Lecture Notes in Electrical Engineering 431

Bruno Andò
Francesco Baldini
Corrado Di Natale
Giovanna Marrazza
Pietro Siciliano
Editors

Sensors

Proceedings of the Third National Conference on Sensors, February 23–25, 2016, Rome, Italy

Springer

Lecture Notes in Electrical Engineering

Volume 431

About this Series

"Lecture Notes in Electrical Engineering (LNEE)" is a book series which reports the latest research and developments in Electrical Engineering, namely:

- Communication, Networks, and Information Theory
- Computer Engineering
- Signal, Image, Speech and Information Processing
- Circuits and Systems
- Bioengineering

LNEE publishes authored monographs and contributed volumes which present cutting edge research information as well as new perspectives on classical fields, while maintaining Springer's high standards of academic excellence. Also considered for publication are lecture materials, proceedings, and other related materials of exceptionally high quality and interest. The subject matter should be original and timely, reporting the latest research and developments in all areas of electrical engineering.

The audience for the books in LNEE consists of advanced level students, researchers, and industry professionals working at the forefront of their fields. Much like Springer's other Lecture Notes series, LNEE will be distributed through Springer's print and electronic publishing channels.

More information about this series at http://www.springer.com/series/7818

Bruno Andò · Francesco Baldini
Corrado Di Natale · Giovanna Marrazza
Pietro Siciliano
Editors

Sensors

Proceedings of the Third National Conference on Sensors, February 23–25, 2016, Rome, Italy

Springer

Editors
Bruno Andò
University of Catania
Catania
Italy

Francesco Baldini
IFAC-CNR
Sesto Fiorentino
Italy

Corrado Di Natale
University of Rome Tor Vergata
Rome
Italy

Giovanna Marrazza
University of Florence
Sesto Fiorentino
Italy

Pietro Siciliano
IMM-CNR
Lecce
Italy

ISSN 1876-1100 ISSN 1876-1119 (electronic)
Lecture Notes in Electrical Engineering
ISBN 978-3-319-55076-3 ISBN 978-3-319-55077-0 (eBook)
DOI 10.1007/978-3-319-55077-0

Library of Congress Control Number: 2017934626

Printed on acid-free paper

This Springer imprint is published by Springer Nature
The registered company is Springer International Publishing AG
The registered company address is: Gewerbestrasse 11, 6330 Cham, Switzerland

Preface

This book gathers scientific contributions presented at the 3rd National Conference on Sensors held in Rome, Italy from 23 to 25 February 2016. The conference has been organized by a partnership of the major scientific societies and associations involved in the research area of sensors, the Italian Society of Chemistry (SCI), the Italian Association of Electric and Electronic Measures (GMEE), the Italian Association of Ambient Assisted Living (AITAAL), the Italian Society of Optics and Photonics (SIOF), the Italian Association of Sensors and Microsystems (AISEM), the Italian Society of Pure and Applied Biophysics (SIBPA), the Italian Association of Photobiology (SIFB), the Association Italian Group of Electronics (GE) and the Association NanoItaly.

The third edition of the conference has confirmed a large participation with approximately 60 oral presentations, 80 poster presentations and over 150 delegates. The driving idea of the first conference, to gather scientists having different expertise and with different cultural background, dealing with all the different aspects of sensors, has proved to be indeed successful again.

In this perspective, the book represents an invaluable and up-to-the-minute tool, providing an essential overview of recent findings, strategies and new directions in the area of sensor research. Further, it addresses various aspects based on the development of new chemical, physical or biological sensors, assembling and characterization, signal treatment and data handling. Lastly, the book applies electrochemical, optical and other detection strategies to relevant issues in the food and clinical environmental areas, as well as industry-oriented applications.

Catania, Italy — Bruno Andò
Sesto Fiorentino, Italy — Francesco Baldini
Rome, Italy — Corrado Di Natale
Sesto Fiorentino, Italy — Giovanna Marrazza
Lecce, Italy — Pietro Siciliano

Contents

Physical Sensors

Integrated Thermal Flow Sensors with Programmable Power-Sensitivity Trade-Off

Massimo Piotto[1(✉)], Filippo Dell'Agnello[2], Simone Del Cesta[2], and Paolo Bruschi[2]

[1] IEIIT—Pisa, CNR, Via G. Caruso 16, 56122 Pisa, Italy
massimo.piotto@ieiit.cnr.it
[2] Dipartimento di Ingegneria dell'Informazione, Università di Pisa, Via G. Caruso 16, Pisa, Italy

Abstract. A thermal flow sensor integrated with a programmable electronic interface into the same chip is proposed. The sensing structure is a micro-calorimeter with a double heater configuration fabricated with a simple post-processing technique applied to chip designed with a commercial CMOS process. The electronic interface is based on a low-noise, low-power instrumentation amplifier and a configurable heater current driver. The device characterization in nitrogen confirms the possibility to manage the trade-off between the sensitivity and the power delivered to the device by means of the programmable interface.

Keywords: Thermal flow sensor · Electronic interface · Chopper amplifier · System-on-Chip (SoC)

1 Introduction

Micromachined thermal flow sensors are used in applications that require measurement and control of small fluid flow rates with high accuracy and resolution [1, 2]. Microsensors with fast response times and low power consumption can be integrated with the read-out electronics into the same chip thanks to the development of the silicon micromachining technologies. These devices have matured from the research stage to commercial products with response times in the order of millisecond and power consumptions of a few tens of milliwatts [3]. Nevertheless, emerging battery-power applications are imposing requirements that are more stringent in terms of power consumption. Unfortunately, the sensitivity of thermal flow sensors is proportional to the power delivered to the sensing structure [4], so a trade-off between power and sensitivity has to be considered.

In this work, we propose a smart flow sensor where the power delivered to the sensing structure can be set through the integrated programmable electronic interface that performs signal reading, offset compensation and heater driving. The device belongs to the thermal sensor platform proposed in [5], which includes diverse flow sensors, acoustical particle velocity detectors and a pressure sensor based on the micro-Pirani principle. The flow sensor is a micro-calorimeter made up of two

B. Andò et al. (eds.), *Sensors*, Lecture Notes in Electrical Engineering 431,
DOI 10.1007/978-3-319-55077-0_1

polysilcon heaters placed between two temperature probes. The sensing structure has been fabricated by applying a simple post-processing procedure to chip designed with a commercial CMOS process of STMicroelectronics.

2 Device Description and Fabrication

The sensing structure has been integrated with the electronic interface into the chip shown in Fig. 1. The chip has been designed with the BCD6s process of STMicroelectronics and includes diverse sensors based on a thermal principle, as detailed in [5]. The structure involved in this work has been highlighted in Fig. 1. It is a calorimeter made up of two polysilcon heaters placed between two temperature probes consisting of 10 n-polysilicon/p-polysilicon thermocouples. The heaters and the hot contacts of the thermopile have been placed over suspended silicon dioxide membrane while the cold contacts of the thermopiles are in thermal contact with the silicon substrate. The suspended membranes have been obtained by applying a simple post-processing technique to the chips returned by the silicon foundry. A detailed description of the sensing structure and the fabrication process is reported in [6]. Briefly, the post-processing procedure consists of two main steps. First, dielectric layers have been selectively removed from the front-side of the chip in order to access the bare silicon substrate. The dielectric layers have been etched with a RIE (reactive ion etching) in CF_4/Ar (50%/50%) gas mixture using an 8 μm thick photoresist film (MEGAPOSIT™ SPR™ 220–7.0) as a mask. Second, the silicon substrate has been anisotropically etched for 150 min at 85 °C in a solution of 100 g of 5 wt% TMAH with 2.5 g of silicic acid and 0.7 g of ammonium persulfate.

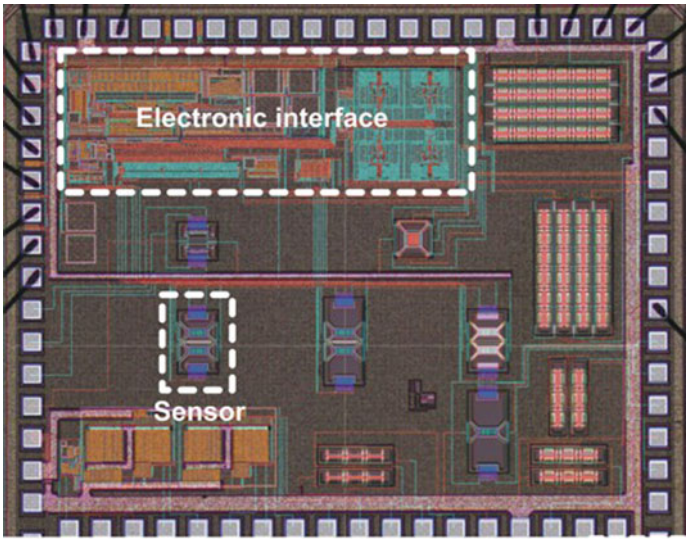

Fig. 1. Photo of the chip with indication of the electronic interface and the sensing structure involved in this work. Note that the chip layout has been superimposed on the optical photograph to show the electronic circuits buried under the planarization dummies

Micrographs of the sensing structure after the silicon removal are shown in Fig. 2. In the optical micrograph, the two polysilicon heaters, placed over rectangular membranes, and the two thermopiles, placed over cantilevers, are clearly visible. In the scanning electron microscopy (SEM) micrograph it can be noted the cavity that allows the thermal insulation of the sensing structures from the substrate.

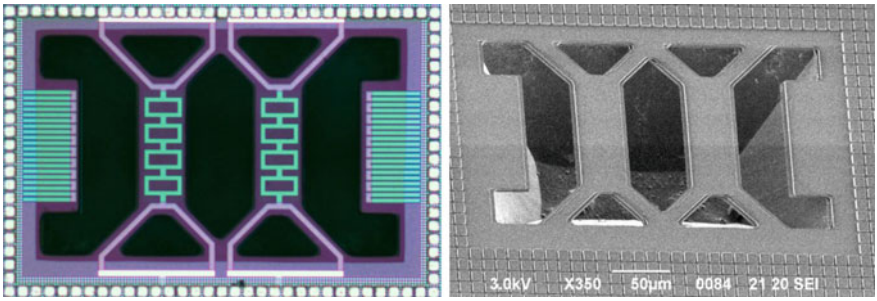

Fig. 2. Optical (*left*) and SEM (*right*) micrograph of the sensing structure after the post-processing

The electronic interface has been optimized with respect to [7] in order to minimize power consumption preserving low noise performances. It includes a low noise, low power instrumentation amplifier based on chopper modulation (gain = 200) and a programmable differential current source for biasing the heaters of the sensing structure. The differential mode component of the dual current source can be digitally tuned (10-bit resolution) to implement drift-free cancellation of the sensor offset [8]. The common mode component can be independently controlled by 2 bits in order to vary the power delivered to the heaters or, equivalently, the sensitivity. In this way, it is possible to bias the heaters with three different current values being the fourth value reserved for the power off condition. A simple digital interface allows control of the current source and instrumentation amplifier parameters.

3 Device Characterization

After post-processing, the chip was packaged in a ceramic DIP28 case and connected to a reference gas line by means of a purposely-built PMMA conveyor [6]. With the application of the conveyor to the chip surface, the sensing structure is included into a flow channel with a 0.5×0.5 mm^2 cross section. The flow channel is connected through 0.6 mm holes to two stainless steel needles used for gas inlet and outlet. The reference gas line is equipped with two precision flow controllers (MKS 1179B), one with a 10 sccm full scale range and the other with 200 sccm full scale range.

The response to a nitrogen flow at room temperature is shown in Fig. 3. The measurement was performed setting the current of both heaters to around 0.53 mA, with a small differential component applied to reduce the output offset to the same level

as the output noise. With these settings, the power delivered to each heater was 0.6 mW, while the total current absorption of the chip, including the electronic interface, is 1.26 mA. This, at a supply voltage of 3.3 V, corresponds to a total power consumption of 4.16 mW. The curve is still monotonic up to flow rates of ±200 sccm even if, as expected, the sensitivity progressively get worse at high flow rates.

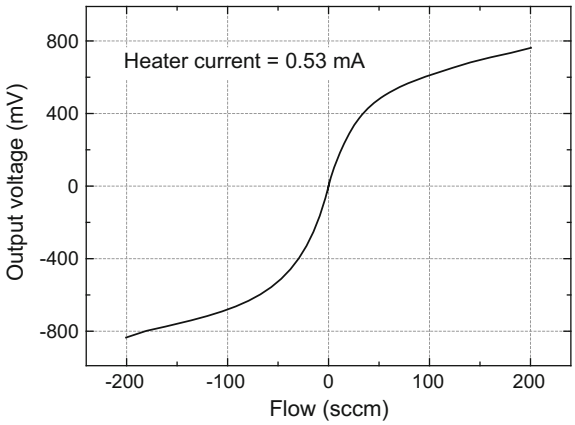

Fig. 3. Amplifier output voltage (gain = 200) as a function of a nitrogen flow at room temperature. Negative flows are obtained by swapping the inlet and outlet connections

The dependence of the sensitivity on power has been verified by setting two different heater current values by means of the electronic interface. The response in ±10 sccm range is shown in Fig. 4. A clear increase in the device sensitivity at the price of greater power consumption has been obtained. This demonstrates the possibility of handling the sensitivity-power trade-off by means of the programmable electronic interface.

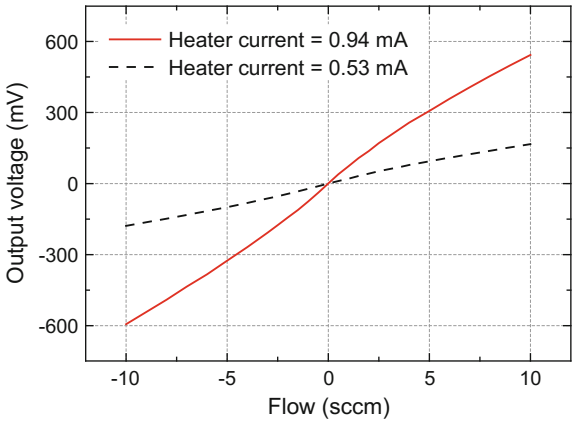

Fig. 4. Response of the device to a nitrogen flow at room temperature with two different settings of the heater current

4 Conclusions

A micro-calorimeter with a double heater configuration has been integrated with a programmable electronic interface into the same chip. The sensing structure has been fabricated with a commercial CMOS process followed by a simple post-processing procedure. The electronic interface includes a low-power, low-noise instrumentation amplifier for the signal reading and a programmable heater driver for the offset compensation and the control of the power delivered to the sensing structure. The dependence of the device sensitivity on power has been demonstrated by means of measurements performed in nitrogen at room temperature. The possibility of handling the power-sensitivity trade-off by means of a programmable interface increases the flexibility of the proposed device.

References

1. Y.-H. Wang, C.-P. Chen, C.-M. Chang, C.-P. Lin, C.-H. Lin, L.-M. Fu, C.-Y. Lee, MEMS-based gas flow sensors. Microfluid. Nanofluid. **6**, 333–346 (2009)
2. J.T.W. Kuo, L. Yu, E. Meng, Micromachined thermal flow sensors—a review. Micromachines **3**, 550–573 (2012)
3. Sensirion Online Product Catalog, [Online]. Available: http://www.sensirion.com/
4. T.S.J. Lammerink, N.R. Tas, M. Elwenspoek, J.H.J. Fluitman, Micro-liquid flow sensor. Sens. Actuators, A **37–38**, 45–50 (1993)
5. F. Del Cesta, P. Bruschi, M. Piotto, An integrated thermal sensor platform for multi-variable detection, in *Proceedings of the XVIII AISEM Annual Conference*, 2015, pp. 1–4
6. M. Piotto, F. Del Cesta, P. Bruschi, Integrated smart gas flow sensor with 2.6 mW total power consumption and 80 dB dynamic range. Microelectron. Eng. **159**, 159–163 (2016)
7. M. Piotto, M. Dei, F. Butti, G. Pennelli, P. Bruschi, Smart flow sensor with on-chip CMOS interface performing offset and pressure effect compensation. IEEE Sens. J. **12**, 3309–3317 (2012)
8. P. Bruschi, M. Dei, M. Piotto, An offset compensation method with low residual drift for integrated thermal flow sensors. IEEE Sens. J. **11**, 1162–1167 (2011)

Single-Chip CMOS Capacitive Sensor for Ubiquitous Dust Detection and Granulometry with Sub-micrometric Resolution

Marco Carminati(✉), Pietro Ciccarella, Marco Sampietro, and Giorgio Ferrari

Dipartimento di Elettronica, Informazione e Bioingegneria, Politecnico di Milano, P.za Leonardo da Vinci 32, 20133 Milan, Italy
marcol.carminati@polimi.it

Abstract. A monolithic CMOS chip able to count single airborne particles down to a diameter of 1 μm is presented. This mm-sized ASIC addresses the growing need for portable and miniaturized solid-state sensors monitoring air quality to be disseminated in the environment within pervasive wireless sensors networks. Particle counting and sizing are based on high-resolution capacitive detection. State-of-the-art performances (65 zF resolution with 40 Hz bandwidth) are enabled by the combination on the same chip of interdigitated microelectrodes (separated by 1 μm distance, matched with the particle size), and ultra-low-noise electronics connected to them achieving the lowest possible parasitic input capacitance. Chip design and characterization are illustrated.

1 Introduction

The relevance of the measurement of airborne particulate matter (PM) does not require extensive explanation. The adverse effects for the environment, the cultural heritage and the human health due to high concentrations of PM in the atmosphere have been abundantly demonstrated. Nevertheless, the strategies proposed and implemented so far, particularly in urban environments, such as vehicular traffic restrictions, have proved to be ineffective, mainly because of the complexity of such a multi-scale problem (involving the spatiotemporal variability of meteorological conditions and of emission sources and targets, from local street canyons to global levels). Dust suspension in the atmosphere is both due to natural phenomena (erosion, volcanic eruptions, and dust storms originated from the Sahara desert, considered the largest source of airborne dust in the world, producing about 70 millions of tons of dust per year transported by eastbound winds, 30% of which deposit in the eastern Mediterranean countries) as well as to anthropogenic sources, significantly varying from rural to urban areas.

Limiting only to the threats for health, they span from pathologies of the cardio-respiratory system to more subtle cell-level and gene-level interactions, which are object of wide on-going research [1]. The World Health Organization estimates that

B. Andò et al. (eds.), *Sensors*, Lecture Notes in Electrical Engineering 431,
DOI 10.1007/978-3-319-55077-0_2

in the year 2000 in Europe the average life expectancy loss due to exposure to $PM_{2.5}$ was 8.6 months, ranging from 3 months in Finland to 12–36 months in the Po valley [2]. Other reports account for 3 million deaths worldwide ascribable to $PM_{2.5}$ [3]. Regardless of the specific toxicological pathway, the risk due to the exposure to high concentrations of PM depends on the size and the chemical composition of the particles. Even particles of inert materials can be the carrier of dangerous pathogens. As illustrated in Fig. 1, the penetration inside the respiratory tract strongly depends on the particle diameter (for non-spherical particles, an equivalent aerodynamic diameter is defined). The distribution of the particles diameter is called *granulometric* spectrum. The smaller the diameter, the lower the filtering and the deeper is the penetration and the higher the risk of diffusion in the body and endocytosis inside the cells.

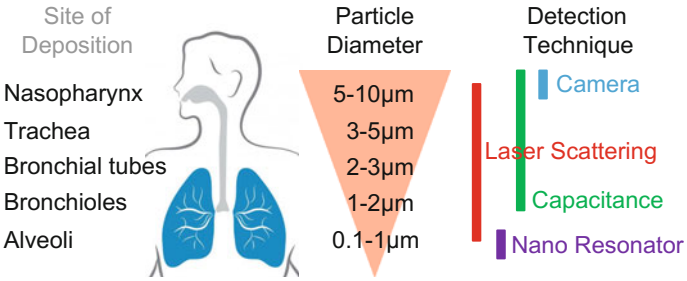

Fig. 1. Depth of PM penetration in the human respiratory system varying according to particle size and corresponding technologies allowing single-particle detection and granulometry

A broad range of instruments and techniques are currently employed for the characterization of PM, which can be analyzed either on-line (i.e. in the field) and off-line. The latter are mostly sophisticated laboratory techniques, based on the collection of PM on filters by means of samplers and impactors, often requiring preliminary sample preparation, such as metallization for electron microscopy or digestion for chemo-physical assays (such as elemental analysis by means of X-ray fluorescence spectroscopy [4]). On-line techniques comprise gravimetric accumulation and weighting, absorption of beta rays and laser scattering [5]. The latter, relying on the size-dependent intensity of the light pulse originated from the scattering of a laser beam focused on a stream of PM, is the only technique allowing single-particle analysis and granulometry. Unfortunately, the cost and bulkiness of these instruments prevent a massive deployment.

In the last years, several paradigm-shifting trends including smartphone-based participatory sensing [6], aimed at gaining a better insight in such a complex problem and mostly enabled by the fast development and pervasiveness of consumer-grade sensors, are emerging also in the environmental field. New interesting horizons are disclosed by wireless sensor networks. As summarized in Fig. 1, different emerging solutions based on solid-state miniaturized sensors, thus embeddable in low-cost and compact sensing nodes, but still allowing single-particle resolution, include CMOS

cameras with pixels of area comparable with larger PM, mass-sensitive MEMS and nano-resonators machined in silicon and micro-capacitance sensing [7].

2 Capacitive Dust Detection

In order to address the challenges described in the previous section, a non-optical technique based on the combination of microelectrodes and high-resolution capacitive sensing can be adopted [8]. As illustrated in Fig. 2, when a single particles enters the electric field between a pair of electrodes, the capacitance increases due to its larger dielectric constant with respect to air ($\varepsilon_r = 1$). In order to maximize the sensitivity, the capacitor volume should be matched to the single particle size. For a parallel-plate geometry (facing electrodes of area A and distance d as in Fig. 2a), the capacitance value can be computed with the well-known expression (neglecting border effects):

$$C = \varepsilon_0 \cdot \varepsilon_r \cdot \frac{A}{d} \tag{1}$$

where ε_0 is the dielectric constant of vacuum and ε_r the relative dielectric constant of the material between the plates. With a spherical particle of radius r inside, the capacitance variation due to a change of a small volume fraction, can be estimated as:

$$\Delta C = \frac{4}{3} \cdot \pi \cdot \frac{r^3}{d^2} \cdot \Delta\varepsilon_r \cdot \frac{\varepsilon_0}{\varepsilon_r} \tag{2}$$

where $\Delta\varepsilon_r$ is the difference between the ε_r. As apparent from Eq. (2), the signal is increases with the dielectric contrast between the particle and the surrounding medium and by reducing the distance between the plates. If $\Delta\varepsilon_r$ is known, it is also possible to estimate r from ΔC, clearly showing the potential for granulometry. Furthermore, the uncertainty in the estimation of an average ε_r (analogously to the average refractive index assumed in laser scattering) is mitigated by the fact that $r \sim \Delta\varepsilon_r^{-1/3}$.

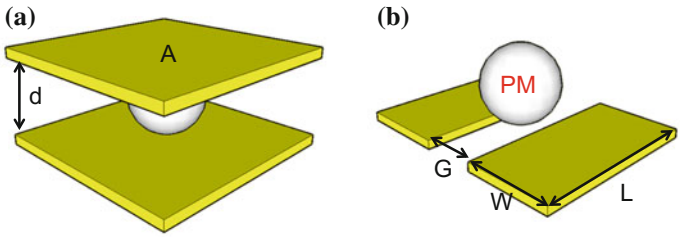

Fig. 2. Parallel-plate **a** and coplanar **b** microelectrodes configurations, both suitable for single particle capacitive detection when d and G are matched with the particle diameter

The advantage of this geometry the homogeneity of the electric field, allowing simple analytical expressions for the design. On the other hand, the major limit is the

risk of clogging when shrinking down d in the micrometric domain. A coplanar geometry (Fig. 2b) composed by a pair of electrodes (W by L) separated by a distance G, allows overcoming this risk, at the price of spatially inhomogeneous field that requires of the use of conformal mapping expressions [9] to estimate the capacitance:

$$C = 2\varepsilon_0 \cdot \frac{\varepsilon_r}{\pi} \cdot \ln\left[\left(1+\frac{2W}{G}\right)+\sqrt{\left(1+\frac{2W}{G}\right)^2-1}\right] \cdot L \tag{3}$$

Thanks to lithography, micrometric values for G can be easily achieved. A first proof-of-concept that capacitive detection of single micrometric airborne particles has been demonstrated with gold microelectrodes (G = 4 μm) patterned on glass and coupled with a low-noise amplifier realized with off-the-shelf discrete components [8]. The minimum resolution of this system was ~1 aF, resulting in a minimum detectable diameter of ~7 μm. In order to detect smaller particles, a single-chip solution has been developed, leveraging the combination of CMOS lithography and minimum stray capacitance at the input of the amplifier integrated on the same chip.

3 Design of a CMOS Monolithic PM_1 Detector

3.1 Electrodes and Architecture

The design starts from sizing the microelectrodes. The electrodes are fabricated on the topmost metal layer (metal 4 in the AMS 0.35 μm process here employed) and exposed to air by opening a window in the nitride passivation the same way used to expose bonding pads. Interestingly, this approach does not require any additional post processing of the chip that can be fabricated in any CMOS foundry and can be used as received. Under the electrodes no metal is present, in order to reduce the stray capacitance and the distance from the silicon substrate is 4 μm (Fig. 3a). An interdigitated geometry is chosen in order to cover uniformly the detection area. Finite-element numerical simulations (Fig. 3b) have been employed for optimal sizing of the electrodes. Targeting PM_1, W and G have been set to 1 μm, (slightly larger than the minimum 0.6 μm allowed by this technology for reliability considerations). With these dimensions, a sphere of 1 μm diameter (and minimum ε_r = 2) produces a capacitance change ΔC = 700 zF.

Having set the electrode width and spacing, the second major choice concerns the total collection area and its partition into smaller "pixels". From system level considerations, mostly related to the interfacing with proper fluidics forcing the collection of PM, the minimum detection area is set to 1 mm^2. If this area were covered by a single couple of interdigitated electrodes, the total sensor capacitance would be 15 pF (with a stray capacitance to ground of about 3 pF). In these conditions, it would be impossible to detect the signal due to a single particle, being ΔC/C = 50 ppb (corresponding to a dynamic range of 146 dB and an environmental stability better than 50 parts per billion). In order to reduce the dynamic range, allowing single particle resolution, two solutions have been adopted:

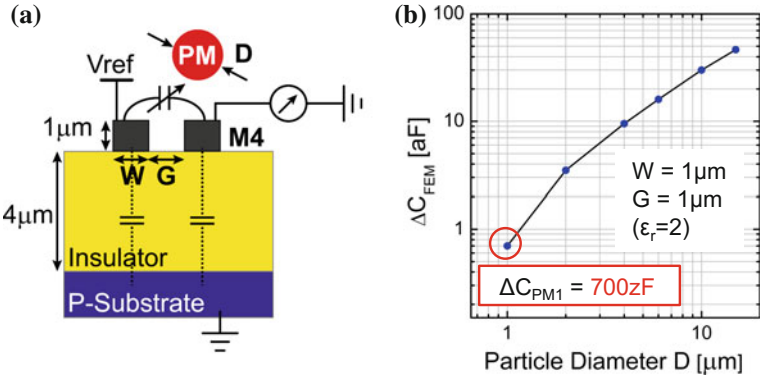

Fig. 3. **a** Cross-section of the CMOS PM sensor showing the capacitance-sensing electrodes fabricated in the highest metal level (M4) and exposed to air. **b** COMSOL simulations of the expected capacitance variation ΔC obtained when a single particle of diameter D deposits between these electrodes

- a *differential* architecture is chosen, so that only the differential signal is amplified by the chain when an unbalance is created by the deposition of a particle on one of the two combs. In order to avoid the risk that a large particles covering both couples produces a zero signal, the layout of the electrode has been arranged (Fig. 4) separating the positively-excited electrodes (+), from the negatively-excited electrodes (−). In one half of the array, the interdigitation is between (+) electrodes and the common input of the amplifier (virtual ground), while analogously, in the other half, the serpentine gaps separate (−) electrodes and the amplifier input. The symmetry is thus maintained and the two halves (C_{UP} and C_{DW}) are separated by a ground line. Furthermore, the differential configuration allows rejection of common mode disturbances (including thermal drifts) as well as the noise due to the voltage generator [10]. The only minor complication implied by this architecture is that the signal can be either positive or negative, depending on which half of the array the particle lands.
- the total sensing area has been *partitioned* in 32 slices of area 500 μm by 70 μm. Correspondingly, the analog conditioning chains are replicated in 32 parallel channels. The pixel area corresponds to an input capacitance smaller than 0.5 pF, suitable for achieving excellent noise performance.

The whole architecture of the readout circuit is shown in Fig. 4. It consists of 32 identical channels including the electrodes and the conditioning chain, which comprises the amplification stages, the square-wave multiplier (synchronous with the square-wave stimulation of the electrodes at 100–500 kHz, biased alternatively at V_{REF} and GND, as commonly performed to read half-bridge differential capacitive sensors such as in inertial MEMS [11]) and a g_m-C low-pass filter with a selectable bandwidth (40, 85, 360, 750 Hz) completing the *lock-in* block.

A sensor bandwidth of 85 Hz per channel is enough to correctly sample single deposition events considering typical PM concentrations (max ∼50 particles/liter for

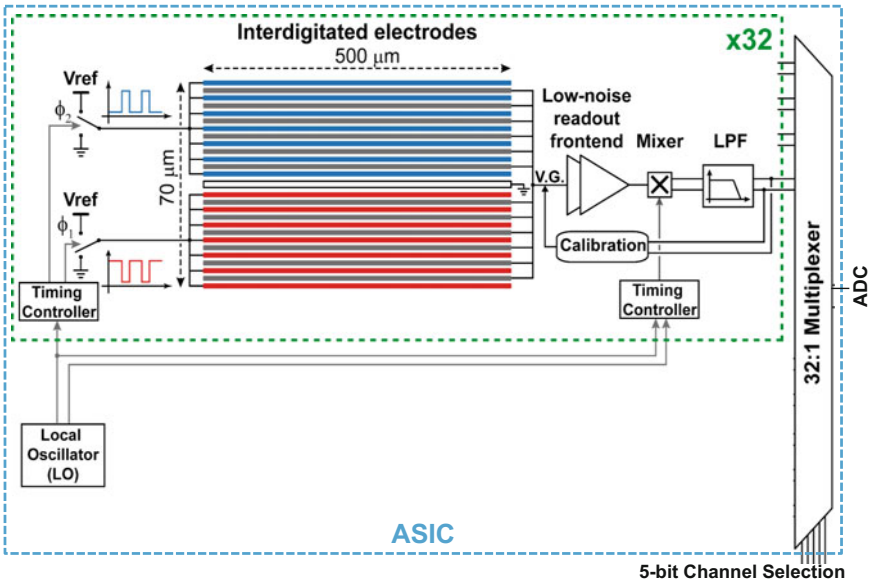

Fig. 4. Architecture of the electronics: each of the 32 channels comprises two sets of interdigitated differential electrodes and a low-noise signal conditioning chain

PM_{10}) and sampling flow-rates ($\sim$liter/min), with a very low coincidence probability, giving a total data rate of $\sim$3 kSa/s. Given such a relatively slow rate of information to be processed, the chip is connected to an external ADC with a single output by means of a 32:1 multiplexer (MUX) controlled by 5 parallel bits. It should be noted that the low-pass filter must be placed before the MUX (thus requiring 32 filters instead of a single one and, unfortunately, much more silicon area) in order to avoid the long settling time required by a single filter which should update its voltage after each switching of the MUX (and would be limiting the scanning frequency to $\sim$1.6 Hz in the case of the narrowest bandwidth).

3.2 Front-End

Given the capacitive nature of the sensor, the optimal choice for the front-end amplifier is a transimpedance stage with capacitive feedback (Fig. 5). This allows frequency-independent gain and minimum noise [12]. The size of the input transistors is set in order to match the amplifier input capacitance with the sensor capacitance, in order to achieve minimum noise. The feedback capacitance C_F of the first stage is set equal to 20 fF. A transistor in feedback operating in sub-threshold regime handles the input DC leakage current. A second stage with a similar topology and high gain (40) is cascaded in order to reduce the impact of the g_m-C filter.

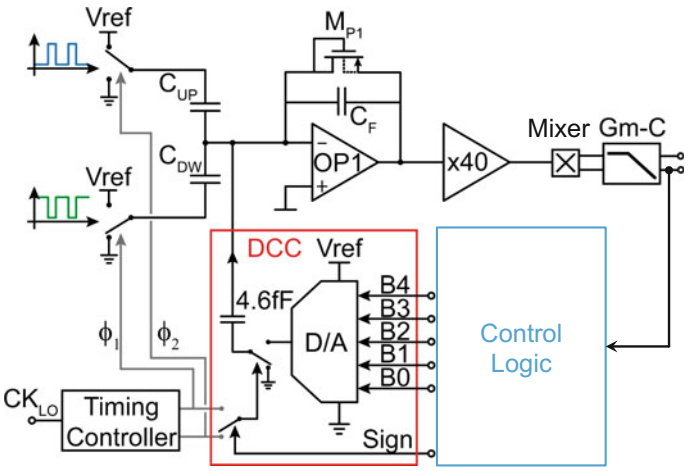

Fig. 5. Scheme of the analog amplification chain

In order to compensate the mismatch between the two pairs of electrodes, an automatic auto-zeroing network has been also implemented. It is composed by a Digital-to-Capacitance Converter (DCC) and a control logic. The DCC comprises a fixed compensation capacitor of 4.6 fF connected at the chain input and driven by a 5-bit resistive DAC featuring a LSB = 150 aF and measured DNL of 15 aF. Finally, a current-subtracting network allows reducing the noise at low frequency by a factor 4.

4 Experimental Results

The fabricated prototype is shown in Fig. 6. The total chip area is 2.5 mm by 2.4 mm and current consumption is 25 mA (at 3.3 V power supply) [13]. The bonding pads are located on one side, in order to leave the other sides free from bonding wires for easier coupling the chip with proper fluidics. After the functional tests confirmed the circuit performances, such as amplifier bandwidth (10 kHz–2 MHz) and noise (65 zF at 40 Hz) are in agreement with the simulations, the chip has been validated with the real-time deposition of single particles.

Consistently with the previous experiments with the discrete-component setup, mineral talc (abundant, nontoxic, with an average diameter of 8 μm and $\varepsilon_r = 2.4$) is employed. Talc powder was suspended in air by means of a properly-driven vibrating loudspeaker, placed in the same Faraday cage. Before starting the experiments, microphotographs of the electrodes surface are taken. Then the speaker is activated and, when a channel displays a capacitance step, the experiment is stopped and another photograph of that channel is taken, in order to correlate the measured ΔC with a microscope image of the deposited particle. By adjusting the concentration of talc loaded on the loudspeaker and its distance from the detector, it is possible to easily achieve the condition of single depositions with rates of a few events per minute. Fixed defects or previously deposited particles act as reference points, useful when comparing images taken in different moments.

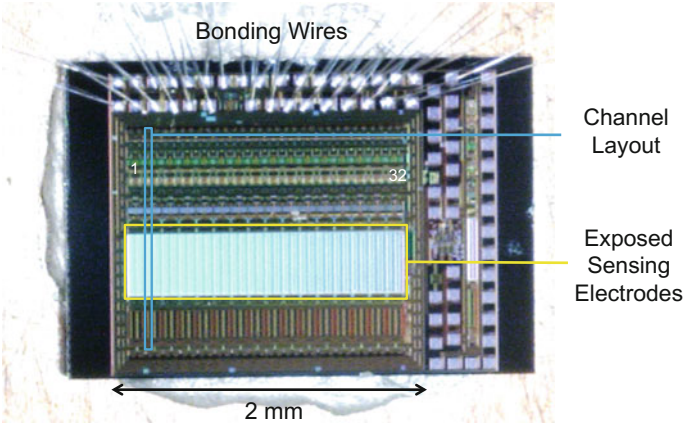

Fig. 6. Chip microphotographs: 32 parallel channels are visible, the sensing area is 1.15 mm^2

A typical deposition event is shown in Fig. 7: the capacitance recording (sampled with a temporal resolution better than 100 ms) shows a clear jump of 1 aF, due to the deposition of a single talc particle with a diameter of about 1.5 µm, extracted from the microscope image. Despite the uncertainties in the estimation of the equivalent diameter of non-spherical particles from bidimensional microscope image, good agreement is observed between the measured jumps, the imaged particles and the simulation of Fig. 3b. Thanks to the measured noise floor of 65 zF, a 1 µm particle (giving a ΔC = 700 zF for the minimum ε_r) is detected with a SNR >20 dB.

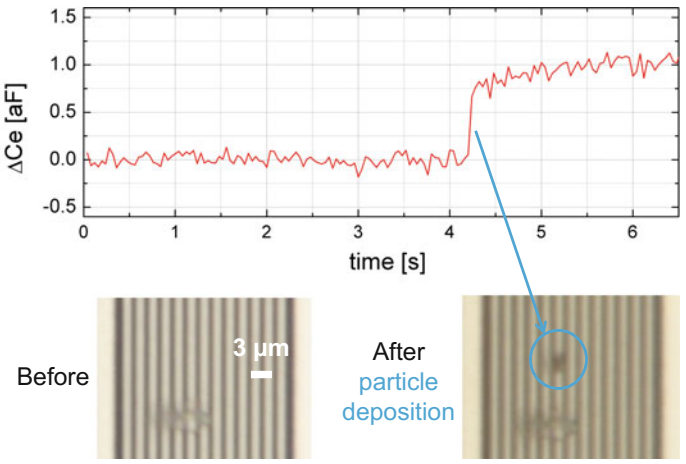

Fig. 7. Real-time capacitive tracking of the deposition on the interdigitated electrodes of a single dust particle (ε_r = 2.4) of 1.5 µm diameter producing a capacitance increase of 1 aF

Figure 8 reports several deposition events, corresponding to two dust clouds, showing the operation of the acquisition system (based on the acquisition board NI PCI-6289 controlled by a custom LabView program) in multichannel tracking.

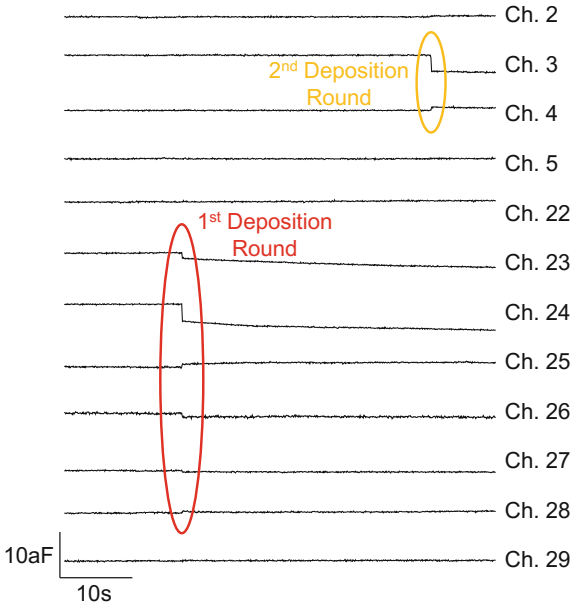

Fig. 8. Multichannel tracking of several PM particles depositing from talc clouds in two rounds

5 Conclusions

The first single-chip CMOS sensor for counting and granulometry of particles in the 20–1 μm range has been presented, illustrating the key design aspects required to achieve deep sub-attoFarad resolution (and improving by more than two orders of magnitude what achieved with discrete components).

Conductive particles do not represent a sever risk of shorting thanks to the insulating layer constituted by the thin native aluminum oxide that naturally forms on the exposed electrodes. Instead, humidity in the form of water droplets can produce large artifacts and false counts (due to the large $\varepsilon_r = 80$ of water). To prevent this issue, analogously to laser-scattering instruments, heated probes can be employed, as well as on-chip heaters or proper layout of the hottest power dissipating areas on chip.

Thanks to the abrupt change in capacitance produced by the PM deposition, slow drifts (due for instance to temperature drifts which, in any case, are mitigated by the differential architecture) do not prevent detection on long measuring times.

Finally, for the deployment in the environment in a pervasive and ubiquitous ways, the micro-system should be completed with:

1. a particles concentration and capture system. For instance, electric fields, fluido-dynamic impactors or thermophoretic forces could be combined with this CMOS platform for enhanced low-concentration operation.
2. a surface cleaning system for periodical removal of deposited PM and restoring of the initial condition for long term operation (based for instance of vibrating mechanical energy or local air jets). The low cost of silicon for large production volumes, allows also considering alternative employment scenarios including disposable cartridges.

The feasibility of the capacitive technique has been demonstrated down to PM_1 and the detector has been optimized from the point of view of noise. Further engineering is clearly required: power dissipation, electrode geometry, total detection area and number of channels can be tuned and adapted to the final application of the chip, spanning from fixed urban nodes, to portable dosimeters or even embedment inside consumer devices such as smartphones.

References

1. G. Sancini et al., Health risk assessment for air pollutants: alterations in lung and cardiac gene expression in mice exposed to Milano winter fine particulate matter (PM2.5). PLoS ONE **9**, 109685 (2014)
2. WHO (2006) Air quality guidelines—global update 2005
3. S.S. Lin et al., A comparative risk assessment of burden of disease and injury attributable to 67 risk factors and risk factor clusters in 21 regions, 1990–2010: a systematic analysis for the global burden of disease study 2010. Lancet **380**, 2224 (2012)
4. A. Zacco et al., Analysis of settled dust with X-ray fluorescence for exposure assessment of metals in the province of Brescia, Italy. J. Environ. Monitoring **11**, 1579 (2009)
5. A. Chung, D.P.Y. Chang, M.J. Kleeman, K.D. Perry, T.A. Cahill, D. Dutcher, E.M. McDougall, K. Stroud, Comparison of real-time instruments used to monitor airborne particulate matter. J. Air Waste Manage. Assoc. **51**, 109 (2001)
6. E.G. Snyder et al., The changing paradigm of air pollution monitoring. Environ. Sci. Tech. **47**, 11369 (2013)
7. M. Carminati, G. Ferrari, M. Sampietro, Emerging miniaturized technologies for airborne particulate matter pervasive monitoring. Measurement (in press)
8. M. Carminati, L. Pedalà, E. Bianchi, F. Nason, G. Dubini, L. Cortelezzi, G. Ferrari, M. Sampietro, Capacitive detection of micrometric airborne particulate matter for solid-state personal air quality monitors. Sens. Actuators A **219**, 80 (2014)
9. J.Z. Chen, A.A. Darhuber, S.M. Troian, S. Wagner, Capacitive sensing of droplets for microfluidic devices based on thermocapillary actuation. Lab Chip **4**, 473 (2004)
10. M. Carminati, G. Gervasoni, M. Sampietro, G. Ferrari, Note: differential configurations for the mitigation of slow fluctuations limiting the resolution of digital lock-in amplifiers. Rev. Sci. Instrum. **87**, 026102 (2016)
11. J. Wu, G.K. Fedder, L.R. Carley, A low-noise low-offset capacitive sensing amplifier for a 50-μg/√Hz monolithic CMOS MEMS accelerometer. IEEE J. Solid-State Circ. **39**, 722 (2004)

12. M. Crescentini, M. Bennati, M. Carminati, M. Tartagni, Noise limits of CMOS current interfaces for biosensors: a review. IEEE Trans. Biomed. Circ. Syst. **8**, 278 (2014)
13. P. Ciccarella, M. Carminati, M. Sampietro, G. Ferrari, Multichannel 65 zF rms resolution CMOS monolithic capacitive sensor for counting single micrometer-sized airborne particles on chip. IEEE J. Solid-State Circ. (submitted)

PDMS Template Generator for Wearable Thermoelectric Energy Harvesting Applications

L. Francioso[1(✉)], C. De Pascali[1], A. Grazioli[2], V. Sglavo[2], and L. Lorenzelli[3]

[1] CNR-IMM Institute of Microelectronics and Microsystems, via Monteroni, University Campus, A3 Building, Lecce, Italy
luca.francioso@le.imm.cnr.it
[2] Department of Industrial Engineering, University of Trento, via Sommarive 9, Trento, Italy
[3] FBK, Fondazione Bruno Kessler, via Sommarive, 18, Trento, Italy

Abstract. Thermoelectric pastes based on Sb, Bi, Te powders were prepared, characterized and used to fabricate a flexible thermoelectric generator (TEG) for wearable harvesting applications. By Finite Element Method (FEM) simulations, the TEG design was finalized to optimize electrical model and match typical thermal resistances of human body skin, in order to maximize its thermoelectric performance. The thermopile is composed by 450 couples of p-Sb_2Te_3 and n-Bi_2Te_3 deposited by blade coating into vertical parallel cavities of a patterned polydimethylsiloxane (PDMS) through-holes layer. Each leg has diameter of 1.5 mm and height of 2.5 mm. The p-n couples were electrically connected by printed silver contact. By preliminary functional tests, a Seebeck coefficient of about 75 μV/K for p-n couple on best conditions was measured.

Keywords: Thermoelectric generator · Energy harvesting · Screen printing

1 Introduction

Energy harvesting represents a new promising technology, by means of which fully exploitation of self-powered wearable devices in practical implementations can be achieved. The human body heat can be directly converted into electricity by Seebeck effect to partially or totally supply ultra-low power wearable health monitoring sensors. TEGs are particularly attractive devices, because compact, robust, lightweight, silent, maintenance-free and devoid of moving parts. The flexible technology represents a key for their unobtrusive application in wearable systems, which integrate different materials and functionalities on the same flexible support. A flexible TEG adapts better to the natural curvature of the human body, with the advantage of enhancing the heat transferred from the human body to the device.

B. Andò et al. (eds.), *Sensors*, Lecture Notes in Electrical Engineering 431,
DOI 10.1007/978-3-319-55077-0_3

Depending on how the thermocouples and substrate are oriented respect to the direction of the heat flow, transversal (cross-plane) or lateral (in-plane) configuration can be used to build a thermopile. Several works on flexible TEGs were reported in literature [1–5]. To maximize the thermal gradient between junctions, an optimized package is often required to be designed for planar TEGs [6–11].

In this paper, screen printable p-Sb_2Te_3 and n-Bi_2Te_3 thermoelectric pastes were developed and morphologically and electrically characterized. The filling with silver particles was also considered, with the aim to increase the figure of merit of the materials. The inclusion of metallic nanoparticles into the material matrix introduces scattering points for phonons, with the result to reduce the thermal conductivity of the material. The metallic particles can also create favourite pathways for the electron transport, giving rise to a reduction of the electrical resistivity of the material. The thermoelectric pastes were used to fabricate a heat sink-free flexible thermoelectric generator, designed for wearable harvesting applications. Preliminary results of functional characterization of the developed device were presented.

2 Preparation and Characterization of Thermoelectric Pastes

High-purity Bi, Sb and Te powders from Sigma Aldrich were ball-milled for 24 h under purified argon atmosphere, in order to minimize oxygen contamination, for obtaining stoichiometric Sb_2Te_3 and Bi_2Te_3 powders. The alloy powders were incorporated into a solution constituted of 2 wt% polystyrene polymer and alpha-Terpineol for a reliable printable pastes production. The solid load of p- and n-type pastes was 56 and 60%. The viscosity of the prepared pastes was adjusted by using the solvent, in order to facilitate the following printing of the slurries. Ag-filled p- and n-type pastes were also prepared by adding silver particles (5–6 μm, from Sigma Aldrich) to the thermoelectric powder with a 2 vol.% load. Figure 1 shows SEM images of as-prepared pastes, after the milling and mixing of components.

The electrical conductivity of the materials was determined by four-point probe measurements, performed on 150–200 μm thick screen-printed films after hot-pressing and firing under nitrogen gas flow at 250 °C for 1 h (heating rate of 5 °C min^{-1}), in order to compact the materials and to remove the solvent in excess. The mean bulk resistivity of the investigated films is reported in Fig. 2. Poor effect of the metal filling on the film resistivity was noted, with a small decrease of resistivity for Ag filled n-alloy and a small increase for the other one. The latter result is explained by the Ag particles behaviour as metal micro-inclusions embedded between the grain boundaries, forming new interfaces and defects which give rise to a decrease in the material electrical conductivity. Nevertheless, the expected Ag inclusion effect is related to thermal phonon modulation and specific measurements are ongoing for experimental confirmation [12].

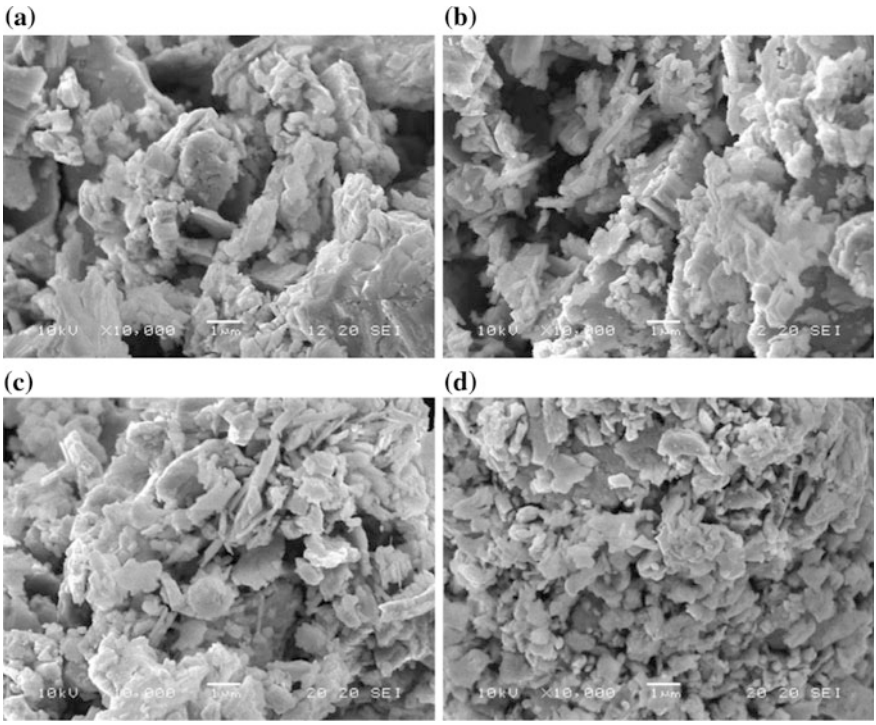

Fig. 1. SEM images of **a** Sb_2Te_3, **b** Bi_2Te_3, **c** Ag-Sb_2Te_3, **d** Ag-Bi_2Te_3, after the milling and mixing of components and before the firing

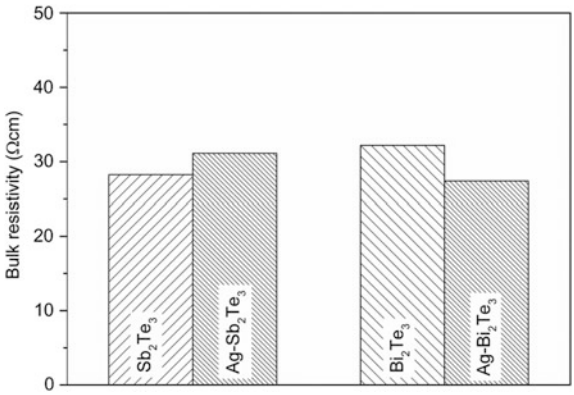

Fig. 2. Bulk resistivity of pristine and Ag-filled p- and n-alloys

3 Design, Fabrication and Electrical Characterization of TEG

Human body produces heat in response to metabolic and muscular activities. The thermoregulatory system keeps the body core temperature within a narrow range around to 37 °C, whereas the heat loss occurs primarily through the skin. Although depending on the body location and environment conditions, the average heat flow observed on human open skin under typical indoor conditions is in the range 1–10 mW cm^{-2}, but it decreases to 4–5 mW cm^{-2} on areas covered by clothes [13].

In this work, an optimal design of the TEG was obtained by matching the thermal and electrical properties of the device at contact with the human body. Heat transfer FEM simulations were performed by using Comsol Multiphysics software, with the aim to optimize the TEG dimensioning for maximizing the output electrical power. A heat flow of 10 mW cm^{-2} was imposed at the hot side of the TEG (supposing thermal contact with human body wrist) [13] and natural convection heat transfer with the environment. The designed TEG is composed by an array of 450 couples of p-n thermoelectric materials, each leg has diameter of 1.5 mm and height of 2.5 mm and the thermopile occupies an area of 74 × 74 mm^2. The thermoelectric alloys were deposited by blade coating into vertical parallel cavities of a patterned PDMS through-holes layer. After printing, hot-pressed annealing in a conventional tubular oven under nitrogen gas flow at 250 °C for 1 h (heating rate of 5 °C min^{-1}) was performed to dry and to compact the materials and to remove the solvent in excess. Silver printed contacts between the p-n legs were optimized to obtain low contact electrical resistance and good adhesion to the PDMS. The electrical functional characterization of the device was performed on a prototype of 45 thermocouples of p-Sb_2Te_3 and n-Bi_2Te_3. The thermal gradient between the hot/cold thermocouples junctions was imposed by two aluminium plates, whose temperature was set by two commercial MCU Peltier controllers, with a temperature set point control of 0.01 °C. Table 1 shows preliminary experimental data obtained for different temperature difference between junctions and increasing load connected at the TEG output ends. Figure 3 shows the fabricated device tested with a custom bench for controlled temperature gradients.

Table 1. Preliminary results obtained by a 45 thermocouples-based TEG, for different temperature difference between junctions and increasing load connected at the output

Thermal gradient (K)	1	2	3	4	5	6
Open circuit						
Output voltage (mV)	2.69	5.43	8.13	10.82	14.55	17.25
Seebeck coefficient per thermocouple (μV/K)	59.11	60.35	60.20	60.11	64.67	63.89
Output power (nW)	7.17E−3	2.91E−8	6.51E−7	1.15E−7	2.08E−7	2.93E−7
Load resistance: 1.0 kΩ						
Output voltage (mV)	3.24	6.45	10.27	13.80	17.32	20.47
Seebeck coefficient per thermocouple (μV/K)	71.97	71.65	76.05	76.68	76.99	75.81
Output power (nW)	0.17	0.68	1.73	3.13	4.93	6.88
Load resistance: 6.8 kΩ						
Output voltage (mV)	2.39	5.29	7.04	9.10	11.77	13.38
Seebeck coefficient per thermocouple (μV/K)	53.02	58.68	52.16	50.56	52.30	53.07
Output power (nW)	0.20	0.99	1.77	2.95	4.94	6.38

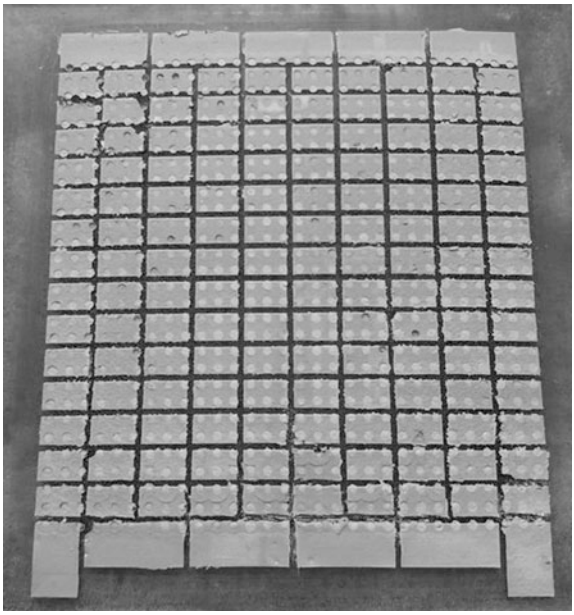

Fig. 3. Fabricated thermoelectric generator with silver metal connections

A Seebeck coefficient of about 75 μV/K for the p-n couple was experimentally measured as a function of the thermal gradient, while silver metal contact resistivity effects are included into average Seebeck coefficient and will be investigated vs different metal films.

Further measurements are in progress in order to evaluate the thermoelectric properties of the materials, in particular the effect of the silver filling on the thermal conductivity of the alloys. Further functional characterization is in progress in order to test a complete system composed by TEG and an ASIC DC-DC converter, the latter designed and realized for the power management of the harvested power on 65 nm technology node. Experimental measurements on pristine and Ag filled alloys are still in progress.

References

1. L. Francioso, C. De Pascali, P. Siciliano, Experimental assessment of thermoelectric generator package properties: simulated results validation and real gradient capabilities. Energy **86**(15), 300–310 (2015)
2. F. Jiao, Di C-a, Y. Sun, P. Sheng, W. Xu, D.Zhu, Inkjet-printed flexible organic thin-film thermoelectric devices based on p- and n-type poly(metal 1,1,2,2-ethenetetrathiolate) s/polymer composites through ball-milling. Phil. Trans. R. Soc. A **372**, 20130008 (2014). doi:10.1098/rsta.2013.0008

3. Z. Lu, M. Layani, X. Zhao, L.P. Tan, T. Sun, S. Fan, Q. Yan, S. Magdassi, H.H. Hng, Fabrication of flexible thermoelectric thin film devices by inkjet printing. Small **10**(17), 3551–3554 (2014). doi:10.1002/smll.201303126
4. K. Suemori, S. Hoshino, T. Kamata, Flexible and lightweight thermoelectric generators composed of carbon nanotube–polystyrene composites printed on film substrate. Appl. Phys. Lett. **103**, 153902 (2013)
5. L. Francioso, C. De Pascali, I. Farella, C. Martucci, P. Cretì, P. Siciliano, A. Perrone, Flexible thermoelectric generator for ambient assisted living wearable biometric sensors. J. Power Sources **196**(6), 3239–3243 (2011)
6. L. Francioso, C. De Pascali, A. Taurino, P. Siciliano, A. De Risi, Wearable and flexible thermoelectric generator with enhanced package. Proc. SPIE Int. Soc. Opt. Eng. Conf. Smart Sensors Actuators MEMS VI **8763**, 876306 (2013)
7. L. Francioso, C. De Pascali, R. Bartali, E. Morganti, L. Lorenzelli, P. Siciliano, N. Laidani, PDMS/kapton interface plasma treatment effects on the polymeric package for a wearable thermoelectric generator. ACS Appl. Mater. Interfaces **5**(14), 6586–6590 (2013)
8. J.P. Carmo, L.M. Goncalves, R.F. Wolffenbuttel, J.H. Correia, A planar thermoelectric power generator for integration in wearable microsystems. Sens. Actuators A **161**(1–2), 199–204 (2010)
9. P.H. Kao, P.J. Shih, C.L. Dai, M.C. Liu, Fabrication and characterization of CMOS-MEMS thermoelectric micro generators. Sensors **10**, 1315–1325 (2010)
10. Z. Yuan, K. Ziouche, Z. Bougrioua, P. Lejeune, T. Lasri, D. Leclercq, A planar micro thermoelectric generator with high thermal resistance. Sensors Actuators A **221**, 67–76 (2015)
11. E.J. Bae, Y.H. Kang, K.S. Jang, S.Y. Cho, Enhancement of thermoelectric properties of PEDOT: PSS and tellurium-PEDOT: PSS hybrid composites by simple chemical treatment. Scientific Reports 6, Article number: 18805 (2016)
12. Q. Zhang, X. Ai, L. Wang, Y. Chang, W. Luo, W. Jiang, L. Chen, Improved thermoelectric performance of silver nanoparticles-dispersed Bi_2Te_3 composites deriving from hierarchical two-phased heterostructure. Adv. Funct. Mater. **25**, 966–976 (2015). doi:10.1002/adfm.201402663
13. V. Leonov, Human machine and thermoelectric energy scavenging for wearable devices. ISRN Renewable Energy **2011**, Article ID 785380, 11 p. (2011)

Nanostructured Superconductive Sensors Based on Quantum Interference Effect for High Sensitive Nanoscale Applications

C. Granata[1(✉)], B. Ruggiero[1], O. Talamo[1], M. Fretto[2], N. De Leo[2], V. Lacquaniti[2], D. Massarotti[3,4], F. Tafuri[3,5], P. Silbestrini[6], and A. Vettoliere[1]

[1] Institute of Applied Sciences and Intelligent Systems "E. Caianiello", National Research Council, Pozzuoli, Naples, Italy
carmine.granata@cnr.it
[2] Istituto Nazionale di Ricerca Metrologica, Turin, Italy
[3] Istituto Superconduttori, Materiali innovativi e Dispositivi, National Research Council, Naples, Italy
[4] Dipartimento di Fisica, Università di Napoli "Federico II", Naples, Italy
[5] Dipartimento di Ingegneria Industriale e dell'Informazione, Seconda Università di Napoli, Aversa, Caserta, Italy
[6] Dipartimento di Matematica e Fisica, Seconda Università di Napoli, Aversa, Caserta, Italy

Abstract. Recently it has been proven that the magnetic response of magnetic nano-objects such as nanoparticles, nanobeads, and small cluster of molecules can be effectively measured by using a Superconducting Quantum Interference Device (SQUID) with a small sensitive area. Here, we present a high sensitivity nanoSQUID based on deep submicrometer Josephson tunnel junctions fabricated by a Focused Ion Beam (FIB) sculpting method. The nanosensor consists of a niobium superconducting loop (0.4×1.0 μm^2) interrupted by two sandwich nanojunctions (Nb/Al-AlOx/Nb) having an area of about (300×300) nm^2. An experimental investigation of the main characteristics of such nanodevice as a function of the temperature is presented.

Keywords: Quantum sensor · nanoSQUID · Spin sensitivity

1 Introduction

In the last years, great efforts have been devoted to the development of Superconducting Quantum Interference devices (SQUIDs) having a flux capture area lower that 1 μm^2 [1–9]. In fact, it can be shown that the magnetic moment sensitivity increases by decreasing the SQUID loop area. Employing the nanofabrication techniques is possible to fabricate nanoSQUIDs having sensitive enough to explore new stimulating nanoscience topics such as the study of magnetic nanoparticles, single electron and molecular magnets. Typically a nanoSQUID consists of a submicron superconducting loop with two nano-constrictions acting as a Josephson elements (Dayem nanobridges) [1–4]. However, due to a non-sinusoidal current-phase relationship, a SQUID based on

B. Andò et al. (eds.), *Sensors*, Lecture Notes in Electrical Engineering 431,
DOI 10.1007/978-3-319-55077-0_4

Dayem bridges exhibits a quite different behavior compared to a standard one based on Josephson tunnel junctions [10]. For this motivation, in the last years the researchers are developing nanoSQUID based on tunnel Josephson nano-junctions [1, 8, 9]. In this paper, we report niobium nanoSQUIDs based on sandwich nano-junctions and their characterization as a function of the temperature down to 300 mK.

2 Nanodevice Fabrication

The nanosensors reported here are realized joining two Josephson junctions with a Nb/Al-AlOx/Nb SNIS (Superconductor-Normal metal-Insulator-Superconductor) structure, through a nano-superconducting loop. These devices have been fabricated by means of a Focused Ion Beam (FIB) sculpting method, used as lithographic technique to define the various elements of the SQUID.

The entire technological process includes a few fabrication steps. At first, the Nb/Al-AlOx/Nb multilayered structure is patterned by optical lithography, deposited by a radio frequency sputtering system, in a high vacuum chamber, and subsequently defined by a lift-off procedure. The thickness of the two Niobium electrodes is 250 nm, while the Al layer is 6 nm thin, with an oxidation exposure of about 3700 Pa s. Afterwards, driving ion beam on the sputtered structure and opportunely orienteering the sample surface with respect to the beam trajectory, a multilayered lamella (around 400 nm) is realized through a consecutive removal of the material in excess, with the working surface perpendicular to the beam line. A rectangular hole ($1 \times 0.4\ \mu m^2$) was realized in the center of the strip, resulting in two parallel lamellae and defining both the Josephson junction's width and the loop of the nanoSQUID device. Afterwards the sample is oriented parallel to the beam trajectory and two side cuts through the two lamellae were performed defining the length of the junctions. Figure 1 depicts a sketch showing the main fabrication steps and a Scanning Electron Micrograph (SEM) image of a nanoSQUID. The aspect-ratio (ratio between the height and the width) referred to the single lamella is about 2, resulting in a three dimensional structure.

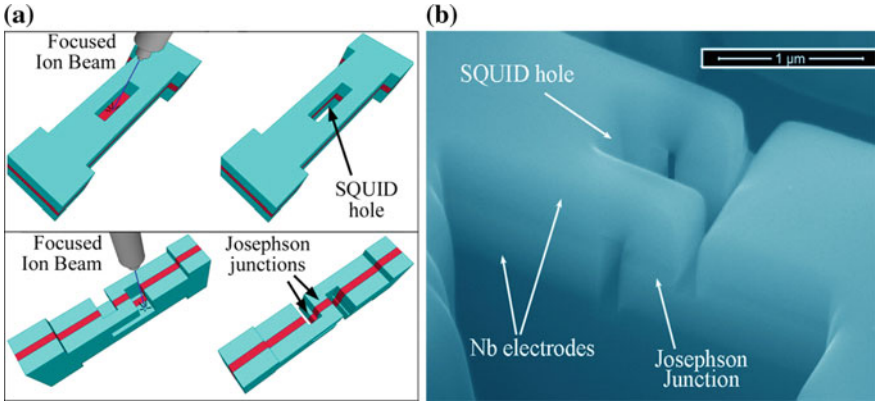

Fig. 1 **a** Sketch of the main fabrication steps of a nanoSQUID. The fabrication is based on a combination of the optical lithography and Focused Ion Beam (*FIB*) sculpting technique. **b** Scanning electron micrograph of a three-dimensional nanoSQUID

3 Characterization and Performances

The nanoSQUID characterization consisted in measurements of current-voltage characteristics, critical current versus external magnetic field and switching current distributions, for different temperature ranging from 9 K to 300 mK. The above measurements give us the behaviors of the critical current, of the modulation depth and of the magnetic flux noise as function of the temperature. In Fig. 2a, the current-voltage characteristics of the nanodevice for two temperatures are reported. The curves do not exhibit hysteresis for temperature higher than 4 K. It is due to both small critical current values as well thermal rounding. As expected, by decreasing the temperature, the β_c (hysteresis parameter) value increases and the hysteresis occurs. It becomes more evident by decreasing the temperature. However, the occurrence of the hysteresis does not prevent to employ the nanodevice as a high sensitive magnetic sensor [11]. The critical current as a function of the external magnetic flux (I_c-Φ) for different temperatures is shown in Fig. 2b. The curves show smooth maxima and cusped-like minima, nominally signature of a sinusoidal current-phase relationship, typical of standard SQUIDs [12]. From the figure is possible to obtain the current responsivity ($I_\Phi = \partial I_c/\partial\Phi_{ext}$) by taking the derivative of the I_c-Φ curves (Fig. 2b) at the point where the slope is steepest. The magnetic flux noise of the sensor is given by $\Phi_N = I_{c,N}/(\partial I_c/\partial\Phi_{ext})$ where $I_{c,N}$ is the measurement error of the critical current which can be obtained by measuring the switching current distributions (Fig. 3a). The $I_{c,N}$ can be assumed as the minimum current variation corresponding to two distinguished distributions. Performing small thermal shifts, we have measured an $I_{c,N} = 100$ nA, which results independent on the temperature in the whole range of temperature investigated. In the Fig. 3b, the values of Φ_N as a function of the temperature is reported. The noise decreases by diminishing the temperature assuming a minimum value of about $1.4 \times 10^{-4}\ \Phi_0$ for T = 300 mK.

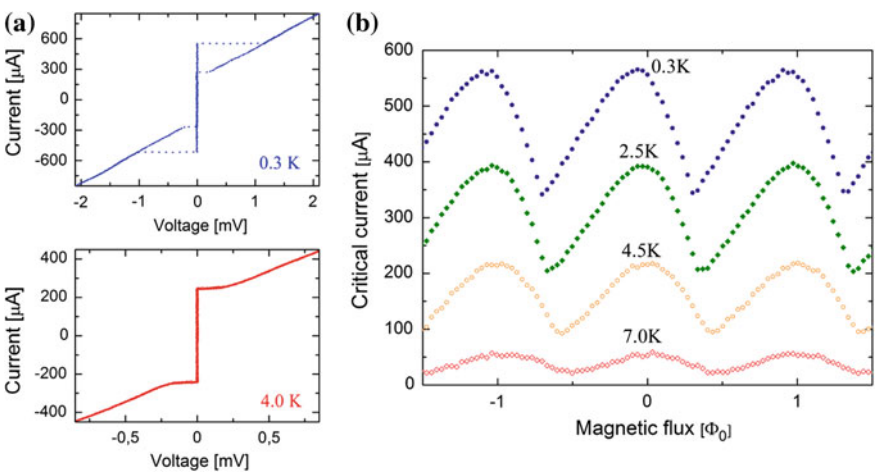

Fig. 2 **a** Current versus voltage characteristics of a nanoSQUID measured at two different temperatures. **b** Critical current versus magnetic flux curves measured at temperature ranging from 7.0 K to 300 mK

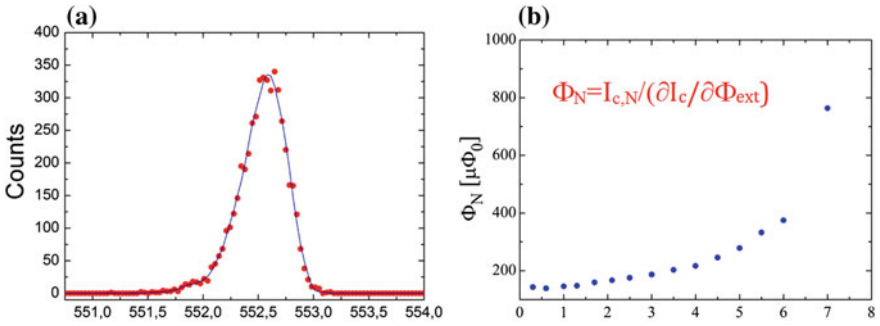

Fig. 3 **a** Critical current switching distribution of a nanoSQUID measured at 300 mK by using the time of flight technique [11]. **b** Magnetic flux noise of the nanosensor obtained by the ratio of the critical current resolution and the current responsivity

4 Conclusions

A fabrication and characterization of a quantum magnetic nanosensor has been reported. Measurements of current-voltage, critical current-magnetic flux characteristics and switching current distributions from the zero voltage state for different temperatures have been performed. The high critical current modulation depths and the low intrinsic dissipation exhibited by these devices ensure a suitable sensitivity for nanoscale applications in the whole temperature range investigated.

References

1. C. Granata, A. Vettoliere, Nano superconducting quantum interference device: a powerful tool for nanoscale investigations. Phys. Rep. **614**, 1–69 (2016)
2. C.P. Foley, H. Hilgenkamp, Why NanoSQUIDs are important: an introduction to the focus issue. Supercond. Sci. Technol. **22**, 064001 (2009)
3. W. Wernsdorfer, From micro-to-nano-SQUIDs: applications to nanomagnetism. Supercond. Sci. Technol. **22**, 064013 (2009)
4. A.G.P. Troeman, et al., NanoSQUIDs based on niobium constrictions. Nano Lett. **7**, 2152 (2007)
5. J.P. Cleuziou et al., Carbon nanotube superconducting quantum interference device. Nat. Nanotech. **1**, 53 (2006)
6. D. Vasyukov et al., A scanning superconducting quantum interference device with single electron spin sensitivity. Nat. Nanotech. **8**, 639 (2013)
7. L. Hao et al., Detection of single magnetic nanobead with a nano-superconducting quantum interference device. Appl. Phys. Lett. **98**, 092504 (2011)
8. J. Nagel et al., Superconducting quantum interference devices with submicron Nb/HfTi/Nb junctions for investigation of small magnetic particles. Appl. Phys. Lett. **99**, 032506 (2011)
9. R. Wölbing et al., Nb nano superconducting quantum interference devices with high spin sensitivity for operation in magnetic fields up to 0.5T. Appl. Phys. Lett. **102**, 192601 (2013)

10. C. Granata et al., Noise theory of dc nano-SQUIDs based on Dayem nanobridges. Phys. Rev. B **84**, 224516 (2011)
11. C. Granata et al., Critical current noise investigations in underdamped Josephson devices. Phys. Rev. B **83**, 092504 (2011)
12. C. Granata, A. Vettoliere, M. Russo, Miniaturized superconducting quantum interference magnetometers for high sensitivity applications. Appl. Phys. Lett. **91**, 122509 (2007)

A Sensor for the Measurement of Liquids Density

Nicola A. Lamberti(✉), Monica La Mura, Valerio Apuzzo, Nicola Greco, and Pasquale D'Uva

Dip. d'Ingegneria Industriale, Università di Salerno, via Giovanni Paolo II 132, 84084 Fisciano, SA, Italy
taulab@unisa.it

Abstract. Density is one of the characteristic properties of a substance, that can be used to understand other physical and chemical properties. On-line density sensors are of interest in many applications: the radioactive monitoring in waste storage tanks, in pipelines for process control in the petrochemical industry, in the production of chemical reagents, in food processing, in the production of paper and textiles and so on. In this paper, a piezoelectric density sensor is proposed and analyzed with FE methods. The idea at the base of the present work relies in the well-known property of piezoelectric structures to vary their resonant behavior depending on load conditions. The active element of the proposed density sensor is a cheap piezoceramic bimorph, widely used in buzzers and telephone receivers. The bimorph is clamped all around by tightening its border to the edge of a rigid open chamber in which the liquid is poured; the flexural resonance frequency of the membrane is modified by the liquid mass. The liquid volume is the volume of the chamber and therefore the membrane resonance frequency can be related to the liquid mass density. We analyze the proposed sensor by a FEM commercial code (ANSYS®) to test the device capability and to design the chamber in which the liquid is poured, in order to maximize the device sensitivity; we computed the sensor resonance frequency by varying the chamber height and for three different values of the chamber radius. The obtained results demonstrate that best sensitivity is obtained with smaller values of both height and radius.

Keywords: Liquid density measurements · Resonant sensor · Piezoelectric bimorph

1 Introduction

Density is a physical characteristic of substances related to several other physical, chemical and mechanical properties [1]. Its measurement is frequently required in many industrial and research applications, from nuclear to pharmaceutical, from paper to textiles, from food to petrochemical industries [2, 3].

Resonant density sensors are highly suitable for these applications, due to their high sensitivity and precision. The sensor proposed in this work is realized by placing a piezoelectric bimorph, widely used in buzzers and telephones receivers, into a metallic chamber, hosting a fixed quantity of liquid. The mass of the liquid causes a variation in

B. Andò et al. (eds.), *Sensors*, Lecture Notes in Electrical Engineering 431,
DOI 10.1007/978-3-319-55077-0_5

the flexural resonance frequency of the piezoelectric bimorph; the volume is fixed and therefore the frequency variations can be related to the liquid density.

A finite elements model of the bimorph was realized, including the boundary conditions associated to the mechanical constraint operated by the metallic structure. The bimorph material parameters were determined by fitting the measured electrical impedance of the unconstrained bimorph with the electrical impedance obtained by a Finite Elements Analysis, performed by using the software ANSYS® (ANSYS, Canonsburg, PA, USA) [4].

FE Analysis was also used in order to maximize the device sensitivity, varying the chamber height and radius.

2 The Bimorph

The active element of the device is a cheap piezoelectric bimorph, composed of a piezoelectric ceramic glued by means of an epoxy resin to a thin disk of metal, which acts as both electrode and mechanical support. Since one of the circular surfaces of the ceramic is bounded to the metal layer, radial resonance of the piezoelectric element is prevented, obtaining a flexural vibration of the bimorph. The piezoceramic upper surface is metallized, obtaining the second electrode. In Fig. 1 the three piezoelectric bimorphs used in the device realization are shown; from left to right, their names are: CT31, SP18 and SP17 respectively.

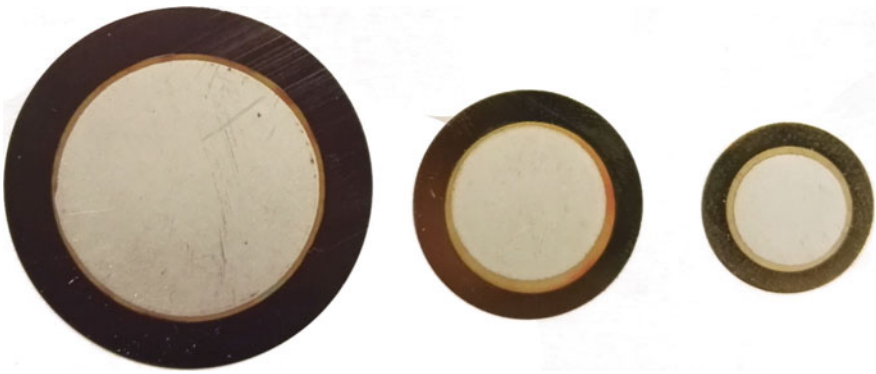

Fig. 1 Picture of the bimorphs used to develop the sensor

In Table 1 the dimensions and the most important characteristics of the three elements are reported; the resonance frequency is the frequency of the first symmetrical vibration mode of the element, i.e. the resonance of the first mode with a nodal circle.

Table 1 Dimensions and characteristics of the three commercial bimorphs

	CT31	SP18	SP17
Metal material	Nickel	Brass	Brass
Metal diameter (mm)	31	20	15
Ceramic diameter (mm)	23	15	11
Metal thickness (mm)	0.1	0.2	0.1
Ceramic thickness (mm)	0.1	0.2	0.1
Resonance frequency (kHz)	1.531	6.215	6.477

3 Device FEM Analysis and Optimization

In order to evaluate the device resonance frequency, the three piezoelectric bimorphs were analyzed by means of the FEM commercial code ANSYS. As mentioned in the introduction, ANSYS was used, first of all, in order to fit the parameters for both the piezoelectric and metal material. The fitting procedure was performed by means of the automatic method described in [4]. In Fig. 2, the fitted curve obtained for the unconstrained CT31 bimorph is shown.

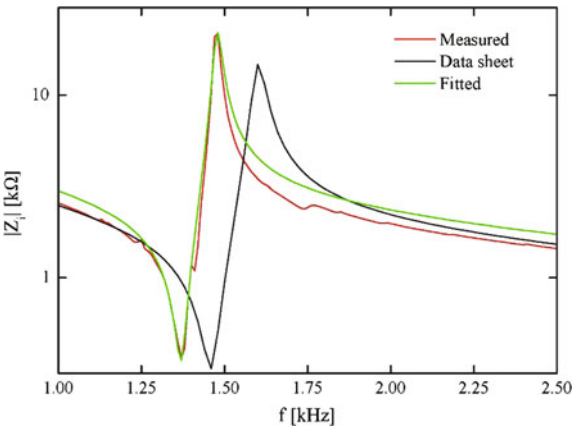

Fig. 2 Comparison between the measured $|Z_i|$ of the unconstrained CT31 bimorph and the same curve computed by FEM, both using the parameters in the manufacturer datasheet and the result of the fitting procedure

As can be seen, the result obtained by using the fitted parameters is practically superimposed to the measured curve.

The sensor design was carried out pursuing the optimization of the height of the chamber *t*, in order to maximize the device sensitivity. Finite Elements Analysis was

performed for the constrained bimorph interacting on its upper surface with a cylinder of water ($\rho = 1000$ kg/m^3) of height t. The height of the chamber and the thickness of the liquid under test are equals, because a cap fixes the volume of the liquid to the volume of the chamber and the metallic structure fixes the area of the base. The cylinder was meshed with solid elements, in order to have the displacements as degrees of freedom. The inner surface of the chamber prevents the liquid movements along the radial coordinate; this was taken into account by setting the radial displacement u_r to zero for all the elements in the outer surface of the cylinder modeling the liquid under test.

FE modal analysis was performed by varying t from 1 to 10 mm, with steps of 1 mm. Figure 3 shows the first resonance frequencies of the sensors equipped with the three bimorphs, evaluated for each value t of the cylinder height.

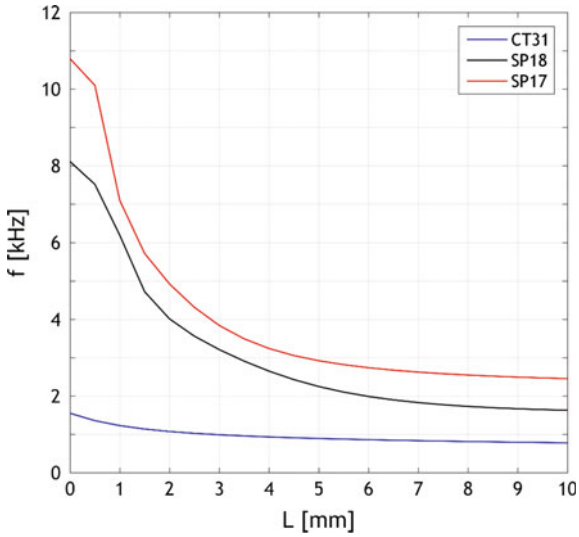

Fig. 3 Resonance frequency computed by ANSYS varying the chamber height. The liquid is water

As can be seen, the frequency values f decrease by increasing the chamber height t and f is not linear with t.

In order to determine the t value that maximizes the sensor sensitivity, we computed the sensor electric input impedance amplitude, $|Z_i|$, by means of the ANSYS harmonic analysis, varying the liquid density from 700 to 1500 kg/m^3. Figure 4 shows the first resonance frequency computed for $t = 1$ mm, i.e., the liquid thickness showing the maximum slope in Fig. 3.

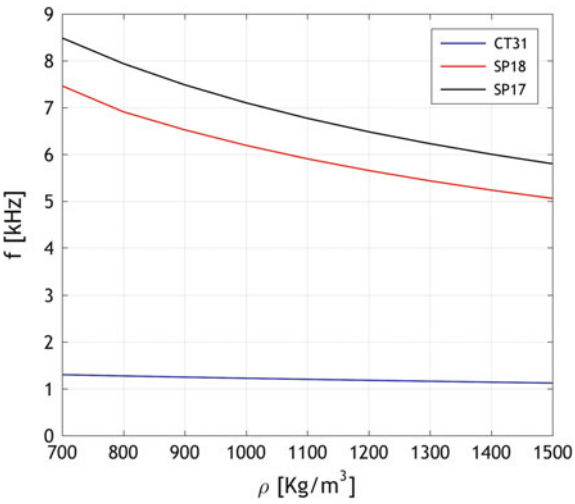

Fig. 4 Device resonance frequency computed by ANSYS, varying the liquid density (t = 1 mm)

It can be noticed in Fig. 4 that the dependence of f from the density ρ is not linear, so the slopes are not constant; highest slopes are obtained by the devices made with the SP17 and SP18 bimorphs.

As it is well known, the sensor sensitivity is defined as

$$S = \frac{\partial y}{\partial x} \tag{1}$$

where y is the electrical output variable and x the input non-electrical variable. For this resonant density sensor S becomes

$$S = \frac{\partial f}{\partial \rho} \tag{2}$$

since the electrical output is the frequency f and the non-electrical input is the density ρ.

In order to compare the sensor sensitivity for the three cases described above, the quantity

$$S \cong \left| \frac{\Delta f}{\Delta \rho} \right| \tag{3}$$

was computed for the sensors equipped with the three bimorphs and the result is reported in Fig. 5.

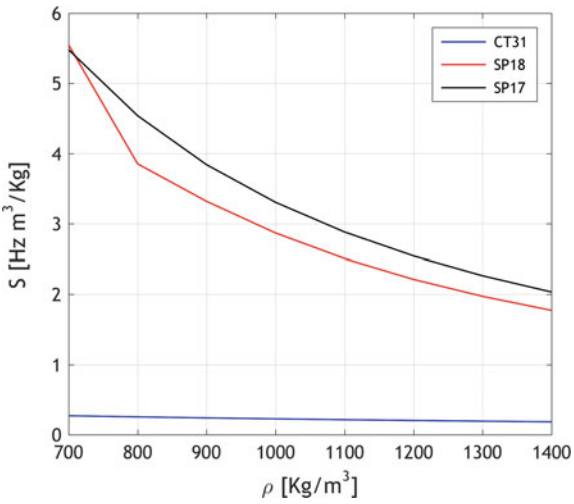

Fig. 5 Device sensitivity computed by ANSYS, varying the liquid density (t = 1 mm)

As it can be seen, the sensors made by the SP17 and SP18 bimorphs show almost the same sensitivity, while the device equipped with the CT31 bimorph shows worse results.

In order to complete the device sensitivity analysis, we computed S by ANSYS, using Eq. (3) and considering t = 2.5 mm and t = 5 mm. The computed sensitivities are reported in Fig. 6.

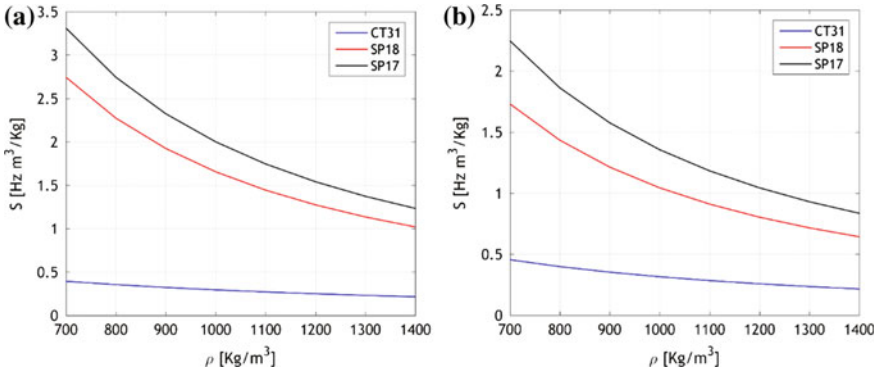

Fig. 6 Device sensitivity computed by ANSYS, varying the liquid density; in **a** we assumed the liquid height t = 2.5 mm, in **b** we considered t = 5 mm

As shown in Figs. 5 and 6, the sensitivity S decreases increasing the liquid height t, for all the considered bimorphs. Further, the best sensitivity is always obtained by using the SP17 bimorph, i.e. the device with the smaller diameter. On the other side,

worse results are always obtained by using the bigger bimorph CT31. The obtained results suggest that better performance in terms of sensitivity are obtained by minimizing the liquid volume in the sensor.

4 Conclusions and Future Work

In this paper a piezoelectric sensor, able to measure the density of liquids, is proposed and analyzed with FE methods. The idea at the basis of the device relies in the well-known property of piezoelectric structures to vary their resonant behavior depending on load conditions. The active element of the proposed density sensor is a cheap piezoceramic bimorph, widely used in buzzers and telephone receivers. The bimorph is clamped all around by tightening its border to the edge of a rigid open chamber in which the liquid is poured; the flexural resonance frequency of the bimorph is modified by the liquid mass. The liquid volume is the volume of the chamber and therefore the bimorph resonance frequency can be related to the liquid mass density. We analyzed the proposed sensor by ANSYS to design the chamber in which the liquid is poured, in order to maximize the device sensitivity; we computed the sensor resonance frequency by varying the chamber height and for three different values of the chamber radius, obtained by considering three commercially available bimorphs. The obtained results demonstrate that best sensitivity is obtained by minimizing both the chamber height and radius.

We are realizing some prototypes in order to experimentally verify the FEM results; first results confirm the device capability.

References

1. B. Lagourette, C. Boned, H. Saint-Guirons, P. Xans, Densimeter calibration method versus temperature and pressure. Meas. Sci. Technol. **3**, 699–703 (1992)
2. M.S. Greenwood, J.R. Skorpik, J.A. Bamberger, On-line sensor to measure the density of a liquid or slurry. *Science and Technology for Disposal of Radioactive Tank Waste*, eds. by W. S. Wallace, J.L. Nichoals (Plenum Press: New York, 1998), pp. 497–506
3. M.S. Greenwood, J.R. Skorpik, J.A. Bamberger, R.V. Harris, On-line ultrasonic density sensor for process control of liquids and slurries. Ultrasonics **37**, 159–171 (1999)
4. N.A. Lamberti, A. Iula, A. Caputo, A method for the automatic characterization of piezoelectric ceramic elements, in *19th International Congress on Acoustics, Rev. Acust*, vol. 38 (3–4) (2007), ISBN: 84-87985-12-2, paper no. ULT-03-003-IP (invited paper)

Temperature Sensing Properties of High Density Polyethylene Loaded with Oxidized Multi Walled Carbon Nanotubes

Heinz-Christoph Neitzert(✉), Giovanni Landi, and Maria Rossella Nobile

Dipartimento di Ingegneria Industriale (DIIn), Università di Salerno, Via Giovanni Paolo II 132, 84084 Fisciano, SA, Italy
neitzert@unisa.it

Abstract. Good temperature sensing properties from room temperature up to 100 °C have been obtained, with high density polyethylene/carbon nanotube composites even for nanotube concentrations slightly above the percolation threshold in the case that oxidized multi-walled carbon nanotubes have been used. Due to the low conductivity no Joule heating has to be considered.

Keywords: 07.07.Df · 07.20.Dt · 72.80.Tm · 88.30.rh

1 Introduction

Carbon nanotube based temperature sensors with electrical readout have been realized in a great variety of geometries, ranging from very small sensors, based on the temperature dependence of the single nanotube conductivity [1], up to large area sensors, based on carbon nanotube networks, often embedded into a matrix material. The matrix material can range from hydrogel [2] to polymers [3], epoxy resins [4, 5] or even biological cells [6]. The sensing properties depend on the type of carbon nanotubes [7], their concentration [8] the matrix material [9] and last, but not least, the electrical contact material and geometry [10]. It should be mentioned that, even for the same type of nanotube networks, as well positive temperature coefficient (PTC) [11, 12] as negative temperature coefficient (NTC) [5] behaviour has been observed. Combining different layers with PTC and NTC effect, zero temperature coefficient (TC) material can be obtained [13]. Recently, however, it has been shown that nanocomposite material with near zero TC can also be obtained by a simple one-layer flexible thin film of poly-(amide-imide) highly loaded with carbon black with applications as high temperature, flexible electrical heater foil without need for temperature compensation [14]. Applying high voltages to nanocomposite based temperature sensors with nanoparticle concentrations far above the electrical percolation threshold, Joule heating has to be taken into account. This effect can be exploited for the realization of current limiting devices [15]. On the other hand Joule-heating can modify the contact properties [16] and hence lead to an instability of the sensing characteristics. Therefore it can be of interest to realize low-conductance temperature sensors, using for example polymer/CNT composites with CNT concentrations slightly above percolation

B. Andò et al. (eds.), *Sensors*, Lecture Notes in Electrical Engineering 431,
DOI 10.1007/978-3-319-55077-0_6

threshold. It should be mentioned, that in the case of LLDPE/CNT composites also high electric fields during high temperature cycling can lead to conductivity changes of the composite sample [17]. Here we report on the realization of high density polyethylene (HDPE)/multi-walled carbon nanotube (MWCNT) based temperature sensors with low conductance and their sensing properties for relatively high temperatures from room temperature up to 100 °C. In order to favour a more homogeneous nanotube distribution, oxidized MWCNTs have been used [18].

2 Experimental

2.1 Sample Preparation

High-density polyethylene (HDPE0390) (Qenos) with an average molecular weight of Mw ~ 58.886 g/mol and polydispersity of 5.8 was chosen as matrix. Multi-walled carbon nanotubes (MWNTs) were synthesized by chemical vapor deposition at CSIRO (Commonwealth Scientific and Industrial Research Organization, Australia) with an average diameter of 50 nm. Non-functionalized (MWNTs) and functionalized (OXI MWNTs) carbon nanotubes were used. The functionalization treatment consists of oxidative treatment in a tube furnace at 500 °C for 1 h, in a 95% nitrogen and 5% oxygen atmosphere.

Nanocomposites with different nanotube concentrations (between 0.5 and 7 wt%) in the HDPE matrix (named MWNT/HDPE and OXI MWNT/HDPE) were prepared by melt mixing in a micro-twin screw extruder (Haake MiniLab Rheomex CTW5). Thanks to a re-circulating channel, this extruder is capable of cycling the melt, ensuring a good mixing and making good-quality samples from a limited amount of material. Each nanocomposite was mixed for 10 min, with a screw speed of 50 rpm. Finally coplanar gold electrodes have been evaporated on the top of the samples. In this work we report exclusively on the samples with a CNT concentration of 2.5 wt%.

2.2 Structural Sample Characterization

In order to analyse the dispersion of the filler in the polymeric matrix, the samples were investigated by means of scanning electron microscopy (SEM). A typical SEM images of the etched fracture surface of the HDPE/CNT composite with 2.5 wt% oxidized MWCNTs is shown in Fig. 1. The image demonstrates a homogeneous dispersion of the carbon nanotubes in the sample.

It should also be mentioned that rheological and electrical measurements have shown that the HDPE/MWCNT nanocomposites with 2.5 wt% carbon nanotube content are above the percolation threshold, independently of the surface treatment of the nanotubes [19].

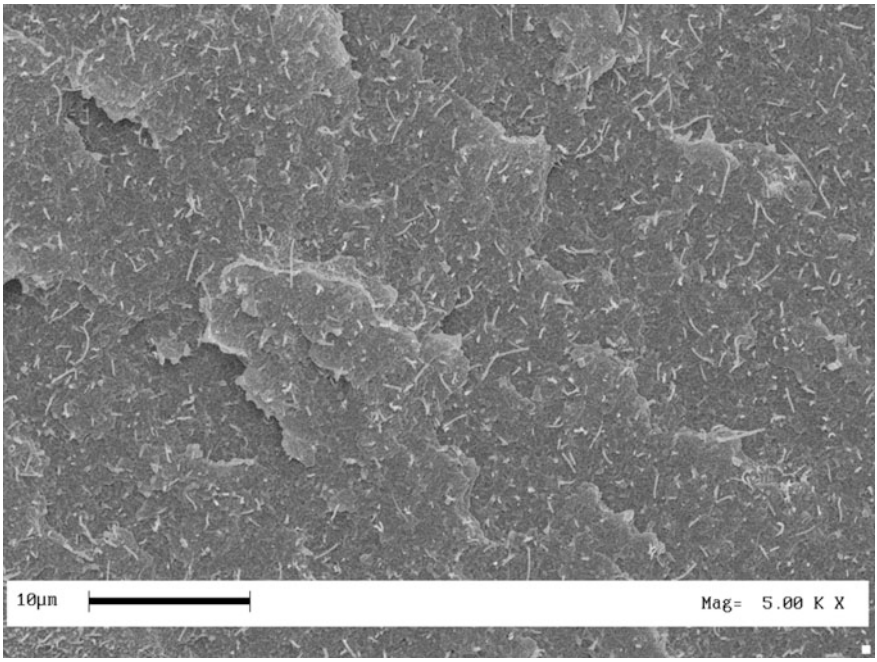

Fig. 1. Scanning electron microscopy image, showing the morphology of the etched fracture surface of the HDPE/CNT composite with 2.5 wt% oxidized MWCNTs

2.3 Measurement Setup for the Temperature Dependent Electrical Characterization

The electrical measurements of the HDPE/MWCNT composites, reported in this paper, have all been performed in a 2-point contact geometry using a Keithley model "2400" Source-Measurement-Unit (SMU). For the temperature dependent conductivity measurements, the samples have been subjected to slow temperature cycles in an electronically regulated oven. The oven temperature has been measured using a thin-film thermo-element, positioned on top of the composite sample, to be characterized.

In a previous work it has been shown, that these composite type has a percolation threshold of the electrical conduction and of the rheological properties between 1 and 2.5 wt% addition of CNTs to the polymer matrix [19, 20]. In the case of highly conducting samples of this kind of composites (CNT concentrations of 5 and 7 wt%) have been shown to have a variety of interesting applications for low temperature sensing [21], current limiting [22] and microwave shielding [23].

Here we investigated the temperature sensing properties above room temperature up to 100 °C of a low CNT concentration composite sample (2.5 wt% of MWCNTs) with oxidized nanotubes. It has been shown, that the oxidation lowers the conductivity by some orders of magnitude as compared to the samples with non-oxidized CNTs. Often it is found that low-conductivity polymer/CNT composites have rather instable characteristics due to the low number of percolation paths involved in the conduction.

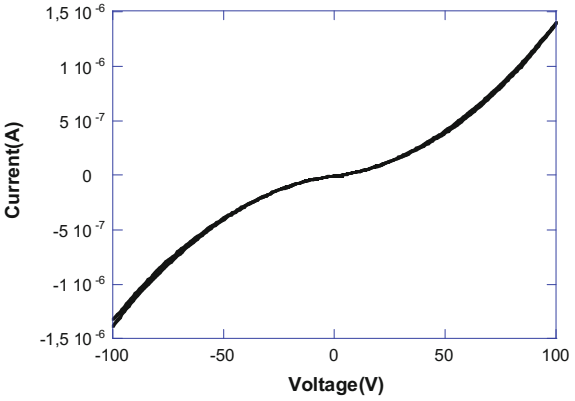

Fig. 2. Current-voltage characteristics of HDPE/MWCNT composites with 2.5 wt% oxidized MWCNT's

3 Results and Discussion

The current-voltage characteristics of the investigated HDPE/CNT composite sample with 2.5 wt% oxidized MWCNTs (see Fig. 2) is not linear, as shown earlier for the case of the high conductance samples [5], but after an initial burn-in procedure rather stable. Typically we found conductivity values of about 1×10^{-6} S/cm for the samples with 2.5 wt% of non-oxidized MWCNTs and values of about 5×10^{-9} S/cm for the samples with 2.5 wt% of oxidized MWCNTs.

Measuring the sample current and temperature (applied voltage: 100 V) during multiple temperature cycling above room temperature for a sample with non oxidized and a sample with oxidized multi walled carbon nanotubes with the same concentration of 2.5 wt% (see Fig. 3), we observed a very unstable characteristics in the case of the sample with non-oxidized CNTs (Fig. 3a). In particular for this sample during the cooling period a non-monotonic behaviour, sharp switching and a successively with increasing cycle number decreasing sensitivity has been found.

For the sample with the oxidized CNTs, however, a rather stable characteristics, as it can be seen in Fig. 3b, was obtained. Only after the first cycle we see a small decrease of the conductivity, that remains further on stable. In this latter case, during the cooling periods a monotonic increase of the conductivity with increasing temperature can be observed.

Because the cooling process, however, was very slow, it can be assumed that the sample is in thermal equilibrium during cooling and hence sample and thermo-element temperature coincide. A good reproducibility of the current-temperature traces during cooling for all the cycles is observed. This confirms that not only the current-voltage characteristics, but also the sample resistance-temperature characteristic has a good stability.

The same monitoring has been also performed for smaller voltages. In Fig. 4 the temperature-conductivity relation of the nanocomposite, as measured during the last cooling cycle has been plotted for different applied voltages of 100 and 10 V. For

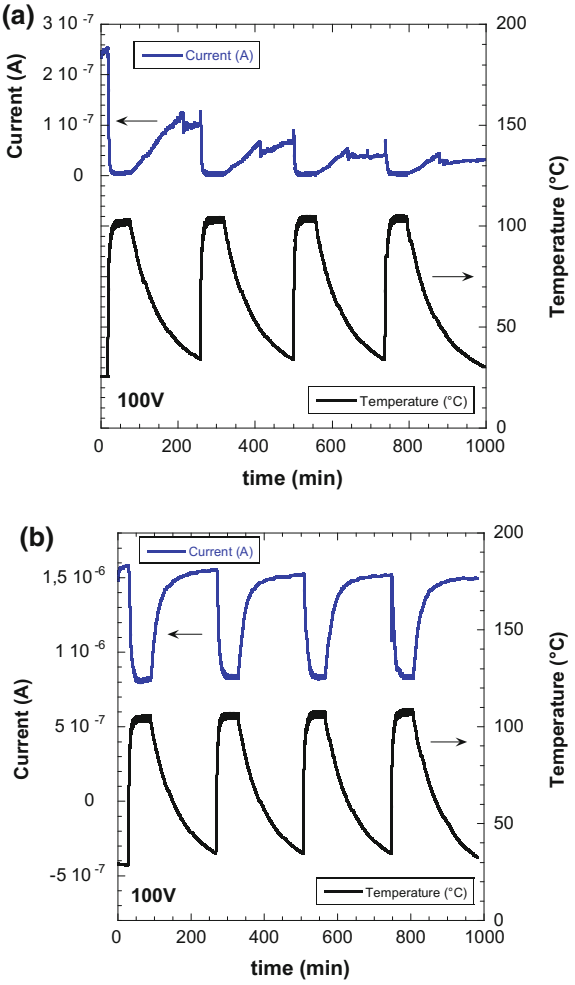

Fig. 3. Current and temperature monitoring during 4 slow thermal cycles for HDPE/CNT samples with **a** non oxidized and **b** oxidized MWCNTs with a concentration of 2.5 wt%

comparison, the conductivities have been normalized to their value at 30 °C. We see a very smooth characteristics for the 100 V curve and a much more noisy characteristics with slightly different behaviour for the curve, taken at 10 V. This has been most probably to be attributed to interface problems either between nanotubes and the metallization or to noisy intertube connections. As it is also seen in the inset of Fig. 4 the characteristics, measured at 100 and 10 V, can be nicely fitted by 3rd order polynomial fits. The sensitivity of the sample is higher than the one previously reported for highly conductive epoxy/CNT [5].

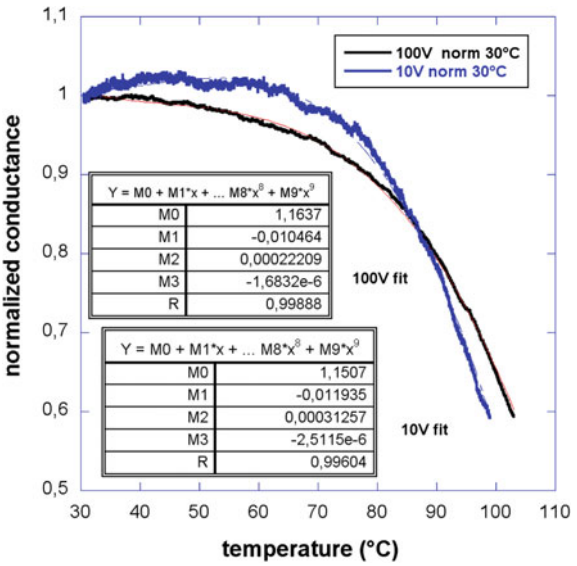

Fig. 4. Comparison of the temperature dependence of the conductance (normalized to the value at 30 °C) of a HDPE/MWCNT composite sensor, measured during the last cooling cycle with different applied voltages (10 and 100 V) and 3rd order polynomial fits of the characteristics (*Insets*)

4 Conclusions

It has been shown that stable temperature sensors for the temperature range up to 100 °C can be realized with low-conductance high density polyethylene/carbon nanotube composites, realized with oxidized multi-walled carbon nanotubes with a filler-concentration of 2.5 wt% and evaporated gold contacts, whereas composites with the same filler-concentration of non-oxidized carbon nanotubes a higher conductivity could be achieved but no stable temperature sensing was possible.

Acknowledgements. The authors thank Prof. Dr. George P. Simon from Monash University (Australia) for the CNT and composite preparation and Dr. Olga Valentino from Polimeri Europa for the composite sample preparation and the structural characterization.

References

1. Y. Arai, C. Ng, P. Liu, L. Dong, Y. Imaizumi, K. Maeda, H. Maruyama, A. Ichikawa, T. Kukuda. Ultra-small site temperature sensing by carbon nanotube thermal probes, in *Proceedings of the 4th IEEE Conference on Nanotechnology*, (2004), 146–148
2. E. Manek, B. Berke, N. Miklósi, M. Sajbán, A. Domán, T. Fukuda, O. Czakkel, K. László, Thermal sensitivity of carbon nanotube and graphene oxide containing responsive hydrogels. Exp. Polym. Lett. **10**, 710–720 (2016)

3. C. Barone, S. Pagano, H.C. Neitzert, Transport and noise spectroscopy of MWCNT/HDPE composites with different nanotube concentrations. J. Appl. Phys. **110**, 113716 (2011)
4. Y. Alamusi, N. Li, L. Hu, W. Wu, X. Yuan, B. Peng, C. Gu, Y. Chang, H. Liu, J. Ning, S. Li, S. Atobe, H. Fukunaga, Temperature-dependent piezoresistivity in an MWCNT/epoxy nanocomposite temperature sensor with ultrahigh performance. Nanotechnology **24**, 455501 (2013)
5. H.C. Neitzert, L. Vertuccio, A. Sorrentino, Epoxy/MWCNT composite as temperature sensor and electrical heating elements. IEEE Trans. Nanotechnol. **9**, 688–693 (2010)
6. R. Di Giacomo, B. Maresca, A. Porta, P. Sabatino, G. Carapella, H.C. Neitzert, Candida albicans/MWCNTs: a stable conductive bionanocomposite and its temperature sensing properties IEEE Trans. Nanotechnol. **12**, 111–114 (2013)
7. A. Naeemi, J.D. Meindl, Physical modeling of temperature coefficient of resistance for single- and multi-wall carbon nanotube interconnects. IEEE Electron Dev. Lett. **28**, 135–138 (2007)
8. C. Barone, G. Landi, C. Mauro, H.C. Neitzert, S. Pagano, Universal crossover of the charge carrier fluctuation mechanism in different polymer/carbon nanotubes composites. Appl. Phys. Lett. **107**, 143106 (2015)
9. W.R. Fahrner, G. Landi, R. Di Giacomo, H.C. Neitzert. Multi-walled carbon nanotube network-based sensors and electronic devices, in *The Nano-Micro Interface: Bridging the Micro and Nano Worlds*, eds. by H.-J. Fecht, M. Werner, M. Van de Voorde, (Wiley-VCH, Verlag, 2015), pp. 225–242
10. H.C. Neitzert, G. Landi. Influence of the contact metallization on the characteristics of resistive temperature sensors based on EPOXY/MWCNT composites, Chapter 58, in *Sensors, Proceedings of the Second National Conference on Sensors*, Rome 19–21 February, 2014 Series. Lecture notes in electrical engineering, vol. 319, (Springer, Berlin, 2015), pp. 333–337
11. X.L. He, J.H. Du, Z. Ying, H.M. Cheng, X.J. He, Positive temperature coefficient effect in multiwalled carbon nanotube/high-density polyethylene composites. Appl. Phys. Lett. **86**, 062112 (2005)
12. S.P. Bao, G.D. Liang, S.C. Tjong, Positive temperature coefficient effect of polypropylene/carbon nanotube/montmorillonite hybrid nanocomposites. IEEE Trans. Nanotechnol. **8**, 729–736 (2009)
13. K. Chu, S.C. Lee, S. Lee, D. Kim, C. Moon, S.H. Park, Smart conducting polymer composites having zero temperature coefficient of resistance. Nanoscale **7**, 471–478 (2015)
14. S. Liparoti, G. Landi, A. Sorrentino, V. Speranza, M. Cakmak, H.C. Neitzert, Flexible poly (amide-imide)-carbon black based microheater with high-temperature capability and an extremely low temperature coefficient. Adv. Electron. Mater. **2**, 1600126 (2016)
15. H.C. Neitzert, O. Valentino, M. Sarno, M.R. Nobile, P. Ciambelli, PTC elements based on high density polyethylene loaded with multi-walled carbon nanotubes, in *Proceedings of the 7*th *International Conference on Nanostructured Polymers and Nanocomposites (ECNP)*, Prague, 24–27 April 2012, pp. 383–385
16. Y. Woo, G.S. Duesberg, S. Roth, Reduced contact resistance between an individual single-walled carbon nanotube and a metal electrode by a local point annealing. Nanotechnology **18**, 095203 (2007)
17. M. Ferrara, H.C. Neitzert, M. Sarno, G. Gorrasi, D. Sannino, V. Vittoria, P. Ciambelli, Influence of the electrical field applied during thermal cycling on the conductivity of LLDPE/CNTs composites. Phys. E **37**, 66 (2007)
18. M.R. Nobile, E. Somma, O. Valentino, G. Simon, H.C. Neitzert, Influence of the nanotube oxidation on the rheological and electrical properties of CNT/HDPE composites. AIP Conf. Proc. **1736**, 020150 (2016)

19. Olga Valentin, PhD thesis, Salerno (2008)
20. O. Valentino, M. Sarno, N.G. Rainone, M.R. Nobile, P. Ciambelli, H.C. Neitzert, G. P. Simon, Influence of the polymer structure and nanotube concentration on the conductivity and rheological properties of polyethylene/CNT composites. Phys. E **40**, 2440–2445 (2008)
21. C. Barone, S. Pagano, H.C. Neitzert, Effect of concentration on low-frequency noise of multiwall carbon nanotubes in high-density polyethylene matrix. Appl. Phys. Lett. **97**, 152107 (2010)
22. H.C. Neitzert, O. Valentino, M. Sarno, M.R. Nobile, P. Ciambelli, PTC elements based on high density polyethylene loaded with multi-walled carbon nanotubes, in *Proceedings of the 7th International Conference on Nanostructured Polymers and Nanocomposites (ECNP)*, Prague, 24–27 April (2012), pp. 383–385
23. R. Di Giacomo, H.C. Neitzert, HDPE/MWCNT composite as microwave absorber. AIP Conf. Proc. **1593**, 282–285 (2014)

RF Rectifier Toward Terahertz Integrated Image Detector

Volha Varlamava[1], Giovanni De Amicis[2], Andrea Del Monte[2], Rosario Rao[1(✉)], and Fabrizio Palma[1]

[1] Department of Information Engineering, Electronics, Telecommunications, Sapienza University of Rome, Eudossiana str. 18, 00184 Rome, Italy
varlamava@die.uniromal.it, rosario.rao@uniromal.it, palma@diet.uniromal.it
[2] LFoundry S.r.l, A. Pacinotti str. 7, 67051 Avezzano, Italy
{giovanni.deamicis,andrea.delmonte}@lfoundry.com

Abstract. We present a new CMOS compatible direct conversion terahertz detector operating at room temperature. The rectenna consists of an integrated antenna, realized on the surface of the integrated circuit and connected to a nanometric metallic whisker at one of its edges. The whisker reaches the semiconductor substrate that constitutes the antenna ground plane. The rectifying device can be obtained introducing some simple modifications of the charge storage well in conventional CMOS APS devices, making the proposed solution easy to integrate with existing imaging systems. No need of scaling toward very scaled and costly technological node is required, since the CMOS only provides the necessary integrated readout electronics. On-wafer measurements of RF characteristics of the designed rectifying junction are reported and discussed.

Keywords: Image detector · THz antennas · Rectifying antenna (rectenna) · Double barrier junction

1 Introduction

THz imaging and spectroscopy applications have a great potential in time-domain spectroscopy [1], communications [2], security control [3], and biomedical imaging [4]. For this reason in past decades a great interest of the research community has been attracted by this region of the electromagnetic spectrum, pushing the microwave and optical THz devices through a constant progress in the development and the improvement of detectors in terms of noise equivalent power.

Currently the main interest is the development of low cost, fast, highly sensitive, compact and room temperature THz detectors. The feasibility of rectifying antennas (rectennas) for the detection of freely propagating THz radiation has been demonstrated [5]. The radiative part of these devices is typically formed by an antenna that focuses the energy of the impinging electromagnetic field into a localized spot called active region, where the rectifying element is placed. The latter produces a continuous current proportional to the energy of the impinging electromagnetic wave.

B. Andò et al. (eds.), *Sensors*, Lecture Notes in Electrical Engineering 431,
DOI 10.1007/978-3-319-55077-0_7

Recently we presented a new structure resulting from the integration of a 3D antenna with widely produced commercial CMOS image detector [6]. The fabrication process, described in [7], permits to integrate the three dimensional antenna directly on the surface of the chip, by means of MEMS technology, and ensures a very low parasitic capacitance, because of the distance between antenna spires and the chip surface.

A further step of the development of this THz technology is the development of low cost, fast, highly sensitive, compact and room temperature detectors. The integration in arrays, in standard CMOS technology, is also mandatory to make exploitable readout and elaboration electronics capabilities. This paper presents a new approach resulting from the direct integration of the antenna with a rectifying device obtained by modification of commercial CMOS Image Sensors (CMOS ISs) [8].

Nowadays CMOS Image Sensors (CMOS ISs) are predominant electronic devices in the field of digital imaging [9]. The photosensitive element of the pixel is the pinned photodiode, i.e. a p-n-p structure constituting the charge storage well (SW) dedicated to the photocurrent integration during the exposure time. In the readout cycle the integrated charge is transferred to a capacitance ("floating diffusion", FD) inducing a voltage difference that is sampled with a transistor in source follower configuration. The complete charge transfer from photodiode to the floating diffusion allows the elimination of the thermal reset noise of the capacitor, referred as kTC noise, by means of the correlated double sampling. This property in combination with the extremely low dark current produced by pinned photodiode contributes to the high image quality of CMOS ISs.

The semiconductor structure implemented in the detector is suitable to perform the rectification of terahertz radiation and to permit accumulation of the rectified charge into a storage capacitance and its readout, by means of a technology compatible with CMOS ISs. The rectifying device with vertical extension of few tenths of nanometers can be created at the base of the nano-whisker previously described, using one of its metal edges as part of the electronic device itself.

This work is organized as follows. In Sect. 2, the structure of the detector is presented and its principle of operation is discussed. Section 3 is dedicated to the presentation of a test structure of the rectifying device and to the characterization of its performance. The effect of doping distribution due to different implantation processes is presented.

2 The Rectifying Device

In Fig. 1 the structure of the rectenna and its connection with the photodetector is presented. The structure is designed as a combination of an antenna fabricated on the surface of the chip with a rectifying junction capable to produce the direct conversion of terahertz electromagnetic field into dc current [10]. The necessity to adopt an approach as close as possible to the existing CMOS photodetectors technology suggests to use a rectifying semiconductor structure realized by a double barrier formed by the metal of the whisker, chosen with working function similar to an n^+-doped semiconductor, a properly designed p^+-doped surface layer and by the weakly n-doped

semiconductor of the storage well (SW). Both the SW and the p^+-type implanted surface layer are commonly used in CMOS image detectors respectively to collect the detected charge and to separate it from the semiconductor surface [9].

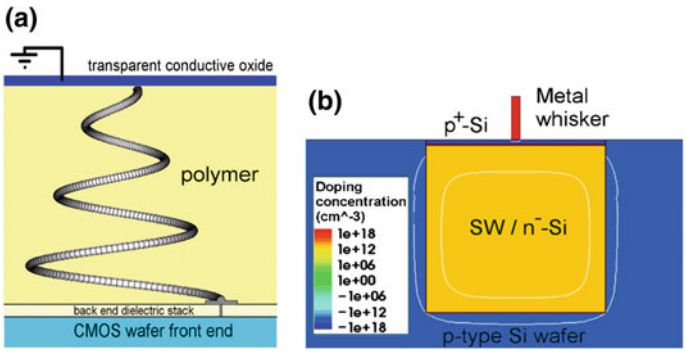

Fig. 1. **a** Schematics of rectenna geometry; **b** front view of the metallic whisker facing the storage well

In the double barrier, a rectifying effect arises from the different extension of two depletion regions, very short for the so called "first junction", formed between the metal and the p+ layer, and much more extended for the so called "second junction", formed between the p^+-doped layer and the SW. The rectifying effect can be explained as follows: the electric field variations induced by the antenna and focused by the whisker on the rectifying device, induce variations of voltage drop through the depleted zones of the two barriers. The majority of the voltage drop occurs through the second depletion region, mainly extending into n-doped region of the SW, much wider that the depletion region related to the first junction. As a consequence, with positive voltage applied to the metal, a reduction of the barrier of the second junction occurs, and electrons preliminarily stored in the SW can be extracted. On the contrary, with negative voltage, electrons present in the metal layer are injected in a much lower number into SW, since the barrier of the first junction is reduced by a much smaller amount due to its shorter extension.

Numerical simulations of the semiconductor device were performed by means of Synopsys Sentaurus TCAD tools using the two-dimensional hydrodynamic model. This model includes "hot electron" phenomenon that become important in submicron devices. It is not included in the conventional drift-diffusion model. Moreover, the hydrodynamic model reproduces the velocity overshoot effects. Simulator engine allows to perform 2.5D simulations setting to 100 nm $\times$ 100 nm the area of the metal contact. As reference, these contact dimensions are achievable by means of 193 nm ArF DUV photolithography process. The use of a not deeply scaled CMOS technology is not a limiting factor. In fact, simulations results [11] demonstrate that these dimensions are suitable to achieve a very high focusing capability of the antenna coupled to the device, and that a further reduction would not bring to a substantial advantage.

Since the structure is supposed to be zero-biased, the resulting barrier must be sufficiently low in order to produce an appreciable rectified current, even under presumably low voltage variations induced by the THz radiation. Figure 2 reports the 2D distribution of conduction band energy besides the rectifying device, assuming a p^+-doped region 30 nm thick, with constant doping concentration of 1.0E18 cm^{-3}. The presence of the barrier along the vertical central cut of the contact is easily observed.

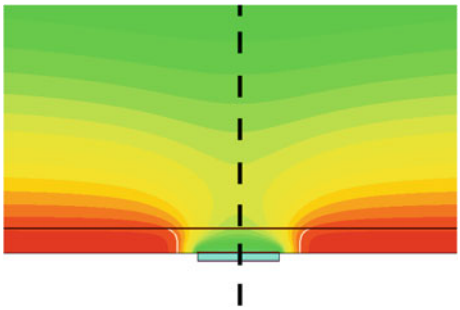

Fig. 2. 2D plot of conduction band energy inside the region in which the rectification takes place. Distribution calculated in equilibrium state with titanium metallic contact

Figure 3 reports the amplitudes of electrons current densities induces by 50 mV voltage variations applied to the metallic contact, with the p-type substrate connected to ground, as simulated by TCAD, along the 1D cut shown by the dashed line in Fig. 2. Curves are obtained for different frequencies between 1 GHz and 1 THz.

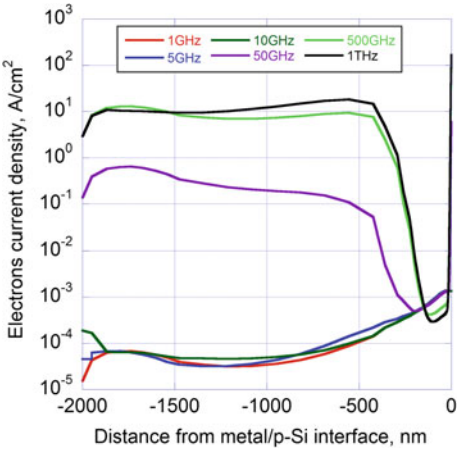

Fig. 3. Amplitude of electrons current densities variations along a section of the rectifying barrier

For all curves, one can note a relevant frequency dependence of the electrons current density at the contact (i.e. calculated at distance zero from the metal/p-Si interface) and inside the SW. In particular, electrons current density at the contact is higher at higher frequencies, as expected due to the presence of the barrier capacitance in series to the contact. At each simulated frequency, the electrons current density is lower inside the SW that at the contact, that is the effect of the current redistributing over a larger section. A saturation effect is evident over 500 GHz; it can be attributed to the resistance of the SW that limits the current at higher frequencies. Furthermore, over 500 GHz we observe the thinning of the depletion layer at the junction, caused by the lack of the charge fed to the barrier depletion layer. With the decrease of the frequency the electrons current inside the SW drops dramatically, due to the effect of the distributed capacitance that SW forms with the surrounding substrate.

It is important to notice that the electrons current across the barrier remains unchanged up to around 500 GHz, and with greater evidence at 1 THz, where the current start decreasing. In these cases, semi-periods of the excitation signal equal to, respectively, 1 and 0.5 ps, become shorter than the time of flight of electrons through the barrier [12].

The rectification capability of the structure is demonstrated in Fig. 4, where a magnification of simulated curves of electrons current density absolute values beside the junction barrier is presented. Reported values are evaluated at the end of two linear voltage ramps, the positive one going between 0 V and 50 mV (continuous line) and the negative one going between 0 and −50 mV (dashed line). Different colors represent voltage ramp rise time of 1 ns, 100, 10 and 1 ps. All curves in Fig. 4 are simulated with SW contacted to ground by means of an ohmic contact, so that there is no current drop effect at low frequencies due to SW capacitance.

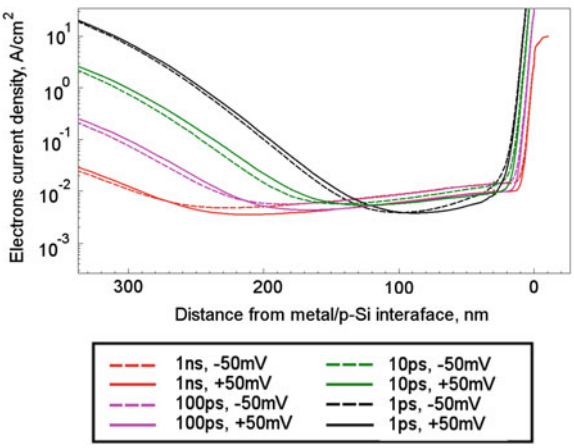

Fig. 4. Absolute values of the electrons current density along the section of the rectifying barrier induced by voltage ramps with different characteristics

One can note that the residual electrons current density through the barrier is many orders of magnitude below the absolute current density injected at the contact; nevertheless, the difference between values of this conduction current density calculated under positive and negative solicitation ramps is of up to about 50%. The rectification effect of the device is supposed to be due to this difference.

In Fig. 4, an increase the rectified current can be observed as the voltage ramp rise time changes from 1 ns to 10 ps. This increment represents an effective improvement of the rectifying capability, which can be explained as due to the decrease of the depletion layer at higher values of voltage ramp rates, i.e. at higher frequencies.

Curves derived for 1 ps rise time show the decrease of electrons current density beside the rectification region. This phenomenon can be explained observing that 1 ps rise time is shorter than the time of flight of electrons through the barrier. The resulting drop of the number of electrons crossing the barrier within the ramp time produces the drop of the current.

3 On-Wafer Measurements

We developed a test structure to verify the rectification properties of the detector. The test structure, reported in Fig. 5, does not include the antenna and is designed for tests at frequencies well below THz range in order to be handled with standard microwave probes and available instrumentation. The signal is applied by a radio frequency generator to emulate the excitation coming from the receiving antenna. This latter measurement setup choice may appear somewhat arbitrary, however in the following we show that with proper modelling it is still possible to provide expected results at THz range combining RF range measurements and numerical simulations.

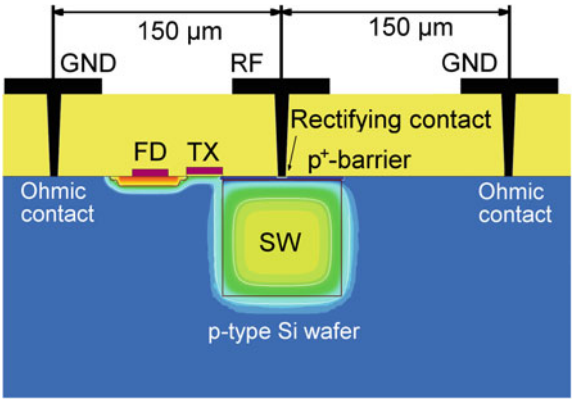

Fig. 5. A schematic description of the test structure. Dimensions of the RF and GND pads and of SW are not in scale

The test structure is realized with minor changes from a standard configuration of a CMOS commercial photodetector using the Aptina/ON Semiconductor 0.15 µm

technology node. The additional technological step requested for the pixel reconfiguration for THz range operation consists in an extra p-type doping implantation below the whisker, forming the p^+-Si layer described in the previous section. The main effect of this step is the barrier height and shape trimming, the phenomenon that hardly affects the rectifying capability of the device. Such implantation can be performed through a properly designed window through which also the metal used for the realization of contact, titanium (Ti), is further deposited. Metal deposition is performed to obtain a via hole between the pad metallization and the rectifying contact. Figure 6 reports layout and SEM cross-section image of the detector, with the SW, metal whisker, rectifier and the TX transistor. Labels TX and FD denote, respectively, the gate and the floating diffusion nodes of transfer gate transistor included in the standard photo detector configuration.

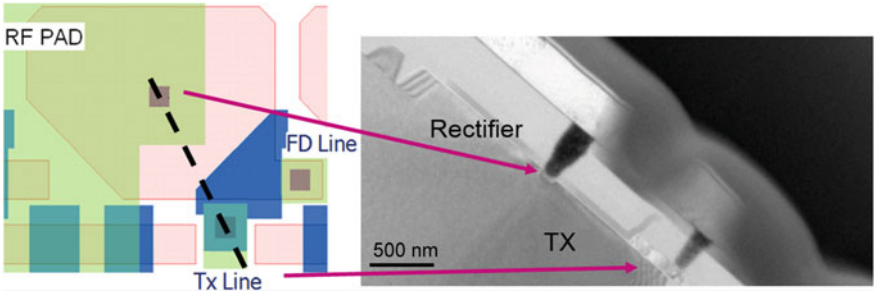

Fig. 6. Layout and SEM cross-section of SW, metal whisker rectifier and TX transistor

Finally, at top metallization level, a planar pattern with three pads is realized with sizing suitable to be contacted by standard RF microprobes. In particular, Microtech Cascade ACP-150 GSG microprobes were used during measurements. The central pad (labeled RF in Fig. 5) is connected to the rectifying contact to be tested, and the two external pads (labeled GND in Fig. 5) are electrically connected to the p^+-Si layer and to the doped substrate surrounding the SW, by means of via holes and ohmic contacts.

The equivalent circuit of the measurement setup is shown in Fig. 7. The gate voltage on TX gate node, V_{TX}, switches the transistor between two states: in TX OFF state the SW is isolated from FD node, permitting the accumulation of the rectified charge, meanwhile in TX ON state the transfer of the accumulated charge from SW to the readout node is performed. Capacitances of FD and of SW are denoted as C_{FD} and C_{SW}, respectively. A Keithley 617 pico-ammeter, shown by the circled capital A, is connected to FD through a low pass filter, represented by the inductance L_{LPF} connected in series.

In order to test experimentally the device rectification capability and to evaluate the rectification efficiency, we performed measurement on two samples with different parameters of the p-type doping implantation, as reported in Table 1. In particular, sample 4E had a higher dose and lower energy with respect to sample 1C. All measurements reported in the following are performed at test frequency of 40 GHz.

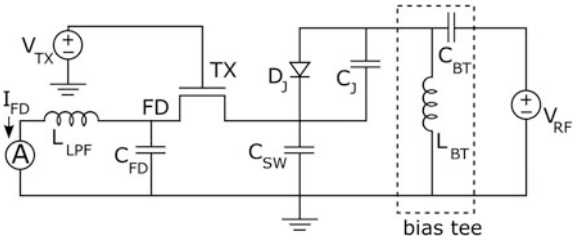

Fig. 7. Equivalent circuit of the measurement setup

Table 1. Implantation scheme

Group	Energy, keV	Dose, cm^{-2}
1C	13.5	1.0E13
4E	5.0	5.0E13

Figure 8 reports the rectified current measured by pico-ammeter versus the RF power applied to the signal pad, for 4E and 1C devices. The voltage level at TX gate node was 4 V for both curves, ensuring TX ON state.

A linear approximation of curves in Fig. 8 can be used to evaluate the detector efficiency. We approximate as linear the relationship between the RF power expressed in decibel-milliwatts, P_{dBm}, and ten times the logarithm of the current, I_{dBA}, as given by

$$P_{dBm} = P_{dBm,0} + k\left(I_{dBA} - I_{dBA,0}\right), \tag{1}$$

where ($P_{dBm,0}$, $I_{dBA,0}$) is an arbitrary chosen reference point on (P_{dBm}, I_{dBA}) curve, and the coefficient k can be calculated from geometrical regression of measured data. Figure 8 shows a different slope of the two curves.

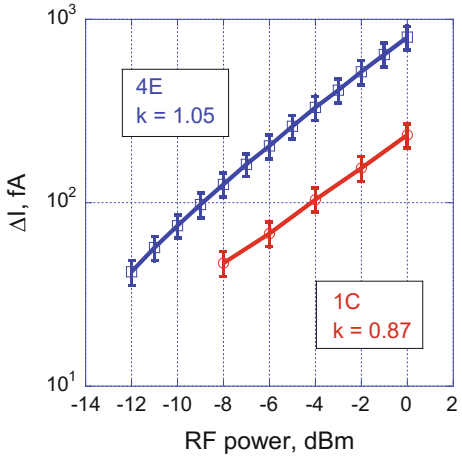

Fig. 8. Rectified current versus applied RF power for the two structures: 4E and 1C

Recalling that the plot is logarithmic, the different k means a different exponential coefficient in the nonlinear relationship rectified current —RF power. This parameter allows to account the actual modulation of the barrier under the rectification process. From the sample 4E we obtained $k = 1.05$, while for the sample 1C the coefficient resulted $k = 0.87$. This effect can be explained as due to the steeper and superficial distribution of the superficial dopant in sample 4E if compared to the sample 1C. As highlighted by TCAD process simulations, the higher dose and the lower energy of the implantation process lead to the rectifying device with higher but more asymmetric double barrier. As the rectification efficiency is strongly affected by the asymmetry degree of the barrier, the obtained rectified current is higher for the sample 4E, although its greater barrier height. At large RF power values, the deformation of the barrier partially compensates the higher current expected in the lower barrier of the sample 1C. Nevertheless, the values of sensitivity calculated for the two samples are comparable due to different k values.

Numerical simulations the semiconductor device reported in Fig. 3 can be used jointly with measurements in Fig. 8 to evaluate the noise equivalent power (NEP) of the sensor.

From the measurements, we may extract the 40 GHz voltage applied to the junction by the RF power generator. For the sake the test structure S_{11} measurement, obtained with an input power of −10 dBm and reported in Fig. 9, is used.

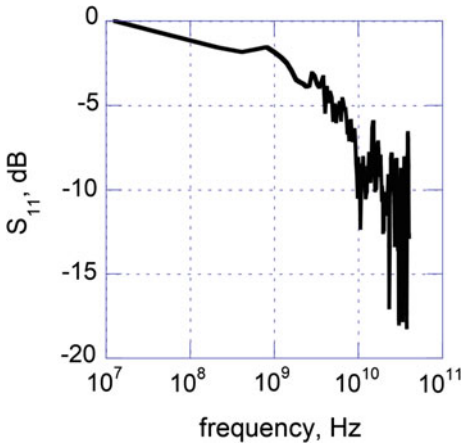

Fig. 9. Scattering parameter S11 measured on the RF test pad

The measure indicates the good matching of the structure at frequencies between 10 and 40 GHz, meaning that the real part of the test structure is nearly 50 Ω, mostly due to the series resistance of the semiconductor structure. S_{11} has a cutoff frequency of $f_H = 1$ GHz, thus at 40 GHz most of the voltage drops onto the resistance. The voltage applied to the pad and to the rectifying structure can be approximated by:

$$V_J \cong \sqrt{\frac{2R_S}{P}\frac{f_H}{f}}, \tag{2}$$

where V_J is the voltage at the rectifying junction, P is the applied RF power, R_S is the series resistance of the test structure. This expression takes into account its one-pole behaviour with respect to the voltage imposed by the RF voltage generator.

From measurements reported in Fig. 8 we extrapolate that the RF power at 40 GHz necessary to generate a rectified current equal to the noise current. The latter, defined as a mean square value of noise measure in photodetector, was measured to be of 5 el/s, value comparable with data reported in literature [9]. For sample 4E, we find a noise equivalent RF power of −60 dBm. Accordingly to (2), this power corresponds to a voltage drop at the rectifying junction of 7.9 μV.

The rectified current depends dramatically on the shape and the height of the barrier. The nonlinearity parameters were thus obtained directly from the measurements. Besides that, from the simulation we extract the frequency behavior in order to extend the results at 1 THz. We note that simulations reported in Fig. 4 clearly indicate that, under the same amplitude of voltage applied to the junction, the rectified current has the same value for a ramp of 25 ps (as interpolation from the 10 and 100 ps curves) and for the ramp of 1 ps. Thus we can extend at 500 GHz, the value of 7.9 μV as the voltage at the junction necessary to equate the noise. We can now use the simulation of Fig. 3 to scale down the value of the density of current at the contact at this frequency. From the amplitude of 167 A/cm^2, obtained under 50 mV solicitation, scaled to the voltage value just found of 7.9 μV, we obtain a density of current 260E−3 A/cm^2, that corresponds to an electric field amplitude of 0.1 V/cm. The latter quantity is the electric field value that must be concentrated by the antenna and the whisker onto the rectifying junction.

We can now recall that the field enhancement capability of the 3D antenna coupled to the device, FE, was shown to be at least a value of 40,000 [11]. Simulations reported in [11] were performed in conditions of the ideal load, i.e. the whisker with radius of 50 nm distant 10 nm from a ground plane; such structure has an equivalent impedance different from that shown by the actual semiconductor device. The impedance of the designed rectifier can be evaluated from simulation reported in Fig. 3, as the ratio of applied voltage and current obtained with contact area equal to the whisker base area in the test structure, 100 nm × 100 nm. The high impedance of the device reduces the FE to a rather low value of 52. The combination of this result with the value of the electric field that must be induced into the junction to produce equivalent current allows the calculation of the external electric field reaching the antenna, and thus of the final value of the $NEP_{500\,\mathrm{GHz}} = 2.7\,\mathrm{pW}/\sqrt{\mathrm{Hz}}$, referred to the sample 4E. With the same procedure, we obtained $NEP_{500\,\mathrm{GHz}} = 1.7\,\mathrm{pW}/\sqrt{\mathrm{Hz}}$ for the sample 1C.

Taking into account the decrease of the rectified current with frequency shown by TCAD simulations, we obtain $NEP_{1\,\mathrm{THz}} = 10.8\,\mathrm{pW}/\sqrt{\mathrm{Hz}}$ for sample 4E, and $NEP_{1\,\mathrm{THz}} = 6.7\,\mathrm{pW}/\sqrt{\mathrm{Hz}}$ for sample 1C.

4 Conclusions

In this work, a new THz detector for direct conversion operating at room temperature and compatible with existing CMOS ISs is presented and experimentally evaluated. We demonstrate that a modification of a limited region of the surface of the CMOS ISs pixel, placed in contact with the metallic antenna pad, provides an efficient rectifying device in THz range. The antenna and the rectifying device, i.e. the rectenna structure, exposed to electromagnetic radiation gives rise to charge injection into the storage well of APS device that is evaluated by the readout electronics. We present measurements at a frequency of 40 GHz demonstrating the effectiveness of the rectifying device and confirming the rectification effect due to the formation of a double barrier just below the antenna whisker. Experimental results supported by 2D numerical TCAD simulations permit an evaluation of NEP at 1 THz. The experimental investigation at 1 THz of the device with the integrated antenna is the target of the future work.

Acknowledgements. The authors want to thank Aptina-OnSemi for allowing the realization of the test structure in the state-of-art CMOS ISs technology.

References

1. B. Fischer, M. Hoffmann, H. Helm, G. Modjesch, P. Jepsen, Chemical recognition in terahertz time-domain spectroscopy and imaging. Semicond. Sci. Technol. **20**, S246 (2005)
2. R. Piesiewicz et al., Short-range ultra-broadband Terahertz communications. IEEE Antennas Propag. Mag. **49**, 24 (2007)
3. F.J. Federici et al., THz imaging and sensing for security applications-explosives, weapons and drugs. Semicond. Sci. Technol. **20**, 266–280 (2005)
4. A. Menikh, S.P. Mickan, H. Liu, R. Maccoll, X.C. Zhang, Labelfree amplified bioaffinity detection using terahertz wave technology. Biosens. Bioelectron. **20**, 658–662 (2004)
5. K.M. Strohm, J. Buechler, E. Kasper, SIMMWIC rectennas on high-resistivity silicon and CMOS compatibility. IEEE Trans. Microwave Theory Tech. **46**, 669–676 (1998)
6. V. Varlamava, F. Palma, P. Nenzi, M. Balucani, Terahertz sensor for integrated image detector. Procedia Eng. **87**, 1131–1134 (2014)
7. P. Nenzi, F. Tripaldi, V. Varlamava, F. Palma, M. Balucani, On-chip THz 3D antennas, in *Proceedings of Electronic Components Conference* (2012), pp. 102–108
8. A. Del Monte, F. Palma, Italian Patent No. RM2014A000323 (2004)
9. E.R. Fossum, D.B. Hondongwa, A review of the pinned photodiode for CCD and CMOS image sensors. IEEE J. Electron Devices Soc. **2**, 33–43 (2014)
10. F. Palma, Italian Patent No. RM2010A000268 (2010)
11. V. Varlamava, F. Palma, P. Nenzi, M. Balucani, Electric field enhancement in 3-D tapered helix antenna for terahertz applications. IEEE Trans. Terahertz Sci. Technol. **4**, 360–367 (2014)
12. M.A. Stettler, M.S. Lundstrom, A microscopic study of transport in thin base silicon bipolar transistors. IEEE Trans. Electron Devices **41**, 1027–1033 (1994)

Chemical Sensors

A New Chemical Sensing Material for Ethanol Detection: Graphene-Like Film

B. Alfano[1,2(✉)], M. Alfè[3], V. Gargiulo[3], T. Polichetti[1], E. Massera[1], M.L. Miglietta[1], and G. Di Francia[1]

[1] ENEA C.R. Portici, P.le E. Fermi 1, 80055 Portici, Naples, Italy
brigida.alfano@enea.it
[2] Department of Physical Sciences, University of Naples Federico II, via Cinthia, 80126 Naples, Italy
[3] Institute for Research on Combustion (IRC)—CNR, p.le V. Tecchio 80, 80125 Naples, Italy

Abstract. The development of volatile organic compounds (VOCs) sensor, operating at room temperature (RT), is a challenge for the research community. In this framework, we present a device based on a graphene-like (GL) material suitably tested as sensing layer for the ethanol detection. GL material was obtained through a two steps oxidation/reduction method starting from a nanostructured carbon black. GL material combines a defect-free basal plane graphenic structure with the presence of oxygen functional groups, mainly carboxylic, located on the layer edges. A GL-based device was realized and investigated for the detection of ethanol. The experiments were performed under atmospheric pressure, in a dry air and at RT. Results showed that GL material is a promising candidate for the detection of low concentration of ethanol at RT.

Keywords: Graphene-like materials · Oxidized carbon black · Gas sensors · VOCs detection · Ethanol sensing device · Room-temperature device

1 Introduction

Metal-oxide semiconductors are widely used as sensing layers for the detection of VOCs, due to their high sensitivity, fast response, recovery and stability. However, one major drawback of this type of sensors is the high temperatures required for their operation (200–450 °C) [1–3] and the consequent high power consumption. Although the introduction of nanocrystals and nanowires have improved the sensing performances and lowered the operating temperatures of metal oxides based sensors [4–6] in the last years, also other materials have been considered for the development of new gas sensors. Carbon-based nanomaterials proved to be promising for this scope due to their intrinsic electrical properties, high surface area, high chemical and thermal stability and functionalization capability [7]. Among the large family of carbon-based nanomaterials, graphene and graphene related materials (GRMs) in the last years have been explored for the detection of a widespread range of chemicals, including VOCs [8].

B. Andò et al. (eds.), *Sensors*, Lecture Notes in Electrical Engineering 431,
DOI 10.1007/978-3-319-55077-0_8

Graphene-like (GL) layers are carbon-based nanomaterials obtained through a two steps oxidation/reduction method starting from a carbon black (CB) [9, 10], consisting in small graphenic flakes (about four graphenic layers of thickness) decorated at the layer edge with oxygen functional groups (mainly carboxylic/carbonylic). Differently from graphite oxide (GO), in GL material the basal planes of the graphitic network are preserved from defect, which represents a clear advantage for the conductivity and the electronic properties. GL layers in aqueous suspension are a versatile material as testified by its use in the preparation of a large variety of hybrid materials. When intercalated in insulating Metal-Organic Frameworks (MOFs), GL layers allow to produce composites with tunable electrical conductivity [11]; when combined with Eumelanin by a copolymerization approach, GL layers produced a biocompatible interface with conductive and adhesive properties very promising for biosensoristic applications [12] and when covered by TiO_2-nanoparticles by a co-precipitation strategy GL layers produced a material with improved photocatalytic activities [13].

In this framework, we have realized a prototypal chemiresistive sensing device for ethanol detection based on GL film. The device was tested under atmospheric pressure, in dry air and at RT. The results showed that GL material is a promising candidate for the detection of low concentration of ethanol at RT.

2 Experimental

2.1 Realization of the Prototypal Chemiresistive Sensing Device

Analytical grade chemicals were purchased from Sigma Aldrich and used as received. CB (furnace black, N110 type, 15–20 nm primary particle diameter, specific BET area 139 m^2/g) was obtained by Sid Richardson Carbon Co.

GL layers in aqueous suspension were produced from a nanostructured CB following a synthetic approach that consists in an oxidation step followed by a chemical reduction with hydrazine. A detailed description of the synthetic procedure is reported elsewhere [9, 10]. Briefly: 500 mg of CB were oxidized for 90 h with 10 mL of HNO_3 (67 wt%) at 100 °C under reflux and stirring. The oxidized material was recovered by centrifugation and washed many times with distilled water in order to remove any acid traces. After the oxidation step 60 mg of oxidized material were dispersed in 60 mL of distilled water and treated with 1.35 mL of hydrazine hydrate (50%) for 24 h at 100 °C under reflux. The excess of hydrazine was neutralized with nitric acid (4 M) allowing the precipitation of a black solid (GL layers). GL layers were recovered by centrifugation and washed two times with distilled water in order to remove salts and acid traces. The GL layers were stored as aqueous suspension at 1 mg/L of concentration and pH 3.7.

GL film was obtained by drop-casting the GL water dispersion onto transducers and dried at RT, realizing a prototypal chemiresistive device. The transducers employed for the electrical and sensing characterization of the GL films, have 5 pairs of gold interdigitated electrodes (IDEs) electrodeposited onto rough alumina substrate: each electrode finger is 350 μm wide and 4650 μm long. The spacing between fingers is 350 μm.

2.2 Characterization Equipment

X-ray photoemission spectroscopy (XPS) was performed in a ultra-high vacuum chamber (base pressure of 1×10^{-10} mbar) equipped with a Specs Phoibos 150 electron analyzer, using Al K_α (photon energy: 1486.6 eV) X- ray source.

GL aqueous suspensions (100 μL of a 1 mg/mL GL suspension) were drop-casted onto the device, allowed to dry in air at ambient temperature and analyzed by atomic force microscopy (AFM). The AFM images were acquired on a XE100 Park instrument operating in noncontact mode (amplitude modulation, silicon nitride cantilever from Nanosensor) at room temperature and in ambient conditions.

The ethanol for gas-sensing characterizations comes from certified cylinder containing calibrated vapour balanced in dry air at 100 ppm (Ossi gas srl). The gas flow mixing rates were precisely and rapidly manipulated using computer mass flow controllers (MKS) and electro-pneumatic valves. A bias voltage fixed at 1 V was applied to the electrodes with a Precision Power Supply TTi QL355T and the conductance values were registered using a high resolution picoammeter Keithley 6485.

The gas-sensing performances of the sensing device were characterized towards ethanol under atmospheric conditions (24 ± 2 °C and 1.00 ± 0.05 bar) in a sealed stainless steel chamber. A constant flux of synthetic dry air of 500 sccm as gas carrier was flowed and mix with the desired concentration of ethanol. After 30 min in dry air (baseline), the sensing device was exposed to the analyte concentration for 30 min and the air flux was then restored for 60 min. The percentage response (S) is defined as the maximum of the conductance variation reached by the device during the analyte exposure that is $[|G - G_0|/G_0] \times 100$, where G and G_0 are the conductance recorded during analyte exposure and baseline acquisition steps, respectively.

3 Results and Discussion

GL film was prepared as described in the Experimental section. A detailed characterization of the material was reported in [9, 10] and here summarized for sake of clarity. The synthesis procedure allow high yields (55 wt% of recovery) of GL layers with a multi-layered graphenic structure (about four layers) characterized by a preserved graphitic network, i.e. with functionalization only at the borders of the graphenic layers [9, 10]. The H/C atomic ratio is 0.32 and the O/C atomic ratio: 0.56. The functionalization consists of residual oxygen functional groups, mainly carboxylic groups (pKa 3.4, number of sites 900 mmol/g). Lactones and anhydrides are also present (pKa 5.5, number of sites 240 mmol/g). The oxygen functional groups allow establishing a zeta potential around −30 mV at pH 2 and around −45 mV at pH 12 [10].

Characterization by X-ray Photoemission Spectroscopy (XPS) on powders and imaging by Atomic Force Microscopy are reported in the following.

XPS spectrum is reported in Fig. 1 along with its deconvolution into Gaussian components after Shirley background subtraction using a home-made software.

C1s XPS spectrum on GL sample and its deconvolution in Gaussian shape peaks demonstrate the presence of different oxygen functional groups. In particular, there are

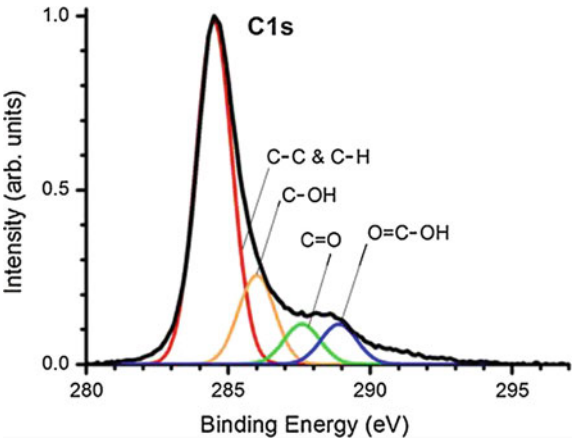

Fig. 1. C1s XPS spectrum on GL film, and its deconvolution in Gaussian shape peaks corresponding to different functional groups (modified from [10])

four components located at 284.5 eV (carbon involved in C=C and C–H bonding), 286 eV (C–OH), 287.5 eV (C=O), 289 eV (COOH).

AFM morphological characterization on a film obtained on mica substrate by drying in air a drop-casted GL layers suspension (pH 3.7, 1 mg/mL) provided an estimation of the surface roughness, as shown in Fig. 2.

AFM topographic image shows a flat morphology over a large area (5 × 5 μm). The roughness, estimated by the scan profile (Fig. 2b) is about 0.1 nm peak to peak over a distance of 3 μm. This value clearly indicate flatness at atomic level, characteristic of the GL layers allowed to self-assembly on a flat surface from suspension at pH 3.7 [10].

I–V measurements performed on GL film showed linear behavior (Fig. 3a), which implies an Ohmic contact between GL sheets and gold electrodes. Figure 3b displays the dynamic response of the device exposed to 50 ppm of ethanol at RT in dry air. GL material is responsive to ethanol, exhibiting a conductance variation equal to 3% (Fig. 3b). This result is even more astonishing when compared to the detection limits of other devices operating at RT reported in the literature [15], including pristine graphene which results as totally insensitive to ethanol.

Employing the mathematical model shown in our previous work [16], it is possible calibrate the device correlating directly the time derivative of the device conductance to the interacting analyte concentration. In particular, defining the reactivity as the maximum of the device conductance rate, it is possible to correlate the reactivity to the analyte concentration. Besides, reaction time is here defined as the time in which the aforementioned maximum of the conductance rate is reached; by extension, the reaction time can be regarded as the time taken by the device to detect a given analyte concentration. The exposure to several sequential steps at different analyte concentrations (black solid squares in Fig. 4), ranging from 0 ppm down to 100 ppm, discloses a linear correlation between the device reactivity and the analyte concentration.

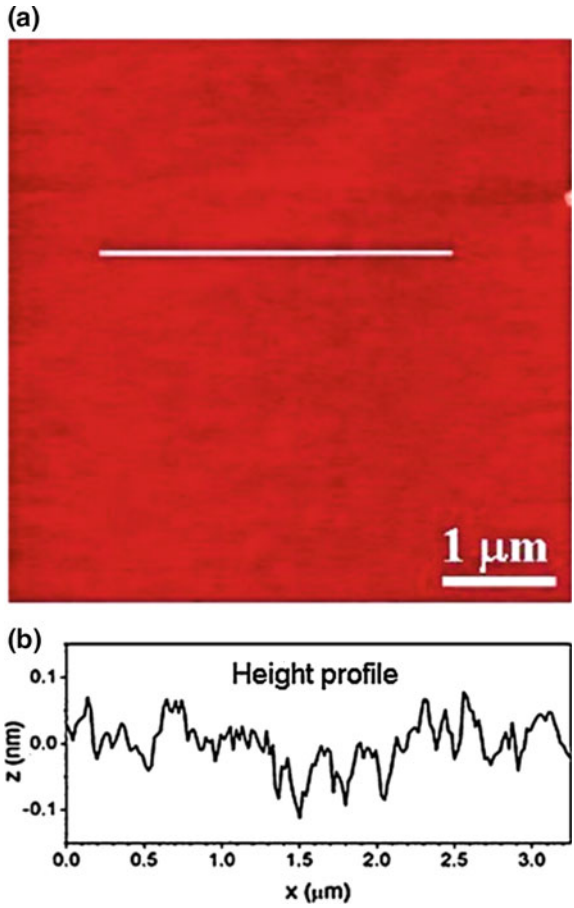

Fig. 2. AFM topographic image (scan area 5 μm × 5 μm, **a**) with a line profile (**b**) (modified from [10])

The black solid squares represent the data of the maxima of the device conductance rate corresponding to different concentrations. The red straight line represents the best fit for the collected data. Taking into account the error bars, it can be evaluated that the limit of detection (LOD) for this device is around 10 ppm.

The device reaction time shows a non-linear relation with the analyte concentration (blue squares in Fig. 4). For concentrations in the range 40–100 ppm the device responds in about 40 s while in the low concentration range, i.e. from 10 to 20 ppm, a clear increase of the reaction time is observed. Nevertheless, the device takes less than 60 s to detect 20 ppm of ethanol.

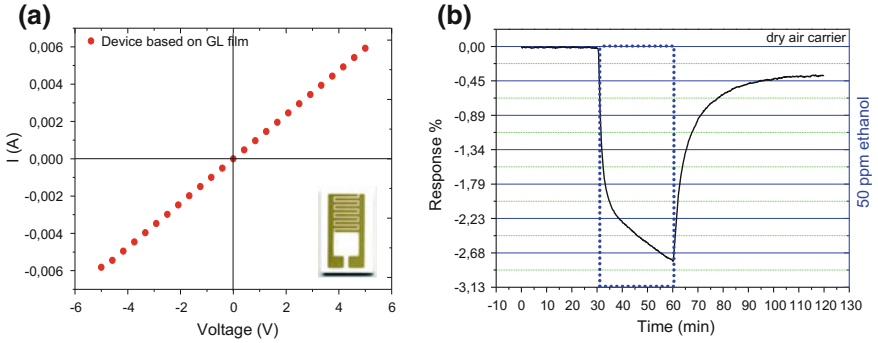

Fig. 3. Electrical characterizations: **a** typical I–V curves of device based on GL film. Data were collected in the range [−5, 5 V], in the inset, an image of the transducer; **b** response to 50 ppm of ethanol in dry air using a GL based sensor

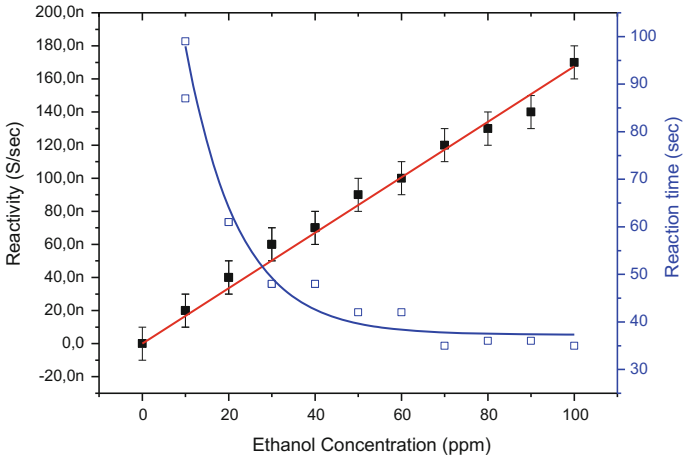

Fig. 4. Ethanol-sensing calibration at RT of the GL film based device in the range 0–100 ppm in dry air carrier. The *red straight line* fits the points of maximum of the conductance rate (reactivity) collected at different ethanol concentrations. Reaction times are plotted versus ethanol concentration (*blue squares*) (Color figure online)

4 Conclusions

We have realized a prototypal chemiresistive sensing device for ethanol detection based on GL film obtained by the self-assembly of GL layers, a carbon-based nanomaterial consisting in small graphenic flakes obtained through a two steps oxidation/reduction method starting from a nanostructured carbon black. The prototypal device was tested under atmospheric pressure, in dry air and at RT and exhibiting a conductance variation equal to 3% to low ethanol concentration (50 ppm). The LOD results around 10 ppm. This result showed that GL material is a promising candidate for the detection of low concentration of ethanol at RT.

References

1. A. Umar, J.-H. Lee, R. Kumar, O.A. Dossary, A.A. Ibrahim, S. Baskoutas, Mat. Des. **105**, 16–24 (2016)
2. C.C. Yang, X. Su, F. Xiao, J. Jian, J. Wang, Sens. Actuators B **158**, 299–303 (2011)
3. N. Hongsith, C. Viriyaworasakul, P. Mangkorntong, N. Mangkorntong, S. Choopun, Ceram. Int. **34**, 826–834 (2008)
4. G. Neri et al., Sens. Actuators B **130**, 222–230 (2008)
5. J.M. Wu. Nanotechnol. **21**, 235501 (6 pp) (2010)
6. M. Mabrook, P. Hawkins, Sens. Actuators B Chem. **75**, 197–202 (2001)
7. E. Llobet, Sens. Actuators B **179**, 32–45 (2013)
8. S.S. Varghese, S. Lonkar, K.K. Singh, S. Swaminathan, A. Abdala. Sens. Actuators B **218**, 160–183 (2015)
9. F. Schedin, A.K. Geim, S.V. Morozov, E.W. Hill, P. Blake, M.I. Katsnelson, K.S. Novoselov. Nat. Mater. 6652–655 (2007)
10. M. Alfè, V. Gargiulo, R. Di Capua, F. Chiarella, J.-N. Rouzaud, A. Vergara, Anna Ciajolo, ACS Appl. Mater. Interfaces **4**, 4491–4498 (2012)
11. M. Alfè, V. Gargiulo, R. Di Capua, Appl. Surf. Sci. **353**, 628–635 (2015)
12. M. Alfè, V. Gargiulo, L. Lisi, R. Di Capua, Mater. Chem. Phys. **147**(3), 744–750 (2014)
13. V. Gargiulo, M. Alfè, R. Di Capua, A.R. Togna, V. Cammisotto, S. Fiorito, A. Musto, A. Navarra, S. Parisi, A. Pezzella, J. Mater. Chem. B **3**, 5070 (2015)
14. M. Alfè, D. Spasiano, V. Gargiulo, G. Vitiello, R. Di Capua, R. Marotta, Appl. Catal. A Genl. **487**, 91–99 (2014)
15. T. Wang, D. Huang, Z. Yang, S. Xu, G. He, X. Li, L. Zhang, Nano-Micro Lett. **8**, 95–119 (2016)
16. F. Ricciardella, E. Massera, T. Polichetti, M.L. Miglietta, G. Di Francia, Appl. Phys. Lett. **104**(18), 183502 (2014)

Iron Oxides Nanoparticles Langmuir-Schaeffer Multilayers for Chemoresistive Gas Sensing

S. Capone[1(✉)], M. Benkovicova[2], A. Forleo[1], M. Jergela[2], M.G. Manera[1], P. Siffalovic[2], A. Taurino[1], E. Majkova[2], P. Siciliano[1], I. Vavra[3], S. Luby[2], and R. Rella[1]

[1] CNR-IMM, Via Monteroni, 73100 Lecce, Italy
{simona.capone, angiola.forleo, mariagrazia.manera, antonietta.taurino, pietro.siciliano, roberto.rella}@le.imm.cnr.it
[2] I. of Physics, S. Ac. of Sc, Dubravska 9, 84511 Bratislava, Slovakia
{monika.benkovicova, matej.jergel, peter.siffalovic, stefan.luby}@savba.sk, majkova@up.upsav.sk
[3] I. of Electrical Eng, S. Ac. of Sc, Dubravska 9, 841 04 Bratislava, Slovakia
ivo.vavra@savba.sk

Abstract. Gas sensors based on mixtures of iron oxides nanoparticles (NPs) modified with Pd NPs at the different NPs Pd: Fe_3O_4/γ-Fe_2O_3 proportions were prepared and characterized. Nanoparticles diameter was 6–7 nm. NPs films were deposited from the mixtures of Fe_3O_4/γ-Fe_2O_3 and Pd NPs colloidal solutions by modified Langmuir-Schaeffer technique onto alumina substrates. Samples were composed from 4 Fe_3O_4/γ-Fe_2O_3 NP monolayers (MLs). Sensors were tested toward acetone vapors and NO_2 at concentration range of 5–200 and 0.5–12 ppm respectively in dry air, and at different working temperatures. Pd-doped Fe_3O_4/γ-Fe_2O_3 sensors showed p-type gas response, higher conductance and higher conduction activation energies compared to pure Fe_3O_4/γ-Fe_2O_3 sensor that gives n-type gas response. Results were tentatively explained in terms of surface interactions with oxidizing and reducing species, and Nearest Neighbor Hopping conduction model (NNH).

Keywords: Iron oxides · Nanoparticles · Langmuir-Schaeffer · Gas sensor · Nearest Neighbor Hopping

1 Introduction

Iron oxide nanoparticles (NPs) have been emerged as significant nanomaterials mainly due to its superparamagnetic properties and their extensive range of application in various fields [1]. A less used application of iron oxides is chemiresistive gas sensors, i.e. sensors based on resistance modulation of semiconducting oxides by chemical adsorbed gas species [2–4]. Several studies on α-Fe_2O_3 (hematite), γ-Fe_2O_3 (maghemite) and Fe_3O_4 (magnetite) phases, indicated suitable sensing characteristics towards LPG, carbon monoxide, ethanol and acetone supporting their employment in gas sensing applications [5–17].

B. Andò et al. (eds.), *Sensors*, Lecture Notes in Electrical Engineering 431,
DOI 10.1007/978-3-319-55077-0_9

In this work we studied the Pd-doping of Fe_3O_4/γ-Fe_2O_3 nanoparticle (NP) multilayers and we tested their gas sensing properties towards two reference species, i.e. nitrogen dioxide (NO_2, oxidizing gas) and acetone (C_3H_6O, a reducing volatile organic compounds. We prepared Pd-doped Fe_3O_4/γ-Fe_2O_3 nanoparticles by high-temperature decomposition of organic precursors. We preferred a simple method of the deposition of sensing nanoparticle mono- or multilayers from the mixture of two colloid solutions of γ-Fe_2O_3 and Pd nanoparticles covered by the similar surfactant by modified Langmuir-Schaeffer technique [4, 5, 18].

2 Materials and Methods

Fe_3O_4/γ-Fe_2O_3 NPs in the form of colloidal solution with nanoparticles size of 6.4 ± 0.6 nm were synthesized by high-temperature solution phase reaction in difenylether from Fe acetylacetonate with 1.2 hexadekandiol as reducing agent. NPs are covered by a surfactant capping approx. 1 nm thick composed by oleic acid and oleyl amine. Pd NPs (6–7 nm sized) capped with oleyl amine surfactant were purchased.

Three different mixtures of the Pd-NPs with the Fe_3O_4/γ-Fe_2O_3 NPs at different Pd:(Fe_3O_4/γ-Fe_2O_3) NPs proportions were prepared. By repeating four times the LS deposition, 4 NPs-based monolayers (MLs) from the different prepared NPs solutions were deposited on alumina sensor substrates in order to get compact films with suitable thicknesses.

Four samples at different Pd:100 Fe_3O_4/γ-Fe_2O_3 nanoparticles proportions were prepared; an undoped Fe_3O_4/γ-Fe_2O_3 sensor was prepared as reference. A list of the as prepared gas sensor samples is shown in the table of Fig. 1. The alumina substrates (2×2 mm^2) were equipped by Ti (20 nm)/Pt (200 nm) comb electrodes to read the measuring current (under constant polarization) and by integrated Ti/Pt heater.

Before testing the sensor structures, the insulating surfactant capping all the nanoparticles was removed in ultraviolet (UV) reactor by ozone generating mercury lamp ($h\nu = 4.9$ and 6.6 eV) for 40 min; the irradiation power was 2 mW/cm^2. The samples were processed by 3 day heating at 500 °C in dry air to stabilize them and to oxidize some initial Fe_3O_4 NP component to Fe_2O_3. This oxidation was confirmed by XANES (X-ray absorption near-edge structure) analysis [18]. Coalescence of NPs was not observed.

The sensor operating temperature T was varied from 200 to 500 °C at the 50 °C step. The gas sensing tests were carried out by a test bench for gas sensors calibration equipped with a gas mixing station and instrumentation for electrical characterization.

The current response of NPs-based sensors was measured by electrometer at the voltage of 1 V. Acetone and NO_2 were mixed with dry air at concentrations ranges of 5–200 and 0.5–12 ppm respectively.

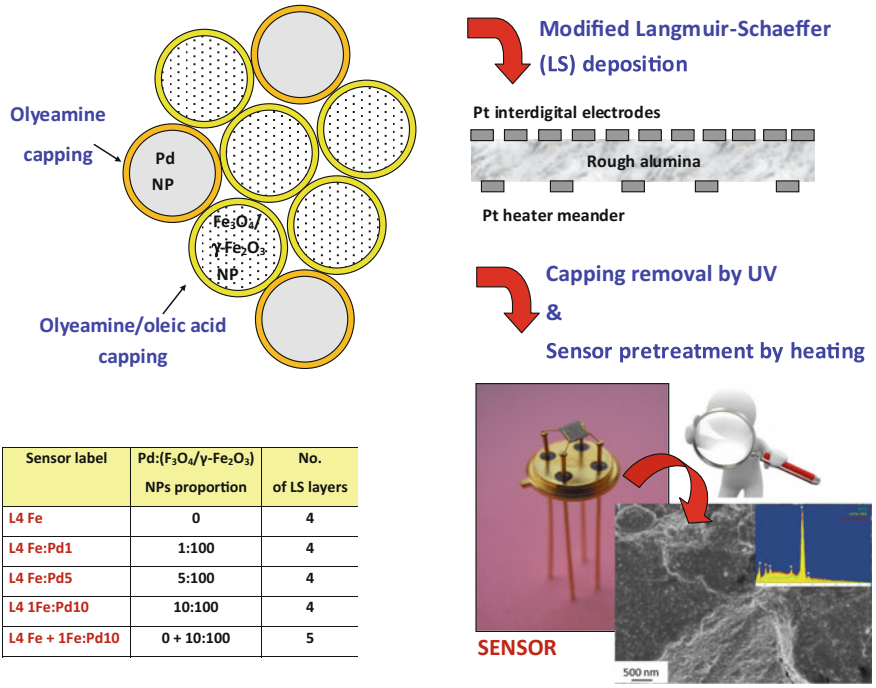

Sensor label	Pd:(F_3O_4/γ-Fe_2O_3) NPs proportion	No. of LS layers
L4 Fe	0	4
L4 Fe:Pd1	1:100	4
L4 Fe:Pd5	5:100	4
L4 1Fe:Pd10	10:100	4
L4 Fe + 1Fe:Pd10	0 + 10:100	5

Fig. 1. Scheme of Pd and iron oxides nanoparticles layers and the steps for the sensors preparation

3 Results

SEM observations (and EDS spectra) of all the Pd-doped sensors were carried out after the gas sensing tests. The inset in Fig. 1 shows the SEM image of the L4Fe + Fe1: Pd10 sensor; the micrograph evidences the morphology of the film, following the rough topography of the alumina substrate. The film shows the presence of spherical details, with size of few tens of nm, very likely corresponding to nanoparticles agglomerate; these features are peculiar of all the observed sensors.

The main experimental evidence concerning gas sensing results is that undoped Fe_3O_4/γ-Fe_2O_3 nanoparticles (NPs) based sensors showed an n-type electrical conduction, on the contrary the Pd-doped Fe_3O_4/γ-Fe_2O_3 nanoparticles (NPs) based sensors showed a p-type electrical conduction. As a consequence, n-type responses for the undoped iron oxides NPs-based sensors, and p-type responses for the Pd-doped iron oxides NPs-based sensors to the considered chemical species were registered. In order to compare the relative responses of the different sensors, we defined the n-type and p-type gas response towards NO_2 (oxidizing species) and acetone (reducing species) as follows:

	n-type response	p-type response
Oxidizing species	$G_{Air}/G_{Ox} > 1$	$G_{Ox}/G_{Air} > 1$
Reducing species	$G_{Red}/G_{Air} > 1$	$G_{Air}/G_{Red} > 1$

so that it's always higher than unit; where G_{Air} and G_{Ox} or G_{Red} are the electrical conductance G in air and under exposure to oxidizing and reducing species respectively (at constant polarization).

The gas sensing experiments were carried out at different working temperatures in order to find out the optimum operating temperature for the specific gas detection.

The gas responses (as defined above) of a typical set of undoped and Pd-doped Fe_3O_4/γ-Fe_2O_3 NPs-based sensors towards 4 ppm NO_2 and 40 ppm acetone in dry air at three different working temperatures is reported in Table 1. For each type of sensing material three equivalent samples were tested and the responses were found comparable (within 10%) within the experimental errors.

Table 1. Responses of a typical set of undoped and Pd-doped Fe_3O_4/γ-Fe_2O_3NPs-based sensors towards 4 ppm NO_2 and 40 ppm acetone in dry air

T (°C)	L4 Fe (n-type resp.)	L4 Fe:Pd1 (p-type resp.)	L4 1Fe:Pd10 (p-type resp.)	L4 Fe+1Fe:Pd10 (p-type resp.)
	4 ppm NO_2 in dry air			
350	422	1.95	1.60	1.68
400	173	1.92	1.45	1.63
450	47	1.68	1.17	1.52
	40 ppm acetone in dry air			
350	1.09	1.33	1.72	1.43
400	1.87	1.44	2.31	1.56
450	4.92	2.85	4.67	2.67

The electrical conductance variation of the prepared sensors upon exposure to different concentrations of NO_2 (0.5–12 ppm) in dry air followed by recovering in air after each gas exposure at an operating temperature of 350 °C is shown in Fig. 2. The n-type gas response of the undoped Fe_3O_4/γ-Fe_2O_3 NPs-based sensors is 2 order of magnitude higher than the p-type responses of the Pd-doped Fe_3O_4/γ-Fe_2O_3 NPs-based sensors. Among the Pd-doped Fe_3O_4/γ-Fe_2O_3 NPs based sensors, the sensor L4Fe: Pd1 has a response a little bit higher than the others, but we can consider the p-type responses roughly comparable among them. At 350 °C there is the highest response, whereas at 400 °C there is a higher speed of response and recovery for the undoped sensor L4Fe. The periods of exposure to gas and recovery in air were 30 and 60 min respectively.

In order to compare the gas sensing properties at the same temperature, in Fig. 3 we report the conductance variation of a typical set of undoped and Pd-doped Fe_3O_4/γ-Fe_2O_3 NPs-based sensors to increasing acetone concentrations (5–200 ppm) in dry air at 350 °C. All the NPs-based iron oxides sensors (undoped and Pd-doped) showed appreciable responses in the explored range of acetone concentration (5–200 ppm) in dry air.

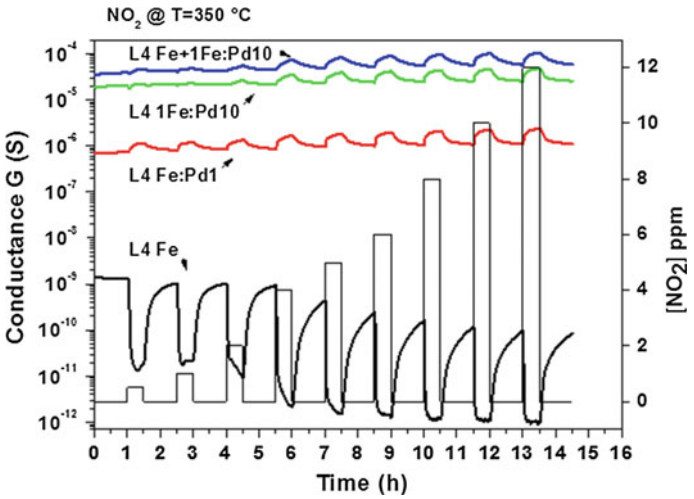

Fig. 2. Dynamic response (G vs. time) of a typical set of undoped and Pd-doped Fe_3O_4/γ-Fe_2O_3 NPs-based sensors to increasing NO_2 concentrations (0.5–12 ppm range) at an operating temperature of 350 °C

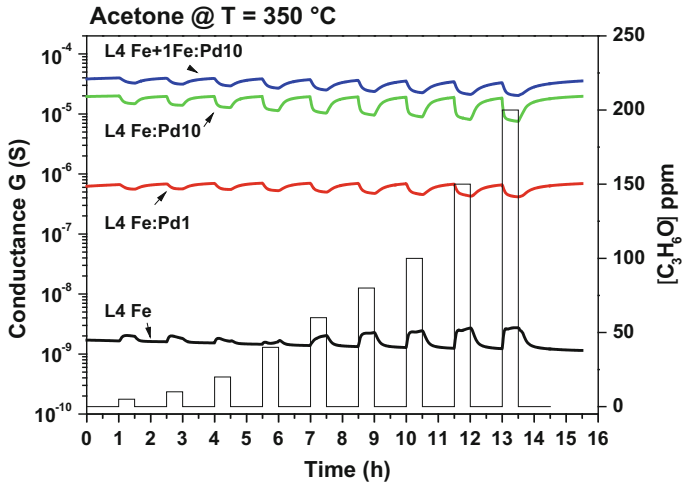

Fig. 3. Dynamic response (G vs. time) of a typical set of undoped and Pd-doped Fe_3O_4/γ-Fe_2O_3 NPs-based sensors to increasing acetone concentrations (5–200 ppm range) at an operating temperature of 350 °C

It can be observed that after NO_2 injection electrical conductance decreases for the Pd-undoped sensor (L4 Fe), whereas it increases in Pd-doped sensors (i.e. L4 Fe:Pd1, L4 1Fe:Pd10, L4 Fe+ Fe1:Pd10). Similarly, after acetone vapours injection electrical conductance increases for the Pd-undoped sensor (L4 Fe), whereas it decreases in Pd-doped sensors (i.e. L4 Fe:Pd1, L4 1Fe:Pd10, L4 Fe+ Fe1:Pd10). Moreover, it can be observed that

the Pd-doped sensors are much more conductive than undoped sensor. The conductance G increases also at increasing the amount of Pd NPs ($G_{L4Fe} < G_{L4Fe:Pd1} < G_{L41Fe:Pd10} < G_{L4Fe+Fe1:Pd10}$) leading to suppose a different electrical conduction regime.

The conductivity is dominated by these spin-polarized charge carriers that may contribute to conduction by hopping process by Nearest Neighbor Hopping (NNH) (Fig. 4).

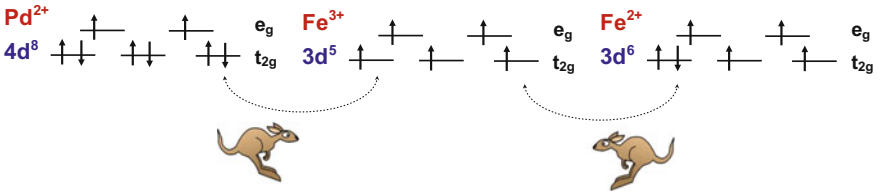

Fig. 4. Scheme of the proposed mechanism of hopping electrical conduction by NNH in the Pd-Fe oxides nanoparticles layers

4 Conclusion

In this work Fe_3O_4/γ-Fe_2O_3 nanoparticles (NPs) by high-temperature decomposition of organic precursors were synthetized and mixed with Pd nanoparticles. The prepared NPs solutions were deposited more times by Langmuir-Schaeffer technique in order to get compact multilayered films. The LS films were deposited onto alumina substrates equipped with Pt interdigital electrodes and integrated heater to test them as a chemiresistor type gas sensors. The gas sensing tests towards NO_2 and acetone showed different sensing behaviour for undoped and Pd-doped Fe_3O_4/γ-Fe_2O_3 NPs-based sensors, i.e. n-type response for the undoped sensors and p-type response for the Pd-doped sensors. In particular, the undoped Fe_3O_4/γ-Fe_2O_3 NPs based sensor (n-type response) resulted more efficient compared to the Pd-doped sensors to detect NO_2 (p-type response), whereas comparable responses toward acetone were obtained with undoped and Pd-doped NPs-based sensors.

The different type of response (n-type and p-type) of the sensing materials may be due to different electrical conduction mechanisms. The electrical transport in iron oxides was proposed as open issue to discussion to the scientific community. We proposed that the conductivity is dominated by spin-polarized charge carriers that may contribute to conduction by hopping process by Nearest Neighbor Hopping (NNH).

References

1. S. Laurent, D. Forge, M. Port, A. Roch, C. Robic, L. Vander Elst, R.N. Muller, Magnetic iron oxide nanoparticles: synthesis, stabilization, vectorization, physicochemical characterizations, and biological applications. Chem. Rev. **108**, 2064–2110 (2008)
2. D. Ramimoghadam, S. Bagheri, S. Bee, S.B.A. Hamid, Review-progress in electrochemical synthesis of magnetic iron oxide nanoparticles. J. Magn. Magn. Mater. **368**, 207–229 (2014)

3. M. Mohapatra, S. Anand, Synthesis and applications of nanostructured iron/oxides/hydroxides—a review. Int. J. Eng Sci. Technol. **2**(8), 127–146 (2010)
4. D. Ling, T. Hyeon, Chemical design of biocompatible iron oxide nanoparticles for medical applications. Small **9**(9–10), 1450–1466 (2013)
5. N. Viet Long, Y. Yang, M. Yuasa, C. Minh Thi, Y. Cao, T. Nann, M. Nogami, Controlled synthesis and characterization of iron oxide nanostructures with potential applications for gas sensors and the environment. RSC Adv., **4**, 6383–6390 (2014)
6. D. Patil, V. Patil, P. Patil, Highly sensitive and selective LPG sensor based on α-Fe2O3 nanorods. Sens. Actuators B **152**, 299–306 (2011)
7. I. Ray, S. Chakraborty, A. Chowdhury, S. Majumdar, A. Prakash, R. Pyare, A. Sen, Room temperature synthesis of γ-Fe_2O_3 by sonochemical route and its response towards butane. Sens. Actuators B, **130**, 882–888 (2008)
8. C.V. Gopal Reddy, K. Kalyana Seela, S.V. Manorama, Preparation of γ-Fe_2O_3 by the hydrazine method application as an alcohol sensor. Int. J. Inorg. Mater. **2**, 301–307 (2000)
9. R.C. Biswal, Pure and Pt-loaded gamma iron oxide as sensor for detection of sub ppm level of acetone. Sens. Actuators B **157**, 183–188 (2011)
10. D.H. Kim, Y.-S. Shim, J.-M. Jeon, H.Y. Jeong, S.S. Park, Y.-W. Kim, J.-S. Kim, J.-H. Lee, H.W. Jang, Vertically ordered hematite nanotube array as an ultrasensitive and rapid response acetone sensor. Appl. Mater. Interfaces. **6**, 14779–14784 (2014)
11. Z.-F. Dou, C.-Y. Cao, Q. Wang, Q. Jin, Y. Yu, W.-G. Song, Synthesis, self-assembly, and high performance in gas sensing of X-shaped iron oxide crystals. Appl. Mater. Interfaces **4**, 5698–5703 (2012)
12. N.D. Cuong, D.Q. Khieu, T.T. Hoa, D.T. Quang, P.H. Viet, T. Dai Lam, N.D. Hoa, N. Van Hieu, Facile synthesis of α-Fe_2O_3 nanoparticles for high-performance CO gas sensor. Mater. Res. Bull. **68**, 302–307 (2015)
13. N.V. Long, Y. Yang, M. Yuasa, C.M. Thi, Y. Cao, T. Nann, M. Nogami, Gas-sensing properties of p-type α-Fe_2O_3 polyhedral particles synthesized via a modified polyol method. RSC Adv. **4**, 8250–8255 (2014)
14. X. Gou, G. Wang, X. Kong, D. Wexler, J. Horvat, Juan Yang, J. Park, Flutelike porous hematite nanorods and branched nanostructures: synthesis, characterisation and application for gas-sensing. Chem. Eur. J. **14**, 5996–6002 (2008)
15. M. Ivanovskaya, D. Kotsikau, S. Capone, P. Siciliano, Effect of gamma-Fe_2O_3/In_2O_3 nano-heterostructure on its sensitivity to methane. *Proceedings of International Conference on Physics, Chemistry and Application of Nanostructures*, Minsk, RUSSIA, 26–29 MAY 2009, Published: 2009, pp. 601–604, ISBN: 978-981-4280-35-8
16. G. Neri, A. Bonavita, G. Rizzo, S. Galvagno, S. Capone, P. Siciliano, Methanol gas sensing properties of CeO_2-Fe_2O_3 thin films. Sens. Actuators B **114**(2), 687–695 (2006)
17. G. Neri, A. Bonavita, G. Rizzo, S. Galvagno, S. Capone, P. Siciliano, A study of the catalytic activity and sensitivity to alcohols of CeO_2-Fe_2O_3 thin films. Sens. Actuators B **111–112**, 78–83 (2005)
18. S. Capone, M.G. Manera, A. Taurino, P.A. Siciliano, R. Rella, S. Luby, M. Benkovicova, P. Siffalovic, E. Majkova, Fe_3O_4/γ-Fe_2O_3 nanoparticle multilayers deposited by Langmuir Blodgett technique for gas sensing. Langmuir **30**, 1190–1197 (2014)

Multianalyte Biosensor Patch Based on Polymeric Microneedles

P. Dardano[1(✉)], A. Caliò[1], V. Di Palma[2], M.F. Bevilacqua[2], A. Di Matteo[2], and L. De Stefano[1]

[1] IMM-CNR uos Napoli, Naples, Italy
principia.dardano@na.imm.cnr.it
[2] ST Microelectronics, Arzano, Italy

Abstract. Multianalyte biosensor patch based on polymeric microneedles (MNs) have been fabricated by photolithography of poly (ethylene glycol) diacrylate (PEGDA) and have been dynamically characterized by means of quartz crystal microbalance and electrochemical measurements. The resulting flexible device acts as multianalyte working electrodes detecting glucose and lactic acid into interstitial liquid by means of redox reaction with glucose oxidase (GOx) and lactose oxidase (LOx) enzymes. Sensitivities of the order of nA mM^{-1} in the mM range are revealed in both case, after five minutes of swelling time and ten second of interaction.

Keywords: Microneedles · Polymers · Swelling · Dynamic characterization

1 Introduction

In the age of smart devices, the integration of health sensor follows the general attention on nutrition and sport activity, indicated as primary prevention means of diseases as obesity, diabetes as well as cancer. However, the low invasiveness constraint of such devices inhibits the monitoring of substances as glucose, although diabetes is one of the most widespread ailments. Commercial electrochemical glucose sensor are based on the redox reaction of glucose oxidase (GOx) with glucose, that creates a charge transfer, resulting in a current proportional to the glucose concentration in blood [1]. Another intermediate key in anaerobic glycolytic pathway metabolism is the lactate or lactic acid, detectable by means of the redox reaction with lactose oxidase (LOx). The determination of lactate concentration in blood is essential in sport medicine where lactate concentration in blood indicate the training activity [2]. This kind of blood biosensor needs a macroscopic needle or cutter wherewith injure a finger till the leakage of a blood droplet.

Microneedles (MNs) are widely applied in biomedicine both in diagnostics and in therapeutics, as being the perfect painless interface between the patient and a sensing or dispenser device [3–6]. In particular, polymeric microneedles act as a molecular filter that is able to lock enzymes and to allow the analyte molecules diffusion from the interstitial liquid [4, 5, 7]. In this work, we present the *in vitro* dynamic characterization of two sensing devices based on tree electrodes system and integrating polymeric MNs arrays for the measure of glucose and lactate level in the subcutaneous interstitial liquid. The MNs arrays are microfabricated by direct photopolymerization

B. Andò et al. (eds.), *Sensors*, Lecture Notes in Electrical Engineering 431,
DOI 10.1007/978-3-319-55077-0_10

PolyEthylene Glycol DiAcrylate (PEGDA) hydrogel containing enzymes (GOx and LOx) and vynilferrocene (VF) molecules, as redox mediator that speeds up the electrochemical conduction. Experimental results show that, after waiting about five minutes for the hydrogel swelling, the sensor sensitivity is stable after ten seconds.

2 Materials and Methods

2.1 Materials

To fabricate the two microneedles based electrodes the following materials have been used: PEGDA with average molecular weight (M_n) of 250, phosphate buffered saline (PBS) 10 mM (NaCl 0.138 M, KCl^- 0.0027 M) at pH 7.4, vynilferrocene powder (VF), D-(+)-glucose, GOx (from *Aspergillus niger*, type II, $\geq$15,000 units/g solid, EC 1.1.3.4), L-(+)-lactic acid and LOx (from *Pediococcus sp.* lyophilized powder, $\geq$20 units/mg solid, EC 1.13.12.4) (from Sigma Aldrich, USA); the photoinitiator (PI), 2-hydroxy-2-methyl-1-phenyl-propan-1-one (Darocur© 1173), (from BASF, Germany); a gold target (from Emitech, Italy) for spattering; silicone rubber (from Saratoga, Italy).

To characterize the sensor the following materials have been used: phosphate buffered saline (PBS) 10 mM (NaCl 0.138 M, KCl^- 0.0027 M) at pH 7.4, VF, magnesium chloride ($MgCl_2$) 0.48 mM, solutions of glucose and lactic acid prepared in PBS solution and stored at 4 °C in the dark. In order to reach sugar muta-rotation equilibrium, D-(+)-glucose solutions have been stored overnight at room temperature before using.

All chemicals were reagent grade or higher and have been used as received unless otherwise specified. All aqueous solutions have been prepared with ultrapure water by means of a MilliporeMilli-Q system (18.2 MΩ cm).

2.2 Fabrication

Fabrication of microneedles devices follows the fabrication steps presented in [4] and [8] and shown in Fig. 1. Briefly, 1 ml of the solution, containing PEGDA, VF (1% w/v) and PI (2% v/v), has been casted on quartz slide and exposed to UV light for 10 s (Fig. 1, step 1).

The obtained PEGDA layer has been used as flexible support for the MN array and is about 1 mm thick. The MN arrays have been fabricated by direct photopolymerization of the former solution mixed with the enzymatic solutions in 9:1 ratio, where the enzymatic solutions have been obtained dissolving GOx in PBS (pH 6.0) at 20 mg/mL concentration and LOx in PBS (pH 6.5) at 15 mg/mL concentration and stirring the solutions for 4 h at 4 °C, as done in [7]. A silicone vessel (1.5 × 1.0 0.4 cm^3) has been fulfilled with the last solutions and the PEGDA layer is overturned on the silicone vessel (Fig. 1, step 2). The direct contact of the PEGDA layer with the solutions allows the adhesion of the MNs to flexible substrate. The UV exposure has been performed for 25 s through a quartz/chrome photomask in soft contact mode (Fig. 1, step 3). For the UV exposure the MA6/BA6 mask aligner (by Karl Suss AG, Germany) at 18 mW/cm^2 and 365 nm has been used.

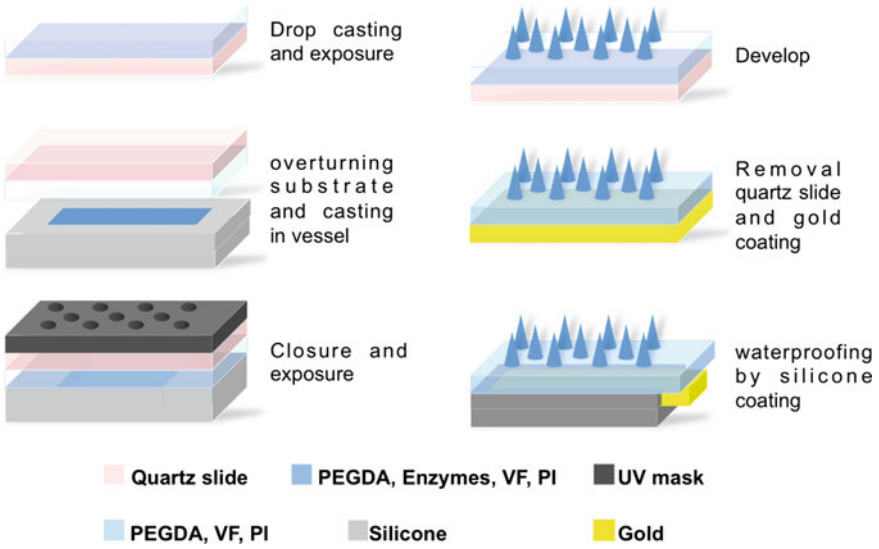

Fig. 1. Flow chart of the fabrication of the working electrodes

After the develop in deionized water for 2 min (Fig. 1, step 4), the quartz support has been removed by means of tweezers and a gold layer has been deposited on the back of the PEGDA layer by the K975X sputter (by Emitech, Italy) at 30 mA current, room temperature and for 240 s, obtaining a 160 nm thick layer (Fig. 1, step 5). In order to prevent the direct contact between gold layer and electrolytic solution during the electrochemical characterizations, the gold layer has been covered with a commercial liquid silicone rubber (Saratoga, Italy), hardened at room temperature in 2 h (Fig. 1, step 6). In order to realize the electric contact between the electrochemical cell setup and the fabricated working electrodes, silicone rubber uncovers a small area of the gold layer. However, during electrochemical characterization the uncovered gold stayed out of the electrolytic solution.

2.3 Quartz Microbalance Measurements

Quartz Crystal Microbalance (QCM) technology is currently used in measuring with high sensitivity small mass changes. Standard nanogravimetry exploits the piezoelectric quartz resonators (QR) properties in quantifying the resonance frequency shift Δf when a mass m is adsorbed to or desorbed from their surface, according to Sauerbey's equation (1):

$$\Delta f/f_0 = \Delta m/A\rho l \tag{1}$$

where f_0 is the fundamental frequency of QR, A is the gold area, Δm is the adsorbed mass variation corresponding to frequency shift Δf and ρ and l are the quartz density and thickness, respectively [9, 10].

In [11] homogeneous matrices of polyethylene glycol (PEG) have been used as malleable inert support to selectively detect carbon dioxide (CO_2) via nanogravimetric method in atmosphere-controlled chamber. Similarly, a QR sample covered by a PEGDA droplet has been fabricated in order to dynamically characterize the swelling of the PEGDA matrix in PBS solution. The sample is fabricated by exposing at UV for 25 s a 1 µl of PEGDA, PI and VF solution casted on a gold plate of the QR (Fig. 2a). To this purpose, QCM by Novaetech S.p.A. (Italy) and quartz resonator by I.E.V. (Italy) have been used in a chamber with a volume of 30 µl fulfilled with PBS (Fig. 2a).

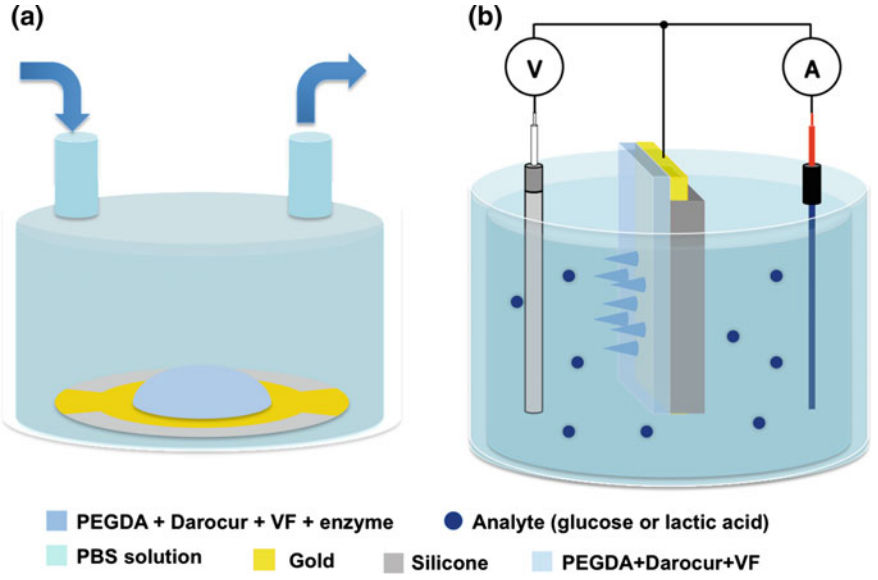

Fig. 2. Experimental set-ups for dynamic characterization: **a** Set-up for dynamic characterization of swelling of PEGDA matrix in PBS solution via nanogravimetric measurements; **b** Set-up for chronoamperometric electrochemical characterization of enzymes doped PEGDA MNs

2.4 Electrochemical Measurements

To provide a dynamic in vitro electrochemical characterization, chronoamperometric (CA) measurements in a three electrodes BASi C-3 Cell Stand have been performed. Figure 2b shows a sketch of the experimental set-up: a saturated silver chloride (Ag/AgCl 3 M) reference electrode, a platinum wire auxiliary electrode and the enzymes doped PEGDA MNs (for glucose or for lactic acid detection) as working electrode. Moreover, the interstitial liquid has been mimicked by electrolytic solution: PBS (pH 7.4) mixed with $MgCl_2$. During the measurements (at room temperature) the electrolytic solution has been deoxygenated with nitrogen. Generally, the CA technique give information about the influence of the analyte (glucose or acid lactic) concentration on the electrons production that follows the proper redox reaction in presence of VF as redox mediator as reported in [4] and [7].

During CA measurements, the potential between working and reference electrodes has been fixed at 300 mV and the current, flowing from working to auxiliary electrodes, has been registered as function of time. The CA characteristics have performed 5 min after addition of aliquots at known concentration of analyte (glucose or lactic acid), in order to allow the diffusion inside the electrolytic solution, Glucose and lactic acid have been detected at 0, 2, 4, 6, 8, 10 mM and 0, 1, 2, 3 and 4 mM concentrations, respectively. Reported results have been graphed and processed by Origin® software.

3 Results

The systems are proposed as proof-of-concept of a wearable electrochemical biosensors, useful for monitoring of glucose and lactic acid levels in the interstitial fluid. The photolithographic fabrication of MNs has been optimized to lock into the polymeric matrix enzymes and the redox mediator without less in their activity. In particular, the temperature during the exposure has been measured by a thermo couple placed on the sample holder of the mask aligner and changes from 25 to 27 °C. Therefore the low exposure time guarantees that the temperature is ever lower than the degradation temperature of enzymes. Figure 3 shows a photo of an enzymes doped PEGDA MNs working electrode: the device is completely flexible and could be deformed without breaking or loosing the electrical contact.

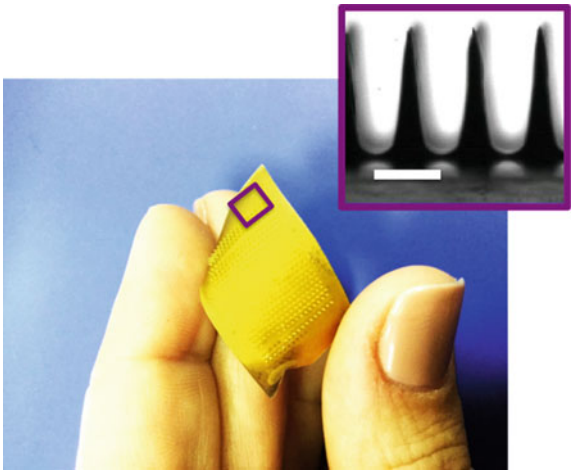

Fig. 3. An enzymes doped PEGDA MNs working electrode. The picture acquired by digital camera shows the flexibility of the system. In the *inset*, a detail of the MNs arrays has been captured by means of the water contact angle camera (scale bar is 400 μm)

By soaking the system into the electrolytic solution, polymeric swelling allows the analyte molecules (glucose or lactic acid) diffusion inside the PEGDA matrix and the interaction with the enzymes (GOx or LOx), resulting in the generation of electrons

current collected by auxiliary electrode. The swelling dynamics has been monitored by QCM measurements by means of a QR covered by a solidified PEGDA droplet. Figure 4 shows the resonance frequency of the modified QR as function of time. In the inset of Fig. 4, a picture of the solidified and soaked PEGDA droplet on the quartz resonator has been captured by means of the water contact angle camera (scale bar is 750 μm). The frequency of the quartz resonator decreases when the PBS solution diffused in MNs PEGDA structure with a constant time, estimated by fitting data ($R^2 = 0.99$), of about 2 min (1.99 ± 0.02 min), and is stable after about 5 min. These data are representative of swelling kinetic in MNS.

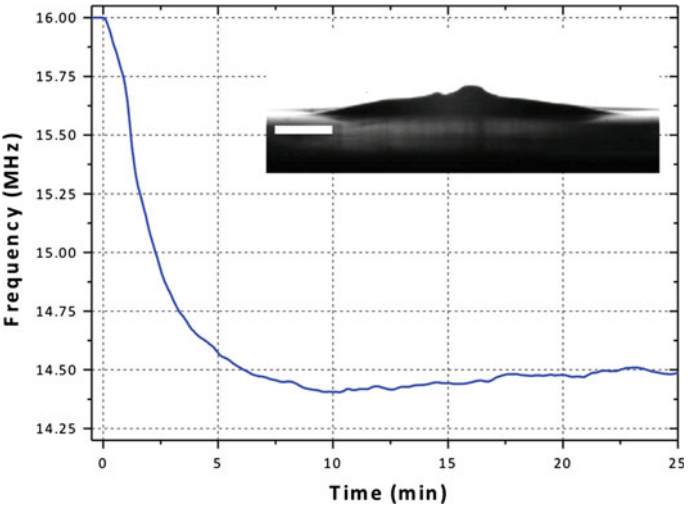

Fig. 4. QCM nanogravimetric measurement of a PEGDA on the quartz resonator interaction with saturated aqueous fluorescein solution as function of time. In the *inset*, a picture of the solidified and soaked PEGDA droplet on the quartz resonator has been captured by means of the water contact angle camera (scale bar is 750 μm)

Moreover, the CA measurements register the enzymatic kinetics and quantify the biosensor responses as current value at several concentrations of glucose and lactic acid, in concentration ranges of interest for the detection in human interstitial fluid [12, 13]. In a recent publication (Ref. [4]), the stationary current value has been considered to determine the calibration curves for glucose and lactic acid. In this way, the reported sensitivity of the biosensor is 18 ± 3 nA mM^{-1} in the range from 0 to 4 mM for glucose and 3.5 ± 0.2 nA mM^{-1} in the range from 0 to 1 mM for lactic acid. However, as reported in Ref. [14], faster response time (30 s) can be obtained in the case of MN array enzymatic based biosensor. Indeed, after waiting a swelling time of two minutes and considering the response of the biosensors at 10, 20, 30 and 60 s, a greater and stable linear range is found after 10 s in both cases and a comparable sensitivity is found after 10 s (Fig. 5).

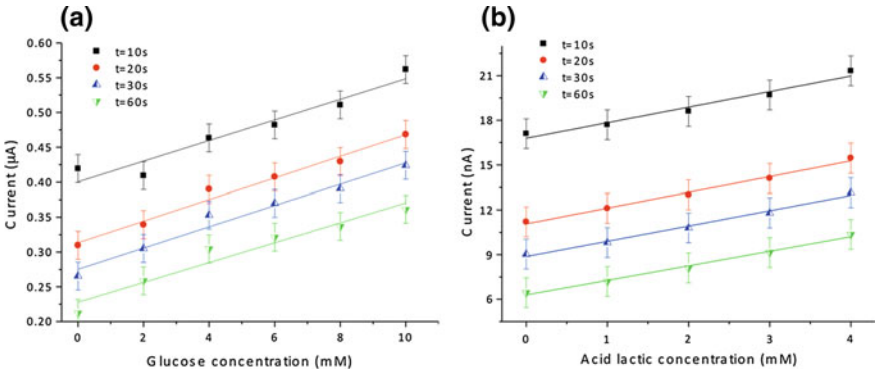

Fig. 5. Calibration curves for glucose (**a**) and acid lactic (**b**) at 10, 20, 30 and 60 s. Linear response and the sensitivity are stable after 10 s in both cases biosensors

In particular, for glucose biosensor a linear range from 0 to 10 mM is found with a sensitivity 15 ± 2 nA mM^{-1} considering the current after 10 s of interaction. Moreover, data and fit results (showed in Fig. 5a and summarized in Table 1) clearly show that the linearity range is the same and the sensitivity is comparable after 10, 20, 30 and 60 s.

Table 1. Sensitivity of the glucose biosensor calculated by the fit results in Fig. 5a

Time (s)	Sensitivity (nA/mM)
10	15 ± 2
20	15 ± 1
30	15 ± 1
60	14 ± 2

For glucose biosensor a linear range from 0 to 4 mM is found with sensitivity 1.0 ± 0.1 nA mM^{-1} considering the current after 10 s of interaction. Similarly, data and fit results (showed in Fig. 5b and summarized in Table 2) show that the linearity range is the same and the sensitivity is comparable after 10, 20, 30 and 60 s.

Table 2. Sensitivity of the acid lactic biosensor calculated by the fit results in Fig. 5b

Time (s)	Sensitivity (nA/mM)
10	1.0 ± 0.1
20	1.05 ± 0.06
30	1.02 ± 0.06
60	0.98 ± 0.05

Finally, considering the limits of detection (LoD) as $3\sigma/S$, where σ is the standard deviation of the measured current at 0 mMol and S is the sensor sensitivity, as done in [14], LoD is about 0.5 mM for both biosensor, respectively.

4 Conclusions

Enzymes doped PEGDA MNs working electrodes have been fabricated by standard photolithography of a solution of enzymes (GOx/LOx), redox mediator (VF) and a photoinitiator (PI) in PEGDA. Swelling dynamics of the polymeric matrix has been characterized by QCM measurements and have a constant time of about 2 min (1.99 ± 0.02 min) and a stabilization time of about 5 min. The devices have been characterized by CA measurements and show sensitivities of the order of nA mM^{-1} with a limit of detection of 0.5 mM. The biosensors are suitable for wearable patch for continuous monitoring of glucose in diabetes patients or for sensing the acid lactic levels in athletes with minimum invasiveness. The technology of Enzymes doped PEGDA MNs working electrodes has been patented [15].

Acknowledgments. This work was partially supported by Italian National Operative Program FUZI (00029_3148467) of IMAST Scarl. The Authors gratefully acknowledge Prof. A. Lombardi of University of Naples Federico II and her team, for electrochemical characterizations.

References

1. J. Wang, Electrochemical glucose biosensors. Chem. Rev. **108**(2), 814–825 (2008)
2. N. Nikolaus, B. Strehlitz, Amperometric lactate biosensors and their application in (sports) medicine, for life quality and wellbeing. Microchim. Acta **160**(1–2), 15–55 (2008)
3. L. Ventrelli, L.M. Strambini, G. Barillaro, Microneedles for transdermal biosensing: current picture and future direction. Adv. Healthc. Mater. (2015). doi:10.1002/adhm.201500450
4. A. Caliò et al., "Polymeric microneedles based enzymatic electrodes for electrochemical biosensing of glucose and lactic acid." Sens. Actuators B: Chem. **236**, 343–349 (2016)
5. P. Dardano et al., "Optically monitored drug delivery patch based on porous silicon and polymer microneedles." Biomed Opt. Express. **7**(5), 1645–1655 (2016)
6. Gabriela Valdés-Ramíreza et al., Multiplexed and switchable release of distinct fluids from microneedle platforms via conducting polymer nanoactuators for potential drug delivery. Sens. Actuators B: Chem. **161**(1), 1018–1024 (2012)
7. J. Yan et al., Immobilizing enzymes onto electrode arrays by hydrogel photolithography to fabricate multi-analyte electrochemical biosensors. ACS Appl. Mater. Interfaces **2**(3), 748–755 (2010)
8. P. Dardano et al., A photolithographic approach to polymeric microneedles array fabrication. Materials, **8**(12), 8661–8673 (2015). doi:10.3390/ma8125484
9. C. Nicolini et al., High-sensitivity biosensor based on LB technology and on nanogravimetry. Sens. Actuators B Chem. **24**, 121–128 (1995)
10. R. Spera et al., NAPPA based nanogravimetric biosensor: preliminary characterization. Sens. Actuators B **182**, 682–688 (2013)

11. T. Bezerra Correia, V. Bavastrello, C. Nicolini, Calcium oxide matrices and carbon dioxide sensors. Sensors (Basel) **12**, 5896–5905 (2012)
12. N.Y. Shim, D.A. Bernards, D.J. Macaya, J.A. DeFranco, M. Nikolou, R.M. Owens, G.G. Malliaras, All-plastic electrochemical transistor for glucose sensing using a ferrocene mediator. Sensors **9**(12), 9896–9902 (2009)
13. N. Thomas, I. Lähdesmäki, B.A. Parviz, A contact lens with an integrated lactate sensor. Sens. Actuators B: Chem. **162**(1), 128–134 (2012)
14. L. Strambini, A. Longo, S. Scarano, T. Prescimone, I. Palchetti, M. Minunni, D. Giannessi, G. Barillaro, Biosens. Bioelectron. **66**, 162 (2015)
15. V. Di Palma, M.F. Bevilacqua, A. Di Matteo, P. Dardano, Microneedle array device for biosensor applications. US Application Patent 14558779

Effective Tuning of Silver Decorated Graphene Sensing Properties by Adjusting the Ag NPs Coverage Density

Maria Lucia Miglietta[1(✉)], Brigida Alfano[1,2], Tiziana Polichetti[1], Ettore Massera[1], Chiara Schiattarella[2], and Girolamo Di Francia[1]

[1] ENEA C.R. Portici, P.le E. Fermi 1, 80055 Portici (Naples), Italy
mara.miglietta@enea.it
[2] Department of Physical Sciences, University of Naples Federico II, Via Cinthia, 80126 Naples, Italy

Abstract. Noble-metal decorated graphene nanohybrids are expected to be a new type of sensing material with high sensitivity and excellent selectivity, since the metal nanoparticles can act as a mediator in the interaction between analytes and graphene, determining peculiar mechanisms of charge transfer according to chemical or electronic sensitization. In particular, the decoration by silver nanoparticles (Ag NPs) can improve the sensing behavior of carbon nanostructures towards ammonia. In this work, graphene/Ag nanoparticles (GR/AgNPs) hybrids were prepared by a one-step microwave-assisted reduction method by irradiating a water/isopropyl alcohol solution of pristine graphene and $AgNO_3$. Two different concentrations of silver precursor were tested obtaining graphene hybrids with different surface coverage. The effect of the metal decoration was investigated by probing the sensing properties of the chemiresistive layers towards NO_2 and NH_3 at concentrations, respectively, of sub-ppm and hundreds of ppm in air, which are considered as standard marker levels of environmental pollution. The results show that the high specificity of bare graphene towards NO_2 in ppb levels was reversed towards NH_3 by addition of Ag NPs. Noteworthy, a low areal density of Ag NPs allowed the material to gain sensitivity towards ammonia while still retaining sensitivity to NO_2. At higher surface coverage an almost complete reversal of the sensitivity occurred and the silver decorated material appeared highly sensitive towards ammonia.

Keywords: Graphene · Silver nanoparticles · Graphene-nanohybrids · Gas sensor · NO_2 · NH_3

1 Introduction

The potential of graphene in the sensing field stems from the unusual combination of singular properties in the same material such as the large specific surface area, the high charge mobility, the low electrical noise and the molecular sensitivity [1]. The interaction of graphene with gaseous molecules can vary in fact in relation to the outermost electron shell structure of the adsorbates [2–4]. Another advantage is that sensitivity,

B. Andò et al. (eds.), *Sensors*, Lecture Notes in Electrical Engineering 431,
DOI 10.1007/978-3-319-55077-0_11

chemical affinity and selectivity towards specific molecules can be tuned by modifying the graphene structure [4, 5].

Among the several approaches considered for this aim, noble-metal decorated graphene nanohybrids are expected to be a new type of sensing material with high sensitivity and excellent selectivity since the metal nanoparticles can act as a mediator in the interaction between analytes and graphene determining different mechanisms of charge transfer according to chemical or electronic sensitization [6]. For instance, it is known that decoration by silver nanoparticles (Ag NPs) greatly improves the sensing behavior of carbon nanostructures towards ammonia [7]. Another interesting features of these systems is that when metal nanoparticles are integrated with graphene sheets, a synergistic effect activates a RT operating mechanism whereas sensors based on noble metals usually require high operating temperatures. Composite materials made by reduced graphene oxide (RGO) and silver nanostructures showed indeed excellent sensitivity towards NH_3 at room temperature [8–10].

In this work, graphene/Ag nanoparticles (GR/AgNPs) hybrids were prepared by a one-step microwave-assisted reduction method by irradiating a water/isopropyl alcohol solution of pristine graphene and $AgNO_3$. Graphene hybrids with different surface coverage in relation to the concentration of the silver precursor were easily obtained and their sensing performances towards NO_2 and NH_3 were investigated.

2 Experimental

Graphene was prepared through a sonication-assisted liquid phase exfoliation of natural graphite as described in Ref. [11]. Graphite flakes (NGS Naturgraphit GmbH Winner Straβe 9 D-91227 Leinburg-Germany) were dispersed at 2.5 mg/ml into 80 ml of an ultrapure water/i-propyl alcohol mixture (7:1 v/v) and sonicated in an ultrasonic bath for 48 h (Transsonic Digital S, 40 kHz, Elma Schmidbauer GmbH). Unexfoliated graphitic crystallites were removed by centrifugation at 500 rpm for 45 min.

Silver NPs decoration of graphene (GR/AgNPs) was accomplished as described in Ref. [13]. Graphene suspension (1 ml) was mixed with 1 ml of ethylene glycol ($C_2H_6O_2$, Sigma Aldrich, CAS 107-21-1) and 1 ml of $AgNO_3$ in purified water (Sigma Aldrich, CAS 7761-88-8) at 0.01 and 0.1 M and named GR/AgNPs1 and GR/AgNPs2, respectively. The suspensions were exposed to cyclic microwave exposures for a total of 4500 s, separated by 10 s off-time steps, by means of Microwave Digestion System equipped with a 700 W magnetron (Perkin Elmer/Anton Paar Multiwave). Afterwards, suspensions were centrifuged and the solid residue washed with ultrapure water.

The morphology of the GR/AgNPs hybrids were studied using Field Emission Scanning Electron Microscopy, coupled with an Energy Dispersive X-ray Analysis System (EDS), and Atomic Force Microscopy. The samples were prepared by drop-casting few microliters of the solutions directly onto Si substrates. The FESEM images were taken with a FESEM/EDS, LEO 1530-2 working at an acceleration voltage of 5 kV. Atomic Force Microscope (AFM-Nanoscope IV Veeco) was used to map topography, operating in tapping mode with a n-doped Si tip (model RTESP Veeco, resonant frequency 257–328 kHz; spring constant 20–80 N/m; radius of curvature <10 nm) under ambient condition, with a scanning rate of 0.5 Hz and 256

scanning lines. Raman spectra were acquired on films drop-casted onto oxidized silicon wafers (SiO_2 300 nm) using a Raman spectrometer (Renishaw inVia Reflex) @ 514 nm excitation, in backscattering configuration. Raman spectra were acquired and averaged mapping the samples in more than 10 different points.

Chemiresistor devices were fabricated by direct drop casting of few microliters of each mixtures onto transducers and dried in air at 100 °C on a hot plate. The transducers have 5 pairs of gold interdigitated electrodes (IDE) electrodeposited onto alumina substrate: each electrode finger is 350 μm wide and 4650 μm long. The spacing between fingers is 350 μm.

The sensing devices were placed in an air-tight chamber with electrical feedthroughs. A constant voltage was applied and the variation of resistance was monitored and recorded with the changes in the gas environment using a high resolution picoammeter Keithley 6485. A typical measurement cycle foresees three continuous steps:

1. Flushing of carrier gas for 1200 s (baseline),
2. Introducing analyte gas in the carrier stream for 600 s (sensing response),
3. Flushing of carrier gas for 1200 s (sensor recovery).

Synthetic air was used as carrier gas and as balance gas for sample gases dilutions. The measurements were performed setting the flow at 500 sccm with relative humidity (RH) at 50% and temperature at 22 °C.

3 Results and Discussion

Figure 1 summarizes the morphological features of the bare graphene obtained by the LPE method (Fig. 1a, b). The presence of nanosheets with an average lateral size around 500 nm is observed.

Raman spectrum, in particular, shows the evidence of the effective exfoliation of the natural graphite (Fig. 1c). The increase of the $2D_1$ component and the concurrent decrease of the $2D_2$ peak is the typical signature of graphene nanosheets with an average number of layers less than five [12].

Graphene-silver hybrids retain most of the morphological features of the bare graphene, as can be observed in FESEM and AFM images reported in Fig. 2. FESEM images (Fig. 2a, b) display graphene nanosheets with silver nanoparticles uniformly distributed all over the surfaces. AFM Phase (Fig. 2c, d) and topography (Fig. 3e, f) images of GR/AgNPs1 and GR/AgNPs2 show a granular structure with nanoparticles anchored onto the GR surface [13]. The corresponding profiles indicate that the height of the Ag nanoparticles on the graphene nanosheets is in the range 2–4 nm with an average diameter of 20–30 nm.

The metal NPs decoration of graphene results evident from the Raman analysis, where an intensity enhancement of the graphene bands due to surface-enhanced Raman scattering (SERS) effects was observed. Information about the changes in the spatial frequency of the enhanced spectra were drawn by mapping a $5 \times 5\ \mu m^2$ area at 1 μm-steps.

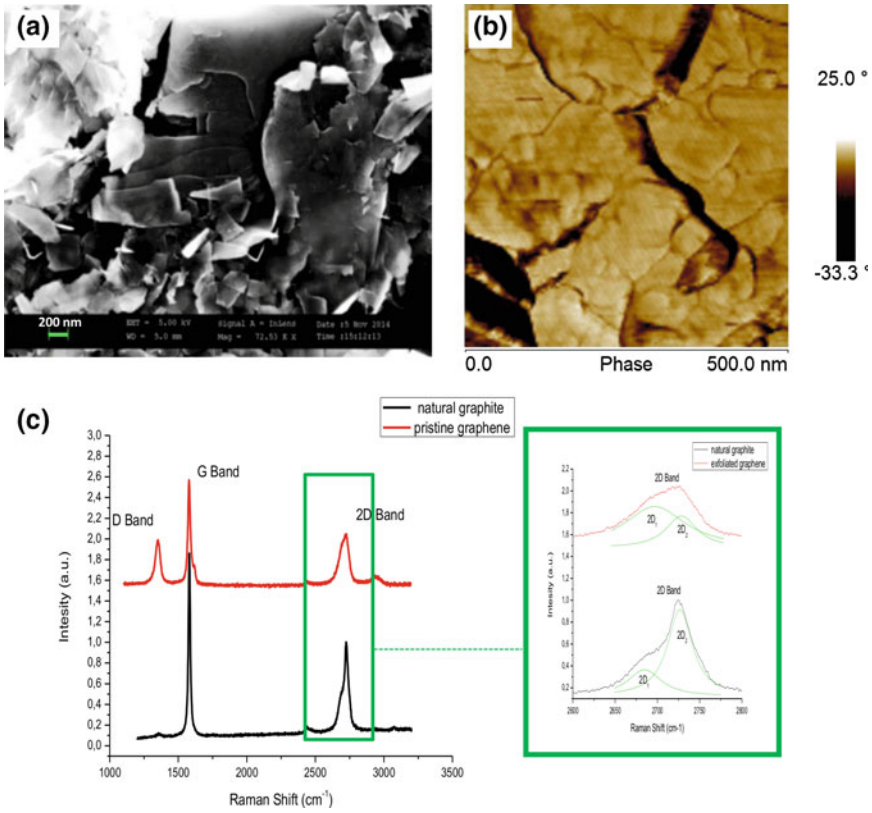

Fig. 1. Morphological characterizations of pristine graphene: **a** FESEM image, **b** AFM phase image, and **c** Raman spectrum of GR and graphite on Si/SiO_2; the *inset* shows the deconvolution of the 2D band into the $2D_1$ e $2D_2$ components. When graphite is exfoliated into less than five layers, the $2D_1$ component increases, whereas the opposite trend is observed for the $2D_2$ peak

For GR/AgNPs1 (Fig. 3a), a SERS effect was observed in around 11% of the sampled area, while for GR/AgNPs2, around 30% of the sampling points gave rise to a Raman enhancement (Fig. 3b), giving confirmation of the denser distribution of NPs on graphene observed in AFM and FESEM images. In addition, the amplification factors observed permits to infer that, in both samples, a charge-transfer between graphene nanosheets and metal nanoparticles is established [14].

The effect of the metal decoration was investigated by probing the sensing properties of these layers towards NO_2 and NH_3. The percentage response (S) is defined as the maximum of the conductance variation reached by the device during the analyte exposure, that is $[|G - G_0|/G_0] \times 100$ where G and G_0 are the conductance values recorded during analyte exposure and baseline acquisition steps, respectively. Absolute values are used for a better comparison among responses to both analytes, the conductance variations being in positive for NO_2 and negative for ammonia, according to their different electrical behaviour [4, 15]. The responses to 300 ppb of NO_2 and to

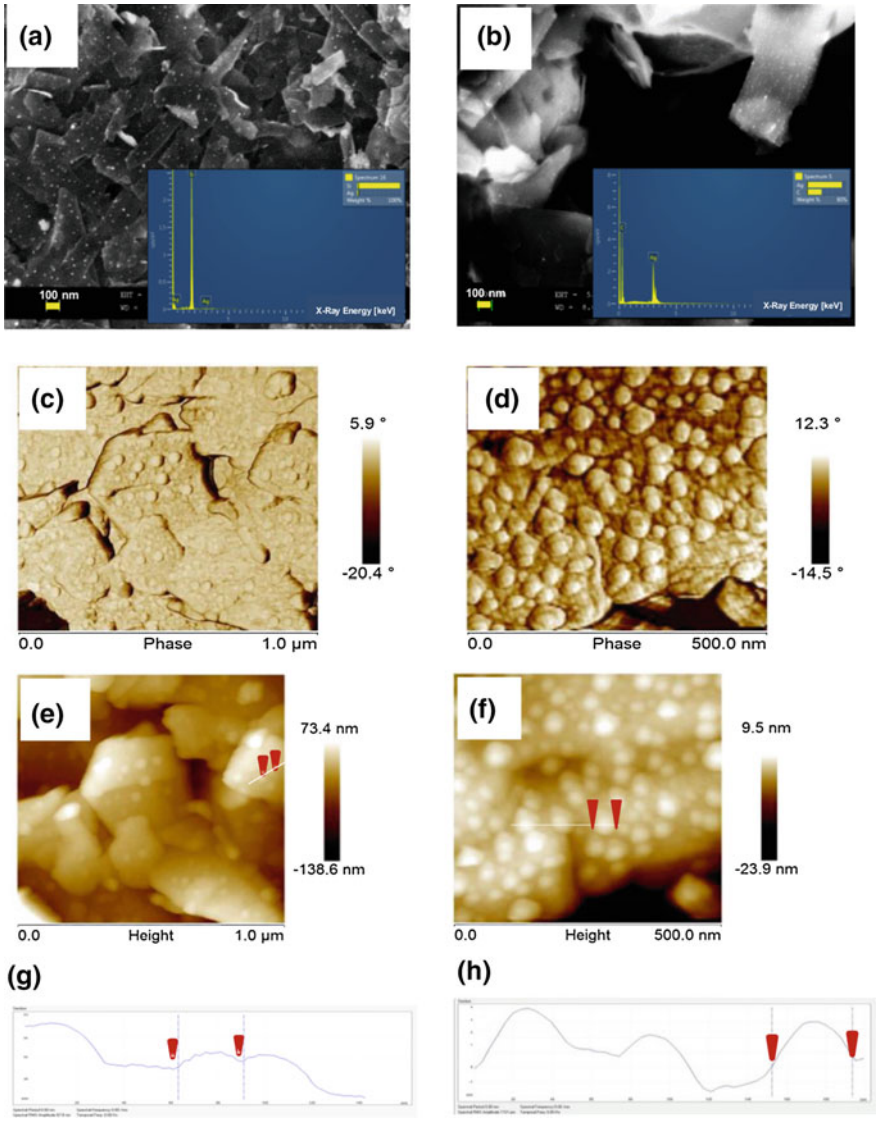

Fig. 2. Morphological characterizations of GR/AgNPs1 and GR/AgNPs2: **a** FESEM image of GR/AgNPs1, **b** FESEM of GR/AgNPs2; the *insets* show the relative EDS spectra performed focusing on the Ag nanoparticles. AFM image of GR/AgNPs1 and GR/AgNPs2 deposited on Si/SiO_2 substrate: **c** phase image of GR/AgNPs1, **d** phase image of GR/AgNPs2; topographic image and the corresponding height profile of GR/AgNPs1 (**e**, **g**) and GR/AgNPs2 (**f**, **h**)

250 ppm of NH_3 gases are reported in Fig. 4. This graph clearly show that the sensitivity towards NO_2 decreases in the order GR > GR/AgNPs1 $\gg$ GR/AgNPs2. Since graphene has a specific response to NO_2, this behavior could actually be addressed to the decrease in free graphene surface available for specific adsorption. To the highest

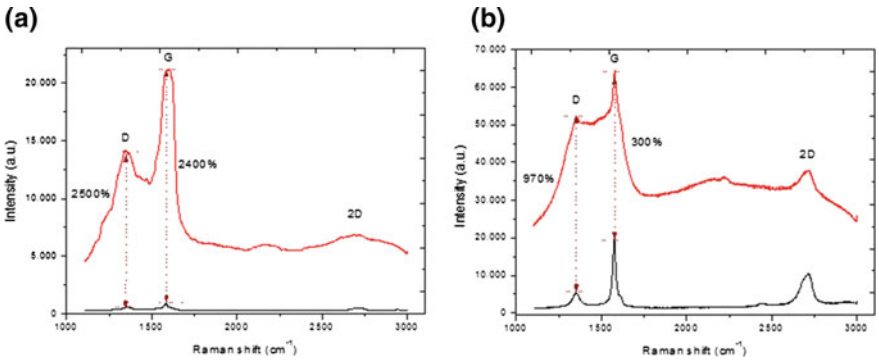

Fig. 3 Raman spectra of **a** GR/AgNPs1 and **b** GR/AgNPs2 deposited on Si/SiO_2 substrate. A comparison between a Raman spectrum acquired in a region covered by metal NPs (*red solid line*) and one recorded in an area not covered by NPs (*black solid line*) is reported. The intensity of the G band, enhanced due to the surface-enhanced Raman scattering effect of AgNPs, is about 2400% greater than that of GR in the case of GR/AgNPs1 and 300% in the case of GR/AgNPs2

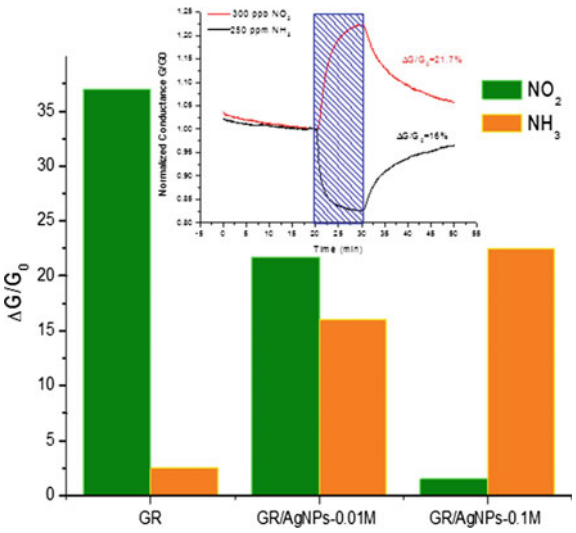

Fig. 4 Summary of the sensing responses of devices based on graphene (GR) and graphene hybrids with different Ag NPs loadings (GR/AgNPs-0.01 M and GR/AgNPs-0.1 M) towards NO_2 (240 ppb) and NH_3 (250 ppm). For a better comparison, on the y-axis the absolute values of the device responses are drawn. The *inset* shows the dynamic responses of the GR/AgNPs1 based device towards NO_2 and NH_3. On the y-axis the normalized conductance is reported

extent of surface coverage by Ag NPs, achieved for the GR/AgNPs2 sample, the response to NO_2 was indeed almost completely hindered. With regard to the ammonia sensing, hybrid materials showed noteworthy responses, above 15 and 21.5% for GR/AgNPs1 and GR/AgNPs2 respectively, after exposure to 250 ppm of NH_3. Under the same exposure conditions, pristine graphene showed only a modest 2.5% response.

Also in this case, the enhanced sensitivity to ammonia of the hybrids material with different Ag NP loadings can be addressed to an increased adsorption ability by the specific sensing element, i.e. Ag NPs. This result is in agreement with previous observation from Cui et al. [8] whose found out that sensitivity of RGO layer benefits from the increasing of the Ag NPs loadings.

The most interesting aspect of these results is that the sample GR/AgNPs2 presents an almost complete reversal of the sensitivity from NO_2 to NH_3 with respect to bare GR while preserving the functionality of the underlying graphene itself. This demonstrates that the tuning of the sensing properties of the material was effective. A lower areal density of Ag NPs allows instead the material to keep the sensitivity to both the analytes and, since the responses are opposite in sign, it can be possible to exploit this feature for a sensing device able to be employed in a wide range of scenarios.

4 Conclusion

We have shown a practical method to prepare a graphene composite with silver nanoparticles. This decoration modulates the sensitivity of the graphene towards analytes that are representative of compounds with completely opposite electronic behaviors. The noteworthy effect of Ag decoration was the enabling of the layer response towards hundreds of ppm of NH_3 in air. The results indicate that the sensitivity was affected by the graphene surface coverage by Ag NPs. In fact, depending on the areal density of the Ag NPs, it was possible to retain the sensitivity to both the analytes or to completely switch it, attaining a material highly sensitive to NH_3.

References

1. K.R. Ratinac, W. Yang, S.P. Ringer, F. Braet, Environ. Sci. Technol. **44**(4), 1167–1176 (2010)
2. T.O. Wehling, K.S. Novoselov, S.V. Morozov, E.E. Vdovin, M.I. Katsnelson, A.K. Geim, A.I. Lichtenstein, Nano Lett. **8**(1), 173–177 (2008)
3. T.O. Wehling, M.I. Katsnelson, A.I. Lichtenstein, Chem. Phys. Lett. **476**, 125–134 (2009)
4. Y.H. Zhang, Y.B. Chen, K.G. Zhou, C.H. Liu, J. Zeng, H.L. Zhang, Y. Peng, Nanotechnology **20**(18), 185504 (2009)
5. Y.H. Zhang, K.G. Zhou, K.F. Xie, J. Zeng, H.L. Zhang, Y. Peng, Nanotechnology **21**(6), 065201 (2010)
6. M.E. Franke, T.J. Koplin, S. Ulrich, Small **2**(1), 36–50 (2006)
7. S. Cui, H. Pu, G. Lu, Z. Wen, E.C. Mattson, C. Hirschmugl, M.G. Josifovska, M. Weinert, J. Chen, ACS Appl. Mater. Interfaces **4**, 4898–4904 (2012)
8. S. Cui, S. Mao, Z. Wen, J. Chang, Y. Zhang, J. Chen, Analyst **138**(10), 2877–2882 (2013)
9. Q.T. Tran, H.T.M. Hoa, D.H. Yoo, T.V. Cuong, S.H. Hur, J.S. Chung, P.A. Kohl, Sens. Actuators B: Chem. **194**, 45–50 (2014)
10. B. Alfano, T. Polichetti, M. Mauriello, M.L. Miglietta, F. Ricciardella, E. Massera, G. Di Francia, Sens. Actuators B: Chem. **222**, 1032–1042 (2016)
11. F. Fedi, M.L. Miglietta, T. Polichetti, F. Ricciardella, E. Massera, D. Ninno, G. Di Francia, Mater. Res. Express **2**, 03560 (2015)

12. A.C. Ferrari, J.C. Meyer, V. Scardaci, C. Casiraghi, M. Lazzeri, F. Mauri, S. Piscanec, D. Jiang, K.S. Novoselov, S. Roth, A.K. Geim, Phys. Rev. Lett. **97**(18), 187401 (2006)
13. Y. Li, X. Fan, J. Qi, J. Ji, S. Wang, G. Zhang, F. Zhang, Nano Res. **3**, 429–437 (2010)
14. K. Jasuja, V. Berry, ACS Nano **3**, 2358–2366 (2009)
15. O. Leenaerts, B. Partoens, F.M. Peeters, Phys. Rev. B **77**(12), 125416 (2008)

CuO-Modified Cu Electrodes for Glucose Sensing

C. Espro, S.G. Leonardi, A. Bonavita, S. Galvagno, and G. Neri(✉)

Department of Engineering, University of Messina, Messina, Italy
gneri@unime.it

Abstract. Electrochemical sensors are largely used for rapid, sensitive and accurate measurement of glucose in many applications such as clinical diagnostics, ecological field, biotechnology and food industry. Among the various methods, the amperometric one is the most popular due to its simplicity and high sensitivity. Furthermore, due to their higher intrinsic stability, electrochemical glucose sensors based on inorganic materials are preferred with respect to enzymatic ones for applications in severe conditions. Herein, we present a simple method to prepare an electrochemical sensor for the determination of glucose by modification of planar copper electrodes in order to obtain a high sensitive copper oxide-modified electrode. In particular, we show the versatility of the preparation method comparing the electrochemical sensing properties towards glucose of two modified copper electrodes, commercial and homemade, respectively.

Keywords: Electrochemical sensors · Glucose sensor · CuO-modified electrode

1 Introduction

The determination of glucose is essential in many fields such as clinical diagnostics, biotechnology and food industry [1]. Therefore, over the past few decades great attention has been paid to the development of glucose sensors [2]. Various analytical methods have been employed for glucose monitoring such as spectrophotometry, spectrofluorometry and liquid chromatography [3–5]. However, due to the simplicity, low cost and the possibility to realize practical sensor devices with excellent sensing properties, the electrochemical methods have been the most studied and adopted in the last decades. The commonly studied amperometric glucose detectors are enzymatic biosensors based on glucose oxidase. The main drawback is related to the nature of enzymes, indeed they are susceptible to environmental conditions such as temperature, pH value, humidity and toxic chemicals. Furthermore, glucose oxidase sensors suffer from instability, high cost of enzymes, complicated immobilization procedures and critical operating conditions associated with cross-linking and entrapment in an electropolymerized and biocompatible matrix [6]. Therefore, the development of a cheap, highly selective, fast and reliable non-enzymatic glucose sensor is still highly desirable.

Noble metals, metal alloys and metal nanoparticles [7, 8] have shown excellent potential in the development of non-enzymatic sensors, however these electrodes have some drawback as low selectivity, high cost, surface etching during electrochemical

B. Andò et al. (eds.), *Sensors*, Lecture Notes in Electrical Engineering 431,
DOI 10.1007/978-3-319-55077-0_12

processes or surface poisoning by intermediate species. In this context, electrochemical glucose sensors based on nanostructured metal-oxide materials such as zinc oxide (ZnO), manganese oxide (MnO_2), titanium oxide (TiO_2), cerium oxide (CeO_2), silicon oxide (SiO_2) and copper oxides (CuO, Cu_2O) have offered many advantages compared to enzymatic or noble metal-based glucose sensors [9]. Among them, nanostructured CuO is a promising candidate for the development of non-enzymatic glucose sensors because of its high specific surface area, good electrochemical activity then excellently high sensitivity, stability and anti-interference ability [10–12]. However, the preliminary synthesis of CuO and the successive modification of the electrode is often tedious. So, the development of simple method for the synthesis of CuO nanostructures and the fabrication of electrode for electrochemical sensors still remains a challenging topic. In order to overcome these problems, in recent years new in situ techniques of synthesis have been proposed for the growth of CuO nanostructures directly on copper substrates [13, 14]. On this basis, we present a simple method to prepare an electrochemical sensor for the determination of glucose by modification of planar copper electrodes in order to obtain a nanostructured copper oxide-based electrode. In particular, we show the versatility of the preparation method comparing the electrochemical sensing properties towards glucose of both commercial and homemade modified copper electrodes prepared with the same technique.

2 Experimental

2.1 Sensors Fabrication

Three electrode planar devices were used to fabricate electrochemical glucose sensors based on CuO nanostructured working electrode. A homemade device was prepared in according to what reported previously [15]. It consists in a three-electrode planar configuration with a circular copper working electrode of 3 mm in diameter, a silver pseudo-reference electrode and a graphite counter electrode. The commercial one is a Dropsens CU10 consisting in a copper working electrode of 4 mm in diameter, a silver pseudo-reference electrode and a graphite counter electrode.

To obtain the modified electrodes, CuO nanostructures were grown in situ on the copper working electrodes following a simple and fast two-step procedure.

In the first step the Cu electrode is immersed into an aqueous solution containing 7.5 mM $CuSO_4 \times 5H_2O$ and 0.4 M Na_2O_2, for 20 min at room temperature, in order to obtain the hydroxyl phase $Cu(OH)_2$. In the second step a drying at 120 °C for 3 h and a subsequent thermal treatment at 180 °C for 3 h promote the complete transformation of hydroxyl phase to CuO.

2.2 Characterization

Working electrodes of both commercial and homemade sensors were characterized by scanning electron microscopy before and after chemical modification of their surfaces.

Electrochemical measurements were performed with a DropSens μStat 400 potentiostat/galvanostat. All electrochemical experiments were carried out using the same three electrodes of each device with un-modified Cu or CuO nanowires modified working electrode. Cyclic voltammetry (CV) was used to evaluate and compare the

electrochemical behaviors and the sensing performance of developed sensors. All electrochemical tests were carried out in alkaline solution (0.1 M KOH) in order to promote the glucose oxidation on the electrodes surfaces recording the CV curves at 100 mV/s in absence and presence of different concentrations of glucose.

3 Results

3.1 Morphological Characterization

For both homemade and commercial devices the working electrodes surface were investigated before and after chemical modification. In Fig. 1a, d is shown the SEM micrographies of homemade and commercial un-modified electrodes respectively. Each one shows a different surface roughness. In the case of the homemade electrode the presence of parallel grooves is due to mechanical abrasion carried out in order to remove possible surface oxides before the chemical treatment. For commercial one has not been performed any kind of pretreatment and the shown surface morphology is as-bought. In Fig. 1b, c, e, f is shown the SEM micrographs at different magnifications, for homemade and commercial electrode respectively, after chemical modification. In the micrographs at lower magnification, it is possible to observe a uniform coverage of the surface of both electrodes in comparison to the respective un-modified ones due to the growth of the CuO phase on them. At higher magnification similar nanostructures can observed for both electrodes with fibrous and needle-like shapes. As obtained suggests that the adopted technique of synthesis, in spite of the different starting copper support, can effectively lead to the formation the required CuO nanostructure with no special precautions.

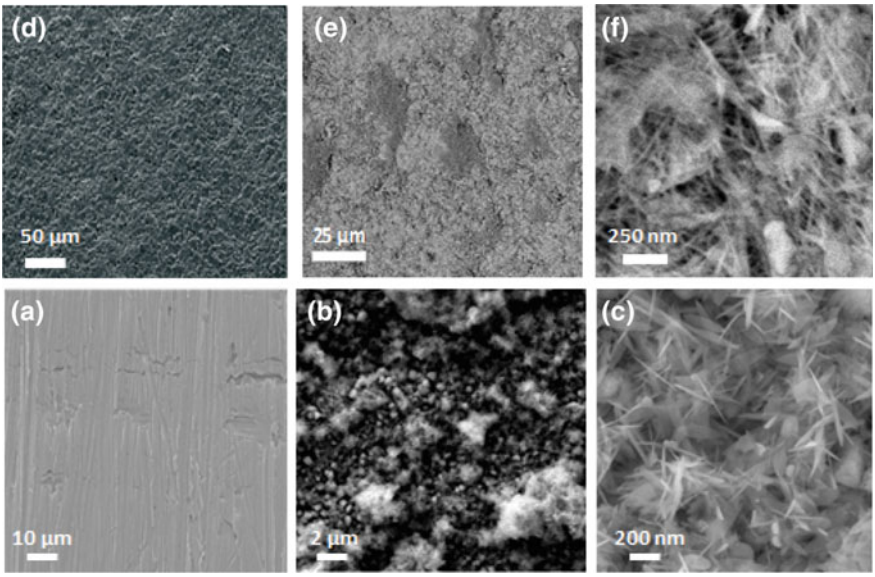

Fig. 1 SEM images of electrodes. **a** Cu unmodified homemade. **b**, **c** CuO modified homemade. **d** Cu unmodified commercial. **e**, **f** CuO modified commercial

3.2 Electrochemical Characterization

CV was used to investigate the electrochemical behavior of Cu and CuO modified electrodes towards glucose oxidation. The electrochemical behavior and the sensing performance of the homemade sensor are detailed in an our previous paper [15]. Here we focus on the electrochemical characterization of the commercial sensor with unmodified and CuO nanostructure modified electrode and the comparison with the previous homemade sensor. In Fig. 2a, b is shown the CVs obtained for commercial unmodified and modified electrodes in absence and presence of 5 mM of glucose in 0.1 M KOH respectively. From the CVs recorded in blank 0.1 M KOH solution (Fig. 2a) a large difference in the area of the cycles between unmodified and modified electrodes can be observed. This could be due to the larger surface area of CuO modified electrode compared to unmodified one as effect of an increased capacitance of double layer directly related to the real surface of electrode. Furthermore, CV of CuO modified electrode shows a weak oxidation peak during anodic scan and a subsequent marked broad reduction peak during cathodic scan close to the potential of 0.55 V, which might be correspond to redox couple Cu(II)/Cu(III) in according to previously reported [13]. However, compared to the previous one, unmodified electrode shows a very narrow cycle, though a weak reduction peaks during cathodic scan can be also observed for it. Indeed, as effect of strong alkaline solution, some oxidized group could be formed on the copper surface which might justify the observed reduction peak. In presence of 5 mM of glucose in 0.1 M KOH solution both unmodified and CuO modified electrodes show marked anodic peaks due to the glucose oxidation. The absence of reduction peaks suggests the irreversible oxidation of this species. Although both electrodes are able to detect the presence of glucose, the CuO modified one shows a remarkable increase in anodic current and a slight decrease of the oxidation over-potential. In fact, while for the unmodified electrode the glucose oxidation peak is centered at about 0.63 V with onset potential at 0.4 V, in the case of the CuO modified electrode the maximum of the oxidation peak occurs at 0.55 V with onset potential close to 0.3 V. This excellent electrochemical properties showed by CuO modified electrode may be due to the high reactivity of such material to catalyze the oxidation of the glucose, and the larger specific surface, typical of this nanostructure, which would favor the increase of the oxidation current, and then the sensitivity.

Figure 3a shows the CVs recorded for different concentrations of glucose in 0.1 M KOH solution for CuO modified commercial electrode. The anodic peak current increases with increasing of glucose concentration in according to a linear trend. In Fig. 3b is plotted the peak current density, obtained normalizing the peak currents to the respective geometric area of each electrode, for both commercial and homemade electrodes before and after the surface modification.

Table 1 summarizes the features and performance of the electrodes. Each electrode shows an excellent linearity of response in the investigated range, i.e. 0–4 mM of glucose. Both commercial and homemade electrodes modified by CuO nanostructures show increased sensitivity in comparison to the respective unmodified electrodes. In particular, the Cu unmodified commercial electrode shows a slightly higher sensitivity compared to the homemade one probably due to the greater roughness, which lead to a higher active surface. Unlike, in the case of CuO modified electrodes, both ones show a

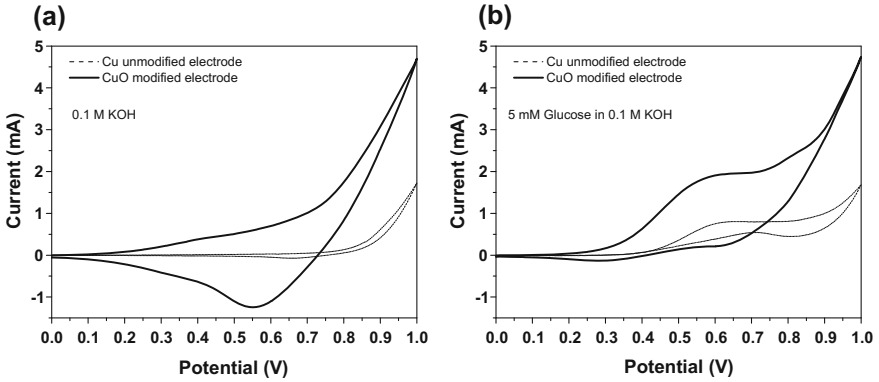

Fig. 2 CVs of both Cu unmodified and CuO modified commercial electrodes in absence (**a**) and presence of 5 mM glucose (**b**) in 0.1 M KOH solution

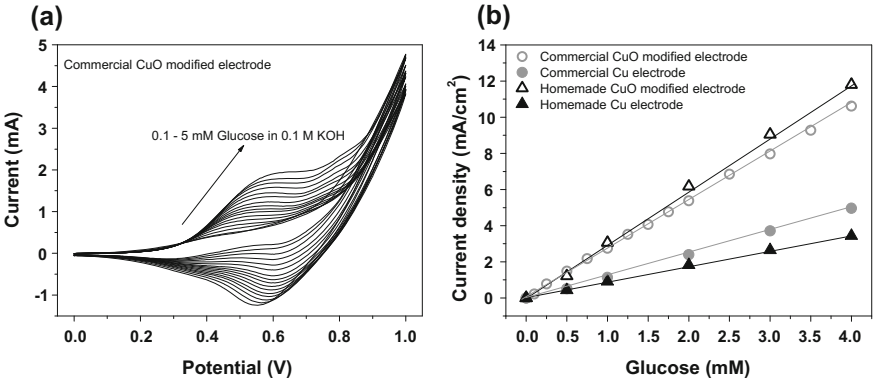

Fig. 3 **a** CVs at different glucose concentrations of commercial CuO modified electrode. **b** Peak current densities at different glucose concentrations for each electrode

Table 1 Comparison of the features and performances of the electrodes

Electrode	Working electrode area (cm^2)	Peak potential E_p (V)	Sensitivity ($\mu A/mM\ cm^{-2}$)	Liner fit R^2
Cu unmodified homemade	0.07	0.75	860	0.999
CuO modified homemade	0.07	0.65	2920	0.998
Cu unmodified commercial	0.125	0.63	1300	0.999
CuO modified commercial	0.125	0.55	2760	0.998

very similar sensitivity suggesting that, after modification, they present a very similar active surface. The difference in potential observed comparing the oxidation potential of glucose for commercial and homemade electrodes, is only due to the different reference electrode adopted. However, for both electrodes after modification with the CuO nanostructures the oxidation peak is shifted of about 0.1 V towards lower potentials.

4 Conclusion

Three electrode planar electrochemical sensors were fabricated and tested to monitor glucose in alkaline media. By a simple oxidative treatment, CuO nanostructures were directly grown on the surface of commercial and homemade Cu working electrodes. The morphological characterization shows the formation of fibrous and acicular nanowires for both homemade and commercial electrodes. Furthermore, both CuO modified electrodes show similar electrochemical behavior towards glucose oxidation in alkaline medium suggesting a high versatility of the employed method.

References

1. M.M. Farid, L. Goudini, F. Piri, A. Zamani, F. Saadati, Molecular imprinting method for fabricating novel glucose sensor: Polyvinyl acetate electrode reinforced by MnO_2/CuO loaded on graphene oxide nanoparticles. Food Chem. **194**, 61–67 (2016)
2. K. Tian, M. Prestgard, A. Tiwari, A review of recent advances in nonenzymatic glucose sensors. Mater. Sci. Eng. C **41**, 100–118 (2014)
3. J. Wang, Z. Fang, Enzymatic determination of glucose by optical-fiber sensor sequential injection renewable surface spectrophotometry. Chem. Res. Chin. Univ. **22**(3), 287–291 (2006)
4. T. Larsen, Fluorometric determination of free glucose and glucose 6-phosphate in cows' milk and other opaque matrices. Food Chem. **166**, 283–286 (2015)
5. C. Ma, Z. Sun, C. Chen, L. Zhang, S. Zhu, Simultaneous separation and determination of fructose, sorbitol, glucose and sucrose in fruits by HPLC–ELSD. Food Chem. **145**, 784–788 (2014)
6. M. Yang, Y. Yang, Y. Liu, G. Shen, R. Yu, Platinum nanoparticles-doped sol–gel/carbon nanotubes composite electrochemical sensors and biosensors. Biosens. Bioelectron. **21**(7), 1125–1131 (2006)
7. L.-H. Li, W.-D. Zhang, Preparation of carbon nanotubes supported platinum nanoparticles by an organic colloidal process for nonenzymatic glucose sensing. Microchim. Acta **163**(3–4), 305–311 (2008)
8. Y. Sun, H. Buck, T.E. Mallouk, Combinatorial discovery of alloy electrocatalysts for amperometric glucose sensors. Anal. Chem. **73**(7), 1599–1604 (2001)
9. M.M. Rahman, A. Ahammad, J.-H. Jin, S.J. Ahn, J.-J. Lee, A comprehensive review of glucose biosensors based on nanostructured metal-oxides. Sensors **10**(5), 4855–4886 (2010)
10. W. Zhang, R. Li, L. Xing, X. Wang, X. Gou, Carnation-like CuO Hierarchical Nanostructures Assembled by Porous Nanosheets for Nonenzymatic Glucose Sensing. Electroanalysis **28**, 2214–2221 (2016)

11. W. Lu, Y. Sun, H. Dai, P. Ni, S. Jiang, Y. Wang, Z. Li, Z. Li, CuO nanothorn arrays on three-dimensional copper foam as an ultra-highly sensitive and efficient nonenzymatic glucose sensor. RSC Adv. **6**(20), 16474–16480 (2016)
12. C. Li, H. Yamahara, Y. Lee, H. Tabata, J.-J. Delaunay, CuO nanowire/microflower/nanowire modified Cu electrode with enhanced electrochemical performance for non-enzymatic glucose sensing. Nanotechnology **26**(30), 305503 (2015)
13. Z. Zhuang, X. Su, H. Yuan, Q. Sun, D. Xiao, M.M. Choi, An improved sensitivity non-enzymatic glucose sensor based on a CuO nanowire modified Cu electrode. Analyst **133** (1), 126–132 (2008)
14. Z. Li, Y. Chen, Y. Xin, Z. Zhang, Sensitive electrochemical nonenzymatic glucose sensing based on anodized CuO nanowires on three-dimensional porous copper foam. Sci. Rep. **5**, 16115 (2015)
15. C. Espro, N. Donato, S. Galvagno, D. Aloisio, S.G. Leonardi, G. Neri, CuO nanowires-based electrodes for glucose sensors. Chem. Eng. Trans. **41**, 415–420 (2014)

Stable Aqueous Solution for the Fabrication of α-Fe_2O_3 Thin Film-Based Chemoresistive Sensors

A. Mirzaei[1], M. Bonyani[1], S.G. Leonardi[2], N. Donato[2], and G. Neri[2(✉)]

[1] Department of Materials Science and Engineering, Shiraz University, Shiraz, Iran
[2] Department of Engineering, University of Messina, 98166 Messina, Italy
gneri@unime.it

Abstract. In this paper, stable water solution using a Pechini sol-gel process was prepared. The solution was used for the direct printing of iron oxide precursor on alumina substrates. To convert the precursor to the desired iron oxide phase, an annealing step was carried out at elevated temperatures (>450 °C). In this work a α-Fe_2O_3 thin film-based chemoresistive sensors for ethanol detection in air were fabricated. The device developed was investigated for evaluate the sensing characteristics such sensitivity, selectivity and stability.

Keywords: Iron oxide · Thin films · Ethanol sensors

1 Introduction

The ability to pattern oxide structures at the microscale directly on different substrates is important for a broad range of emerging applications, including sensors, micro-fuel cells and batteries, photocatalysts, solar arrays, and photonic band gap (PBG) materials. Sol-gel can be used to prepare suitable inks for direct patterning. For example, by designing sol-gel inks based on organometallic precursors, Duoss et al. [3] have recently demonstrated direct ink writing of oxide structures.

Iron oxide (Fe_2O_3) is being currently explored diverse applications such as magnetic storage media, environment protection, sensors, catalysis, etc. In the pursuit to prepare Fe_2O_3 nanomaterials, a variety of synthesis routes like precursor, precipitation, sol-gel, hydrothermal, combustion, solvent evaporation etc. have been reported [2, 4, 7, 8]. However, most of these methods are associated with some limitations such as use of expensive compounds as starting materials, use of strong bases as precipitating agent and formation of mixed or undesired crystalline phases.

Therefore, development of a simple synthetic methodology for preparation of pure Fe_2O_3 nanostructures is a major challenge till now. Herein, we report a synthesis methodology for preparation of single phase -Fe_2O_3 thin film to use as a sensitive layer for ethanol sensors.

B. Andò et al. (eds.), *Sensors*, Lecture Notes in Electrical Engineering 431,
DOI 10.1007/978-3-319-55077-0_13

The important features of the methods reported here are: no impurity phase formation; the use of simple and cheap starting materials and water as solvent. The simplicity of the method to produce nanostructured pure Fe_2O_3 makes it attractive as compared to other synthetic methods.

Ethanol (C_2H_5OH) is one of the most commonly and widely used alcohols and has many applications in food, biomedical, transportation and chemical industries, therefore the detection of ethanol vapor at ppm levels is of great importance [1, 6]. Consequently, the possibility to have cheap, reliable, and simple to prepare sensors is very appreciated. Because the iron oxide has been shown several times an excellent, stable then a promising material for the monitoring of ethanol [5, 9], in this work we will focus our attention to it.

2 Experimental

2.1 Preparation of the Printable Aqueous Solution

For synthesis of α-Fe_2O_3 thin films iron (III) sulfate, was used as Fe (III) source, polyethyleneglycole was used as esterification agent and citric acid was used as chelating agent. All equipment was cleaned thoroughly by soaking in ethanol and washed with distilled water. Figure 1 shows schematic representation of steps to obtain iron oxide precursors ink.

In a typical synthesis process two aqueous solutions were prepared. The first solution was prepared by dissolving of appropriate amount of iron sulfate into 50 ml of hot (70 °C) distilled water (to make 0.1 M solution) under magnetic stirring vigorously until a homogeneous solution was formed.

The second solution was prepared by dissolving of appropriate amount of citric acid in hot distilled water (50 ml) at 70 °C (Molar ratio between citric acid and metallic Fe was 2). The separate solutions were kept under magnetic stirring until complete dissolution. Then these two solution were mixed and appropriate amount of polyethyleneglycol (molar ratio between PEG and metallic iron was 2) was added. The resulting mixture was refluxed at 120 °C for 2 h, obtaining a clear yellow-colored solution.

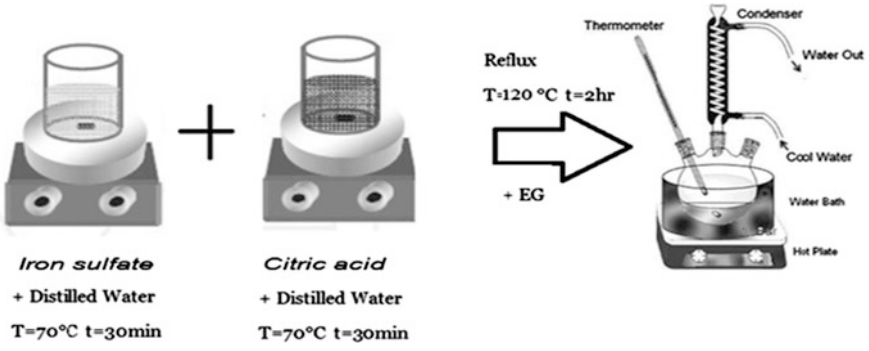

Fig. 1. Schematic representation for the preparation of printable iron oxide precursors ink

2.2 Sensor Preparation and Sensing Tests

Sensor devices were fabricated dropping an appropriate volume of above solution on alumina substrates (3×6 mm^2) supplied with interdigited Pt electrodes and heating element on the back side. The sensors prepared were let drying at room temperature then heat treated at two different temperature 450 and 600 °C to obtain pure crystalline thin film iron oxides.

Measurements were performed under a dry air total stream of 100 sccm, collecting the sensors resistance data in the four points mode by means of an Agilent 34970A multimeter. Electrical measurements were carried out in the working temperature 400–450 °C. Sensing tests were performed in a lab apparatus which allows to operate at controlled temperature and to perform resistance measurements while varying the ethanol concentration from 12.5 to 500 ppm. The gas response was defined as the ratio R_{air}/R_{gas} and R_{gas}/R_{air} for reducing and oxidizing gas respectively, where R_{air} represents the electrical resistance of the sensor in dry air and R_{gas} is electrical resistance of the sensor at different ethanol (or another gases) concentration. Response time, t_{res}, was defined as the time required for the sensor resistance to reach 90% of the equilibrium value after ethanol is injected and recovery time, t_{rec}, was taken as the time necessary for the sensor resistance to reach 90% of the baseline value in air.

3 Results

The sensor devices were treated at high temperatures in order to promote the complete transformation of precursors in a stable iron oxide phase. Two different temperature 450 and 600 °C respectively were used and the effect on the sensing performance was then investigated. Figure 2a, b show the dynamic responses of both sensors recorded at operation temperature of 450 °C during pulses at different concentrations of ethanol. Both sensors show a decrease of resistance when the sensitive films are exposed to ethanol pulses in agreement to the effect of a reducing gas on a n-type semiconductor material [5]. In Fig. 2c are reported the calibration curves extrapolated from the previous dynamic responses to different concentrations of ethanol. As it can be observed, the sensor treated at 600 °C shows a decreased sensitivity compared to the sensor treated at 450 °C. This effect could be due to an excessive sintering of the iron oxide which leads to a compact thin film characterized by low surface area. In the case of the sample treated at 450 °C, the lower annealed temperature while ensuring the transformation into iron oxide precursors thus favoring the stability to the sensitive film, it would not enable the complete sintering of the material. Consequently, the possible formation of a porous structure with a higher specific surface could justify the greater sensitivity shown by this sensor. Having the best performance, the sensor treated at 450 °C was chosen for further investigation.

A good sensor should be as fast as possible so it is very important to understand the relationship between response/recovery time and ethanol concentrations. Figure 3 reports the response and recovery times of the sensor recorded at the operation temperature of 450 °C as function of ethanol concentration. As shown, increasing the ethanol concentration the response time becomes shorter and recovery time becomes

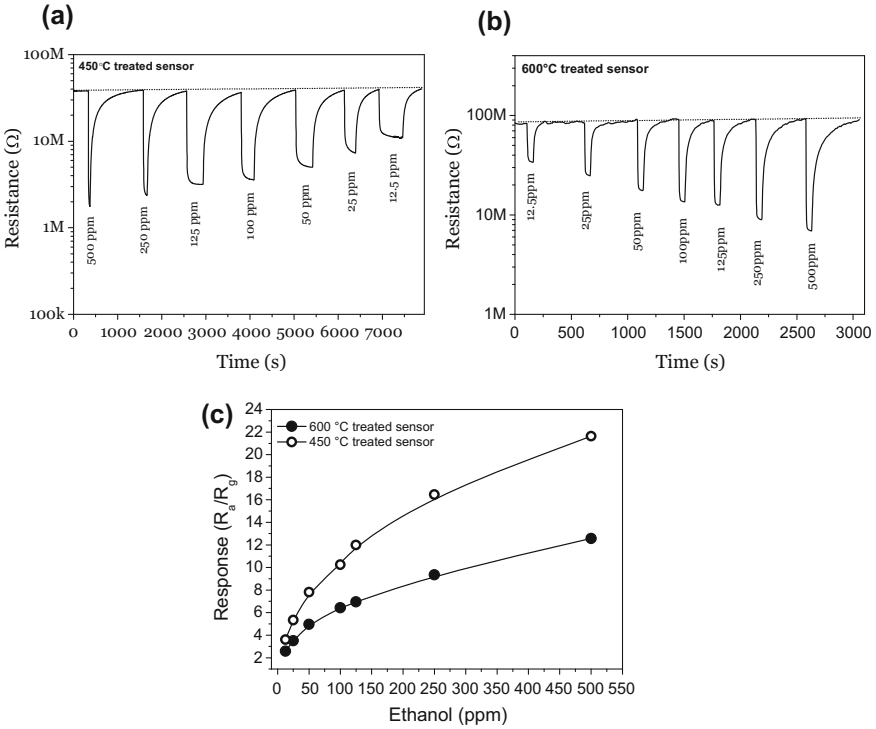

Fig. 2. Dynamic responses to ethanol of 450 °C (**a**) and 600 °C (**b**) treated sensors recorded at operation temperature of 450 °C (**c**) calibration curves

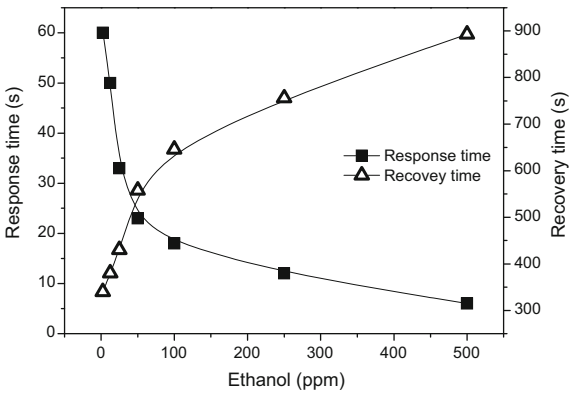

Fig. 3. Response and recovery times as function of ethanol concentrations recorded at operation temperature of 450 °C

longer. The shortest response time recorded is 6 s to 500 ppm ethanol, and the shortest recovery time is 360 s to 12.5 ppm ethanol. The response time and recovery depend on the reaction rate of ethanol molecules with the active sites on the sensitive material and by their time of desorption respectively. When the ethanol concentration is low, the ethanol molecules may spend relatively long time reacting with the active sites represented by oxygen ions. With the concentration increasing, the reaction time decreases, and the response time decreases accordingly. Unlike, because recovery time is due to the desorption rate of molecule from the surface of sensitive material, a higher concentration means a large number of molecules adsorbed which require long time to completely desorb. Both reaction and desorption processes of the gas molecules from sensitive surface are energetically activated processes so, the operating temperature has a large effect on their kinetics. In this case, although temperatures below 450 °C improved the sensitivity to ethanol, they also increased the response and recovery times of the sensor.

Reliability is another important parameter of the sensors. For a sensor this means to be stable and not have false positive then response only to the species of interest; in other words, it should be selective. Figure 4a compares the response to ethanol of the sensor as fabricated and after 8 days of operation. As observed, the sensor shows an excellent match in the responses recorded in the two different days. This aspect and the preservation of the baseline during the days suggest a good stability of the developed sensor.

The sensing response of sensor towards different reducing and oxidizing vapors and gases such as nitrogen dioxide, carbon monoxide, acetone, carbon dioxide, methane, ammonia, hydrogen, oxygen at different concentrations is shown in Fig. 4b. As observed, the response to the lowest concentration of ethanol tested (12.5 ppm) is about 2.5 times higher than the responses to other vapors and gases for typical their concentration in the main applications. As obtained suggests also an excellent selectivity of the here reported α-Fe_2O_3 thin film based sensor.

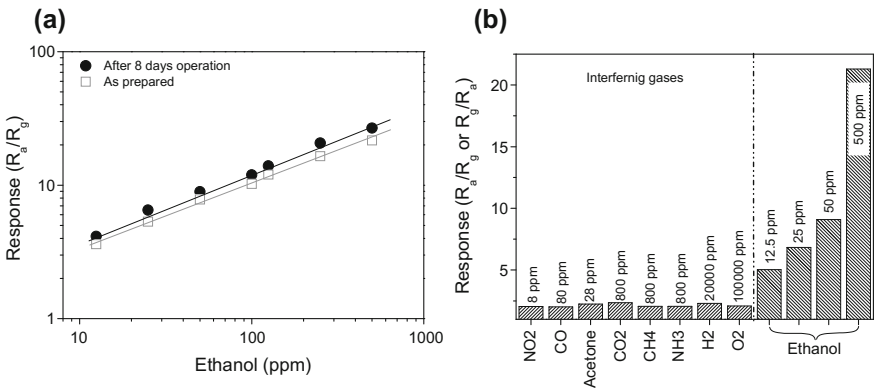

Fig. 4. **a** Comparison of the response to ethanol of the sensor as fabricated and after 8 days of operation. **b** Response of the sensor to different gases

4 Conclusion

In this paper, stable water solution using a Pechini sol-gel process was prepared and used to print a thin film on ceramic sensor substrates. The effect of annealing temperature has been investigated identifying 450 °C as the best condition to obtain a stable and sensitive film. The α-Fe_2O_3 thin film based sensor exhibits a highly selective sensing behavior towards ethanol and very stable response in time. The simple preparation method and the excellent sensing performance represent a promising and encouraging way for practical development of ethanol sensors.

References

1. R. Ab Kadir, R.A. Rani, A.S. Zoolfakar, J.Z. Ou, M. Shafiei, W. Wlodarski, K. Kalantar-zadeh, Nb_2O_5 Schottky based ethanol vapour sensors: effect of metallic catalysts. Sens. Actuators, B Chem. **202**, 74–82 (2014)
2. A.A. Ayachi, H. Mechakra, M.M. Silvan, S. Boudjaadar, S. Achour, Monodisperse α-Fe_2O_3 nanoplatelets: synthesis and characterization. Ceram. Int. **41**(2), 2228–2233 (2015)
3. E.B. Duoss, M. Twardowski, J.A. Lewis, Sol-gel inks for direct-write assembly of functional oxides. Adv. Mater. **19**(21), 3485–3489 (2007)
4. C. Han, Y. Wang, T. Lu, S. Yang, L. Wang, X. Song, Fabrication and magnetism of α-Fe_2O_3 nanotubes via a multistep ac electrodeposition. Chem. Phys. Lett. **633**, 47–51 (2015)
5. A. Mirzaei, K. Janghorban, B. Hashemi, M. Bonyani, S. Leonardi, G. Neri, Highly stable and selective ethanol sensor based on α-Fe_2O_3 nanoparticles prepared by Pechini sol-gel method. Ceram. Int. **42**(5), 6136–6144 (2016)
6. P. Patnaik, *A Comprehensive Guide to the Hazardous Properties of Chemical Substances* (John Wiley & Sons, 2007)
7. R. Ramesh, K. Ashok, G. Bhalero, S. Ponnusamy, C. Muthamizhchelvan, Synthesis and properties of α-Fe2O3 nanorods. Cryst. Res. Technol. **45**(9), 965–968 (2010)
8. A. Umar, M. Akhtar, G. Dar, S. Baskoutas, Low-temperature synthesis of α-Fe_2O_3 hexagonal nanoparticles for environmental remediation and smart sensor applications. Talanta **116**, 1060–1066 (2013)
9. Y. Wang, J. Cao, S. Wang, X. Guo, J. Zhang, H. Xia, S. Zhang, S. Wu, Facile synthesis of porous α-Fe_2O_3 nanorods and their application in ethanol sensors. J. Phys. Chem. C **112**(46), 17804–17808 (2008)

Optimization of Cyclic Voltammetric Curve Parameters to Measure Lactate Concentration in Urine Samples

Giulio Rosati[1(✉)], Matteo Scaramuzza[2], Elisabetta Pasqualotto[1,2], Alessandro De Toni[2], and Alessandro Paccagnella[1]

[1] Department of Information Engineering, University of Padova, via G. Gradenigo 6/b, 35131 Padua, Italy
rosatigiulio@gmail.com
[2] ARC - Centro Ricerche Applicate s.r.l, via J. da Montagnana, 49, 35132 Padua, Italy

Abstract. In this work, veal urine dilutions in Hepes-buffered Ringer's solution (HBRS) are tested by both UV-visible absorption spectroscopy and Cyclic Voltammetry (CV) to assess their viability as mediums for the detection of lactate, through the Lactate Dehydrogenase enzyme (LDH) reaction which involves the formation of NADH. Several data analysis algorithms for the recorded CV data are proposed and compared, in order to optimize the NADH detection in the urine samples dilutions. UV-visible spectroscopy was adopted as reference for NADH quantification.

Keywords: Biosensors, Cyclic Voltammetry, Lactate, SPCE, NADH, Urine

1 Introduction

Lactate detection in cattle urine samples is a non-invasive method which could help to prevent syndromes, e.g., sub-acute ruminal acidosis (SARA), that alter the quality of dairy products and seriously injure the animals in the herds [1, 2]. Electrochemical biosensors employing the Lactate Dehydrogenase enzyme (LDH) for the Lactate detection are a well-known technology [3, 4]. These sensors are based on the LDH catalysis, which reduces NAD^+ to NADH in presence of Lactate, and on the NADH electrochemical quantification (Scheme 1).

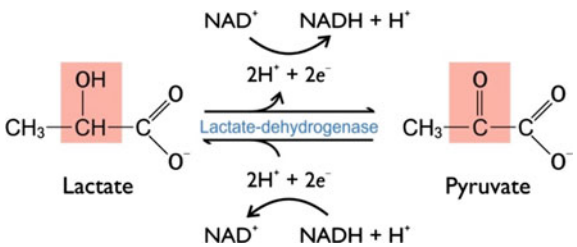

Scheme 1 Lactate Dehydrogenase (LDH) enzyme catalysis (elte.prompt.hu paragraph 7.6)

B. Andò et al. (eds.), *Sensors*, Lecture Notes in Electrical Engineering 431,
DOI 10.1007/978-3-319-55077-0_14

The NADH detection can be performed both optically (absorbance at 340 nm or fluorescence at 460 nm) and electrochemically, e.g. by Cyclic Voltammetries (CVs) which oxidize NADH generating an electrical current proportional to its concentration [5, 6]. However, since the NADH oxidation is an irreversible reaction which usually requires a high overpotential, two approaches are currently adopted: using a mediator to perform an electrocatalytic oxidation requiring lower overpotentials [7, 8], or developing new materials for the mediatorless oxidation at lower potentials [9, 10].

With the latter approach, no standard data analysis methods are reported for the construction of the NADH calibration curve [11]. Therefore, we introduce and compare six parameters extracted from the cyclic voltammograms, to quantify the NADH concentration produced by the LDH enzyme in presence of the different Lactate dilutions in Hepes Buffered Ringer's Solution (HBRS). Lastly, we validate these parameters by performing the same measurements with Lactate in veal urine diluted in HBRS at 1, 10 and 100%.

2 Materials and Methods

All the chemicals and biochemicals used in this work were purchased from Sigma Aldrich. The Nicotinamide Adenine Dinucleotide reduced (NADH) and oxidized (NAD^+) coenzymes were purchased in powder form, with a purity ≥ 97 and 96.5% (HPLC), respectively, and dissolved in the mediums prior to use. Lactic acid was purchased with a purity $\geq 98\%$ in powder form, dissolved in the mediums with a 100 mM concentration and conserved at 4 °C for maximum 5 days. The rabbit muscle Lactate dehydrogenase enzyme was purchased dehydrated, dissolved in PBS to a concentration of 100 U/ml, and aliquoted in 1 ml tubes stored at −20 °C.

The veal urine samples were provided by the Venetian Zooprophylactic Experimental Institute of Legnaro (Padova), from a 6 months old veal, and stored at −80 °C.

The sensors were purchased from Dropsens Inc. (Dropsens 110). They consist of screen-printed electrodes on ceramic substrate composed by carbon (working and counter electrodes) and silver (pseudo-reference electrode and contacts), respectively. The sensors were used with a Dropsens adapter both in the three and two electrodes configurations, for CV and EIS measurements, respectively.

The measurement techniques involved in this work are Cyclic Voltammetry (CV), and UV-Visible spectrometry (UV-Vis). The CVs were recorded using a CH Instruments Inc. 440a potentiostat with 100 µl of solution, while the UV-Vis measurements were performed using a Mapada UV 1600PC spectrophotometer with 4 ml quartz cuvettes (1 cm path length) filled by 2 ml of solution, i.e., a sufficient volume to completely cover the incident light spot.

The data analysis was performed by Matlab 2012a, using its native curve fitting tool for the linear fits.

3 Results and Discussion

The veal urine sample was diluted in HBRS to several concentrations ranging from 1 to 100% (pure sample).

The dilutions were characterized by UV-Visible spectroscopy and CV in order to define the level of interference which the sample exhibits at 340 nm, and at 456 mV, respectively. The former value is usually associated to the NADH absorption peak, while the latter to oxidation on the carbon electrodes. The results are depicted in Fig. 1.

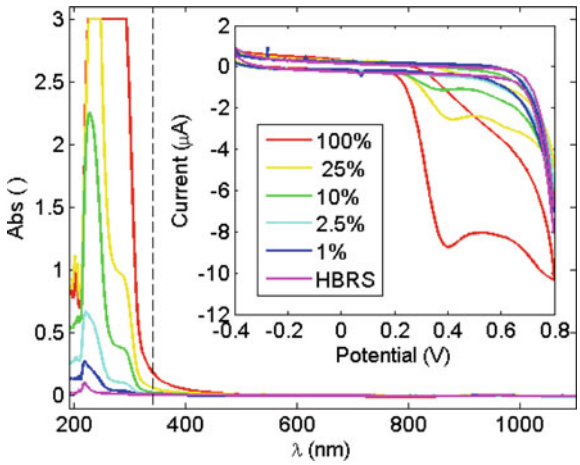

Fig. 1. UV-Visible absorption spectra of veal urine dilutions in HBRS. The *inset* shows the CV data of the same solutions

The adsorption at 340 nm is slightly disturbed by the urine sample. Conversely, the oxidation of one or more interfering species appears over 300 mV in the CVs, and the associated current is relevant at high sample concentrations.

Four urine sample dilutions in HBRS were selected for the next experiments, i.e. 100% (pure sample), 10, 1, 0% (HBRS). Each urine sample solution was spiked by 10 Lactate dilutions, ranging from 1 μM to 50 mM.

The prepared dilutions were tested by UV-Vis kinetic measurements at 340 nm for 300 s by mixing in the quartz cuvette 625 μM NAD^+ in the respective sample dilution (1.6 ml), 100 U/ml LDH in PBS (0.2 ml), and each Lactate dilution (0.2 ml). Then, at the end of the NADH formation kinetics, 100 μl of the cuvette solution were drop-casted on 3 electrochemical sensors for the CV NADH measurement.

Figures 2 and 3 show the UV-Vis kinetics and CVs for the Lactate dilutions in pure HBRS. The 300 s absorbance values, obtained from the UV-Vis kinetics allow the calculation of the final NADH concentration through the Lambert-Beer equation and the millimolar absorption coefficient 6.22 Abs mM^{-1} cm^{-1}.

Depending on which parameter of the CV curves is considered, different NADH calibration curves can be obtained, with respect to the UV-Vis determined NADH

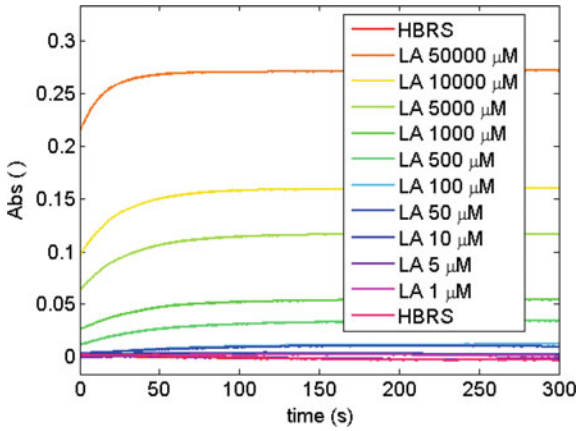

Fig. 2. UV-Vis kinetics at 340 nm of the Lactate dilutions in pure HBRS

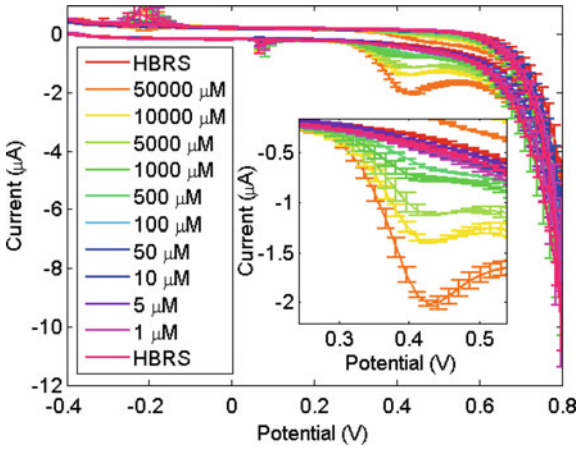

Fig. 3. CVs on the sensors of 100 µl of the Lactate testing solutions in the quartz cuvette at the end of the UV-Vis kinetic measurements

concentration. Therefore, we propose six CVs parameters for the NADH quantification in each urine sample dilution, defined as:

- P1: current value at 456 mV;
- P2: area under the CV curve;
- P3: area under the CV curves between 0.2 and 0.8 V;
- P4: area under the CV curves between 0.2 and 0.55 V;
- P5: current recorded at the potential which give the maximum R^2 value of the linear fit of the currents against the NADH concentrations;
- P6: current at the potential which give the absolute maximum slope of the linear fit of the currents against the NADH concentrations.

The definitions of these parameters reflect all the possible interpretations of the CV data. For example, P1 represent the current values at a fixed potential (obtained as the average of the NADH dilutions oxidation peak potentials). Conversely, P2, P3 and P4 are related to the charge accumulation, i.e., to the capacitance, developed by the NADH oxidation. They become more specific for this reaction as the boundaries of the area calculation becomes closer to the NADH oxidation potential. Finally, P5 and P6 are focused on the NADH calibration curve instead on the single CV.

Figures 4 and 5 show the absolute values of the slopes and the R^2 values of the linear fits of the NADH calibration plots, obtained by the six parameters considered from the UV-Vis and the CV measurements in the Lactate dilutions. The slopes represent the NADH detection sensitivity by the sensors while the R^2 values are a good indicator of the linearity of the detection in the considered range.

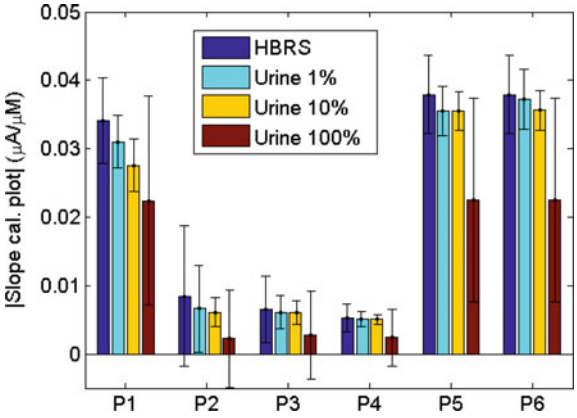

Fig. 4. Average modules of the NADH calibration plot linear fits' slopes and respective 95% confidence intervals, obtained by the CV parameters with respect to the 300 s UV-Vis kinetics determined NADH concentrations

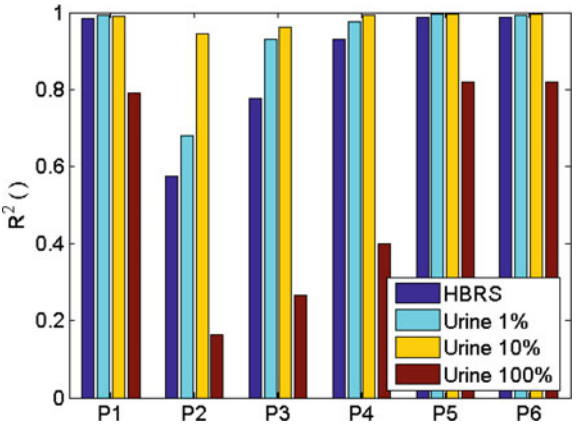

Fig. 5. R^2 values obtained from the linear fits of the CV parameters with respect to the 300 s UV-VIS kinetics determined NADH concentrations

From Fig. 4 it's evident that the P5 and P6 parameters allow a higher sensitivity, but the Lactate measurements in the pure urine sample shows a drastic sensitivity reduction and a standard deviation boost, most probably caused by the interferences observed in Fig. 1 inset.

Since the R^2 values represent the linear fit quality, it is interesting to notice that the P1 and P6 show a fit quality very similar to P5, which has the highest R^2 as it is formulated to maximize it. Moreover, as expected, the R^2 values of the area related parameters tend to those of P1, P5 and P6 as the portion of area is limited around the 456 mV current peak.

Another way to define the quality of the linear fits is to consider the fitted slope 95% confidence intervals. The linear fits which maximize the slope and minimize the interval is the best candidate as CV-related parameter for the NADH sensitive quantification. Therefore, the maximization of the ratio between the slope and its confidence interval becomes an important quality factor (QF), as described in Eq. 1, and shown in the inset of Fig. 6.

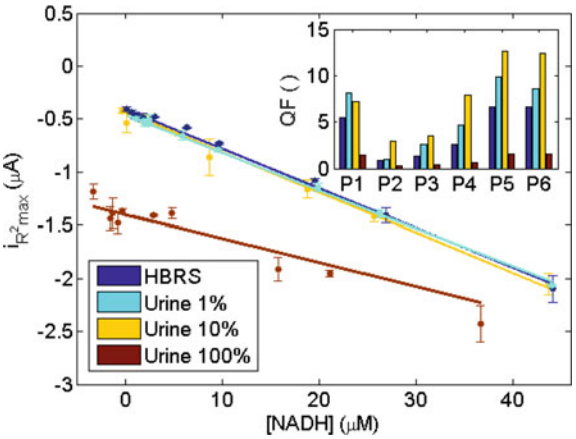

Fig. 6. NADH calibration plots and linear fits obtained by the P5 parameter for the Lactate concentrations in 100, 10, 1, and 0% sample urine. The *inset* shows the quality factor defined by the ratio between the linear fit slope and its 95% confidence interval for the NADH calibration plots of the CV parameters, with respect to the 300 s UV-Vis kinetics determined NADH concentrations

$$QF = |m| / cf_m^{95\%} \tag{1}$$

Where m is the considered parameter linear fit slope, and $cf_m^{95\%}$ is its 95% confidence interval obtained by the fitting procedure.

Again P5 and P6 result the best parameters and the measurements in the pure urine sample show very low values. However, the solutions which show the best ratios are 10 and 1% sample urine instead of HBRS, as could be expected.

Figure 6 shows the calibration plots and the respective linear fits obtained from the P5 parameter for the CV analysis, which proved to be the best in terms of quality of the linear fit (by definition), slope of the fit (and thus NADH sensitivity), and ratio between the slope and its 95% confidence interval.

4 Conclusions

In this work we have proved that the Lactate detection and quantification in veal urine is possible both optically by standard techniques such as UV-Visible spectroscopy, and electrochemically by Cyclic Voltammetries on low-cost disposable carbon screen-printed electrodes.

Furthermore, we have proposed several methods to analyze the CV data obtained after the stabilization of the LDH enzyme Lactate catalysis, and thus the produced NADH concentration. We compared these methods by evaluating their linearity, their sensitivity, and their linear fitting errors, with respect to the NADH concentration produced by the LDH catalysis.

We found that the best CV parameters are the currents recorded at the potentials that maximize the slope, i.e., the sensitivity (P6) of the linear fit of the calibration curve, and that maximize its R^2 value (P5). Therefore, the best approach to the data analysis in this case is to define in this way the potential by the calibration curve and then to use this parameter for the quantification of unknown Lactate concentrations.

Acknowledgements. The research activities reported here have been partially supported by the project «Sistema microelettronico per l'individuazione tempestiva di trattamenti illeciti sugli animali da allevamento», co-founded by Avepa (Veneto Region): Programma di sviluppo rurale, Misura 124 —Cooperazione per lo sviluppo di nuovi prodotti, processi e tecnologie nel settore agricolo, alimentare e forestale. We particularly thank UNICARVE for their contribution to the project activities.

References

1. J.M.D. Enemark, The monitoring, prevention and treatment of sub-acute ruminal acidosis (SARA): a review. Vet. J. **176**(1), 32–43 (2008). doi:10.1016/j.tvjl.2007.12.021
2. J.C. Plaizier, D.O. Krause, G.N. Gozho, B.W. McBride, Subacute ruminal acidosis in dairy cows: the physiological causes, incidence and consequences. Vet. J. **176**(1), 21–31 (2008). doi:10.1016/j.tvjl.2007.12.016
3. M.M. Rahman, M.J. Shiddiky, M.A. Rahman, Y.B. Shim, A lactate biosensor based on lactate dehydrogenase/nictotinamide adenine dinucleotide (oxidized form) immobilized on a conducting polymer/multiwall carbon nanotube composite film. Anal. Biochem. **384**(1), 159–165 (2009). doi:10.1016/j.ab.2008.09.030
4. H.C. Yoon, H. Kim, Electrochemical characteristics of a carbon-based thick-film L-lactate biosensor using L-lactate dehydrogenase. Anal. Chim. Acta **336**, 57–65 (1996)
5. A. Radoi, D. Compagnone, Recent advances in NADH electrochemical sensing design. Bioelectrochemistry (Amsterdam, Netherlands). **76**(1–2), 126–34 (2009). http://doi.org/10.1016/j.bioelechem.2009.06.008

6. J. Hart, S. Wring, Recent developments in the design and application of screen-printed electrochemical sensors for biomedical, environmental and industrial analyses. TrAC Trends Anal. Chem. **76**(2), 89–103 (1997)
7. Z.-H. Dai, F.-X. Liu, G.-F. Lu, J.-C. Bao, Electrocatalytic detection of NADH and ethanol at glassy carbon electrode modified with electropolymerized films from methylene green. J. Solid State Electrochem. **12**(2), 175–180 (2007). doi:10.1007/s10008-007-0378-1
8. L. Gorton, Electrocatalytic oxidation of NAD(P)H at mediator-modified electrodes. Rev. Mol. Biotechnol. **82**, 371–392 (2002)
9. E. Katekawa, F. Maximiano, L.L. Rodrigues, M. Flávia Delbem, S.H. Serrano, Electrochemical oxidation of NADH at a bare glassy carbon electrode in different supporting electrolytes. Anal. Chim. Acta **385**(1–3), 345–352 (1999). doi:10.1016/S0003-2670(98)00694-1
10. K.S. Prasad, J.-C. Chen, C. Ay, J.-M. Zen, Mediatorless catalytic oxidation of NADH at a disposable electrochemical sensor. Sens. Actuators, B: Chem. **123**(2), 715–719 (2007). doi:10.1016/j.snb.2006.10.012
11. P.E. Whitson, H.W. Vanden Born, D.H. Evans, Acquisition and analysis of cyclic voltammetric data. Anal. Chem. **45**(8), 1298–1306 (1973). http://doi.org/10.1021/ac60330a016

Inkjet Printed Graphene-Based Chemiresistive Sensors to NO_2

C. Schiattarella[1], T. Polichetti[2], F. Villani[2(✉)], F. Loffredo[2], B. Alfano[2], E. Massera[2], M.L. Miglietta[2], and G. Di Francia[2]

[1] Department of Physical Sciences, University of Naples Federico II, via Cinthia, 80126 Naples, Italy
[2] ENEA C.R. Portici, P.le E. Fermi 1, 80055 Portici (Naples), Italy
fulvia.villani@enea.it

Abstract. In this work, the possibility of manufacturing chemiresistive gas sensing devices by inkjet printing different LPE (Liquid Phase Exfoliation) graphene suspensions, formulated in standard organic solvents or aqueous mixtures, on rigid and flexible substrates has been studied. The sensing film has been obtained by printing a different number of graphene layers, depending on the specific ink/substrate system. The device performances have been investigated upon exposure to different concentrations of NO_2 at ambient pressure and temperature, addressing the device-to-device variation as function of the number of printed layers and the base conductance.

Keywords: Liquid phase exfoliation graphene · Ink-jet printing · Aqueous dispersion · Chemiresistive gas sensors

1 Introduction

Graphene is a material with surprising properties, that catalyzed the attention of the scientific community in the last years for its potential applications in different fields, from electronics to sensors.

Several techniques have been investigated for the graphene fabrication. With respect to mechanical exfoliation methods [1], which are not suited for the industrial scalability though providing highest quality material, the processes Chemical Vapor Deposition (CVD) [2], Chemical Exfoliation (CE) [3] and Liquid Phase Exfoliation (LPE) [4] are the most promising for a potential large-scale production of graphene. Anyhow, also these approaches are not discharged from some drawbacks: for instance, the CVD, due to the high temperatures required for the synthesis of graphene, is an energy consuming method; in addition, the material needs to be transferred from the growth to final substrate, with a potential degradation of the film properties. The CE method through the chemical reduction of graphite oxide (GO) is commonly employed to synthesize graphene for industrial, large-scale applications thanks to the good solubility of the insulating GO in a common and simple solvent as water; as a counterweight, the reduction step, needed to obtain the conductive material (reduced-graphene oxide, R-GO), leaves many structural defects in the crystal lattice, decreases the water solubility and, additionally, generally employs highly dangerous chemicals, such as

B. Andò et al. (eds.), *Sensors*, Lecture Notes in Electrical Engineering 431,
DOI 10.1007/978-3-319-55077-0_15

hydrazine. In comparison with the above described methods, LPE is a more sustainable process: it allows to produce graphene through the exfoliation of graphite in standard organic solvents [5–7] or simply hydro-alcoholic mixtures [8]. Furthermore, LPE-based graphene can be deposited by solution-processable techniques, like inkjet printing (IJP), a technology which allows to selectively deposit in a controlled manner minimizing the process steps and the waste materials.

In the present work, chemiresistive gas sensing devices have been fabricated by inkjet printing different LPE graphene suspensions on rigid and flexible substrates. The device performances have been investigated upon exposure to different concentrations of the gas NO_2 in environmental conditions.

2 Experimental

Different LPE graphene-based inks have been prepared. Starting from commercial graphite powder (Sigma-Aldrich, product 332461), a first ink (INK1) has been formulated by dispersing it in N-methyl-pirrolidone (NMP) (10 mg/mL) followed by a sonication for 3 h, and a second ink (INK2) by using a mixture of water/isopropanol (IPA/H_2O (1:7)) as solvent and sonicating the obtained dispersion for about 48 h. Then, each suspension has been centrifuged to remove the larger graphitic structures or the unexfoliated flakes and the surnatant has been taken as ink [9].

In order to analyze the surface morphology of the produced graphene, atomic force microscopy (AFM) measurements have been carried out in tapping mode by the Veeco Dimension Digital Instruments Nanoscope IV system. Moreover, the inkjet printed material has been also investigated by scanning electronic microscopy (SEM, LEO 1530).

Commercial alumina and glossy paper substrates with interdigitated gold electrodes have been employed as transducers.

The inkjet equipment was a Dimatix Materials Printer 2831 (DMP2831) of FUJIFILM—USA suitable for the print of functional inks onto flexible and rigid substrates. This system uses a piezoelectric drop-on-demand technology to eject droplets through a multi-nozzles printhead. The pattern of the printed sensing material was a rectangular surface. The chemi-resistor devices have been manufactured by printing a different number of graphene-based sensing layers, depending on the specific ink/substrate system. After printing, in order to remove the residual solvent a thermal treatment has been performed by keeping the devices on hot-plate at 100 °C for 15 min.

Tests for sensing measurements upon the analyte NO_2 have been performed in a stainless steel chamber placed in a thermostatic box, keeping constant the temperature (T = 22 °C), the relative humidity (RH = 50%) and under a controlled environment at atmospheric pressure.

The sensing analysis has been carried out by biasing the single device at 1 V. Specifically, the measurement protocol has consisted of several sequential exposures at different analyte concentrations, where each exposure step has been preceded and followed by baseline and recovery phases, respectively, in inert atmosphere.

3 Results and Discussion

In our previous work [10], we demonstrated that IJP is able to deposit LPE graphene-based ink in a controlled manner so as to produce sensor devices with reproducible performances in terms of electrical response upon gas exposures. In that case, the ink was a dispersion of graphene in NMP and the employed substrate was alumina. Here we aim to further investigate the device-to-device variation as function of the number of printed layers and the base conductance. Therefore, by fixing the employed materials, chemiresistive sensor devices have been fabricated by inkjet printing the INK1 (see experimental section) onto gold/alumina transducers, and the sensing film has been obtained by printing a different number of overlapped layers (n). Just after their fabrication, the device have been electrically characterized in terms of initial resistance and sensing properties. The measurement results are summarized in Table 1. In detail, the initial resistance (R) has been detected in inert atmosphere under bias of 1 V, while the sensing properties have been analyzed through tests upon 10 min long exposure to the gas NO_2 and evaluating the conductance variation ($\Delta G/G_0$), namely the percentage variation of the conductance with respect to its initial value detected at the beginning of the exposure (G_0).

Table 1. Initial resistance (R) and conductance variation ($\Delta G/G_0$) values of the chemiresistive sensor devices fabricated by inkjet printing the INK1 (LPE graphene in NMP) onto gold/alumina transducers by varying the number of overlapped layers (n) to form the sensing film

Device	Printed layers	Initial resistance (kΩ)	Conductance variation (%) exp. to 1 ppm of NO_2
GR_NMP_IJP_2	2	400	3.5 (very noisy)
GR_NMP_IJP_3	3	10.2	2.5
GR_NMP_IJP_4	4	1.5	1.7
GR_NMP_IJP_5	5	0.6	1.5
GR_NMP_IJP_15	15	0.05	Unresponsive

As expected, by increasing the number of printed layers, and, hence, the deposited material, the devices become more conductive and the $\Delta G/G_0$ decreases. In Fig. 1, R and $\Delta G/G_0$ as function of n are reported. As it can be observed, both the parameters are well fitted by hyperbolic functions. This can be easily explained by assimilating the device as schematized in Fig. 2, where a section of the printed layer and the electrical contacts are displayed. Referring to that scheme, R follows the Ohm's law, $R = \rho * l/(w * t)$, where ρ is the resistivity. Assuming that each printed layer has always the same thickness (t_0) so that the final thickness of the sensing film is $t = n * t_0$, then R increases as $1/n$ increases. Similarly, since $\Delta G/G_0$ depends on the specific surface (S/V, where $S = l * w$ is the exposed surface and $V = l * w * t$ is the volume), then also $\Delta G/G_0$ increases as $1/n$ increases.

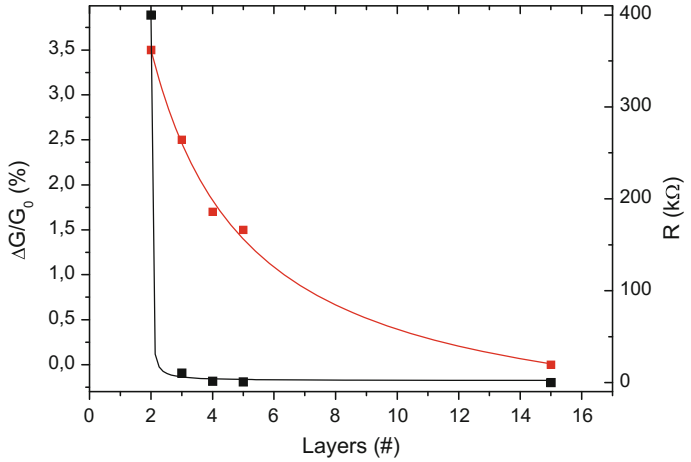

Fig. 1. Initial resistance (*R*) (*black*) and conductance variation ($\Delta G/G_0$) (*red*) values versus the number of overlapped printed layers (*n*) and related fit curves (Color figure online)

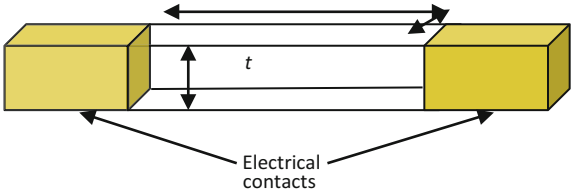

Fig. 2. Scheme of a section of the printed sensing layer and the electrical contacts of the manufactured chemiresistive device

Moreover, in order to investigate the possibility to fabricate graphene-based sensor devices by employing eco-friendly materials, the INK2 has been formulated by dispersing graphite flakes in a hydro-alcoholic mixture and printed onto glossy paper substrate.

The morphology of the printed material has been characterized by AFM analysis and the detected phase image is shown in Fig. 3. The AFM investigation shows a presence of restacked aggregates formed by planar-structured flakes. These structures are randomly distributed with cracks and gaps between neighbouring sheets.

SEM analysis confirmed this distribution of the printed material as AFM pointed out. By observing SEM image, displayed in Fig. 4, the deposition appears rather inhomogeneous and regions with overlapped flakes are clearly visible.

The material electrical property has been also investigated through the volt-amperometric characterization and the measurement results are reported in Fig. 5. The detected data I–V have been well interpolated by a linear fit showing the evident ohmic behavior of the material.

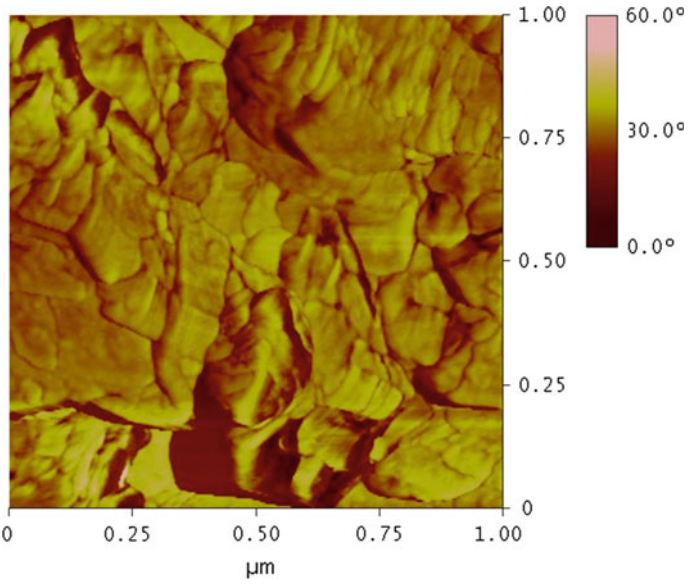

Fig. 3. AFM phase image of the sensing film printed by an aqueous graphene dispersion (scan size 1 × 1 μm^2)

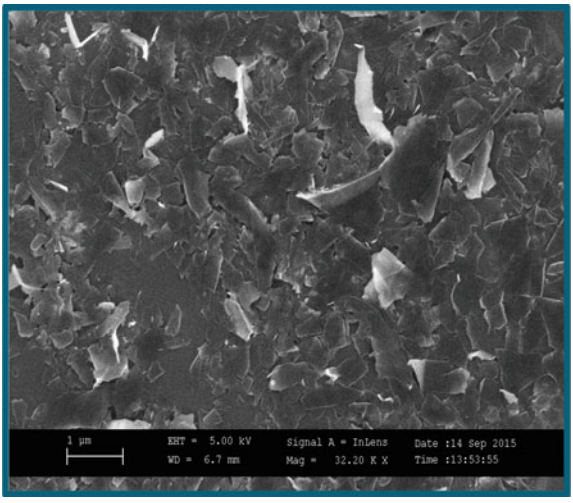

Fig. 4. SEM image of the printed graphene film

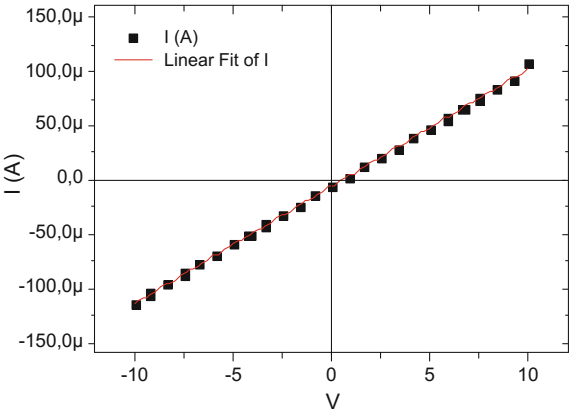

Fig. 5. I–V and related linear fit curve

The sensing property of the printed aqueous LPE-graphene chemiresistors has been tested by exposing them gas vapours of NO_2. Specifically, sequential cyclic exposures to the analyte at different concentrations have been performed, and the device outputs are reported in Fig. 6. As expected, during the exposure window to an acceptor analyte gas as NO_2, a conductance increase has been observed since LPE graphene is a p-type material [9]. It is worth noting that the device does not recover to the initial conductance value, so indicating that the material is not able to completely desorb the analyte. This also affects the sensitivity curve plotted by correlating the $\Delta G/G_0$ values to the NO_2 concentrations (Fig. 7).

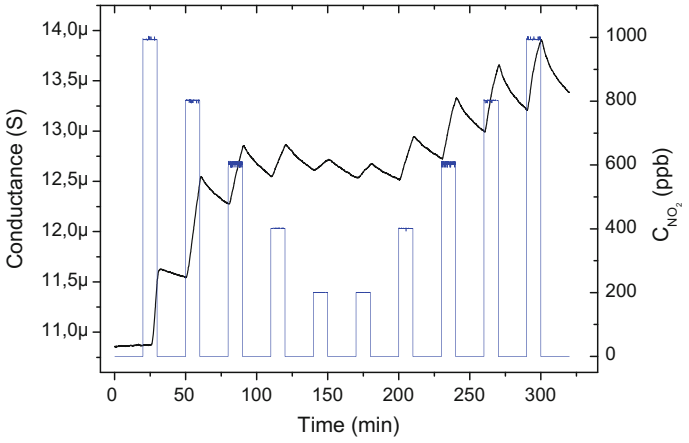

Fig. 6. Typical conductance behaviour of the chemiresistive device upon sequential analyte 10 min-long pulses (*dashed areas*) at different concentrations

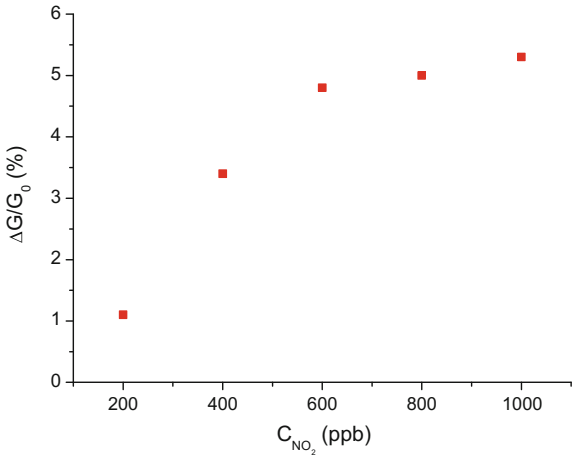

Fig. 7. Sensitivity curve: $\Delta G/G_0$ as function of NO_2 concentration

As it can be seen, at higher concentrations of the target analyte the curve diverges from a linear behavior, due to a poisoning effect of the sensing material. Nonetheless, good repeatability of the electrical responses upon identical exposures have been observed in the forward and backward cycles, as displayed in Table 2, where the $\Delta G/G_0$ values upon different concentrations of NO_2, ranging from 200 to 1000 ppb, are reported.

Table 2. Conductance variation ($\Delta G/G_0$) values of the chemiresistive sensor devices fabricated by inkjet printing the INK2 (LPE graphene in IPA/H_2O) onto gold/paper transducers upon different concentrations of NO_2 from 200 to 1000 ppb and vice versa

C_{NO_2} (ppb)	$\Delta G/G_0$ (%)	
	1000 ppb → 200 ppb	200 ppb → 1000 ppb
1000	6.8	5.3
800	8.5	5.0
600	4.6	4.8
400	2.5	3.4
200	0.8	1.1

4 Conclusion

In this work, we have manufactured chemiresistive gas sensing devices by inkjet printing different LPE (Liquid Phase Exfoliation) graphene suspensions, formulated in standard organic solvents (N-methyl-pirrolidone) or aqueous mixtures (water/isopropanol), on rigid (alumina) and flexible substrates (paper). The device performances have been investigated upon exposure to different concentrations of NO_2 and the device-to-device

variation as function of the number of printed layers to form the sensing film and the base conductance has been investigated. By increasing the inkjet printed layers a higher conductivity has been obtained, and both the parameters of the initial resistance and $\Delta G/G_0$ decrease with a hyperbolic behaviour.

Furthermore, we demonstrated that the inkjet printing can be successfully adopted to fabricate graphene-based sensor devices by employing eco-friendly materials in order to address a sustainable approach in the processing chain, including functional (sensing) materials, substrates and technology.

References

1. F. Bonaccorso, A. Lombardo, T. Hasan, Z. Sun, L. Colombo, A.C. Ferrari, Mater. Today **15**, 564–589 (2012)
2. W. Wu, Z. Liu, L.A. Jauregui, Q. Yu, R. Pillai, H. Cao, J. Bao, Y.P. Chen, S.-S. Pei, Sens. Actuators B **150**, 296–300 (2010)
3. S. Stankovich, D.A. Dikin, R.D. Piner, K.A. Kohlhaas, A. Kleinhammes, Y. Jia, Y. Wu, S.T. Nguyen, R.S. Ruof, Carbon **45**, 1558–1565 (2007)
4. G. Lu, S. Park, K. Yu, R.S. Ruoff, L.E. Ocola, D. Rosenmann, J. Chen, ACS Nano **5**, 1154–1164 (2011)
5. Y. Hernandez, V. Nicolosi, M. Lotya, F.M. Blighe, Z. Sun, S. De, I.T. McGovern, B. Holland, M. Byrne, Y.K. Gun'Ko, J.J. Boland, P. Niraj, G. Duesberg, S. Krishnamurthy, R. Goodhue, J. Hutchison, V. Scardaci, A.C. Ferrari, J.N. Coleman, Nat. Nanotechnol. **3**, 563–568 (2008)
6. J.N. Coleman, Acc. Chem. Res. **46**, 14–22 (2012)
7. Y. Hernandez, M. Lotya, D. Rickard, S.D. Bergin, J.N. Coleman, Langmuir **26**, 3208–3213 (2009)
8. F. Fedi, M.L. Miglietta, T. Polichetti, F. Ricciardella, E. Massera, D. Ninno, G. Di Francia, Mater. Res Express **2**(035601), 1–8 (2015)
9. F. Ricciardella, E. Massera, T. Polichetti, M.L. Miglietta, G. Di Francia, Appl. Phys. Lett. **104**, 183502_1–183502_5 (2014)
10. F. Ricciardella, B. Alfano, F. Loffredo, F. Villani, T. Polichetti, M.L. Miglietta, E. Massera, G. Di Francia, AISEM XVIII IEEE, 1–4 (2015)

Optical Sensors

Integration of Amorphous Silicon Photosensors with Thin Film Interferential Filter for Biomolecule Detection

Domenico Caputo[1(✉)], Emanuele Parisi[1], Augusto Nascetti[2], Mario Tucci[3], and Giampiero de Cesare[1]

[1] D.I.E.T., University of Rome "La Sapienza", via Eudossiana 18, 00184 Rome, Italy
domenico.caputo@uniromal.it
[2] S.A.E., University of Rome "La Sapienza", via Salaria 851/881, 00138 Rome, Italy
[3] ENEA Research Center Casaccia, via Anguillarese 301, 00123 Rome, Italy

Abstract. This work presents a thin film device, combining, on the same glass substrate, photosensors and long-pass interferential filter to achieve a compact and efficient sensor for biomolecule detection. The photosensors are amorphous silicon stacked structures, while the interferential filter is fabricated alternating layers of silicon dioxide and titanium dioxide, directly grown over the photosensors. The system has been optimized to effectively detect the natural fluorescence of Ochratoxin A, a highly toxic mycotoxin present in different food commodities. In particular, the long-pass interferential filter has been designed to reject the wavelengths arising from the excitation source (centered at 330 nm) thus transmitting the OTA emission spectrum (centered at 470 nm). Experimental results show that the filter strongly reduces the photosensors quantum efficiency below 420 nm, while keeps it nearly constant at higher wavelength.

Keywords: Thin film · Amorphous silicon · Interferential filter · Photosensors · Ochratoxin A

1 Introduction

Detection techniques of biomolecules have received and continue to receive a great attention due to their relevance in biology, chemistry, medicine and agriculture. Therefore, innovative methods are coming up beside the standard techniques [1]. As an example, in food related applications, established procedures rely on enzyme-linked immunosorbent assay (ELISA) or on chromatographic procedures. The ELISA kit [2, 3] are usually competitive enzyme immunoassays based on specific antibodies optimized to cross react primarily with the target molecules, while the chromatographic techniques rely on high-performance liquid chromatography (HPLC), through extraction of the analyte from the sample, clean-up (or purification) by ImmunoAffinity Columns (IAC) [4] and chromatographic analysis. ELISA based method are

B. Andò et al. (eds.), *Sensors*, Lecture Notes in Electrical Engineering 431,
DOI 10.1007/978-3-319-55077-0_16

friendly-to-use, less expensive and less time-consuming than HPLC techniques, which on the other hand are much more reliable in terms of analyte quantification.

To overcome the disadvantages of these standard methods, many research efforts are currently committed to develop lab-on-chip (LoC) systems [5, 6], integrating on single substrate devices and techniques for the thermal treatment [7], handling, recognition and quantification of biomolecules [8]. The main advantages of the LoC are the low reagent consumption and the shortening of analysis time. These characteristics coupled with the possibility to automatize the analysis procedure make LoCs the ideal systems easy-to-use, low-cost and low pollution devices. However, even though LoCs tend to be as compact as possible, their scaling down is slowed by the need of bulky external connections [9] and off-chip detection [10].

Our work addresses the effective LoC miniaturization integrating, on the same glass substrate, amorphous silicon (a-Si:H) photosensors [11–15] and interferential filter to achieve on-chip detection of fluorescent molecules. In particular, the integrated device has been developed for the detection of Ochratoxin A (OTA) [16], a mycotoxin present in different food commodities such as red wine, beer, coffee and peanuts. Indeed OTA has received a great attention by scientists and dietary organizations, because this mycotoxin is carcinogenic (Group 2B) [17], can have weak mutagenic effects [18] and immunotoxicity activity in animals [19].

2 Device Structure

The device structure is showed in Fig. 1. The system is designed to detect the natural fluorescence of OTA molecules by means of a-Si:H photosensors.

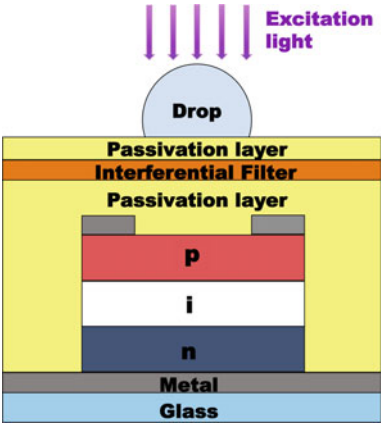

Fig. 1. Device structure

An appropriate radiation source excites the fluorescence of OTA molecules contained in a solution drop, while the thin film interferential filter, integrated onto the structure, rejects the excitation radiation and only transmits the OTA fluorescence. The a-Si:H photosensors absorb the transmitted light and generate photocarriers collected at

the metal electrodes, giving rise to a current proportional to the number of photons and then to the number of OTA molecules contained into the drop.

The design of photosensors and filter started from the OTA emission and absorption spectra shown in Fig. 2. The absorption spectrum is centered at 330 nm, while the emission spectrum is centered at 470 nm.

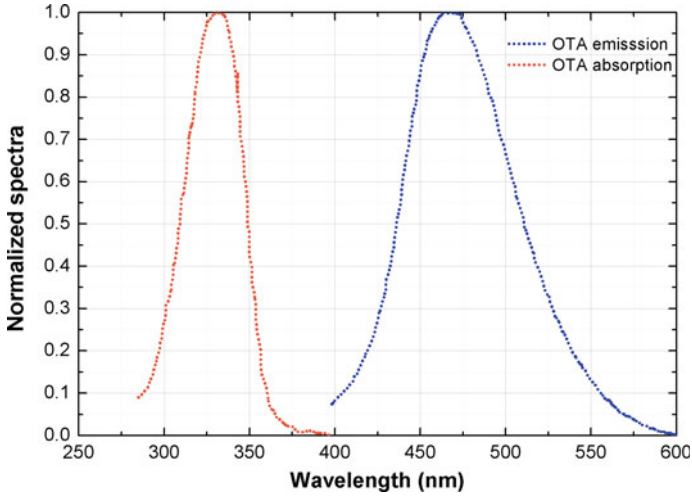

Fig. 2. Emission (*orange dotted line*) and absorption (*blue dotted line*) spectra of Ochratoxin A (Color figure online)

From these data, we infer the requirements for the excitation source, the spectral response of the photodiodes and the interferential filter. A laser diode or a light emitting diode, able to provide an ultraviolet light, is chosen as excitation source.

3 Amorphous Silicon Photodiodes

The photosensors used to detect the emission of OTA are a-Si:H photodiodes. Their structure is a p-type/intrinsic/n-type (p-i-n) stacked junction, deposited by Plasma Enhanced Chemical Vapor Deposition (PECVD) at temperatures below 300 °C. The deposition parameters are listed in Table 1.

The thicknesses and energy gaps of the different layers within the a-Si-H device have been tuned to maximize the matching between OTA emission spectrum and photosensor quantum efficiency, keeping the dark current as low as possible.

The achieved quantum yield (QY) is showed in Fig. 3 as black squares. The measured value at 470 nm is 185 mA/W. The current density, measured in dark conditions at 100 mV of low reverse voltage, is in the order of 10^{-10} A/cm^2. This reflects in a dark current noise in the order of few fA/cm^2.

Table 1 Deposition parameters of the a-Si:H layers

Material	SiH_4 (sccm)	B_2H_6 (sccm)	CH_4 (sccm)	PH_3 (sccm)	T_{dep} (° C)	P_{dep} (Torr)	P_{RF} (mW/cm^2)	t_{dep} (s)
p/a-SiC:H	40	5	40		210	0.7	25	50
i/a-Si:H	40				280	0.68	25	2100
n/a-Si:H	40			10	300	0.3	25	180

The gases are: SiH_4 pure silane, PH_3 silane diluted (5%), B_2H_6 helium diluted (5%), CH_4 pure methane. P_{dep} is the process pressure, P_{RF} the radio-frequency power density, T_{dep} the substrate temperature and t_{dep} the deposition time

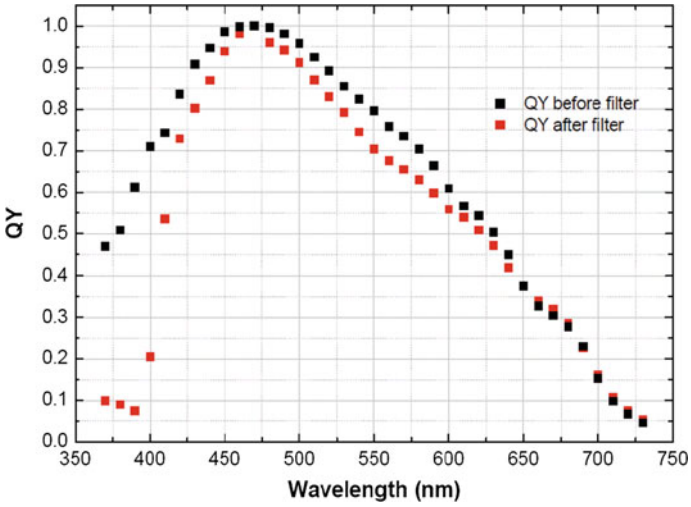

Fig. 3. Quantum yield of the a-Si:H photodiodes before (*black squares*) and after (*red squares*) the deposition of the interference filter (Color figure online)

4 Interferential Filter Design

As can be deduced comparing Figs. 2 and 3, the quantum yield of the photosensors is not negligible in the absorption spectrum of the OTA molecules, therefore a long-pass filter is necessary to reject the light coming from the excitation source.

The modeled thin-film filter is a multi-dielectric interferential filter, designed according to Distributed Bragg Reflector's theory (DBR). The periodic structure is composed by alternating two films with high and low refractive index. The optical thickness of the two layers is equal to a quarter of the incident wavelength.

$$n_h d_h = n_l d_l = \lambda_0/4$$

where n_h and d_h are, the refractive index and the thickness of high refractive index layer respectively, n_l and d_l are, the refractive index and the thickness of low refractive index layer respectively, $\lambda_0 = c_0/f_0$ is the wavelength of the incident radiation.

The wavelength-pass region can be made flat by setting the thicknesses of the first and last high-index layers equal to $\lambda_0/8$. The filter response has been modeled with the IMD extension of the freeware software XOP. The chosen materials are TiO_2 and SiO_2 and the designed filter structure is schematically reported in Fig. 4.

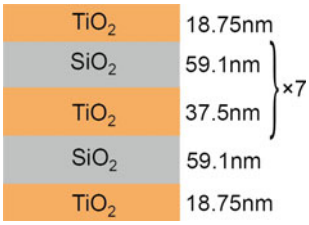

Fig. 4. Structure of the thin film multi-dielectric interferential OTA filter

The modeled transmittance (T) and reflectance (R), reported as continuous lines in Fig. 5, show that the filter provides a stop-band attenuation of three orders of magnitude (optical density OD = 3.0 at 340 nm). Furthermore, its cut-off wavelength (50% of T) is 408 nm, while the roll-off (20 nm from 10 to 90% of T) permits an almost unperturbed transmission of the OTA emission.

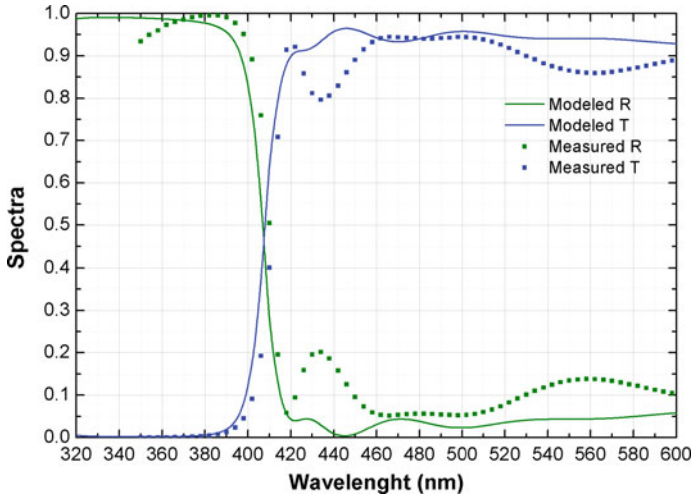

Fig. 5. Modeled (*continuous lines*) and measured (*symbols*) spectral characteristics of the interferential filter

5 Experimental Results

At first, the designed filter has been deposited by Electron Beam Physical Vapor Deposition at 250 °C on a plain borosilicate glass. This deposition temperature is lower than the maximum temperature reached during the a-Si:H photosensors fabrication. The spectral characteristics of the filter have been then measured with a *Perkin Elmer Lambda 950* spectrophotometer.

The measured transmittance (T) and reflectance (R) are showed in Fig. 5 as blue and green squares, respectively. An excellent agreement between measurements and simulations has been achieved. Indeed, both the measured cut-off wavelength and the stop-band attenuation are very close to the simulated value, thus demonstrating that the fabricated filter satisfies very well the design requirements.

Finally, using the same deposition parameters adopted for the plain borosilicate glass, the filter has been deposited directly onto the photosensors. The spectral response, measured after the filter deposition, is reported as red squares in Fig. 3. We can observe that the quantum efficiency remains almost unchanged in the OTA emission range, while it experiments a sharp decrease at wavelength below 420 nm. These data confirm, therefore, the filter effectiveness in rejecting the excitation radiation and its successful integration with the photosensors.

6 Conclusion

This work has reported design, fabrication and characterization of a device based on thin film technologies suitable for selective detection of the natural fluorescence of Ochratoxin A molecules. A multi dielectric interferential long-pass filters have been designed through a freeware software, according to Distributed Bragg Reflector's theory. The filter, directly deposited onto an a-Si:H photosensors array, is able to reject the excitation UV light and to transmit the OTA emission light. Indeed the filter measurements show excellent agreement with simulations.

The photodiode quantum yield, measured before and after the filter deposition, demonstrates the successful integration of filter with sensors and the suitability of the system to effectively reject the excitation radiation thus accomplishing the specimen desired. Works are currently in progress to test the performances of the integrated device on standard samples of Ochratoxin A.

References

1. F. Costantini, C. Sberna, G. Petrucci, C. Manetti, G. de Cesare, A. Nascetti, D. Caputo, Lab-on-chip system combining a microfluidic-ELISA with an array of amorphous silicon photosensors for the detection of celiac disease epitopes. Sens. Bio-Sens. Res. **6**, 51–58 (2015)
2. http://www.sigmaaldrich.com/catalog/product/sigma/se120014?lang=it&region=IT
3. http://www.biooscientific.com/Mycotoxin-test-kits/MaxSignal-Ochratoxin-A-ELISA-Test-Kit

4. H. Meng, Z. Wang, S. De Saeger, Y. Wang, K. Wen, S. Zhang, J. Shen, Determination of Ochratoxin A in cereals and feeds by ultra-performance liquid chromatography coupled to tandem mass spectrometry with immunoaffinity column clean-up. Food Anal. Methods **7**(4), 854–864 (2014)
5. A. Manz, N. Graber, H.M. Widmer, Miniaturized total chemical-analysis systems—a novel concept for chemical sensing. Sens. Actuat. B-Chem. **1**(1–6), 244–248 (1990)
6. L. Gervais, N. de Rooij, E. Delamarche, Microfluidic chips for point-of-care immunodiagnostics. Adv. Mater. **23**(24), H151–H176 (2011)
7. D. Caputo, G. de Cesare, M. Nardini, A. Nascetti, R. Scipinotti, Monitoring of tempera-ture distribution in a thin film heater by an array of a-Si: H temperature sensors. IEEE Sens. J. **12** (5), 1209–1213 (2012)
8. D. Caputo, M. Ceccarelli, G. de Cesare, A. Nascetti, R. Scipinotti, Lab-on-Glass system for DNA analysis using thin and thick film technologies. Proceedings of material research symposium, vol. 1191, OO06-01 (2009)
9. K. Lewotsky, Microfluidics streamlines laboratory operations. SPIE Newsroom (2010). doi:10.1117/2.2201012.01
10. F. Berthold, M. Hennecke, J. Wulf, Instrumentation for chemi-luminescence and bioluminescence, in *Chemiluminescence and Bioluminescence—Past, Present and Future*, ed. by A. Roda (RSC, Cambridge, 2011), pp. 113–139
11. D. Caputo, G. de Cesare, A. Nascetti, R. Negri, Spectral tuned amorphous silicon p-i-n for DNA detection. J. Non-Cryst. Solids **352**(9-20 SPEC. ISS.), 2004–2006 (2006)
12. A.C. Pimentel, A.T. Pereira, V. Chu, D.M.F. Prazeres, J.P. Conde, Detection of chemiluminescence using an amorphous silicon photodiode. IEEE Sens. J. **7**(3–4), 415–416 (2007)
13. C.R. Vistas, S.S. Soares, R.M.M. Rodrigues, V. Chu, J.P. Conde, G.N.M. Ferreira, An amorphous silicon photodiode microfluidic chip to detect nanomolar quantities of HIV-1 virion infectivity factor. Analyst **139**(15), 3709–3713 (2014)
14. F. Costantini, A. Nascetti, R. Scipinotti, F. Domenici, S. Sennato, L. Gazza, F. Bordi, N. Pogna, C. Manetti, D. Caputo, G. de Cesare, On-chip detection of multiple serum antibodies against epitopes of celiac disease by an array of amorphous silicon sensors. RSC Adv. **4**(4), 2073–2080 (2014)
15. M. Mirasoli, A. Nascetti, D. Caputo, M. Zangheri, R. Scipinotti, L. Cevenini, G. de Cesare, A. Roda, Multiwell cartridge with integrated array of amorphous silicon photosensors for chemiluminescence detection: development, characterization and comparison with cooled-CCD luminograph. Anal. Bioanal. Chem. **406**(23), 5645–5656 (2014)
16. D. Caputo, G. de Cesare, C. Fanelli, A. Nascetti, A. Ricelli, R. Scipinotti, Innovative detection system of ochratoxin a by thin film photodiodes. Sensors **7**(7), 1317–1322 (2007)
17. H.A. Clark, S.M. Snedeker, Ochratoxin A: its cancer risk and potential for exposure. J. Toxicol. Environ. Health. Part B, Crit. Rev. **9**(3), 265–296 (2006)
18. N. Palma, S. Cinelli, O. Sapora, S.H. Wilson, E. Dogliotti, Ochratoxin A-induced mutagenesis in mammalian cells is consistent with the production of oxidative stress. Chem. Res. Toxicol. **20**(7), 1031–1037 (2007)
19. L. Al-Anati, E. Petzinger, Immunotoxic activity of ochratoxin A. J. Vet. Pharmacol. Ther. **29** (2), 79–90 (2006)

Chemical Sensors Based on Surface Plasmon Resonance in a Plastic Optical Fiber for Multianalyte Detection in Oil-Filled Power Transformer

Nunzio Cennamo[1(✉)], Maria Pesavento[2], Antonella Profumo[2], Daniele Merli[2], Letizia De Maria[3], Cristina Chemelli[3], and Luigi Zeni[1]

[1] Department of Industrial and Information Engineering, Second University of Naples, via Roma 29, Aversa, CE, Italy
nunzio.cennamo@unina2.it
[2] Department of Chemistry, University of Pavia, via Taramelli 12, Pavia, Italy
[3] RSE S.p.A, via Rubattino 54, Milan, Italy

Abstract. The combination of a D-shaped plastic optical fiber (POF) and a Molecularly Imprinted Polymer (MIP) receptor is an effective way to obtain a highly selective and sensitive surface plasmon resonance (SPR) optical platform, especially suitable for the detection of chemical marker in the oil of Power Transformers. In this work Authors present the preliminary results for determination of two important analytes, dibenzyl disulfide (DBDS) and furfural (2-FAL), whose presence in the transformer oil is an indication of underway corrosive or ageing process, respectively, in power transformers. The low cost of the POF-MIP platforms and the simple and modular scheme of the optical interrogation layout make this system a potentially suitable on-line diagnostic tool for power transformers.

Keywords: Dibenzyl disulfide · Furfural (furan-2-carbaldehyde) · Molecularly imprinted polymers · Plastic optical fibers · Power transformers

1 Introduction

Oil-filled power transformers are a key component of a Transmission and Distribution (T&D) network. Their failure can have relevant impact on maintenance costs due to out-of-services. Nowadays the increasing energy peak demand and its timing change can often expose power transformers to irregular stresses and/or overloads, that can compromise their long term integrity.

The availability of reliable and potentially low-cost sensors to be used as diagnostic tools for detecting ageing and failures of these components is of significant interest to improve management of the electric power system assets. In particular, for oil-filled transformers, the on-line continuous detection of chemical parameters (Dissolved Gases and chemical agents) in the insulating oil could provide an early warning of

B. Andò et al. (eds.), *Sensors*, Lecture Notes in Electrical Engineering 431,
DOI 10.1007/978-3-319-55077-0_17

incipient failures (partial discharges, over temperature, hot spot) or of occurring accelerated aging on dielectric parts of transformers.

Surface Plasmon Resonance (SPR) based Plastic Optical Fibers (POF) sensors are good candidates for an on-line detection of different diagnostic markers directly in oil environment. This methodology potentially allow to overcome problems, foreseen by current practices, of periodical collections of oil samples from the transformer and application of more expensive and time-consuming standard analysis (by gas chromatography for instance).

The SPR is an optical phenomenon that appears at a metal-dielectric interface, widely used in a large number of sensors for label-free detection [1–4]. The Kretschmann configuration is widely used in practice, but the setup usually require expensive optical equipment. Incorporating optical fiber makes it possible to reduce the sensor cost and dimensions, with the possibility to integrate the SPR sensing platform in telecommunication systems [5–8]. Using a molecularly imprinted polymer (MIP) layer as an artificial receptor, the rapid and selective detection of different analytes in aqueous matrices has been demonstrated [9, 10]. Also, MIP-POF-SPR optical platform has been demonstrated to be potentially useful for the determination of 2-furaldehyde (2-FAL) directly in transformer oil, without any previous extraction procedure [11].

MIPs are synthetic receptors obtained by molecular imprinting methods, presenting a number of favorable aspects for sensing in comparison to bioreceptors, as for example antibodies, including high stability, reproducibility and low cost. They are porous solids containing specific sites interacting with the molecule of interest, according to a "key and lock" model [12]. Indeed, a distinctive feature of MIPs, in comparison with other receptors, is the selectivity. Moreover, the polymer layer may contain a relatively high density of recognition elements, included in a three-dimensional matrix, which should help the recognition by SPR even for relatively low molecular mass molecules.

In this work, as a case-study, we experimentally analyse the behavior of a newly developed POF-MIP-SPR multichannel sensor system, specialized for simultaneous and selective detection of dibenzyl disulfide (DBDS) and 2-furaldehyde (2-FAL) in transformer oil.

2 Optical Sensor System

The fabricated optical sensor system was realized removing the cladding of a plastic optical fiber along half the circumference, by mechanically polishing the plastic optical fiber without jacket embedded in a resin block, spinning on the exposed core a buffer of Microposit S1813 photoresist, and finally sputtering a thin gold film using a sputtering machine [13].

The chosen plastic optical fiber has a PMMA core of 980 μm and a fluorinated polymer cladding of 20 μm, the gold film is 60 nm thick and the thickness of the photoresist buffer layer is about 1.5 μm. The realized sensing region is about 10 mm in length (see Fig. 1).

The gold film so obtained presents a good adhesion to the substrate, verified by its resistance to rinsing in de-ionized water, and it is also easy to functionalize with bio/chemical receptors.

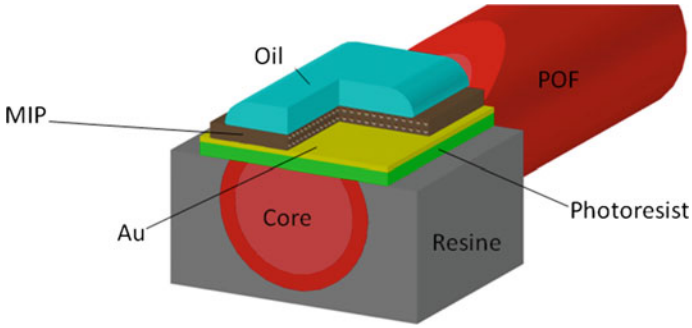

Fig. 1. Optical chemical sensor based on D-shaped POF

The experimental measurements for the characterization of the SPR-POF sensors have been previously carried out in different ways, i.e. spectral and amplitude mode. In this work we have used a particular setup based on the spectral mode configuration. It consists of a halogen lamp, a beam splitter (50/50) illuminating simultaneously the two optical chemical sensors, with different MIP (see Fig. 2a), and two identical spectrometers. The here used halogen lamp exhibits a wavelength emission range from 360 to 1700 nm, while the spectrum analyzer detection range was from 330 to 1100 nm. Two spectrometers were finally connected to a computer (see Fig. 2b).

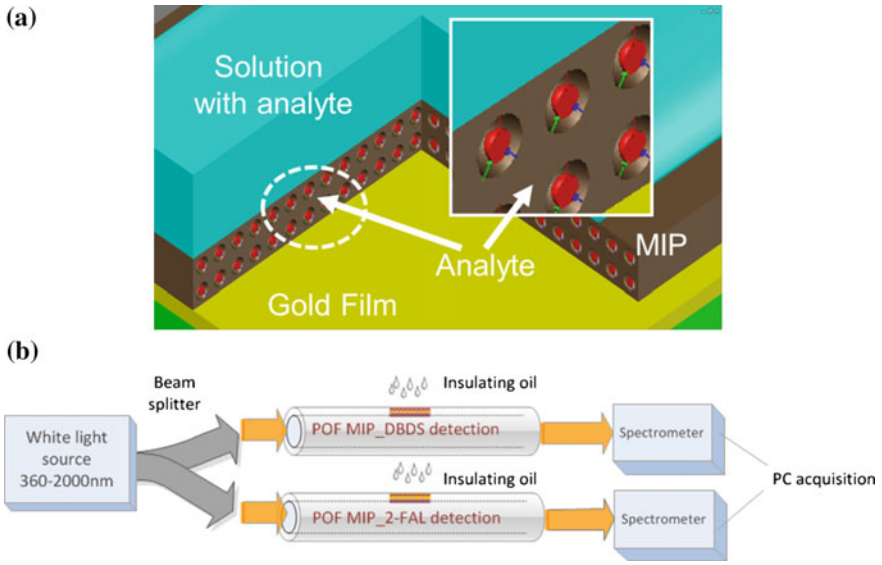

Fig. 2. **a** Zoom of the sensing area. **b** Schematic view of the experimental setup based on two POF-MIPs sensors for different analytes

3 The Sensitivity in Spectral Mode Operation

In SPR sensors with spectral interrogation, the resonance wavelength (λ_{res}) is determined as a function of the refractive index of the sensing layer (n_s). If the refractive index of the sensing layer is altered by δ_{ns}, the resonance wavelength shifts by $\delta\lambda_{res}$. The sensitivity (S_n) of an SPR sensor with spectral interrogation is defined as [13–15]:

$$S_n = \frac{\delta\lambda_{res}}{\delta n_s}\left[\frac{nm}{RIU}\right] \tag{1}$$

Owing to the fact that the vast majority of the field of an SPW is concentrated in the dielectric, the propagation constant of the SPW is extremely sensitive to changes in the refractive index of the dielectric itself. This property of SPW is the underlying physical principle of affinity SPR bio/chemical sensors.

In the case of artificial receptors, as molecular imprinted polymers (MIPs), the polymeric film on the surface of metal selectively recognizes and captures the analyte present in a liquid sample so producing a local increase in the refractive index at the metal surface. The refractive index increase gives rise to an increase in the propagation constant of SPW propagating along the metal surface which can be accurately measured by optical means. The magnitude of the change in the propagation constant of an SPW depends on the refractive index change and its overlap with the SPW field. If the binding occurs within the whole depth of the SPW field, the binding-induced refractive index change produces a change in the real part of the propagation constant, which is directly proportional to the refractive index change.

The chemical sensor's sensitivity (S) is defined as the shift in resonance wavelength per unit change in analyte concentration [16]:

$$S = \frac{\delta\lambda_{res}}{\delta C_{analyte}}\left[\frac{nm}{M}\right] \tag{2}$$

4 Experimental Results

Measurements were simultaneously carried out on two SPR-POF-MIP optical chemical sensors based on different MIP receptors: one for dibenzyl disulfide (DBDS) and one specific for furfural (2-FAL). A rapid and selective detection of these analytes is, actually, very important for an on-line control of oil in transformers to prevent their damages and/or failure.

Samples were obtained by dissolving the analyte in a mineral oil (Nytro Libra) widely used for power transformers, which does not contain DBDS and 2-FAL and is also used as a blank.

All the measurements were carried out by dropping 30 µl of the liquid sample (oil with analyte) directly over the two POF-MIPs sensor platform, which were maintained in horizontal position. Steady state wavelength shift were obtained after 3 min incubation.

Several plasmonic resonances were observed in the considered wavelength range (300–1100 nm) of the transmission spectra, when the binding interaction occurs between MIP and the analyte under investigation [9–11]. In this preliminary analysis only the red-shift of the SPR resonance (in the wavelength range 700–820 nm) will be taken into account hereafter.

Figures 3 and 4 report some preliminary results of DBDS and 2-FAL detection in transformer oil samples, respectively. They clearly show that the resonance wavelength is shifted to higher values (red shifted) when the DBDS (Fig. 3) and 2-FAL (Fig. 4) concentration increases, indicating that DBDS and 2-FAL effectively combines with MIP from the oil matrix.

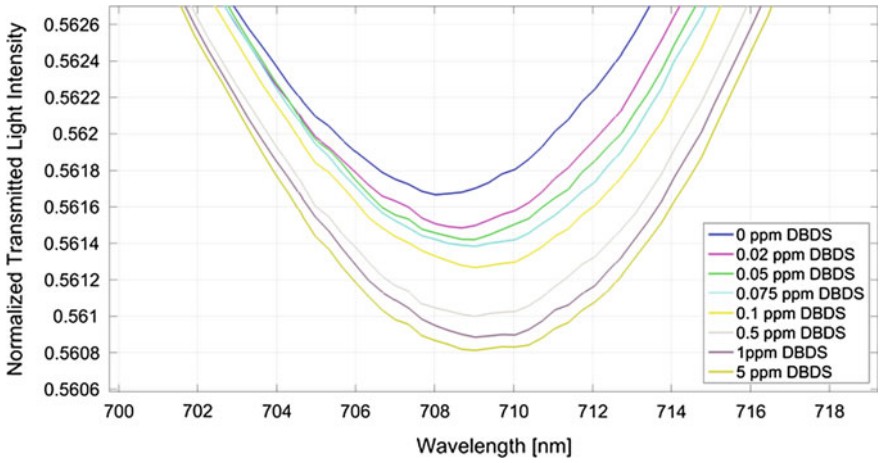

Fig. 3. Zoom of experimental SPR transmission spectra for different DBDS (ppm) in transformer oil

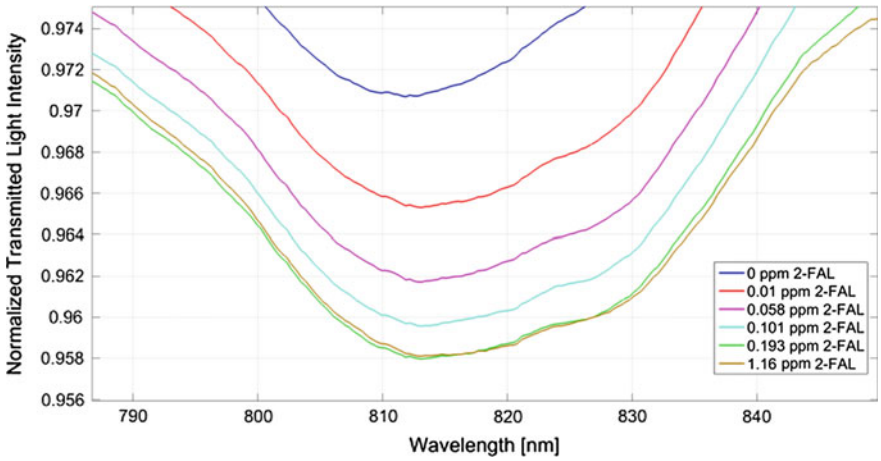

Fig. 4. Zoom of experimental SPR transmission spectra for different 2-FAL (ppm) in transformer oil

5 Conclusions

Preliminary experimental results on a multichannel chemical SPR sensor, for the detection of two markers (DBDS and 2-FAL) directly in transformer oil, have demonstrated an attractive feature in industrial application. In particular, for oil-filled transformers, the frequent control of chemical markers in the insulating oil could provide an early warning of incipient failures (partial discharges, over temperature, hot spot) or of occurring accelerated aging on dielectric parts of transformers [17–21].

Acknowledgements. This work has been financed by the Research Fund for the Italian Electrical System under the Contract Agreement between RSE and the Ministry of Economic Development-General Directorate for Energy and Mining Resources stipulated on 29 July 2009 in compliance with the Decree of 19 March 2009.

References

1. R. Narayanaswamy, Optical chemical sensors and biosensors for food safety and security applications. Acta. Biol. Szeged **50**, 105–108 (2006)
2. E.M. Munoz, S. Lorenzo-Abalde, Á. González-Fernández et al., Direct surface plasmon resonance immunosensor for in situ detection of benzoylecgonine, the major cocaine metabolite. Biosens. Bioelectron. **26**, 4423–4428 (2011)
3. D. Habauzit, J. Armengaud, B. Roig, J. Chopineau, Determination of estrogen presence in water by SPR using estrogen receptor dimerization. Anal. Bioanal. Chem. **390**, 873–883 (2008)
4. J. Homola, Present and future of surface plasmon resonance biosensors. Anal. Bioanal. Chem. **377**, 528–539 (2003)
5. A. Gowri, V.V.R. Sai, Development of LSPR based U-bent plastic optical fiber sensors. Sens. Actuators B **230**, 536–543 (2016)
6. A. Trouillet, C. Ronot-Trioli, C. Veillas, H. Gagnaire, Chemical sensing by surface plasmon resonance in a multimode optical fibre. Pure Appl. Opt. **5**, 227–237 (1996)
7. K. Anuj, R.J. Sharma, B.D. Gupta, Fiber-optic sensors based on surface plasmon resonance: a comprehensive review. IEEE Sens. J **7**, 1118–1129 (2007)
8. X.D. Wang, O.S. Wolfbeis, Fiber-optic chemical sensors and biosensors (2008–2012). Anal. Chem. **85**, 487–508 (2013)
9. N. Cennamo, G. D'Agostino, R. Galatus, L. Bibbò, M. Pesavento, L. Zeni, Sensors based on surface plasmon resonance in a plastic optical fiber for the detection of trinitrotoluene. Sens. Actuators B **188**, 221–226 (2013)
10. N. Cennamo, G. D'Agostino, M. Pesavento, L. Zeni, High selectivity and sensitivity sensor based on MIP and SPR in tapered plastic optical fibers for the detection of L-nicotine. Sens. Actuators B **191**, 529–536 (2014)
11. N. Cennamo, L. De Maria, G. D'Agostino, L. Zeni, M. Pesavento, Monitoring of low levels of furfural in power transformer oil with a sensor system based on a POF-MIP platform. Sensors **15**, 8499–8511 (2015)
12. L. Uzun, A.P.F. Turner, Molecularly-imprinted polymers sensors: realising their potential. Biosens. Bioelectron. **76**, 131–144 (2016)
13. N. Cennamo, D. Massarotti, L. Conte, L. Zeni, Low cost sensors based on SPR in plastic optical fiber for biosensor implementation. Sensors **11**, 11752–11760 (2011)

14. M. Iga, A. Sekib, K. Watanabe, Gold thickness dependence of SPR-based hetero-core structured optical fiber sensor. Sens. Actuators B Chem. **106**, 363–368 (2005)
15. M. Kanso, S. Cuenot, G. Louarn, Sensitivity of optical fiber sensor based on surface plasmon resonance: modeling and experiments. Plasmonics **3**, 49–57 (2008)
16. J. Homola, Present and future of surface plasmon resonance biosensors. Anal. Bioan. Chem. **377**, 528–539 (2003)
17. Y. Lin, L. Yang, R. Liao, W. Sun, Effect Of Oil Replacement On Furfural Analysis And Aging Assessment Of Power Transformers. IEEE Trans. Dielectr. Electr. Insul. **22**, 2611–2619 (2015)
18. R. Blue, D.G. Uttamchandani, O. Farish, A novel optical sensor for the measurement of furfuraldehyde in transformer oil. IEEE Trans. Instrum. Meas. **47**, 964–966 (1998)
19. F. Scatiggio, V. Tumiatti, R. Maina, M. Tumiatti, M. Pompili, R. Bartnikas, corrosive sulfur in insulating oils: its detection and correlated power apparatus failures. IEEE Trans. Power Delivery **23**, 508–509 (2008)
20. R.M. Morais, W.A. Mannheimer, M. Carballeira, J.C. Noualhaguet, Furfural analysis for assessing degradation of thermally upgraded papers in transformer insulation. IEEE Trans. Dielectr. Electr. Insul. **6**, 159–163 (1999)
21. S. Toyama, J. Tanimura, N. Yamada, E. Nagao, Highly sensitive detection method of dibenzyl disulfide and the elucidation of the mechanism of copper sulfide generation in insulating oil. IEEE Trans. Dielectrics Elect. Insul. **16**, 509–515 (2009)

Surface Plasmon Resonance Sensor in Plastic Optical Fibers. Influence of the Mechanical Support Geometry on the Performances

Nunzio Cennamo[1(✉)], Letizia De Maria[2], Cristina Chemelli[2], Maria Pesavento[3], Antonella Profumo[3], Ramona Galatus[4], and Luigi Zeni[1]

[1] Department of Industrial and Information Engineering, Second University of Naples, via Roma 29, Aversa, CE, Italy
nunzio.cennamo@unina2.it
[2] RSE S.p.A, via Rubattino 54, Milan, Italy
[3] Department of Chemistry, University of Pavia, via Taramelli Pavia, Italy
[4] Basis of Electronics Department, Technical University of Cluj-Napoca, Memorandumului 28, Cluj-Napoca, Romania

Abstract. A performance analysis on Surface Plasmon Resonance (SPR) sensor based on D-shaped Plastic Optical Fibers (POFs) is reported. It is a very low cost sensor for determining refractive index variations at the interface between a metallic layer and a dielectric medium. This POF-SPR optical platform can be used in many bio and chemical applications. The advantage of using POFs is that the sensor platforms based on POF are simpler to manufacture than those made using silica optical fibers. For low-cost sensing systems, POFs are especially advantageous due to their excellent flexibility, easy manipulation, great numerical aperture, large diameter, and the fact that plastic is able to withstand smaller bend radii than glass. In this work the authors investigate the role of the geometric shape of the resin block, used to obtain a D-shaped POF. In fact, different resin blocks can produce different performances. Two different POF-SPR sensors, based on two different geometric shapes of the resin block, with numerical and experimental results, are presented.

Keywords: Surface Plasmon Resonance · Plastic Optical Fibers · Optical sensors · D-shaped plastic optical fiber

1 Introduction

The SPR is an optical phenomenon that appears at a metal-dielectric interface, widely used in a large number of sensors for label-free detection [1–4]. The Kretschmann configuration is widely used in practice, but the setup usually require expensive optical equipment. Incorporating optical fiber makes it possible to reduce the sensor cost and dimensions, with the possibility to integrate the SPR sensing platform in telecommunication systems [5–8]. Using a molecularly imprinted polymer (MIP) layer as an artificial receptor, the rapid and selective detection of different analytes, as for example

B. Andò et al. (eds.), *Sensors*, Lecture Notes in Electrical Engineering 431,
DOI 10.1007/978-3-319-55077-0_18

trinitrotoluene (TNT) or L-nicotine, in aqueous matrices has been demonstrated [9, 10]. Also, MIP-POF-SPR optical platform has been demonstrated to be potentially useful for the determination of 2-furaldehyde (2-FAL) directly in transformer oil, without any previous extraction procedure [11]. In comparison with biosensors based on biological receptors, the polymeric receptors have an improved reproducibility and shelf-life, and a lower cost, so that they are suitable for mass production of sensors [12]. The planar gold surface and the useful refractive index ranging from 1.33 to 1.42 are two good factors for successful bio/chemical sensors implementation. Moreover the flat surface of the optical platform, characteristic of the D-shaped platform here proposed, makes it possible the reproducible deposition of the receptor, particularly in the case of MIP.

The performances of the optical sensor platform (sensitivity and signal-to-noise ratio) are very important to the implementation of the platform in bio/chemical applications.

In this work the authors investigate the role of the geometric shape of the resin block. In fact, different resin blocks can produce different performances. To this aim, a numerical model of the sensor, with different sensing regions, has been developed and subsequent experimental testing has been conducted to confirm the simulation results.

2 Optical Sensor System

The fabricated optical sensor system was realized removing the cladding of a plastic optical fiber along half the circumference, by mechanically polishing the plastic optical fiber without jacket embedded in a resin block, spinning on the exposed core a buffer of Microposit S1813 photoresist, and finally sputtering a thin gold film using a sputtering machine [13]. In this work the authors investigate the role of the geometric shape of the resin block. We have realized two different SPR-POF sensor platforms based on two different geometric shapes of the resin block (see Fig. 1).

The chosen plastic optical fiber has a PMMA core of 980 μm and a fluorinated polymer cladding of 20 μm, the gold film is 60 nm thick and the thickness of the photoresist buffer layer is about 1.5 μm. The realized sensing region is about 10 mm in length (see Fig. 1).

The gold film so obtained presents a good adhesion to the substrate, verified by its resistance to rinsing in de-ionized water, and it is also easy to functionalize with bio/chemical receptors.

The experimental setup is arranged to measure the light spectrum transmitted through the SPR-POF sensor and is characterized by a halogen lamp, illuminating the optical sensor system and a spectrum analyzer (see Fig. 2). The employed halogen lamp exhibits a wavelength emission range from 360 to 1700 nm, while the spectrum analyzer detection range is from about 330 to 1100 nm. An Ocean Optics USB2000 + VIS-NIR spectrometer, controlled by a computer, has been used. The spectral resolution of this spectrometer ($\delta\lambda_{DR}$) was 1.5 nm (full width at half maximum).

Fig. 1. Sensors with two different geometric shapes of the resin block

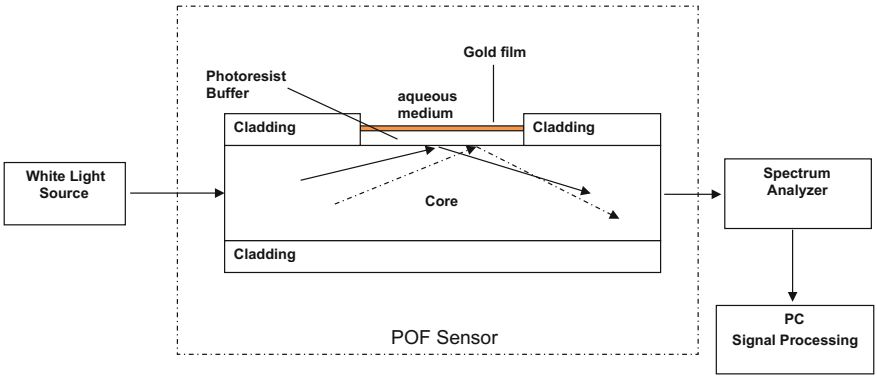

Fig. 2. Schematic view of the experimental setup and section of the SPR platform

3 Sensor's Parameters in Spectral Mode Operation

In SPR sensors with spectral interrogation, the resonance wavelength (λ_{res}) is determined as a function of the refractive index of the sensing layer (n_s). If the refractive index of the sensing layer is altered by δ_{ns}, the resonance wavelength shifts by $\delta\lambda_{res}$. The sensitivity (S_n) of an SPR sensor with spectral interrogation is defined as [13–15]:

$$S_n = \frac{\delta\lambda_{res}}{\delta n_s}\left[\frac{nm}{RIU}\right] \quad (1)$$

Owing to the fact that the vast majority of the field of an SPW is concentrated in the dielectric, the propagation constant of the SPW is extremely sensitive to changes in the refractive index of the dielectric itself. This property of SPW is the underlying physical principle of affinity SPR bio/chemical sensors. In the case of artificial receptors, as molecular imprinted polymers (MIPs), the polymeric film on the surface of metal selectively recognizes and captures the analyte present in a liquid sample so producing a local increase in the refractive index at the metal surface. The refractive index increase gives rise to an increase in the propagation constant of SPW propagating along the metal surface which can be accurately measured by optical means. The magnitude of the change in the propagation constant of an SPW depends on the refractive index change and its overlap with the SPW field. If the binding occurs within the whole depth of the SPW field, the binding-induced refractive index change produces a change in the real part of the propagation constant, which is directly proportional to the refractive index change.

The resolution (Δn) of the SPR-based optical sensor can be defined as the minimum amount of change in refractive index detectable by the sensor. This parameter (with spectral interrogation) definitely depends on the spectral resolution ($\delta\lambda_{DR}$) of the spectrometer used to measure the resonance wavelength in a sensor scheme. Therefore, if there is a shift of $\delta\lambda_{res}$ in resonance wavelength corresponding to a refractive index change of δn_s, then resolution can be defined as [13–15]:

$$\Delta n = \frac{\delta n_s}{\delta \lambda_{res}} \delta \lambda_{DR} = \frac{1}{S} \delta \lambda_{DR} [RIU] \tag{2}$$

The Signal-to-Noise Ratio (SNR) of an SPR sensor depends on how accurately and precisely the sensor can detect the resonance wavelength and hence, the refractive index of the sensing layer. This accuracy in detecting the resonance wavelength depends on the width of the SPR curve.

The narrower the SPR curve, the higher the detection accuracy. Therefore, if $\delta\lambda_{SW}$ is the spectral width of the SPR response curve corresponding to some reference level of transmitted power, the detection accuracy of the sensor can be assumed to be inversely proportional to $\delta\lambda_{SW}$.

The signal-to-noise ratio of the SPR sensor with spectral interrogation is, thus, defined as [13–15]:

$$SNR(n) = \left(\frac{\delta \lambda_{res}}{\delta \lambda_{SW}} \right)_n \tag{3}$$

where $\delta\lambda_{SW}$ can be calculated as the full width at half maximum of the SPR curve (FWHM). SNR is a dimensionless parameter strongly dependent on the refractive index changes.

4 Numerical and Experimental Results

Two different POF sensors, based on two different geometric shapes of the resin block, are numerically and experimentally tested: first, the D-shaped POF configuration with a square (cubic) resin block (see Fig. 1); second, the D-shaped POF configuration with a round (cylindrical) resin block (see Fig. 1).

Figure 3 shows the simulation of the Poynting vector, for a round (cylindrical) resin block (see the layout with the geometry in Fig. 3, after the polishing process). The model was made with beam propagation method (BPM). In the simulation we have considered one wavelength and one mode, the fundamental mode (because it contains the maximum energy). Figure 3 shows how the power increases in the middle of the sensing area, because of the lens effect at the entrance (convergent lens). At the end of the sensing area the lens effect is divergent and it is possible that some modes are lost in the cladding (exceed the critical angle).

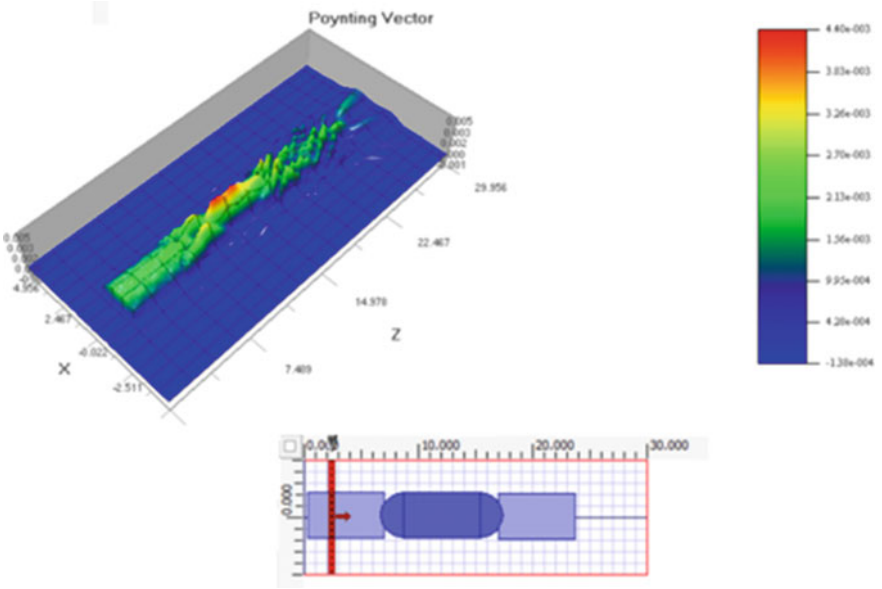

Fig. 3. Numerical results (based on BPM) for POF sensor with round (*cylindrical*) resin block

The preliminary experimental results are plotted in the Fig. 4. SPR transmission spectra of these two different sensors with two different geometric shapes of the resin block, when a water solution (1.332 RIU) is present on a gold layer, are reported in Fig. 4. The results clearly demonstrate that the geometric shape of the resin block has a relevant role in the performances of the optical platform. In particular, the square (cubic) resin block presents a deeper resonance than the round (cylindrical) resin block. This phenomenon is very important to the signal-to-noise ratio (SNR) of the SPR sensor.

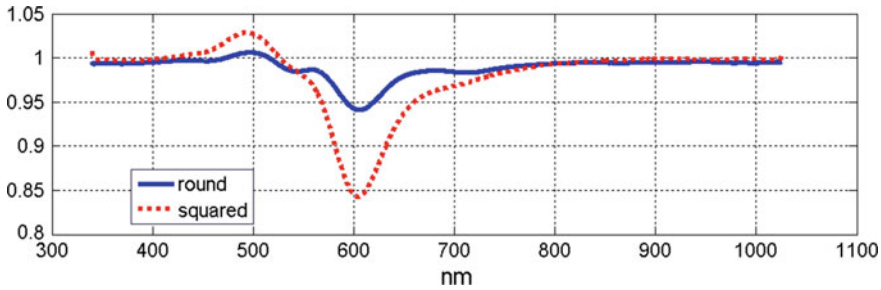

Fig. 4. Experimentally obtained SPR transmission spectra, normalized to the air spectrum, for two POF sensors with different geometric shapes of the resin block (*round* and *square*), when a water solution (1.332 RIU) is present on a gold layer

5 Conclusions

In this work the role of the geometric shape of the resin block (used to obtain a D-shaped POF) is investigated. This has been suggested by a numerical simulation carried out considering that the sensor actually consists of different sensing regions, possibly formed during the preparation of the sensor, in particular during the removal of the cladding. Subsequent experimental testing has been conducted to confirm the simulation.

Acknowledgements. This work has been financed by the Research Fund for the Italian Electrical System under the Contract Agreement between RSE and the Ministry of Economic Development-General Directorate for Energy and Mining Resources stipulated on 29 July 2009 in compliance with the Decree of 19 March 2009.

References

1. R. Narayanaswamy, Optical chemical sensors and biosensors for food safety and security applications. Acta. Biol. Szeged **50**, 105–108 (2006)
2. E.M. Munoz, S. Lorenzo-Abalde, Á. González-Fernández et al., Direct surface plasmon resonance immunosensor for in situ detection of benzoylecgonine, the major cocaine metabolite. Biosens. Bioelectron. **26**, 4423–4428 (2011)
3. D. Habauzit, J. Armengaud, B. Roig, J. Chopineau, Determination of estrogen presence in water by SPR using estrogen receptor dimerization. Anal. Bioanal. Chem. **390**, 873–883 (2008)
4. J. Homola, Present and future of surface plasmon resonance biosensors. Anal. Bioanal. Chem. **377**, 528–539 (2003)
5. A. Gowri, V.V.R. Sai, Development of LSPR based U-bent plastic optical fiber sensors. Sens. Actuators B **230**, 536–543 (2016)
6. A. Trouillet, C. Ronot-Trioli, C. Veillas, H. Gagnaire, Chemical sensing by surface plasmon resonance in a multimode optical fibre. Pure Appl. Opt. **5**, 227–237 (1996)

7. K. Anuj, R.J. Sharma, B.D. Gupta, Fiber-optic sensors based on surface plasmon resonance: a comprehensive review. IEEE Sens. J **7**, 1118–1129 (2007)
8. X.D. Wang, O.S. Wolfbeis, Fiber-Optic Chemical Sensors and Biosensors (2008–2012). Anal. Chem. **85**, 487–508 (2013)
9. N. Cennamo, G. D'Agostino, R. Galatus, L. Bibbò, M. Pesavento, L. Zeni, Sensors based on surface plasmon resonance in a plastic optical fiber for the detection of trinitrotoluene. Sens. Actuators B **188**, 221–226 (2013)
10. N. Cennamo, G. D'Agostino, M. Pesavento, L. Zeni, High selectivity and sensitivity sensor based on MIP and SPR in tapered plastic optical fibers for the detection of L-nicotine. Sens. Actuators B **191**, 529–536 (2014)
11. N. Cennamo, L. De Maria, G. D'Agostino, L. Zeni, M. Pesavento, Monitoring of low levels of furfural in power transformer oil with a sensor system based on a POF-MIP platform. Sensors **15**, 8499–8511 (2015)
12. L. Uzun, A.P.F. Turner, Molecularly-imprinted polymers sensors: realising their potential. Biosens. Bioelectron. **76**, 131–144 (2016)
13. N. Cennamo, D. Massarotti, L. Conte, L. Zeni, Low cost sensors based on SPR in plastic optical fiber for biosensor implementation. Sensors **11**, 11752–11760 (2011)
14. M. Iga, A. Sekib, K. Watanabe, Gold thickness dependence of SPR-based hetero-core structured optical fiber sensor. Sens. Actuators B Chem. **106**, 363–368 (2005)
15. M. Kanso, S. Cuenot, G. Louarn, Sensitivity of optical fiber sensor based on surface plasmon resonance: Modeling and experiments. Plasmonics **3**, 49–57 (2008)

An Integrated Interferometric Sensor for Electromagnetic Field

Mario Medugno(✉)

Institute for Microelectronics and Microsystems, Consiglio Nazionale delle Ricerche, Naples, Italy
mario.medugno@na.imm.cnr.it

Abstract. We propose in this chapter an integrated optical electromagnetic field sensor suitable for sensing in the Fresnel region over a wide frequency range. This device, based on a coherent symmetric interferometer implemented on $LiNbO_3$ substrate, yields minimal coupling with critical radiating structures and enables their near-field monitoring. The principle and technologies of this optical sensor are described and applications of more complex platforms based on the optical device are discussed.

Keywords: Optical interferometer · Electromagnetic field sensor · Fresnel region

1 Introduction

Electromagnetic field sensors are widely used in several industrial, scientific and medical applications and can be used for measurements of fields yield by communication systems and devices. Electromagnetic field monitoring is a necessary task in several critical RF communication systems, both spatially localized services as Wi-Fi or InFly Wi-Fi for airplane connectivity, point to point communication links, medical devices for tissue irradiation and imaging (e.g. RFA, EMT, etc.), and distributed as in radar and radio antenna systems. The electromagnetic field coverage of mission-critical distributed communication systems in large area, can in turn be monitored by satellite or other network systems for security and quality of service purposes. Recently optical fiber links and fast modulators support RF photonic links [1] and distributed RF networks as in Radio Frequency Over Fibers [2], therefore optical monitoring of RF subsystems seems viable and could make "all-optic" the communication infrastructure. Optical communication provides low-power communication systems with respect to the electronic-based devices, and are used for the space segment of satellite systems and in Small Form-factor Pluggable (SFP) transceiver interconnecting massively parallel supercomputers processors sustaining Terabit per second communication and an aggregate performance in the order of exaFLOPS.

The optical electromagnetic field sensor we present in this paper is based on an integrated interferometer driven by optical fiber transmission lines. The optical probe is mainly made by dielectric materials making such device suitable to monitor electromagnetic fields (EMF) radiated by antennas also in near field region. Here no simple

B. Andò et al. (eds.), *Sensors*, Lecture Notes in Electrical Engineering 431,
DOI 10.1007/978-3-319-55077-0_19

theory is available in order to evaluate the fields, and mutual coupling between antennas and standard probes strongly affect the measurements [3]. Therefore the optical probe avoids the coupling of the fields with metallic structures occurring in standard metallic probes [4], wherever measurement errors could also be caused by the loss of antenna calibration. Optical EMF sensor thereby results dramatically less invasive then a standard EMF probe [5], and yield a new feedback signal of the radiated power. Optical probes enable the implementation of large-scale electric field monitoring for communication systems [6], providing a better power control in the respect of the laws on electromagnetic field limits in the far-field, and the optimization of the quality of service (QOS).

Expensive probes for electric and magnetic field measurements (also in the Fresnel region) made by dielectric materials with optical transmission lines are recently been developed. Their measure heads need a power source and electronics in order to (i) conditioning and processing the signals received by an external antenna, (ii) electro-optical (EO) signal conversion to drive the optical link of the measure equipment. In recent papers [7, 8] the authors proposed an optically interrogated electromagnetic power sensor based on an all-silicon Fabry-Perot interferometer, where detuning occurs by the field power dissipation in the silicon etalon. This device has a low cost and a very simple structure but relies on the thermo-optic effect, therefore shows low-frequency and transient response limitations. In order to overcame such limitations we describe an integrated optical sensor for fast response electromagnetic field sensing: in the Sect. 2 the design and fabrication aspects, in the Sect. 3 the experimental setup and the measurements performed.

2 Design and Fabrication

The mutual coupling of EMF with the standard metallic probe is the source of precision loss, which can strongly be reduced by a completely optical probe. We propose an integrated optical device for fast response electromagnetic field sensing, suitable for electromagnetic field measurements also in the Fresnel region. The probe is based on a resistively loaded travelling wave antenna approach operating on a wide frequency range including ELF-UHF band.

2.1 Electric Formulation

The design of a suitable tapered antenna is derived according to the Wu-King approximation [9]: a resistively loaded antenna, where only the progressive wave has to be present, is characterized by an impedence distribution:

$$Z(x) = 60g(h, k, a)/(h/2 - |x|) \tag{1}$$

where:

$$g(h,k,a) = 2\{[sinh^{-1}(h/a) - C_i(2ka,kh) + j[2(1-e^{-jkh})/kh - S_i 2ka,kh \quad (2)$$

and h is the dipole length, λ is the wavelength, $k = 2\pi/\lambda$ is the *wavenumber* and a is the thickness of the antenna, C_i is the cosine integral, S_i is the sine integral. *Z(x)* can be realized as a pure resistance because when $a < \lambda$ the imaginary part of *g(h, k, a)* is smaller than the real part.

For this kind of antenna $|Z_a|$, the module of the antenna impedance, is a monotone decreasing function of the frequency and can be shown that the peak corresponding to the resonance frequency are smoothed with respect to one occurring in an ordinary metal dipole.

Following such approach we realized a very tiny (1400 nm) Indium Tin Oxide (ITO) resistively loaded antenna, with a flat response in the frequency range considered for the EMF probe.

2.2 The Sensor Design

The sensor is based on an integrated optical interferometer device, with input and output optical fibers respectively connecting it to a remote laser source and a fast response photo-detector. The resistively loaded antenna, with a flat response in a wide band, yields the voltage input for an integrated modulator. This is composed of two y-branch couplers connecting two optical waveguide arms. Several authors (e.g. [5]) improperly refer to this optical structure as Mach-Zehnder interferometer (MZI), which has a different optical scheme with two mirrors M, two beam-splitter and two detection points 0 and 1, as shown in Fig. 1. The detectors reveal different signals as destructive and constructive interference occur due to different phase shift along the optical paths.

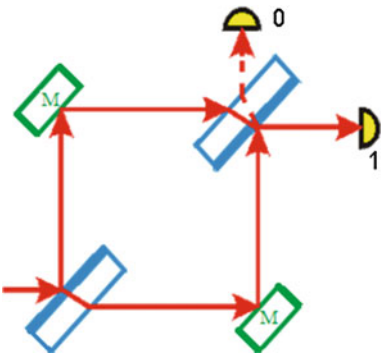

Fig. 1. Schematic of an optical Mach-Zehnder Interferometer

The integrated interferometer in our sensor conversely has only one constructive detection point at the output y-branch, and the optical signal decreases when a detuning signal is detected.

The sensor moreover hybridize an optical device with an electric one, and can be examined as an electric and optical transduction chain which equivalent model is given in Fig. 2. The antenna equivalent yields the electric circuit input, it is a voltage generator V (V equals the field E times the antenna effective length h_e) and two series impedances: the antenna impedance at the gap Z_a with antenna loading Z_l. The electrodes are supplied with the signal induced by a suitable resistively loaded dipole antenna, implementing a progressive wave in order to suppress the typical resonance of metal dipoles.

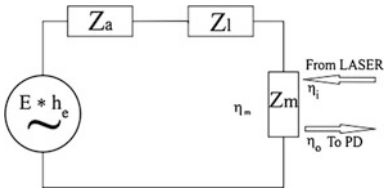

Fig. 2. The sensor equivalent circuit model

The modulator impedance has an optical input port and an output optical port both characterized by two efficiency parameters η_i, η_o, therefore it converts the electric signal at the electrodes into an optical signal according to the Thevenin complex equations and the optical power budget. An optimal modulator working point has been used introducing a constant bias signal [10]. The optical probe is fabricated on a $LiNbO_3$ substrate with X-cut, Y-propagating waveguides substrate (with the antenna superimposed on the modulator substrate) in order to exploit the Pockel effect which results in a linear change of the refractive index due to an external E-field [11].

The X-cut $LiNbO_3$ substrate has been chosen for the much greater thermal stability with respect to z-cut $LiNbO_3$ interferometers, caused by pyroelectric and electrostatic effects occurring when the temperature changes [12].

2.3 Sensor Fabrication

The optical sensor has a "push-pull" electrode configuration such that a dual phase change is induced in the interferometer arms, yielding a doubled effect in the optical output.

Figure 2 shows a transverse section of the optical modulator. Planar optical waveguides (the two ellipses in in the Fig. 3) were manufactured by using high energy ion implantation technique of oxygen ions at 5 meV [13]. The substrate has X-cut, Y-propagating waveguides, as the extraordinary index of the Z axis n_e is lower than the ordinary index n_o of the X axis, where the relatively large electro-optic coefficient is $r_{33} = 32.2$ pm/V. The phase shift Γ is:

$$\Gamma = \pi V r_{33} L n_e^3 / \lambda G_{EL} \tag{3}$$

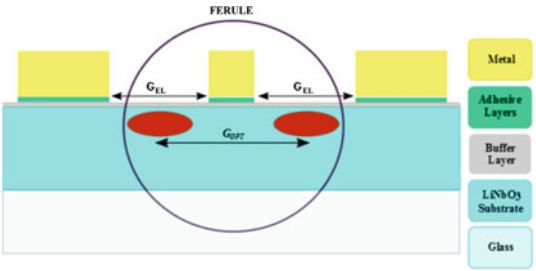

Fig. 3. The sensor transverse section

where L is the electrodes lenght and G_{EL} their spacing. This phase shift produces at the constructive interference output branch an amplitude modulated optical output.

The antenna elements are made by the following process:

- Deposition of a 1.4 μm film of ITO by sputtering on the substrate (1 mm glass);
- Deposition by spinning of reversible photoresist;
- Lithography of the ITO film by the antenna element mask;
- Subsequent development of photoresist (negative process);
- Wet etching of ITO elements by HCl solution.

Then the antenna and modulator substrates are bonded and two micro wires are soldered to electrically supply the modulator, and Table 1 reports a sensor characterization.

Table 1. Electric characterization of the sensor

Element length [m]	5.0 e^{-3}
Element tickness [m]	1.4 e^{-6}
Modulator capacity [F]	2.2 e^{-11}
Modulator resistence [Ω]	1.0 e^{8}

The output of the Y branches interferometer has one constructive interference point, therefore in the detector output we have to filter the large DC component of the signal in order to obtain an amplitude modulated useful signal [10].

3 Measurement

The first experimental setup used is shown in Fig. 4, where the source is a 150 mW in fiber LASER diode (LD) at 980 nm pigtailed with a polarization maintaining fiber, and multi-mode output fiber connecting to fast response amplified photo-detector (PD) with a conversion gain of 200 V/W.

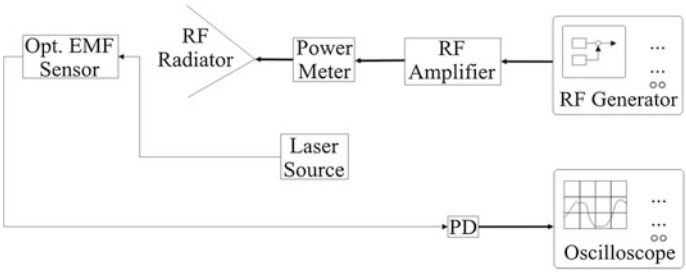

Fig. 4. The sensor transverse section structure

Performance figures will be shown: S11 parameter strongly depends on the wafer interface to fiber. The optical power budget of the interferometer provides a total loss of 28 dB, obtained with accurate optical polishing. Damages in fibers or near the grooves, pigtails, connectors require an accurate optical segment rework soldering.

A power laser is necessary to match the optical power budget used in this experimental phase, that is:

$$L_T = L_D + L_{FC} + L_S = (3\,\mathrm{dB/cm} \cdot 7\,\mathrm{cm}) + (2 \cdot 3\mathrm{dB}) + (2 \cdot 0.5\,\mathrm{dB}) = 28\,\mathrm{dB} \quad (4)$$

where L_T is the sum of losses due to interferometer device L_D, the two fiber coupling L_{FC} and the two optical fiber soldering L_S.

The measurements where performed both in an anechoic chamber with an open-ended wave guide RF radiator, and in laboratory with standard dipole antennas with anti-inductive stands. Measurement in ELF band where performed with capacitive plane cells. The external noise measured in large band in our lab was lower than 300 mV/m, negligible with respect to the test fields used for the probe exposition. Automated measurements were performed connecting the instruments with standard bus for frequency response measurement.

The sensor can be designed for a suitable V_π value, in order to avoid phase-wrapping in strong electric near-field field measurements.

Due to damages in the optical fibers or optical interconnections, optical signal reflections occurred in the measurement chain causing strong LD detuning. This condition produced several harmonics in the optic signal and then in the output waveform, and to detect it we substituted in the setup of Fig. 4 the oscilloscope with a spectrum analyser; narrow and spread spectrum RF sources were characterized for frequency selective measurements [11].

4 Conclusion

We propose an integrated optical probe, a small dimension devices mainly made by non-metallic parts, thereby dramatically less invasive then standard EMF probes. This is an appealing feature where space and time electromagnetic field has to be detected as in EMT [13]. A very tiny resistively loaded antenna with a flat response in a wide band,

yields the electric input for the integrated optical interferometer. The sensor, its technological implementation steps and performance as well as applications to monitoring systems are described. The proposed device technology is compatible with photonic antennas and is a step toward an all-optical communication system. Due to the suitable physical properties of the substrate [14], optical devices integrating the proposed sensor with other sensor on the same complex chip [15] could be implemented in the future.

References

1. Y. Yashchyshyn, et al., Study on active integrated photonic antenna. IEEE ECAP 2009, pp. 3507–3510
2. F. Vacondio, M. Mirshafiei, J. Basak, A. Liu et Al., A silicon modulator enabling rf over fiber for 802.11 OFDM signals, IEEE J.S.T. Quantum Elect. **16**(1) January 2010
3. A. D. Yaghian, An Overview of near-field antenna measurement, IEEE Trans. Ant. Propag. vol. AP-34, 1986
4. M. Kanda, Standard probes for electromagnetic field measurements IEEE Trans. Ant. Propag. **41**(10), 1349–1364 (1993)
5. R. Kobayashi, K. Tajima, N. Kuwabara and M. Tokuda, Optical bias angle control method for electric-field sensor using Mach-Zehnder. inteferometer, IEICE Trans. vol. J81-B-II, no.5, pp. 542–549, May 1998
6. M. Medugno, Electric and optical sensing in nir environmental monitoring. in Proceedings 12th National Conference on Sensors and Microsystems, Naples, 12–14 Feb, 2007, Word Scientific, ISBN 13 978-981-283-358-7 e 10 981-283-358-7 pp. 458–463
7. I. Rendina, F.G. Della Corte, M. Iodice, R. Massa, G. Panariello, G. Cocorullo, All-silicon optically-interrogated power sensor for microwaves and millimetre waves. Elect. Lett. **35**, 1748–1749 (1999)
8. S. Grasso, M. Bellucci G. Cocorullo, F. Della Corte, M. Iodice and I. Rendina, Thermo-optic design for microwave and millimetre-wave electromagnetic power microsensors, Appl. Opt. **41**(18), pp. 3601–3611, 2002
9. T. T. Wu, R. W. P. King, The cylindrical antenna with nonreflecting resistive loading. IEEE Trans. Ant. Propag. AP-**13**(3), 369–373, 1965
10. L. Ciccarelli, M. Medugno, I. Rendina, Electric field measurement by a $LiNbO_3$ Probe, in Proceeding of SPIE, vol 6593, 18 June 2007, Spain, doi:10.1117/12.722513
11. M. Medugno, I. Rendina, V. Striano, A $LiNbO_3$ Electric field optical sensor, in Proceeding 2nd of EOSAM, October 2008, Paris, France, ISBN 978-3-00-024188-8
12. P. Skeath, C.H. Bulmer, S.C. Hiser, W.K. Burns, Novel electrostatic mechanism in the thermal instability of z-cut $LiNbO_3$ Interferometers. Appl. Phys. Lett. **49**, 1221–1223 (1986)
13. M. Jalilvand, Chuanren Wu, J. Schmid and T. Zwick, Quantitative imaging of numerically realistic human head model using microwave tomography. Elect. Lett. **50**(4), 255–256, 2014
14. P. Ferraro, S. Grilli, P. Di Natale, Ferroelectric crystals for photonic applications including nanoscale fabrication and characterization techniques. Springer Series in Materials Science, 2014, ISBN: 978-3-642-41085-7
15. S. Fathpour, Emerging heterogeneous integrated photonic platforms on silicon. Nanophotonics **4**, 143–164 (2015)

Moisture Measurement in Masonry Materials Using Active Distributed Optical Fiber Sensors

Aldo Minardo[1(✉)], Ester Catalano[1], Luigi Mollo[2], Roberto Greco[2], and Luigi Zeni[1]

[1] Department of Industrial and Information Engineering, Seconda Università di Napoli, Via Roma 29, Aversa, CE, Italy
aldo.minardo@unina2.it
[2] Dipartimento di Ingegneria Civile Design Edilizia e Ambiente, Seconda Università degli Studi di Napoli, Via Roma 29, 81031 Aversa, Italy

Abstract. A Brillouin Optical time-domain analysis (BOTDA) sensor has been used to perform distributed temperature measurements along a fiber optic cable with an electrically conductive armoring heated via electrical resistance. The thermal response of a fibre-optic probe put in contact with yellow tuff samples at different moisture content is measured by the BOTDA sensor, paving the way to distributed measurements of moisture content in masonry materials.

Keywords: Distributed optical fiber sensors · Active thermometry · Moisture measurements

1 Moisture Measurement by Active Thermometry

Yellow tuff is a very common building material in Campania (Southern Italy), and tuff masonry often presents damages due to water uptake phenomenon [1, 2]. Capillary rise can have potentially devastating consequences for buildings (biological corrosion, worsening of indoor comfort parameters, worsening of thermal resistance, etc.). Therefore, measuring moisture in building structures is still a current research issue.

Among the methods for non-destructive and continuous measurement of moisture content, the heat-pulse method determines the thermal properties of a material by monitoring the temperature transient resulting from the application of electrical heating. As the moisture content affects the thermal conductivity of the material, the heat-pulse method can be used to determine the moisture after proper calibration. Heat-pulse techniques based on fiber-optic distributed temperature sensors (DTS) has several advantages compared to other technologies, including the capability to monitor the temperature at several locations simultaneously [3–8]. In addition, by using an armored cable, the same cable can be used to perform the measurement of the temperature through the embedded fiber, as well as to apply the heat pulse by injecting electrical current in its conductive armoring. Finally, it is worth to mention that the cable can be simply put in contact with the material, with minimum invasiveness compared to other methods such as the hot-ball probe [9].

B. Andò et al. (eds.), *Sensors*, Lecture Notes in Electrical Engineering 431,
DOI 10.1007/978-3-319-55077-0_20

2 Experimental Results

Distributed temperature sensors (DTS) based on stimulated Brillouin scattering (SBS) retrieve the temperature profile along an optical fiber with high spatial resolution and accuracy [10]. In the Brillouin Optical Time-Domain Analysis (BOTDA), a continuous wave probe signal and a frequency-shifted, pulsed pump signal are injected at the two opposite ends of an optical fiber. Provided that the frequency offset between the two waves is close to the Brillouin Frequency Shift (BFS) of the fiber, the two optical waves interact via stimulated Brillouin scattering (SBS), so that the pump field is backscattered reinforcing the probe field. The gain of the emerging probe beam is measured as a function of the time, for an interval of pump-probe frequency shifts. At each section along the fiber, the local BFS is determined by fitting a spectral shape to the measured Brillouin gain spectrum (BGS). Sensing is based on the (linear) dependence of the BFS from the temperature (about 1 MHz/°C).

The experimental set-up schematically shown in Fig. 1.

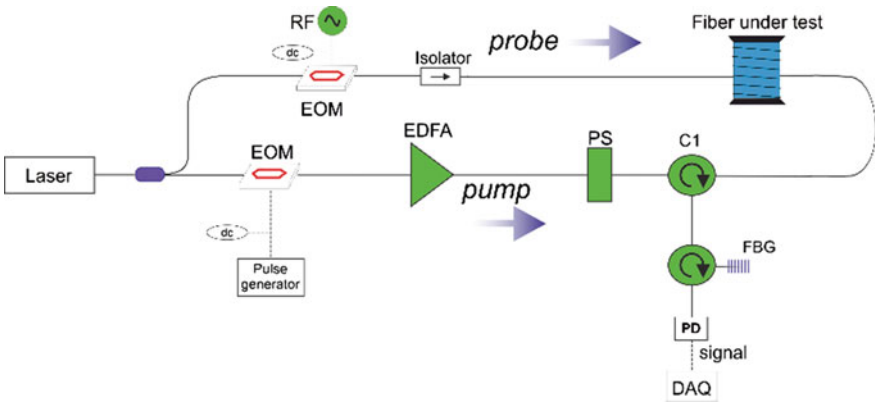

Fig. 1. Experimental set-up for distributed measurement of temperature in optical fibers. *EOM* electro-optic modulator, *PS* polarization scrambler, *EDFA* erbium-doped fiber amplifier, *PD* photodetector, *FBG* fiber Bragg grating

Light from a 1.55 μm distributed feedback (DFB) laser diode is split in two arms to generate the pump and the probe fields. A spectral shift between the two fields is achieved by double sideband, carrier-suppressed modulation in the upper branch: at the modulator output, the sideband with lower frequency acts as the probe beam, while the upper sideband is filtered out through a fiber Bragg grating (FBG) placed before the detector. The latter is a 125 MHz photoreceiver, connected to a data acquisition card (DAQ) with a sampling rate of 250 MS/s. Spatial resolution is dictated by the pump pulse duration, with a 10-ns pulse width giving rise to a 1-m spatial resolution. The set-up allowed us to measure the temperature with a spatial resolution of 1 m, a digital sampling step of 40 cm, an accuracy of 0.1 °C and a temporal resolution of a few seconds.

For the experimental test, a fiber-optic heatable cable with a diameter of 4.0 mm was employed. The cable comprises a central loose tube with two single-mode fibers and two multimode fibers, a copper conductor with an overall cross-section of 0.83 mm^2 for active sensing, stainless steel strength members and double layer polyamide (PA) outer sheath. The amplitude of the electrical current is a trade-off between sensitivity and the requirement of keeping temperature disturbance at minimum, in order to have minimal redistribution of moisture. As an example, we show in Fig. 2 the BFS profile retrieved along the fiber at 1-m spatial resolution and 1-min temporal resolution, after application of a 30-A electrical pulse and with the heatable cable exposed to air.

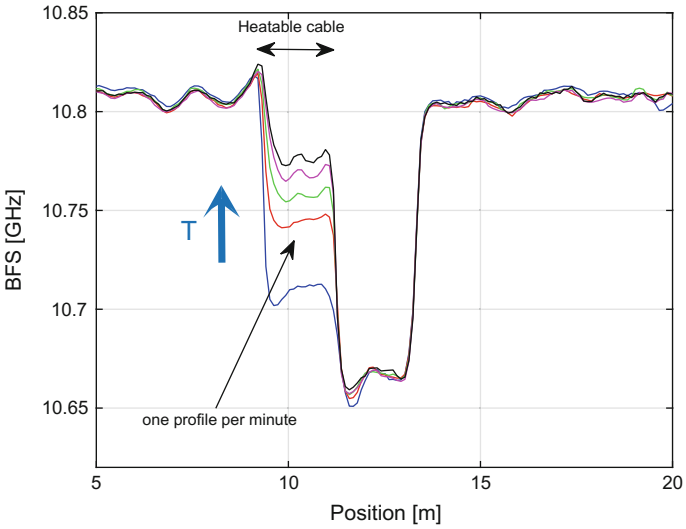

Fig. 2. BFS profile along the sensing fiber, as retrieved by the distributed sensor

In Fig. 3, we show the thermal response acquired by the DTS in a point of the heatable cable, upon the application of a 10-A electrical pulse. Note that the response was acquired at a reading frequency of 0.14 Hz and with the cable exposed to air.

In order to calibrate our sensor for moisture content measurements in the tuff, a relationship must be found between the moisture content and the acquired thermal response. For soil moisture monitoring, two main approaches are being followed. The former derives the thermal conductivity from the slope and intercept of a line fit to the temperature response following an extended heat pulse [4, 5]. Rise time or fall time (or both) can be used to infer the moisture content. The second approach makes use of the cumulative temperature increase over a certain period of time [6, 7], i.e.:

$$T_{cum} = \int_0^{t_0} \Delta T(dt) \tag{1}$$

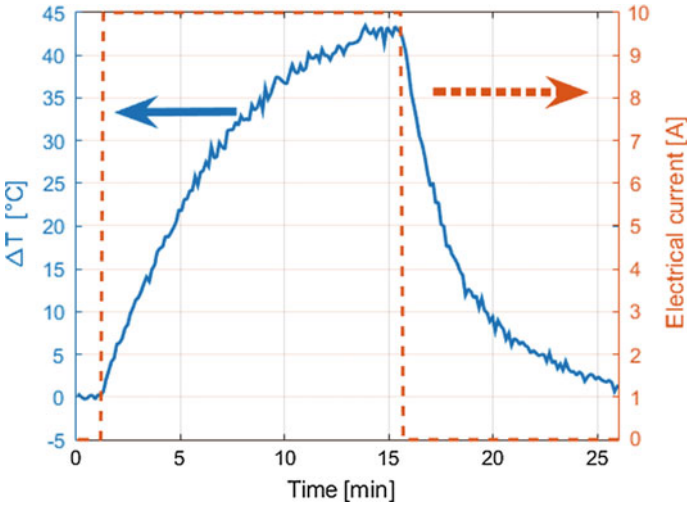

Fig. 3. Example of thermal response acquired upon injection of a 10-A electrical pulse in the active optical cable in air

where T_{cum} is the cumulative temperature increase (°C · s) during the time of integration t_0, and ΔT is the DTS reported temperature change from the prepulse temperature, as in Fig. 3. The integral approach leverages the sensitivity to moisture content of the overall magnitude of the temperature change. Furthermore, there is an intrinsic improvement in sensitivity found in integral methods compared to derivative (slope) approaches. On the other hand, the integral approach has the drawback of being sensitive to the amount of injected energy. In particular, any change in the injected electrical current will result in a change of the cumulative temperature, which may be erroneously ascribed to moisture content changes. Due to this reason, we have opted for the former (derivative) approach.

Measurements were carried out over a Neapolitan yellow tuff sample with size 37 cm × 25 cm × 3 cm, porosity about 50% and an oven-dried weight of 1610 g. The tuff stone was firstly immersed into water for 24 h, in order to reach the saturated state. The weight of the saturated tuff was 2315 g. The thermal response of the tuff was acquired in successive tests, in order to follow the variations of thermal conductivity with the moisture content. The moisture content was calculated in each test by weighting the tuff stone with an electronic scale having a resolution of 5 g. Thus, we measured the gravimetric water content (moisture) by taking the ratio between the mass of water and the mass of the oven-dried material, while the thermal response was acquired by the DTS and post-processed in order to determine the fall time of the thermal response. Each measurement was carried out by applying an electrical pulse having the same characteristics (10 A amplitude, 15 min duration) and by putting a 1-m piece of the cable in contact with the tuff sample.

We report in Fig. 4 the inverse of the fall time of the thermal response as a function of the moisture, together with the fitting (third-order polynomial) curve. As expected, the fall time of the thermal response is inversely related to the moisture content.

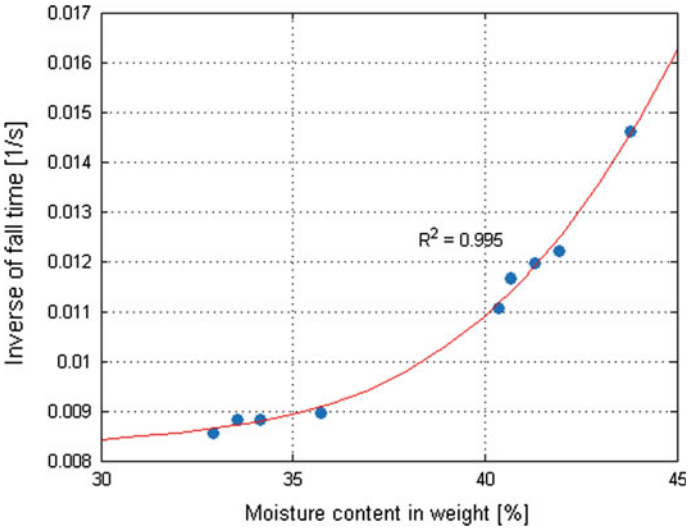

Fig. 4. Slope of the thermal response as a function of the moisture content: experimental (*dots*) and fitted data (*solid curve*)

3 Conclusions

The BOTDA technique has been used for acquiring the thermal response of an optical fiber cable put in contact with a tuff sample at varying moisture contents. A heat-pulse is applied to the sensor by injecting electrical current in the armoring of the optical cable. The relationship between the thermal conductibility measured by the BOTDA sensor, and the volumetric water content measured gravimetrically, has been experimentally determined over samples of yellow tuff. The obtained results show that thermal conductivity is sensitive to moisture variations, suggesting that the DTS technology is a promising tool for moisture measurement in building materials. The obtained results confirm that the BOTDA sensor provides reliable readings of temperature, which can be correlated to the water content in the tuff rock. However, further investigation is needed in order to get more insight about the thickness of tuff rock actually affecting the observed thermal response at the surface. Future work will be also devoted to the design of a custom probe capable of ensuring a good and stable thermal contact between the fiber cable and the sample.

References

1. R. Agliata, L. Mollo, R. Greco. Use of TDR to compare rising damp in three tuff walls made with different mortars. Accepted for publication in Journal of Materials in Civil Engineering (2016)
2. L. Mollo, R. Greco. Moisture measurements in masonry materials by time domain reflectometry. J. Mater. Civ. Eng., 441–444 (2014). doi:10.1061/(ASCE)MT.1943-5533.0000188
3. L. Zeni, L. Picarelli, B. Avolio, A. Coscetta, R. Papa, G. Zeni, C. Di Maio, R. Vassallo, A. Minardo, Brillouin optical time-domain analysis for geotechnical monitoring. J. Rock Mech. Geotech. Eng. **7**, 458–462 (2015)
4. J.D. Weiss, Using fiber optics to detect moisture intrusion into a landfill cap consisting of a vegetative soil barrier. J. Air Waste Manage. Assoc. **53**, 1130–1148 (2003)
5. S. Perzlmaier, M. Aufleger, M. Conrad. Distributed fiber optic temperature measurements in hydraulic engineering—prospects of the heat up method. in *Proceedings of 72nd ICOLD Annual Meeting Workshop on Dam Safety Problems and Solutions Sharing Experience*, Korean Natl. Comm. on Large Dams, Seoul, 16–22 May 2004
6. C. Sayde, C. Gregory, M. Gil-Rodriguez, N. Tufillaro, S. Tyler, N. van de Giesen, M. English, R. Cuenca, J.S. Selker, Feasibility of soil moisture monitoring with heated fiber optics. Water Resourc. Res. **46**, W06201 (2010)
7. D. Cao, B. Shi, H. Zhu, G. Wei, S. Chen, J. Yan, A distributed measurement method for in-situ soil moisture content by using carbon-fiber heated cable. J. Rock Mech. Geotech. Eng. **7**, 700–707 (2015)
8. J. Benítez-Buelga, C. Sayde, L. Rodríguez-Sinobas, J.S. Selker. Heated fiber optic distributed temperature sensing: a dual-probe heat-pulse approach. Vadose Zone J. **13**(11) (2014)
9. V. Boháč, D. Fidríková, V. Vretenár, T. Durmeková, I. Šimková, V. Greif, J. Vlčko. Moisture probe calibration for open air measurements in rock dwellings locality in Brhlovce. in *Proceedings of the 9th International Conference on Measurement* (Smolenice, Slovakia, 2013)
10. X. Bao, L. Chen, Recent progress in Brillouin scattering based fiber sensors. Sensors **11**, 4152–4187 (2011)

Biosensors

Electrochemical Preparation of a MIP-Glassy Carbon Electrode for the Determination of Dimethoate

Denise Capoferri[1(✉)], Michele Del Carlo[1], Nomaphelo Ntshongontshi[2], Emmanuel I. Iwuoha[2], and Dario Compagnone[1]

[1] Faculty of Biosciences and Technology for Food, Agriculture and Environment, University of Teramo, Via Renato Balzarini 1, 64100 Teramo, Italy
dcapoferri@unite.it
[2] SensorLab, Department of Chemistry, University of the Western Cape, Bellville 7535, South Africa

Abstract. In this work a dimethoate-polypyrrole (dim-PPy) MIP films were electropolymerized by cyclic voltammetry (CV) on the surface of glassy carbon electrode (GCE), using pyrrole (Py) as the monomer and dimethoate (dim) as the template. Dimethoate is electro-inactive, therefore an electroactive $K_3[Fe(CN)_6]$ solution was used as probe in the CV and square wave voltammetry (SWV) for the evaluation of the performance of the imprinted (MIP) and non-imprinted (NIP) films. To investigate the analytical performance of the MIP system in the dimethoate detection, the dim-free MIP films electrode, obtained after the removal of the dimethoate, was placed in solutions containing dimethoate at different concentrations for the analyte rebinding. After the rebinding step, for the MIP films there was a decrease of the response and the current was lower than that for the dim-free MIP films. The decrease of the response could thus be used to indirectly detect the analyte quantitatively. For the NIP films, the response of $K_3[Fe(CN)_6]$ was very small and showed no obvious difference with different dimethoate concentrations in the rebinding step. These results illustrated that the dim-PPy MIP film system is simple to construct and easy to operate and could be used to recognize dimethoate.

Keywords: Dimethoate · Molecularly imprinted polymer · Polypyrrole · Electrochemical sensor

1 Introduction

Dimethoate is an organophosphate pesticide (OP) that has an inhibitory effect on the function of the enzyme acetylcholinesterase (AChE); the latter hydrolyses the neurotransmitter acetylcholine and this effect leads to a pathologic excess of acetylcholine in the body. Toxicity of OPs affect many organs [1], particularly the nervous system [2]. Detection of organophosphate pesticides in food samples has been extensively studied using biosensors based on AChE [3, 4]; this system is quite sensitive but the selectivity

B. Andò et al. (eds.), *Sensors*, Lecture Notes in Electrical Engineering 431,
DOI 10.1007/978-3-319-55077-0_21

is poor. Because of wide use and acute toxicity of OPs, it is important to develop rapid, sensitive and selective detection methods.

Molecularly imprinted polymers (MIPs) have received considerable attention in analytical chemistry, primarily because specific recognition sites are formed in the MIP matrix, and excellent selectivity toward the analyte is achieved [5]. Molecularly imprinting is a process by which selected functional monomers are polymerized around a target analyte (template). After polymerization, the template molecule is extracted and a polymer matrix, which is complementary in shape and functionality to the template, is obtained. Thus, the polymer has the ability to selectively link to the target analyte. The chemical and mechanical stability, the facility of preparation and the relatively low cost of the polymers make them attractive for several analytical applications and in some cases they are used as replacers of natural receptors and enzymes [6]. The electropolymerization process is frequently used in the development of molecularly imprinted electrochemical sensors. The advantages are the control of the polymer thickness, which can be regulated by electrochemical conditions, the simple preparation procedure and the formation of very thin films that are beneficial to rapid response [7]. The electropolymerization of polypyrrole (PPy) has been widely used for the preparation of molecularly imprinted electrochemical sensors, due to its excellent biocompatibility and the facility of the immobilization of different compounds [8].

In the present study, MIPs were prepared by electropolymerization of pyrrole (Py) in the presence of dimethoate (template) on the glassy carbon electrode surface, for the electrochemical detection of pesticide. Dimethoate (dim) is electro-inactive, therefore an electroactive $K_3[Fe(CN)_6]$ solution was used as the probe in the cyclic voltammetry (CV) and square wave voltammetry (SWV). To investigate the analytical performance of the MIP system in the dimethoate detection, the dim-free MIP films electrode, obtained after the removal of the dimethoate, was placed in solutions containing dimethoate at different concentrations for the analyte rebinding. After the rebinding step, for the MIP films there was a decrease of the response and the current was lower than that for the dim-free MIP films. The decrease of the response is indirectly related to the amount of the analyte.

2 Materials and Methods

2.1 Chemicals and Apparatus

All the chemicals were obtained from Sigma-Aldrich. Pyrrole was distilled under vacuum until a colorless liquid was obtained, purged with argon and kept in darkness at −30 °C.

Electrochemical studies were carried out using a BASi potentiostat-galvanostat controlled by a Bas100 Software. A three-electrode system was used for all measurements: a MIP-glassy carbon electrode (3 mm diameter) as the working electrode, a platinum wire as the counter electrode and an Ag/AgCl/NaCl (3 M) as the reference electrode.

2.2 Preparation of MIP Film Electrodes and Electrochemical Measurements

A bare glassy carbon electrode (GCE) was polished using 1, 0.3 and 0.05 μm alumina paste on microcloth pads and rinsed thoroughly with distilled water until a mirror-like surface was obtained. Then it was sonicated in 1:1 (v/v) ethanol and distilled water for 10 min. Finally the electrode was washed with distilled water and allowed to dry at room temperature before use. Then the GCE was immersed in PBS solution containing 30 mM pyrrole and 10 mM dimethoate for the electropolymerization step by using cyclic voltammetry in the potential range between −0.4 and +1.5 V during 10 cycles at a scan rate of 50 mV/s. After the electropolymerization, in order to extract dimethoate from the imprinted polymer, the dim-PPy MIP films were immersed in a pH 2 HCl solution and stirred for 20 min (dim-free MIP films). The dimethoate molecules were extracted from the polymer matrix to give a surface complimentary in shape and functionality to the template. For rebinding step, the MIP films after the dimethoate removal were incubated into dimethoate solutions at different concentrations (0.01–10 nM) for 15 min (dim-rebinding MIP films).

Electrochemical measurements for the characterization of the electrodes were performed by using CV and SWV in a pH 7 PBS containing 1 mM $K_3[Fe(CN)_6]$ and 0.1 M KCl solution in the potential range from −0.3 to +0.8 V (CV-SWV) and from +0.8 to −0.3 V (SWV). The $K_3[Fe(CN)_6]$ was used as the probe because the dimethoate is electro-inactive. All measurements were performed at room temperature. A control electrode (non imprinted polymer electrode, NIP) was prepared under the same conditions but without adding dimethoate during the electropolymerization.

3 Results and Discussion

The dim-PPy MIP films were obtained by electropolymerization on the surface of GCE using CV in potential range between −0.4 and +1.5 V during 10 cycles (scan rate 50 mV/s) in PBS solution containing 30 mM pyrrole and 10 mM dimethoate (Fig. 1). An oxidation peak of pyrrole was observed on the first scan at about 1 V, then the peak decreased under continuous cyclic scans. The decrease is related to the formation of PPy films that hinder pyrrole monomer further access to the surface of the GCE. Figure 2a shows cyclic voltammogram obtained with bare GCE and a well-defined redox peaks were observed. After the electropolymerization, for the dim-PPy MIP films no response was observed (Fig. 2b) because of the polymeric matrix and the dimethoate molecules that cover the surface of the electrode. After washing with HCl solution for the dimethoate removal a redox peak appeared again (Fig. 2c) because the electrochemical probe had easier access to the electrode surface. After the template removal, the electrode was incubated in dimethoate solution with different concentration for 15 min for the rebinding step. After incubation in a dimethoate solution, a decrease in the redox peaks currents was observed (Fig. 2d) and the current was lower than that for the dim-free MIP films, because of the ability of the electrode to incorporate again the dimethoate molecules, blocking the diffusion of the probe. ΔIp was the difference between the catodic (ΔIpc) or anodic peak (ΔIpa) current of the probe at a

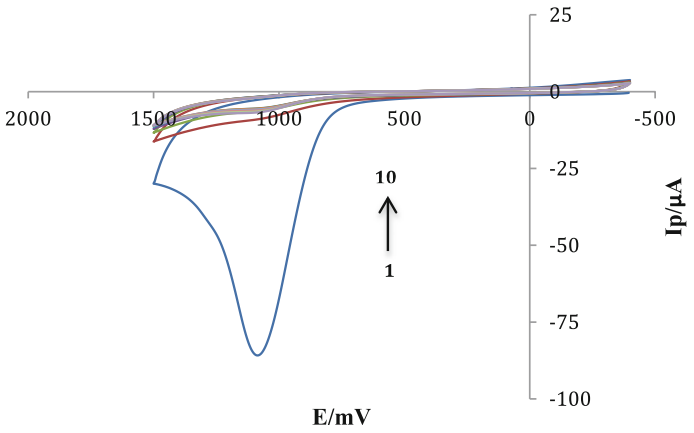

Fig. 1. Cyclic voltammogram for the electropolymerization of 30 mM Py at GCE surface in PBS containing 10 mM dimethoate; scan rate 50 mV/s; 10 cycles

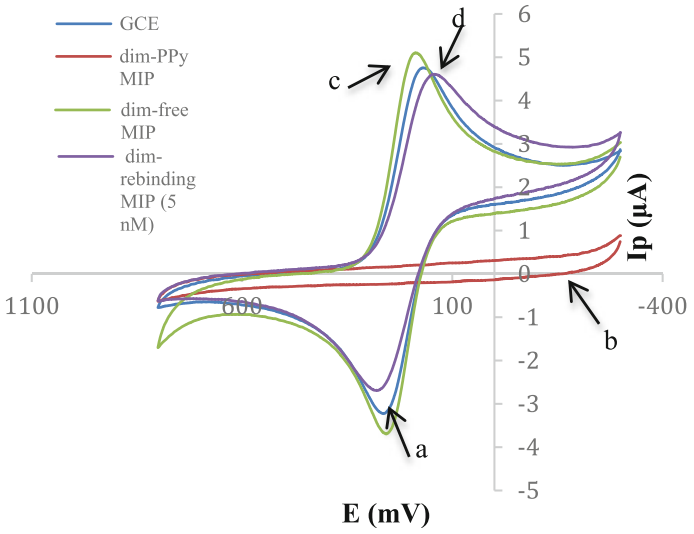

Fig. 2. CVs of 1 mM $K_3[Fe(CN)_6]$ at 10 mV/s in pH 7.0 PBS at **a** bare GCE, **b** dim-PPy MIP film electrode, **c** dim-free MIP film electrode and **d** dim-rebinding MIP film electrode after 5 nM dimethoate rebinding

dim-free MIP film electrodes and that at the dim-rebinding MIP film electrodes. A relationship between the ΔIp and the logarithm of the concentration was evaluated in the range 0.01–10 nM and a linear response was observed. These results indicate that the decrease of the response could thus be used to indirectly detect the analyte quantitatively. For the NIP films, the response of $K_3[Fe(CN)_6]$ was very small and showed no obvious difference with different dimethoate concentrations in the rebinding step

because there is no recognition site for dimethoate (Fig. 3). An initial evaluation of the selectivity of the MIP sensor was carried out using other organophophate pesticides, such as malathion and parathion during the rebinding step. There was no significant decrease of the peak currents for the interferents after the rebinding step (Fig. 4), indicating a very promising selectivity of the sensor. The reproducibility of the MIP-GCE was estimated by determination of 5 nM dimethoate using three different electrodes that were prepared under the same conditions. The relative standard deviation was found to be 3.2% for the ΔIpa and 1.8% for the ΔIpc, demonstrating that the preparation of sensor has a good reproducibility.

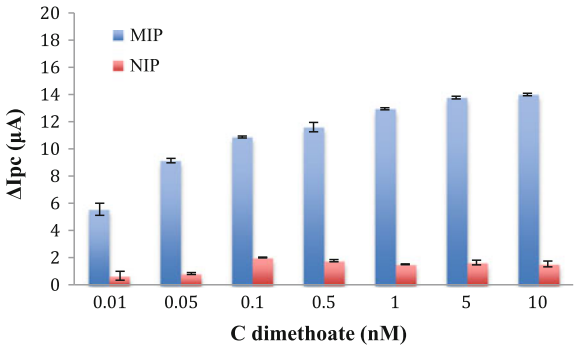

Fig. 3. ΔIpc (SWV) of the MIP and NIP films where ΔIpc represents the difference between the reduction peak current of the probe for the dim-free MIP or NIP films and that after the dimethoate rebinding for 15 min

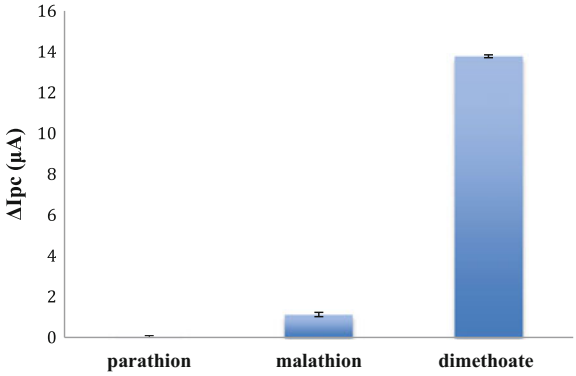

Fig. 4. ΔIpc (SWV) of the MIP films where ΔIpc represents the difference between the reduction peak current of the probe for the dim-free MIP films and that after the dim-free MIP films were placed in 5 nM dimethoate, parathion and malathion solutions for 15 min

4 Conclusion

In this work, a MIP-GCE for the determination of dimethoate was developed, by cyclic voltammetric electropolymerization of a polypyrrole film on the surface of GCE. The difference of the catodic or anodic peak current of probe (ΔIpc or ΔIpa) at electrodes between dim-free MIP and dim-rebinding MIP films could be used to measure dimethoate quantitatively. The developed sensor showed a good reproducibility, repeatability and selectivity. These results illustrated that the dim-PPy MIP film system is simple to construct and easy to operate and could be used to selectively detect dimethoate in real samples.

Acknowledgements. The Authors acknowledge the financial contribution of the Ministry of Foreign Affairs for the Project "Materiali nanostrutturati per sistemi (bio)chimici sensibili ai pesticidi"-Sudafrica.

References

1. A. Betrosian, M. Balla, G. Kafiri, G. Kofinas, R. Makri, A. Kakouri, Multiple systems organ failure from organophosphate poisoning. J. Toxicol. Clin. Toxicol. **33**, 257–260 (1995)
2. I. Desi, L. Nagymajteny, A. Papp, H. Schulz, Experimental model studies of pesticide exposure. Neurotoxicology **19**, 611–616 (1998)
3. M. Del Carlo, M. Mascini, A. Pepe, G. Diletti, D. Compagnone, Screening of food samples for carbamate and organophosphate pesticides using an electrochemical bioassay. Food Chem. **84**, 651–656 (2004)
4. M. Del Carlo, A. Pepe, M. Mascini, M. De Gregorio, A. Visconti, D. Compagnone, Determining pirimiphos-methyl in durum wheat samples using an acetylcholinesterase inhibition assay. Anal. Bioanal. Chem. **381**, 1367–1372 (2005)
5. X. Ding, P.A. Heiden, Recent developments in molecularly imprinted nanoparticles by surface imprinting techniques. Macromol. Mater. Eng. **299**, 268–282 (2014)
6. H. da Silva, J.G. Pacheco, J.M.C.S. Magalhães, S. Viswanathan, C. Delerue-Matos, MIP—graphene-modified glassy carbon electrode for the determination of trimethoprim. Biosens. Bioelectron. **52**, 56–61 (2014)
7. P.S. Sharma, M. Dabrowski, F. D'Souza, W. Kutner, Surface development of molecularly imprinted polymer films to enhance sensing signals. Trends Anal. Chem. **51**, 146–157 (2013)
8. P. Jara-Ulloa, P. Salgado-Figueroa, R. Moscoso, J. Arturo Squella, Polypyrrole molecularly imprinted modified glassy carbon electrode for the recognition of gallic acid, J. Electrochem. Soc. **160**, H243–H246 (2013)

Self Assembled and Electrochemically Deposed Layers of Thiols on Gold Compared with Electrochemical Impedance Spectroscopy and Atomic Force Microscopy

J. Castagna[1], F. Malvano[2], D. Albanese[2], and R. Pilloton[3(✉)]

[1] CNR—IIA, c/o Polifunzionale Unical, Rende, CS, Italy
[2] Dipartimento di Ingegneria Industriale (DIIN), Università di Salerno, Fisciano, SA, Italy
[3] CNR—IIA, AdR RM1, Via Salaria km. 29, 3, 00015 Rome, RM, Italy
roberto.pilloton@cnr.it

Abstract. Self-Assembling is based on a spontaneous process in which organic molecules (alkanethiols, silanes) are adsorbed on a substrate (gold, glass, silicon). Although the implementation is extremely easy, it shows a big disadvantage in timing, because the solution has to be in contact overnight with the substrate under mild shaking. An alternative method of molecular deposition is the Electrochemically Deposed Multilayers commonly used in our laboratory for further immobilization of biological molecules in order to obtain specific biosensors for several analytes. It consists in applying a constant potential on gold working electrode (1.3 V vs. Ag/AgCl) for driving molecules in proximity of the electrode and allow them to react on the surface and form a layer similar to self assembled ones. Both the layers, self assembled and electrochemically deposed ones, were tested with Electrochemical Impedance Spectroscopy and Atomic Force Microscopy. The substrate electrochemically covered shows a higher and a more homogeneous deposition than self assembled one and the deposition time is extremely reduced from several hours to a few of seconds (50 s).

Keywords: Self assembled monolayer · Electrochemical deposition · Thiols · Biosensors · Sensors

1 Introduction

Self-Assembly is a spontaneous process in which organic molecules (alkanethiols or silanes) are chemisorbed on a 2D substrate (gold, glass, silicon, ceramic materials as well as Al_2O_3, TiO_2, ZnO_2 et cetera) forming a highly ordered monolayer architecture. Self Assembled Monolayers (SAMs) of thiols behave like building elements for which the term "nanoLego" has been coined for similarity with the toys for children. So (bio) sensors could be designed to detect analytes as well as Hg(0), Hg(II), ochratoxin-A, *E. coli*. Figure 1 shows some examples of sensing nano-structures built on gold

B. Andò et al. (eds.), *Sensors*, Lecture Notes in Electrical Engineering 431,
DOI 10.1007/978-3-319-55077-0_22

electrodes starting from a thiol precursor ranging from poly-oligonucleotides (poly-thymine), antibodies (anti-ochratoxin A) and specific polymers (limonene).

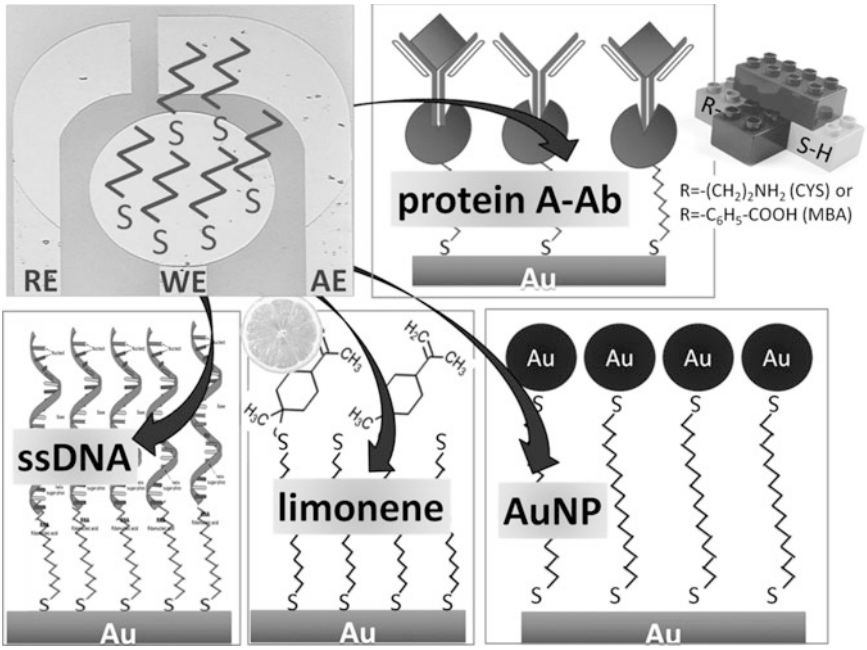

Fig. 1. Sensing nano-structures (oligonucleotides, antibodies, polymers) realized on gold electrodes via thiol precursor

Although the implementation is extremely easy, an overnight treatment after cleaning of the substrate (Au electrodes) with cyclic voltammetry (CV) (inset in Fig. 2) is required. By this way SAMs are deposed not only on working electrode (WE) but also on reference (RE) and auxiliary (AE) ones. Electrochemically Deposed Multilayers (EDMs) are commonly adopted in our lab [1–3] for immobilization of molecular structures in order to obtain (bio)sensors for several analytes [4–7].

2 Materials and Methods

Thiols, as well as Cysteamine (CYS) or 4-mercaptobenzoic acid (MBA), were purchased from Sigma-Aldrich and deposed on a commercial gold three electrodes—Micrux Technologies (Oviedo, Spain). The electrode cleaning, the thiol deposition and the impedimetric analysis were obtained with PalmSens3 (Netherlands), a portable potentiostat/galvanostat and impedance analyzer. At first, the cleaning of Au WE was performed with cyclic voltammetry (CV) at ±1.2 V versus Ag/AgCl pseudo-RE in H_2SO_4, 0.1 M, then Electrochemical Impedance Spectroscopy (EIS) has been performed on the bare electrode in equimolar potassium hexacyanoferrate $K_3[Fe(CN)_6]$/

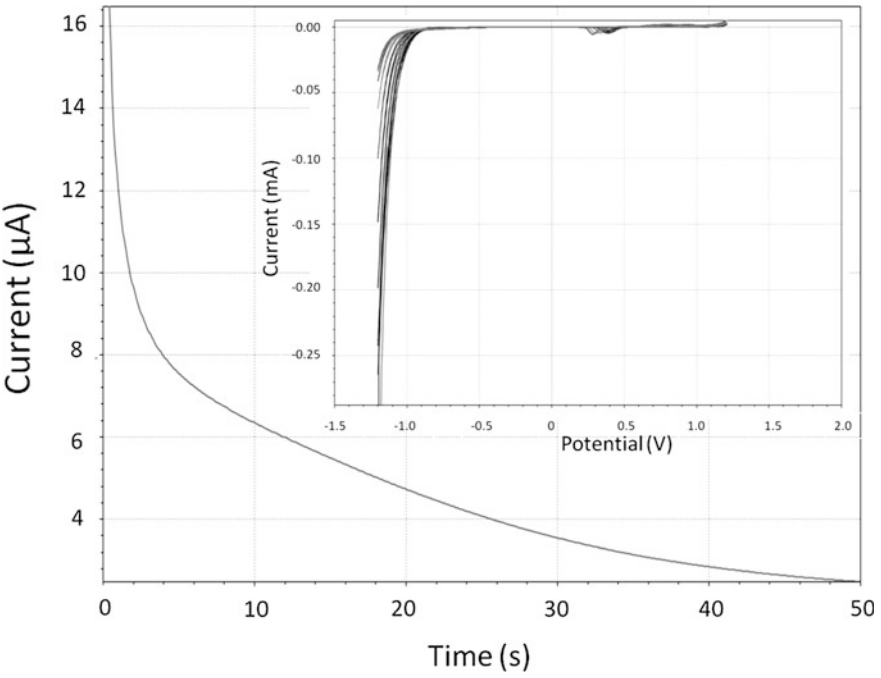

Fig. 2. Current intensity of CYS (20 mM) deposition on Au WE at +1.3 V versus RE. *Inset* Cleaning of AuWE by CV (±1.2 V) in H_2SO_4, 0.1 M, scan rate = 1 V/s, E_{step} = 5 mV

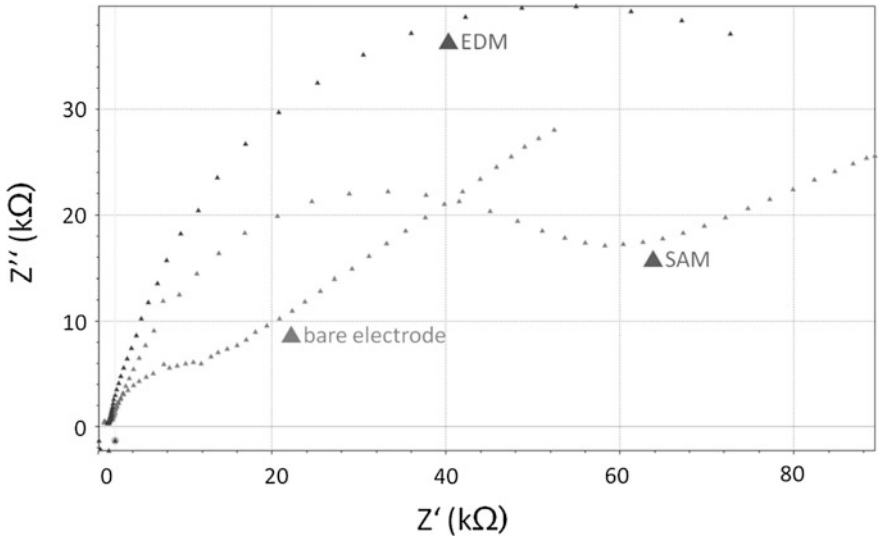

Fig. 3. EIS of bare and cleaned, CYS-SAM, and CYS-EDM AuWEs in 1 mM $K_4/K_3Fe(CN)_6$

$K_4([Fe(CN)_6]$ 0.1 M, at 0.0 V versus RE and with an alternate potential of 10 mV exploring a frequency range between 1 Hz and 20 kHz. The thiol deposition was made with a 20 mM solution by self-assembling overnight or by chronoamperometry at +1.3 V versus RE (50 s). Successively, a new EIS of the thiolated electrode was performed. Surface analysis were obtained with Atomic Force Microscopy (AFM, a Nanosurf Flex-ANA).

3 Experimental and Results

Constant potential drives thiols in proximity of a single AuWE (not AE or RE) allowing addressing in an electrode array (Fig. 4) and reaction on the Au surface with formation of an EDM in only 50 s (Fig. 2) instead of hours as needed for SAMs. Thiols as well as cysteamine (CYS) or 4-mercaptobenzoic acid (MBA) have been deposed as SAMs or EDMs on AuWEs.

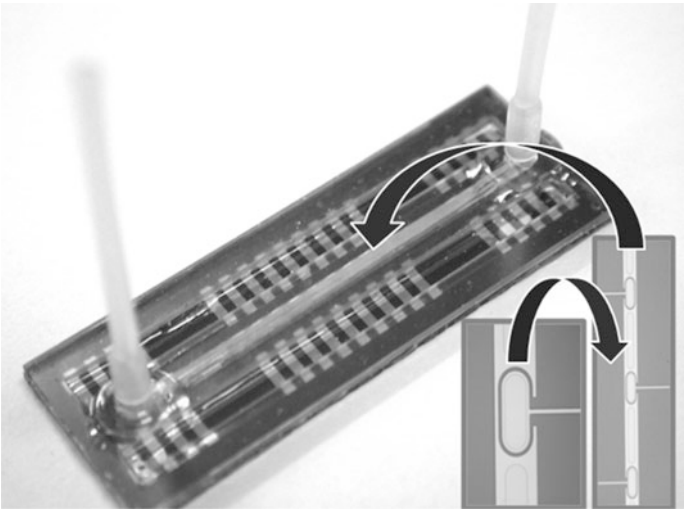

Fig. 4. Multiplexed 16 AuWEs μ-array and μ-flow-cell

Both the layers have been studied with EIS (Fig. 3) and AFM (Fig. 5). By comparison of the impedance spectra for SAMs and EDMs, we can deduce that EDMs shows higher impedance values (Fig. 3), on the other hand, thanks to AFM images, we establish that EDMs is thicker (Fig. 4) than SAMs. SAM shows Au electrodes poorly covered with a thinner film with holes where the bare Au electrode is exposed (poor electrochemical performances of further obtained biosensors). On the contrary the substrate covered with EDMs shows a more homogeneous and smooth surface (Table 1).

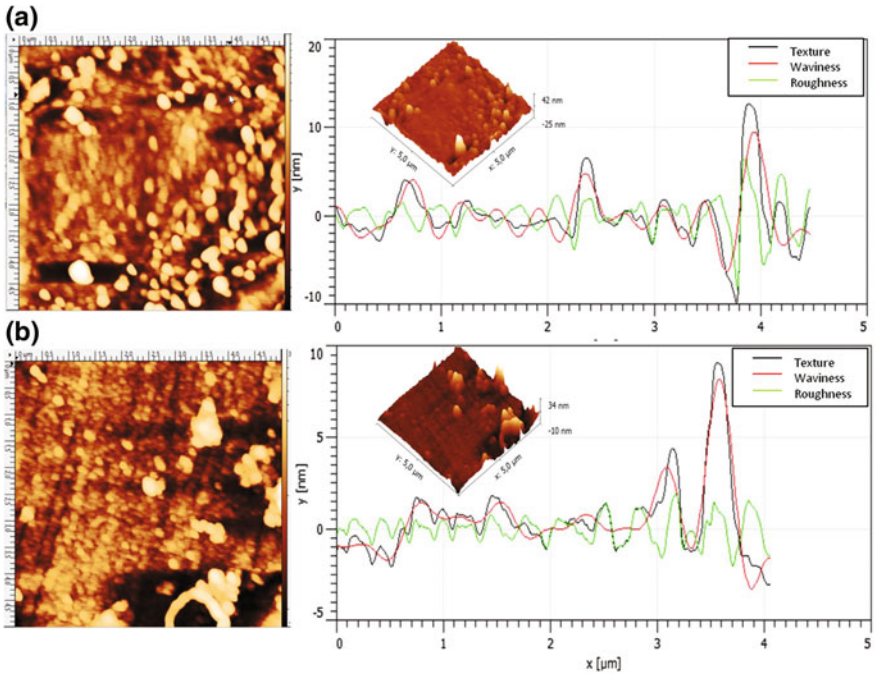

Fig. 5. AFM scans: topographies, 3D views and roughness parameters of SAMs and EDMs on AuWE

Table 1. Comparison between roughness and waviness values for SAM and EDM

	SAM (nm)	EDM (nm)
Ra	1.37	0.56
Rt = Rv + Rp	14.83	3.93
Rv	8.35	2.02
Rp	6.48	1.91

Ra average roughness, *Rp* highest peak, *Rv* deepest valley, *Rt* total roughness

4 Conclusions

EDMs are faster to realize (in 50 s) than SAMs (overnight). They allow molecular addressing on a specific electrode in an array for obtaining multiparametric biosensors. Nano-structures can be easily removed from gold surface at −1.3 V versus RE allowing reversible deposition of new molecules on gold electrode [3]. Additionally, the multilayer offers a higher impedance in EIS although is thicker and more homogeneous than SAMs. Furthermore, the EDMs surface is smoother with a minor number of holes as described by several roughness parameters as Ra, Rt, Rp and Rv.

Acknowledgements. Thanks to Dr. E. Zampetti (CNR-IIA) for AFM images of thiolated surfaces.

References

1. W. Vastarella, L. Della Seta, A. Masci, J. Maly, M. De Leo, L.M. Moretto, R. Pilloton, Biosensors based on gold nanoelectrode ensembles and screen printed electrodes. Int. J. Environ. Anal. Chem. **87**(10–11), 701–714 (2007)
2. J. Maly, M. Ilie, V. Foglietti, E. Cianci, A. Minotti, L. Nardi, A. Masci, W. Vastarella, R. Pilloton (2005) Continuous flow micro-cell for electrochemical addressing of engineered bio-molecules, Sens. Actuators B Chem. **111**, 317–322 (2005)
3. J. Maly, C. Di Meo, M. De Francesco, A. Masci, J. Masojidek, M. Sugiura, A. Volpe, R. Pilloton, Reversible immobilization of engineered molecules by Ni-NTA chelators. Bioelectrochemistry **63**(1), 271–275 (2004)
4. F. Malvano, D. Albanese, R. Pilloton, M. Di Matteo, A highly sensitive impedimetric label free immunosensor for Ochratoxin measurement in cocoa beans. Food Chem (2016). doi:10.1016/j.foodchem.2016.06.034. (Accepted, in press)
5. F. Malvano, D. Albanese, A. Crescitelli, R. Pilloton, E. Esposito, Impedimetric label free immunosensor on disposable modified screen-printed electrodes for ochratoxin A, Biosensors (2016) (in press)
6. N.B. Cramer, J.P. Scott, C.N. Bowman, Photopolymerizations of thiol-ene polymers without photoinitiators. Macromolecules **35**(14), 2002 (2002)
7. C. Tortolini, P. Bollella, M.L. Antonelli, R. Antiochia, F. Mazzei, G. Favero, DNA-based biosensor for Hg(II) determination by polythymine–methylene blue modified electrodes. Biosens. Bioelectron. **67**(2015), 524–531 (2015)

Hybrid Hydrophobin/Gold Nanoparticles: Synthesis and Characterization of New Synthetic Probes for Biological Applications

Jane Politi[1(✉)], Luca De Stefano[1(✉)], Paola Giardina[2], Sandra Casale[3,4], Ilaria Rea[1], and Jolanda Spadavecchia[3,4]

[1] Unit of Naples-National Research Council, Institute for Microelectronics and Microsystems, Via P. Castellino 111, 80127 Naples, Italy
{jane.politi,luca.destefano}@na.imm.cnr.it
[2] Department of Chemical Sciences, University of Naples Federico II, Via Cintia, 80126 Naples, Italy
[3] Laboratoire de Réactivité de Surface, CNRS, UMR 7197, 75005 Paris, France
[4] Laboratoire de Réactivité de Surface, Sorbonne Universités, UPMC Paris 06, 4 Place Jussieu, 75005 Paris, France

Abstract. We report a simple and original method to synthesize gold nanoparticles in which a fungal protein, the hydrophobin Vmh2 from *Pleurotus ostreatus*, mixed to cetyltetrammonium bromide (CTAB) has been used as additional component in a one-step synthesis, leading to shell-like hybrid protein-metal nanoparticles (NPs). The nanoparticles have been characterized by ultra-violet/visible and infrared spectroscopies, and also by electron microscopy imaging. The results of these analytical techniques highlight nanometric sized, stable, hybrid complexes of about 10 nm, with a micelles-like hydrophobins rearrangement.

Keywords: Hybrid gold nanoparticles · Hydrophobins · CTAB

1 Introduction

Gold Nanoparticles (AuNPs) are attracting considerable interest as viable biomedical materials and the research effort about this subject is continuously growing, due to their unique physical and chemical properties [1–4].

The utilization of biomolecules to tune the surface properties and the assembly of AuNPs is a very attractive approach that has received considerable attention: this technology combines the advantages of green chemistry, since harmless biological substances are used instead of some aggressive chemical compound, with the unique properties of biological probes, leading to a next generation of nanometric complexes. Biomolecules and/or biopolymer-conjugated AuNPs are largely used as biomarkers in diseases early detection and as in vivo drugs delivery vehicles in medicine/pharmacy applications, and also in cosmetic products [5, 6].

In the past decades, many synthetic strategies have been developed to prepare AuNPs in organic or aqueous solvent [7, 8]. A commonly employed method for

B. Andò et al. (eds.), *Sensors*, Lecture Notes in Electrical Engineering 431,
DOI 10.1007/978-3-319-55077-0_23

synthesis of AuNPs involves the use of cetyl-tetrammonium bromide (CTAB) as the best candidate among different surfactants with the scope of stabilizing the metallic nanoparticle in solution.

The ionic detergents can be usefully exploited as stabilizers agents during the synthesis of nanoparticles, since they not only prevent particles aggregation but also help in tuning their functional properties. To date, a variety of stabilizers have been employed for the synthesis of AuNPs [1, 9, 10]. In general, surfactants play an important role in contemporary pharmaceutical biotechnology, since they are largely utilized in various drug dosage forms to control wetting, stability, bioavailability, among other properties [11, 12]. Association colloids such as micelles, on the other hand, can form spontaneously under certain conditions (self-assembling systems), and are thermodynamically more stable towards both dissociation and aggregation [13].

This work presents new synthesized hybrid nanoparticles as possible tools for biological applications by using fungal proteins called hydrophobins (HFB). HFB are small (about 100 amino acid residues), amphiphilic, highly surface-active, and self-assembling proteins [14] with different roles in the fungal growth and development. Indeed their biological functions are linked to the reduction of the water surface tension, and to their ability to self-assemble into an amphipathic membrane when they reach an interface, thus allowing fungi to escape from aqueous environment and to facilitate air dispersal of the spores [15, 16]. On the surface of the folded molecules, there is a coherent hydrophobic patch, which makes the molecule amphiphilic. The amphiphilicity gives the protein the ability to strongly stick to hydrophobic surfaces [17], forming a highly stable coating which can be used to promote biocompatibility [18–21], and as an intermediate to attach cells, proteins, or other type of molecules to surfaces.

In this work, HFB Vmh2 purified from *Pleurotus ostreatus* was used. The properties of Vmh2 were studied at the air-water interface, at surfaces, and in solution. We engineered hybrid nanoparticles in which Vmh2 molecules formed a nano-complex with cationic surfactant as CTAB, thus changing chemical and optical properties of Au nanoparticles.

2 Experimental Section

2.1 Materials

All chemicals were reagent grade or higher and were used as received unless otherwise specified. Tetrachloroauric acid ($HAuCl_4$), cetyltetrammonium bromide (CTAB), sodium borohydride ($NaBH_4$), Polyethylene glycol 600 Diacid (PEG), Sodium Dodecyl Sulfate (SDS), methanol (CH_3OH), chloroform ($CHCl_3$) and ethanol (C_2H_5OH) were purchased from Sigma Aldrich.

2.2 Preparation of HFB

White-rot fungus, *P. ostreatus* (Jacq.: Fr.) Kummer (type: Florida; ATCC No. MYA-2306) was maintained through periodic transfer at 4 °C on potato dextrose

agar (Difco) plates in the presence of 0.5% yeast extract. Mycelia were inoculated in 2 L flasks containing 500 mL of potato-dextrose broth (24 g/L) supplemented with 0.5% yeast extract, grown at 28 °C in shaken mode (150 rpm). After 10 days of fungal growth, mycelia were separated by filtration through gauze, treated twice with 2% SDS in a boiling water bath for 10 min, washed several times with water and once with 60% ethanol to completely remove the detergent. The residue was dried under nitrogen, grinded and treated with 100% trifluoroacetic acid (TFA) in a water bath sonicator (Bandelin Sonorex Digitec) for 10 min. The supernatant was dried, dissolved in 60% ethanol and centrifuged (10 min at 3200 g). The new supernatant was lyophilized, and lipids were extracted in a mixture of water-methanol-chloroform 4:4:1 v/v (5 min in bath sonicator). After centrifugation, proteins appeared as a solid aggregate at the interface. They were recovered by upper phase removal, methanol addition and centrifugation. The precipitate was again dried, treated with TFA for 30 min in bath sonicator, re-dried, and dissolved in 80% ethanol. This sample was centrifuged (90 min at 12,000 g) and the supernatant dried, treated with TFA as above-described and re-dissolved in 60% ethanol.

2.3 Synthesis of Hybrid CTAB-Hydrophobin Gold Nanoparticles (Hyb-CTAB-HFB-AuNPs)

CTAB-HFB-AuNPs were prepared using 5 ml of HFB solution (150 μg/ml) mixed with 5 ml of CTAB solution (10^{-4}M) and then added 5 ml of 0.0001 M aqueous $HAuCl_4$ solution for 10 min. To the resulting solution 1.8 ml of $NaBH_4$ (0.01 M) was added dropwise followed by rapid stirring. After 1 h without agitation, the solution became red-violet. The product was centrifuged and purified at the same conditions.

2.4 UV/Vis Measurements

Absorption spectra were recorded using a Jasco V-570 UV/VIS/NIR Spectrophotometer from Jasco Int. Co. Ltd., Tokyo, Japan. 1 mL of nanoparticles solution were acquired in the range between 200 and 800 nm after 60 min from synthesis.

2.5 TEM Measurements

Transmission electron microscopy measurements were recorded on a JEOL JEM 1011 microscope operating at an accelerating voltage of 100 kV. The TEM graphs were taken after separating the surfactant from the metal particles by centrifugation. Typically 1 mL of the sample was centrifuged for 20 min at a speed of 14,000 rpm/min. The upper part of the colourless solution was removed and the solid portion was re-dispersed in 1 ml of water. 2 μL of this re-dispersed particle suspension was placed on a carbon coated copper grid and dried at room temperature.

2.6 PM-IRRAS Measurements

PM-IRRAS spectra were recorded on a commercial Thermo (Les Ulis—France) Nexus spectrometer. The external beam was focused on the sample with a mirror, at an optimal incident angle of 80°. A ZnSe grid polarizer and a ZnSe photoelastic modulator, modulating the incident beam between p- and s-polarizations (HINDS Instruments, PEM 90, modulation frequency = 37 kHz), were placed prior to the sample. The light reflected at the sample was then focused onto a nitrogen-cooled MCT detector. The presented spectra result from the sum of 128 scans recorded at a 8 cm^{-1} resolution. Each spectra shown represent the average of three measurements.

3 Results and Discussion

The synthesis of CTAB-HFB-AuNPs was carried out, mixing HFB and CTAB solutions, and then reducing tetrachlororoauric acid ($HAuCl_4$) by sodium borohydride ($NaBH_4$). TEM images of HFB-CTAB-AuNPs show nanoparticles with an average size of 10.0 ± 0.9 nm (Fig. 1). Conventionally surfactants such as CTAB typically form spherically shaped micelles at low concentration [18].

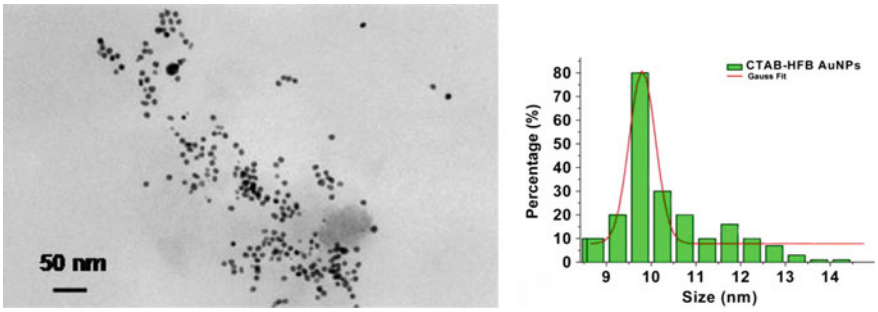

Fig. 1. TEM images and size distribution histogram of CTAB-HFB-AuNPs

As reported by earlier authors [7], the extraordinarily strong binding of $AuBr^{2-}$ to the positive CTA^+ head group could stabilize the Au^+ species in aqueous solution. This is due to the cooperative effect of micelles and Br^-, which favored the emergence of soluble Au^+ species. In the beginning, a small part of Au^+, disproportionate to Au^{3+} and Au^0 species where the complexion between Au^{3+} and Br^- in the presence of CTAB micelles resulted in the appearance of yellowish-red solution [7]. The binding on cationic surfaces was proposed to be due to local charge-charge interactions and as a result, local charges on the surface of the protein were of greater interest than the overall isoelectric point of the protein. For this reason, when HFB molecules were mixed with CTAB solution, the charged residues opposite to the hydrophobic patch of the amphiphilic HFB proteins were thought to interact with the polar surface of CTAB in such a way as the hydrophobic patch was turned outwards against the solution resulting in a hydrophilic coating of the gold surface (see Fig. 2).

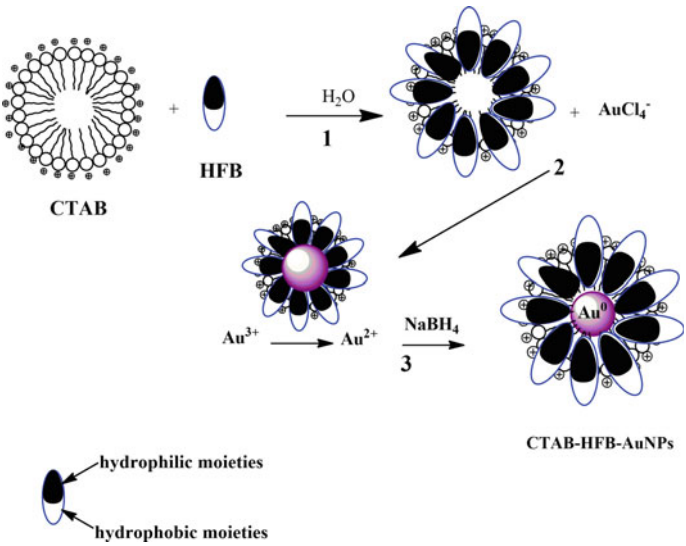

Fig. 2. Schematic of proposed mechanism of AuCl4-reduction and particle formation in the presence of CTAB and HFB protein as surfactants

This steric arrangement of HFB in CTAB micelles before reduction of $HAuCl_4$ during synthetic process of gold nanoparticles, was confirmed by PM-IRRAS analysis, reported in the following.

CTAB-HFB-AuNPs (Fig. 3 green curve) showed a strong resonance band at around 530 nm and a weaker one at 300 nm. This optical behavior was due to steric arrangement like inverse micelle of HFB into CTAB as stabilizers during synthetic process.

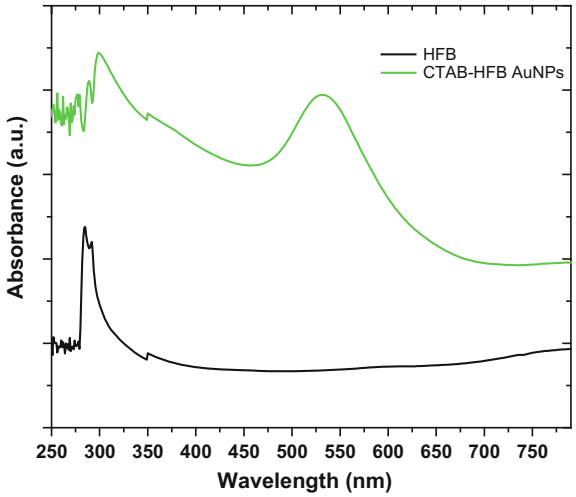

Fig. 3. UV-Vis absorption spectra of (*black curve*) HFB, CTAB-HFB-AuNPs (*green curve*) (color figure online)

The infrared spectrum of CTAB-HFB-AuNPs (Fig. 4 curve 3) shows a peak at 1460 cm^{-1} attributed to the asymmetric and symmetric C–H scissoring vibrations of CH_3–N^+ moieties and to the CH_2 scissoring mode, respectively due to the presence of CTAB. The peaks centred at 2920 and 2850 cm^{-1} are assigned of C–H vibration stretching mode of CH_2 and CH_3 groups respectively. The region corresponding of amide bands is very attenuated. This result is in agreement of UV-Vis spectra in which the absorption peak of HFB is very weak, probably due to a steric arrangement of HFB protein into micelles of CTAB.

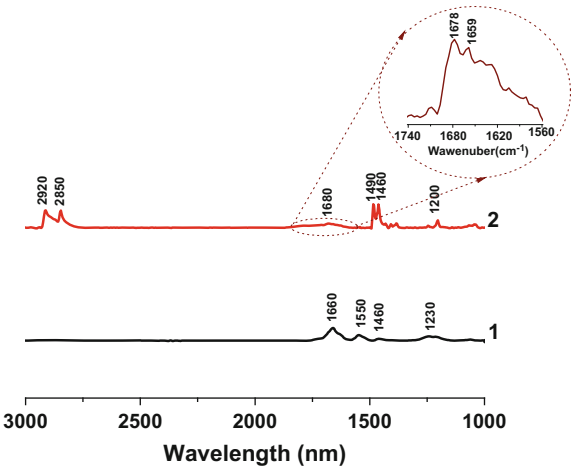

Fig. 4. PM-IRRAS spectra of (*1*) HFB, CTAB-HFB-AuNPs (*2*)

4 Conclusions

In the present work we showed that hybrid HFBAuNPs can be synthesized via a simple one step method. The key role of the HFB molecules during the growth process of nanoparticles was investigated by mixing with cetyltetrammonium bromide as standard surfactant in the synthesis. Stable nanometric hybrid protein-organic-metal NPs have been obtained, with average diameter of 10 nm. These results open a route to simple, effective, and also green chemistry synthesis of a new class of hybrid multipurpose NPs which will be tailored for different biomedical application, such as imaging, targeting and drugs delivery.

References

1. Y. Xia, Y. Xiong, B. Lim, S.E. Skrabalak, Shape-controlled synthesis of metal nanocrystals: simple chemistry meets complex physics? Angew. Chem. Int. Ed. **48**(1), 60–103 (2009)
2. E.E. Bedford, J. Spadavecchia, C.-M. Pradier, F.X. Gu, Surface plasmon resonance biosensors incorporating gold nanoparticles. Macromol. Biosci. **12**, 724–739 (2012)

3. J. Politi, J. Spadavecchia, M. Iodice, L. de Stefano, Oligopeptide–heavy metal interaction monitoring by hybrid gold nanoparticle based assay. Analyst **140**(1), 149–155 (2015)
4. J. Politi, J. Spadavecchia, G. Fiorentino, I. Antonucci, S. Casale, L. De Stefano, Interaction of *Thermus thermophilus* ArsC enzyme and gold nanoparticles naked-eye assays speciation between As (III) and As (V). Nanotechnology **26**(43), 435703 (2015)
5. C.X. Song, V. Labhasetwar, H. Murphy, X. Qu, W.R. Humphrey, R.J. Shebuski, R.J. Levy, Formulation and characterization of biodegradable nanoparticles for intravascular local drug deliver, J. Contr. Rel. **43**, 197–212 (1997)
6. N. Reum, C. Fink-Straube, T. Klein, R.W. Hartmann, C.M. Lehr, M. Schneider, Multilayer coating of gold nanoparticles with drug-polymer coadsorbates. Langmuir **26**(22), 16901–16908 (2010)
7. C. Li, F. Fan, B. Yin, L. Chen, T. Ganguly, Z. Tian, Au^{+}cetyl-trimethylammonium-bromide solution: a novel precursor for seed-mediated growth of gold nanoparticles in aqueous solution. Nano Res. **6**(1), 29–37 (2013)
8. R. Cui, C. Liu, J. Shen, D. Gao, J.-J. Zhu, H.-Y. Chen, Gold nanoparticle–colloidal carbon nanosphere hybrid material: preparation, characterization, and application for an amplified electrochemical immunoassay. Adv. Funct. Mat. **18**(15), 2197–2204 (2008)
9. N. Li, P. Zhao, D. Astruc, Anisotropic gold nanoparticles: synthesis, properties, applications, and toxicity. Angew. Chem. Int. Ed. **53**(7), 1756–1789 (2014)
10. T. Sakai, P. Alexandridis, Spontaneous formation of gold nanoparticles in poly (ethylene oxide)-poly (propyleneoxide) solutions: solvent quality and polymer structure effects. Langmuir **21**(17), 8019–8025 (2005)
11. C.A. Smith, C.A. Simpson, K. Ganghyeok, C.J. Carter, D.L. Feldheim, Gastrointestinal bioavailability of 2.0 nm diameter gold nanoparticles. ACS Nano **7**(5), 3991–3996 (2013)
12. R.K. Gangwar, V.A. Dhumale, D. Kumari, U.T. Nakate, S.W. Gosavi, R.B. Sharma, S.N. Kale, S. Datar, Conjugation of curcumin with PVP capped gold nanoparticles for improving bioavailability. Mat. Sci. Eng. **32**(8), 2659–2663 (2012)
13. B.G. Yu, T. Okano, K. Kataoka, G. Kwon, Polymeric micelles for drug delivery: solubilization and haemolytic activity of amphotericin B. J. Contr. Rel. **53**(1–3), 131–136 (1998)
14. A. Caliò, I. Rea, J. Politi, P. Giardina, S. Longobardi, L. De Stefano, Hybrid bio/non-bio interfaces for protein-glucose interaction monitoring. J. Appl. Phys. **114**(13), 134904–134906 (2013)
15. A. Armenante, S. Longobardi, I. Rea, L. De Stefano, M. Giocondo, A. Silipo, A. Molinaro, P. Giardina, The *Pleurotus ostreatus* hydrophobin Vmh2 and its interaction with glucans. Glycobiology **20**(5), 594–602 (2010)
16. M. Ballero, E. Mascia, A. Rescigno, E.S. Teulada, Use of Pleurotus for transformation of polyphenols in waste waters from olive presses into proteins. Micol. Italiana **19**, 39–41 (1990)
17. M.I. Janssen, M.B.M. van Leeuwen, T.G. van Kooten, J. de Vries, L. Dijkhuizen, H.A.B. Wösten, Promotion of fibroblast activity by coating with hydrophobins in the -sheet end state. Biomaterials **25**(14), 2731–2739 (2004)
18. B. von Vacano, R. Xu, S. Hirth, I. Herzenstiel, M. Rückel, T. Subkowski, U. Baus, Hydrophobin can prevent secondary protein adsorption on hydrophobic substrates without exchange. Anal. Bioanal. Chem. **400**(7), 2031–2040 (2011)
19. A.M. Gravagnuolo, S. Longobardi, A. Luchini, M.S. Appavou, L. De Stefano, E. Notomista, L. Paduano, P. Giardina, Class I hydrophobin Vmh2 adopts atypical mechanisms to self-assemble into functional amyloid fibrils. Biomacromolecules **17**(3), 954–964 (2016)

20. J. Politi, L. De Stefano, S. Longobardi, P. Giardina, I. Rea, C. Methivier, J. Spadavecchia, The amphiphilic hydrophobin Vmh2 plays a key role in one step synthesis of hybrid protein–gold nanoparticles. Colloids Surf. B Biointerfaces **136**, 214–221 (2015)
21. J. Politi, L. De Stefano, I. Rea, A.M. Gravagnuolo, P. Giardina, C. Methivier, J. Spadavecchia, One-pot synthesis of a gold nanoparticle–Vmh2 hydrophobin nanobio-complex for glucose monitoring. Nanotechnology **27**(19), 195701 (2016)

Real Time Flow-Through Biosensor

Immacolata Angelica Grimaldi(✉), Genni Testa, Gianluca Persichetti, and Romeo Bernini

Institute for Electromagnetic Sensing of the Environment (IREA), National Research Council (CNR), Naples, Italy
grimaldi.a@irea.cnr.it

Abstract. An all polymeric platform based on planar microring resonator employing a microfluidic flow-through approach is presented and exploited for biosensing applications. A micromilled hole in the center of the microring resonator drives the analyte flow towards the sensing surface, so optimizing the transport kinetic. A simulated and experimental evaluation of the improved performances in terms of kinetic transport and response time is also presented. Biosensing experiments with bovine serum albumin (BSA) based solutions at different concentrations are performed. Optical characterizations by resonance peak shift show a linear behaviour up to 200 nM and a saturation condition at higher concentrations in SU-8 based microring resonators. A reduction of more than 4 times of the response times, as compared with the standard flow-over approach, is obtained with the proposed flow-through approach. The proposed sensing architecture, allowing the single addressing of ring resonator, gives numerous advantages related to time responses and multiplexing of different analytes for a label-free biosensing.

Keywords: Microring resonator · Flow-through · Biosensing · Optical biosensor

1 Introduction

Detection of bioanalytes is becoming a prominent interest for different fields of application such as environmental monitoring, healthcare, pharmaceuticals and diagnostics. Among the various sensing approaches, one of the most promising is based on optical microring resonator for label-free analyte detection. Microring resonators are constituted by a ring-shape waveguide structure, evanescently coupled with one or more linear waveguides. Microring resonators support wave resonant modes that recirculate along the ring, allowing a repeated interaction with the surrounding sample medium. The surface sensing, involving the binding of analyte molecules on the sensor surface, modifies the effective refractive index of the guided mode and, hence, the resonance wavelengths. Microring resonators offer different advantages such as label-free and high integration capability, thanks to standard fabrication photolithographic techniques, for a simple lab-on-chip integration [1, 2].

B. Andò et al. (eds.), *Sensors*, Lecture Notes in Electrical Engineering 431,
DOI 10.1007/978-3-319-55077-0_24

Usually, the fluidic approaches employed in microfluidic sensors are two: flow-over and flow-through. In the flow-over approach the liquid flows in a microchannel parallel to the sensor surface and the analyte diffuses towards the sensor surface. In the flow-through approach, instead, the analyte flows orthogonally to the sensor surface being driven towards the sensing surface. This configuration can, hence, significantly improve the detection time thanks to the efficient transport of the analyte [3].

In this work, biosensing experiments with microring resonators in a flow-through configuration, realized by means of a precise hole drilled in the center of the ring, are exploited. The processing feasibility of the polymeric materials with mechanical micromilling systems allows a unique, simple and precise method for the realization of the micro-hole on the final sensing device. The biomolecule sensing capability is demonstrated by using BSA protein at different concentrations. The red shift of the resonance peak is then correlated to the BSA concentration, obtaining a calibration curve of the devices. The sensor response times are also evaluated and an improving of more than four times is demonstrated in flow-through configuration respect to flow-over one.

2 Experimental

SU-8 based microring resonators are fabricated on 3 mm-thick poly(methyl methacrylate) (PMMA) substrate. The PMMA sheets are cleaned with isopropyl alcohol and dried on hot plate at 70 °C for 30 min. Negative SU-8 2002 (Microchem Corp.) is spin-coated at 3000 rpm onto PMMA substrate to obtain 2 μm thick layers. A pre-bake of 10 min at 70 °C to evaporate the solvent is followed by UV curing by direct laser writing photolithographic process. After the UV exposure, the film is post-baked for polymer crosslinking. The ring resonators have a diameter of 280 μm and are coupled with a straight bus waveguide, 3 μm wide and 2 μm height preserving the monomodal condition at 1550 nm.

High precision computer numerical control (CNC) micromilling machine is employed for the realization of 240 μm diameter holes in the centre of the ring resonators.

The microfluidic channel (500 μm width and 100 μm height), used to deliver the sample to the ring, is manufactured in PDMS by a standard replica molding process.

For biosensing experiments, bovine serum albumin (BSA, molecular weight 66 kD) is dissolved at different concentrations in deionized water and stirred for 20 min at ambient temperature before using.

A fibre coupled tunable laser, over a range of wavelengths 1545–1565 nm, is used to interrogate the ring resonators.

Syringe pumps are used to dispense precise amount of analytes at different flow rates. The tubing are connected to the chip by steel needles, with an outer diameter of 500 μm and inner diameter of 260 μm, glued to the inlet of PDMS based microfluidic part.

3 Results and Discussions

The schema of the experimental setup is reported in Fig. 1. The polymeric ring resonator is top-sealed by the PDMS microchannel. In the flow-over configuration the analyte flows parallel to surface (Fig. 1a) while in the flow-through configuration passes through the drilled hole in the center of the ring (Fig. 1b).

Finite element method (FEM) simulations by using COMSOL Multiphysics software are performed for both flow-over and flow-through configuration. The steady state flow profiles obtained by solving the incompressible Navier–Stokes equation by using a 3D model for both configurations are reported in Fig. 2. The left side channel is used as inlet in order to inject a water based solution (density $\rho = 1000$ kg/m^3) with a flow rate of 6 μL/min. The outlet was set to fixed-pressure boundary condition. The flow over scheme (Fig. 2a) the flow has a parabolic profile with a fast convective flow in the centre of the microchannel and a very slow flow near the sensing surface. In the flow-through configuration (Fig. 2b) the analyte is driven towards the bottom, passing through the hole, with an increasing of the convective flow around the sensing surface. The presence of a flow velocity different from zero near the sensing area in the flow-through configuration modify the transport kinetic of the analyte that is more efficiently collected in the sensing area respect to flow-over one. As results, the response times of both configurations are significantly affected from the transport kinetic and it is absolutely predictable a reduction of the response time in the flow-through approach.

Having confirmed the feasibility of our approach, we study the sensor response in the flow-over and flow-through conditions at fixed flow rate.

In Fig. 3a is reported an example of transmission spectrum of the polymeric microring resonator measured around 1560 nm. The highest Q factor, estimated by evaluating the linewidth full width at half maximum of the Lorentzian-shaped dips, is about 5.7×10^3. The main aspect that limits the Q-factor can be ascribed to the roughness on the ring sidewalls, an intrinsic effect of the direct writing system. Nevertheless, this Q-factor value is widely suitable for the biosensing experiments to be performed.

The calibration curve in biosensing experiments is measured by pumping in flow-over condition the BSA solutions and evaluating the resonance peak shift respect

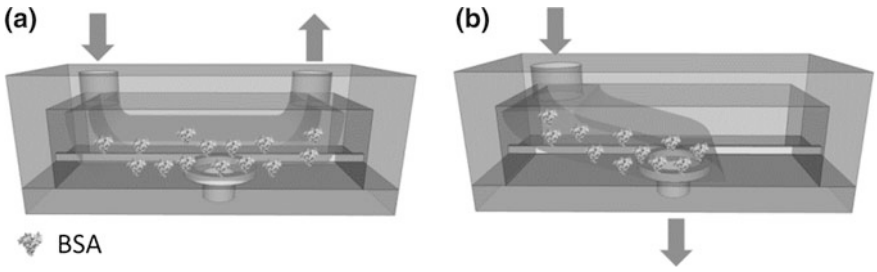

Fig. 1. Schema of the optofluidic microring resonator in (**a**) flow-over and (**b**) flow-thorough configurations

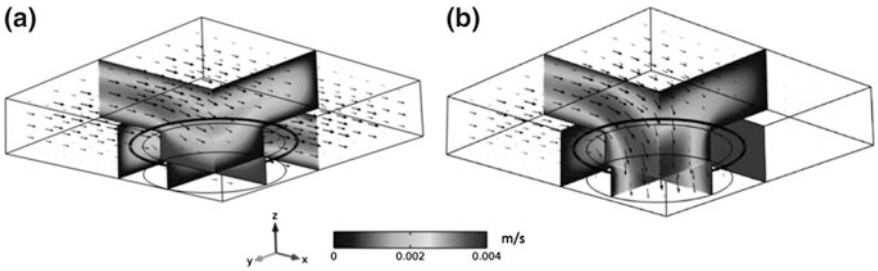

Fig. 2. 3D steady state flow profile for both (**a**) flow-over and (**b**) flow-through profile obtained by solving incompressible Navier-Stokes equations

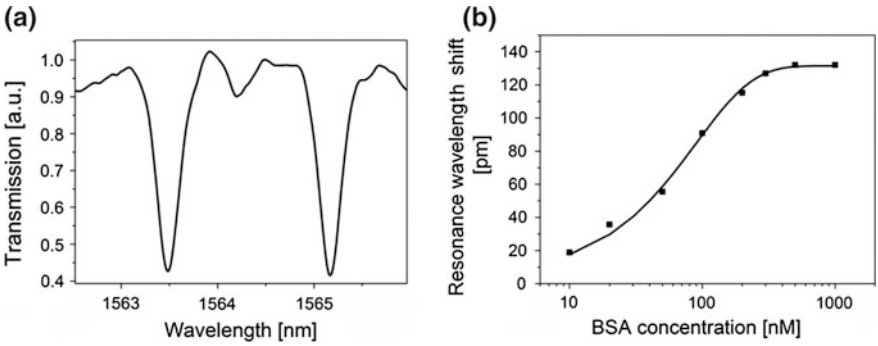

Fig. 3. **a** Transmission spectrum of the microring resonator. **b** Resonance peak shift in transmission spectra of the ring resonators for different BSA concentrations. The *straight line* is a sigmoidal fit of the experimental points

to zero concentration. The results are reported in Fig. 3b. The experimental points are well fitted with a sigmoidal curve, a clear indication of binding site limited reactions. The sensor response is almost linear up to 200 nM and saturated at higher concentration, a clear indication of a full coverage of the surface with the BSA molecules. The surface mass detection sensitivity can be estimated by the following equation:

$$S_m = \frac{\Delta\lambda}{\sigma_p} \tag{1}$$

where $\Delta\lambda$ is the peak shift at the saturation condition and σ_p is the surface density of the molecular monolayer of BSA. The measured $\Delta\lambda$ is equal to 132 pm while the surface density of the molecular BSA layer is $\sigma_p = 2.96$ ng mm^{-2} [4], giving a calculated sensitivity of $S_m = 44.6$ pm ng^{-1} mm^2.

The dynamic experiments for biochemical sensing of 20 nM BSA solution are performed on both flow-over and flow-through configurations with flow rate of 6 μL min^{-1}. The results of the experiments are reported in Fig. 4. The evaluated sensor response times, defined as the rise time to move from 10 to 90% of the equilibrium

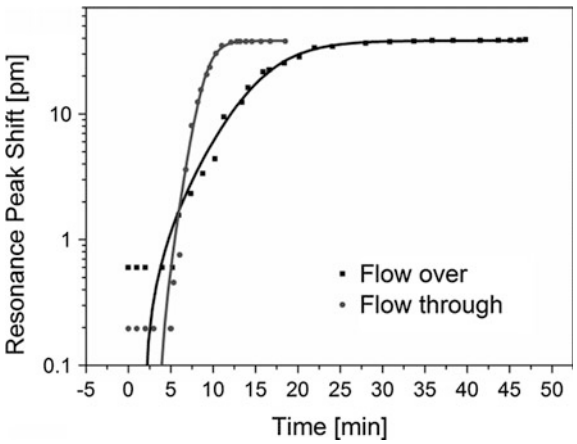

Fig. 4. Response times of microring resonators with 240 μm drilled hole for detecting 20 nM BSA solution in flow-over (*dark square*) and flow-through (*red circle*) experiments with a flow rate of 6 μL/min

value, are 14.8 and 4.1 min for flow-over and flow-through, respectively. The analysis indicates an improvement factor of more than 4 times of the response time for the active configuration. Indeed, an active transport of the molecules is achieved in the flow-through case, which enables a greater number of analyte molecules to reach the sensor respect to flow-over configuration, so reducing the response times.

4 Conclusions

The successful realization of a polymeric platform based on flow-through approach of all polymer microring resonators has been reported. A drilled hole in the center of the microring resonator significantly modify the flow profile, improving the transport kinetic respect to standard flow-over one. Preliminary biosensing experiments, employing BSA protein, are performed on both configurations and the response times are also measured. The analysis highlights that the flow-through approach led to a reduction of the sensor response time of more than 4 times respect to standard configuration.

Acknowledgements. This research has been partially supported by Italian Minister of University and Research (MIUR) under the project I-AMICA (I High Technology Infrastructure for Environmental and Climate Monitoring—PONa3_00363) and Futuro in Ricerca (FIR) programme under the grant No. RBFR122KL1 (SENS4BIO).

References

1. Y. Sun, X. Fan, Optical ring resonators for biochemical and chemical sensing. Anal. Bioanal. Chem. **399**, 205–211 (2011)
2. M.H.M. Salleh, A. Glidle, M. Sorel, J. Reboud, J.M. Cooper, Polymer dual ring resonators for label-free optical biosensing using microfluidics. Chem. Comm. **49**, 3095–3097 (2013)
3. I.A. Grimaldi, G. Testa, R. Bernini, Flow through ring resonator sensing platform. RSC Adv. **5**, 70156–70162 (2015)
4. X. Fan, I.M. White, H. Zhu, J.D. Suter, H. Oveys, Overview of novel integrated optical ring resonator bio/chemical sensors. Proc. SPIE **6452M**, 1–20 (2007)

Amorphous Silicon Temperature Sensors Integrated with Thin Film Heaters for Thermal Treatments of Biomolecules

Nicola Lovecchio[1(✉)], Domenico Caputo[1], Giulia Petrucci[1], Augusto Nascetti[2], Marco Nardecchia[2], Francesca Costantini[2,3], and Giampiero de Cesare[1]

[1] D.I.E.T., University of Rome "La Sapienza", Via Eudossiana 18, 00184 Rome, Italy
nicola.lovecchio@uniromal.it
[2] S.A.E., University of Rome "La Sapienza", Via Salaria 851/881, 00138 Rome, Italy
[3] Department of Chemistry, University of Rome "La Sapienza", Piazzale Aldo Moro 5, 00138 Rome, Italy

Abstract. This work combines a lab-on-chip device with an electronic system for the achievement of a small-scale and low-cost thermal treatment of biomolecules. The lab-on-chip is a 1.2 mm-thick glass substrate hosting thin film resistor acting as heater and, on the other glass side, amorphous silicon diodes acting as temperature sensors. The electronic system controls the lab-on-chip temperature through a Proportional-Integral-Derivative algorithm. In particular, an electronic board infers the temperature measuring the voltage across the amorphous silicon diodes, which are biased with a constant forward current of 50 nA, and drives the heater to achieve the set-point temperature. The characterization of the whole system has been carried out implementing the thermal cycles necessary in the polymerase chain reaction technique for amplification of DNA. To this purpose, the lab-on-chip has been thermally coupled with another glass hosting a microfluidic network made in polydimethilsiloxane, and the time evolution of temperature has been carefully monitored. The measured performances in terms of heating rate, cooling rate and settling time demonstrate that the proposed system completely fulfills the requirements of the investigated biological application.

Keywords: Lab-on-chip · Thin film heaters · Temperature sensors · Amorphous silicon diodes · Polymerase chain reaction

1 Introduction

Lab-on-chip (LoC) technology is receiving a lot of attention thanks to their potential applications in biology and in genomics. The strength of these devices relies in the integration of multiple functionalities in a single chip [1, 2].

The development of LoC devices for biochemical analysis has several advantages including reduced volume of reagents and samples, portability, and low power

B. Andò et al. (eds.), *Sensors*, Lecture Notes in Electrical Engineering 431,
DOI 10.1007/978-3-319-55077-0_25

consumption [3–6]. Several clinical diagnostics techniques, such as Polymerase Chain Reaction (PCR) or cell lysis, require thermal treatments of the analyte [7–9], and therefore the temperature control is a critical parameter in managing many physical, chemical and biological applications. The thermal power can be provided by a bulky metal block thermally coupled with the LoC or by an integrated thin film heater. The standard on-chip heating approach uses a thin metal film (i.e. platinum) as both heater and temperature sensor, taking advantage of the resistance temperature dependence [10]. This way presents many advantages but is limited by the resistance temperature coefficient (TCR) of the heater: for some conductor the TCR is very low and in these cases is hard to obtain a good sensitivity. Furthermore, it is impossible to infer local information as the temperature in different points of the heated area since the resistor variation depends on the average temperature of the whole heater surface. Another approach relies on the integration of thin film temperature sensors and thin film heater in the same LoC to achieve high sensitivity regardless of the heater material [11].

In this context, we present the integration of amorphous silicon (a-Si:H) p-i-n structure and thin film heaters on the same glass substrate combined with a compact electronic board able to drive the heaters and monitor the temperature measuring the drop voltage across the diodes. Indeed, a-Si:H diodes are appealing as thin film temperature sensor since the voltage across them varies linearly with the temperature, when they are biased with a constant current, with a sensitivity greater than those found in crystalline silicon [12].

2 System Description

The proposed system, whose block diagram is depicted in Fig. 1, is constituted by the following components:

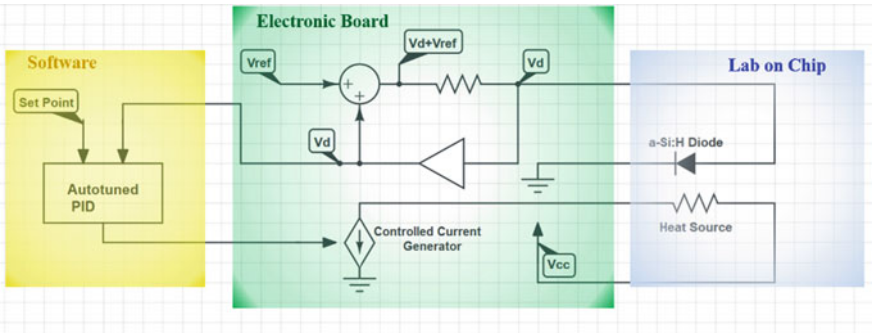

Fig. 1. Block diagram of the system

1. a lab-on-chip device;
2. an electronic board that controls the lab-on-chip temperature;
3. a software that controls the electronic circuit board.

A Graphical User Interface was developed in order to control all the functionalities of the electronic board. In particular, the set-point temperature (specified by the user) is achieved using a software Proportional-Integral-Derivative algorithm, which takes, as input, the temperature inferred by the diode. This is possible since the voltage across the diode varies linearly with the temperature when it is biased with a constant current. The output of the software is then used to provide a controlled current to the heater. The following parts of this section report the detailed descriptions of the lab-on-chip device and the electronic circuit board.

2.1 Lab-on-Chip System

The LoC integrates on a 1.2 mm-thick glass substrate different thin film technologies in order to develop a multifunctional platform suitable for thermal treatments. In particular, a 5 × 5 cm^2 glass substrate hosts:

- a thin metal film acting as heating sources on one side of the glass;
- a set of a-Si:H diodes, acting as temperature sensors, to monitor the temperature distribution on the active area of the heater.

A cross section of the fabricated device is shown in Fig. 2.

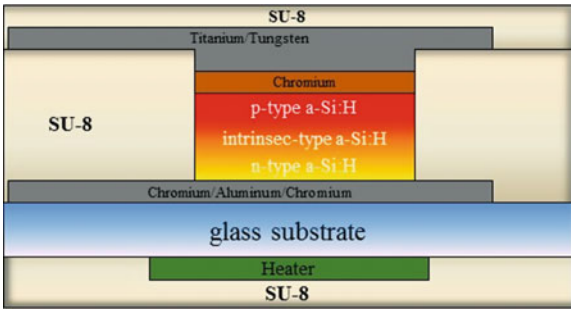

Fig. 2. Detailed cross section of the lab-on-chip

2.1.1 Heater Design, Fabrication and Characterization

The thin film metal resistor, deposited on a glass substrate, features an area comparable to the active area of the thermal treatment and low power consumption. The selected materials and thicknesses, determining the value of the electrical resistance, are mainly defined by the power requirement, while the resistor geometry is determined by the specification of uniform spatial temperature distribution over the thermal process area. Starting from the results published in previous works [13], we have developed a double concentric spiral with a heated area of about 120 mm^2.

The heater geometry was designed using finite element simulations with COMSOL Multiphysics software, coupling the electrical and the thermal problems with the Joule effect and obtaining the temperature profiles due to a potential difference applied across

the resistor. Basing on the simulations results, the thin film heater has been fabricated through vacuum evaporation of a 100/600/100 nm-thick Chromium/Aluminum/Chromium stacked layer and defined by conventional photolithography using the mask depicted in Fig. 3. The 5 × 5 cm^2 glass substrate hosts two mirrored heaters with elliptical shape. Each heater has four electrical contacts: the two external pads provide the current, while the voltage is measured between the internal ones. The obtained resistance was around 11 Ω.

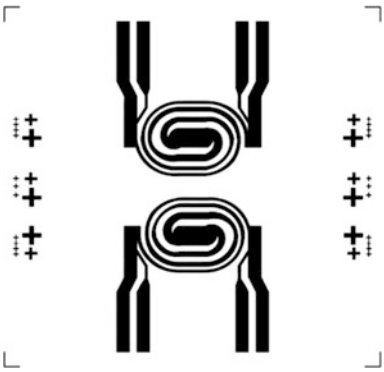

Fig. 3. Heater mask

An infrared thermo-camera (FLIR A325) has been used to measure the thermal distribution over the heated area in steady state condition. Results obtained applying a

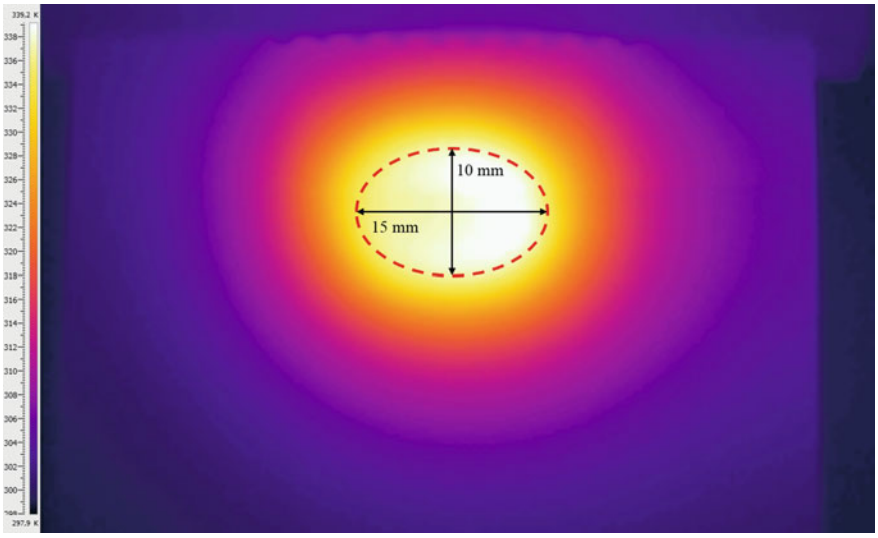

Fig. 4. Measured temperature distribution over the heater area

voltage equal to 2.9 V to the heater are reported in Fig. 4 in color scale. The elliptical shape, where the temperature is uniform, reproduces the heater geometry. In particular, inside the area (≈120 mm^2) defined by the dashed red line, an average temperature of 338 K with a standard deviation of ±1 K is achieved.

2.1.2 Sensors Fabrication

On the other side of the glass, the a-Si:H devices have been fabricated through Plasma Enhanced Chemical Vapor Deposition (PECVD) and standard microelectronic techniques (evaporation, sputtering, photolithography and etching). In particular, the fabrication steps are the following:

1. vacuum evaporation of 30/150/30 nm-thick Cr/Al/Cr stacked layer, which acts as bottom contact of the diodes;
2. patterning of the metal stack by conventional photolithography and wet etching process;
3. deposition by PECVD of the a-Si:H stacked structure n-type/intrinsic/p-type;
4. deposition by vacuum evaporation of a 50 nm-thick chromium layer, which acts as top contact of the sensors;
5. wet etching of the chromium and dry etching of the a-Si:H layers for the mesa patterning. The area of the diodes is 0.8 × 0.8 mm^2;
6. deposition by spin coating of a 5 μm-thick SU-8 3005 (from MicroChem, MA, USA) passivation layer and its pattering for opening via holes over the diodes;
7. deposition by sputtering of a 150 nm-thick titanium/tungsten alloy layer and its patterning for the definition of the top contacts and of the connection to the pad contacts;
8. deposition by spin coating of a 5 μm-thick SU-8 3005 passivation layer.

2.2 Electronic Circuit Board

The electronic board includes:

- a power circuit that drives the heater with the current required to achieve the specified temperature;
- a power circuit that drives a fan used to enhance the cooling of the LoC during thermal cycles;
- an electronic circuit that biases the diode at a constant current and reads the diode voltage.

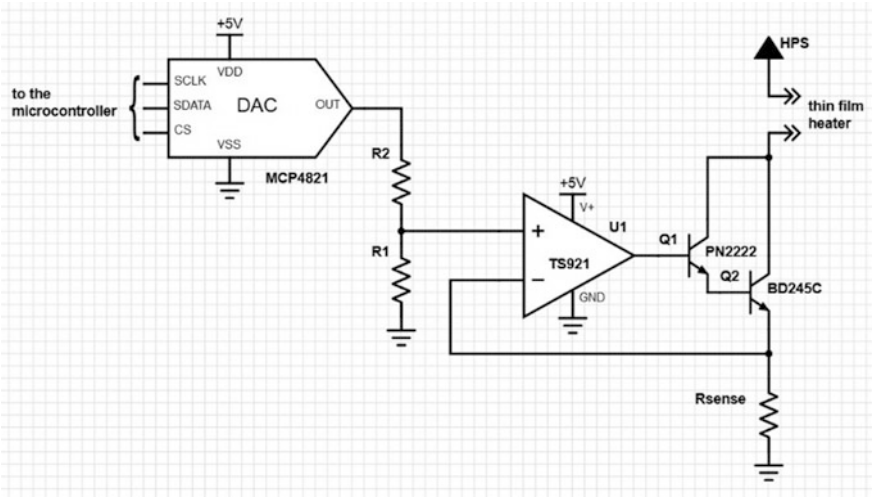

Fig. 5. Schematic of the current generator that drives the heater

In order to drive the thin film resistor we have used a simple current generator driven by a Digital to Analog Converter (DAC). The schematic of this electronic board section is reported in Fig. 5.

The most of the current that flows in the heater comes from the collector of the transistor Q2 (BD245C from Bourns®) that is a NPN silicon power transistor with very high maximum continuous collector current (10 Amps) and a minimum forward current transfer ratio (h_{FE}) of 20. Taking into account this small value of the h_{FE}, we decided to use the Darlington configuration adding to the circuit the transistor Q1 (PN2222 from Fairchild Semiconductor), which is a general-purpose small signal transistor.

The operational amplifier is the TS921 from STMicroelectronic. This is a rail-to-rail single BiCMOS operational amplifier that exhibits very low noise, low distortion and low offset. The current provided to the heater is set by the MCP4821 converter (from Microchip), which is a single channel 12-bit DAC. The devices operate from a single 2.7–5.5 V supply. A Serial Peripheral Interface allows us to control the DAC through a PIC18F4550 microcontroller (also from Microchip). The device has a high precision internal voltage reference (V_{REF} = 2.048 V), and the user can configure the full-scale range to be 2.048 V or 4.096 V.

The value chosen for the sense resistance R_{sense} is 0.2 Ω, while the values of R_1 and R_2 are respectively 1 and 36 kΩ. With these values, we achieved a maximum driving current of 550 mA.

The same topology of circuit has been used to drive the fan that is necessary to quickly cool the LoC when thermal cycles are required.

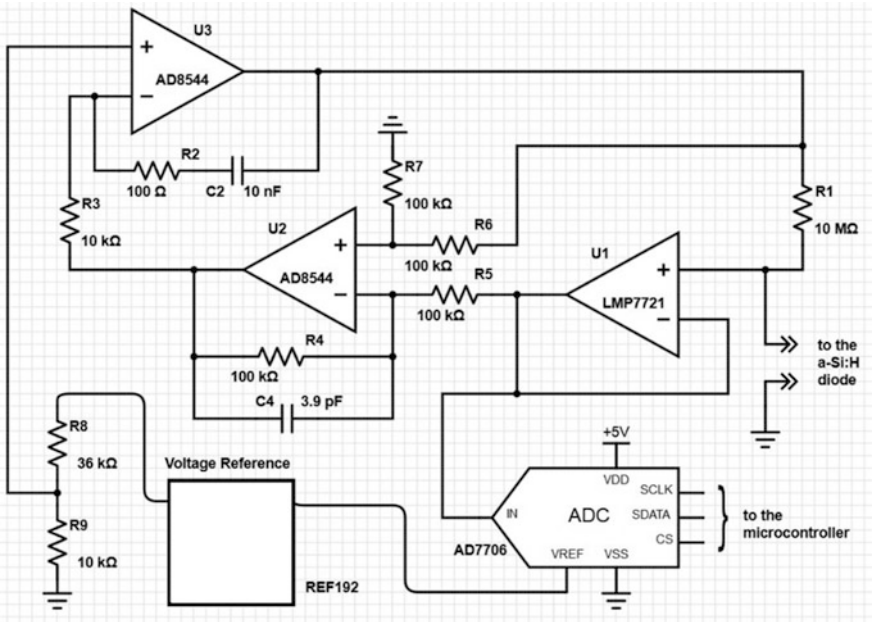

Fig. 6. Schematic of the circuit which senses the temperature biasing with a constant forward current the a-Si:H diode

The circuit that infers the heater temperature through the a-Si:H diode is instead depicted in Fig. 6. It drives the diode with a constant current in forward condition and at the same time reads the voltage across the diode. A detailed description of the circuit mode of operation was reported in [14].

Briefly, a voltage reference of 2.5 V (provided by the REF192 from Analog Devices) is partitioned with the resistances R_8 and R_9 obtaining a voltage reference for the circuit equal to

$$V_{ref} = 2.5\,\mathrm{V} \cdot \frac{10\,\mathrm{k\Omega}}{10\,\mathrm{k\Omega} + 36\,\mathrm{k\Omega}} \approx 0.543\,\mathrm{V} \tag{1}$$

This voltage is reported, through the feedback loop, across the resistance R_1. In this way, the current that flows in the diode is

$$I_{diode} = \frac{V_{ref}}{10\,\mathrm{M\Omega}} = 54.3\,\mathrm{nA} \tag{2}$$

The same 2.5 V reference together with the ADC-gain of 4 were chosen for the DAC, obtaining a minimum detectable signal V_{min} equal to

$$V_{min} = \frac{2.5\,\text{V}}{(2^{16} \cdot 4)} \approx 9.5\,\mu\text{V} \tag{3}$$

All DA and AD Converters included on the board are driven by the PIC18F4550 microcontroller, which incorporate a fully featured Universal Serial Bus (USB) communications module that is compliant with the USB Specification Revision 2.0. This module allows us to control all the functionalities of the electronic board with a common personal computer equipped by the developed GUI.

3 Experimental Results

This section reports the performances of the whole system during the thermal cycles of a PCR experiment.

3.1 System Calibration

In order to control the temperature of the LoC system, we performed a preliminary calibration of the a-Si:H diodes combining the realized system and the FLIR A325. We monitored the temperature of the diode through the thermo-camera while the electronic board kept constant the temperature of the diode actuating the developed PID control on the heater and simultaneously recording the diode voltage.

Measurement results are reported for one diode in Fig. 7. Equation inside the figure is the linear fitting of the measured values. The slope of the fitting straight line (about

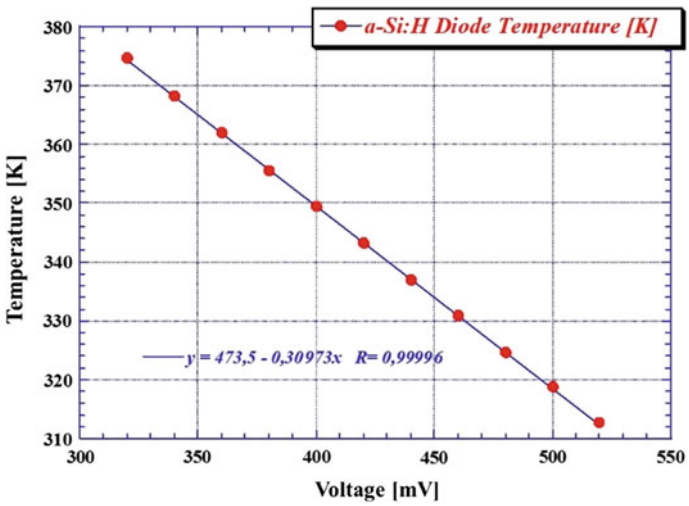

Fig. 7. Measured voltage-temperature characteristics of an a-Si:H diode integrated in the lab-on-chip

0.31 K/mV) represents the inverse of the diode thermal sensitivity, which is around 3.2 mV/K. Taking into account the minimum voltage variation that the ADC can discern (see Eq. (3)) and the diode sensitivities, the minimum temperature change that can be detected by our system is around 3 mK. This value satisfies the requirements of the routine biological applications, which demand, at mostly, to monitor temperature change of tens of degrees.

3.2 Testing of the Whole System

The performances of the developed system have been characterized through the implementation of a Polymerase Chain Reaction experiment, suitable for DNA amplification. In particular, the test has been accomplished carrying out the standard three-temperature cycling technique. In this approach, each PCR cycle consists of the melting of the double-stranded DNA (around 370 K), annealing of the specific primers

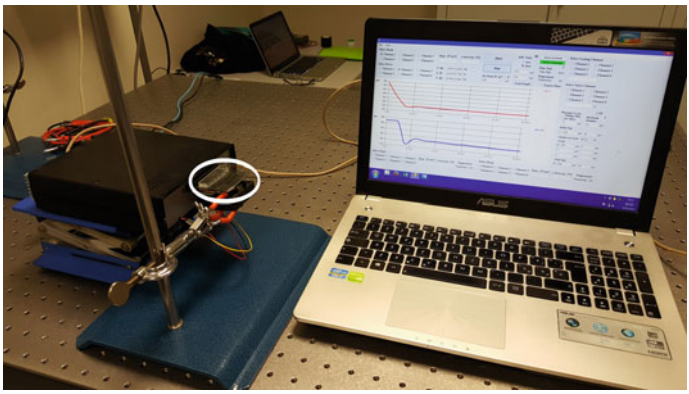

Fig. 8. Picture of the setup used for the PCR experiment. The *white circle* indicates the lab-on-chip, while the *black box* contains the electronic circuits (Color figure online)

to their target gene (usually between 323 and 338 K) and extension of primers with thermo-stable polymerase enzymes such as Taq polymerase (around 345 K).

In order to reproduce the operating conditions of a PCR experiment, the LoC has been thermally coupled with another glass hosting a microfluidic network made in polydimethilsiloxane (PDMS). In this way, apart from the few microliters of biological solution contained in the microfluidic network, this set-up includes all the elements to

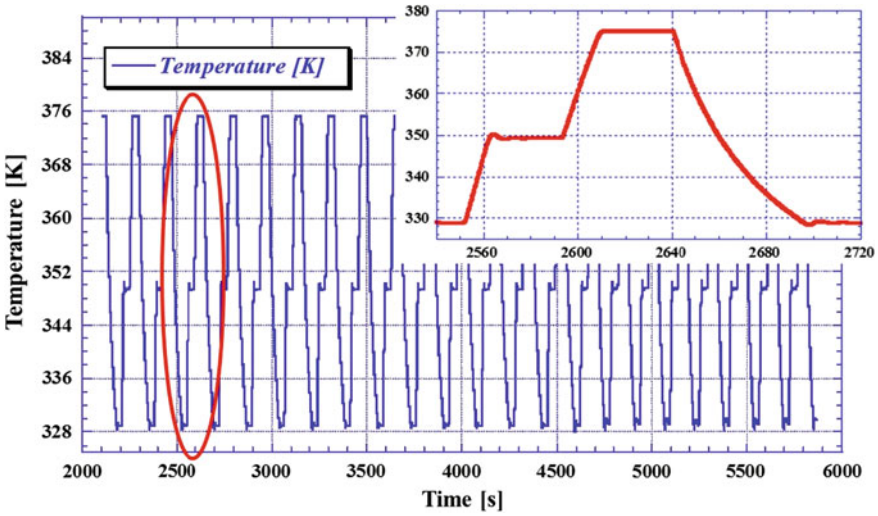

Fig. 9. Time evolution of the temperature during the PCR experiment. The zoom shows a detail of one PCR cycle

implement the DNA amplification through the PCR technique. A picture of the complete setup is shown in Fig. 8.

The sensor temperature during the PCR experiment is shown in Fig. 9. The inset shows a detail of one PCR cycle. Each cycle foresees 30 s at 329 K, 30 s at 349 K and 30 s at 375 K. The time evolution of the reported curves, and in particular the fall time, the rise time and the setting time, depends on the temperature control performed through the PID algorithm. We found that the rise rate was 2 K/s and that the fall rate, controlled by the fan, was 1 K/s. Furthermore, the curve showed absence of overshoot and a displacement from the set-point temperature below ± 0.5 K.

These values meet the characteristics of the standard thermo-cyclers used for the PCR experiments in the biological laboratories and therefore demonstrate the suitability of the proposed LoC for thermal treatments of biomolecules.

4 Conclusions

This work has presented a very compact system able to perform controlled thermal treatments of biomoleculels. It is based on thin film technologies to avoid the use of bulky external metal block heaters. In particular, the realized lab-on-chip integrates on the same glass substrate thin film metal heaters on one side and amorphous silicon diodes, acting as temperature sensors, on the other side.

The experimental characterization of the single electronic devices (thin film heater and a-Si:H diodes) and of the whole system has demonstrated that the proposed LoC fully satisfies the requirements for the implementation of the PCR technique, the nowadays prevalent biological process for DNA amplification.

References

1. C.H. Ahn, J.W. Choi, G. Beaucage, J.H. Nevin, J.B. Lee, A. Puntambekar, J.Y. Lee, Disposable smart lab on a chip for point-of-care clinical diagnostics. Proc. IEEE **92**(1), 154–173 (2004)
2. S.C. Jakeway, A.J. de Mello, E.L. Russell, Miniaturized total analysis systems for biological analysis. Fresenius' journal of analytical chemistry **366**(6–7), 525–539 (2000)
3. D. Caputo, M. Ceccarelli, G. de Cesare, A. Nascetti, R. Scipinotti, Lab-on-glass system for DNA analysis using thin and thick film technologies, in *Proceedings of Material Research Symposium*, vol. 1191, 2009, OO06-01
4. D. Caputo, A. de Angelis, N. Lovecchio, A. Nascetti, R. Scipinotti, G. de Cesare, Amorphous silicon photosensors integrated in microfluidic structures as a technological demonstrator of a "true" lab-on-chip system. Sens. Bio-Sens. Res. **3**, 98–104 (2015)
5. P. Abgrall, A.M. Gue, lab-on-chip technologies: making a microfluidic network and coupling it into a complete microsystem—a review. J. Micromech. Microeng. **17**(5), R15 (2007)
6. J.W. Hong, S.R. Quake, Integrated nanoliter systems. Nat. Biotechnol. **21**(10), 1179–1183 (2003)
7. V. Miralles, A. Huerre, F. Malloggi, M.C. Jullien, A review of heating and temperature control in microfluidic systems: techniques and applications. Diagnostics **3**(1), 33–67 (2013)
8. A.I. Lao, T.M. Lee, I.M. Hsing, N.Y. Ip, Precise temperature control of microfluidic chamber for gas and liquid phase reactions. Sens. Actuators A **84**(1), 11–17 (2000)
9. T.M. Hsieh, C.H. Luo, F.C. Huang, J.H. Wang, L.J. Chien, G.B. Lee, Enhancement of thermal uniformity for a microthermal cycler and its application for polymerase chain reaction. Sens. Actuators B Chem. **130**(2), 848–856 (2008)
10. K. Tsutsumi, A. Yamashita, H. Ohji, The experimental study of high TCR Pt thin films for thermal sensors, in *Sensors, 2002. Proceedings of IEEE*, vol. 2. IEEE, pp. 1002–1005
11. D. Caputo, G. de Cesare, M. Nardini, A. Nascetti, R. Scipinotti, Monitoring of temperature distribution in a thin film heater by an array of a-Si: H temperature sensors. IEEE Sens. J. **12** (5), 1209–1213 (2012)
12. G. de Cesare, A. Nascetti, D. Caputo, Amorphous silicon pin structure acting as light and temperature sensor. Sensors **15**(6), 12260–12272 (2015)
13. G. Petrucci, D. Caputo, A. Nascetti, N. Lovecchio, E. Parisi, S. Alameddine, A. Zahra, G. de Cesare, Thermal characterization of thin film heater for lab-on-chip application, in *Proceedings of the 18th AISEM Annual Conference, AISEM 2015.* Art. no. 7066835
14. N. Lovecchio, G. Petrucci, D. Caputo, S. Alameddine, M. Carpentiero, L. Martini, E. Parisi, G. de Cesare, A. Nascetti, Thermal control system based on thin film heaters and amorphous silicon diodes, in *6th IEEE International Workshop on Advances in Sensors and Interfaces, IWASI 2015.* Art. no. 7184977, pp. 277–282

Opto-Plasmonic Biosensors for Monitoring Wheat End-Products Quality

C. Galati[1(✉)], M.G. Manera[2], A. Colombelli[2], M. De Pascali[1], P. Rampino[1], C. Perrotta[1], and R. Rella[2]

[1] Department of Biological and Environmental Sciences and Technologies, University of Salento, Via Monteroni, 73100 Lecce, Italy
chiara.galati@unisalento.it
[2] CNR-IMM-Unit of Lecce, Via Monteroni, 73100 Lecce, Italy

Abstract. The aspect of food quality is of increasing interest for both consumers and food industry. Detection of chemical contaminants and specific quality-related components are required. In this sense, biosensors can play a prime role, because these devices allow cheap and continuous monitoring of contaminants along the pasta production chain and are also useful to identify allelic variants of genes coding for protein associated to bad or good quality of wheat end-products. In this work we report the production of a whole-cell biosensor based on bacterial cells genetically modified to respond to the presence of metal ions by fluorescence or luminescence emission, and of a biosensor based on Localized Surface Plasmon Resonance (LSPR), that is able to detect nucleic acid sequences characterizing different allelic variants.

Keywords: Food quality · Durum wheat · Whole-cell biosensor · Localized surface plasmon resonance

1 Introduction

Important factors that determine qualitative characteristics of durum wheat end-products are mainly related to the quality of grains, that are in turn due to the genetic background, but are also strongly influenced by environmental factors and crop management. An important environmental factor affecting quality is the presence of metal ions as food contaminants deriving from the growing environment or released by the processing industry. Reliable analytical methods for the detection and quantification of chemical contaminants and for the determination of genetic quality-related components are required: in this sense, biosensors can play a prime role. In general biosensors are analytical devices composed by a biological recognition element associated to a physical transducer generating a signal proportional to analytes concentration. The aim of this work is the development of biosensors for the detection of factors influencing quality of durum wheat end-products. We started the development of two kinds of biosensor based on different biological recognition devices: a whole-cell biosensor for the detection of metal ions and a Localized Surface Plasmon Resonance (LSPR) biosensor, based on DNA/DNA interaction, for the detection of allelic variants of genes specifically related to quality in different durum wheat

B. Andò et al. (eds.), *Sensors*, Lecture Notes in Electrical Engineering 431,
DOI 10.1007/978-3-319-55077-0_26

cultivars. The first kind of biosensor uses the whole prokaryotic or eukaryotic cell as a single reporter, incorporating both bioreceptor and transducer elements into the same cell. The sample toxicity is estimated from the degree of inhibition of a cellular activity or a specific reporter gene expression [1]. In this case the presence of metal ions activated the transductions of a reported protein.

In the LSPR kind of biosensor, light interacts with particles much smaller than the incident wavelength. This leads to a plasmons that oscillates locally around the nanoparticle with a frequency known as the LSPR. When metal nanostructures interact with a light beam, part of the incident photons are absorbed and part are scattered in different directions [2]. In particular, in this work the LSPR biosensor was used to study the *Lpx* gene coding for lypoxigenase, enzyme responsible of the carotenoid pigments degradation and, consequently, of the color change of wheat end-products.

2 Experimental Details

2.1 Whole-Cell Biosensor

The whole-cell biosensor consists of K12 MG1655 and DH5α *Escherichia coli* cells transformed with plasmids in which the reporter gene (GFP or *lux*CDABE), whose expression is quantitatively monitored, is under control of metal-responsive promoters such as *zntA*, *groE* and *dnaK*. Tobacco protoplasts were transformed with a plasmid containing the GFP gene driven by a promoter of a sunflower small HSP gene known to be activated also by metal ions. The *E. coli* and tobacco cells genetically engineered as above reported, emit fluorescence or luminescence in response to metal exposure. Bacteria and tobacco protoplasts were mixed with an agarose matrix (2%) and dispensed into the wells of a *96-well* plate to be immobilized. After immobilization, *E. coli* and tobacco cells were treated, first, with different concentrations of Al, Cd, Co, Ni and Zn salts for different times (0–24 h), and then with various by-products and final product of the pasta processing industry. The signal was measured by a fluorimeter.

2.2 LSPR Biosensor

Au nanoparticles were prepared onto corning glass substrates (10 × 10 × 2 mm) by e-beam evaporation. The technique used allows to obtain spherical nanoparticles with a diameter of 30 nm (Fig. 1).

The immobilization of the DNA molecules (probe-10 μM) occurred by depositing a drop of the solution containing the probes in a saline buffer for 20 h. The probe is 5′ thiol-modified and contains a $(CH_2)_{15}$tail. After rinsing in water, the transducer was left for 20 h in the passivation buffer and, after a new rinsing in water, the solution containing the oligonucleotides (target-1 μM) resuspended in hybridization buffer was injected into the measuring cell using a peristaltic pump: the interaction was monitored for 30 min. Finally, the probe was regenerated by HCl 20 mM. The optical characterization was conducted by using a Varian Cary® 500 UV-Vis Spectrophotometer.

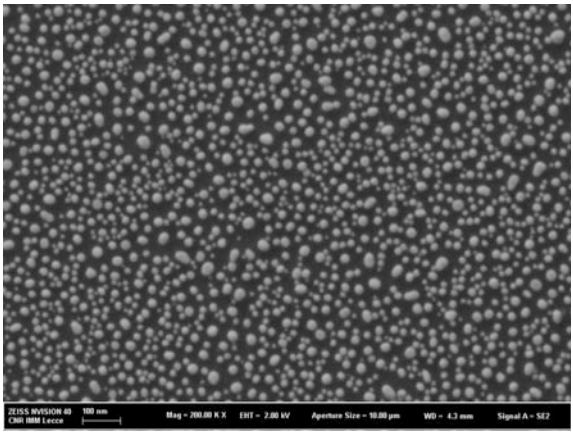

Fig. 1. Au nanoparticles observed at electronic microscope. Diameter: 28 ± 11 nm, Distance: 15 ± 6 nm, Coverage 34 ± 2%, h_m = 17.6 nm

3 Results and Discussion

3.1 Whole-Cell Biosensor

The first step was to assess the ability of the genetically engineered bacteria and tobacco protoplasts to sense, after immobilization, the presence of metal ions. In fact, a detectable signal was evaluated after treatments with different concentrations of Al, Cd, Co, Cu, Ni and Zn salts. In general, genetically modified *E. coli* and tobacco cells produce detectable signal in the presence of all metal ions. In particular, the highest signal was detected after 16 h of treatment in all samples when the GFP reporter was used, on the contrary *lux*CDABE reporter is elicited in bacteria at highest level after 2 h. The variation of signal intensity is related to both promoter and reporter gene used; *zntA* and *groE* promoters are the most sensitive, *luxCDABE* reporter gene has faster response time and higher short-term sensitivity.

Subsequently, *E.coli* cells genetically engineered with *zntA* or *groE* promoter were chosen to analize various by-products and the final product of the pasta processing industry.

The results obtained, reported in Table 1, indicate that the bacterial whole-cell biosensor is activated by certain food matrices analyzed; allowing to say that the biosensor is able to detect the presence of metal ions in food matrices.

Table 1. List of analyzed food matrices obtained from durum wheat

Food matrix	Promoter	
	zntA	*groE*
Wheat bran[a]	×	×
Wheat midds[a]	–	–
Uncooked semolina pasta[a]	×	×
Cooked semolina pasta[a]	×	×
Uncooked barley pasta[b]	–	–
Cooked barley pasta[b]	–	–
Cooking water/semolina pasta[a]	–	–
Cooking water/barley pasta[b]	–	–
Uncooked β-glucan enriched pasta[c]	–	×
Cooked β-glucan enriched pasta[c]	–	×

[a]Semolina pasta: 100% Pietrafitta *cv* flour
[b]60% Pietrafitta *cv* flour, 40% barley flour
[c]90% Pietrafitta *cv* flour, 10% β-glucan extract

3.2 LSPR Experiment

Localised surface plasmon resonance measurements were conducted by the immobilization of the Lpx2s probe, identifying the intermediate quality haplotype of *Lpx* gene, on the surface of gold nanoparticles.

In Fig. 2a the typical optical absorption curves of gold nanostructured substrate (black color) are shown. As one can see, the absorption curves were obtained through the immobilization procedure of Lpx2s probe on gold nanoparticles (red color), the passivation (green color) and the hybridization with the target Lpx2p (blue color). Obviously, the target sequence is complementary to the sequence of the probe.

It was observed a wavelength shift of the peak of the absorption curves from 547 nm, in the presence of the only metallic nanoparticles, to 570 nm, after the hybridization of the probe with the complementary target. In addition it was also observed an increase of the signal intensity from 0.24 (only gold nanoparticles) to 0.28 (after hybridization). This effect is due to the variation of the refractive index of the surface. A relative variation of the light absorbed as a function of wavelength is also reported in Fig. 2b where giving the opportunity to choose the wavelength corresponding to the maximum variation in the optical absorption. In fact, after the binding of the complementary target to the probe, it was observed, in addition to a wavelength shift of the absorption peak, a variation of the intensity of light absorbed, which is maximum in correspondence of the spectral region where the absorption curve have the greater slope. Therefore it can also be detected a small variation in the refractive index. The wavelength shift values and the signal intensity increase, calculated in the different step of the experiment, are shown in Table 2.

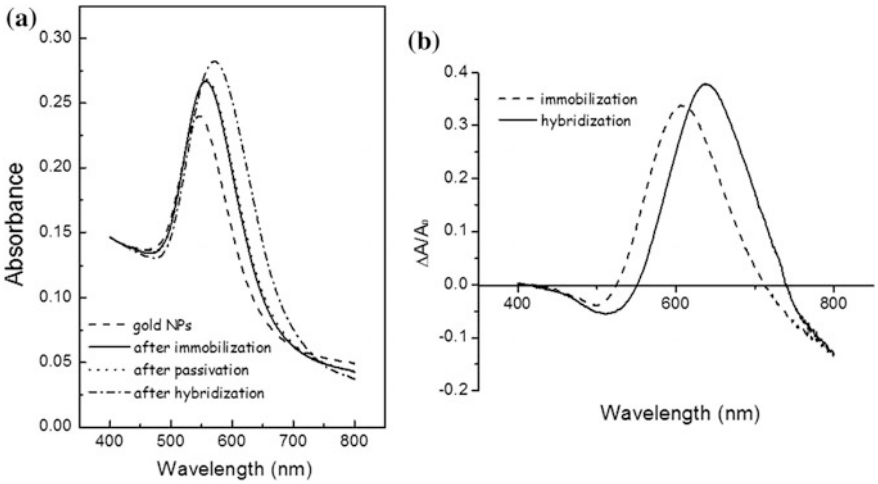

Fig. 2. Typical absorption curves obtained for the Lpx2s probe during the DNA/DNA interaction (**a**) and absorption relative variation of the light absorbed moving from immobilization to hybridization process (**b**)

Table 2. Wavelength shift values and signal intensity increase in the different step of the experiment

Experimental step	$(\Delta A/A)_{max}$	$\Delta\lambda$ (nm)
Immobilization	0.34	10
Hybridization	0.39	13

4 Conclusions

A biosensor based on bacterial whole cells genetically engineered with metal responsive expression cassettes was realized, that is useful to detect specifically, rapidly and with high sensitivity the presence of contaminants in wheat end-products. This device can be used "on the field" to monitor pasta-production plants in order to asses food safety along the production chain. Furthermore, as a proof of concept a LSPR biosensor that allow to identify allelic variants of genes coding for protein associated to bad or good quality of wheat end-products has been also demonstrated.

Acknowledgements. This work was supported by the Italian Ministry of Education, University and Research: projects PON01-01145 "ISCOCEM" and PRIN 2010-2011 prot.2010Z77XAX_002.

References

1. J.C. Gutiérrez, F. Amaro, A. Martin-Gonzalez, Heavy metal whole-cell biosensors using eukaryotic microorganism: an update critical review. Front. Microbiol. **48**, 1–6 (2015)
2. K.A. Willets, R.P. Van Duyne, Localized surface plasmon resonance spectroscopy and sensing. Annu. Rev. Phys. Chem. **58**, 267–297 (2007)

Design, Fabrication and Testing of a Capillary Microfluidic System with Stop-and-Go Valves Using EWOD Technology

M. Nardecchia[1(✉)], P. Rodríguez Llorca[1], G. de Cesare[2], D. Caputo[2], N. Lovecchio[2], and A. Nascetti[1]

[1] D.I.A.E.E, University of Rome "La Sapienza", Via Salaria 851/881, 00138 Rome, Italy
marco_nardecchia@libero.it
[2] D.I.E.T, University of Rome "La Sapienza", Via Eudossiana 18, 00184 Rome, Italy

Abstract. This article presents the successful design, fabrication and testing of a miniaturized system integrating capillarity and electrowetting-on-dielectric (EWOD) technology in a microfluidic network. In particular, the change in hydrophobicity occurring at the interphase between a capillary channel and a hydrophobic layer has been exploited using EWOD as a stop-go fluid valve. The combination of capillary forces and EWOD technology to control the fluid movement opens the possibility to implement a wide variety of microfluidic configurations to perform different biomedical assays with a low-power consumption process. These assays could be easily and inexpensively integrated in lab-on-chip systems featuring small size and high-throughput characteristics.

Keywords: Lab-on-chip · Microfluidic system · Electrowetting-on-dielectric · Capillarity · Fluid · Stop-and-go valve

1 Introduction

Lab-on-chip (LoC) devices are miniaturized systems able to perform bio-chemical and biological analysis by integrating, in a small chip of few square centimeters, several modules that implement the functionalities of a standard laboratory for biomedical applications [1, 2]. Even though LoC systems tend to be simplest, they usually have bulky connections and external fluid injection systems that impede their effective miniaturization.

Currently, research on LoC applications is being addressed towards eliminating external instrumentation—syringes, pumps, radiation sources and complex optical systems [3, 4]—to perform the analysis. Developing a technology that is reliable, simple, light and small is a challenge for researchers.

In this framework, this paper combines two different techniques to drive liquid samples through a microfluidic network without using external bulky connections. These techniques are the capillarity that takes advantage of the surface tension effect, and the electrowetting-on-dielectric (EWOD) approach, that through an electric field

B. Andò et al. (eds.), *Sensors*, Lecture Notes in Electrical Engineering 431,
DOI 10.1007/978-3-319-55077-0_27

changes from a hydrophobic to a hydrophilic status the wettability of a surface. The main idea is to use the capillary forces to move the fluid and the EWOD technique to implement a stop-and-go system [5], by using the electrodes as fluidic-electric valves.

The two technologies have been integrated in a test-chip, which includes structures for different functions and in particular a set of EWOD electrodes acting as stop-and-go valves. To this aim the technological steps needed for the fabrication, on a single glass substrate, of regions characterized by different hydrophobicity have been designed and optimized. The performed tests prove the suitability of the proposed microfluidic chip as low-power consumption, autonomous and compact lab-on-chip system.

1.1 Electrowetting-on-Dielectric

Digital microfluidics, based on the Electrowetting-On-Dielectric (EWOD) mechanism, has shown great potential for a wide range of applications in lab-on-a-chip device. Indeed, EWOD technology allows to isolate samples of fluid, digitally control its movement and improve the mixing efficiency [6]. It presents low-power consumption and a faster response to control signals when compared to other systems that modulate the surface tension [7].

EWOD relies on the ability to vary the contact angle of an electrically conductive liquid droplet on a hydrophobic surface by means of an external electric field [8, 9]. The contact angle change as a function of applied voltage is regulated by the Lippmann-Young equation:

$$\cos\theta = \cos\theta_0 + \frac{\varepsilon_0 \varepsilon_r}{2 d_{EDL} \gamma_{lv}} (V - V_0)^2 \tag{1}$$

where γ_{lv} is the liquid-vapor surface tension, d_{EDL} the thickness of the dielectric layer, ε_0 is the permittivity of the free space, ε_r is its relative dielectric constant and V the applied voltage. θ is the contact angle at the applied voltage V, while θ_0 is the contact angle without applied voltage [10, 11]. The droplet wets the electrode surface as the contact angle decreases and the surface becomes effectively less hydrophobic, along the solid-liquid contact line, as voltage is increased. The variation of contact angle or wettability shift is mainly caused by the charge-induced change in the solid-liquid interfacial tension [12]. In order to take advantage of this effect for droplet manipulation, a polarizable and conductive liquid droplet is sandwiched between the two plates and surrounded by a filler fluid, which may be air or an immiscible liquid such as silicone oil to prevent evaporation of the droplet. Both plates are covered with a hydrophobic coating that is electrically insulating on the bottom-plate, and may or may not be insulating on the top-plate. To achieve a droplet movement, an array of driving electrodes is patterned on the surface of an EWOD device to spatially control the surface wettability electrode by electrode. Generally, movement is obtained by placing the drop on an electrode and by applying the voltage to the adjacent electrodes. EWOD can be performed in an open configuration, where the electrodes are placed only in a bottom plate, or in a closed configuration, which includes also a continuous electrode in a top plate, which acts as the ground connection. Both plates are treated with a

hydrophobic material deposition. In the closed EWOD system, the generated electric field is stronger than in the open configuration and, thus, it is easier—a smaller voltage is needed—to move the sample droplets. A sketch of the closed configuration can be seen in Fig. 1.

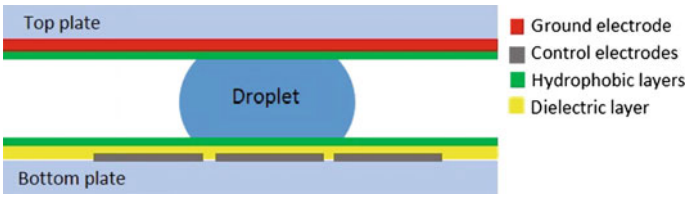

Fig. 1 Cross section of closed electrowetting-on-dielectric configuration

1.2 Capillary Forces

Capillary forces result from the interaction of liquid, gas and solid surfaces, at the interface between them. In the liquid phase, molecules are held together by cohesive forces. In the bulk of the liquid, the cohesive forces between one molecule and the surrounding molecules are balanced. However, at the edge of the liquid, the cohesive forces with other liquid molecules are larger than the interaction with air molecules. As a result, the liquid molecules at the interface are pulled together towards the liquid. The overall effect of these forces minimizes the free surface of the liquid that is exposed to air. The proportionality between the decrease in energy of the surface that results from decreasing the surface is described by the surface tension:

$$\gamma = \frac{dG}{dA} \tag{2}$$

where dG is the change in energy [N/m], dA is the change in area [m^2] and γ is the surface tension [N/m]. Of interest for capillary forces is the contact between three phases: liquid, solid and vapor (air) (see Fig. 2). Three forces are present, trying simultaneously to minimize the contact area between the three phases. Two of them are in the same plane and a third one that forms the so called "contact angle" at the

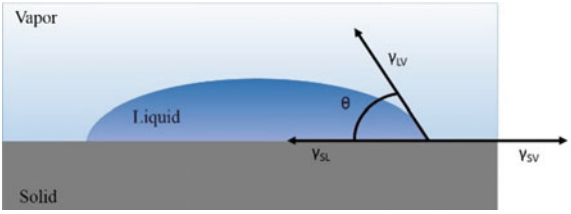

Fig. 2 Forces acting at the triple interface line

solid-liquid interface. At equilibrium, the forces at the triple interface are balanced and the relationship between them is described by the Young's equation:

$$\gamma_{SV} - \gamma_{SL} - \gamma_{LV} \cdot \cos\theta_0 = 0 \tag{3}$$

where γ represents an interfacial tension and the subscripts *L, V* and *S* stand for liquid, vapor and solid, respectively.

Analyzing the horizontal equilibrium of forces, the Young's equation is reached. Since the surface energy in an interface is a physical constant that depends on the nature of both the substances involved (it depends on the attraction forces between molecules), the droplet has to change shape and reach the contact angle that permits static equilibrium. Molecules at an interface are subjected to both cohesion forces (molecules attracting each other) and adhesion forces (attraction to the other side surface). Surfaces where adhesion forces are greater than cohesion forces are said to be hydrophilic, or wettable, and are characterized by a contact angle smaller than 90°. On the other hand, when surface experiences cohesion forces stronger than adhesion forces, it is called a hydrophobic, or not wettable, surface. In this case the contact angle is greater than 90°.

In a capillary tube, the fluid that is not in contact with the walls of the conduit adopts a concave (convex) meniscus shape if the surface is hydrophilic (hydrophobic)

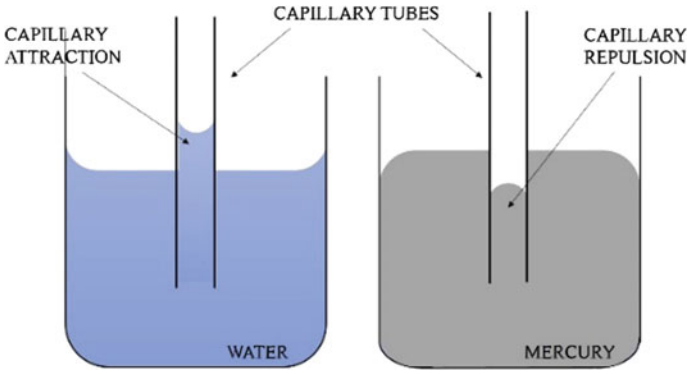

Fig. 3 Hydrophilic and hydrophobic meniscus

(see Fig. 3). In a capillary tube, a column of water can move through the conduit due to capillary pressure. This magnitude is the difference in pressure across the interface of two immiscible fluids and has a value calculated by the Young-Laplace equation:

$$p_c = \frac{2\,\gamma\,\cos\theta}{r} \tag{4}$$

In the previous equation p_c is the capillary pressure, γ is the interfacial tension, θ the contact angle and r is the effective radius of the interface. According to Eq. 4, the further to 90° is the contact angle (either towards 0° or 180°), or the greater the interfacial tension, the greater is the capillary pressure. Also, the smaller the effective radius of curvature of the meniscus, the greater is the capillary pressure. A microscale flow is characterized by a small Reynolds number and subsequently by a laminar flow (which is self powered) that hinders the mixing of two different substances.

2 Designed Device

Taking into account the advantages of both capillarity (self-powered and autonomous systems) and EWOD approach (low power consumption, possibility to electrically control the movement of liquid drops), we developed a microfluidic network as a test-chip for the integration of these two techniques.

The main idea is to use the capillary forces to move the fluid and the EWOD technique to implement a stop-go system, by using the electrodes as fluidic-electric valves. Top view of the basic device is shown in Fig. 4. A fluid inserted in the

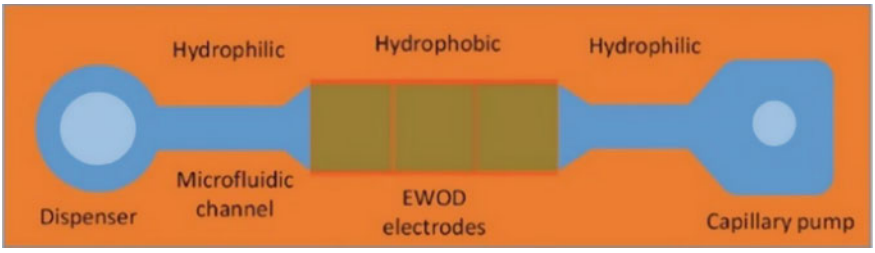

Fig. 4 Schematic top view of the device

dispenser will go along the hydrophilic channel until it reaches the hydrophobic region, where are located the EWOD electrodes. Only when an appropriate sequence of voltages is applied to the electrodes, the fluid will get to the second hydrophilic channel and then to the capillary pump.

Before the system design, we solved the technological issue related to the fabrication on the same glass substrate of hydrophilic and hydrophobic regions. This has been achieved through the optimization of the different fabrication processes and in particular of the deposition parameters of the Teflon® layer that covers the EWOD electrodes. Figure 5 demonstrates the successful fabrication of a glass substrate having a hydrophobic surface with hydrophilic spots that capture droplets of water.

The whole system design, comprised in a 5×5 cm^2 glass substrate, is reported in Fig. 6 where are reported and explained the different parts of the microfluidic circuits.

In particular, the blue regions refer to the microfluidic circuit, while the red ones to the EWOD electrodes. Independently on the specific function implemented in each

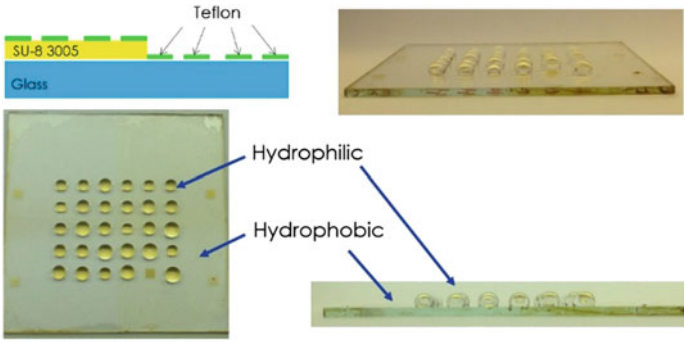

Fig. 5 Glass substrate with an alternate sequence of hydrophilic and hydrophobic regions

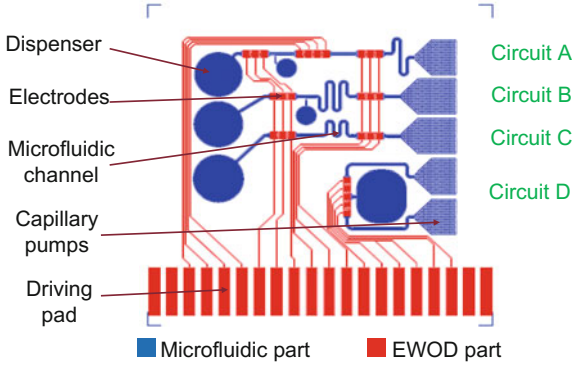

Fig. 6 Design of the tested device

microfluidic circuit (from A to D), each network includes the basic structure reported in Fig. 4, where the EWOD pads are used as stop-and-go valves.

3 Device Fabrication and Testing

To fabricate this device different technological steps need to be performed. A cross section of the basic device, together with the used materials, is shown in Fig. 7.

The process steps for the fabrication of the bottom layer are:

1. Cleaning glass with “piranha process”.
2. Metal electrodes: evaporation of the Cr/Al/Cr metal stack (thickness 300/1500/300 Å) and lithography with a mask that leaves the electrical part unexposed.
3. Dielectric layer: deposition by spin coating of a SU-8 3005 layer and its lithography to cover all the metal electrodes.

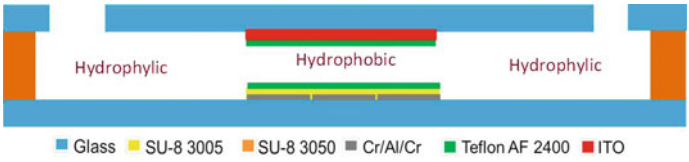

Fig. 7 Cross section of the basic device

4. Hydrophobic layer: spinning of Teflon AF2400 and its patterning through lift-off process to cover all the metal electrodes.
5. Microfluidic channel: deposition by spin coating of a SU-8 3050 layer and its lithography for defining the microfluidic channels.

The process steps for the fabrication of the top layer are:

6. Cleaning the glass already covered with Indium Tin Oxide (ITO).
7. Conductive layer: wet etching of ITO to define a conductive layer corresponding to the bottom layer's electrodes.
8. Hydrophobic layer: Teflon AF2400 patterned with same process of bottom layer.
9. Microfluidic channel: SU-8 3050 deposited with same process described above for defining microfluidic channel, dispenser, capillary pumps and the space over the electrodes.

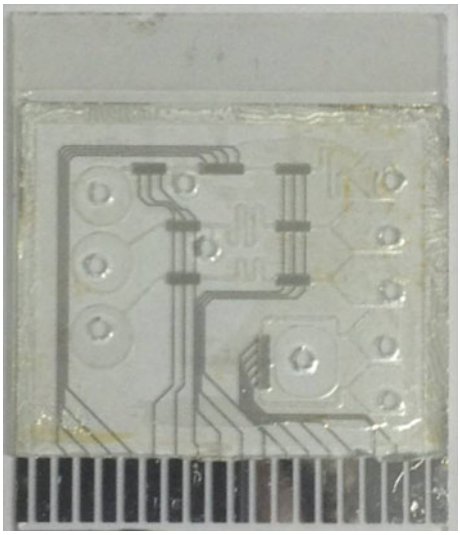

Fig. 8 Picture of the fabricated device

10. Drilling hole on corresponding of the end of the capillary pumps and at the inlets.

The last step is the bonding of the two substrates (top and bottom) using a clip to apply a pressure. The device is finally baked for 40 min at 160 °C.

The device fabricated is shown in Fig. 8.

After fabrication, the system has been tested using circuit B. A detail sequence of the system operation is shown in Fig. 9. We observed that the fluid flows through the hydrophilic channels and stops at the border of the hydrophobic region (Fig. 9a).

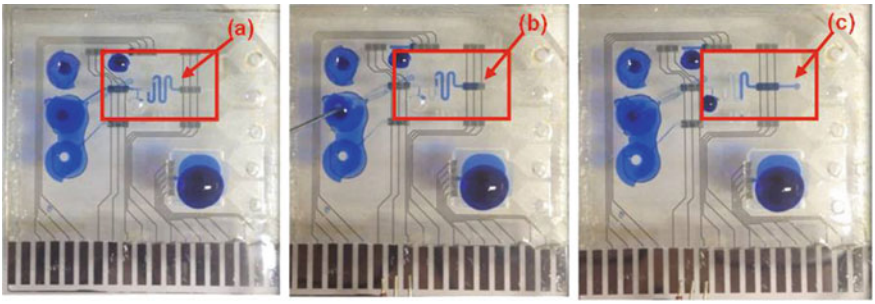

Fig. 9 Sequence of device operation showing the EWOD electrodes working as stop-go valves

Subsequently, driving the EWOD electrodes with a voltage as low as 35 V, the fluid passes over the hydrophobic layer (Fig. 9b) and fills the successive hydrophilic channel (Fig. 9c). These pictures demonstrate the successful combination of the capillarity and the EWOD technique on the same glass substrate and the effectiveness of the electric field as driving force for the stop-and-go EWOD valves.

4 Conclusion

This paper has reported the combination of two microfluidic techniques (capillarity and EWOD) for the development of autonomous and compact microfluidic networks, whose operations are electronically controlled. The EWOD stop-go valve has been demonstrated to correctly work as the fluid stopped at the electrode border and moved once the voltage was applied to it.

Therefore, the idea of enclosing a sample in the channel between two valves can be implemented. This is a very important result because the capillary action permits the development of autonomous, low-consumptions systems while the EWOD technique, and its application as stop-go valves, allow the design of microfluidic networks dense of functions (triggering, mixing, dispensing, separation).

References

1. P. Abgrall, A.M. Gue, Lab-on-chip technologies: making a microfluidic network and coupling it into a complete microsystem—a review. J. Micromech. Microeng. **17**(5), R15–R49 (2007)
2. D. Caputo, M. Ceccarelli, G. de Cesare, A. Nascetti, R. Scipinotti. Lab-on-glass system for DNA analysis using thin and thick film technologies. Proceedings of Material Research Symposium, vol. 1191, OO06-01 (2009)
3. M.A. Miled, G. Massicotte, M. Sawan, Dielectrophoresis-based integrated lab-on-chip for nano and micro-particles manipulation and capacitive detection. IEEE T. Bio-Med. Eng. **7** (4), 557 (2013)
4. D. Caputo, G. de Cesare, M. Nardini, A. Nascetti, R. Scipinotti, Monitoring of temperature distribution in a thin film heater by an array of a-Si: H temperature sensors. IEEE Sens. J. **12** (5), 1209–1213 (2012)
5. A.P. Washe, P. Lozano-Sanchez, D. Bejarano-Nosas, B. Teixeira-Dias, I. Katakis, Electrochemically actuated passive stop–go microvalves for flow control in microfluidic systems. Microelectron. Eng. **111**, 416–420 (2013)
6. V. Kumar, N. Sharma, SU-8 as hydrophobic and dielectric film in electrowetting-on-dielectric based microfluidics device. J. Nanatechnol, ID312784. 1–6 (2012)
7. G.M. Washizu, Electrostatic actuation of liquid droplets for microreactor applications. IEEE Trans. Ind. Appl. **34**(4), 732–737 (1998)
8. B. Shapiro, H. Moon, R.L. Garrell, C.-J. Kim et al., Equilibrium behavior of sessile drops under surface tension, applied external fields and material variations. J. Appl. Phys. **93**(9), 5794–5811 (2003)
9. F. Mugele, J.-C. Baret, Electrowetting: from basics to applications. J. Phys. Condens. Matter **17**(28), R705 (2005)
10. G. Lippmann, Relations entre les phenomenes electriques et capillaires. Ph.D. dissertation, Gauthier-Villars, 1875
11. Y.-Y. Lin, E.R.F. Welch, R.B. Fair, Low voltage picoliter droplet manipulation utilizing electrowetting-on-dielectric platforms. Sens Actuators B Chem. **173**, 338–345 (2012)
12. D. Caputo, G. de Cesare, N. Lovecchio, R. Scipinotti, A. Nascetti, Electrowetting-on-dielectric system based on polydimethylsiloxane. *Proceedings of the 5th IEEE International Workshop on Advances in Sensors and Interfaces*, IWASI, 99–103 (2013)

Electrochemical and Photoelectrochemical Biosensors for Biomarker Detection

Andrea Ravalli, Francesca Bettazzi, Diego Voccia, Giovanna Marrazza, and Ilaria Palchetti(✉)

Dipartimento di Chimica "Ugo Schiff", Università degli Studi di Firenze, Via della Lastruccia 3, 50019 Sesto Fiorentino, FI, Italy
ilaria.palchetti@unifi.it

Abstract. A rapid and accurate medical diagnosis is essential in order to determine the health status of a patient. Nowadays, most of the clinical analyses are performed in specialized laboratory, which required specific instrumentation and trained personal, resulting in an increase of analysis costs and time. In this context, biosensors represent ideal tools capable to provide a specific and fast response together with low cost, easy use and portable size features. This work attempts to provide a review of the research progresses of electrochemical and photoelectrochemical biosensor platforms in clinical applications that have been published in recent years. Special emphasis will be devoted to discuss examples for breast cancer biomarker detection, because breast cancer, is considered the leading cause of cancer-related deaths worldwide in women, representing 15% of all cancer related amongst women, with a 6% mortality rate (based on overall cancer deaths). The manuscript is focused on aptamer-based biosensors, because, due to their stability and their relatively low cost, they have been successfully applied in many biosensor formats for breast cancer biomarker detection.

Keywords: Biosensors · Breast cancer · Biomarker · Aptamer

1 Introduction

Cancer represents one of the leading causes of death worldwide. There are more than 100 different types of cancer affecting different human organs. Following statistics, in Europe in 2012 the most common primary cancer sites in men were prostate, lung, colorectal and bladder. In women, breast cancer was by far the most frequently diagnosed neoplasm, followed by colorectal, lung and corpus uteri cancers. Breast cancer, represents 15% of all cancer related amongst women, with a 6% mortality rate (based on overall cancer deaths) [1].

It is now well known that early detection of cancer represents the best opportunity to increase the survival rate of patients. In this perspective the discovery and the clinical validation of cancer-related biomarkers represent and ideal tool.

In clinical analysis, a biomarker represents a bio-molecule whose concentration increases/decreases over a threshold level (named also as clinical cut-off) in a body fluids, tissue, etc. in the presence/absence of a disease. Rigorous definition was given

B. Andò et al. (eds.), *Sensors*, Lecture Notes in Electrical Engineering 431,
DOI 10.1007/978-3-319-55077-0_28

both by Food and Drug Administration (FDA) and European Union National Institute of Health which defined a biomarker as a "characteristic that is objectively measured and evaluated as an indicator of normal biological processes, pathogenic processes, or pharmacologic responses to therapeutic intervention. The biomarkers act as indicators of a normal or a pathogenic biological process. They allow assessing the pharmacological response to a therapeutic intervention. A biomarker shows a specific physical trait or a measurable biologically produced change in the body that is linked to a disease or a particular health condition" [2].

These molecules should ideally possess the following properties:

- Biomarker expression should be related to the process that causes cancer and to the type of the cancer.
- Biomarker level should be higher enough, in biological fluids or tissue, to be measured in an easy and trustworthy way.
- Biomarker concentration (increasing or decreasing) should be strictly correlated to the disease variation and to the treatment outcome.

Because proteins influence the molecular pathways in the cells and they are strictly related to disease state and they are released in biological fluids, the cancer-related proteins are one of the most studied and used biomarkers in clinical analysis [3–6].

In the cancer biomarker analysis, biosensors play an interesting role because they allow fast, accurate, sensitive, selective and low cost analysis coupled with the possibility of device miniaturization and multi-analysis detection in contrast with the conventional clinical procedure (such as ELISA test, fluorescent or chemiluminescent assays) [7–9].

In this work, we focus our attention on the development of electrochemical and photoelectrochemical biosensor for determination of breast cancer biomarkers reported in the literature in the last three years.

2 Aptamer

Aptamers are synthetic oligonucleotides sequences (both DNA, in particular ssDNA, and RNA) or peptide capable to bind a target protein with affinity and selectivity comparable of those of monoclonal antibodies. Due to their advantages respect to antibodies (such as high stability, chemical synthesis, low dimension, affinity for small molecules, etc.) aptamers were successfully applied in many fields including drug discovery and delivery, tissue bio-imaging and also as therapeutic agents and as bioreceptors in biosensor applications for clinical, environmental and food analysis [10–12].

2.1 Nucleic Acid Aptamers

Nucleic acid aptamers (both DNA and RNA), which exhibits a high affinity for a specific target, are synthetized through a process named as systematic evolution of ligands by exponential enrichment (abbreviated as SELEX) developed in 1990s by two independents research groups [13, 14].

The original process (conventional SELEX) consists in a series of binding, elution and amplification steps repeated several times (about 20) which led to the selection of a pool of aptamers with high affinity for a specific target. In particular, an initial library of 10^{15}–10^{16} random sequences (each one composed by a 20–30 bp variable region and a 15–25 bp flanked region, used to anneal the primer during the Polymerase Chain Reaction, PCR, amplification step) is incubated, in controlled experimental conditions (pH, ionic strength, temperature, incubation time etc.), with the target molecules. After the affinity reaction, the unbound oligonucleotides are removed while the DNA sequences bound to the analyte are eluted and subsequently amplified by PCR process. The binding/elution/amplification steps are then repeated, in more stringent experimental conditions, with the new pool of oligonucleotides. For RNA aptamer selection, the initial DNA library is transcribed into a RNA library, which is incubated with the target molecules; after the elution step, selected RNA aptamers are converted again into DNA sequences, amplified by PCR, and transcribed back to RNA for the next round. In both cases, at the end, the selected aptamer are sequenced and characterized by thermodynamics and kinetic measurements in terms of affinity constant (K_a), dissociation constant (k_d) and the ratio ($K_D = K_d/K_a$) [15].

In order to overcome some drawbacks of SELEX conventional procedure (such as long working time, high operative and instrumentation costs), some variants were studied and introduced (i.e. in capillarity and micro-flow electrophoresis SELEX, magnetic meads-based SELEX or cell- and in vivo SELEX)

All these processes are generally followed by a post-modification step in which various positions of the oligonucleotide chain (i.e. 2′, 3′ and 5′) can be functionalized with specific molecules (polyethylene glycol tag, PEG, -SH, -NH2, biotin, sugar, etc.) for particular applications. In some cases, in order to avoid the decreasing of aptamer affinity, chemically modified DNA/RNA sequences can be directly introduced into the initial library [16].

2.2 Peptide Aptamer

Peptide aptamers have been defined by Colas et al. in 1996 [17] as combinatorial protein molecules in which a variable peptide sequence with affinity for a given target protein is displayed on an inert, constant scaffold protein. They are extremely simple molecules, selected from combinatorial libraries on the basis of their affinity to the target protein or small molecule, and, generally, expressed in bacterial cells, such as *E. coli.* [10, 17]. There are many protein scaffolds reported in the literature and they have been intensely reviewed in the past [1, 10].

Among this class of bioreceptor, Affibody® molecules are commercially available. The Affibody molecule is an engineered version (Z domain) of one of the five stable three-a-helix bundle domains from the immunoglobulin Fc-binding region of staphylococcal protein A. This molecule is constituted by only 58 amino acids without disulphide bonds and can therefore be produced in simpler organism such as prokaryote, rather than the animal system required in antibody synthesis. Affibodies

can include specific labels, such as fluorophores, radioactive labels and other moieties, such as biotin, which can be used to couple the affibody to surfaces or other molecules, including enzymes [18, 19].

3 Biomarkers in Breast Cancer

Some specific biomarkers are often useful for selecting the appropriate treatment options in breast cancer. Some of them are here described.

CA15.3 (also known as MUC1 from the coding gene) is a type I transmembrane glycoprotein, that is mainly overexpressed in breast and ovarian carcinomas. It possesses a molecular mass ranging from 300 to 600 kDa and consists of two subunits (a C-terminal cytoplasmic domain and an extracellular subunits containing the variable number tandem repeat, VNTR, domain). The disease status in breast and recently in ovarian cancer patients is routinely assessed by monitoring the serum levels of circulating CA15.3 protein and its elevated levels (>20 U/mL) are always associated with poor survival [20].

Human epidermal growth factor receptor 2 (HER2), also known as ErbB2, c-erbB2 or HER2/neu, is a 185 kDa protein belongs to a family composed of four structurally related members, HER1 (ErbB1, also known as EGFR), HER2 (ErbB2), HER3 (ErbB3) and HER4 (ErbB4). In particular, HER2 is a type 1 transmembrane glycoprotein which includes three distinct regions: an N-terminal extracellular domain (ECD), a single α-helix transmembrane domain (TM), and an intracellular tyrosine kinase domain. Overexpression of HER2 usually results in malignant transformation of cells accounts for $\sim$25% of all breast cancer cases (clinical cut off: 15 ng/mL). Furthermore, it was also found that survival rate and recurrence probability of the tumor for HER2 positive breast cancer patients are significantly shorter than patients without HER2 overexpression. HER2 can be also found at high concentration in blood in the presence of other cancer types such as gastric, ovarian and prostate [21].

Vascular endothelial growth factor term is referred to a family of dimer glycoprotein (covalently linked by 2 disulfide bridges) which includes five members (VEGF-A, VEGF-B, VEGF-C, VEGF-D, placenta growth factor, PGF) and their associated receptors (VEGFR-1, VEGFR-2, VEGFR-3). Homologs of VEGF protein are also discovered in the genome of some viruses (VEGF-E) or in the venom of some snakes (VEGF-F). Because VEGF-A was the first and the most studied protein (in particular related to carcinogenesis and cancer biology), often, in literature, the term VEGF strictly indicate the VEGF-A member. From biological point of view, VEGF and its receptors play a main role in the formation of cardiovascular system; in presence of a cancer process VEGF is mainly involved carcinogenesis and in tumor metastasis. VEGF concentration in blood and serum (which values is much higher than 100 pM in pathological condition) can be thus used as biomarker associated with diagnosis and prognosis of different type of cancer diseases with particular reference to the presence of metastasis processes [22].

4 Electrochemical and Photoelectrochemical Biosensor for Breast Cancer Biomarker Detection

4.1 Electrochemical-Based Biosensors

Electrochemical techniques as transduction mechanism in aptasensors development were widely known. The common electrochemical techniques used for the detection of the analyte include potentiometry, amperometry, voltammetry, conductometry and electrochemical impedance spectroscopy. Further and complete description of these electrochemical techniques can be found in Ref. [23].

Herein, some examples of electrochemical aptasensors development for breast cancer biomarkers detection using label and label-free approaches are briefly discussed.

An aptamer sandwich-based assay for MUC1 detection was reported by Florea et al. [24]. In this work, anti-MUC1 primary aptamer was immobilized on the surface of streptavidin-coated magnetic beads, followed by reaction with biotin (as blocking agent) and with MUC1 protein. Then, incubation with a biotinylayed secondary anti-MUC1 aptamer and with streptavidin-alkalin phosphatase were carried out. The electrochemical detection of alpha-naphthol (obtained by the hydrolysis of alpha-naphthyl phosphate) by the use of differential pulse voltammetry (DPV) technique allowed the detection of MUC1 in the range between 0.05 and 0.28 nM MUC1 with a detection limit of 0.07 nM. The proposed aptasensor showed also a high selectivity for MUC1 protein in the presence of mucin 4 and mucin 16 (as non-specific proteins) and the ability to detect MUC1 in cancer patient serum sample.

In a recent work, the development of a label-free biosensor for HER2 cancer biomarker detection based on the use of anti-HER2 Affibody, as bioreceptor, and of gold nanoparticles (AuNPs)-modified graphite screen-printed electrode, as nanostructured electrochemical transducer, was proposed (Fig. 1) [25]. In particular, after the electrodeposition of AuNPs on the working electrode surface, the sensor was modified by the incubation with the anti-HER2 Affibody. Mixed-SAM formation (by the use of the use 6-mercapto-1-hexanol) and surface blocking step (by the use of BSA) were performed. Affinity reaction with HER2 protein was then evaluated by means of electrochemical impedance spectroscopy, EIS (linear range: 1–40 μg/L HER2, detection limit: 6 μg/L). The proposed affibody-based biosensor showed also good response in HER2-spiked serum samples.

An aptamer-based sandwich assay for VEGF detection was reported by Ravalli et al. [26]. After the modification of the graphite working electrode surface by the use of AuNPs, the incubation with thiolated primary anti-VEGF aptamer was carried out, followed by blocking step (by the use of 6-mercapto-1-hexanol) and affinity reaction with VEGF. The assay was then completed by the addition of a biotinylated secondary anti-VEGF aptamer and by streptavidin-alkaline phosphatase. The electrochemical evaluation of alpha-naphthol (produced by the enzyme in the presence of alpha-naphthyl phosphate) allowed the construction of the calibration curve in a linear range between 40 and 250 nM with a limit of detection of 30 nM.

Recently, Baydemir et al. [27] described the use of Affibody molecule for TNF-α detection. TNF-α is an inflammatory cytokine produced by the immune system. Serum TNF-α level is elevated in some pathological states such as septic shock, graft

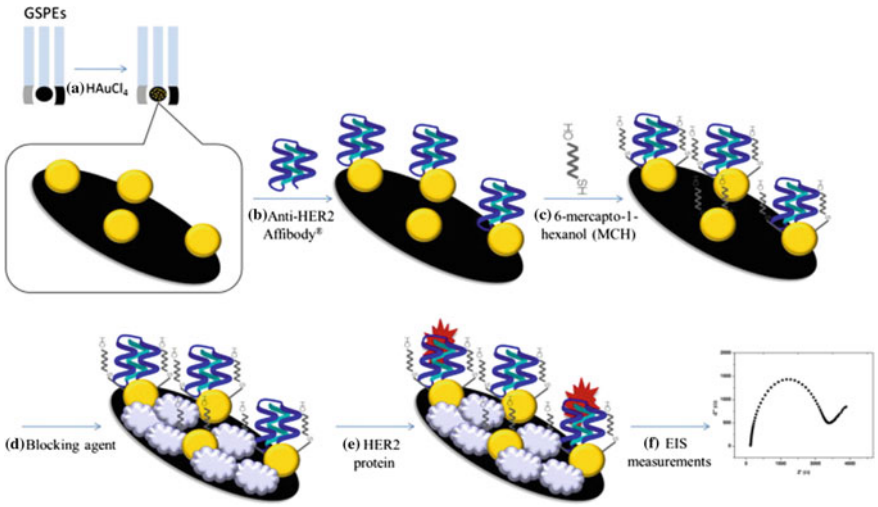

Fig. 1 Schematic representation of label-free HER2 cancer biomarker detection using anti-HER2 Affibody-modified gold nanostructured graphite screen-printed electrodes (GSPEs) (reproduced with permission from [25])

rejection, HIV infection, neurodegenerative diseases, rheumatoid arthritis and cancer. Detecting trace amount of TNF-α is, also, very important for the understanding of tumor biological processes [28]. Magnetic beads were used as support for Affibody immobilization and screen printed carbon electrodes were used as transducers. TNF-α calibration curve was performed, obtaining a detection limit of 38 pg/mL, the quantification range of 76–5000 pg/mL and RSD% 7.

4.2 Photoelectrochemical-Based Biosensors

Photoelectrochemical biosensors are based on the use of photoactive materials for the development of the transducer. The photoactive material is responsive to a light excitation, generating a photocurrent on a conductive substrate. Inorganic and organic semiconductors can be used as photoactive materials.

An anodic photocurrent occurs when the conduction electrons are transferred to the electrode, and valence holes neutralized by electrons supplied by an electron donor in solution [29]. If the conduction electrons are transferred to a solution-solubilized electron acceptor, a cathodic photocurrent is measured. The presence of an efficient electron donor/acceptor prevents the electron-hole recombination and thus increases and stabilizes the photocurrent.

Nowadays, inorganic semiconductors are mainly fabricated using nanomaterials like SnO_2, TiO_2 nanoparticles (NPs) as well as CdS, CdSe quantum dots (QDs). Frequently, these nanomaterials are assembled on a conductive substrate, such as gold, Indium-Tin-Oxide (ITO) or F-doped SnO_2 (FTO). Organic photoactive materials include small molecules such as porphyrin, phtalocyanine, and their derivatives, azo

dyes, metal complexes as well as polymers. The light excites the molecules that can react with an electron donor or an electron acceptor, producing anodic or cathodic photocurrents, respectively.

Hybrid semiconductors can be obtained by coupling two inorganic semiconductors with different band gaps or organic complexes combined with inorganic materials; in this sense improved conversion efficiency is obtained by coupling semiconductors with different band gap.

Photoelectrochemical detection offers some peculiar advantages, such as miniaturized and low cost instrumentation. Moreover, by using light for excitation and electrochemistry for detection, photoelectrochemistry can reach high level of sensitivity because of the reduced background associated with it. According to the mode of signal transduction photoelectrochemical biosensors could be classified as potentiometric or amperometric photoelectrochemical biosensors.

Recently, Tan et al. described the use of TiO_2 nanotube arrays (TiO_2 NTs), grown on a titanium foil and decorated with Au nanoparticles (AuNPs) for the detection of MUC1 (Fig. 2) [30]. AuNPs were used for improving the electrical conductivity of TiO_2 NTs and for the immobilization of the MUC1 aptamers. CdTe QDs-labeled complementary single-stranded DNAs (c-DNA@QDs) are hybridized with the MUC1 aptamer to form a TiO_2 NT/aptamer/c-DNA@QD aptasensor. In the absence of target MUC1, under the irradiation of visible light, a high photocurrent response was observed due to the light absorption of CdTe QDs and the photoinduced electron transfer from CdTe QDs to TiO_2 NTs through DNA chain. However, in the presence of MUC1, MUC1 combined with its aptamer and CdTe QDs-labeled c-DNAs left the

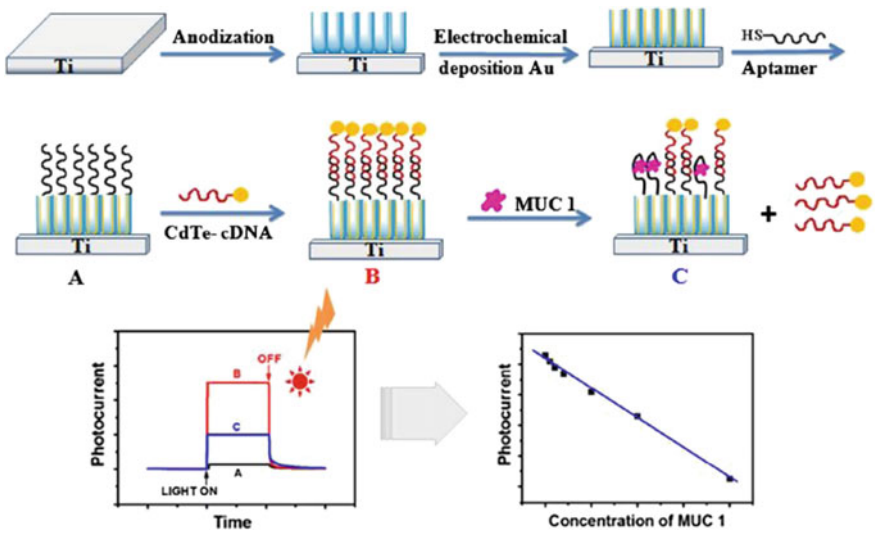

Fig. 2 Schematic representation of TiO_2 NT/aptamer/c-DNA/QD-based photoelectrochemical aptasensor for MUC1 cancer biomarker detection (reproduced from [30] with permission of The Royal Society of Chemistry)

TiO_2 NTs, leading to a decreasing of photocurrent value. Therefore, the detection of target MUC1 could be sensitively transduced via detection of the photocurrent reduction.

5 Conclusions

Nowadays, aptamers have been proposed as innovative, synthetic bioreceptors in biosensing. Within this review, different applications of both nucleic acid and peptide aptamers have been discussed in the field of breast cancer biomarker monitoring.

Acknowledgements. I.P. thanks financial support from Ministero dell'Istruzione, dell'Università e della Ricerca (MIUR), PRIN 2012 grant no. 20128ZZS2H.

References

1. I. Palchetti, Affinity biosensors for tumor-marker analysis. Bioanalysis **6**, 3417–3435 (2014)
2. R. Mayeux, Biomarkers: potential uses and limitations. NeuroRX **1**, 182–188 (2004)
3. N.L. Henry, D.F. Hayes, Cancer biomarkers. Mol. Oncol **6**, 140–146 (2012)
4. I. Diaconu, C. Cristea, V. Hârceagă, G. Marrazza, I. Berindan-Neagoe, R. Săndulescu, Electrochemical immunosensors in breast and ovarian cancer. Clin. Chim. Acta **425**, 128–138 (2013)
5. S. Centi, S. Tombelli, M. Puntoni, C. Domenici, M. Franek, I. Palchetti, Detection of biomarkers for inflammatory diseases by an electrochemical immunoassay: the case of neopterin. Talanta **134**, 48–53 (2015)
6. S. Centi, L.B. Sanmartin, S. Tombelli, I. Palchetti, M. Mascini, Detection of C reactive protein (CRP) in serum by an electrochemical aptamer-based sandwich assay. Electroanalysis **21**, 1309–1315 (2009)
7. Z. Taleat, A. Ravalli, M. Mazloum-Ardakani, G. Marrazza, CA125 immunosensor based on poly-anthranilic acid modified screen-printed electrodes. Electroanalysis **25**, 269–277 (2013)
8. Q.A.M. Al-Khafaji, M. Harris, S. Tombelli, S. Laschi, A.P.F Turner, M. Mascini, G. Marrazza, An electrochemical immunoassay for HER2 detection. Electroanalysis **24**, 735–742 (2012)
9. A. Ravalli, L. Lozzi, G. Marrazza, Micro-flow immunosensor based on thin-film interdigitated gold array microelectrodes for cancer biomarker detection. Curr. Drug Deliv. **13**, 400–408 (2016)
10. M. Mascini, I. Palchetti, S. Tombelli, Nucleic acid and peptide aptamers: fundamentals and bioanalytical aspects. Angew. Chem. Int. Ed. **51**, 1316–1332 (2012)
11. I. Palchetti, M. Mascini, Electrochemical nanomaterial-based nucleic acid aptasensors. Anal. Bioanal. Chem. **402**, 3103–3114 (2012)
12. I. Palchetti, M. Mascini, Nucleic acid biosensors for environmental pollution monitoring. Analyst. **133**, 846–854 (2008)
13. A.D. Ellington, J.W. Szostak, In vitro selection of RNA molecules that bind specific ligands. Nature **346**, 818–822 (1990)
14. C. Tuerk, L. Gold, Systematic evolution of ligands by exponential enrichment: RNA ligands to bacteriophage T4 DNA polymerase. Science **249**, 505–510 (1990)

15. M. Blind, M. Blank, Aptamer selection technology and recent advances. Mol. Ther. Nucleic Acids **4**, e223 (2015)
16. S. Gao, X. Zheng, B. Jiao, L. Wang, Post-SELEX optimization of aptamers. Anal. Bioanal. Chem. 1–7 (2016)
17. P. Colas, B. Cohen, T. Jessen, I. Grishina, J. McCoy, R. Brent, Genetic selection of peptide aptamers that recognize and inhibit cyclin-dependent kinase 2. Nature **380**, 548–550 (1996)
18. H. Ilkhani, M. Mascini, G. Marrazza, The potential affibodies in new cancer marker immunosensors, in *Sensors and Microsystem*, ed. by A. D'Amico, C. Di Natale, L. Mosiello, G. Zappa (Springer, US, Boston, MA, 2012), pp. 15–18
19. M.D. Harris, S. Tombelli, G. Marazza, A.P.F. Turner, Affibodies as an alternative to antibodies in biosensors for cancer markers. in *Biosensors for Medical Applications*, ed. By S. Higson, (Woodhead Publishing, Cambridge, UK, 2012) pp. 217–232
20. D.W. Kufe, Mucins in cancer: function, prognosis and therapy. Nat. Rev. Cancer **9**, 874–885 (2009)
21. C. Gutierrez, R. Schiff, HER2: biology, detection, and clinical implications. Arch. Pathol. Lab. Med. **135**, 55–62 (2011)
22. N. Ferrara, H.-P. Gerber, J. LeCouter, The biology of VEGF and its receptors. Nat. Med. **9**, 669–676 (2003)
23. D. Grieshaber, R. MacKenzie, J. Vörös, E. Reimhult, Electrochemical biosensors—sensor principles and architectures. Sensors **8**, 1440–1458 (2008)
24. A. Florea, A. Ravalli, C. Cristea, R. Sandulescu, G. Marrazza, An optimized bioassay for mucin1 detection in serum samples. Electroanalysis **27**, 1594–1601 (2015)
25. A. Ravalli, C.G. da Rocha, H. Yamanaka, G. Marrazza, A label-free electrochemical affisensor for cancer marker detection: the case of HER2. Bioelecrochemistry **106**, 268–275 (2015)
26. A. Ravalli, L. Rivas, A. De La Escosura-Muñiz, J. Pons, A. Merkoçi, G. Marrazza, A DNA aptasensor for electrochemical detection of vascular endothelial growth factor. J. Nanosci. Nanotechnol. **15**, 3411–3416 (2015)
27. G. Baydemir, F. Bettazzi, I. Palchetti, D. Voccia, Strategies for the development of an electrochemical bioassay for TNF-alpha detection by using a non-immunoglobulin bioreceptor. Talanta **151**, 141–147 (2016)
28. F. Bettazzi, L. Enayati, I. Campos, Electrochemical bioassay for the detection of TNF-a using magnetic beads and disposable screen-printed array of electrodes. Bioanalysis **5**(1), 11–19 (2013)
29. D. Voccia, I. Palchetti, Photoelectrochemical biosensors for nucleic acid detection. J. Nanosci. Nanotechnol. **15**, 3320–3332 (2015)
30. J. Tian, T. Huang, J. Lu, A photoelectrochemical aptasensor for mucin 1 based on DNA/aptamer linking of quantum dots and TiO_2 nanotube arrays. Anal. Methods **8**, 2375–2382 (2016)

Impedance Sensors Embedded in Culture Media for Early Detection of Bacteria Growth

Michela Borghetti, Marco Demori, Marco Ferrari, Vittorio Ferrari, Emilio Sardini, and Mauro Serpelloni(✉)

Department of Information Engineering, Università degli Studi di Brescia, Via Branze 38, Brescia, Italy
mauro.serpelloni@unibs.it

Abstract. In this work, the ability of an impedance sensor to rapidly detect bacteria growth in a culture medium has been investigated. A test configuration with two electrodes embedded in a Petri dish has been proposed. Impedances corresponding to a sterile medium and one inoculated with bacteria have been measured and compared during the growth process. Remarkable differences have been observed in the time evolutions of the two behaviors. In particular, impedance behavior measured at 100 Hz allows such achievement after only 1 h. An equivalent circuit of the measured impedances have been proposed. Considerations regarding the effects of the bacteria growth on the components describing the electrode-medium interface have been reported. The variations of these elements have been identified as the more significant for the early detection. From these promising results, improved configurations consisting of a matrix of electrodes can be proposed for localized and rapid detection by means of automated analysis systems.

1 Introduction

Early and objective detection of bacteria growth in culture media is a desired important improvement in microbiology and medicine. It can reduce the time necessary to determine the specie of a pathogen, thus allowing, for example, a rapid correction of an antibiotic therapy. The detection by impedance measurements represents an objective method, in fact, the growth can be observed in the variations of the culture medium impedance caused by the bacteria activity [1–3]. Growth devices that can allow the detection of bacteria can be obtained by placing sensing electrodes, in contact with the growth media and embedded in the media holder [4–6]. Moreover, impedance sensors are suitable to the purpose when low concentrations of bacteria grow not uniformly in the medium. In fact, it is possible to focus the detection in localized regions of the medium by placing a distributed matrix of electrodes [6]. Petri dishes are a typical grow

B. Andò et al. (eds.), *Sensors*, Lecture Notes in Electrical Engineering 431,
DOI 10.1007/978-3-319-55077-0_29

medium holder also adopted in automated systems for the manipulation of a large number of bacteria cultures. In this work, a test configuration with an impedance sensor embedded in a Petri dish has been proposed. The sensor consists of two steel electrodes, which has been fixed to the Petri dish structure and immersed, in the culture medium. The time evolution of the impedance has been measured during the growth process and the effect of the bacteria growth has been studied for an objective detection. The detection time has been estimated to demonstrate the possibility of an early detection. In addition, the effect of the temperature variations and the drying of the medium that can affect impedance the variations, during the growth process, has been investigated. To separate the effects of these phenomena from the bacteria growth comparative measurements between the impedances of a sterile culture medium and one inoculated with bacteria have been performed. The investigation of the measured impedances has been also carried out by proposing an electrical equivalent circuit of the sensor with the culture medium between the electrodes [1, 3]. In this way, the elements of this model, which are mainly affected by the bacteria during the growth, can be identified and conveniently considered for an early detection.

2 Petri Dish with Impedance Sensor

2.1 Impedance Sensor Description

In the proposed test configuration of the Petri dish with embedded impedance sensor, two steel electrodes have been fixed to the bottom of the dish. As shown in Fig. 1, the electrodes consist of two planar slats, which have been placed faced each other at a fixed distance. The Petri dish has a diameter of 85 mm and the electrodes have a width W = 60 mm and a distance d = 60 mm between them. In this way, a large portion of the culture medium is in the spacing between the electrodes and this is used as the area for the bacteria growth. The electrodes are fixed to the dish by two steel pins that protrude from the bottom side of the dish and act as the terminals for the measurements. The electrodes are partially immersed in the culture medium that consists of Tryptone Soya and it has a height $h \approx 4$ mm.

2.2 Frequency Behavior of the Culture Media Impedance and Equivalent Circuit

The impedance behavior as a function of the frequency has been measured by connecting the electrode terminals to an impedance analyzer HP 4194A. Figure 2a shows an example of culture medium impedance measured in the frequency range between 100 Hz and 500 kHz for a sterile culture medium at ambient temperature of 25 °C. As it can be observed, two different regions can be identified in the measured frequency behavior. At the low frequencies, it presents a decreasing magnitude and a negative

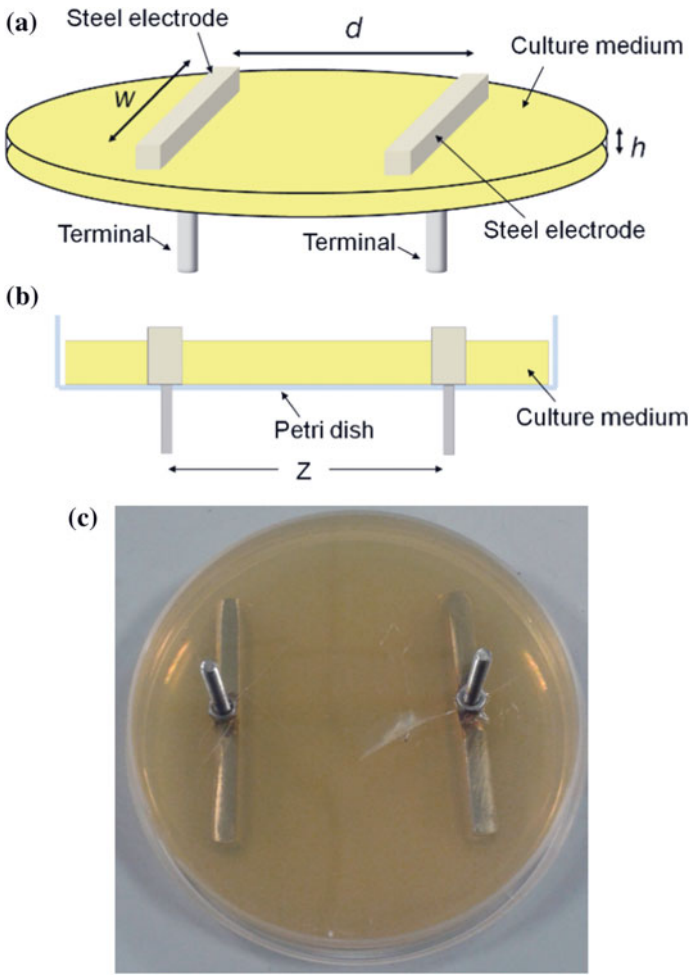

Fig. 1. **a** Schematization of the petri dish with embedded impedance sensor; **b** cross-section of the proposed test configuration; **c** picture of the bottom side of the Petri dish with the embedded electrodes immersed in the culture medium

phase that tends to 0° with the increase of the frequency. At higher frequencies, the phase remain close to 0° and the magnitude tends to assume a constant value.

The obtained behavior can be described by a typical electrical equivalent circuit, reported in Fig. 2b, where an electrolyte, as the adopted culture medium, is interfaced to metal electrodes [1–3]. The equivalent circuit consists of the series of a resistor R_M and the parallel between a capacitor C_{DL} and a resistor R_{Ct}. The R_M resistor describes the electrical behavior of the medium that is dominated by the conductivity.

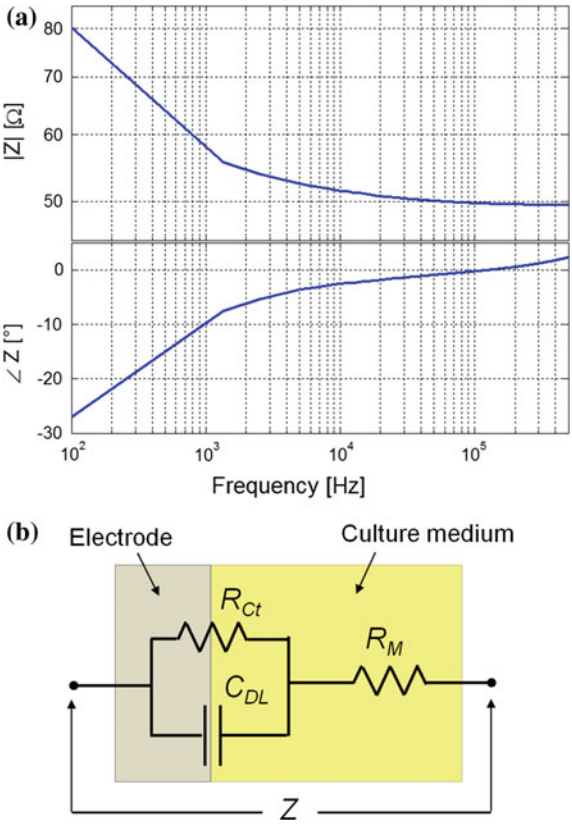

Fig. 2. **a** Magnitude and phase of the measured impedance between the electrodes embedded in the Petri dish; **b** electrical equivalent circuit of the sensor impedance. The interface components at both the electrodes have been grouped in a single R_{Ct} and C_{DL} components for simplicity

The parallel $R_{Ct} - C_{DL}$ describes the electrical behavior of the interface, where, the resistor R_{Ct} accounts for the charge transfer between the medium and the electrode, and the capacitor C_{DL} accounts for the double layer capacitance in the medium at the interface with a metal electrode. Following this equivalent circuit, in Fig. 2a the effect of the interface components at the low frequencies can be observed in the magnitude and phase of the measured impedance. Increasing the frequency the reactance of C_{DL} decreases neglecting thus also the effect of R_{Ct} and the measured impedance assumes the behavior of the medium resistance R_M.

Considering the obtained behavior of the sensor impedance, the effect of the bacteria growth on it can be conveniently evaluated only at two representative frequencies. On one hand, a frequency f_l in the "low" range where the interface components present a relevant contribution has been considered. Thus, the effect of the bacteria growth on C_{DL} and R_{Ct} can be observed in the measured impedance. On the other hand, a frequency f_h in the "high" range, where the interface components can be neglected, has been considered and the effect of the bacteria growth can be observed on R_M.

A f_l = 100 Hz has been used as the low frequency. A f_h = 100 kHz has been chosen as the high frequency value to avoid the effect of possible inductive contributions of the connections.

3 Bacteria Growth Detection

3.1 Experimental Procedure

Two Petri dishes with embedded electrodes have been used in the experiment. The culture medium of one Petri dish has been inoculated with bacteria while the other one has been maintained sterile to be used as reference. The bacteria have been inoculated with a solution of 16 μg/ml Escherichia Coli. The comparison experiment has been performed by placing the Petri dishes, which start from the ambient temperature of 25 °C, in a thermostatic chamber to carry out the bacteria growth at 35 °C. The impedances of the culture medium with inoculated bacteria, $\boldsymbol{Z_{batt}}$, and of the sterile one, $\boldsymbol{Z_{st}}$, have been measured by connecting the electrodes of the two different Petri dishes to two HP4194A impedance analyzers controlled and synchronized via GPIB by a specific LabWiew program on a PC. For the comparison of their time evolution, the two impedances $\boldsymbol{Z_{batt}}$ and $\boldsymbol{Z_{st}}$ have been measured simultaneously every 2 min for 12 h. The measurements have been started after the bacteria inoculation at the beginning of the growth process in the thermostatic chamber. Figure 3 reports the time evolution of $\boldsymbol{Z_{batt}}(f_{l,h})$ and $\boldsymbol{Z_{st}}(f_{l,h})$ measured at the two representative frequencies, where the suffix l or h indicates the different frequencies f_l or f_h. As it can be observed, at both the considered frequencies the two compared impedances present a different trend. On the one hand, the impedances $\boldsymbol{Z_{st}}(f_{l,h})$ of the sterile medium present variations only due to the temperature settling and the drying of the medium. On the other hand, the different trend of $\boldsymbol{Z_{batt}}(f_{l,h})$ of the medium with inoculated bacteria can be associated to the added effect of the bacteria growth.

3.2 Growth Detection by Impedance Comparison

The comparison of the time behavior between the impedances $\boldsymbol{Z_{batt}}(f_{l,h})$, and $\boldsymbol{Z_{st}}(f_{l,h})$, can be conveniently made using magnitudes and phases referred with respect their initial values. In this way, the impedances can be compared despite the differences in their values due to the slight dimensional discrepancies between the two Petri dishes.

The magnitude $|\boldsymbol{Z}(f_{l,h})|*$ and the phase $<\boldsymbol{Z}(f_{l,h})*$ can be defined as follows:

$$\left|Z(f_{l,h})\right|* = \frac{\left|Z(f_{l,h})\right|}{\left|Z(f_{l,h})\right|_{t=0}} \tag{1}$$

$$\angle Z(f_{l,h})* = \angle Z(f_{l,h}) - \angle Z(f_{l,h})_{t=0} \tag{2}$$

where $|\boldsymbol{Z}(f_{l,h})|_{t\,=\,0}$ and $<\boldsymbol{Z}(f_{l,h})_{t\,=\,0}$ is the magnitude and the phase values measured at the beginning of the experiment.

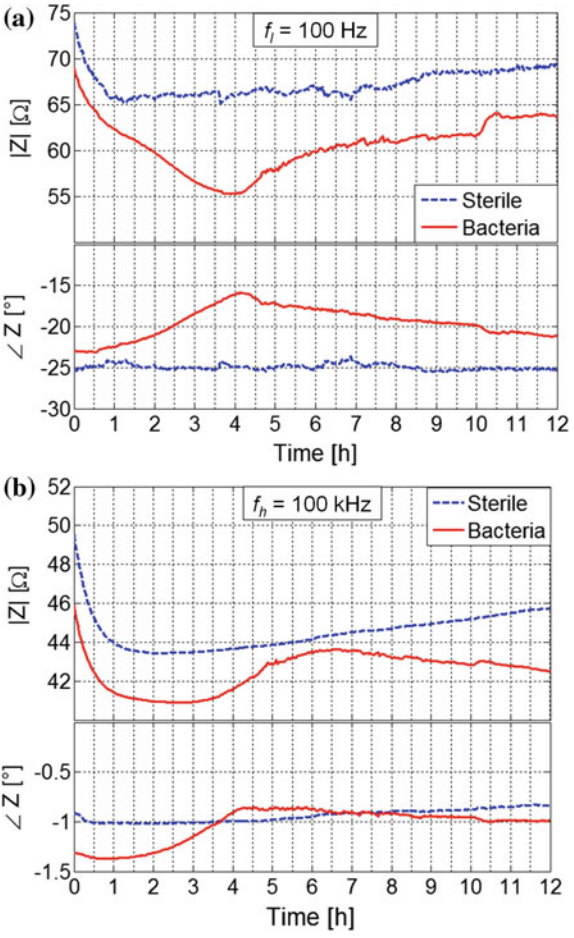

Fig. 3. Comparison of the time evolution of the magnitude and phase of $\boldsymbol{Z}_{batt}$ and $\boldsymbol{Z}_{st}$ measured at f_l = 100 Hz (**a**) and f_h = 100 kHz (**b**)

The possibility to detect the bacteria growth by the proposed impedance measurements can be observed in the comparisons of Fig. 4. In fact, at the frequency f_l of 100 Hz, after about 1 h, the trends of $|\boldsymbol{Z}_{batt}(f_l)|^*$ and $<\boldsymbol{Z}_{batt}(f_l)^*$ present large differences with respect the trends of $|\boldsymbol{Z}_{st}(f_l)|^*$ and $<\boldsymbol{Z}_{st}(f_l)^*$. In particular, $|\boldsymbol{Z}_{batt}(f_l)|^*$ presents an additional decrease until about 4 h follow by a more rapid increase with respect $|\boldsymbol{Z}_{st}(f_l)|^*$. At the same frequency, the phase $<\boldsymbol{Z}_{batt}(f_l)^*$ presents a positive shift which assumes the maximum value after 4 h. The detection of the bacteria growth can be obtained from the comparison also at the frequency f_h of 100 kHz. In particular, after about 3 h magnitude $|\boldsymbol{Z}_{batt}(f_h)|^*$ presents a different trend with respect the reference $|\boldsymbol{Z}_{st}(f_h)|^*$. It consists in a rapid increase of $|\boldsymbol{Z}_{batt}(f_h)|^*$ between 3 and 6 h followed by a slow decrease which is not present in the trend of $|\boldsymbol{Z}_{st}(f_h)|^*$.

The detection time can be better observed in Fig. 5 where the comparison is shown as the ratio between the magnitudes $|\boldsymbol{Z}_{batt}\ (f_{l,h})|^*/|\boldsymbol{Z}_{st}(f_{l,h})|^*$ and difference between the phases $<\boldsymbol{Z}_{batt}(f_{l,h})^* - <\boldsymbol{Z}_{st}(f_{l,h})^*$. At the frequency f_l the ratio starts to decrease from the unitary value and the phase difference starts to increase from the zero after about

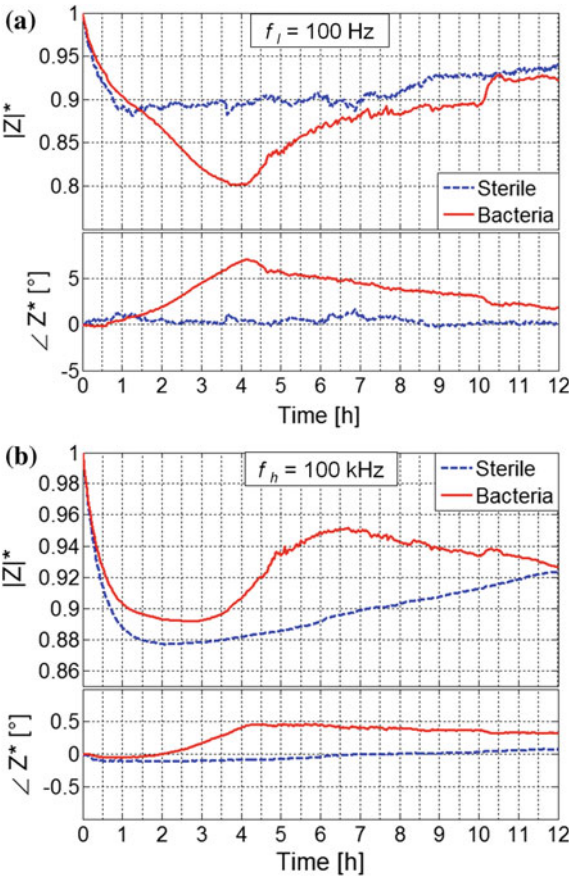

Fig. 4. Comparison of the time evolution of the magnitudes $|\boldsymbol{Z}_{batt}|^*$ and $|\boldsymbol{Z}_{st}|^*$, and the phases $<\boldsymbol{Z}_{batt}{}^*$ and $<\boldsymbol{Z}_{st}{}^*$ measured at f_l = 100 Hz (**a**) and f_h = 100 kHz (**b**)

1 h which can be assumed as the detection time. Considering the different phases of bacteria growth, the initial phase, where the impedance trend of $\boldsymbol{Z}_{batt}(f_l)$ has the same behavior of $\boldsymbol{Z}_{st}(f_l)$, can be associated to the lag phase where the multiplication of the bacteria has not yet started. In the subsequent log and stationary phases of the growth, $\boldsymbol{Z}_{batt}(f_l)$ reaches a maximum reduction of about 10% with respect the reference trend of $\boldsymbol{Z}_{st}(f_l)$. This maximum reduction verifies after about 4 h where the maximum bacteria activity can be assumed. The comparison reported in Fig. 5 shows also that the bacteria growth presents a different effect on $\boldsymbol{Z}_{batt}$ at the frequency f_h. In fact, the ratio $|\boldsymbol{Z}_{batt}(f_h)|^*/|\boldsymbol{Z}_{st}(f_h)|^*$ starts to significantly increase from the unitary value after about 3 h, while the phase difference $<\boldsymbol{Z}_{batt}(f_h)^* - <\boldsymbol{Z}_{st}(f_h)^*$ presents only a slight deviation from zero. The ratio increase reaches a maximum value of about 5% from the 5th and the 6th hour of the grow process.

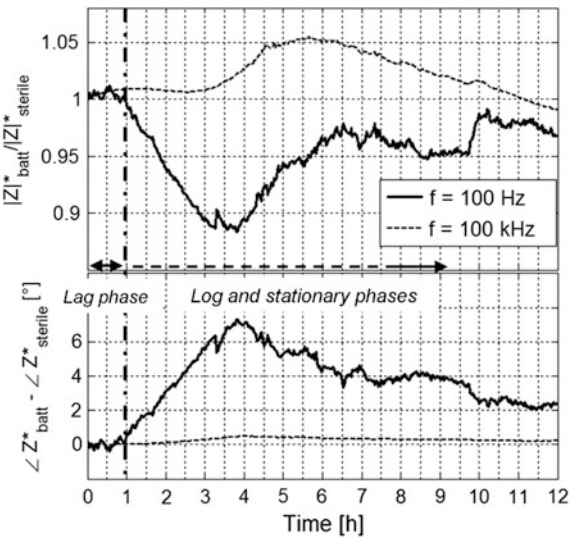

Fig. 5. Time evolutions of the magnitude ratio $|\boldsymbol{Z_{batt}}|^*/|\boldsymbol{Z_{st}}|^*$ and phase difference $<\boldsymbol{Z_{batt}}^* - <\boldsymbol{Z_{st}}^*$ at the frequencies f_l = 100 Hz and f_h = 100 kHz. The correspondent lag, log and stationary phases of the bacteria growth are outlined

4 Effect of Bacteria Growth on the Equivalent Circuit Components

The experimental results discussed in the Sect. 3 shows that the bacteria growth affects in different way the measured impedance behavior at the different frequencies f_l and f_h. It implies that the bacteria growth presents different actions on the different components of the equivalent circuit of the sensor impedance, proposed in Fig. 2b. An evaluation of the bacteria growth effects on these components can be useful for the design of impedance sensors in order to maximize sensitivity and minimize thus the detection time. The value of the components R_{Ct}, C_{DL} and R_M can be obtained from the impedance measurements at two frequencies:

$$C_{DL} = \frac{2\pi f_h \mathrm{Im}[Z(f_l)] - 2\pi f_l \mathrm{Im}[Z(f_h)]}{\mathrm{Im}[Z(f_h)]\mathrm{Im}[Z(f_l)]((2\pi f_h)^2 - (2\pi f_h)^2)} \tag{3}$$

$$R_{Ct} = \sqrt{-\frac{\mathrm{Im}[Z(f_l)]}{2\pi f_l C_{DL} + \mathrm{Im}[Z(f_l)](2\pi f_l)^2 {C_{DL}}^2}} \tag{4}$$

$$R_M = Z(f_h) - \frac{R_{Ct}}{1 + j2\pi f_h C_{DL}} \tag{5}$$

where $\mathrm{Im}[\boldsymbol{Z}(f_{l,h})]$ is the imaginary part of the impedance measured at f_l or f_h. The time evolutions of the components C_{DL}, R_{Ct}, R_M have been calculated for both impedances $\boldsymbol{Z_{batt}}$ and $\boldsymbol{Z_{st}}$. The different effect of the bacteria growth on the components of the equivalent circuit can be observed in Fig. 6 where the comparisons of their time evolutions are reported.

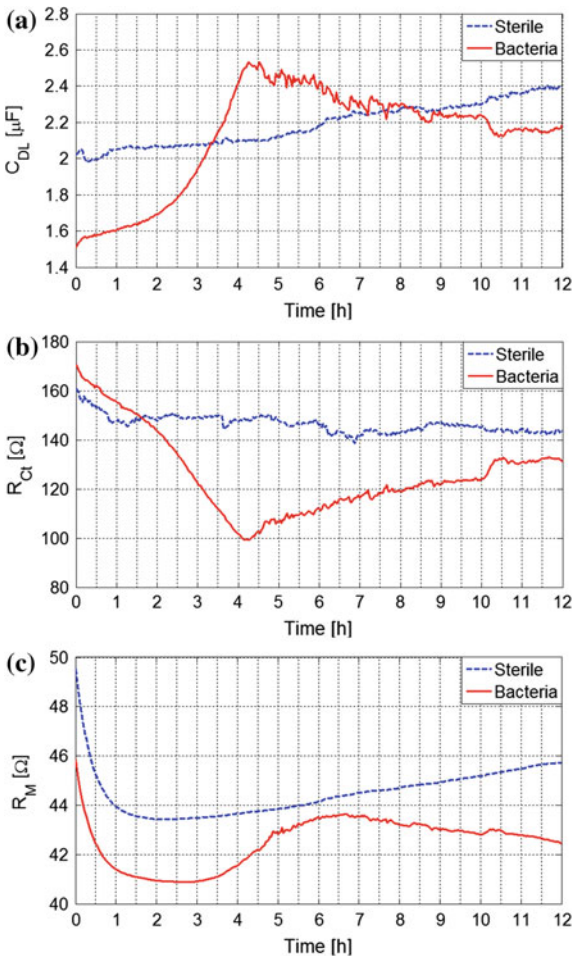

Fig. 6. Time evolutions of the equivalent circuit components C_{DL} (**a**), R_{Ct} (**b**) and R_M (**c**) derived for the compared impedances $\boldsymbol{Z_{batt}}$ and $\boldsymbol{Z_{st}}$

Figure 6a, b show that the bacteria growth has a strong effect on the components C_{DL} and R_{Ct}, which accounts for the phenomena at the interface between the electrodes and the medium. In fact, after an initial phase of about 1 h, the trends of the double layer capacitance presents an evident increase and the contact resistance presents an evident decrease with respect the trends derived for the impedance of the sterile medium. The maximum variation rate of C_{DL} and R_{Ct}, derived for $\boldsymbol{Z_{batt}}$, has been obtained between the 2nd and the 4th hour of the growth process which probably corresponds to the phase where the bacteria presents the higher multiplication rate. These variations reach the maximum magnitudes at the same time after about 4.5 h followed by a slow variation towards the initial values. In this phase, which follows the maximum variations, it can be assumed that the bacteria growth is in the stationary phase where the number of bacteria presents an equilibrium between the bacteria multiplication and the bacteria death.

Differently, Fig. 6c shows that the medium resistance R_M is less affected by the bacteria growth with respect C_{DL} and R_{Ct}. Both the R_M trends can be mainly associated to the temperature settling and the drying of the medium during the experiment. The effect of the bacteria growth on R_M can be clearly seen only after about 3 h where the resistance of the medium with inoculated bacteria presents a different behavior with respect the sterile one.

5 Conclusion

The possibility of an early detection of bacteria growth in a culture media has been demonstrated by proposing and testing a Petri dish with an embedded impedance sensor. The comparisons of impedance measurements, operated during a growth process, on a culture medium with inoculated bacteria and a sterile one show that a detection time as low as 1 h has been obtained. In fact, the time evolutions of the compared impedances present different behaviors, which allow the detection of the bacteria growth. In addition, the different growth phases can be identified with different impedance trends at different times during the experiment. The effects of the bacteria growth on the components of the equivalent circuit of the sensor impedance have been evaluated. Bacteria growth affects the components that describe the electrical behavior of both the medium and the electrode-medium interface. The major and earlier variations have been obtained in the capacitance and in the resistance that describe the interface. Thus, these variations have been identified as the most effective ones for the early detection of bacteria growth. Therefore, the detection time would be highly reduced by a sensor design that emphasizes the contribution of the interface components on the comprehensive sensor impedance. Such a result can be obtained by positioning small area electrodes at short distance from one another. In this way, on the one hand, a reduced area increases the magnitude of the interface reactance and resistance, on the other hand, reduced distance between the electrodes reduces the magnitude of the medium resistance. This solution matches also the perspective to focus the detection in localized regions of the medium by placing a distributed matrix of electrodes. In fact, multiple localized sensors are suitable for the detection of low concentrations of bacteria that grow not uniformly in the medium. A culture media holder, such as a Perti dish, with embedded a distributed matrix of electrodes, can be proposed for the early and automatic detection of bacteria growth in automated systems for the manipulation of bacteria cultures.

References

1. L. Yang, R. Bashir, Electrical/electrochemical impedance for rapid detection of foodborne pathogenic bacteria. Biotechnol. Adv. **26**, 135–150 (2008)
2. M. Varshneya, Y. Li, Interdigitated array microelectrodes based impedance biosensors for detection of bacterial cells. Biosens. Bioelectron. **24**, 2951–2960 (2009)

3. L. Yang, C. Ruan, Y. Li, Detection of viable *Salmonella typhimurium* by impedance measurement of electrode capacitance and medium resistance. Biosens. Bioelectron. **19**, 496–502 (2003)
4. J. Paredes, S. Becerro, S. Arana, Label-free interdigitated microelectrode based biosensors for bacterial biofilm growth monitoring using petri dishes. J. Microbiol. Methods **100**, 77–83 (2014)
5. J. Paredes, S. Becerro, F. Arizti, A. Aguinaga, J.L. Del Pozo, S. Arana, Interdigitated microelectrode biosensor for bacterial biofilm growth monitoring by impedance spectroscopy technique in 96-well microtiter plates. Sensor. Actuat. B-Chem. **178**, 663–670 (2013)
6. J. Paredes, S. Becerro, F. Arizti, A. Aguinaga, J.L. Del Pozo, S. Arana, Real time monitoring of the impedance characteristics of Staphylococcal bacterial biofilm cultures with a modified CDC reactor system. Biosens. Bioelectron. **38**, 226–232 (2012)

Ampicillin Measurement Using Flow SPR Immunosensor and Comparison with Classical Amperometric Immunosensor

Mauro Tomassetti[1(✉)], Giovanni Merola[1], Elisabetta Martini[1], Luigi Campanella[1], Maria Pia Sammartino[1], Gabriella Sanzò[2], Gabriele Favero[2], and Franco Mazzei[2]

[1] Department of Chemistry, University of Rome "La Sapienza", P.le A. Moro, 5, 00185 Rome, Italy
mauro.tomassetti@uniromal.it
[2] Department of Chemistry and Pharmaceutical Technologies, University of Rome "La Sapienza", P.le A. Moro, 5, 00185 Rome, Italy

Abstract. An analytical comparison of a flow SPR immunosensor method and a conventional amperometric immunosensor has been carried out. Different formats were used, respectively, main analytical data have been checked and affinity constant values evaluated and compared.

Keywords: Direct SPR · Amperometric competitive · Immunosensors · Ampicillin · Analysis

1 Introduction

Recently we developed and standardized [1] classical immunoamperometric sensors for β-Lactam antibiotics determination and studied the possibility of their use for the analysis of real samples [2]. At present we have started to investigate also the possibility to fabricate and apply new immunosensor methods, such as those based on flow SPR, to check possible advantages and disadvantages, in comparison with classical immunoamperometric devices above developed. In the latter case, peroxidase as enzymatic marker and a "competitive" format were used. Conversely, the SPR transduction technique, used in the present research, allowed a "direct" measurement format to be used, working in flow mode.

2 Methods

2.1 Conventional Amperometric Immunosensor Method

For the ampicillin determination using, the conventional amperometric immunosensor, the "following competitive format" was used: the ampicillin free in solution, to be determined, was allowed to compete with a fixed supply of the penicillin-G labeled with biotin-avidin-peroxidase, for the ampicillin antibody immobilized on the membrane (Immobilon), in order to produce the antigen- antibody immunocomplex [1].

B. Andò et al. (eds.), *Sensors*, Lecture Notes in Electrical Engineering 431,
DOI 10.1007/978-3-319-55077-0_30

2.2 Flow-Immunosensor SPR Method

For the determination of ampicillin using flow SPR immunodevice (Fig. 1) and direct measurement format, first of all a modified (with mercaptoundecanoid acid) gold sensor (SAM) disk, was placed on the prism of SPR; then the antibody was immobilized using ethyl(dimethylamminopropyl)carbodiimide and N-hydroxysuccinimide, and, after washing with buffer solution, the non-reacted, activated groups were deactivated by treatment with ethanolamine. For the measurement, the following sequence was used: firstly the baseline in the presence of the flowing buffer (0.1 M sodium phosphate buffer, pH 7.4) was recorded, then ampicillin solution was allowed to flow into the cell, thus generating a signal increase; when a plateau was reached, the phosphate buffer was allowed to flow and finally the surface was regenerated by allowing a 0.1 mM glycine–HCl, pH 2.5 solution to flow in the SPR cell, producing the dissociation of anti-ampicillin–ampicillin complex, before restarting a new measurement.

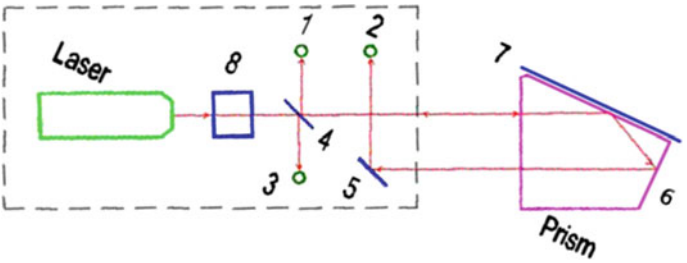

Fig. 1. SPR immunodevice: a semiconductor laser is used as a light source in the device. Polarized light of the laser is split into two beams by beam splitting means (*8*). These two beams provide two-channel device operation mode. Beam in the first channel falls on the measurement prism (*6*) and further on the sensor chip (*7*), passing the transparent plate (*4*) that serves for take-off of the part of the beam energy on the photodiode (*3*) and part on photodiode (*1*) for laser power control. The point of incidence of beam on the chip coincides with the table rotation axis. The beam reflected from the chip falls on the photodiode (*2*) of the registration system after turning by 90° prism angle and turn mirror (*5*). The accepted optical arrangement provides design compactness and weak dependence of positions of light spot on the chip and on the registration system photodiode what is important for ensuring of accuracy of the SPR curve measurement

3 Results

In Fig. 2 the calibration curve of the conventional amperometric immunosensor has been reported. While, in Fig. 3 the calibration curve obtained using the flow SPR immunodevice has been displayed. In the same two figures also the equations of calibration curves and respectively main analytical data found using two immunosensors, are reported. Lastly K_{aff} values, obtained using both the SPR device operating in flow mode and the conventional amperometric immunosensor, are respectively collected and compared in Table 1.

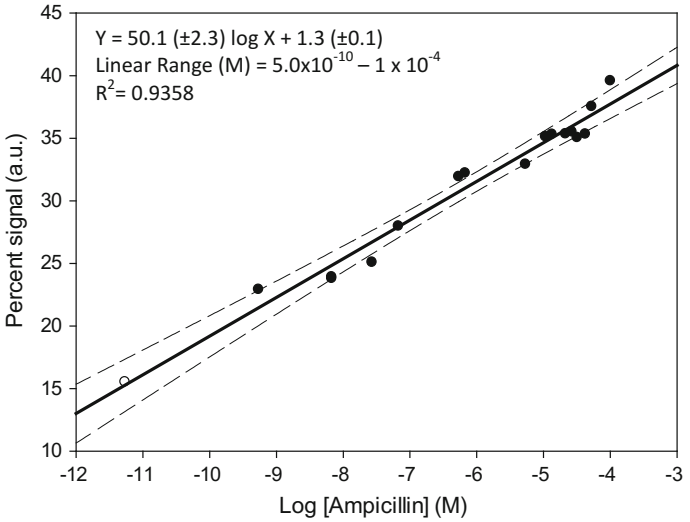

Fig. 2. Calibration curve for the conventional amperometric immunosensor and confidence interval using the competitive format for ampicillin determination obtained using a semilogarithmic scale

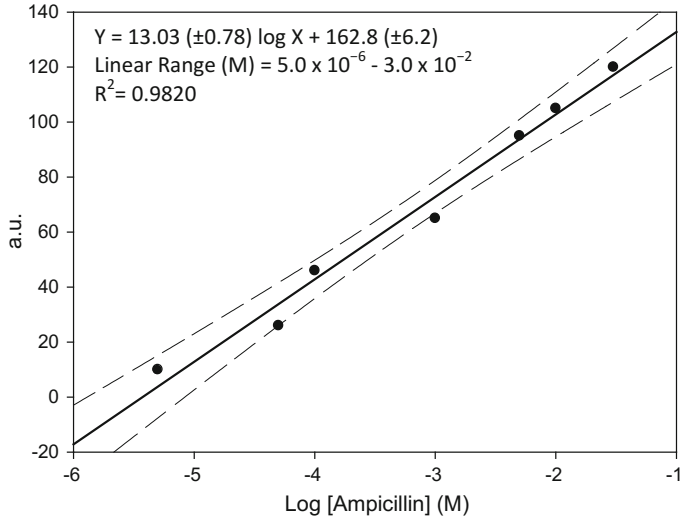

Fig. 3. Calibration curve and confidence interval, obtained by the direct method, based on flow surface plasmon resonance (SPR), for ampicillin determination as a function of increasing ampicillin concentration

Table 1. K_{aff} value for the ampicillin obtained by the SPR immunosensor and comparison with the value found using the conventional amperometric immunosensor

Method	K_{aff} (M^{-1}) n = 5; RSD% $\leq$ 5
Conventional immunosensor for ampicillin using "Competitive" format	3.7×10^7
Direct SPR immunosensor for ampicillin	2.0×10^3

4 Discussion and Conclusions

In conclusion a comparison of the main analytical data between SPR and classical amperometric immunosensor shows that even if the linearity range of the SPR method results only of about 4 decades (10^{-6}–10^{-2} M), so that it is less wide of the traditional immuno-amperometric method and, owing this reason, above all displaced only towards lower values, nevertheless the sensitivity of the SPR method is, for instance, still satisfactory for environmental analysis [3–7].

Acknowledgements. This work was funded by University of Rome "La Sapienza", Center "Protezione dell'Ambiente e dei Beni Culturali (CIABC)" and "Istituto per lo Studio dei Materiali Nanostrutturati (ISMN)" of CNR.

References

1. G. Merola, E. Martini, M. Tomassetti, L. Campanella, New immunosensor for β-lactam antibiotics determination in river waste waters. Sens. Actuators. B, Chem. **199**, 301–313 (2014)
2. G. Merola, E. Martini, M. Tomassetti, L. Campanella, Simple and suitable immunosensor for β-Lactam antibiotics analysis in real matrixes: milk, serum, urine. J. Pharm. Biomed. Anal. **106**, 186–196 (2015)
3. D.N. Heller, M.L. Smith, O.A. Chiesa, LC/MS/MS measurement of penicillin G in bovine plasma, urine, and biopsy samples taken from kidneys of standing animals. J. Chromatogr. B Analyt. Technol. Biomed. Life Sci. **830**, 91–99 (2006)
4. M.G. Pikkemaat, M.L. Rapallini, S.O. Dijk, J.W. Elferink, Comparison of three microbial screening methods for antibiotics using routine monitoring samples. Anal. Chim. Acta **637**, 298–304 (2009)
5. D. Li, M. Yang, J. Hu, Y. Zhang, H. Chang, F. Jin, Determination of penicillin G and its degradation products in a penicillin production wastewater treatment plant and the receiving river. Water Res. **42**, 307–317 (2008)
6. I. Michael, L. Rizzo, C.S. McArdell, C.M. Manaia, C. Merlin, T. Schwartz et al., Urban wastewater treatment plants as hotspots for the release of antibiotics in the environment: a review. Water Res. **47**, 957–995 (2013)
7. T. Christian, R.J. Schneider, H.A. Färber, D. Skutlarek, M.T. Meyer, H.E. Goldbach, Determination of antibiotic residues in manure, soil, and surface waters. Acta Hydrochim. Hydrobiol. **31**, 36–44 (2003)

Looking If Any Correlation Exists Between the Total Antioxidant Capacity and Polyphenol Concentration (Measured Using Two Different Enzyme Sensors) in Several Food or Feed Based Vegetables and Pharmaceutical Integrators

Mauro Tomassetti(✉), Riccardo Angeloni, Elisabetta Martini, Mauro Castrucci, Luigi Campanella, and Maria Pia Sammartino

Department of Chemistry, University of Rome "La Sapienza", P.le A. Moro 5, 00185 Rome, Italy
mauro.tomassetti@uniromal.it

Abstract. The principal aim of the present research has been to check if any correlation exists between the total antioxidant capacity (TAOC) value and the total polyphenols content (TPC) of several food, or beverages and feed samples based vegetables. The research was also extended to several food supplements currently sold as pharmaceutical integrators.

Keywords: Antioxidant capacity · Polyphenols · Correlation · Foods · Seeds · Pharmaceutical supplements

1 Introduction

The measurement of antioxidant capacity, linked to numerous natural plant products, has been aroused in recent years increasing interest. Really, while the antioxidant capacity of the principal vegetables products is now sufficiently well known through the publication of numerous reports on the subject (some of which by the authors of the present communication), little or nothing is actually known from the experimental standpoint about the antioxidant capacity of many food supplements, most of which have appeared on the market recently and can be found in drugstores, side by side with actual pharmaceutical products. Furthermore, although numerous methods are described in the literature to measure antioxidant capacity, the situation has become complicated ever since the United States Department of Agriculture [1] severely criticized and also withdrew from its catalogue the principal and widely known ORAC fluorimetric method [2, 3]. Numerous researchers have therefore recently gone back to using the polyphenol content of vegetables or vegetables based products as a measure of antioxidant properties rather than using methods based for instance on Hydrogen Atom Transfer (HAT), such as ORAC method.

B. Andò et al. (eds.), *Sensors*, Lecture Notes in Electrical Engineering 431,
DOI 10.1007/978-3-319-55077-0_31

2 Results and Discussion

In recent years our research team has developed an original biosensor method based on superoxide dismutase enzyme [4–6] for the purpose of measuring the total antioxidant capacity (TAOC) in many vegetables matrices. This new method has been found to correlate highly with methods of Electron Transfer (ET) type [7]. In the present research this biosensor method has been used to determine the TAOC of several different food supplements available in drugstores and advertised above all as having antioxidant properties that can act as radical scavengers. At the same time, in the same products, the total concentration of polyphenols content (TPC), which are deemed to be the main and most effective radical scavengers of plant origin, was measured using a classical enzymatic-amperometric tyrosinase sensor pointed out in the past years by our group [8]. Lastly we checked if any correlation exists between TAOC and polyphenols content values (TPC). Results show that TAOC values and total polyphenol concentration measured in food supplements do not always correlate closely (Fig. 1), not only because of the presence of other non phenolic molecules, which also have a their significant antioxidant capacity, in several of the supplements tested, but due in addition to the different antioxidant capacity of the various polyphenols present.

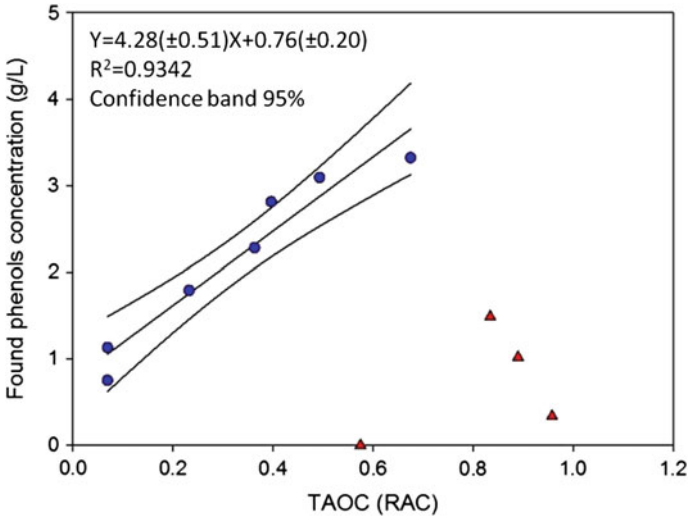

Fig. 1. It can be shown as a correlation between TPC and TAOC exists for several (*filled circle*), but not for all (*filled triangle*) pharmaceutical integrators

Lastly this investigation was extended to several food (beverages) or feed based vegetables already considered in previous researches [4–6, 9–12]. In the case of these food and feed based vegetables, on the contrary, this correlation between TAOC and TPC seems to be usually in a rather evident, as our experimental data have shown (see Figs. 2, 3 and 4).

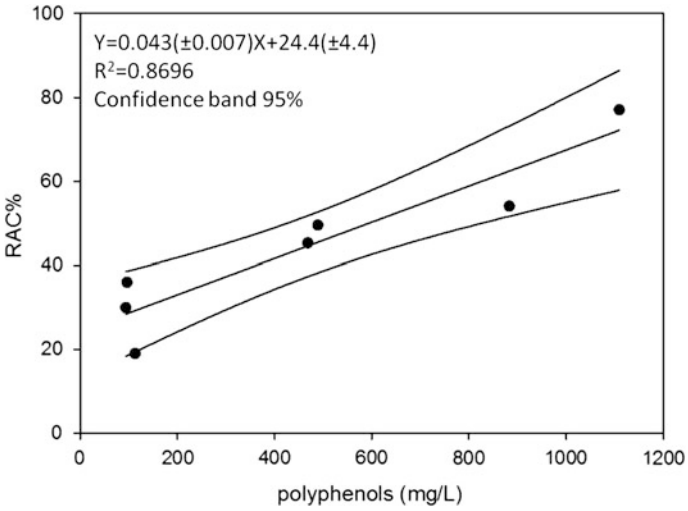

Fig. 2. Correlation between TPC and TAOC for beverages based vegetables product, i.e. common, green and detheinated tea, black and white wines (*filled circle*)

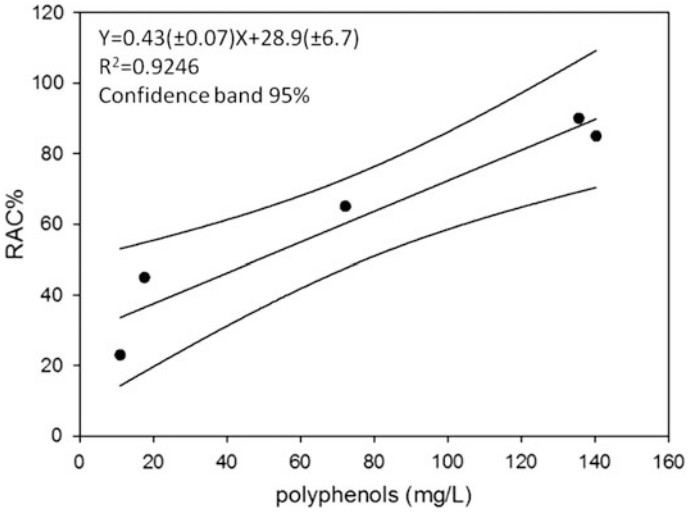

Fig. 3. Correlation between TPC and TAOC for food based vegetables product, i.e. aromatic herbs: anise, basil, majoran, rosemary and juniper (*filled circle*)

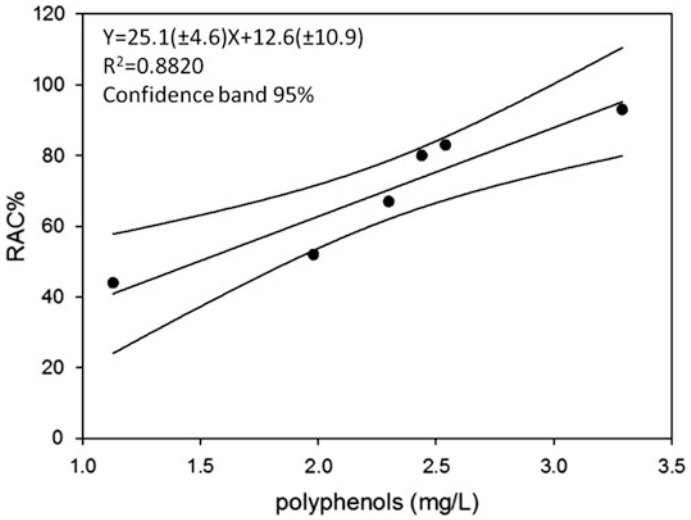

Fig. 4. Correlation between TPC and TAOC for feeds based vegetables product, i.e. maize, bean, mixture of barley maize and bean, grass hay, poultry feed (*filled circle*)

3 Conclusions

One conclusion that may therefore be drawn from this research is that it was confirmed as two used biosensors are very suitable for measurement in foods, feeds and integrators real matrices. Nevertheless the polyphenol concentration alone cannot always be taken as a completely reliable indicator of the total antioxidant capacity of matrices, like those represented by pharmaceutical food supplements. While the polyphenol content represent on the contrary a good indicator of the TAOC value, for food and feed based vegetables.

Acknowledgements. This work was funded by University of Rome "La Sapienza", Center "Protezione dell'Ambiente e dei Beni Culturali (CIABC)" and "Istituto per lo Studio dei Materiali Nanostrutturati (ISMN)" of CNR.

References

1. United States Department of Agriculture. Available online: http://www.ars.usda.gov/services/docs.htm?docid=15866. Accessed 13 Jan 2015
2. G. Cao, C.P. Verdon, A.H.B. Wu, H. Wang, R.L. Prior, Automated assay of oxygen radical absorbance capacity with the COBAS FARA II. Clin. Chem. **41**, 1738–1744 (1995)
3. T. Hatano, H. Kagawa, T. Yasuhana, T. Okuda, Two new flavonoids and other constituents in licorice root: their relative astringency and radical scavenging effects. Chem. Pharm. Bull. **36**, 2090–2097 (1988)

4. L. Campanella, A. Bonanni, M. Tomassetti, Determination of the antioxidant capacity of samples of different types of tea, or of beverages based on tea or other herbal products, using a superoxide dismutase biosensor. J. Pharm. Biomed. Anal. **32**, 725–736 (2003)
5. L. Campanella, G. Favero, L. Persi, M. Tomassetti, New biosensor for superoxide radical used of evidence molecules of biomedical and pharmaceutical interest having radical scavenging properties. J. Pharm. Biomed. Anal. **23**, 69–76 (2000)
6. L. Campanella, G. Favero, M. Tomassetti, Superoxide dismutase biosensors for superoxide radical analysis. Anal. Lett. **32**(13), 2559–2581 (1999)
7. V. Fogliano, V. Verde, G. Randazzo, A. Ritieni, Method for measuring antioxidant activity and its application to monitoring the antioxidant capacity of wines. J. Agric. Food Chem. **47**, 1035–1040 (1999)
8. L. Campanella, G. Favero, M.P. Sammartino, M. Tomassetti, Enzymatic immobilisation in kappa-carrageenan gel suitable for organic phase enzyme electrode (OPEE) assembly. J. Mol. Catal. B Enzym. **7**, 101–113 (1999)
9. L. Campanella, A. Bonanni, E. Finotti, M. Tomassetti, Biosensors for determination of total and natural antioxidant capacity of red and white wines: comparison with other spectrophotometric and fluorimetric methods. Biosens. Bioelectron. **19**, 641–651 (2004)
10. L. Campanella, E. Gregori, F. Marini, M. Tomassetti, Biosensors, colorimetric tests and chemometrics to check antioxidant and prooxidant properties of several animal feeds. J. Food Agric. Environ. **6**, 326–332 (2008)
11. A. Bonanni, L. Campanella, T. Gatta, E. Gregori, M. Tomassetti, Evaluation of the antioxidant and prooxidant properties of several commercial dry spices by different analytical methods. Food Chem. **102**, 751–758 (2007)
12. L. Amati, L. Campanella, R. Dragone, A. Nuccilli, M. Tomassetti, S. Vecchio, New investigation of the isothermal oxidation of extra virgin olive oil: determination of free radicals, total polyphenols, total antioxidant capacity, and kinetic data. J. Agric. Food. Chem. **56**, 8287–8295 (2008)

Preliminary Study of a Low-Cost Point-of-Care Testing System Using Screen-Printed Biosensors for Early Biomarkers Detection Related to Alzheimer Disease

Sarah Tonello[1(✉)], Mauro Serpelloni[1], Nicola Francesco Lopomo[1], Giulia Abate[2], Daniela Letizia Uberti[2], and Emilio Sardini[1]

[1] Department of Information Engineering, University of Brescia, Via Branze, 38, 25123 Brescia, Italy
s.tonello@unibs.it

[2] Department of Molecular and Translational Medicine, University of Brescia, Via Branze, 38, 25123 Brescia, Italy

Abstract. Among neurodegenerative diseases, Alzheimer Disease (AD) represents one of the most widespread pathologies, for which an early diagnosis is still missing. A peculiar expression of an altered conformational isoform of p53 protein was reported to be a potential biomarker able to distinguish AD subjects from healthy population, quantifiable using a blood-based enzyme-linked immunosorbent assay (ELISA). In order to overcome ELISA limitations, related to reliability and to improve sensitivity, this study aimed to realize a low cost highly sensitive portable point-of-care (PoC) testing system based on screen printed electrochemical sensors (SPES). The development of the platform specifically included both the design of the sensing probe and of the electronic circuit devoted to the conditioning and acquisition of the transduced electric signal. Preliminary testing of the circuit were performed recording changes in the conductivity of NaCl solution and quantifying electrodes coating with antibodies using Electrochemical Impedance Spectroscopy (EIS) principle. Results obtained with saline solution, showed the ability of the circuit to give the best response corresponding to low changes in NaCl concentration (sensitivity 0.2 mA/(mg/ml)), suggesting a good sensitivity of the platform. Findings obtained from EIS showed the ability of the circuit to discriminate between different concentrations of antibodies coatings (sensitivity 80 μA/μg). Preliminary calibration of the sensor using interleukin IL-8 showed an increase in the maximum peak of current proportional to the increase of protein concentration, achieving a sensitivity of 35 μA/ng and reporting also a good value of reproducibility, really promising in the perspective of lower values of proteins concentrations.

Keywords: Screen printing · Electrochemical biosensors · Voltammetry · Point-of-care testing

B. Andò et al. (eds.), *Sensors*, Lecture Notes in Electrical Engineering 431,
DOI 10.1007/978-3-319-55077-0_32

1 Introduction

Among neurodegenerative diseases, Alzheimer Disease (AD) represents one of the most investigated and serious pathologies, for which an early reliable diagnosis is still missing. However, AD presents a long pre-symptomatic period, that could last up to 20 years, and which is characterized by biochemical and molecular events that can be used to foresee the beginning of the disease itself. Therefore, one of the most pervasive challenges of the research in medical diagnosis is related to the ability to detect this pathology in its earliest development [1, 2] thanks to reliable identification of specific biomarkers, or biological markers (e.g. proteins). Biomarkers represent in fact an indicator of the biological status, which can give useful information concerning physiological or pathological conditions and during the application of different medical treatments. Concerning AD diagnosis, recent studies specifically reported how the presence of a particular altered conformation of a specific protein (p53) could be able to discriminate subjects affected by AD from healthy population [3–5]. In this perspective, clinicians require technologies able to identify, quickly and with a high sensitivity, specific biological biomarkers related to AD disease, overcoming the issues related to the use of blood-based enzyme-linked immunosorbent assay (ELISA), in term of time and cost effectiveness, volume of sample required, reliability and possibility of quantification. In the last decades, new rapid, low cost and easily accessible methodologies and technologies have been increasingly investigated, supported by the interest toward customized and personalized medicine and toward rapid and home-accessible diagnostic systems [6–8]. Thanks to their ability to be functionalized and customized for the detection of different analytes (e.g. DNA, proteins), electrochemical biosensors represent the ideal starting point to realize complete testing platforms.

Printed electronics represents a successful approach to realize low cost and sensitive biosensors for the sensitive and specific quantification of different proteins [9–13]. By implementing biosensors, different methods can be used to detect and quantify specific proteins. The most widely used methodology to detect and quantify specific proteins on immunosensors are Electrochemical Impedance Spectroscopy (EIS) and Voltammetry, both based on the electrode surface functionalization, very similar to those used in the multi-wells standard ELISA [13]. The first one is a label free method, which measures the changes of impedance deriving from a different electrons exchange between the functionalized surface of the electrode and a conductive solution depending on the concentration of the recognized proteins [7, 9, 10]. The second method represents instead the study of variation of electronic current as a function of applied potential, which is able to induce specific redox reaction on the functionalized working electrode (WE). A 3-electrode conformation—including WE, reference electrode (RE) and a counter electrode (CE), used to measure the current—usually allows for optimal measurement within this kind of applications [14, 15]. A very sensitive technique of voltammetry, able to detect both proteins [14] or DNA sequences [16] with limit of detection in the order of ng/ml, is represented by Anodic Stripping Voltammetry (ASV). Using—for instance—the action of specific catalyzing enzymes,

this method is able to obtain a selective chemical deposition of specific metals proportional to the amount of proteins recognized in the sample. In this way, the concentration of proteins can be estimated as proportional to the peak of current measured during a stripping step, varying the potential between WE and RE. To further improve specificity and sensitivity of this technology, limits of detection lower than 100 pg/ml can be achieved thanks to the integration of the SPES with nanostructured materials. Gold nanoparticles, for example, or carbon nanotubes, or a combination of the two, has been used to modify the surface of the working electrode allowing to better recognize antigens and DNA sequences [14, 16–18]. Focusing on the quantification of a specific biomarker for the early detection of AD, the main objective of this work addressed the preliminary analysis of a low-cost portable point-of-care testing platform for the detection and sensitive quantification of the unfolded p53 protein. This study specifically reported the design of the sensing probe, with particular attention to the choice of materials and geometry and of the electronic circuit devoted to the conditioning and acquisition of the electric signal. In particular, the electrodes were designed to be easily implemented by means of screen printing methodology. Considering the whole testing workflow and without losing the possibility of generalization, preliminary results were obtained on controlled concentrations of electrolytic solution, on the quantification of antibodies coating through EIS and of interleukin concentration through ASV.

2 Materials and Methods

The development of the platform (Fig. 1) specifically included both the design of the sensing probe—produced with screen printing technology—with particular attention to the choice of the materials and geometry, and of the electronic circuit devoted to the conditioning and acquisition of the transduced electric signal.

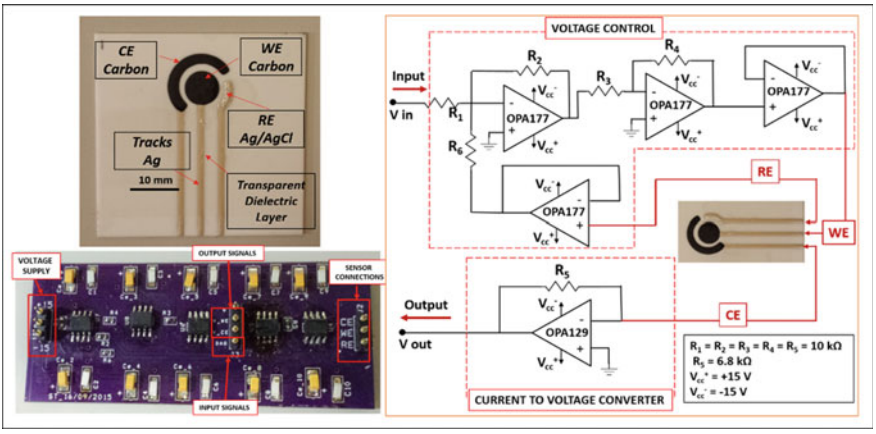

Fig. 1. Final layout of the biosensor and of the conditioning circuit

Specifically, silver, carbon and silver-silver chloride were selected respectively to realize conductive tracks, working and counter electrode, reference electrode in a three-electrodes configuration focusing on anodic stripping voltammetry (ASV).

The design of the circuit was in particular performed by implementing the functionalities of potentiostats. Using four Operational Amplifiers (OpAmp), the input signal applied to WE is regulated precisely during time, with respect to RE. The current from redox reactions of silver, selectively deposited where proteins are recognized on WE surface, is recorded thanks to a current to voltage converter. All SMD components were carefully selected depending on the specific function they had to perform in the circuit, in order to guarantee high accuracy and precision.

After completing the production of biosensor and circuit (Fig. 1), the compatibility of the materials and of the printing process with wet lab practices was evaluated and the protocol for sensor functionalization was optimized.

Preliminary tests of the circuit were then performed recording changes in the conductivity of NaCl solution and quantifying electrodes coating with antibodies using Electrochemical Impedance Spectroscopy (EIS) principle.

The first test was performed varying the concentration of NaCl in order to change the conductivity of the solution and evaluating the ability of the circuit to quantify these variations as changes in the current peak between WE and CE. In the second test, EIS principle was applied in order to measure changes of system impedance, resulting in changes in the current detected between WE and CE deriving from different concentrations of the primary antibodies released and adhered on WE surface after an overnight coating. EIS measurements were performed in presence of a conductive electrolytic an solution of 5 mM $K_3[Fe(CN)_6]$ in 1 M KCl.

In both protocols, drops of 2 ml of the conductive solution were released on WE, CE and RE in order to allow current flow, triangular waves were given as input at specific frequencies using a pulse generator and the output voltage form the measurement circuit, proportional to the current flowing between WE and CE, was recorded using an oscilloscope.

Finally, a preliminary calibration of the platform using ASV measurements was performed quantifying interleukin protein. ASV protocol adopted was characterized by a specific functionalization of the WE using immucomplexes formed by a capture and a detection antibody, using a dedicated kit (DuoSet® development system for ELISA, Human CXCL8/IL-8). In order to perform the detection step, Alkaline Phosphatase (AP) was used to label the secondary antibodies, thus allowing a selective silver deposition, proportional to the amount of proteins detected. Finally, after placing a drop of buffer solution on the three electrodes, a ramp input was given to the WE, causing the oxidation of the deposited silver, and the current flowing between WE and CE was measured, allowing a sensitive quantification of the proteins.

3 Results

Regarding this preliminary testing alumina substrate represented the optimal solution.

Thanks to the intrinsic porosity of the material, electrodes printed on this substrate did not show any variation when washed with water-based solutions during

functionalization steps and moreover appeared to allow an homogeneous passive coating of primary antibodies, confirmed both from optical and from impedance measurements (Fig. 2).

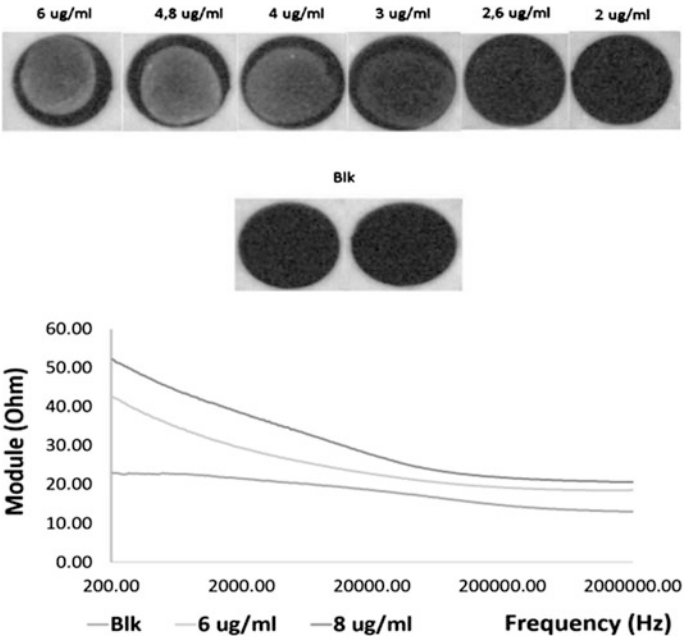

Fig. 2. Comparison between optical analysis and EIS measurements coating electrodes with different primary antibody concentrations

Results from the evaluation of circuit response to changes in saline solution conductivity showed a particular trend, characterized by two different slopes respectively for concentration of NaCl lower and higher than 1.0 mg/ml.

In particular (Fig. 3), a higher sensitivity was shown for concentrations lower than 1.0 mg/ml, indicating a higher sensitivity of the sensor (0.2 mA/(mg/ml)) for small changes of conductivity and small currents, and a lower sensitivity (20 μA/(mg/ml)) for higher concentration.

Results from EIS measurements showed a proportional decreasing of the peak of current flowing between CE and WE, indicating an increased impedance of the system due to an increasing concentration of antibodies coated on WE surfaces resulting in a reduced electrons exchange between WE surface and electrolytic solution (Fig. 4). Increasing the concentration of antibodies coated on the WE resulted in reducing the differences of currents exchanged at different frequencies. The sensitivity of the sensor in detecting the change in antibodies coating concentration was of 80 μA/μg.

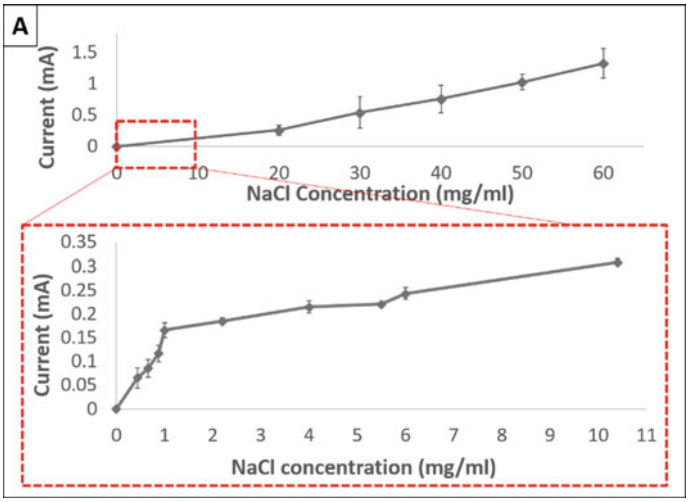

Fig. 3. Calibration of SPES with NaCl solution

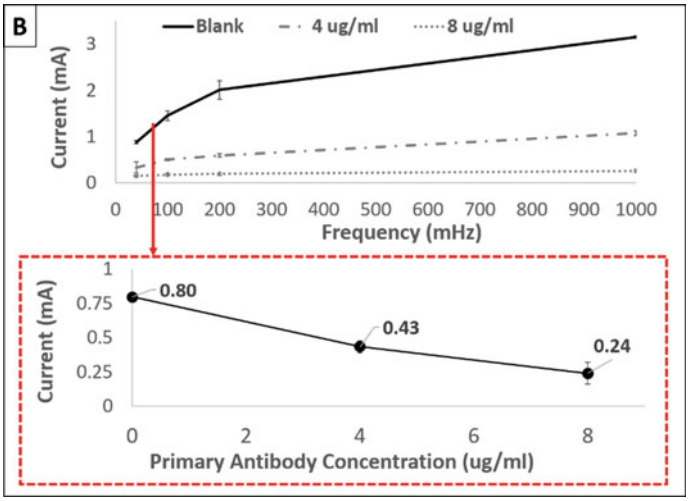

Fig. 4. EIS at low frequencies and at 50 MHz of coating using different primary antibodies

Results from ASV measurements showed an increase in the maximum peak of current proportional to the increase of interleukin concentration. A linear increase of current peaks recorded when increasing the input potential from 0 to 0.6 V could be observed, with a sensitivity of 35 μA/ng (Fig. 5).

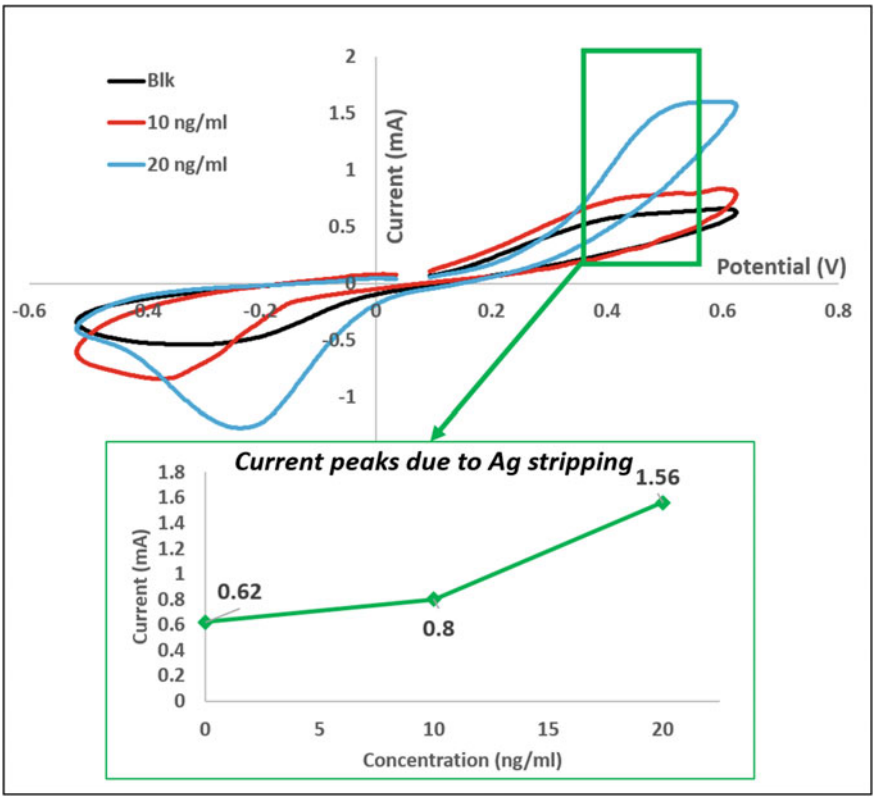

Fig. 5. ASV measurements in a preliminary calibration of SPES using human interleukin proteins

4 Conclusion

In light of the positive results described, the study is on-going and further analyses will include ASV tests of unknown concentration of unfolded p53 in samples of real patients, comparing the results with the ones obtained from ELISA analysis.

Moreover, the activity actually going on refers to the implementation of the ASV protocol with a multi wells conformation of biosensor geometry, in order to optimize the protocol and reduce the variability. After the validation, the proposed methodology and the platform design will be optimized in order to be easily accessible for a routine automatized diagnosis technique in the clinical environment. From these bases, particular attention will be then addressed to increase the sensitivity of the method itself, including both the introduction of nanostructured materials for the working electrodes and proper ASV measurements. All this, with the aim to realize an innovative self-standing portable point-of-care, a low cost, easy to use and highly precise platform able to support clinicians to diagnose AD from its earliest stages.

References

1. Z. Svobodova, M. Reza Mohamadi, B. Jankovicova, H. Esselmann, R. Verpillot, M. Otto, M. Taverna, J. Wiltfang, J.-L. Viovy, Z. Bilkova, Development of a magnetic immunosorbent for on-chip preconcentration of amyloid beta isoforms: representatives of Alzheimer's disease biomarkers. Biomicrofluidics **6**(2), 24126–2412612 (2012)
2. C. Humpel, Identifying and validating biomarkers for Alzheimer's disease. Trends Biotechnol. **29**(1), 26–32 (2011)
3. D. Uberti, C. Lanni, T. Carsana, S. Francisconi, C. Missale, M. Racchi, S. Govoni, M. Memo, Identification of a mutant-like conformation of p53 in fibroblasts from sporadic Alzheimer's disease patients. Neurobiol. Aging **27**(9), 1193–1201 (2006)
4. C. Lanni, M. Racchi, G. Mazzini, A. Ranzenigo, R. Polotti, E. Sinforiani, L. Olivari, M. Barcikowska, M. Styczynska, J. Kuznicki, A. Szybinska, S. Govoni, M. Memo, D. Uberti, Conformationally altered p53: a novel Alzheimer's disease marker? Mol. Psychiatry **13**(6), 641–647 (2008)
5. L. Buizza, G. Cenini, C. Lanni, G. Ferrari-Toninelli, C. Prandelli, S. Govoni, E. Buoso, M. Racchi, M. Barcikowska, M. Styczynska, A. Szybinska, D.A. Butterfield, M. Memo, D. Uberti, Conformational altered p53 as an early marker of oxidative stress in Alzheimer's disease. PLoS ONE **7**(1), e29789 (2012)
6. A.P. Dhawan, W.J. Heetderks, M. Pavel, S. Acharya, M. Akay, A. Mairal, B. Wheeler, C.C. Dacso, T. Sunder, N. Lovell, M. Gerber, M. Shah, S.G. Senthilvel, M.D. Wang, B. Bhargava, Current and future challenges in point-of-care technologies: a paradigm-shift in affordable global healthcare with personalized and preventive medicine. Transl. Eng. Health Med., IEEE J. **3**, 1–10 (2015)
7. D. Polese, A. Convertino, L. Maiolo, A. Ferrone, L. Pazzini, M. Marrani, F. Maita, A. Pecora, G. Fortunato, G. Fiaschi, Investigation on nanostructured biosensor for Biotin detection. *Sensors, 2014 IEEE*, pp. 1627–1630, 2014
8. S. Feng, L.E. Roseng, T. Dong, Quantitative detection of Escherichia coli and measurement of urinary tract infection diagnosis possibility by use of a portable, handheld sensor. *Medical Measurements and Applications (MeMeA), 2015 IEEE International Symposium on*, pp. 586–589, 2015
9. M.M.S. Silva, a.C.M.S. Dias, M.T. Cordeiro, E. Marques, M.O.F. Goulart, R.F. Dutra, A thiophene-modified screen printed electrode for detection of dengue virus NS1 protein. Talanta **128**, 505–510 (2014)
10. R. Elshafey, A.C. Tavares, M. Siaj, M. Zourob, Electrochemical impedance immunosensor based on gold nanoparticles-protein G for the detection of cancer marker epidermal growth factor receptor in human plasma and brain tissue. Biosens. Bioelectron. **50**, 143–149 (2013)
11. Y.H. Yun, B.K. Lee, J.S. Choi, S. Kim, B. Yoo, Y.S. Kim, K. Park, Y.W. Cho, A glucose sensor fabricated by piezoelectric inkjet printing of conducting polymers and bienzymes. Anal. Sci. **27**(4), 375 (2011)
12. A.M. Pernia, M.J. Prieto, I.C. Orille, J.A. Martin-Ramos, A. Costa-Garcia, Development of Optimized Screen-Printed Immunosensors. Instrum. Measur., IEEE Trans. **58**(7), 2181–2188 (2009)
13. R.A.S. Couto, J.L.F.C. Lima, M.B. Quinaz, Recent developments, characteristics and potential applications of screen-printed electrodes in pharmaceutical and biological analysis. Talanta **146**, 801–814 (2016)
14. V. Escamilla-Gómez, D. Hernández-Santos, M.B. González-García, J.M. Pingarrón-Carrazón, A. Costa-García, Simultaneous detection of free and total prostate specific antigen on a screen-printed electrochemical dual sensor. Biosens. Bioelectron. **24**, 2678–2683 (2009)

15. Y.-F. Liang, C.-Y. Huang, B.-D. Liu, A voltammetry potentiostat design for large dynamic range current measurement. *Intelligent Computation and Bio-Medical Instrumentation (ICBMI), 2011 International Conference on*, pp. 260–263, 2011
16. G. Martínez-Paredes, M.B. González-García, A. Costa-García, Genosensor for detection of four pneumoniae bacteria using gold nanostructured screen-printed carbon electrodes as transducers. Sens. Actuators, B Chem. **149**, 329–335 (2010)
17. P. Kara, A. de la Escosura-Muñiz, M. Maltez-da Costa, M. Guix, M. Ozsoz, A. Merkoçi, Aptamers based electrochemical biosensor for protein detection using carbon nanotubes platforms. Biosens. Bioelectron. **26**, 1715–1718 (2010)
18. B. Jeong, R. Akter, O.H. Han, C.K. Rhee, Increased electrocatalyzed performance through dendrimer–encapsulated gold nanoparticles and carbon nanotube–assisted multiple bienzymatic labels: highly sensitive electrochemical immunosensor for protein detection. Anal. Chem. **85**(3), 1784–1791 (2013)

Multisensorial Systems

Modeling Investigation of a Nonlinear Vibrational Energy Harvester

Bruno Andò[1(✉)], Salvatore Baglio[1], Adi Bulsara[2], Vincenzo Marletta[1], and Antonio Pistorio[1]

[1] DIEEI, Università di Catania, v.le A. Doria 6, 95125 Catania, Italy
bruno.ando@dieei.unict.it
[2] Space and Naval Warfare Systems Center Pacific, Code 71000, 92152-5000 San Diego, CA, USA

Abstract. In last years the authors have investigated nonlinear systems for vibrational energy harvesting. Nonlinear configurations have been demonstrated that, under the proper conditions, can provide better performance, compared to linear resonant oscillators, in terms of the amount of energy extracted from environmental wide spectrum mechanical vibrations. In particular, the authors presented the results of investigations on a system exploiting the advantages of a nonlinear bistable Snap-Through-Buckling (STB) configuration and two piezoelectric transducers placed at the locations of the two stable states (the position of the two minima of the bistable potential underpinning the dynamics of the system). The device investigated was shown to be capable of providing sufficient electrical energy to power an RF transmitter. However, in order to properly design the harvester an analytical model is necessary. The authors are investigating different nonlinear models. In this work, a comparison between two different theoretical models for the STB beam is discussed.

Keywords: Nonlinear energy harvester · Bistable systems · Snap through buckling · Piezoelectric materials · Modeling

1 Introduction

The development of systems aimed at powering electronic devices by exploiting the energy scavenged from their operating environment is an important line of research driven by the real needs to reduce the dependency on battery power.

The proliferation of small sensors, often networked or deployed in remote regions makes the dependency on battery power an important issue. For instance, wireless sensors might be placed in isolated locations or unsafe environments without the possibility to connect to the main power supply lines; in this case, it would certainly be inconvenient if a battery had to be replaced regularly [1]. A well designed energy harvester (EH), integrated with the sensor, can reduce or possibly eliminate this dependency.

Many different environmental power sources can be exploited to scavenge energy, well known solutions are the solar energy conversion [2], the thermoelectric power generation [3], the radio-frequency (RF) power conversion [4]. In recent times

B. Andò et al. (eds.), *Sensors*, Lecture Notes in Electrical Engineering 431,
DOI 10.1007/978-3-319-55077-0_33

particular attention has been devoted to the mechanical vibration sources [5] because of their ubiquity and the availability of new high-performance materials that can be used to convert mechanical vibrations to a suitable electrical response.

Typical solutions to scavenge energy from vibrations are based on linear resonant mechanical structures like cantilever beams exploiting piezoelectric, macro-fiber composites, electromagnetic or electrostatic conversion mechanism. Such kind of solutions are able to efficiently harvest energy when stimulated very close to their resonance frequency [6]. On the other hand, it has been demonstrated that the exploitation of nonlinear mechanisms such as bistable systems [7], can outperform traditional (linear) energy harvesters under the right set of operating conditions. A possible configuration implementing a nonlinear bistable energy harvester is the Snap Through Buckling structure. The bistable system is a special type of nonlinear structures underpinned by a two well potential energy [7, 8].

The STB configuration allows the inertial mass embedded in the harvester to travel rapidly between the two (stable) equilibrium positions under external mechanical vibrations regardless of their frequencies. This makes possible to access the energy contained in low amplitude wideband vibrations. Moreover, the bistable dynamics yields enhanced device behavior in terms of an extension of the frequency band within which the device is able to scavenge energy from vibrations [9]. This effect represents the main advantage of the nonlinear harvesting setup over the linear one.

The authors are investigating the mechanical and electrical behavior of buckled beam based nonlinear energy harvesters [9–13] like the one shown in Fig. 1. In particular, in [9] a low cost solution based on a bistable beam and two piezoelectric transducers exploiting the benefits of a Snap Through Buckling (STB) configuration was presented. In [11] the authors presented preliminary experimental results showing the capability of the nonlinear bistable energy harvester discussed in [9] to power (without batteries) a Commercial Off-The-Shelf (COTS) wireless transmitter @ 2.4 GHz. In [12], the use of rapid prototyping techniques for the realization of a nonlinear energy harvester has been introduced. The device exploits the benefits of bistable dynamics and a screen printed piezoelectric layer. The latter was electrically connected using Inter-DigiTed electrodes (IDT) realized by the inkjet printing of a silver based solution on a flexible PET (PolyEthyleneTerephthalate) substrate.

In [13], a comparison between two different theoretical models describing the mechanical behavior of the STB beam has been discussed and quantified by experimental evidence. In addition, preliminary results demonstrating the possibility of exploiting the device in the presence of noise, under some specific operating conditions, were reported.

In [14] preliminary results from the investigations aimed to understand the behavior and the performances of the STB harvester for a different position of the two stable states are presented. In particular, compared to [9] where the two piezoelectric transducers were placed at the stable minima of the potential energy function, here they have been placed near the inflection points of the potential energy function that underpins the dynamics of the nonlinear bistable beam. From a practical point of view and with reference to the schematic shown in Fig. 1, it means that the distance Δx between the two piezoelectrics has been reduced. This makes the STB beam to assume a new "constrained" bistable configuration. The main advantage of this is in the lower

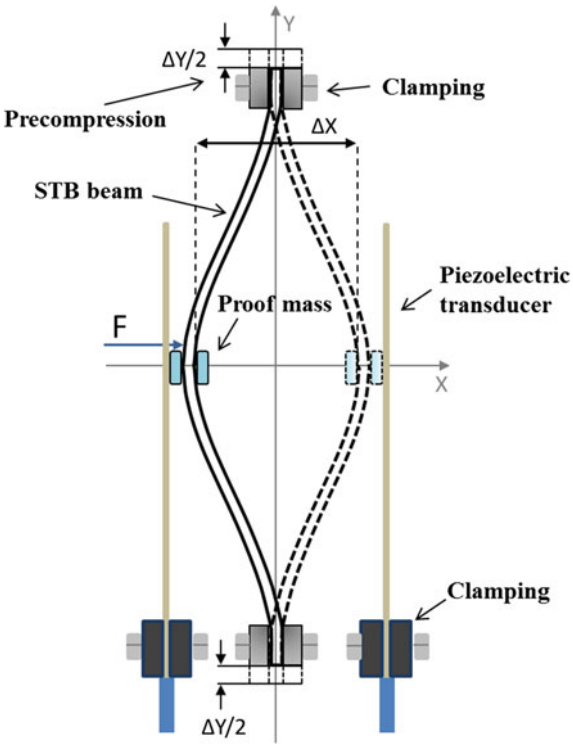

Fig. 1. Schematization of the nonlinear bistable STB harvester [16]

accelerations required to switch the beam between the two new constrained stable states.

It should be highlighted that the availability of an EH with a wide frequency bandwidth, ranging from very low frequency (in the order of 0.5 Hz and below) up to 10 Hz, is important for a number of real applications.

However, in order to understand the system behavior and optimize its performance by properly design the EH, both in the mechanical and electrical domains, an analytical model is necessary. In this paper, a comparison between two different theoretical models for the mechanical behavior of the STB beam is discussed and supported by experimental evidences.

2 The Non Linear Energy Harvester

A schematic of the nonlinear bistable harvester is shown in Fig. 1. It consists of a clamped-clamped cantilever beam with a pre-compression applied along the Y axis (in a STB configuration), a proof mass placed in the middle of the beam and two lateral identical piezoelectric transducers. The beam is a strip of flexible PET whose

dimensions are 9 cm by 1 cm while its thickness is 140 μm. Two dedicated clamps have been used to block the beam on both ends along the Y axis and to adjust the pre-compression. It should be obvious that changing the pre-compression affects the switching dynamics, e.g. the average switching rate, of the device. The behavior of the device for different values of the pre-compression has been investigated in [9]. On the basis of the results obtained in [9], for the device investigated through this paper, the beam pre-compression has been fixed to $\Delta Y = 3$ mm, for the sake of convenience.

In this configuration, the beam exhibits a bistable behavior when a stress is applied perpendicular to its surface. In case the input stimulus exceeds the switching threshold, which is mainly defined by the pre-compression as well as the beam material and geometry, the beam will start switching between its stable positions. In case of a subthreshold signal the beam will vibrate close to one of the two stable states. This behavior is well described and ruled by a two-stable-state potential [9, 12, 13]. It should be obvious that in the bistable potential energy function that describes the dynamics, the energy barrier height as well as the locations of the stable minima of the potential, are a function of the pre-compression.

A proof mass of 9.7 g is used to optimize the trade-off between the operative frequency band and the minimum force that allows the switching. The proof mass has been designed and installed in order to maintain, as much as possible, the device symmetry and to reduce the beam tilt effect.

The piezoelectric transducers, manufactured by Midè (model Volture V21BL), are ultra-thin and light weight devices which convert the beam impacts (in each steady state) into electric charges. The dimensions of the piezoelectric transducers are 9.04 cm by 1.68 cm, while the thickness is 0.8 mm.

The distance between the piezoelectric transducers is fixed to 21 mm, which roughly corresponds to the distance Δx between the two stable positions of the beam.

The behavior of the lab prototype has been experimentally investigated by a dedicated set-up. The main component of the set-up is the shaker, consisting of an aluminum movable platform actuated by a vibration exciter and controlled by a power amplifier. The vibration exciter and the power amplifier are the TV 51110 and the BAA 120 manufactured by TIRA GmbH, respectively. The STB has been fixed on the movable platform of the vibration exciter.

A reference accelerometer, model MMA7331L by Freescale Semiconductor with a sensitivity S = 83.6 mV/g (configured in the operating range of ± 12 g), has been also included in order to perform an independent measurement of the imposed stimulus. Moreover, a distance measurement module, model QTR-1A by Pololu, including a very small reflectance InfraRed (IR) sensor and the conditioning electronics, has been included in the STB architecture to continuously monitor the displacement of the proof mass [15, 16]. The output signals from the piezoelectric transducers, the reflectance infrared sensor and the reference accelerometer have been acquired by the MSO9064A scope by Agilent Technologies with a sampling frequency $f_s = 10$ kHz, saved and processed by dedicated Matlab paradigms.

3 The Models for the STB Beam

As already stated before, the beam exhibits a bistable behavior in response to stresses applied perpendicular to its surface. A second order dynamical model fitting the nonlinear mechanical behavior of the system was presented in [9–12]. A nonlinear quartic potential energy function was used to describe the bistable behavior.

However, the authors are investigating the possibility to adopt new models to better describe the behavior of the device. In this work a first order dynamical model to fit the dynamic nonlinear mechanical behavior, stemming from the experimental observed behavior of the system of Fig. 1 is presented:

$$\tau\dot{x} - \Psi(x) = F(t) \tag{1}$$

where τ is the system time constant, $\dot{x}$ is the velocity of the beam, $F(t)$ is a stochastic source characterizing the external mechanical vibrations, and $\Psi(x) = -\partial U(x)/\partial x$ is the restoring force, with $U(x)$ the potential energy function.

In the following, we compare the model (1) performance with two different nonlinear bistable potentials, a quartic potential and a "soft" hyperbolic one that better reproduces the dynamic behavior observed in the experiments:

$$U_q(x) = \frac{1}{4}a \cdot x^4 - \frac{1}{2}b \cdot x^2 \tag{2}$$

$$U_h(x) = \frac{1}{2} \cdot x^2 - a'ln\ \cosh(b' \cdot x) \tag{3}$$

By substituting Eqs. (2) and (3), in Eq. (1) the following two dynamical models are obtained, respectively:

$$\tau \cdot \dot{x} + a \cdot x^3 - b \cdot x = F(t) \tag{4}$$

$$\tau \cdot \dot{x} + x - a'b' \tanh(b' \cdot x) = F(t) \tag{5}$$

The coefficients (a, b) and (a′, b′) were determined via a Nelder-Mead optimization algorithm implemented through a dedicated Matlab script exploiting the following minimization index:

$$J_{dyn} = \sqrt{\frac{\sum (x_{Meas} - x_{Pred})^2}{\sum x_{Meas}^2}} \tag{6}$$

Here, x_{Meas} and x_{Pred} refer to the measured and predicted displacement of the bistable device, respectively. The values of the parameters in (4) and (5) estimated by the optimization algorithm are a = 6.2e−3 N/m^3, b = 0.86 N/m, a' = 75.9 m/N, b' = 0.16 N/m.

4 Experimental Results and Conclusions

Figures 2 and 3 show the experimental displacement of the beam in response to a sinusoidal stimulation at 5 and 6 Hz, respectively, for two values of the acceleration, 6.3 and 7.3 m/s^2, compared to the displacement predicted by the two models (4) and (5).

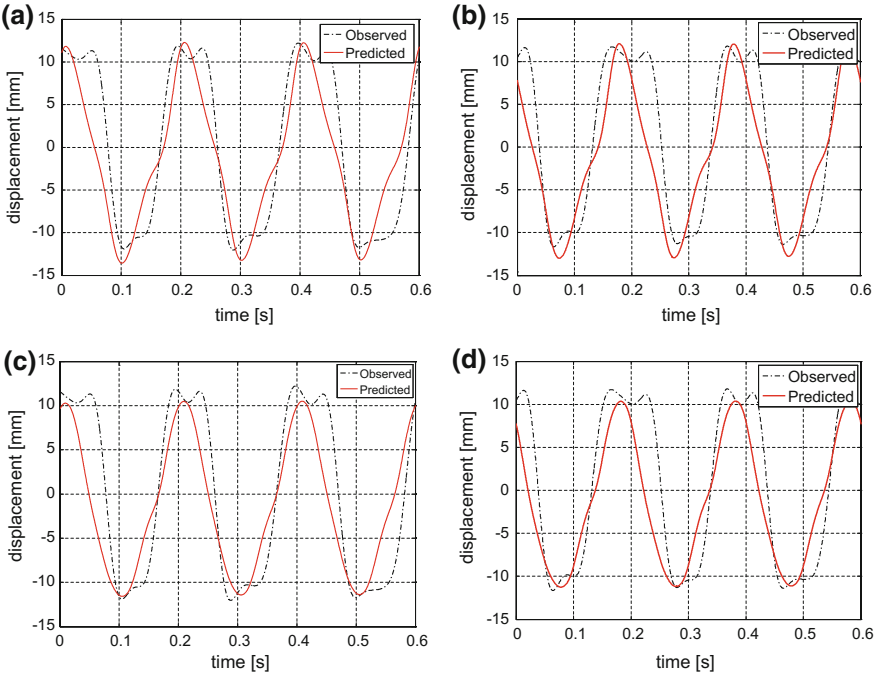

Fig. 2. Comparison of the experimental displacement of the beam in response to a sinusoidal stimulation at 5 Hz, for two values of the acceleration, 6.3 m/s^2 (**a**, **c**) and 7.3 m/s^2 (**b**, **d**) with the displacement predicted by the quartic model (**a**, **b**) and the hyperbolic model (**c**, **d**)

The fitting of the two investigated models with the hysteretic relationship of the accelerations versus displacement, in case of a sinusoidal stimulation of 6.3 m/s^2 at 6 Hz is shown in Fig. 4a, b, respectively.

Finally, a reconstruction of the potential by using the parameters identified for the two models is given in Fig. 5.

The results show a good fitting of both models with real data; however the model (5) shows a slightly better fit than the model (4). This difference stems from the (different) topologies of the potential energy functions in (2) and (3). Actually, potential (3) better describes the observed non-linearity of the device under investigation.

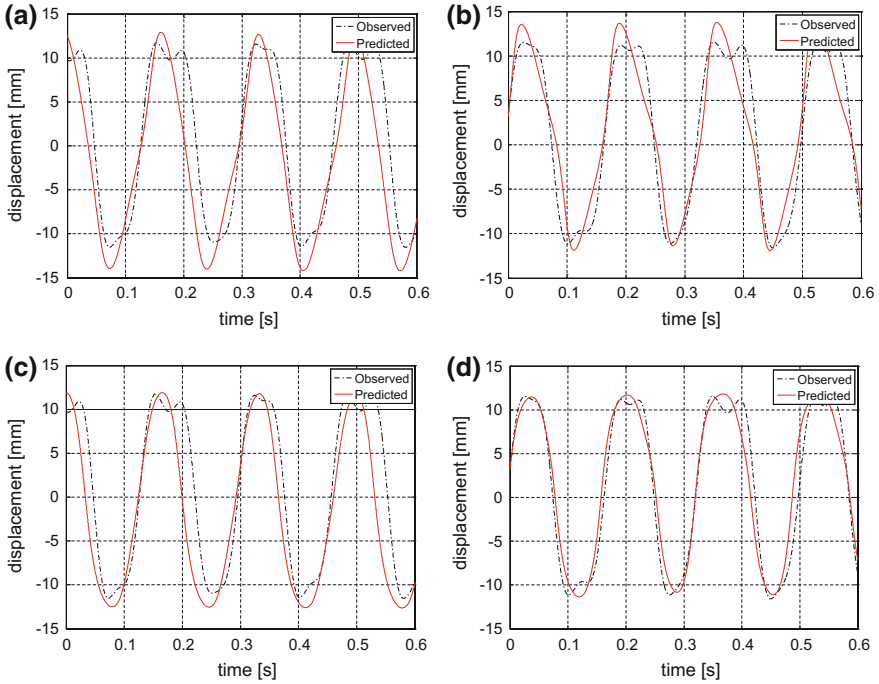

Fig. 3. Comparison of the experimental displacement of the beam in response to a sinusoidal stimulation at 6 Hz, for two values of the acceleration, 6.3 m/s^2 (**a**, **c**) and 7.3 m/s^2 (**b**, **d**) with the displacement predicted by the quartic model (**a**, **b**) and the hyperbolic model (**c**, **d**)

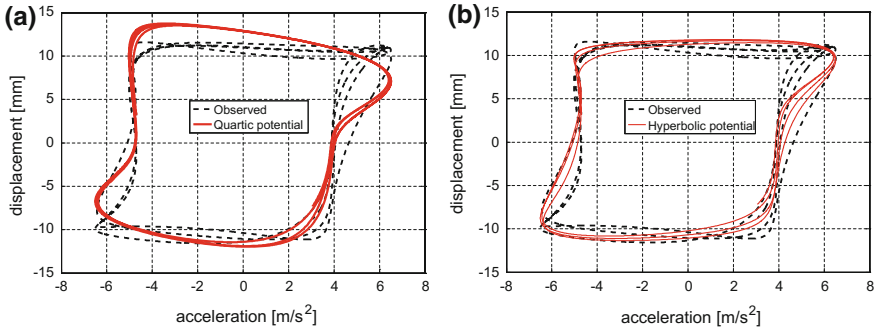

Fig. 4. The observed and predicted hysteresis of displacement versus acceleration in case of a sinusoidal acceleration of 6.3 m/s^2 at 6 Hz

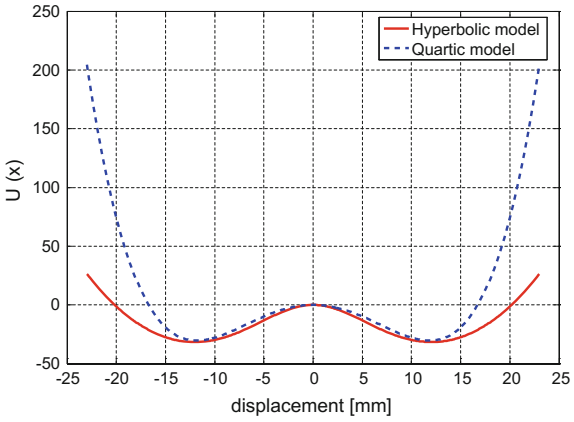

Fig. 5. Double-well potential reconstruction by using the parameters identified for the two models investigated

Acknowledgements. The authors gratefully acknowledge support from the US Office of Naval Research (ONR-30), and the Office of Naval Research Global (ONRG). This research activity is developed under the grant "Advanced nonlinear energy harvesters in the mesoscale: exploiting a Snap-Through Buckling configuration, for the autonomous powering of electronic devices. ONR_N62909-15-1-2015".

References

1. M. Ericka, D. Vasic, F. Costa, G. Poulain, Predictive energy harvesting from mechanical vibration using a circular piezoelectric membrane. Proc. IEEE Ultrason. Symp. **2**, 946–949 (2005)
2. D. Brunelli, C. Moser, L. Thiele, L. Benini, Design of a solar-harvesting circuit for batteryless embedded systems. IEEE Trans. Circ. Syst. I: Regul. Papers **56**(11), 2519–2528 (2009). doi:10.1109/TCSI.2009.2015690
3. S. Dalola, M. Ferrari, V. Ferrari, M. Guizzetti, D. Marioli, A. Taroni, Characterization of thermoelectric modules for powering autonomous sensors. IEEE Trans. Instrum. Measur. **58** (1), 99–107 (2009). doi:10.1109/TIM.2008.928405
4. P. Thurein, E.A. Falkenstein, R. Zane, Z. Popovic, Custom IC for ultralow power RF energy scavenging. IEEE Trans. Power Electron. **26**(6), 1620–1626 (2011). doi:10.1109/TPEL.2010.2096475
5. S. Roundy, P. Wright, J. Rabaey, A study of low level vibrations as a power source for wireless sensor nodes. Comput. Commun. **26**(11), 1131–1144 (2003)
6. M. Ferrari, V. Ferrari, M. Guizzetti, B. Andò, S. Baglio, C. Trigona, Improved energy harvesting from wideband vibrations by nonlinear piezoelectric converters. Procedia Chem. **1**(1), 1203–1206 (2009)
7. S. Baglio, A.R. Bulsara, B. Andò, S. La Malfa, V. Marletta, C. Trigona, P. Longhini, A. Kho, V. In, J.D. Neff, G.W. Anderson, C.C. Obra, B.K. Meadows, A. Palacios, Exploiting nonlinear dynamics in novel measurement strategies and devices: from theory to experiments and applications. IEEE Trans. Instrum. Meas. **60**(3), 667–695 (2011)

8. B. Andò, S. Baglio, A.R. Bulsara, V. Marletta, I. Medico, S. Medico, A double piezo—snap through buckling device for energy harvesting, in *IEEE 17th International Conference on Solid-State Sensors, Actuators and Microsystems (TRANSDUCERS & EUROSENSORS XXVII)*, Barcelona, 16–20 June 2013, pp. 43–45
9. B. Andò, S. Baglio, A.R. Bulsara, V. Marletta, Ass bistable buckled beam based approach for vibrational energy harvesting. Sens. Actuators, A **211**, 153–161 (2013)
10. B. Andò, S. Baglio, V. Marletta, E. Pergolizzi, V. Ferrari, M. Ferrari, A.R. Bulsara, Nonlinear snap-through-buckling devices for energy harvesting from vibrations. Lect. Notes Electr. Eng. **319**, 409–413 (2015)
11. B. Andò, S. Baglio, V. Marletta, A.R. Bulsara, A wireless sensor node powered by nonlinear energy harvester. IEEE Sens. Valencia, Spain, 2–5 Nov 2014
12. B. Andò, S. Baglio, A.R. Bulsara, V. Marletta, V. Ferrari, M. Ferrari, A low-cost snap-through buckling inkjet printed device for vibrational energy harvesting. IEEE Sens. J. **15**(6), 3209–3220 (2015)
13. B. Andò, S. Baglio, A.R. Bulsara, V. Marletta, A. Pistorio, Experimental and theoretical investigation of a nonlinear vibrational energy harvester. Eurosens. XXIX, Procedia Eng. 120, pp. 1024–1027, Freiburg, 2015, doi:10.1016/j.proeng.2015.08.701
14. B. Andò, S. Baglio, A.R. Bulsara, V. Marletta, A. Pistorio, A low threshold bistable device for energy scavenging from vibrations. IEEE Sens. Appl. Symp. (SAS), Catania, Italy, 20–22 April 2016. doi:10.1109/SAS.2016.7479816
15. B. Andò, S. Baglio, A.R. Bulsara, V. Marletta, A. Pistorio, Investigation of a nonlinear energy harvester. IEEE Trans. Instrum. Meas. doi:10.1109/TIM.2017.2663178, available from: http://ieeexplore.ieee.org/document/7858786/, Accessed: 23 March 2017
16. B. Andò, S. Baglio, V. Marletta, A. Pistorio, A.R. Bulsara, Performance investigation of a nonlinear energy harvester with random vibrations and subthreshold deterministic signals. IEEE Trans. Instrum. Meas. doi:10.1109/TIM.2017.2649998, available from: http://ieeexplore.ieee.org/document/7837607/, Accessed: 23 March 2017

Study on Impedance Behavior of a Telemetric System Operating with an Inkjet-Printed Resistive Strain Gauge

M. Bona[1], E. Sardini[1], M. Serpelloni[1(✉)], B. Andò[2], and C.O. Lombardo[2]

[1] Department of Information Engineering, University of Brescia, Via Branze 38, 25123 Brescia, Italy
mauro.serpelloni@unibs.it

[2] Department of Electric, Electronics and Computer Engineering, University of Catania, Viale A. Doria 6, 95125 Catania, Italy

Abstract. Devices that measure the strain applied to a body can find several applications in many fields, especially if they are able to satisfy precise specifications about power supply and transmission of information. Telemetric systems offer a viable solution, since they rely on the inductive coupling between the coils connected to a passive sensor and a readout unit. Therefore, they require neither batteries nor wired connections. The present work illustrates a preliminary analysis on a telemetric device made of Printed Circuit Board (PCB) planar inductors and a resistive strain gauge fabricated through inkjet printing on a flexible substrate. We carried out experimental tests to evaluate system frequency behaviour. Firstly, we measured its impedance phase at readout inductor terminals while varying sensor resistance, with the inductors put at a fixed relative distance. Then, we repeated the same operation when that distance changed, with strain gauge at rest position. Obtained results report a total variation of phase most sensitive point of about 0.12° for a strain equal to 1% of sensor length at rest, suggesting that measuring strain with such a structure is feasible. On the other hand, they highlight that distance variation has a strong influence on that result; thus, it has to be taken into account during measurement process.

Keywords: Impedance phase · Inkjet printing · Strain measurement · Telemetric system

1 Introduction

Measuring strain is fundamental for applications dealing with Structural Health Monitoring (SHM) [1], which range from transportation [2], to building [3] fields. They aim at acquiring important information about the condition of systems, like vehicles and civil infrastructures, in order to prevent their failures [1]. In fact, such events could have a tremendous impact on human safety and have high costs to be solved. Furthermore, strain is a magnitude exploited also in medical sector to control vital parameters like bladder volume [4] or joint angles during movement [5].

B. Andò et al. (eds.), *Sensors*, Lecture Notes in Electrical Engineering 431,
DOI 10.1007/978-3-319-55077-0_34

Currently, there are a lot of devices employed to perform strain measurement. Among all the examples, literature reports the use of strain gauges [6], optical fiber-based instruments [7] and piezoelectric sensors [8]. However, these devices need meeting strict requirements that concern power supplies and data transmission, especially when they have to operate in environments that require to be kept isolated from the outside or are characterized by harsh working conditions. For instance, use of batteries or wired connections is unsuitable, since it would imply a perturbation (at least periodic) of the environment. On the other hand, active circuits could not withstand its harsh characteristics. In addition, device costs and dimensions should not be too high.

A viable solution is given by telemetric systems. They are made of a readout module that supplies a passive sensor and receives strain information from it, thanks to the inductive coupling generated between two inductors, one connected to the former and one to the latter, respectively. With such a structure, sensing circuit composed by sensor and the corresponding inductor can be put inside measurement environment and it can work without batteries or cables. On the other side, information is treated by readout module positioned outside.

Most telemetric systems described in the literature operate with inductive [9] or capacitive [10] sensing elements. They present a LC oscillator as sensing circuit, whose resonant frequency is detected, since it varies as strain changes. On the contrary, this work illustrates an analysis carried out on a device equipped with a strain gauge that has a resistive output. In addition, sensor has been fabricated through inkjet printing on a flexible substrate. This is a promising technology for the easy production of cheap components [6]. In fact, a common CAD software can be used to draw a pattern followed by the printer during ink deposition, whereas its process does not require masks or complex treating steps. Furthermore, realized elements have good characteristics [6] and they can be printed on materials that adapt to different surfaces.

Next section will describe the parts that form this system. Then, performed studies will be illustrated and obtained results will be reported.

2 Telemetric System with an Inkjet-Printed Sensor

Figure 1 represents telemetric system scheme, together with its components. Inkjet-printed strain gauge was made by using silver nanoparticles-based ink Metalon® JS-015, from NovaCentrix, deposited on a flexible substrate of Polyethylene terephthalate (PET). Table 1 lists its characteristics.

In particular, we measured its output at rest with digital multimeter 34401 A, from Agilent, whereas we obtained an estimation for its gage factor through a specific analysis for its characterization.

Planar inductors were realized through common PCB techniques, on a rigid substrate of FR4 epoxy glass. The one joined to printed strain gauge is called “sensing inductor”, whereas that connected to readout module is named “readout inductor”. Their properties are reported in Table 2.

Electrical characteristics, i.e. inductance, parasitic resistance and parasitic capacitance, are the elements of an equivalent circuit used to represent the inductors [11]. We

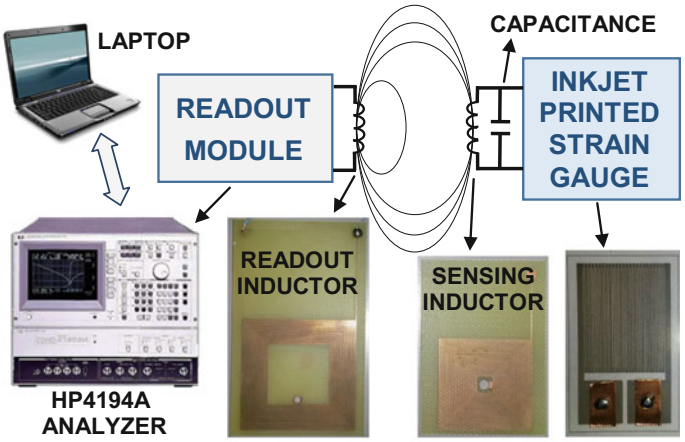

Fig. 1. Scheme of the presented telemetric system with its components

Table 1. Printed sensor characteristics

Property	Value
Length at rest position	27 mm
Width at rest position	20 mm
Ink layer thickness	1.9 μm
PET substrate thickness	200 μm
Ink resistivity	4.5 μΩ cm
Output at rest position	2.3 kΩ
Gage factor	3.6

Table 2. Planar inductors characteristics

Property	Value for readout inductor	Value forsensing inductor
Outer side (mm)	50	27
Inner side (mm)	27	5
Number of windings	28	27
Windings width (μm)	150	200
Space between windings (μm)	300	250
Inductance (μH)	47.7	11.6
Parasitic resistance (Ω)	35.3	9.4
Parasitic capacitance (pF)	3.3	2.1

found them with an HP4194A impedance analyzer. Then, we added a commercial capacitance equal to about 560 pF in parallel to sensing inductor in order to adjust its resonant frequency to a desirable value.

Finally, readout module is composed of HP4194A impedance analyzer for system frequency analysis, which interfaces with a laptop via a GPIB-USB high-speed controller from National Instruments.

3 Study on the System

We analyzed system frequency behavior to investigate the possibility of measuring strain through telemetric techniques, by measuring its electrical impedance at readout inductor terminals.

3.1 Experimental Setup

We performed experimental tests on the setup whose scheme is illustrated in Fig. 2. Strain gauge was kept at the right position through the apparatus shown in Fig. 3. We immobilized one of its edges to a fixed support, while the other was clamped to another structure that could move along its longitudinal axis thanks to a micrometric screw with a resolution of 10 μm.

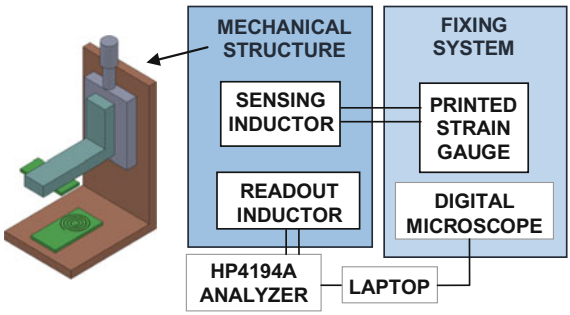

Fig. 2. Scheme of the setup used to carry out the experimental tests

We used both screw graduated scale and a digital microscope to evaluate such movement. Then, we maintained the inductors parallel and coaxial thanks to a mechanical structure whose supports can be moved through micrometric screws. It is exploited also to set the correct distance between them. Finally, readout inductor was connected to HP4194A analyzer, driven by laptop for impedance detection.

3.2 Strain Variation

During the first kind of tests, we applied an increasing pulling force on the sensor, with the aid of fixing system micrometric screw, in order to induce different levels of deformation to it, until about 1% of its length at rest was achieved. After each step, we have been maintaining the reached position for about a minute. We used the digital

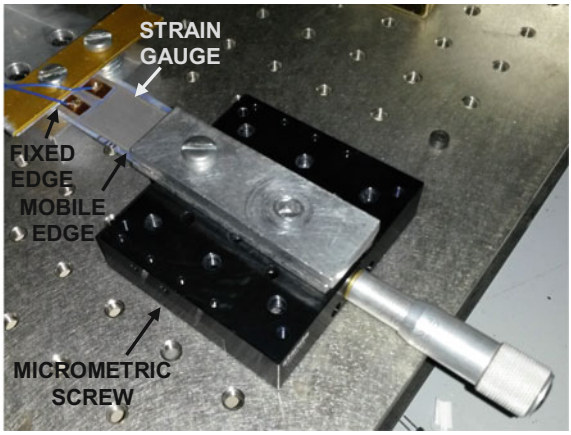

Fig. 3. System for strain gauge fixing

microscope as an aid to assess the actual elongation. Distance between the inductors was kept fixed at 12 mm. At the same time, we continuously executed a frequency sweep from 1.5 to 2.3 MHz and we acquired data about impedance phase variation due to a change in sensor output. Furthermore, readout module saved all the information for further elaboration.

3.3 Distance Variation

During the second tests, we moved mechanical structure supports to change the distance between the inductors from 6 to 20 mm, whereas we maintained the strain gauge at rest position. As before, for each distance reached (verified through screws graduated scale), we detected impedance phase in a frequency interval from 1.5 to 2.3 MHz, and we saved all the data.

4 Results and Discussion

4.1 Strain Variation

Figure 4 shows some of the obtained curves of impedance phase φ as a function of frequency f, each corresponding to an achieved strain level. An inset highlights the frequency range around phase minimum φ_{min}. It helps to appreciate that impedance varies when an increasing pulling force is applied to the sensor, for a distance between the inductors kept fixed. In fact, sensor resistance augments, affecting whole system frequency response.

In our analysis, we focused on phase minimum, since it is the point most sensitive to deformation variation. Figure 5 reports its trend as a function of strain ε. We found that, during the entire test, it changed from about 72.79° to about 72.67°, i.e. an average total decrease of about 0.12°. Despite this limited quantity, we were able to distinguish

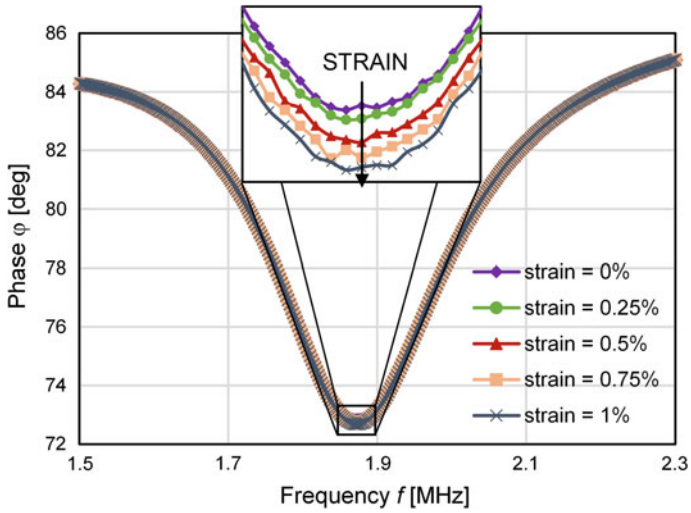

Fig. 4. Curves of system impedance phase φ as a function of frequency f. Each curve corresponds to a different level of achieved strain. Distance between the inductors is fixed to 12 mm

a linear dependence of phase on strain (in fact, coefficient of determination R^2 is more than 0.99). Furthermore, maximum deviation from mean values was about 0.005°. These results allow to observe the feasibility of a methodology based on finding the strain applied to a sensor (in particular, to an inkjet-printed element) in an indirect way, i.e. starting from an analysis of whole system impedance.

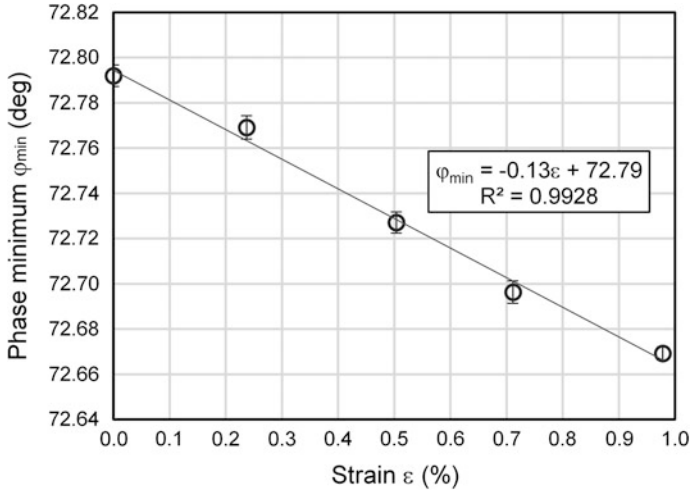

Fig. 5. Impedance phase minimum φ_{min} as a function of strain ε

4.2 Distance Variation

Figure 6 reports some of the phase curves acquired during the second analysis, for every considered distance *d*.

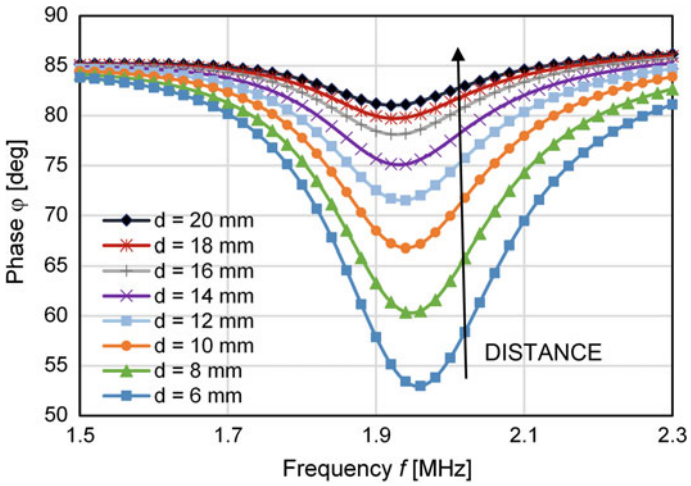

Fig. 6. Curves of system impedance phase φ as a function of frequency *f*, for different distances *d* between the inductors. Strain gauge is at rest position

They highlight that such variable affects heavily system impedance, compared to a change in sensor output (even considering the huge entity of its variation), since it has a big effect on the inductive coupling between the coils [11]. In particular, phase minimum presents a total decrease of about 28° when they get closer up to 6 mm, as illustrated in Fig. 7, which shows it as a function of distance. Therefore, they have to be kept always at a constant relative position during measurement procedure, in order to avoid distance influence to lead to mistakes that could compromise a correct strain estimation. Furthermore, Fig. 6 indicates that, the more they get far from each other, the more difficult is to detect a change in system frequency response. For this reason, they have to be placed in a suitable position.

In addition, we interpolated phase minimum points, finding that their trend follows a second-order polynomial function (with a coefficient of determination R^2 greater than 0.999), whose equation is reported in Fig. 7. Such expression could be exploited to predict system behavior at a specific distance.

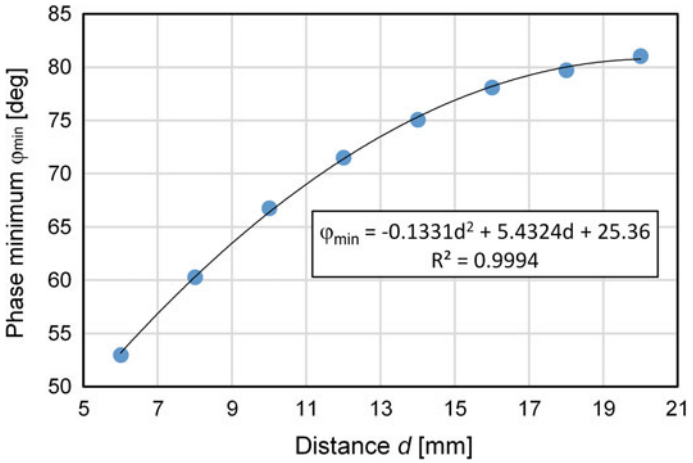

Fig. 7. Impedance phase minimum φ_{min} as a function of distance d between the inductors

5 Conclusions

This work has presented a study on a telemetric device made of PCB inductors and a resistive strain gauge fabricated through inkjet printing on a flexible substrate. Firstly, we analyzed system frequency response by reading its impedance phase when a pulling force was applied to the sensor, while inductors were at a fixed relative distance. Then, we repeated the same measurement, but when the inductors got closer, with strain gauge at rest position. After having illustrated the system, used experimental apparatuses have been described. Afterwards, performed tests and achieved results have been presented. On one side, they demonstrate the feasibility of finding information on the output of an inkjet-printed sensor from a reading of whole system impedance, showing that such a device could be useful when measurement environment does not permit to employ components such as cabled connections, batteries or active circuits. On the other side, distance between the inductors is a variable that could potentially affect final strain estimation; thus, it should be kept fixed during measurement procedure or, as an alternative, its variation should be compensated.

References

1. A. Deivasigamani, A. Daliri, C.H. Wang, S. John, A review of passive wireless sensors for structural health monitoring. Mod. Appl. Sci. **7**(2), 57–76 (2013)
2. R. Matsuzaki, A. Todoroki, Wireless strain monitoring of tires using electrical capacitance changes with an oscillating circuit. Sens. Actuators A Phys. **119**(2), 323–331 (2005)
3. K.J. Loh, J.P. Lynch, N.A. Kotov, Passive wireless strain and pH sensing using carbon nanotube-gold nanocomposite thin films, in *Proceedings of SPIE, Sensors and Smart Structures Technologies for Civil, Mechanical, and Aerospace Systems* **6529**, 652919/1-652919/12 (2007)

4. H. Cao, S.K. Thakar, T. Fu, M. Sheth, M.L. Oseng, V. Landge, Y. Seo, J.-C. Chiao, A wireless strain sensor system for bladder volume monitoring, in *Proceedings of IEEE MTT-S International Microwave Symposium Digest (MTT)*, 5–10 June 2011, Baltimore (MD), 1–4 (2011)
5. H. Nakamoto, H. Ootaka, M. Tada, I. Hirata, F. Kobayashi, F. Kojima, Stretchable strain sensor with anisotropy and application for joint angle measurement. IEEE Sens. J. **16**(10), 3572–3579 (2016)
6. B. Andò, S. Baglio, All-inkjet printed strain sensors. IEEE Sens. J. **13**(12), 4874–4879 (2013)
7. K. Bhowmik, G.-D. Peng, Y. Luo, E. Ambikairajah, V. Lovric, W.R. Walsh, G. Rajan, High intrinsic sensitivity etched polymer fiber Bragg grating pair for simultaneous strain and temperature measurements. IEEE Sens. J. **16**(8), 2453–2459 (2016)
8. T. Kobayashi, T. Yamashita, N. Makimoto, S. Takamatsu, T. Itoh, Ultra-thin piezoelectric strain sensor 5×5 array integrated on flexible printed circuit for structural health monitoring by 2D dynamic strain sensing, in *Proceedings of 29-th International Conference on Micro Electro Mechanical Systems (MEMS)*, 24–28 Jan 2016, Shanghai (China), (2016), pp. 1030–1033
9. J.C. Butler, A.J. Vigliotti, F.W. Verdi, S.M. Walsh, Wireless, passive, resonant-circuit, inductively coupled, inductive strain sensor. Sens. Actuators, A Phys. **102**(1–2), 61–66 (2002)
10. Y. Jia, K. Sun, F.J. Agosto, M.T. Quiñones, Design and characterization of a passive wireless strain sensor. Meas. Sci. Technol. **17**(11), 2869–2876 (2006)
11. D. Marioli, E. Sardini, M. Serpelloni, A. Taroni, A new measurement method for capacitance transducers in a distance compensated telemetric sensor system. Meas. Sci. Technol. **16**(8), 1593–1599 (2005)

Breath Analysis by a GC/MS Coupled to a Gas Sensor Detector

S. Capone[1(✉)], M. Tufariello[2], A. Forleo[1], F. Casino[1], and P. Siciliano[1]

[1] National Research Council of Italy, Institute for Microelectronics and Microsystems (CNR-IMM), Via Monteroni, Campus Universitario, 73100 Lecce, Italy
simonetta.capone@cnr.it, {angiola.forleo, flavio.casino, pietro.siciliano}@le.imm.cnr.it

[2] National Research Council of Italy, Istituto di Scienze delle Produzioni Alimentari, via Monteroni, Campus Universitario, 73100 Lecce, Italy
maria.tufariello@ispa.cnr.it

Abstract. A peculiar experimental configuration of a gas chromatograph (GC) coupled, by a splitter, to two detectors, i.e. a mass spectrometer (MS) and a semiconducting gas sensor (SGS), operating in dual mode, was arranged. A suitable breath sampling system was used to sample the alveolar air volume in a bag from the air volume of a single expiration by discarding the dead volume. Breath volatiles (VOCs) were isolated and preconcentrated by solid-phase microextraction (SPME). Breath tests on alveolar air sampled by a sample of smokers volunteers were carried out. Statistical analysis techniques (descriptive statistics, Mann-Whitney test, PCA, Probit nonlinear regression model) applied to GC-MS data and sensor data showed good results in discriminating the subset of smokers sampled in resting condition ("blank" smokers) and after the action of smoking a cigarette.

Keywords: Gas sensor · Breath analysis · Smokers

1 Introduction

Nowadays it's widely recognized the powerful potential of breath analysis for disease diagnostics and metabolic status monitoring. On one side, scientific research is devoting a lot of efforts in identifying markers of pathologies in exhaled breath by advanced analytical technologies, as gas chromatography combined with mass spectrometry (GC-MS), ion mobility spectrometry (IMS), proton transfer reaction mass spectrometry (PTR-MS), selected ion flow tube mass spectrometry (SIFT-MS) [1–4]. On the other side, instruments as Electronic Noses (e-Noses) mainly based on semiconducting gas sensors (SGS), offer a quick and easy-to-use tool for breath analysis alternative to the above mentioned complex spectrometry techniques. E-Noses devices are small and portable and they have a potential for point of care applications and in disease screening in population [5–8, 18–20].

B. Andò et al. (eds.), *Sensors*, Lecture Notes in Electrical Engineering 431,
DOI 10.1007/978-3-319-55077-0_35

In this work, we try to combine an advanced analytical technique as GC-MS with a semiconducting gas sensor (SGS) in order to study the ability of SGS to detect breath VOCs eluting from the gas chromatographic column. This approach looks to the development of hybrid device based on miniaturized gas chromatographs using gas sensors detector.

As applicative study we used our experimental system in the analysis of the smoking status. From a clinical point of view, there is a need for method to detect active smoking. This is because some patients do not admit to being smokers and recognize smoking a smaller numbers of cigarettes than what has actually been smoked. Moreover, it well recognized that smoking habit is a risk factor for lung diseases, such as lung cancer, chronic bronchitis and emphysema. Different VOCs have been proposed as smoking breath biomarkers (carbon monoxide, 2,5-dimethylfuran, benzene, toluene, xylene, 1,3-butadiene, acetonitrile), but the correlation between a single compound and proof of smoking habit is complex and dependent on other factors (other exogenous sources different from cigarettes, co-indication of other diseases different from smoking, heavily time dependent concentrations, large variability) [9–17].

Here, we identified and quantified the VOCs present in the alveolar breath samples of a small group of smokers, sampled both in resting condition and after a recent action of cigarette smoke. We used the pattern of the only VOCs with statistically relevance to perform statistical analysis (Mann-Whitney test, predictive Progit model) in order to asses recent smoke use. The same statistical analysis techniques were also applied to the continuous sensorgrams (i.e. electrical sensor signals vs. time), preprocessed by Principal Component Analysis (PCA).

2 Materials and Methods

2.1 Subjects

Breath analyses were conducted in 16 healthy adult volunteers with smoking habits. The smokers individuals (cod. Fi_jbag, i = 1, …, 16, j = 1, 2, 3) were asked to fill three bags in different times: 1° bag, early morning fasting before smoking first cigarette (resting condition, “blank smokers”), 2° bag after smoking 1° daily cigarette and 3° bag after n-cigarette daily smoking event. We collected total 48 bags from smokers. In Fig. 1 a scheme of the study design and groups definition is shown.

2.2 Breath Sampling

We sampled the alveolar air of the smokers volunteers by a commercial breath sampling system (QUINTRON, USA). The system consisting in a special 3-way valve and two bags is able to discard the expired air contained in the first respiratory airways (dead-volume) and collect the only alveolar air. A closed 1-way stopcock has to be inserted into a small Luer Port on the alveolar air collecting bag prior to breath sampling. The patient is asked for doing a single deep exhalation through the mouthpiece of the system. When discard bag is full, a membrane-valve opens automatically and the second bag fills with the alveolar breath.

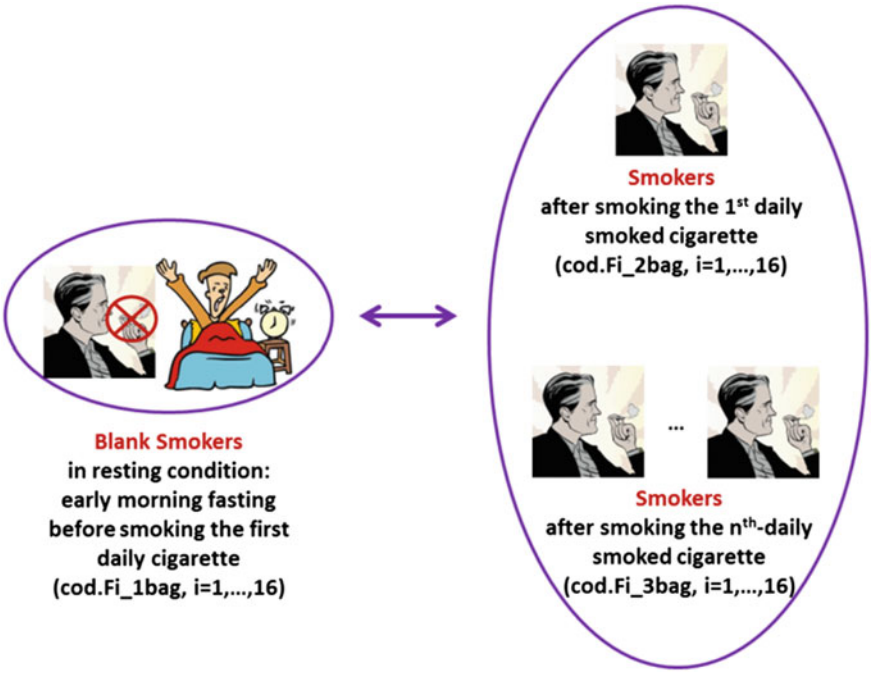

Fig. 1. Scheme of the study design and groups definition

2.3 Experimental Procedure

We arranged an uncommon and peculiar configuration of a gas chromatograph (GC) coupled, by a splitter, to two detectors, i.e. a mass spectrometer (MS) and a semiconducting gas sensor (SGS), operating in dual mode. The experimental set-up is sketched in Fig. 2. The GC-MS analysis was performed on Agilent 5973 mass spectrometer (MSD) coupled with 6890 N series gas chromatograph (Agilent Technologies) with a split-splitless injector. The injector temperature was 250 °C. A DB-WAX capillary column (60 m, 0.25 mm I.D., 0.25 μm thickness) was used. The oven temperature program was as follows: initial 40 °C held for 5 min; them ramped at 3 °C/min to 140 °C held for 10 min, then ramped to 230 °C and held for 3 min. Electron impact ionization was applied at 70 eV. The MS analyses were carried out in full-scan mode with a scan range 30–500 amu at 3.2 scans/s. The identification of the volatile compounds were achieved by comparing mass spectra with those of the data system library (NIST 98, $P > 80\%$). A manual SPME holder with black coated fiber (Supelco, Bellefonte, USA) was introduced in the septum adjusted in the Luer port of the bag, and the fiber exposed to collected alveolar air for 30 min. During SPME exposure the bag was heated at 38 °C to avoid breath sample condensation. Semi-quantitative analysis method by an Internal standard (bromobenzene, 23 ppbv), added by a suitable multi-steps dilution into the collecting bag, was used.

A tiny home-made sensor-chamber in Teflon was adjusted at the second detector port of the gas chromatograph; the reduced size of the cell was necessary not to lose the

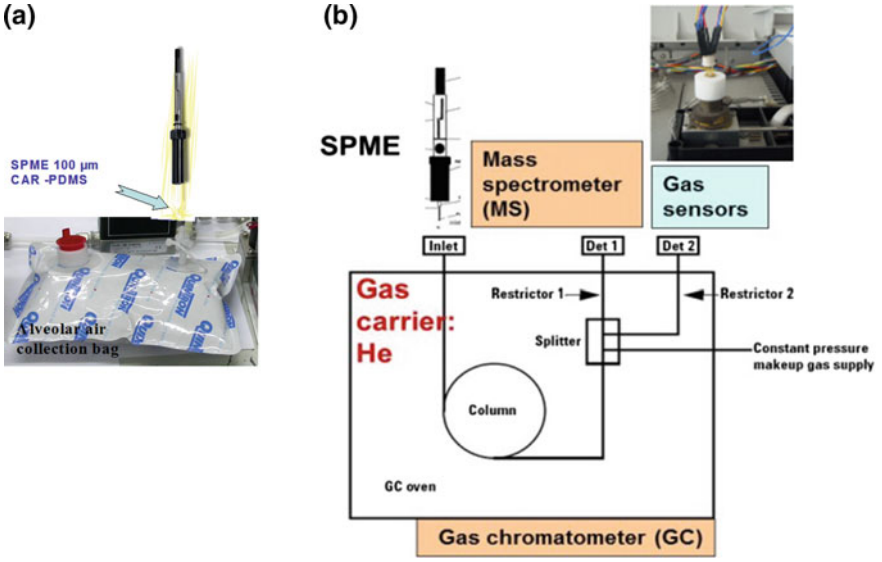

Fig. 2. **a** Exposure of the SPME fiber into the alveolar air collection bag; **b** scheme of the Gas Chromatograph (GC) equipped with a splitter to two ports, where two different detectors, i.e. Mass Spectrometer (MS) and semiconducting gas sensor (SGC), are placed

GC system's ability to temporally separate the compounds eluting from the column. A commercial micromachined SnO_2-based sensor (Silsens srl, Switzerland) was used as semiconducting gas sensor. The sensor resistance was read by a Keithley 2700 multimeter. After SPME injection, for each collected breath sample chromatogram and sensorgram were acquired simultaneously in the same run test.

3 Results

Our experimental set-up gave us the opportunity to join two goals: (1) study the altered breath composition after smoking, by identifying the chemical pattern of VOCs present in the breath of a smoker, and (2) evaluate the sensing properties of a semiconducting gas sensor to these breath VOCs. As an example, a temporal overlapping of a chromatogram and the corresponding sensorgram during a run test is showed in Fig. 3 for a smoker F8 after her 1st daily smoked cigarette (sample cod.F8_2bag). It can be observed that the resistance of the sensor varies during the chromatographic run following the elution of the compounds from the column. Therefore, the modulation of the sensor signal, containing the information on the composition of the sample analyzed, demonstrates the feasibility of using the sensor as a gas chromatograph detector Next, the dual signals (chromatogram and sensorgram) for all the breath samples of the experimental campaign were used in the statistical analysis aiming to identify the VOCs markers of the recent use of tobacco and classify the subset group of smokers after a smoking event to the subset of the same smokers in resting condition.

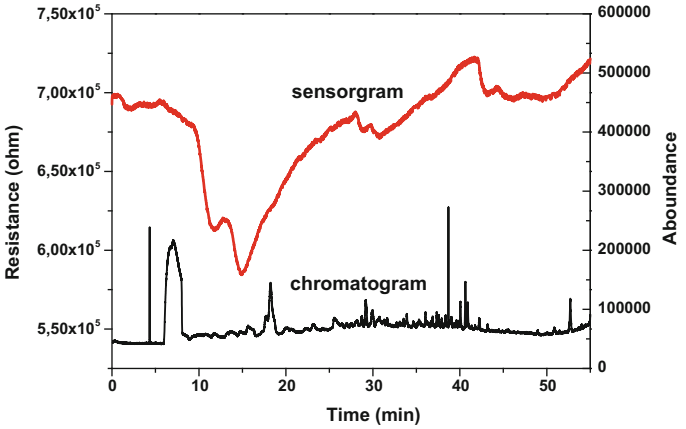

Fig. 3. Run test for a smoker individual after the 1st daily smoked cigarette (cod.F8_2bag)

Eighty-three different compounds were identified in collected breath samples by GC/MS analysis. Their concentration was calculated by normalizing picks areas to internal standard area and referring to its concentration. For calculations of statistical significance, two-sided testing was used, and $p < 0.05$ was considered as significant. In particular, a non-parametric statistical test (Mann-Whitney test) was used to compare the "blank smokers" group with the group of smokers after a smoking action and select the most significant statistical differences in terms of VOCs variables. The statistical relevant variables were: (a) toluene, (b) pyridine, (c) pyrrole, (d) benzene, (e) 2-butanone, (f) 2-pentanone, (g) 1-methyldecyclamine.

Descriptive statistic results (median, 25th–75th percentiles, minimum/maximum) for these compounds were calculated; we found that the action of smoking a cigarette altered the breath pattern by increasing the levels of the identified VOCs with statistical relevance. As an example, the box-whisker plot related to toluene (concentrations are in ppbv) for "blank smokers" and smokers groups is shown in Fig. 4.

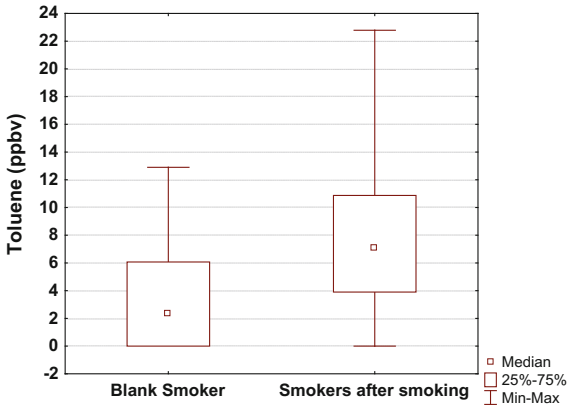

Fig. 4. Box-whiskers box plot related to toluene (concentrations are in ppbv) for "blank smokers and smokers groups"

In a next step we performed a predictive regression analysis. For GC-MS based data, we didn't consider the 7 individual VOCs with statistical relevance as breath markers of the recent use of tobacco, attributing to each of them a predictive power; whereas we used their pattern to assess if a smoking event occurred, hence attributing to the 7-VOCs chemical patterns a marker characteristic. At this aim by non linear Probit Regression was applied to the matrix of 7-VOCs predictors and a prediction of class membership to the groups of "blank" smokers and smokers after smoking was get. In this case a very good prediction ($p < 0.01$) was obtained with both high sensitivity (84%) and specificity (100%) (Table 1). The high sensitivity means that it's possible to correctly detect smokers, who effectively smoked before testing, as smokers after a smoking event. The full specificity means that it's possible to correctly identify smokers, who effectively abstained from smoking before testing. Such information are fundamental for doctors to assess the degree of compliance with a smoking cessation program.

Table 1. Confusion matrix of predictive Progit model ($p = 0.0000016$) applied to GC-MS data

		True condition	
		Condition positive (smoker after smoking)	Condition negative ("blank" smoker)
Predicted condition	Predicted condition positive (smoker after smoking)	**True positive (TP) = 27**	**False positive (FP) = 0**
	Predicted condition negative ("blank" smoker)	**False negative (FN) = 5**	**True negative (TN) = 16**
	Accuracy (ACC) = (TP + TN)/ Total population = 89%	**Sensitivity or true positive rate TPR = TP/ (TP + FN) = 84%**	**False positive rate** (FPR) or Fall-out = 1−SPC = 0%
		False negative rate (FNR), **miss rate = FN/ (FN + TP) = 16%**	**Specificity** (SPC) or true negative rate (TNR) TNR = TN/ (TN + FP) = 100%

For sensor-based data, sensorgrams were preprocessed by Principal Component Analysis. Mann-Whitney test selected the PCs with statistical relevance ($p < 0.05$) and the patterns of these PCs were used as predictive variables in the Probit model. Table 2 shows the confusion matrix of predictive Progit model ($p = 0.0088170$) applied to sensor data. The results can be considered satisfactory.

Table 2. Confusion matrix of predictive Progit model ($p = 0.0088170$) applied to sensor data

		True condition	
		Condition positive (smoker after smoking)	Condition negative ("blank" smoker)
Predicted condition	Predicted condition positive (smoker after smoking)	**True positive** (TP) = 30	**False positive** (FP) = 4
	Predicted condition negative ("blank" smoker)	**False negative** (FN) = 2	**True negative** (TN) = 12
	Accuracy (ACC) = (TP + TN)/ Total population = 87.5%	**Sensitivity** or true positive rate TPR = TP/ (TP + FN) = 93.75%	**False positive rate** (FPR) or Fall-out = 1−SPC = 25%
		False negative rate (FNR), Miss rate = FN/ (FN + TP) = 6.25%	**Specificity** (SPC) or True Negative Rate (TNR) TNR = TN/ (TN + FP) = 75%

4 Conclusion

An unconventional experimental configuration of a gas chromatograph (GC) coupled to two detectors (Mass Spectrometer, MS) and a semiconducting gas sensor was satisfactory arranged. The experimental set-up was exploited in a challenging application of breath analysis. In particular, we consider smokers volunteers as a natural study group of healthy individuals for testing whether breath analysis can be used to recognize the recent use of tobacco. As consequence of an action of smoking a cigarette the levels of some VOCs (toluene, pyridine, pyrrole, benzene, 2-butanone, 2-pentanone, 1-methyldecyclamine) in the exhaled air, increase compared to the reference levels in the breath profile of a "blank" smoker who really observed abstinence from smoking. Our statistical approach to data analysis was based on filtering the statistical relevant variables (VOCs), that highlight the differences between two groups ("blank smokers" and smokers after smoking) by non-parametric Mann-Whitney test, and in using the breath patterns of statistically relevant VOCs to assess the membership to the two classes under analysis by non-linear Probit regression model. The results of the prediction model based on GS-MS dataset showed that it's easily possible recognize with high specificity and sensitivity if a smoking event occur.

Moreover the gas sensor demonstrates its reliability as detector, and the predictive model applied to the sensor-based data (preprocessed by PCA and Mann-Whitney test) gave fair results.

However, at present the small sample size used in this study doesn't allow to establish statistically significant correlations for biomedical considerations. Larger data set are needed. Work is in progress to extend the experimental campaign to non-smokers volunteers aiming to evaluate which pattern of VOCs is able to distinguish a non-smoker from a smoker.

References

1. J. Pereira, P. Porto-Figueira, C. Cavaco, K. Taunk, S. Rapole, R. Dhakne, H. Nagarajaram, J. S. Camara, Breath analysis as a potential and non-invasive frontier in disease diagnosis: an overview. Metabolites **5**, 3–55 (2014)
2. N.J.W. Rattray, Z. Hamrang, D.K. Trivedi, R. Goodacre, S.J. Fowler, Taking your breath away: metabolomics breathes life into personalized medicine. Trends Biotechnol. **32**(10), 538–548 (2014)
3. A.W. Boots, J.J.B.N. van Berkel, J.W. Dallinga, A. Smolinska, E.F. Wouters, F.J. van Schooten, The versatile use of exhaled volatile organic compounds in human health and disease. J. Breath Res. 6, 027108 (21 pp) (2012)
4. G. Pennazza, M. Santonico, E. Martinelli, A.D'Amico, C.Di Natale, Interpretation of exhaled volatile organic compounds. chap.8. Exhaled Breath—Eur. Res. Monogr. **49** September 2010, pp. 115–119
5. A. Bikov, Z. Lázár, I. Horvath, Established methodological issues in electronic nose research: how far are we from using these instruments in clinical settings of breath analysis? J. Breath Res. **9**, 034001 (2015)
6. A.D. Wilson, Advances in electronic-nose technologies for the detection of volatile biomarker metabolites in the human breath. Metabolites **5**, 140–163 (2015)
7. C. Di Natale, R. Paolesse, E. Martinelli, R. Capuano, Solid-state gas sensors for breath analysis: a review. Anal. Chim. Acta **824**, pp. 1–17 (2014)
8. W.H. van Geffen, M. Bruins, H.A.M. Kerstjens, Diagnosing viral and bacterial respiratory infections in acute COPD exacerbations by an electronic nose: a pilot study. J. Breath Res. **10**, 036001 (2016)
9. S.M. Gordon, L.A. Wallace, M.C. Brinkman, P.J. Callahan, D.V. Kenny, Volatile organic compounds as breath biomarkers for active and passive smoking. Environ. Health Perspect. **110**, 689–698 (2002)
10. A.H. Kendrick, Exhaled carbon monoxide devices in smoking cessation: physiology, controversies and equipment. The buyers' guide to respiratory care products, **13**, 180–189, © GASP 0117 955 0101
11. A. Sandberg, C.M. Sköld, J. Grunewald, A. Eklund, Å.M. Wheelock, Assessing recent smoking status by measuring exhaled carbon monoxide levels. PLoS ONE **6**(12), e28864 (2011)
12. N. Al-Sheyab, K. A. Kheirallah, L.J. Thomson Mangnall, R. Gallagher, Agreement between exhaled breath carbon monoxide threshold levels and self-reported cigarette smoking in a sample of male adolescents in Jordan. Int. J. Environ. Res. Public Health **12**, pp. 841–854 (2015)
13. M. Alonso, M. Castellanos, J.M. Sanchez, Evaluation of potential breath biomarkers for active smoking: assessment of smoking habits. Anal. Bioanal. Chem. **396**, 2987–2995 (2010)
14. B. Buszewski, A. Ulanowska, T. Ligor, N. Denderz, A. Amann, Analysis of exhaled breath smokers, passive smokers and non-smokers by solid-phase microextraction gas chromatography/mass spectrometry. Biomed. Chromatogr. **23**, 551–556 (2009)
15. P. Lirk, F. Bodrogi, M. Deibl, Ch. Kähler, J. Colvin, B. Moser, G. Pinggera, H. Raifer, J. Rieder, W. Schobersberger, Quantification of recent smoking behaviour using proton transfer reaction-mass spectrometry (PTR-MS). Wien. Klin. Wochenschr. **116**(1–2), 21–25 (2004)
16. E. Crespo, S. Devasena, C. Sikkens, R. Centeno, S.M. Cristescu, J.M. Harren, Frans, "Proton-transfer reaction mass spectrometry (PTRMS) in combination with thermal

desorption (TD) for sensitive off-line analysis of volatiles". Rapid Commun. Mass Spectrom. **26**, 990–996 (2012)
17. J.J. Jarẽno-Esteban, M. Ángeles Munoz-Lucas, B. Carrillo-Aranda, J.Á. Maldonado-Sanz, I. de Granda-Orive, A. Aguilar-Ros, C. Civera-Tejuca, C. Gutiérrez-Ortega, L.M. Callol-Sánchez, Volatile organic compounds in exhaled breath in a healthy population: effect of tobacco smoking. Arch Bronconeumol. **49**(11), 457–461 (2013)
18. Z.J. Cheng, G. Warwick, D. H. Yates, P.S. Thomas, An electronic nose in the discrimination of breath from smokers and non-smokers: a model for toxin exposure. J. Breath Res. **3**, 036003 (5 pp) (2009)
19. K. Witt, S. Reulecke, A. Voss, Discrimination and characterization of breath from smokers and non-smokers via electronic nose and GC/MS analysis, in *Proceedings of the 33rd Annual International Conference of the IEEE EMBS*, pp. 3664–3667 (2011)
20. S. Capone, L. Mazzotta, L. Francioso, M. Epifani, P. Siciliano, Gas microsensor array for breath analysis: an explorative study of smoking status risk, in *Proceedings of 4th IEEE International Workshop on Advances in Sensors and Interfaces (IWASI)*, pp. 121–124, Article number 6004700 (2011)

Multi-sensor Platform for Detection of Anomalies in Human Sleep Patterns

Andrea Caroppo(✉), Alessandro Leone, Gabriele Rescio, Giovanni Diraco, and Pietro Siciliano

National Research Council of Italy—Institute for Microelectronics and Microsystems, Lecce, Italy
andrea.caroppo@le.imm.cnr.it

Abstract. This work describes a multi-sensor platform for anomalies detection in human sleep patterns. The inputs of the platform are sequences of human postures, extensively used for analysis of activities of daily living and, more in general, for human behaviour understanding. The postures are acquired by using both ambient and wearable sensors that are time-of-flight 3D vision sensor, ultra-wideband radar sensor, and three-axial accelerometer. The suggested platform aims to provide an abstraction layer with respect to the underlying sensing technologies, exploiting the postural information in common to all involved sensors (i.e., Standing, Bending, Sitting, Lying down). Furthermore, in order to fill the lack of datasets containing long-term postural sequences, which are required in human sleep analysis, a simulator of activities of daily living/postures has been proposed. The capability of the platform in providing a sensing invariant interface (i.e., abstracted from any specific sensing technology) was demonstrated by preliminary results, exhibiting high accuracy in sleep anomalies detection using the three aforementioned sensors.

Keywords: Human sleep anomalies · Multi-sensor platform · Time-of-flight 3D sensor · Ultra-wideband radar sensor · Wearable accelerometer

1 Introduction

The demography distribution of the developed world is set to change dramatically over the coming decades. Current trends show that the elderly people population is increasing in size and this phenomenon is predicted to continue in the future [1]. This trend of population ageing is as a result of reductions in fertility combined with increases in life expectancy. Although the latter issue is a positive situation, a number of related effects require consideration. In the last years, two priorities in research are investigated: (a) to establish novel and effective methods for assessment of activity levels in the home, and (b) to establish appropriate methods for the long term monitoring and management of chronic conditions with the purpose of alleviating the increased strain on healthcare resources. The use of sensor technologies within intelligent environments (IEs) is one such approach which has the potential to facilitate these needs. IEs can provide objective data describing behaviour and health status, facilitating the development of novel activity recognition, assisted living, or healthcare monitoring solutions. Moreover, the

B. Andò et al. (eds.), *Sensors*, Lecture Notes in Electrical Engineering 431,
DOI 10.1007/978-3-319-55077-0_36

current technologies, such as smart sensors, allows to keep the privacy and let the end-users to live in their own homes reducing the need for assistance from medical staff or caregiver. Integrated platforms of heterogeneous smart sensors are becoming more and more a key technology player in Ambient Assisted Living (AAL) scenarios. Moreover, advancement in sensor technologies give us the opportunity to recognize ADLs [2] for a long-period of time. Continuous monitoring of ADLs is helpful for detection of lifestyle disorders. Irregular human sleep patterns, for example, may cause health problems, such as disorders of psychological or neurological nature. Consequently, early detection of sleep anomalies can be useful for the prevention of such problems. In literature many approaches have been proposed for only monitoring human behaviour, reporting information about user's health and life patterns [3, 4]. On the other hand, in [5–7] some methodologies for the detection of anomalies in behaviour pattern are described. In the above systems set of features obtained from raw data provided by specific sensor technology are considered (e.g. pressure sensor, motion sensor, IR sensor, wearable sensor…). In these works, using probabilistic approach, the detection of sleep anomalies is reached with a good level of accuracy. However, these systems have some limitations. In fact, they do not have the ability to manage long-term data and in some circumstances a training phase is required.

This paper reports the description of a multi-sensor platform for detection of anomalies in human sleep patterns within AAL context. The input of the system is constituted by sequences of human postures generated using an activity simulation approach specifically designed and implemented within this work. The simulator provides sequences of postures according to a calibrated simulation based on real-life experiments conducted with three different sensors: a Time-of-Flight (TOF) sensor, a Ultra-wideband (UWB) radar and a ST MEMS three-axial accelerometer (ACC). The use of postures is motivated by their extensive use in ADLs modelling [8], besides that ADL sequences allow to model human behaviour. The main contribution of this work is related to the design and development of a platform for automatic detection of anomalies in sleep patterns by using an unsupervised methodology. It is important to highlight the platform capability in providing a technology invariant interface abstract from any specific sensing technology. The preliminary results show the ability of the presented approach to detect with good accuracy sleep/wake phases for subsequent medical evaluation of sleep disorders.

2 Materials and Methods

The platform architecture is organized, as shown in Fig. 1, in three main layers: detection layer, simulation layer, reasoning layer.

2.1 Detection Layer

Human postures can be detected by using several sensing approaches implemented with either ambient or wearable solutions. In this paper, three different kind of sensing approaches are taken into account: (1) TOF 3D vision, (2) UWB radar and (3) ACC. The first two (TOF, UWB) approaches refer to ambient solutions, whereas the last one

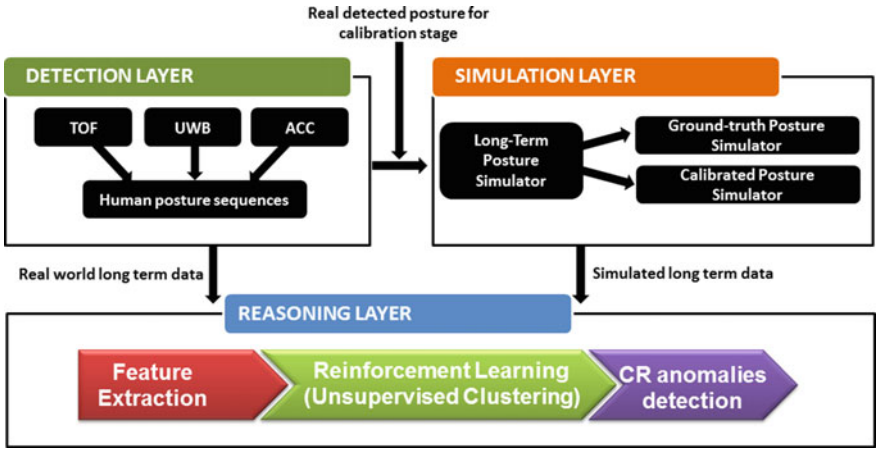

Fig. 1. Implemented logical modules overview

falls into wearable ones. All these posture detection approaches are differently characterized in terms of invasiveness, accuracy, robustness to object occlusion and cluttering and data richness, as summarized in Table 1.

Table 1. Comparison of three posture detectors

Characteristic	TOF	UWB	ACC
Invasiveness	Low	Very low	Medium
Accuracy	Very high	Medium	Medium
Robustness to object occlusion and cluttering	Low	High	Very high
Data richness	Very high	Medium	Medium

The aforementioned devices, the related mounting setups, the logical platforms for posture classification are described in the last works of the authors [9, 10], allowing posture analysis in different ways. For the purpose of this study, four main postures have been considered such as Standing (ST), Bending (BE), Sitting (SI) and Lying down (Ly), although the vision-based system is able to recognize a great number of postures, with greater accuracy (Fig. 2).

For the assessment of the sensor's accuracy with respect to the posture recognition task, a common experimental framework has been used, in which eighteen healthy subjects (9 males and 9 females, age 38 ± 6 years, height 175 ± 20 cm, weight 75 ± 22 kg) have been involved. The participants performed typical ADLs such as household tasks, meal preparation, feeding, sitting and watching TV, relaxing and sleeping. During such experimental sessions, data were collected simultaneously by a TOF sensor, a UWB radar and a MEMS accelerometer worn by participants.

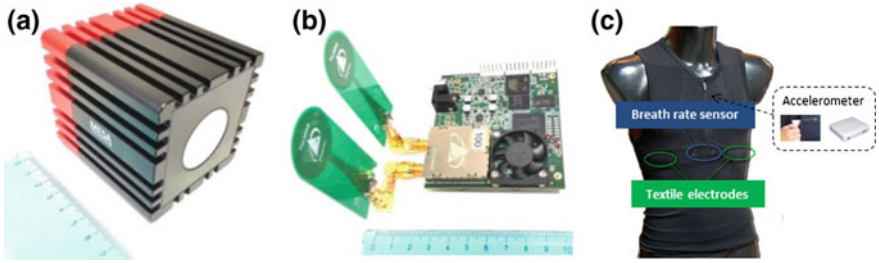

Fig. 2. **a** MESA SR-4000 Time-of-Flight sensor, **b** Time Domain PulseON 410 Ultra-wideband radar in monostatic setup, **c** Smartex WWS composed by a sensorized garment and an electronic device (SEW)

The classification performances are reported in Table 2 (for each detector) in terms of confusion matrix.

2.2 Simulation Layer

Since the availability of datasets for behaviour analysis is limited by difficulties associated with the collection of such data, and considered the lack of datasets containing long-term postural sequences, a simulator of ADLs/postures has been implemented. The simulator provides synthetic data with the ability to rapidly generate a large simulated dataset driven by different parameters which allow to reproduce different normal/abnormal behaviours (in particular human sleep patterns).

The simulator is composed by two stages; the first for simulation of long-term ADLs/postures, the last for a calibrated simulation of long-term postures referred to a specific sensing approach.

Long-term ADL/posture simulator. The general architecture of the simulator is inspired from the work of Noury et al. [11]. The authors assumed that the daily activities of a subject are almost regular. Thus, the simulator (of which a schematic representation with their logic modules is reported in Fig. 3) is based on a Markov model with homogeneous periods. As shown in the figure, the day is segmented into seven periods (e.g., wake up, morning, lunch, afternoon, dinner, going to bed, sleep) and thus seven Markov models corresponding to well identified circadian rhythms are used. Each model is represented by a graph of the transitions in between the different activities that occurs in each period (FSM). The transitions are controlled by their probabilities. This model is heavily based on prior knowledge as the probabilities of transitions are selected by users, as well as the limits of the seven periods of the day. The next step of the simulator is devoted to translate activities in a sequence of actions. In this work it is assumed that each activity is translated always by the same sequence of actions and the only free parameter in this step is the duration of the specific action. Finally, as described in the next subsection, the posture simulator models each action as a sequence of the postures (taking into account the only four postures previously mentioned).

Table 2. Confusion matrices for posture classification related to TOF sensor, UWB sensor and ACC sensor

		Predicted postures (%)											
		St			Be			Si			Ly		
		TOF	UWB	ACC	TOF	UWB	ACC	TOF	UWB	ACC	TOF	UWB	ACC
Actual postures (%)	St	**99**	**82**	**92**	1	13	2	0	5	6	0	0	0
	Be	0	18	2	**97**	**75**	**84**	3	6	2	0	1	12
	Si	3	11	11	0	8	2	**97**	**79**	**87**	0	2	0
	Ly	0	0	0	2	4	5	0	15	1	**98**	**81**	**94**

The recognition rate for each posture class is highlighted in bold

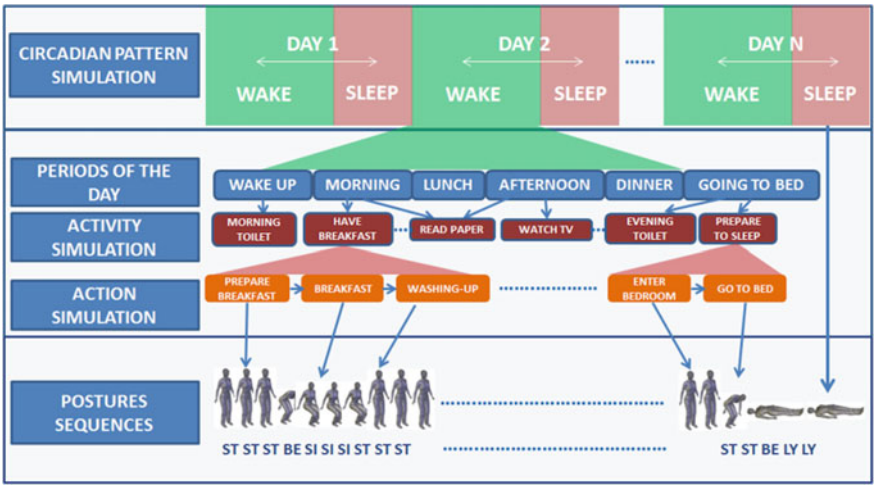

Fig. 3. Posture simulator representation (*SI* sitting, *ST* standing, *BE* bending, *LY* lying down)

Calibrated approach for long-term posture simulator. Starting from the sequence of actions provided by the ADL simulator, the posture sequence is generated by using a calibrated approach based on real observations conducted with real detectors (i.e., TOF, UWB, ACC). Such calibration consists in modelling errors introduced by each specific detector, starting from simulated ground-truth sequences. The Model Error Modelling (MEM) method [12] together with the Expectation-Maximization (EM) algorithm [13] are used to model detection errors. Furthermore, the parameters of the simulated detectors are obtained by minimizing a cost function based on the Prediction Error Method (PEM) [14].

2.3 Reasoning Layer

Given long-term posture sequences referred to the different sensing approaches, the platform includes a feature extraction procedure aimed to identify the starting point of sleep periods and their durations for each day. At this purpose, the most efficient solution is to recognize human actions from patterns of posture sequences, and more specifically to extract starting points of the actions: “going to bed”, “sleep in bed” and “wake up”. The approach implemented in this work allows ADLs recognition using the technique described below. Basically, human actions are recognized by considering successive postures over time periods. A transition action occurs when the person changes the current action to another action. Thus, a transition action might include several transition postures. Transition actions are merged together to form single atomic actions and global events are recognized by using Dynamic Bayesian Networks (DBNs) specifically designed for indoor application scenario, following an approach similar to Park and Kautz [15]. Designed DBNs have a hierarchical structure with three node layers: activity, interaction and sensor. The activity layer stays on top of hierarchy and includes hidden nodes to model high-level activities (i.e. ADLs, behaviours, etc.).

The interaction layer is a hidden layer as well and it is devoted to model the states of evidence for interactions inside the home (i.e. appliances, furniture, locations, etc.). The detector layer, at the bottom of hierarchy, gathers data from detector sensors (postures). Each DBN is hence decomposed in multiple Hidden Markov Models (HMMs) including interaction and sensor layers, and trained on the basis of the Viterbi algorithm [16]. In this way, the detection of sleep start time can be derived from the recognition of the action "going to bed", and the duration of sleep can be obtained evaluating the difference between "wake up" time and "sleep in bed" time.

The extracted features (start time of sleep and relative duration) are used for the detection of sleep periods and also to estimate human sleep trends evaluating their mapping into the two-dimensional space in which the x-axis indicate the start time of sleep and the y-axis its duration (expressed in hours and minutes). This step is explored with a reinforcement learning procedure; in particular, using an incremental clustering technique [17], the last step of the platform provides an unsupervised approach for real-time discovery of changes in a sleep patterns with respect to an initial pattern assumed as reference, namely Reference Sleep Pattern (RSP). This is achieved by incrementally clustering incoming features (extracted from the current day whose postures are simulated) in the aforementioned feature space. When a new cluster appears, a change in the sleep pattern is detected (and thus classified as normal or anomalous) if the features belonging to the new cluster are extracted from N consecutive days (not necessary adjacent), with N set according to physician's indications.

3 Experimental Results

The robustness of the feature extraction step has been evaluated on a series of experiments in which synthetic data obtained after calibrated simulation of real data generated by TOF sensor were affected by different percentages of errors related to: (1) sensor noise and (2) fault situation which can occur in real contexts (e.g. wearable sensor not worn, vision sensor turned off or occluded, resulting in postures not available during a time period). The purpose to simulate situations close to reality has been reached by modeling the noise with two kinds of components: bias noise (uniform distribution) and posture transition noise (Gaussian distribution). Performances have been evaluated in terms of Mean Absolute Error (MAE) by measuring the misalignment between ground-truth sleep phases and detected ones, and also in terms of Mean Relative Error (MRE) related to the percentage of undetected sleep phases. The previous error measures are estimated through 13 synthetic datasets constituted by different time periods, and characterized by an average length of sleep pattern equal to 8 h. The duration of sleep is randomly perturbed by variance values between 0.5 and 1.5 h. The number of simulated days for each experiment, the percentage of errors and relative performances are reported in Table 3.

The results obtained reveal that a total noise level of about 60% can affect the accuracy of the detected sleep phases in terms of temporal misalignment compared with the ground-truth. Moreover, if a fault situation is added to the noise the percentage of undetected sleep phases grows and this happens more if the fault situation occurs during the sleep periods.

Table 3. Experimental results of the feature extraction step

		# Days	Bias noise (%)	Posture transition noise (%)	Fault situation (%)	Alignment MAE (min)	Detection MRE (%)
Experiment	1	120	0	0	0	5	0
	2	90	20	10	0	5.2	0
	3	150	20	30	0	5.3	0
	4	90	30	10	0	5.2	0
	5	90	30	30	0	20.1	5
	6	120	20	10	15	8.4	4
	7	120	20	30	15	9.5	6
	8	90	30	10	15	11.7	7
	9	90	30	30	15	26.8	13
	10	150	20	10	30	14.4	10
	11	120	20	30	30	18.8	10
	12	150	30	10	30	25.1	12
	13	120	30	30	30	36.5	21

For the validation of the incremental clustering step, experiments that simulate different time periods have been carried out reproducing postural time series according to posture classification performance. Three time intervals (60, 120 and 180 days) have been taken into account as reference period M, followed by periods within which a change in the CR pattern was simulated (labelled with N). In Table 4, the detection rate of trend changes, at varying of both M and N, is reported for each detector. It is important to note that at the increasing of M, the incremental clustering achieves good performance if changes in CR pattern persist for a time period N. However, it is important to note that an acceptable detection rate (at least of 80%) is obtained for period N (in days) closely related to each detector: a greater amount of days N is required at the increasing of M.

Table 4. Detection rate (%) of deviations from the reference CR at varying of "M" and "N"

		N (days)							
		Detector	7	14	21	28	35	42	49
M (days)	60	TOF	76.4	**90.2**	90.7	94.6	95	95.8	96.5
		ACC	73.1	**84.6**	86.1	89.5	92.3	93.1	94.5
		UWB	69.7	73.5	77.2	**81.4**	84.5	87.7	90.2
	120	TOF	72.1	74.4	**80.3**	88.7	88.9	89.2	90.5
		ACC	69.8	70.1	73.9	76.8	**80.2**	83.6	86.7
		UWB	65.2	67.6	70.2	73.5	78.5	**81.4**	82.9
	180	TOF	60.4	73.7	79.7	**80.2**	87.4	88.9	90.4
		ACC	58.7	62.6	66.9	70.4	74.2	**79.7**	83.7
		UWB	56.4	60.1	63	67.9	72.7	77.5	**80**

The value in bold is highlighted in order to suggest to the reader how many days N are at least necessary to obtain a minimum detection rate of 80% at varying of the reference period M (in which there is not a change in the circadian rhythm)

4 Discussion and Conclusion

From the analysis of the obtained results, it is evident the platform ability in identification of changes in human sleep patterns with high accuracy. However, the performances are strictly related to the sensing technology involved; in fact, at varying of the detector, a different number of days N is required to reach a satisfactory detection rate. For example, if we consider a reference period of length M = 120 days, a detection rate of about 80% is reached within N = 21 days (TOF), N = 35 days (ACC), N = 42 days (UWB). The platform has been validated by using posture sequences simulated in a calibrated way (with calibration error less than 5%) and referring to common ADLs carried out by older people in their home environment. Furthermore, the solution was tested considering reference periods M very different in order to taking into account any deviations with respect to standard execution of ADLs.

This leads up to believe that the performances that can be reached using real monitoring systems should be included between M = 60 and M = 180, with N corresponding to the sensing technology used. From the usability perspective, the platform is consistent with the independent living context; in fact the detection of changes in sleep patterns can be automatically obtained allowing offline analysis by a caregiver/doctor for subsequent clinical evaluations. Finally, it is important to stress the versatility of the platform which can potentially operate with any kind of detector able to provide postural information.

Acknowledgements. This work was carried out within the project "ACTIVE AGEING AT HOME" funded by the Italian Ministry of Education, Universities and Research, within the National Operational Programme for "Research and Competitiveness" 2007–2013.

References

1. United Nations Programme on Ageing, The ageing of the world's population, 23 June 2008, http://www.un.org/esa/socdev/ageing/popageing.html
2. D.H. Barer, F. Noury, Measurement of activities of daily living. Clin. Rehabil **3**, 179–187 (1989)
3. G. Virone, M. Alwan, S. Dalal, S. Kell, B. Turner, J.A. Stankovic, R. Felder, Behavioral patterns of older adults in assisted living. IEEE Trans. Inf. Technol. Biomed. **12**, 387–398 (2008)
4. A.A. Chaaraoui, J.R. Padilla-López, F.J. Ferrández-Pastor, M. Nieto-Hidalgo, F. Flórez-Revuelta, A vision-based system for intelligent monitoring: human behaviour analysis and privacy by context. Sensors **14**(5), 8895–8925 (2014)
5. G. Virone, N. Noury, J. Demongeot, A system for automatic measurement of circadian activity deviations in telemedicine. IEEE Trans. Biomed. Eng. **49**, 1463–1469 (2002)
6. F. Cardinaux, S. Brownsell, M. Hawley, D. Bradley, Modeling of behavioral patterns for abnormality detection in the context of lifestyle reassurance. LNCS **5197**, 234–251 (2008)
7. J. Shin, B. Lee, K. Park, Detection of abnormal living patterns for elderly living alone using support vector data description. IEEE Trans. Inf. Technol. Biomed. **15**, 438–448 (2011)

8. V. Kellokumpu, M. Pietikäinen, J. Heikkilä, Human activity recognition using sequences of postures, in *MVA*, pp. 570–573 (2005)
9. G. Diraco, A. Leone, P. Siciliano, In-home hierarchical posture classification with a time-of-flight 3D sensor. Gait Posture **39**(1), 182–187 (2014)
10. G. Rescio, A. Leone, P. Siciliano, Supervised expert system for wearable MEMS Accelerometer-Based Fall Detector, J. Sens. **2013**(Article ID 254629), 11 pages (2013)
11. N. Noury, T. Hadidi, Computer simulation of the activity of the elderly person living independently in a health smart home. Comput. Meth. Progr. Biomed. **108**(3), 1216–1228 (2012)
12. L. Ljung, Model validation and model error modelling, in The Astrom symposium on control, Lund, Sweden (1999)
13. R.A. Delgado, G.C. Goodwin, R. Carvajal, J.C. Agüero, A novel approach to model error modelling using the expectation-maximization algorithm, in *CDC*, pp. 7327–7332 (Dec 2012)
14. Y. Zhao, B. Huang, H. Su, J. Chu, Prediction error method for identification of LPV models. J. Process Control **22**(1), 180–193 (2012)
15. S. Park, H. Kautz, Privacy-preserving recognition of activities in daily living from multi-view silhouettes and rfid-based training, in *AAAI Symposium on AI in Eldercare: New Solutions to Old Problems* (2008)
16. F.V. Jensen, T.D. Nielsen, Bayesian networks and decision graphs, in *Information Science and Statistics*, ed. by M. Jordan, J. Kleinberg, B. Schölkopf (Springer Science Business Media, NY USA, 2007)
17. W.A. Barbakh, Y. Wu, C. Fyfe, Online clustering algorithms and reinforcement learning, in *Non-Standard Parameter Adaptation for Exploratory Data Analysis*, pp. 85–108 (2009)

Bioimpedance Measurement in Dentistry: Detection of Inflamed Tissues

Gloria Cosoli[1(✉)], Lorenzo Scalise[1], Graziano Cerri[2], Gerardo Tricarico[3], and Enrico Primo Tomasini[1]

[1] Department of Industrial Engineering and Mathematical Sciences, Università Politecnica delle Marche, v. Brecce Bianche, 60131 Ancona, Italy
{g.cosoli,l.scalise,ep.tomasini}@univpm.it
[2] Department of Information Engineering, Università Politecnica delle Marche, v. Brecce Bianche, 60131 Ancona, Italy
g.cerri@univpm.it
[3] Department of Health Sciences, Università del Piemonte Orientale, v. Solaroli, 28100 Novara, Italy
trigerard@gmail.com

Abstract. This work aims at determining if bioimpedance measurements are able to provide information about the inflammatory state of the tissues; if the presence of an inflamed tissue can be located by means of bioimpedance measure, it would be possible to focus a potential treatment in this site. Different numerical 3D models have been realized to simulate the measurement conditions present in the event of inflamed gingiva around a dental implant. A premolar has been represented and different inflammation volumes have been considered; both geometric and electrical properties have been taken from the literature. In addition, some preliminary measurements have been conducted in three patients with dental implants in different conditions: healthy tissues, inflammation and peri-implantitis. The percentage difference of impedance (ΔZ) between healthy and inflamed tissues has been considered. In addition, also three numerical models of healthy teeth have been realized (i.e. incisor, canine and premolar roots), in order to evaluate the normal range of teeth bioimpedance values. The results obtained from the numerical simulations show ΔZ values of 6–20% for the dental implant, depending on the inflamed volume. The bioimpedance values experimentally measured are in agreement with the ones obtained from the simulations and ΔZ values are also more marked (34% for inflammation, 55% for peri-implantitis), suggesting that in real inflamed tissues not only electrical properties but also dimensions are different with respect to the normal case. As regards the healthy teeth, the modulus of the measured impedance is higher than that of the implant; this was predictable and is due to the presence of bone instead of the implant. In conclusion, it is possible to state that bioimpedance measurements allow the clinician to detect inflamed tissues, so that the therapy can be focused on the impaired zone, limiting the influence in the surrounding healthy tissues and personalizing the therapy according to the inflammation severity.

Keywords: Bioimpedance · Dentistry · Peri-implantitis · Personalized medicine

B. Andò et al. (eds.), *Sensors*, Lecture Notes in Electrical Engineering 431,
DOI 10.1007/978-3-319-55077-0_37

1 Introduction

Biologic tissues are characterized by specific electrical properties (i.e. electrical conductivity and magnetic permittivity) [1–3], which vary together with their physiological/pathological conditions, such as inflammation [4]. Bioimpedance measurements are widely applied for the monitoring of remodeling and changes in the organism, both in normal and in pathological conditions [5]. Its wide application is due to its minimal invasivity and to the ease to use of the required instrumentation [6]. Bioimpedance measurements could be used with diagnostic aims, since inflammation determines an increase of electric conductivity with respect to normal values, due to the presence of liquids (hyperemia and infiltration of the adjacent tissues are typical of the inflammatory process) [4]. So, using the corresponding healthy tissue as the reference, it is possible to diagnose an inflamed site; for example, in a study made on a mammary gland [4], it is reported that the impedance value of the affected tissue is 2–3 fold lower than that of the contralateral one. In dentistry, oral inflammations are very frequent [7] and can have serious consequences (peri-implantitis is the main cause of implant failure [8] and is characterized by bacterial infection, peri-implant bone loss and inflammation, as illustrated in Fig. 1).

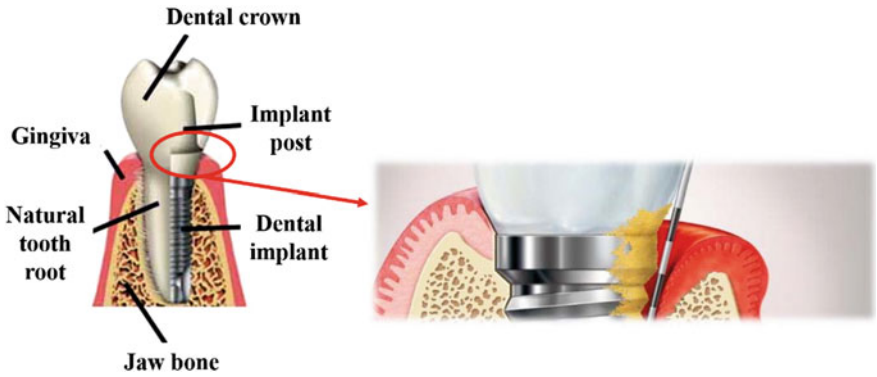

Fig. 1. Scheme of the implant screwed in the jaw bone and enlargement of the portion of the system that can be affected by peri-implantitis; there is a bone loss, the gingiva become *red* and there are bacteria adhering to the implant (Color figure online)

So, bioimpedancemetry could be used as a mean to locate the inflamed area of a periodontal tissue, like the oral mucosa. These measurements would allow personalized therapies possible, according to the position and the severity of the detected inflammation, since the current densities and pathways are strongly influenced by the electrical properties of the tissue [9]. In this way, the therapy could be focused on the impaired area, minimizing the collateral/undesired effects on the surrounding tissues. Moreover, bioimpedance measurements would allow to follow the inflammation course, since the measured value is linked to the inflammation severity. In this paper, the authors want to show the bioimpedance measurement system by means of

numerical 3D models built in COMSOL [10], used to investigate the sensitivity of the technique for different inflamed volumes. After having demonstrated the feasibility of this approach, bioimpedance measurements on patients were conducted in different clinical cases: healthy tissues, inflammation and peri-implantitis. Both in simulation and experimentally, the impedance measurements have been done by applying a voltage stimulus at 300 kHz, both to avoid Faraday effect [11] and to be in line with the typical frequency range used for bioimpedance measurements [4, 6].

2 Materials and Methods

At first, a numerical analysis of the bioimpedance measurement by means of 3D Finite Element Method (FEM) was conducted. The model (reported in Fig. 2) consists in a first premolar tooth root with a dental implant surrounded by a portion of inflamed tissue; geometric and electrical properties were taken from the literature [1–3, 12, 13], paying particular attention to the inflamed tissue [4], whose conductivity was considered 2 folds higher than that of the corresponding healthy tissue. The relative permittivity of the inflamed gingiva was instead considered equal to the healthy gingiva one. All the electrical properties of the simulated biological tissues are reported in Table 1. For the sake of simplicity, changes in geometric dimensions of the inflamed tissue was not considered, even if the inflammatory process is actually characterized by swollen tissue, causing a further decrease in the measured impedance. So, it can be assumed that the analyzed structure is the worst case situation in the detection of inflammations by means of bioimpedancemetry.

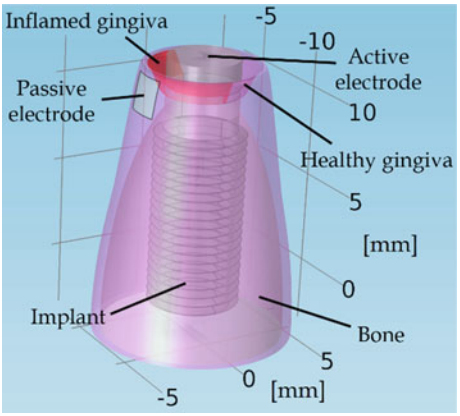

Fig. 2. Numerical 3D model of a dental implant screwed in the jaw bone; a portion of gingiva is inflamed (represented in *red*). The implant is used as active electrode, while the passive one is a square metal electrode adhering to the gingival (Color figure online)

In order to simulate impedance measurements, an AC generator was connected between the active and the passive electrodes; the former is the AC generator terminal (connected to the implant, realized in titanium), while the latter is a metallic square

Table 1. Electrical properties of the model tissues (gingiva, inflamed gingiva and jaw bone, i.e. cortical bone): electrical conductivity, σ (S/m), and relative permittivity, ε_r (adimensional) [1–3]

Tissue	σ (S/m)	ε_r
Gingiva	0.39	245
Inflamed gingiva	0.78	245
Bone (cortical)	0.021	190

surface of about 4 mm^2 adhering to the gingiva and fixed at 0 V potential (ground). In this way, the authors wanted to verify the possibility of distinguishing between healthy and inflamed tissues, by means of two different configurations: passive electrode was first put in contact with healthy gingiva to measure healthy side, then with inflamed gingiva to measure the inflamed side and so to do the comparison. Different inflamed tissue volumes were considered, that is 2, 5 and 13 mm^3. Simulations of bioimpedance measurement were made also on different healthy teeth roots (premolar, canine and incisor, as shown in Fig. 3), in order to evaluate a normal bioimpedance range.

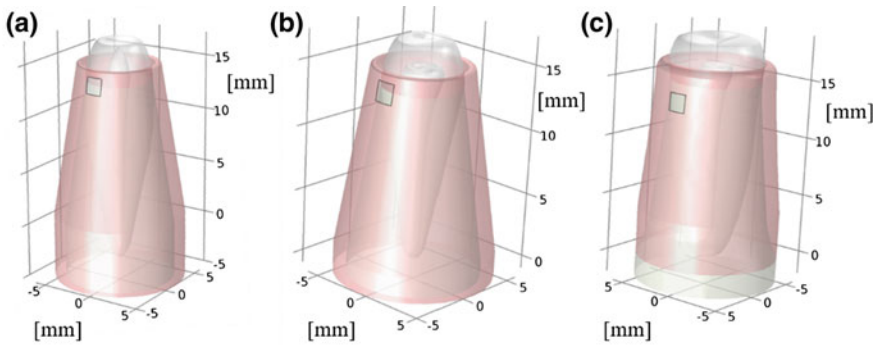

Fig. 3. Numerical 3D models of healthy teeth roots: canine (**a**), incisor (**b**) and premolar (**c**); both active and passive electrodes are metallic squares, put in contact with gingiva on two opposite sides with respect to the tooth root

After having numerically verified the possibility to discriminate between inflamed and healthy periodontal tissues by means of bioimpedancemetry, a few experimental measures were conducted on patients with dental implants, in case of healthy and inflamed tissue, as well as in a case of peri-implantitis. An LCR bridge meter was used (HP LCR Precision Meter 4285A [14]), connected by means of an opposite insulation transformer and equipped with proper electrodes, allowing an adequate electric contact. Typical accuracy of a commercial RLC meter is lower than 1%, so it is suitable for the discrimination between healthy and inflamed tissues (Fig. 4).

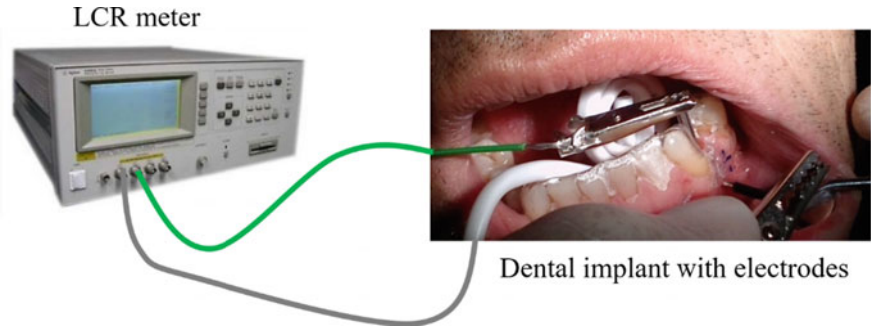

Fig. 4. LCR meter (connected by means of a proper insulation transformer) equipped with proper electrodes for the impedance measurement: active electrode screwed in the dental implant itself, passive electrode put in contact with gingiva

3 Results

3.1 Numerical Simulation

After running the simulations, the impedance was evaluated in its absolute, real and imaginary values. Due to biological tissues electrical properties, the contribution of the imaginary part to the impedance values is always negligible and therefore the modulus reported is mainly given by the resistance component. In dental implant model, ΔZ value was computed to make a comparison between healthy and inflamed sides.

3.1.1 Dental Implant Model

As regards numerical simulations, healthy and inflamed tissues impedances were compared and differences in the range of 6÷20% were calculated, depending on the considered inflamed volume (Table 2).

Table 2. Bioimpedance modulus ($|Z|$) results from numerical simulations with different inflamed volumes: 2, 5 and 13 mm^3

Volume of inflammation (mm^3)	$\|Z\|$ (Ω)—healthy side	$\|Z\|$ (Ω)—inflamed side	ΔZ (%)
2	553	519	6
5	558	498	11
13	551	445	20

ΔZ is the percentage difference between the impedance moduli of inflamed and healthy sides

3.1.2 Healthy Teeth Models

As regards the healthy teeth roots models, impedance values obtained are reported in Fig. 5. It is possible to observe that the real part is the predominant one, so the major contribute to the impedance modulus is due to that and the imaginary part is negligible.

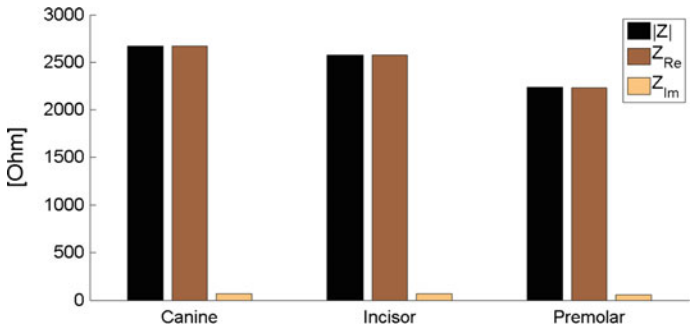

Fig. 5. Impedance results from numerical 3D model of canine (*left*), incisor (*centre*) and premolar (*right*) teeth roots, in modulus, real and imaginary parts

3.2 Experimental Measurements

Experimental measurements were repeated four times for each considered tooth, so to evaluate the repeatability of the measurement. An equivalent circuit was considered, that is a series between resistance and capacitance. The results are reported in Table 3, whose last column is related to the mean value (m) and the standard deviation (σ) of the impedance moduli obtained from the four measurements done on each clinical case.

Table 3. Impedance values experimentally measured on three patients with dental implants in case of peri-implantitis, inflammation and healthy tissues

Clinical case	Measure	Rs (Ω)	Cs (nF)	|Z| (Ω)	(m ± σ) of |Z| (Ω)
Peri-implantitis	1	369	14.40	371	369 ± 10
	2	330	3.37	363	
	3	334	3.81	360	
	4	352	3.46	382	
Inflammation	1	440	1.83	521	549 ± 23
	2	463	1.74	548	
	3	468	1.80	547	
	4	502	1.78	578	
Healthy	1	738	1.51	811	829 ± 43
	2	791	1.75	843	
	3	690	1.38	782	
	4	789	1.30	881	

The impedance modulus (reported as mean ± standard deviation) was equal to (369 ± 10) Ω on the implant with peri-implantitis, to (549 ± 23) Ω on the implant surrounded by inflamed tissue and to (829 ± 43) Ω on the implant surrounded by healthy tissue. So, impedance values are higher in the implant surrounded by healthy tissues; the presence of liquids (due to hyperemia and infiltration) reduces the impedance value in the inflammation case ($\Delta Z = 34\%$) and, even more, in the peri-implantitis case ($\Delta Z = 55\%$).

4 Discussion and Conclusions

A numerical study to investigate the feasibility of a bioimpedancemetry-based instrument to detect inflamed tissues for periodontal applications has been carried out, in case of dental implants (often linked to peri-implantitis phenomena). The diagnosis of the inflammation is based on the comparison between healthy and sick tissues. Numerical results show that the change in impedance values due to the inflammatory process is sufficiently pronounced (i.e. 6–20%, depending on the inflamed volume) to discriminate between healthy and inflamed tissues; as predictable, greater the inflamed volume, higher the percentage difference and so easier the detection of the inflamed area. Once demonstrated the feasibility of the bioimpedancemetric method, a few experimental measures on patients have been conducted in case of dental implants surrounded by healthy or inflamed tissues or with peri-implantitis phenomena. Also experimental results show a significant change in pathological condition with respect to normality (ΔZ of 34% in case of inflammation and of 55% in case of peri-implantitis). As a consequence, it is possible to state that a bioimpedance measuring system integrated in a therapeutic device could allow the clinician to locate the impaired area and to evaluate the severity of the inflammation, thus adjusting the therapeutic dose. Moreover, bioimpedancemetry would permit the monitoring of the pathology course. This monitoring system could be applied not only when an implant is present, but also with natural teeth. So, numerical 3D models of canine, incisor and premolar teeth roots have been realized and the impedance values have been evaluated. They are greater than those related to dental implants, because in natural teeth there is more bone, which is a material with a greater resistivity than the implant (i.e. bone is less conductive, since the implant is a metal, that is the conductor par excellence). In the future, it would be interesting to do experimental measurements of bioimpedance in natural teeth, comparing healthy tissues with inflamed ones; this could find a consistent application in case of periodontitis, that is an inflammatory disease affecting the tissues surrounding tooth. This approach could be applied not only to locate inflammations in mouth environment, but also in other parts of our body, providing an easy, low-cost and non-invasive diagnostic method.

References

1. C. Gabriel, S. Gabriel, E. Corthout, The dielectric properties of biological tissues: I. Literature survey. Phys. Med. Biol. **41**(11), 2231–2249 (1996)
2. S. Gabriel, R.W. Lau, C. Gabriel, The dielectric properties of biological tissues: II. Measurements in the frequency range 10 Hz to 20 GHz. Phys. Med. Biol. **41**(11), 2251–2269 (1996)
3. S. Gabriel, R.W. Lau, C. Gabriel, The dielectric properties of biological tissues: III. Parametric models for the dielectric spectrum of tissues. Phys. Med. Biol. **41**(11), 2271–2293 (1996)
4. Y.V. Tornuev, E.V. Koldysheva, G.A. Lapiy, O.P. Molodykh, S.M. Balakhnin, G.M. Bushmanova, D.E. Semenov, V.K. Preobrazhenskaya, Bioimpedancemetry in the diagnostics of inflammatory process in the mammary gland. Bull. Exp. Biol. Med. **156**(3), 381–383 (2014)
5. A.V. Rodin, V.G. Pleshkov, S.D. Leonov, S.M. Bazhenov, Experimental study of the diagnostic potentialities of bioimpedance measurement in acute intestinal obstruction. Bull. Exp. Biol. Med. **155**(6), 810–813 (2013)
6. D.V. Belik, K.D. Belik, Improvement of the information value of multifrequency impedancometry for detection of small tumor arrays. Biomed. Eng. **41**(4), 157–161 (2007)
7. S. Renvert, A.-M. Roos-Jansåker, N. Claffey, Non-surgical treatment of peri-implant mucositis and peri-implantitis: a literature review. J. Clin. Periodontol. **35**(Suppl 8), 305–315 (2008)
8. Z. Cao, Y. Chen, Y. Chen, Q. Zhao, X. Xu, Y. Chen, Electromagnetic irradiation may be a new approach to therapy for peri-implantitis. Med. Hypotheses **78**(3), 370–372 (2012)
9. D. Miklavčič, N. Pavšelj, F.X. Hart, Electric properties of tissues, in *Wiley Encyclopedia of Biomedical Engineering* (John Wiley & Sons, Inc., 2006)
10. COMSOL Multiphysics, in *Wikipedia*, *the free encyclopedia*. 30 Nov 2015
11. F.P. Branca, Fondamenti di Ingegneria Clinica, vol. 1. Springer
12. S.J.N.D. Ms, *Wheeler's Dental Anatomy, Physiology and Occlusion, 9e*, 9th edn. (Saunders, St. Louis, MO, 2009)
13. K.L. Vandana, B. Savitha, Thickness of gingiva in association with age, gender and dental arch location. J. Clin. Periodontol. **32**(7), 828–830 (2005)
14. LCR Meters & Impedance Measurement Products, Keysight (Agilent) [Online]. Available: http://www.keysight.com/en/pc-1000000391%3Aepsg%3Apgr/lcr-meters-impedance-measurement-products?nid=-536902441.0.00&cc=IT&lc=ita&cmpid=93159. Accessed 01 Dec 2015

Stochastic Comparison of Machine Learning Approaches to Calibration of Mobile Air Quality Monitors

E. Esposito[1], S. De Vito[1(✉)], M. Salvato[1], G. Fattoruso[1], V. Bright[2], R.L. Jones[2], and O. Popoola[2]

[1] DTE-FSN-DIN, ENEA, P.le E. Fermi 1, 80055 Portici, NA, Italy
saverio.devito@enea.it
[2] Department of Chemistry, University of Cambridge, Lensfield Rd., Cambridge, UK

Abstract. Recently, the interest in the development of new pervasive or mobile implementations of air quality multisensor devices has significantly grown. New application opportunities appeared together with new challenges due to limitations in dealing with rapid pollutants concentrations transients both for static and mobile deployments. Sensors dynamic is one of the primary factor in limiting the capability of the device of estimating true concentration when it is rapidly changing. Researchers have proposed several approaches to these issues but none have been tested in real conditions. Furthermore, no performance comparison is currently available. In this contribution, we propose and compare different approaches to the calibration problem of novel fast air quality multisensing devices, using two datasets recorded in field. Machine learning architectures have been designed, optimized and tested in order to tackle the cross sensitivities issues and sensors inherent dynamic limitations to perform accurate prediction and uncertainty estimation. Comparison results shows the advantage of dynamic non linear architectures versus static linear ones with support vector regressors scoring best results.

Keywords: Air quality · Chemical sensors · Calibration · Mobile air quality monitoring · Machine learning

1 Introduction

In 2008, EU Air quality Directive called for the integration of the sparse network of conventional air quality monitoring systems via the so called indicative measurements devices [1]. It also defined Data Quality Objective (DQO) that systems should achieve in order to produce usable measurements. In particular, the DQO were expressed in terms of extended uncertainty.

Solid state based chemical multisensor devices are most appealing candidates for this role for their low cost and low dimensional impacts that enable pervasive or mobile deployments. Recently, they have been a relevant factor in the diffusion of the citizen science concept aiming to personal pollutant exposure assessment while on the move [2, 3]. Unfortunately, notwithstanding the promising performance expressed in

B. Andò et al. (eds.), *Sensors*, Lecture Notes in Electrical Engineering 431,
DOI 10.1007/978-3-319-55077-0_38

laboratory settings, solid state sensors are known to consistently underperform when deployed in real world conditions [4], with performance that are far from being acceptable from the DQO point of view. However, researchers that have attempted to implement multivariate calibration scheme reported interesting results exploiting all the response signals of the sensor array to overcome cross-sensitivities, sensitivities and, to a minor extent, stability issues.

Researchers are well aware of the impacts of chemical sensors slow response dynamic to their capability to follow rapid pollutant transients. These impacts are considered particularly relevant for robotic, mobile or even pervasive deployments where chemical sensors are expected to face rapid transients due to the crossing of chemical plumes. They have tried to implements multiple strategies that, tested in lab environments, have suggested the possibility to achieve at least a partial solution to the involved issue [5]. Esposito et al. [6] have recently tested one of these methodologies by using on field recorded measurements. To the best of our knowledge these proposals have never been compared and a little is known on their generalization capabilities when facing to different conditions. In this work we attempt to give a first response to these needs by comparing several recently proposed approaches to the dynamic calibration of chemical sensor devices by using two different datasets with a relevant number of samples recorded in different conditions, in different cities and with different timeframes and sampling frequencies. In the following, we briefly summarize relevant aspects of calibration techniques and the testing datasets as well as the proposed comparison methodology. Results are then commented in the last sections. To skate over the nonetheless interesting performance ranking results, they will confirm the need for taking into account the dynamic content of the sensor response in order to obtain a fast response from the raw sensor signals and hence overcome dynamic issues.

2 Methods

A set of machine learning (ML) approaches to sensor array calibration have been selected by the available literature and compared for performance results on two datasets. The latter are built up by data collected on the field and include the response of a sensors array and the corresponding ground truth for pollutant concentrations obtained by co-located conventional analyzers. Datasets have been temporally segmented in three non-overlapping subsets for training, validation and test purposes. The order of sampling have been preserved in order to let the technique to exploit information on sensors and process dynamic.

Whenever possible, each ML technique have been developed considering both its static, basic, structure and its dynamic version as capable of taking into account the dynamic features of the considered problem.

Comparison have been carried out with the aim of fairly compare performances of the proposed machine learning approaches. According to common practice, model design and optimization have been carried out by selecting best performing hyperparameters combination within a specific subspace for each of the different experimental conditions. Best hyperparameters combination have been selected by a brute force search conducted on a set of combination obtained by subsampling the different

hyperparameter spaces. Practically, each combination was associated to a specific model and performance have been evaluated with the use of a separated validation set. According to this procedure the best performing hyperparameter combination have been used in order to test the specified model on the devised test set. Obtained performances have been then compared in the results section. It is noteworthy to highlight that each performance evaluation both occurring on the validation set for model design or on the test set, has been carried out by averaging the results obtained during multiple runs of the training procedure. For ANN and RC architecture, for example, the results are in fact dependant from the outcomes of their random initialization procedure.

2.1 Machine Learning Approaches

The selection of tested machine learning approaches include Artificial Neural Network (ANN), Support Vector Regressor (SVR), Reservoir Computing (RC), Gaussian Processes and the base Multilinear Regressor Approach (see Refs. [5–7]).

ANNs have become a de facto standard for non linear multivariate regression in multiple applied machine learning fields. Their basic structure includes three layers (input, hidden and output) of computing nodes. Weighted connections conveys processed input signals to inner layers where non linear evaluation of sigmoidal functions take places. Eventually, processed signals are evaluated by a linear output layer to estimate the value of the output (in our case being the pollutant concentration). Weights are tuned by a training procedure aimed to reduce empirical error to a minimum. SVRs are competing with ANN to set a new reference standard, several studies have highlighted its superior performances in multiple conditions [8–10]. Based on the so called kernel trick, their structure aims to find a subset of relevant training samples to be used for optimal non linear signal interpolation. Optimal selection is carried out with a regularized approach involving simultaneous evaluation of costs of empirical error and solution complexity. RC [11] comprises several emerging architectures that have expressed remarkable performances in selected problems when dynamic behaviour is involved [12]. Based on the interconnection of two basic structures, namely a Reservoir and a Readout, RC architecture embed significant memory and computing capabilities in an intertwined fashion. The reservoir, in particular, is built up by a set of recurrently interconnected computing nodes (also called neurons) each of them is also connected to both input signals and the so called Readout structure. This is generally built up by a multilinear regression block that take as input the output of all the reservoir units, i.e. the state of the RC network, and outputs a linear combination of them. Interestingly enough, the reservoir units interconnection is randomly generated and does not need tuning, practically limiting the training phase to Readout coefficients tuning.

Gaussian Processes are used as supervised machine learning method for estimating the complete posterior joint probability of a process, in signal theory sense [7]. In this framework, they infer the sought calibration function starting with a prior distribution over the relevant function space and using data samples and correspondent ground truth values to refine the assumptions eventually learning the target function.

ANN, GP, SVR and MLR have been tested in their static basic architecture and in their dynamic counterpart formulation by coupling an equally spaced and long tapped

delay line to each of the relevant input signals. Different TD length have been considered for each approach. RC model, for its intrinsic dynamic nature, has been tested in its conventional echo state network version.

As regards as hyperparameters subspace selection, the compared neural networks (static and dynamic NN) have been designed to host 5, 10 or 15 neurons in their hidden layer. For SVR and TD-SVR components the scanned Kernel Functions (KF) were *Radial Basis Function*, *Gaussian Kernel* and *Polynomial Kernel* with $\gamma \in \left(2^{-15}, 2^{5}\right)$, $C \in \left(2^{-5}, 2^{15}\right)$, $\varepsilon \in (0.1{:}0.1{:}10.8)$.

For GPR and TD-GPR, the kernel function was selected to belong to the ('*SquaredExponential*', '*Matern32*', '*Matern52*') set and $\sigma \in (10^{-2} std(Y_{train}), std(Y_{train}))$, where $std(Y_{train})$ is the Standard Deviation of the Target gas data in the training set.

For RC, Spectral Radius (SR) was selected to rest in $(0.1{:}0.1{:}0.9)$ interval, Input Scaling factor (IS) in $(10^{-9}, 10^{-1})$, and the number of reservoir units (RU) in $(20, 50, 100, 150, 200)$. For every relevant architecture, the length of the tapped delay was selected to belong to the (0 min/static, 3 min, 5 min) set for the first dataset and (0 h/static, 3 h and 5 h) for the second dataset.

2.2 Datasets

As above mentioned, two datasets have been selected for the performance evaluation representing the core focus of this contribution.

The first Dataset here used includes data collected during the deployment of a multisensory device called SnaQ (see Ref. [2] for a detailed description) developed by a team led by the Center for Atmospheric Sciences (CAAS) of University of Cambridge (UK). The multisensory device is equipped with the following sensors units:

- 2 NO_2 EC sensor units (Alphasense NO_2-B4);
- 1 NO Alphasense EC sensor unit (Alphasense NO-B4);
- 2 O_3 Alphasense EC sensor units (Alphasense O_3-B4);
- T, RH sensor units;
- Wind speed and direction unit.

The device was located in the Cambridge city centre (University of Cambridge—Dept. of Chemistry) together with a conventional reference station operated by CAAS. While the sampling period of the SnaQ system was set at 20 s, the reference station provides ground truth readings of target gases at 60 s intervals. For the SnaQ sensors, a known cross sensitivity have been reported for, respectively, O_3 and NO_2. Baseline and temperature correction have been implemented on the recorded samples using the procedure detailed in the sensors datasheet. A further preprocessing step has been conducted to remove reference station calibration periods during the night. The dataset encompasses five weeks of continuous measurements with the first week of measurements (10 k samples) set apart as a training set for statistical machine learning tools. The remaining four weeks of data have been used for validation (10 k samples) and testing purposes (30 k samples). This dataset has been selected for the relatively

fast sampling period that has been adopted during the recordings of the sensor responses reasonably embedding information on the dynamic behaviour of the sensors when exposed to rapid transients.

The second dataset is focused on the deploying of a multi-sensor device developed by Pirelli Labs for the use in urban pollution monitoring scenarios [12]. In particular, the device was designed as a low-cost, compact, versatile and reliable tool to support the city air quality monitoring network. The device was characterized by a three-stage design (sensor array, data processing unit, communication unit). The device was built up by a 31 cm × 26 cm × 12 cm metallic case hosting the power management unit, signal conditioning and acquisition electronics, a microcontroller board hosting a microprocessor eventually capable to run simple sensor fusion algorithms, a GSM (Global System for Mobile Communications) data transmission unit and of course a sensor array subsystem. Total weight was 2.5 kg. The microcontroller board took care of first-stage data processing operations, storing up to 72 h measurements at an 8 s sample rate and controlled the communication unit in order to transfer processed data (8, 15 or 60 min mean sampled values) to data sinks. The dataset collects data sampled over a whole year by a multi-sensor device equipped with five metal oxide chemoresistive sensors (CO, NO_x, O_3, NMHC, NO_2; hourly averages recorded) plus commercial temperature and humidity sensors. The device has been co-located with a fixed conventional monitoring station equipped with spectrometer analysers. The conventional fixed station provided reference concentration estimation for five different atmospheric pollutants, i.e. CO (mg/m^3), non-metanic hydrocarbons (NMHC) ($\mu g/m^3$), C_6H_6 ($\mu g/m^3$), NO_x (ppb), NO_2 ($\mu g/m^3$). The dataset is freely available within the UCI dataset repository [13]. The dataset have been partitioned in a training set encompassing 3 months out of 12 of measurements and a validation set encompassing the successive 3 months. The remaining 6 months have been used for testing purposes reflecting the scheme chosen for performance evaluation in this work.

It is worth to note that this dataset is not thought to embed significant information about sensors dynamic behaviour because all dynamic information is obviously lost after hourly averaging procedure. As such dynamic machine learning components, can only exploit the fraction of process dynamic related information captured by the available sensor responses history.

3 Results

The brute force best performing hyper parameter search procedure have been conducted using training and validation sets as above mentioned, producing an hyperparameters values set for each tapped delay line length and ML approach.

For each different tapped delay length, corresponding best performing models have then been used in order to estimate the pollutant concentrations over the dedicated test set sample (see Table 1 for selected values). The Mean Absolute Error (MAE), that retains the same unit of measure as estimated concentrations (ppb for the first dataset, mg/m^3 for the second), has been used as primary performance estimator. Table 2 summarize the obtained results.

Table 1. Best performing hyperparameters set for each experimental settings as resulted by the brute force search conducted over predesigned hyperparameters spaces

Best performing hyperparameters values sets					
First_Dataset target gas = NO_2	*NN*	*SVR*	*MLR*	*GPR*	*RC*
STATIC	$HNN = 5$	$(KF, C, \gamma, \varepsilon) = (\text{'}RBF\text{'}, 2^3, 2^3, 2.7)$	–	$(KF, \sigma) = (SquaredExp, 3.2)$	$(SR, IS, RU) = (0.1, 0.1, 200)$
TDL = 3 min	$HNN = 5$	$(KF, C, \gamma, \varepsilon) = (\text{'}RBF\text{'}, 2^3, 2^3, 0.1)$	–	$(KF, \sigma) = (SquaredExp, 1.7)$	
TDL = 5 min	$HNN = 5$	$(KF, C, \gamma, \varepsilon) = (\text{'}RBF\text{'}, 2^4, 2^4, 0.1)$	–	$(KF, \sigma) = (SquaredExp, 3.2)$	
Best performing hyperparameters values sets					
Second_Dataset CO target gas	*NN*	*SVR*	*MLR*	*GPR*	*RC*
STATIC	$HNN = 5$	$(KF, C, \gamma, \varepsilon) = (\text{'}RBF\text{'}, 2^3, 2^3, 0.1)$	–	$(KF, \sigma) = (SquaredExp, 0.2)$	$(SR, IS, RU) = (0.1, 1e-5, 20)$
TDL = 3 h	$HNN = 5$	$(KF, C, \gamma, \varepsilon) = (\text{'}RBF\text{'}, 2^4, 2^4, 0.1)$	–	$(KF, \sigma) = (SquaredExp, 0.1)$	
TDL = 5 h	$HNN = 5$	$(KF, C, \gamma, \varepsilon) = (\text{'}RBF\text{'}, 2^5, 2^5, 0.1)$	–	$(KF, \sigma) = (SquaredExp, 0.1)$	

Table 2. Results of performance evaluation procedure expressed in terms of Mean Absolute Error (MAE) over true pollutant concentration

MAE (ppb)—(STD)					
First dataset target gas = NO_2	*NN*	*SVR*	*MLR*	*GPR*	*RC*
STATIC	1.52 (0.08)	1.54	1.58	1.69 (0.04)	1.27 (0.08)
TDL = 3 min	1.29 (0.07)	1.23	1.39	1.33 (0.04)	
TDL = 5 min	1.27 (0.09)	***1.20***	1.38	1.31 (0.03)	
MAE (mg/m^3)—(STD)					
Second dataset CO target gas	*NN*	*SVR*	*MLR*	*GPR*	
STATIC	0.85 (0.09)	0.80	0.93	1.05 (0.02)	0.89 (0.01)
TDL = 3 h	0.80 (0.05)	0.77	0.92	1.04 (0.03)	
TDL = 5 h	***0.74 (0.18)***	0.76	0.92	1.04 0.01)	

Different architectures are reported in different columns while the different rows report the performance values obtained at different length of the tapped delay observation window (TDL). Best performing models are highlighted in bold

As we expected, confirming lab based evidences, for each different main architecture (NN, SVR, MLR, GPR) the use of a tapped delay line making use of past sensor response samples significantly ameliorated the performance of the corresponding static version in the first dataset. Concerning the second dataset, interestingly enough, only a fraction of the tested architectures (NN, SVR) seems to be able to exploit process dynamic related information content embedded in the tapped delay line observations.

SVR and ANN expressed a performance advantage with respect to the rest of the proposed architectures over both the dataset.

RC confirms its interesting performances by being able to compete, scoring very similar values, with classic NN while being outcompeted by SVR. In the second dataset, its performances are inferior to SVR and NN but it nonetheless outcompeted GPR and the basic MLR approach. However, Tapped delay line equipped NNs seems capable to express same or better performances in a more concise and elegant fashion, embedding knowledge in less computational units and weights. On the other hand the training of a fully connected NNs is more computationally intensive than what is needed to train the linear readout of the proposed Echo State Network. It is worth to note anyway that NN, GP and RC results are expressed in terms of average performances over 30 repetitions of the training-test procedure due to the stochastic nature of their initialization/training procedures. In facts, when applicable, the standard deviation of the MAE results have been reported in table in brackets.

4 Conclusions

This work reports the results of a comparison exercise conducted with the aim of testing the use of several dynamic ML architectures, recently proposed for solving the slow dynamic issues of chemical multisensing device. In particular, tests have been conducted with on field recorded data in order to obtain performance estimations that could be used for the design of real world operating systems. The overall results

confirmed laboratory studies findings with respect to the performance amelioration obtainable by taking into account sensors response dynamic information. Neural architectures (NN, RC) and SVR obtained best score outcompeting MultiLinear and Gaussian Process regressors. Future works will include a more complete evaluation with particular focus on computational and memory impacts of the varous techniques. The aim will be to select the best suitable algorithm for CMD on-board or fog computing implementation as well as offline centralized implementation in pervasive deployments, where computational load due to incoming data stream to process may represent a serious concern.

Acknowledgements. This work was partially funded by project MAVER (Manutenzione Avanzata dei Veicoli Regionali) under Campania Aerospace District initiative and by COST Action TD1105 EuNetAir (European Network on New Sensing Technologies for Air-Pollution Control and Environmental Sustainability).

References

1. Directive 2008/50/EC of the European Parliament and of the Council on ambient air quality and cleaner air for Europe, Official Journal of European Union, L152/1, 6/2008
2. I. Mead et al., The use of electrochemical sensors for monitoring urban air quality in low-cost, high-density networks. Atmos. Environ. **70**, 186–203 (2013)
3. L. Capezzuto et al., A maker friendly mobile and social sensing approach to urban air quality monitoring, in *IEEE SENSORS 2014 Proceedings* (Valencia, 2014), pp. 12–16
4. L. Spinelle et al., Field calibration of a cluster of low-cost available sensors for air quality monitoring. Part A: Ozone and nitrogen dioxide. Sens. Actuators B Chem. **215**, 249–257 (2015)
5. J. Fonollosa et al., Reservoir computing compensates slow response of chemosensor arrays exposed to fast varying gas concentrations in continuous monitoring. Sens. Actuators B Chem. **215**, 618–629 (2015)
6. E. Esposito et al., Dynamic neural network architectures for on field stochastic calibration of indicative low cost air quality sensing systems. Sens. Actuators B Chem. **231**, 701–713 (2016)
7. J.G. Monroy et al., Probabilistic gas quantification with MOX sensors in open sampling systems—a Gaussian process approach. Sens. Actuators B Chem. **188**, 298–312 (2013)
8. A. Shirzad et al., A comparison between performance of support vector regression and artificial neural network in prediction of pipe burst rate in water distribution networks. KSCE J. Civ. Eng. **18**(4), 941–948 (2014)
9. I. Naquib et al., Support vector regression and artificial neural network models for stability indicating analysis of mebeverine hydrochloride and sulpiride mixtures in pharmaceutical preparation: a comparative study. Spectrochim. Acta A Mol. Biomol. Spectrosc. **86**, 515–526 (2012)
10. R. Balabin et al., Support vector machine regression (SVR/LS-SVM)—an alternative to neural networks (ANN) for analytical chemistry? Comparison of nonlinear methods on near infrared (NIR) spectroscopy data. Analyst **136**(8), 1703–1712 (2011)

11. M.C. Ozturk et al., Analysis and design of echo state networks. Neural Computation **19**(1), 111–138 (2007)
12. De Vito et al., CO, NO_2 and NO_x urban pollution monitoring with on-field calibrated electronic nose by automatic bayesian regularization. Sens. Actuators B Chem. **143**(1), 182–191 (2009). UCI dataset
13. https://archive.ics.uci.edu/ml/datasets/Air+Quality—visited July 2016

A Distributed Sensor Network for Waste Water Management Plant Protection

S. De Vito[1(✉)], G. Fattoruso[1], E. Esposito[1], M. Salvato[1], A. Agresta[1], M. Panico[2], A. Leopardi[3], F. Formisano[1], A. Buonanno[1], P. Delli Veneri[1], and G. Di Francia[1]

[1] DTE-FSN-DIN, ENEA, P.le E. Fermi, 1, 80055 Portici, NA, Italy
saverio.devito@enea.it
[2] Acea Gori Servizi Scarl, Via Ex Aeroporto snc, Pomigliano d'Arco, NA, Italy
[3] Dip. Ing. Civile, UNICLAM, Via G. Di Biase, 43, Cassino, FR, Italy

Abstract. Waste water management process has a significant role in guarantee sea and surface water bodies water quality with direct impact on tourism based economy and public health. Protection of this critical infrastructure form illicit discharges is hence paramount for the whole society. Here, We propose a pervasive monitoring centered approach to the protection of wastewater management plant. An hybrid sensor network is actually deployed along the wastewater network including several different transducers. Incepted data are harmonized and processed with an integrated SWMM model and machine learning based approach in order to forecast water qualitative and quantitative aspects, detect and localize anomalies. An advanced WEBGIS-SOS based interface conveys relevant information to the management entity allowing it to take appropriate actions in a timely way, reducing and mitigating the impacts of illicit discharges.

Keywords: Wastewater management · Distributed sensor network · Water quality monitoring · Plant protection

1 Introduction

Wastewater contains a number of pollutants and contaminants, including plant nutrients, heavy metals, organic pollutants and other kinds of microorganism (viruses, bacteria, protozoa). All of these can cause health and environmental problems and can have economic and financial impacts, when improperly treated or untreated wastewater is released into the environment [1]. Hence, Waste water collection and management process has a significant role in protect tourism based economies and public health. Discharges of toxic substances that reach the waste water management plants may adversely affect the plants themselves, causing the release into the environment of pollutants at illegal and harmful concentrations. Regulatory agencies established in Italy a direct penal responsibility of waste water management company for adverse impact on environment due to management plant malfunction. As such, it is paramount for the company to monitor the waste water network so to detect and predict dangerous

B. Andò et al. (eds.), *Sensors*, Lecture Notes in Electrical Engineering 431,
DOI 10.1007/978-3-319-55077-0_39

and anomalous inputs to the purification plant. Until very recently and, in practice still currently, waste water pollution continuous monitoring is severely affected by several costs and technological issues. Consequently, the information about sewage network environment and receiving surface water bodies is limited, lacking consistence and completeness [2]. In their work, Métadier and Bertrand-Krajewski, among the firsts, proposed a continuous monitoring approach to the evaluation of pollution levels in a stormwater network by using turbidity measurement at catchment outlet. Their work revealed the significant time variability and complexities of interactions that can be found in real world scenarios highlighting the limitations of conventional approaches. However their work focused on single point of measurements obtaining limited information on the pollutant status along the network. Several works have addressed drinking water infrastructure monitoring and protection with a pervasive approach, i.e. using a sensor network for early detection of significant events [3] or source localization. However, only a few works have attempted to test these methodologies on real world stormwater or combined sewage [4, 5], due to the harsh operating conditions and characteristics of wastewater. Summarizing, up to now, monitoring strategies based on routine analytical assessments do not allow to forecast or prevent or mitigate the effect of illicit discharge, because water quality assessment occurs sparsely in space and time. In order to overcome these limitations, we need a completely new paradigm for this critical infrastructure protection that could leverage the opportunities of the integrated use of online continuous and pervasive sensor readings and forecasting models. To this purpose, the SIMONA Project investigates, develops and test new strategies for waste water management plant protection. Funded by Regional Operative Program of Campania (Italy), it involved actual stakeholders and research agencies. It aims to tackle the problem with an innovative and practical approach including on-field trials for testing the developed methodologies. In this work we present the concept and design of the proposed integrated system and the early results of its deployment along the Massa Lubrense waste water network.

2 The Proposed Methodology

In order to avoid unnecessary latencies and delays, and to detect events timely and mitigate impacts, SIMONA proposes a simple data assimilation scheme, consisting of several components interacting in a predetermined scheme. At the core of the architecture ensuring the critical roles lies **a pervasive intelligent sensing network**, responsible for timely measurements of relevant variables and early warning via on board Anomaly Detection algorithm and **forecasting and inverse models**, responsible for diffuse assessment, water quality forecasting, backtracking of illicit emissions. The SIMONA ICT service architecture ensure the inception and storage of incoming data as well as the orchestration of execution of models and data processing algorithm. A separated HCI section provide for GIS data visualization functionalities of forecasting modeling results.

2.1 Sensor Network

The SIMONA sensor network is based on heterogeneous model including several different multisensor devices ensuring monitoring different variables with different accuracies. In particular commercial contact multisensor devices and prototypal sensors developed by ENEA cooperate to near real time assessment of the relevant variables. The basic principle is to deploy a limited number of commercial multisensor device providing high accuracy measurements in focal nodes of the wastewater network integrating their data with a diffuse network of low cost, low maintenance requirements prototypal nodes to reduce total costs of ownership of real world scenario deployments. S::CAN™ commercial multisensor devices have been selected for their reliability by design concept being mostly based on optical transducers but in principle the ICT service infrastructure would be able to integrate different vendors systems. The chosen (s::can™) systems integrate different electrochemical and spectrometric transducers, operating at powerline equipped nodes of the collecting networks [6]. In particular they are able to capture and transmit near real time information (Ts = 1 min) on Chemical Oxygen Demand (COD), Ammonia, Total Suspended Solids (TSS), Water level, pH and Temperature by relying on cell phone infrastructure (see Table 1). To compliment commercial sensors capabilities, Non-contact multisensors device have been designed to record relevant proxies of water pollution levels such as NH3 and H2S off gas, remote water temperature, water level. The aggregate sensed data vector is used to evaluate an overall status that, processed by an onboard or remote anomaly detection algorithm, may detect anomalous conditions that can indicate high pollution events. These detection events may be used to rise warning conditions and trigger enhanced monitoring actions. Their low cost enable, at least in principle, the diffuse deployments of multiple instance of such multisensor device providing a pervasive network of water quality assessment sentinels. Furthermore, special very low power and low maintenance nodes have been deployed for long term unattended detection of wastewater flow in overflows sections of the network that are only used in case of heavy rains. The presence of water in those sections may indicate transport issues like clogging. Both the systems relies on STMicroelectronics Nucleo boards embedding ad hoc developed software and GSM connectivity board to capture, locally process, store and transmit sensor data. Specifically, their duty cycle foresee to send SMS embedded data in case of alert for immediate reaction plus a combo SMS conveying hourly averaged data at a 24 h rate. A further sensor system based on IR and UV reflectance sensing, developed by Water Research Council (UK) and aimed to COD and TSS non-contact estimation, is included in the multisensor set (see ref. [7]).

2.2 Anomaly Detection Algorithm

In order to enable the fast identification of local anomalies caused by illegal drainages or faults on the sensor network, we employ an immune based algorithm for the anomaly detection [8]. If on board encoded, this enable sensors to autonomously send

Table 1. List of the measured parameters by Commercial multisensor devices

	Parameter	Measurement unit	Range
Commercial sensor device	COD	mg/l	0–3750
	TSS	mg/l	0–2500
	PH	–	0–14
	NH4	ppm	0–1000
	Conductivity	mS/cm	0–2000
	Temperature	°C	−5–75
	Water level	cm	0–200
	Flow	l/s	–
	Pluviometer	Impulse	1 pulse × 1 mm of rain

alerts. Biomimetically, these algorithms typically operates using two principal entities, i.e. antibodies and antigens. Particularly, in the initial boot phase (a fixed one week long time window) each sensor measurement is stored in an antibodies set called dynamic B-cells (DBs) reservoir. Each subsequent incoming samples is indicated instead as antigen. The DBs reservoir acts as the "normal" prototypes set, actually representing the algorithm internal knowledge. Each DBs can be described, by means its features vector, as a point in the multivariate space, having an own influence sphere, a stimulation level s and a specific age a. The radius $c * \sigma^2$ of its influence sphere represents the variance of the Gaussian distribution prototyped by each DB. The algorithm, dynamically adapts each DB radius size on the strength of the novel incoming field recorded sensor readings. This allows for the efficient computing of the actual feature space coverage of an antibody, simultaneously adapting it to short term evolutions. The dynamic antibodies characterization is completed with a stimulation and age parameters. Specifically, the stimulation level allows to model, over time, the DB cell local representativeness with regards to the set of incoming sensor readings. Large stimulation levels actively slow down the ageing process of a DB cell rejuvenating its age parameter. The DBs characterization by these parameters guarantees at all times an accurate ad faithful representation of the system evolution. In order to obtain a scalable model, DBs, competing each other for the memory resources, are partitioned in clusters by means of a density based clustering algorithm (DBSCAN). In this way, the problem of the anomalies recognition involves only a set of cluster representative instances (cluster centroids) and not all DBs with considerable computational advantages that enable on board integration. On the basis of the DB based representation, antigens are hence classified as "normal" or otherwise "anomalous" if their feature vector significantly differs from the current normality pattern described by closest hourly DBs (Fig. 1).

2.3 Software Architecture

The ICT service architecture (Fig. 2) first endpoint is based on a data sink system designed to incept data coming from the heterogeneous sensor network. Based on an array of dedicated receiving units it receive data and forward data to a NOSQL scalable

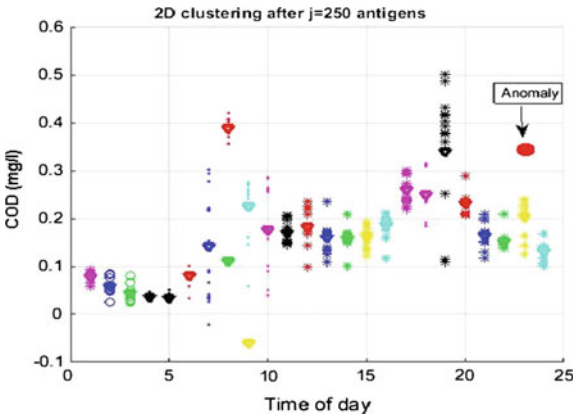

Fig. 1. Offline example of anomaly detection in the stream of incoming normalized COD data

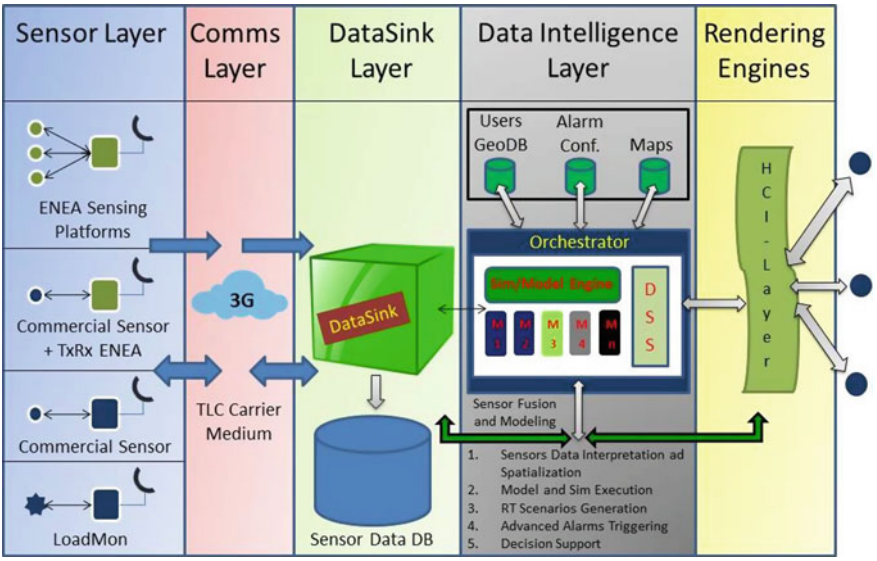

Fig. 2. Sketch of the SIMONA ICT architecture with relevant interaction among main systems

storage system based on MONGODB server. JSON formatting is carried directly from custom components on the commercial sensor systems while a dedicated server based on Raspberry PI + GSM shield provide the receiving end for the prototypal systems. Incoming SMS are parsed to build the appropriate JSON document to be stored in the database. JSON document, in turn, are sent to a Node.js based software component which take the role of MONGODB input interface. The next node in the architecture, the so called orchestrator, take the role of orchestrating the data processing flow

between the primary storage system and the HCI. Data are extracted from the primary storage and processed with a dedicated set of algorithms to extract relevant semantic content. Here, we focus on forecasting models and rule based alerting systems. A rule based system based on Drools [9] open source software has been configured to host simple rules devised to detect rule based anomalies. Relevant examples includes the detection of threshold and location based alerts plus unexpected water presence. In the first case an alert is triggered when a particular threshold levels casted on a single or a set of variables is reached in a particular location of the deployment. In the second case an alert is triggered when water presence is detected and transmitted by a water presence sensor and no rain have been recorded by the rain gauges sensors. Model description is detailed in the following subchapter.

2.3.1 Forecasting and Inverse Model

One of the primary role of focal nodes data is to help calibrating SWMM [10] based water transport models so to achieve accurate prediction of network status in the next hours. By using networked sensors recorded values as an input, the calibrated SWMM model will be able to predict the arrival of heavily polluted water volumes at the plant. In this case, the plant manager could be warned to take appropriate action so to reduce the possibility of harming the bacterial population of the wastewater reactor. In this context we also developed and deployed a methodology for identify source of contamination events in a real SS. This methodology that allow the finding of the input location of contamination is formulated as an optimization problem. For its solution three components are required: sensor measurements along the system; an hydraulic/water quality model and an optimization problem solver. The USEPA's SWMM model [11] is used to perform the hydraulic and water quality simulations, whereas the genetic algorithm library GALib [12] is used to solve the optimization problem. Computational efforts represents the primary limiting factor for applying this methodology to real sewer systems. Actually, they significantly increase with network size and complexity [13]. This drawback is overcomed with a pre-screening procedure that reduces the number of nodes before the optimization routine. First step of this procedure defines the set of candidate nodes through the pollution matrix [14]. This matrix is an $N \times N$ matrix of 0–1 coefficients, where N is the number of nodes and "1" and "0" correspond to contaminated and non-contaminated nodes, respectively. The ith row lists all contaminated nodes due to an accidental pollution in node i. The jth column lists all polluting nodes (sources of pollution) that can contaminate node j. In the second step the unnecessary elements of the network are cut. The flow coming from the cut parts is added to the next node of the remaining scheme, assigning a new average inflow and a new time pattern. The inflow is estimated from the last link of the cut portion, while the time pattern is estimated from the downstream link next to the node, where the value has to be assigned. After the pre-screening procedure, the optimization problem is formulated, minimizing a dimensionless objective function, F, defined as the normalized square difference between simulated and the measured contaminant concentration values:

$$F = \sum_{t=t_0}^{t_c} \sum_{i=1}^{N_s} \left(\frac{C_{it}^{obs} - C_{it}(L, C_0, T_0, D)}{\frac{\left(C_{it}^{obs} + C_{it}(L, C_0, T_0, D)\right)}{2}} \right)^2$$

where i = sensor index; t = time step; C^{obs} it and C_{it} = measured and simulated concentration at sensor i at time step t, respectively; L = intrusion node index; C_0 = release concentration (mg/l); T_0 = release starting time; D = release duration (h); t_0 = time of the first detection of the contaminant at the sensor i; t_c = ending time of simulation; N_s = total number of sensors. The simulated concentrations are computed through a forward quality simulation using EPA-SWMM, fixing the values of the unknown source characteristics, which are herein represented by the four decision variables: pollution injection node, L; pollutant concentration at the source, C_0; injection starting time, T_0; and injection duration, D. Then, the optimal value of the objective function F is obtained by modifying the values of these variables. The result is obtained by a typical Genetic Algorithm (GA) that starts with the generation of a random set of strings (population), then the objective function score is evaluated for each string (individual). Afterwards, the algorithm generates a new set of strings through selection, crossover and mutation. The above steps are repeated until the selected stopping criterion is attained.

2.3.2 Human to Computer Interface

A web based geospatial HCI (Human to Computer Interface) has been developed. This geo-console (i.e. web based map viewer) allows accessing and browsing within maps the various continuous and networked sensors, and browsing, queering and analyzing the observation data both in real time and at prefixed time intervals. The observation data can be real measurements gathered by sensors actually installed along the wastewater networks as well as predictive measurements returned by on line simulation models (see previous chapter). The networked sensors can be visualized as an unique layer or as single layer for each monitoring parameter. For the multi-sensor stations, it is possible to visualize the real time observations of all active sensors (Fig. 3). Within each layer, as thematic map, it is possible to visualize the state of the sensors, especially their alert state when anomaly situations occur as well as prefixed threshold values are met. By means of a toolbar, user can access two specific web-based browser applications. One application is a web SOS client, developed as a extending the open source Sensor Web Client. It acts as an application layer to handle, via web, the rendering of queried observations in the form of graph, time series and geographic maps. The implementation of the described web based map viewer has been deployed by using the framework GeoExt2 and some libraries such as OpenLayers, Sencha-ExtJS 4.2.x.

A SWE (Sensor Web Enablement) architecture has been developed integrating and real time accessing the various networked sensors and their observations, enabling observation data browsing, querying and analyzing capabilities within the geo-console HCI. Essentially, it consists of the services SOS (Sensor Observation Service) by which clients access descriptions of associated sensors and their collected observations by a standardized web service interface. The SWE architecture has been realized by customizing the 52°N framework, version 3.x and, specifically, by using the standards OGC SOS 1.0 and 2.0. The deployed SOS endpoint uses a database PostgreSQL 9.3.1 with a spatial extension PostGIS 2.x to store observation values and sensor metadata.

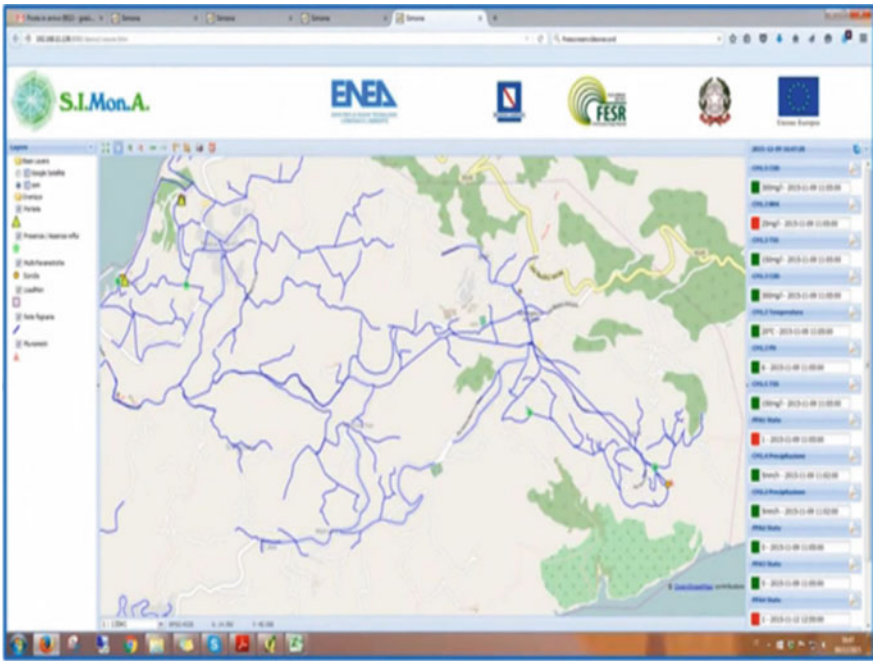

Fig. 3. The web based geo-console: view of all multi-sensor probes installed along the Massa Lubrense network and real time queering observation data

3 Deployment at Massa Lubrense WWMP

After software platform setup, a multi-month pilot study have been performed by deploying an hybrid sensor network on the wastewater network of Massa Lubrense, a 14,000 inhabitants town located near Naples, Italy on the Amalfitan coast. The whole area is interested by significant touristic activities. It is serviced by a combined sewer system, covering an area of 0.75 km^2. The scheme consists of 242 circular conduits connecting 241 junctions, one pump, two storage units and one outfall. The deployment lasted from October 2015 until February 2016 including a stress test experiment in which a pollutant simulant have been allegedly discharged into the sewer system. The networked sensor system was characterized by 4 multisensors prototype located at internodes, 4 Commercial S::CAN devices located at main facilities including pumps and water management plant, 8 Water presence devices distributed in overflow locations and 1 Loadmon device at the water management plant.

3.1 Preliminary Data Analysis and Results

Preliminary results confirms the harshness of the sewage environment with several issues related with sensor operation and data transmission occurring frequently and requiring maintenance and tuning operations. First results, in facts, indicate a relatively

stable behavior of the water quality in the network while contact sensors, with special regard to electrochemical transducers, have been subjected to drift needing recalibration. Instead, fall of water level due to seasonal changes (population, low rainfall levels) was unexpectedly large at one of the sites and caused the sensors to run dry multiple times. The 3G coverage of the monitored site has also caused significant packet losses indicating a strong coverage as a must to ensure continue operation. First results indicate sufficient correlation among analytical control measurements and sensor readings (see Fig. 4). Observing the same figure, it is also clear that relevant information on water quality is embedded at relatively high frequency and cannot be revealed by current monitoring strategies involving a limited number of analytical measurements.

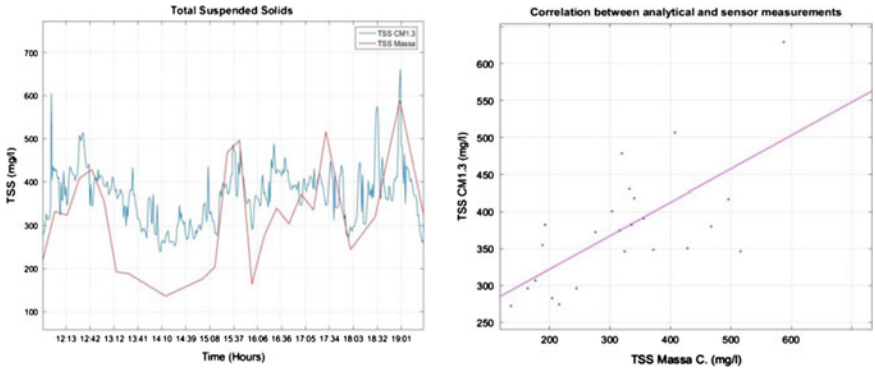

Fig. 4. Correlation among analytical measurements and sensor readings for TSS parameter

Description of correlation among different variables is also made possible as seen in Fig. 5, where continuous monitored COD and TSS express an high correlation factor (r = 0.9) substantially confirmed by analytical control measurements.

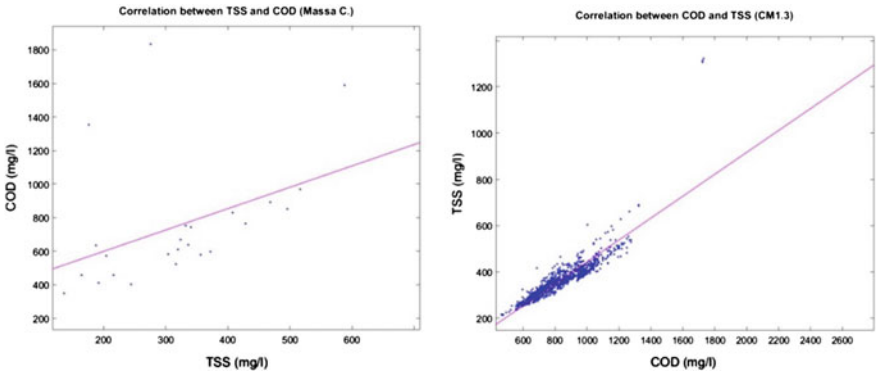

Fig. 5. Correlation among TSS and COD parameters measured by analytical control (*left*) and sensor readings (*right*)

In Fig. 6 the sensor node captures the influence on water quality of the pumps duty cycle. As pumps onset water coming from different sewage network segments mix together cyclically changing COD values. Again, these oscillations are likely to be lost with conventional monitoring strategies.

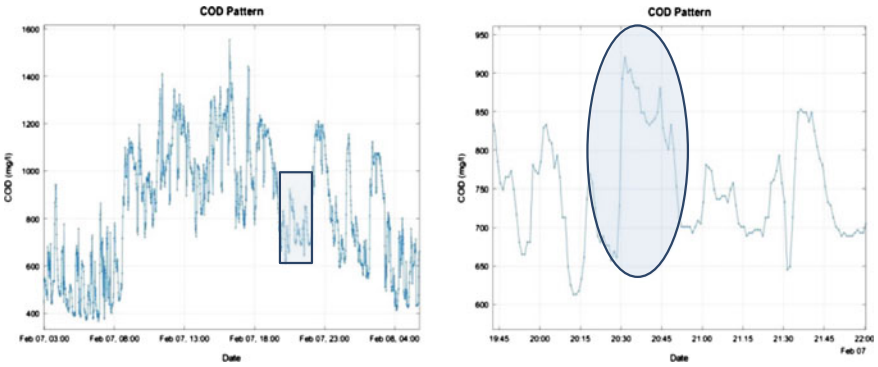

Fig. 6. COD diurnal pattern. It can be identifier the rapid transients, due, for example, to events corresponding to commercial activities

Figure 7 shows the diurnal patterns of COD and TSS, for the commercial sensor devices. Diurnal patterns help to characterize measurement site and identify high load network segments, and can be useful in order to provide feedback on citizen's and company's impact on water quality. In turn, this could improve their environmental awareness eventually leading to behavioral changes. In particular, it is possible to note the typical daytime peak load following by gradual descent towards the night hour regime. At the same time it is possible to identify site CM4.1 as characterized by minimal variance along the 24 h while CM 3.1 as characterized by stronger dynamic in both TSS and COD measurements.

On February 19th, a stress test has been executed with the release of 300 + 300 L of Nutrient™, an organic carbon source for nutrient supply in wastewater treatment plants injected at two different sites:

- Punta Campanella (22 × 25 l in 5 min),
- Patierno (12 × 25 l in 3 min),

with a 6 h interval. As can be seen in Fig. 8, deployed sensors have recorded and transmitted the simulated event propagation throughout the waste water network.

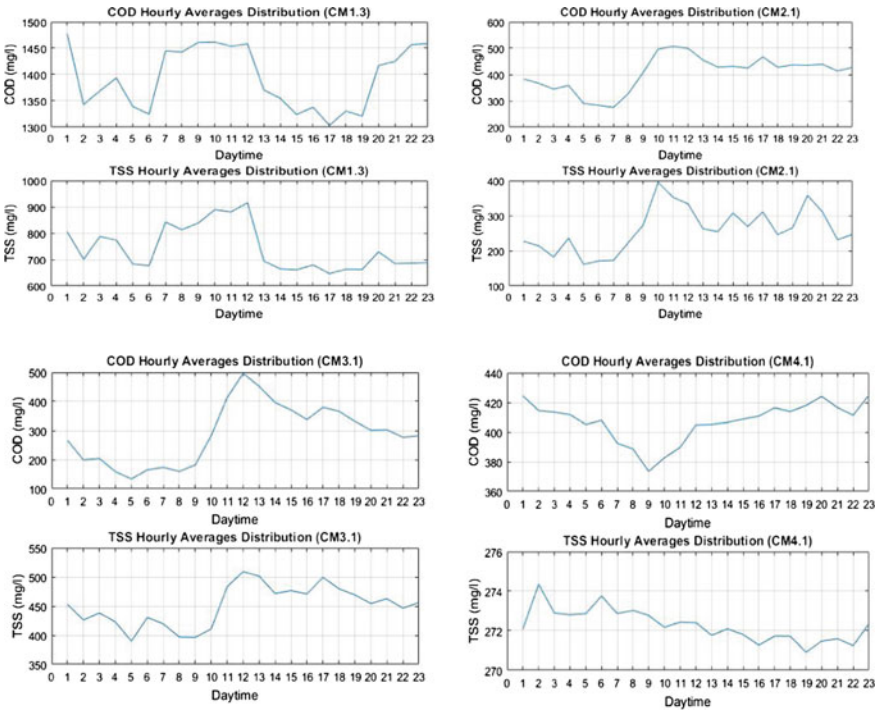

Fig. 7. Averaged diurnal patterns of COD and TSS, for commercial multisensor devices

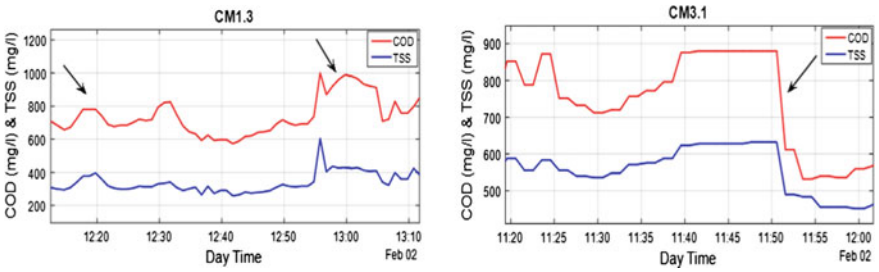

Fig. 8. Deployed sensors have recorded and transmitted the simulated event propagation throughout the waste water network. It can be observed that the first detection of contaminant was read at 12:17 and second at 13:00 by CM1.3, the plumes transition was detected at 11:39 at CM3.1

4 Conclusions

We have presented the design and implementation of an integrated pervasive sensing/model based solution to the waste water management monitoring and protection. The proposed architecture have been deployed during a pilot test in a relatively small town of Sorrento Coast south of Naples. First results of the SIMONA project

pilot tests indicate the advantage of continuous monitoring highlighting high frequency feature that are lost with sparse spatial and temporal conventional measurement patterns. Although affected by several issues due to the peculiarly harsh environment characteristics features can be easily extracted involving site specific pollution fingerprints (pollutant levels and correlations), dynamic patterns (average hourly concentrations) and cross sites correlations.

Acknowledgements. This work has received funding from the Campania Regional Operative Program FESR 2007–2013 under Project Campus SiMonA—"Sistema Integrato di competenze per il MONitoraggio Ambientale" (BURC no. 20, April 2012).

References

1. S. Even, M. Poulin, J.M. Mouchel, M. Seidl, P. Servais, Modelling oxygen deficits in the Seine River downstream of combined sewer overflows. Ecol. Model. **173**(2), 177–196 (2004)
2. M. Métadier, J.L. Bertrand-Krajewski, The use of long-term on-line turbidity measurements for the calculation of urban stormwater pollutant concentrations, loads, pollutographs and intra-event fluxes. Water Res. **46**(20), 6836–6856 (2012)
3. L. Cozzolino, R. Della Morte, A. Palumbo, D. Pianese, Stochastic approaches for sensors placement against intentional contaminations in water distribution systems. Civ. Eng. Environ. Syst. **28**(1), 75–98 (2011)
4. K. Irvine, M.C. Rossi, S. Vermette, J. Bakert, K. Kleinfelder, Illicit discharge detection and elimination: low cost options for source identification and track down in storm water systems. Urban Water J. **8**(6), 379–395 (2011)
5. B.K. Banik, C. Di Cristo, A. Leopardi, G. de Marinis, Illicit intrusion characterization in sewer systems. Urban Water J. 1–11 (2016)
6. S::CAN website: http://www.s-can.at/. Accessed Jan 2016
7. S.L. Russell et al., Non-contact measurement of wastewater polluting load—the Loadmon project. Water Sci. Technol. **47**(2), 79–86 (2003)
8. M. Salvato, S. De Vito, S. Guerra, A. Buonanno, G. Fattoruso, G. Di Francia, An adaptive immune based anomaly detection algorithm for smart WSN deployments, in *AISEM Annual Conference*, *2015*, vol XVIII (IEEE, 2015), pp. 1–5
9. Drools website: http://www.drools.org
10. SWMM website: http://www.epa.gov/water-research/storm-water-management-model-swmm. Accessed Jan 2016
11. L.A. Rossman, Storm water management model user's manual. Version 5.0. National Risk Management Research Laboratory, Office of Research and Development: US Environmental Protection Agency, 2010
12. M. Wall, GAlib: A C++ library of genetic algorithm components. Mechanical Engineering Department: Massachusetts Institute of Technology, 1996
13. C. Di Cristo et al., Closure to "Pollution source identification of accidental contamination in water distribution networks". J. Water Resour. Plann. Manage. **136**(2), 292–294 (2010)
14. A. Kessler et al., Detecting accidental contaminations in municipal water networks. J. Water Resour. Plann. Manage. **124**, 192–198 (1998)

Virtual Olfactory Device In EEG And Olfactory Conditioning Task: an OERP Study

S. Invitto[1(✉)], S. Capone[2], G. Montagna[1], and P. Siciliano[2]

[1] Human Anatomy and Neuroscience Lab, DiSTeBA, University of Salento, via Monteroni, 73100 Lecce, Italy
sara.invitto@unisalento.it, giovanni.montagna@le.imm.cnr.it

[2] National Research Council of Italy, Institute for Microelectronics and Microsystems (CNR-IMM), via Monteroni, Campus Universitario, 73100 Lecce, Italy
{simona.capone,pietro.siciliano}@le.imm.cnr.it

Abstract. Aim of this study is to investigate innovative olfactory applications of cognitive neuroscience in order to improve basic knowledge as well as to develop novel devices for enhancing synaesthetic experiences through olfactory stimulation. We arranged an experiment of olfactive conditioned evoked potentials by analyzing Event Related Potential (ERP) of adult safe volunteers during the conditioning perception of 2 odor stimuli, in an experiment of emotional face recognition task. Specifically, it was developed a paradigm of classical conditioning in which the three types of odors (pleasant, unpleasant, neuter) were conditioned on images of neuter face expression and these results were compared with direct results of olfactory stimulation. The main experimental evidence of our study consists in significant values in ERPs components in direction of a greater amplitude and slower latency in unpleasant condition. On the basis of these results one might assume that an unpleasant odor can modulate, in a cross modal way, the perceptions of emotional and neutral face expressions, and it's highlighted in an early ERPs component (P1) in conditioning way only for neutral expressions.

Keywords: Olfactory conditioned evoked potentials · Chemosensory event related potential · Olfactory perception

1 1 Introduction

The perception of an odor is a two-step process. First, there is a physiological process, i.e. the detection of chemical stimuli (odorous molecules) by olfactory receptors in the olfactory epithelium. Next, there is a neurologic process; olfactory neurons transduce receptors activation into neuronal electrical signals travelling along the olfactory nerve to olfactory bulb and finally, they are processed by subcortical and higher cortical areas, where odor encoding and perception occur. Because of this, olfaction is a complex primal sense highly associated with sexual attraction, mood, detection of danger and odors have the power to evoke distant memories and boost self-confidence.

B. Andò et al. (eds.), *Sensors*, Lecture Notes in Electrical Engineering 431,
DOI 10.1007/978-3-319-55077-0_40

A lot of knowledge on olfaction has to be still get mainly regarding its relationship with other sensory stimuli as audio, visual, taste stimuli [1]. Odor recognition memory is slightly influenced by the length of retention intervals. This was observed for short intervals (few minutes) as well as longer retention period (over a year too) [2]. Odor detection applications are needed by human societies in various circumstances. A recent study of He et al. [3] presents a novel apparatus designed to train maximum 5 mice automatically to detect odors using a new olfactory, relative go no-go, classical conditioning paradigm. The new paradigm offers the chance to measure real-time reliability of individual animal's detection behavior with changing responses.

Another approach to understanding the olfaction links to other senses is to monitor and analyze human brain activity during odors perception. By measuring event-related potentials (ERPs) by electroencephalography, it's possible to measure the brain electrophysiological response to a specific event, i.e. in this case the presentation of olfactory stimuli [4, 5]. Aim of this study is investigate how the olfactory system, which also involves and activates the subcortical areas, can modulate perception during an emotional face recognition task, and how, through a new method of olfactory stimulation we can also obtain a comparable trend analyzing Olfactory Event Related Potentials (OERPs). This study allows to investigate and to implement innovative applications of cognitive neuroscience in order to improve basic knowledge as well as to develop novel devices for enhancing synaesthetic experiences with olfactory stimulations. In order to compare two different olfactory applications, we analyzed a paradigm of classical conditioning and an OERP task [6]. Classical conditioning is a time-related learning process in which a neutral stimulus is associated, through repeated combined presentations, to a different stimulus not related with the neutral one. This means that, the olfactory stimulus, could be highlighted in the EEG, right through an identification and conditioning process related with an associated stimulus.

Moreover, in this work we proposed a contribute to the topic of olfaction exploration by brain activity monitoring during odors perception, by presenting a new measuring system of olfactory event-related potentials during olfactory stimulation. The system allows a Virtual Olfactive Stimulation in EEG (VOS-EEG); it generated and dispensed odorous stimuli and allows a controlled, automated and synchronized acquisition of the EEG signal [7]. The measuring system of new conception has been implemented through the design and implementation of an olfactometer interfaced to an EEG instrumentation. In particular, a two channels olfactometer, interfaced to EEG, allows the occurrence of OERP via the controlled administration of two different chemo-olfactory stimuli to the individual under analysis EEG. We selected some odorous substances for the definition of experiments of interest for the study of brain activity under stimulation from pleasant/unpleasant and neutral odors. We used this approach to study cross-modal effect of smell on perception and to investigate new paradigms of smell administration, as well as to promote new technologies and functional devices for olfactory cognition neuroscience.

In this study we obtain the same effect trend comparing a direct method with an indirect method.

2 2 Materials and Methods

2.1 Smell Tools and Method

We arranged an experiment of olfactory conditioned evoked potentials by analyzing visual ERP of 7 adult safe volunteers during perception of 2 odor stimuli: pleasant (rose, 2-phenyl ethanol $C_2H_4O_2$) and unpleasant (acid, Acetic Acid $C_8H_{10}O$). For the odorous stimuli in the experiment, pure chemical compounds were diluted in distilled water. A dilution ratio (1:4) was suitably considered in order to realize easily perceptible, but not unpleasant, odors; the odorants and their concentration used in the test are listed in Table 1 together with their odor sensory description. In addition, distilled water was used a control for inducing an odorless stimulus. The odorous solutions (5 ml) were put into 20 ml glass vials sealed with septum till the exposure time to the volunteers.

Table 1 Odors used in the conditioning ERPs experiment

Compound	Formula	Concentration (mg/ml)	Odor sensory description
Acetic acid	$C_2H_4O_2$	262.25	Acid, pungent, vinegar-like
2-phenyl ethanol	$C_8H_{10}O$	254.25	Floral, rose

2.2 Psychophysiological Tools and Method

(A) Emo Go-no Go task: We considered ERP components respect to neuter face. The signal was recorded by an EEG 16 channels, Through Brain Amp device and Brain Vision Recorder software (Brain Products). A further electrode was positioned above the right eyebrow for electro-oculogram recording. ERPs analysis was carried out using the Brain Vision Analyzer and the time off-line analysis was from 100 pre-stimulus to 500 ms post-stimulus with −100 ms baseline-correction. Thereafter, trials with blinks and eye movements were rejected on the basis of horizontal electro-oculogram with an ICA component analysis.

(B) Olfactory Event Related Potentials: through the VOS-EEG, synchronization, along with the program of olfactory stimulation, allows us to study in detail the OERP according to the stimulus triggers sent to an interfaced and digitized output that comes from the system (Fig. 1). The olfactory triggers are modulated as a function of the variables intensity and duration of stimulation.

Fig. 1 Subject during VOS EEG olfactory stimulation (pending patent n. PCT/IB2015/055575)

2.3 Experiments

2.3.1 First Experiment (classical condition)

An experiment of olfactive conditioned evoked potentials was arranged by analyzing ERPs of adult safe volunteers during perception of 3 odor stimuli (pleasant: rose odor; unpleasant: acetic acid; neutral: water), during a face recognition task paradigm. Specifically, we proposed a paradigm of classical conditioning in which the three types of odors were conditioned on images of neuter face expression [8]. Aim of the experiment was to understand how the olfactory system, which involves and activates the limbic system, can modulate a perception on emotional face recognition.

The experimental protocol was based on a NimStim Face Stimulus Set [9], during a learning training lasting 5 min, repeated for three times. Subsequently, the subject had to perform an emotional Face recognition task, implemented through NimStimSet, during a Emo No Go Paradigm Presented with E-Prime Presentation (the task had a duration of 10 min). During the face recognition task, the subject had to press a PC key, when he saw emotional neuter face expression in a presentation of randomized emotional expressions (fear, neuter and happy).

The experiments have been performed with a group of 7 safe volunteers (mean age: 35; s.d: 5.3).

Visual stimuli had a dimension of 240 $\times$ 210 pixels, and have been displayed centrally on a light gray background and to the same level of brightness on the computer monitor. The task odd-ball was administered via the E-prime software 2.0. Each trial, composed of a single type of target alternated randomly background-color, has lasted 600s, with a stimulus duration of 2000 and 1000 ms inter-stimulus duration.

The participants were instructed to stand upright with ca 75 cm between the front edge of the chair and the floor. The instruction was: 'Please click a button when you see a neuter face'.

2.3.2 Second Experiment on Olfactive Event-Related Potentials (OERP)

In this experiment we proposed the same odor stimulation (pleasant, unpleasant, neutral) using a novel system consisting of an olfactometer interfaced to an EEG instrumentation (Fig. 1) (pending patent n. PCT/IB2015/055575). The system allows to measure the OERPs under olfactory stimulation in a controlled, automated mode synchronized to the acquisition of the EEG signal.

The subjects had to perform two independent tests, in which each participant had to discriminate: (a) pleasant odor alternated to neutral odor and (b) unpleasant odor alternated to neutral odor. Each stimulation had a duration of 15 min.

3 Statistical Analysis and Main Results

EEG data processing: An artifact rejection criterion of 60 V was used at all other scalp sites to reject trials with excessive EMG or other noise transients; sampling rate was 256 Hz. After a transformation and a re-segmentation of data with the Brain Vision Analyzer, the artifact-free EEG tracks, were averaged in each case to extract the main waveforms, the P1 in the time range 80–150 ms, the N170 in the time range 150–250 and P3 component in the 250–400 ms time interval, according to literature. A semi-automatic peak detection was performed on each ERPs components.

Data analysis: We performed a General Linear Model to repeated measures to analyze ERP component, P1, N170 and P3, with two Odor Conditions (pleasant and unpleasant) and three Emotional Face Expressions (neuter, fear and happy) as Factors and Amplitude and Latency as dependent variables. As main results of our study we found significant value in P1, and in P3 components (see Fig. 2).

Fig. 2 1° *experiment*. Matching ERP *Black Line* Acid Acetic and *Red Line Rose*; Loreta Representations of *Acid Acetic* (*Center*) and *Rose* (*Right*) (Color figure online)

In P100 we found significant value in neutral face conditions in P8 Latency (F = 5277; p = 0035); in PZ Amplitude (F = 6157; p = 0025); in F7 Amplitude (F = 6784; p = 0019) and in F8 Latency (F = 5369; p = 0034).

In P300 we had significant value only for neutral faces in C3 Latency (F = 28,339; p = 0006) and in PZ Latency (F = 7346; p = 0005).

All the results are in direction of a greater amplitude and slower latency in Acid Acetic Condition (Fig. 2).

The red line corresponds to the olfactory stimulus of the odorous substance S2, and the black line corresponds to the olfactory stimuli of neutral substance S1 and S2. AS in the case of the classical paradigm, we have the same results of the first experiment, ERP for unpleasant odor is less activating of the ERP for pleasant odor (Fig. 3).

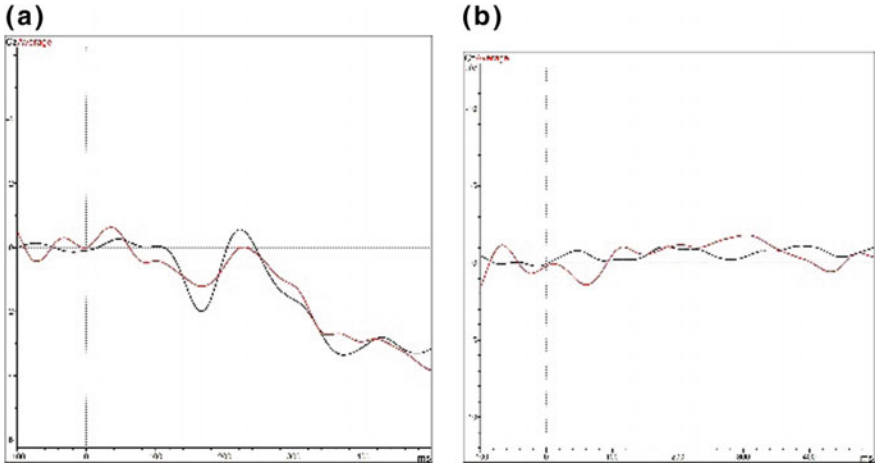

Fig. 3 2° *experiment*. OERP on Cz **a** Neuter (*Black line*) versus unpleasant odor (*red line*); **b** Neuter (*Black line*) versus pleasant odor (*red line*) (Color figure online)

4 Conclusion

In this work we presented the preliminary results of a study on Olfactive response and Crossmodal perception. The study was organized in two different experiments: First Experiment (classical condition), Second Experiment on OERPs by a novel prototype which performs a Virtual Olfactive Stimulation interfaced to EEG (VOS-EEG). According to the results of both experiments, we may suppose that the unpleasant odor can modulate, in a cross modal way, the perceptions of emotional and neutral face expressions, and it can be general in a very early component (P1) and more specific, in conditioning way, in the attentive component (P3), only for neutral expressions. We addressed these issues in the research field and have ventured into the development of Virtual Olfactive Stimulation in EEG device (VOS-EEG), that allows to interface olfactory responses to cortical chemosensory event related potentials.

Acknowledgements. ERPs research has been supported by Università del Salento—co-funded through 5 for Thousand Research Fund. The CNR-IMM authors wish to express gratitude to Dr. Maria Tufariello (CNR-ISPA, Lecce, Italy) for providing kind cooperation and material support in the course of this study.

References

1. G. Ghinea, O.A. Ademoye, Olfaction-enhanced multimedia: perspectives and challenges. MultimediaTools Appl. **55**(3), 601–626 (2011)
2. G.M. Zucco, Anomalies in Cognition: olfactory memory. Eur. Psychol. **8**(2), 77–86 (2003)
3. J. He, J.K. Wei, J.D. Rizak, Y. M. Chen, J. H. Wang, X. T. Hu, Y.Y. Ma, An odor detection system based on automatically trained mice by relative go no-go olfactory operant conditioning, Nature, Scientific Report 5, Article Number 10019 (2015)
4. Y.-K. Kim, S. Watanuki, Characteristics of electroencephalographic responses induced by a pleasant and an unpleasant odor. J. Physiol. Anthropol. Appl. Human Sci **22**, 285–291 (2003)
5. A. Yazdani, E. Kroupi, J.-M. Vesin, T.E Brahimi, Electroencephalogram alterations during perception of pleasant and unpleasant odors. in Proceedings of Fourth International Workshop on Quality of Multimedia Experience (QoMEX), (2012), pp. 272–277
6. R.G. Miltenberger, & K.A. Crosland. Parenting. The Wiley Blackwell handbook of operant and classical conditioning. Wiley (2014). doi:10.1002/9781118468135.ch20
7. S. Invitto, S.Capone, G. Montagna, P.A. Siciliano, Method and related system for measuring physiological parameters of a human subject undergoing an olfactory stimulation, patent n. MI2014A 001344, PCT/IB2015/055575
8. M.J. Banissy, L. Garrido, F. Kusnie, B. Duchaine, V. Walsh, and J. Ward, Superior facial expression, but not identity recognition, in mirror touch synesthesia. J Neurosci. **31**(5), 1820–1824 (2011)
9. N. Tottenham, J.W. Tanaka, A.C. Leon, T. McCarry, M. Nurse, T.A. Hare, D.J. Marcus, A. Westerlund, B.J. Casey, C. Nelson, The NimStim set of facial expressions: judgments from untrained research participants. Psychiatry Res. **168**(3), 242–249 (2009)

Wireless Electromyography Technology for Fall Risk Evaluation

A. Leone(✉), G. Rescio, A. Caroppo, and P. Siciliano

National Research Council of Italy, Institute for Microelectronics and Microsystems, via Monteroni presso, Campus Universitario Palazzina A3, Lecce, Italy
{alessandro.leone, gabriele.rescio, andrea.caroppo, pietro.siciliano}@le.imm.cnr.it

Abstract. The chapter presents a study on an electromyography-based wearable system for fall risk assessment. It has been focused especially on the electrical activity analysis of the user's lower limb muscles in relation to his body movement. For that purpose four wireless electromyography probes (sEMG) have been placed on the Gastrocnemius/Tibialis muscles and an accelerometer-equipped t-shirt has been worn during the Activities of Daily Living (ADLs) and fall events simulations. The results obtained have shown that the simultaneous contraction of the muscles considered appear relevant immediately after the starting of the imbalance condition, when the vertical velocity of the user's body is too low for the commonly used inertial-based pre-fall detection systems. So an sEMG-based platform should be suitable to realize a more efficient platform to prevent the injures due to the fall. The mean lead-time measured, in controlled condition, is more than 750 ms with performance in terms of sensitivity and specificity more than 75%.

Keywords: Electromyography · Inertial-based system · Pre-fall detection · Wearable sensors

1 Introduction

Fall events represent serious problem among older people [1]. The fall detectors appear a very important tool in reducing the time of medical intervention, however it could be desirable the development of a system able to detect falls before the impact on the floor which, working together with an impact reduction systems, can limit the consequences of falls [2, 3]. Several solutions have been proposed in the prevention of falls and high-quality reviews have been presented [4]. They use inertial sensors and threshold-based techniques for the classification of the events. Their performance suggest that specificity and sensitivity values are high, but the lead-time parameter before the impact is low (less than 400 ms). For these reasons a new surface EMG-based system to detect the risk of fall in a faster mode has been investigated. To reduce the invasiveness, only four EMG sensors, placed through the gelled electrodes, have been considered and used for measuring the lower limb muscles activities. The main purpose of the work, is the development of a low-power, wireless, real time,

B. Andò et al. (eds.), *Sensors*, Lecture Notes in Electrical Engineering 431,
DOI 10.1007/978-3-319-55077-0_41

automatic and effective fall risk detection EMG-based framework. The lead-time before the impact has been evaluated by simulating imbalance conditions and fall events through a moveable platform activated by a pneumatic piston. The obtained results show that the system, in simulated and controlled conditions, is able to detect the falls about 780 ms before the impact on the floor. Moreover, an accelerometer-based system have been used during the simulation campaign to evaluate the EMG signals respect to the user's body trunk vertical velocity after an imbalance condition.

2 Materials and Methods

2.1 Hardware Architecture

In this study a multi sensor approach has been used to evaluate the user's muscles behavior and their movement information during the simulation of Activities of Daily Living (ADLs) and fall events. The BTS Bioengineering Freeemg 1000 probes [5] has been chosen to acquire EMG signals of the lower limb muscles, while the accelerometer-based SMARTEX garment [6] has been adopted for the analysis of the movements of the upper part of the body. The accelerometer system has been used to evaluate the vertical velocity profile of the fall events and to create the ground truth during the acquisition campaign for the data collection.

2.1.1 Surface Electromyography Acquisition System

The BTS probes (Fig. 1b) have been chosen since they are small (41.5 × 24.8 × 14 mm for mother electrode and 16 × 12 mm for satellite electrode) and lightweight (less than 10 gr). Moreover they can transmit the data for about eight hours in streaming and wireless mode (Zigbee protocol) up to 20 m in free space. The system allows an accurate acquisition data by using a resolution of 16 bit and a 1 kHz frequency rate.

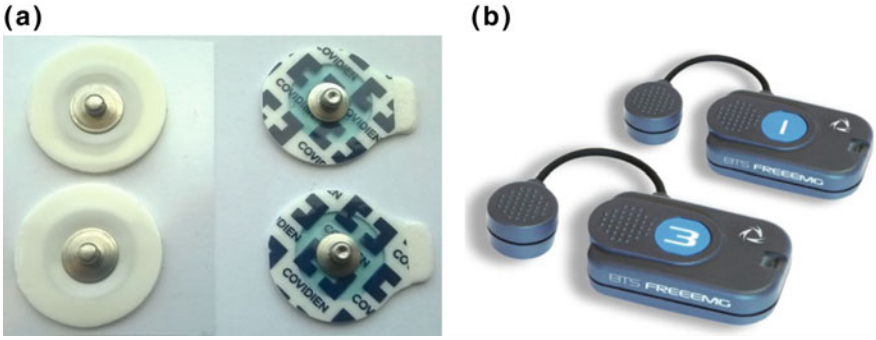

Fig. 1. **a** Fiab and Kendall pre-gelled silver/silver chloride electrodes; **b** BTS Bioengineering Wireless EMG probes

In this study, for the fall risk assessment, the Gastrocnemius lateralis and Tibialis anterior muscles have been chosen for the monitoring of the user's lower limb. The

sensors have been worn through the common pre-gelled silver/silver chloride (Ag/AgCl) electrodes by using clips, allowing a fast, simple and resistant mounting. Several kinds of Ag/AgCl electrodes have been tested and the models that have shown the best trade-off between the signal quality and weareability are the Kendall H124SG model (dimensions 30 × 24 mm) and Fiab PG10C model (dimensions ø26 mm), shown in Fig. 1a. The Ag/AgCl electrodes are very easy to wear but they may induce skin irritation and allergies, moreover their signal quality should be degraded due to the drying of the gel over time [7]. Thus new biocompatible, textile and more comfortable wearable electrodes [8] could be adopted to increase the user acceptability.

2.1.2 Accelerometer-Based Acquisition System

The sensorized garment Wearable Wellness System (WWS) produced by Smartex (Fig. 2), has been used to acquire the acceleration data and to obtain chest movement information, relevant for the posture and fall recognition [9]. The WWS is made up of a washable and comfortable t-shirt and of the electronic board SEW for the data acquisition and communication. The t-shirt integrates the piezo resistive textile sensors for the breathe-rate monitoring and the electrodes for the heart-rate evaluation, while a MEMS tri-axial accelerometer sensor for the movement detection is placed on the SEW. In the presented study only the data coming from the accelerometer have been stored. The accelerometer is DC coupled and allows the evaluation of the static and dynamic acceleration with an acquisition rate of 25 Hz, enough for the movement evaluation [10]. The accelerometer data can be sent by the wireless transmitter, placed on the SEW board for more than eight hours in a streaming mode up to 20 m in free space.

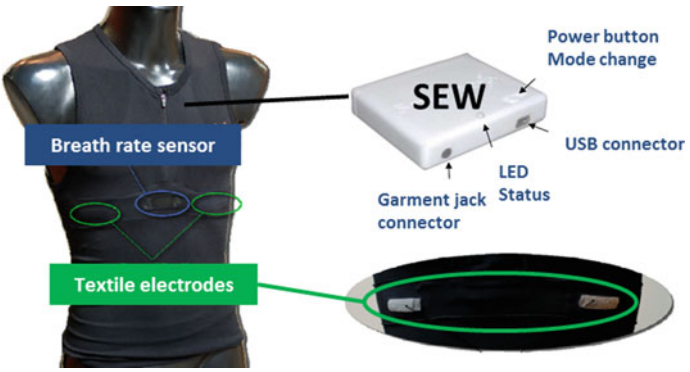

Fig. 2. Smartex wearable wellness system garment

2.2 Data Collection

To analyze the pattern of sEMG signals for fall events and ADLs, a data collection has been accomplished by 5 young healthy actors (4 male and 1 female) with different age (27.5 ± 6.7 years), weight (63.5 ± 9.2 kg) and height (1.72 ± 0.13 m). They have

simulated more than 120 ADLs and 24 fall events wearing the sEMG probes and the WWS garment as described in paragraph 2.1. The data have been collected on a PC host equipped with both Bluetooth and Zigbee receivers. The signals coming from the accelerometer sensor and sEMG probes have been elaborated trough the Mathworks Matlab computing software. The ground-truth of each sequence of simulated events has been recorded and labelled. The posture and events simulated were: sitting, walking, standing, lying down, voluntary/involuntary falling down. For the involuntary fall simulation a movable pneumatic platform has been adopted [11]. It is equipped with an IMU sensor for the evaluation of the perturbation intensity and with a system to detect the precise instant of the impact on the mat. The same platform has been considered in the simulation of the voluntary fall event: the actor dropped himself on the mat without any piston activation. At the end, the combination of the data coming from the two aforementioned wearable systems has allowed the evaluation of the electromyography analysis on the Gastrocnemius/Tibialis muscles during the ADLs and in correspondence to each phase of the falls simulated.

2.3 Computational Data Processing

For the data analysis of the aforementioned wearable systems the pre-processing, calibration and feature extraction phases have been considered. They are described in the following.

2.4 Surface Electromyography Software Steps

Pre-processing. The raw data have been filtered through a 8th FIR (Finite Impulse Response) Filter, with cut frequencies between 20 and 450 Hz reduce the artifact, the noise and the signal aliasing. Moreover, to compare the EMG-tension relationship the signals have been processed by generating their full wave rectification and their linear envelope, using a 10th order low-pass Butterworth filter, with cut-off frequency of 10 Hz.

Calibration. For the calibration procedure the Maximal Voluntary Contraction (MVC) of the Tibialis anterior and gastrocnemius lateralis muscle groups have been calculated. The MVC value has been measured considering the mean amplitude of the highest signal in a window of 5 s. Then each muscle's MVC values have been used to normalize the sEMG data and to decrease the intra-subject variability of the electromyography signals.

Feature extraction. Several features relevant for the analysis of the examined muscles have been tested [12] and those with higher discrimination degree for the pre-fall detection have been considered. The best results in terms of data collected during the simulation campaign, have been obtained considering the simultaneous contraction of the antagonist Gastrocnemius-Tibialis muscles, using the Co-Contraction Indices (CCI) [13] in a sliding windows of 100 ms.

2.4.1 Accelerometer-Based Software Steps

Pre-processing. The acceleration data on three axes were filtered out by a low pass 8th order, 10 Hz cut-off FIR filter to minimize the noise and the human tremors. Moreover the data have been converted into gravitational units to represent acceleration data in the range ± 2 g, in order to make it possible to extract the user posture and to avoid orders of magnitude too different in the features.

Calibration. This phase has been accomplished when the user wore the garment for the first time in standing position for 10 s in order to obtain the baseline of the signal for the feature extraction step.

Feature extraction. The vertical velocity profile and the tilt angle of the trunk [14] have been considered to recognize and to evaluate the movements during the events simulated. These features appear relevant to distinguish falls from normal ADLs [14] and to detect the pre-impact fall with an average lead-time of about 400 ms prior the impact on the floor. From the comparison among the EMG and accelerometer features, it has been possible to study the muscle contraction behavior during the ADLs simulated and each fall phase.

3 Results

For the performance evaluation of the EMG-based system proposed, all data obtain during the campaign simulation have been investigated. The mean vertical velocity measured for all fall simulated has been 2.72 ± 0.61 m/s, while for ADLs the maximum vertical velocity measured has been 1.73 m/s. In the Fig. 3 is reported an example of the accelerometer and electromyography parameters calculated during a backward fall, simulated through the movable platform. From Fig. 1 it is possible to verify that the simultaneous contraction of the gastrocnemius and tibialis muscles starts with the onset of platform motion (the initial phase during an imbalance condition) and an high value for the CCI feature has been obtained before the impact on the mat. For instance, in Fig. 3 the lead time before the impact is about 730 ms, while considering all fall described in the "Data Collection" paragraph the lead-time is about 780 ms. The tilt angle analysis has been considered to produce a more complete study on the fall and on the ADLs dynamic related to the EMG patterns. It is possible to note that the peak of the muscles contraction occurs at the start of the trunk displacement, when the vertical velocity of the trunk is almost zero. This means that the EMG based system could act before the inertial-based pre-impact detection systems. The sensorized movable platform has been able to detect the start of perturbation and the instant of the impact on the mat (see paragraph 2.2); in this way it has been possible to measure the duration of each fall (the mean duration is about 1.5 s). One half of the dataset has been used to calculate the threshold values of features to detect the instability events, while the remaining part has been considered to test the performance in terms of sensitivity and specificity [15] through a threshold-based approach. The best results have been achieved by using the Co-Contraction indices with a threshold value of 28.3 (78.6% for sensitivity and 77.4% for specificity). To reach adequate computation cost regarding the feature extraction, only the CCI have been selected. In Fig. 4 some examples of features obtained for a sequence of ADLs have been reported. According to the results obtained, the system

developed seems to be an efficient starting point to realize a fast and efficient platform for the fall risk assessment. The performance in terms of sensitivity and specificity could be improved monitoring other muscles of the lower limb increasing the number of probes.

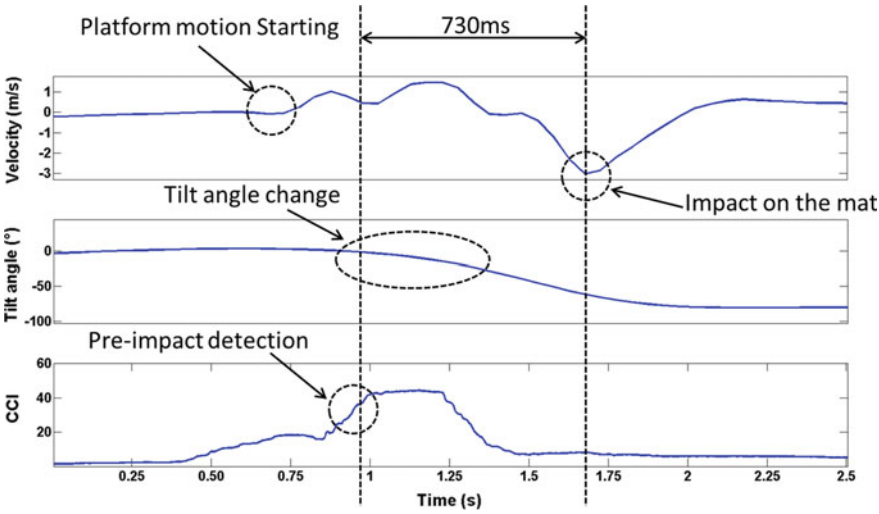

Fig. 3. Example of features extracted for a backward fall event

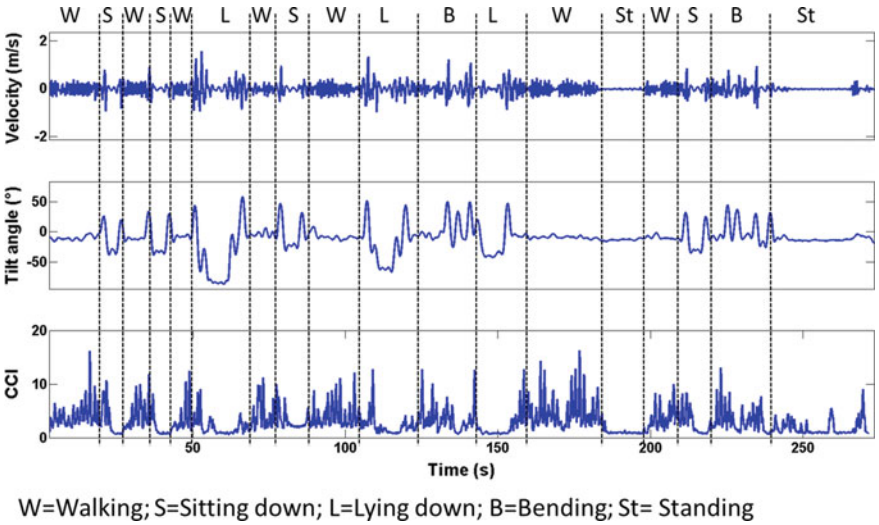

Fig. 4. Example of features extracted for simulated ADLs

4 Conclusion

This work presents a preliminary study of a real-time and minimally invasive pre-fall detection surface Electromyography-based system. During the data acquisition campaign several ADLs and involuntary/voluntary fall events have been simulated, worn four probes on the lower limb and an accelerometer-based garment to compare the two kind of signals during the fall events. In this way it has been possible to analyze the user's muscle behavior in relation with the velocity and the displacement of the user's body trunk. Significant performance in terms of lead-time before the impact on the floor has been measured, in controlled conditions, and the EMG system appears more reactive respect to the inertial-based system. Future works will be focused to improve the performance and the user acceptability of the system increasing the number of probes and using more biocompatible and comfortable electrodes.

References

1. M.C. Chung, K.J. McKee, C. Austin, H. Barkby, H. Brown, S. Cash, J. Ellingford, L. Hanger, T. Pais, Posttraumatic stress disorder in older people after a fall. Int. J. Geriatr. Psychiatry. **24**(9) 955–64 (September 2009)
2. F. Bagalà, C. Becker, A. Cappello, L. Chiari, K. Aminian, J.M. Hausdorff, W. Zijlstra, J. Klenk, Evaluation of accelerometer-based fall detection algorithms on real-world falls. PLoS ONE **7**, e37062 (2012)
3. G. Rescio, A. Leone, and P. Siciliano, Supervised expert system for wearable mems accelerometer-based fall detector. J. Sens. vol. 2013, Article ID 254629, p. 11 (2013)
4. G. Wu, Distinguishing fall activities from normal activities by velocity characteristics. J. Biomech. **33**(11) 1497–1500 (2000)
5. http://www.btsbioengineering.com
6. http://www.smartex.it
7. C. Pylatiuk, M. Muller-Riederer, A. Kargov, S. Schulz, O. Schill, M. Reischl, G. Bretthauer, Comparison of surface EMG monitoring electrodes for long-term use in rehabilitation device control. in IEEE International Conference on Rehabilitation Robotics, ICORR 2009, (2009) pp. 300–304
8. S.M. Lee, H.J. Byeon, J.H. Lee, D.H. Baek, K.H. Lee, J.S. Hong, S.-H. Lee, Self-adhesive epidermal carbon nanotube electronics for tether-free long-term continuous recording of biosignals. Sci Rep. **4**, 6074 (2014)
9. A. K. Bourke, P. W. J. van de Ven, A. E. Chaya, G. M. OLaighin and J. Nelson, The design and development of a long-term fall detection system incorporated into a custom vest for the elderly. in 30th Annual International Conference of the IEEE Engineering in Medicine and Biology Society, Vancouver, BC, 2008, pp. 2836–2839
10. Y. He, Y. Li, Physical Activity Recognition Utilizing the Built-In Kinematic Sensors of a Smartphone. Int. J. Distributed Sen. Networks. vol. 2013, Article ID 481580, p. 10 (2013)
11. G. Rescio, A. Leone, A. Caroppo, F. Casino, P. Siciliano, A minimally invasive electromyography-based system for pre-fall detection. Int. J. Eng. Inno. Technol. (IJEIT), **5**(6) (2015)

12. A. Phinyomark, G. Chujit, P. Phukpattaranont, C. Limsakul, H. Hu, A preliminary study assessing time-domain EMG features of classifying exercises in preventing falls in the elderly. in 9th International Conference on Electrical Engineering/Electronics, Computer, Telecommunications and Information Technology (ECTI-CON), 2012, pp. 1,4, 16–18
13. B. Horsak, et al., A muscle co-contraction around the knee when walking with unstable shoes. J Electromyogr Kinesiol. **25** (2015)
14. A.K. Bourke, K.J. O'donovan, G. Olaighin, The identification of vertical velocity profiles using an inertial sensor to investigate pre-impact detection of falls. Med. Eng. Phys. **30**(7), 937–946 (2008)
15. N. Noury, P. Rumeau, A.K. Bourcke, G. Olaighin, J.E. Lundy, A proposal for the classification and evaluation of fall detectors. IRBM **29**(6), 340–349 (2008)

A Multisensorial Thermal Anemometer System

L. Pantoli[1(✉)], R. Paolucci[2], M. Muttillo[1], P. Fusacchia[1], and A. Leoni[1]

[1] Department of Industrial and Information Engineering and Economics, University of L'Aquila, 67100 L'Aquila, Italy
leonardo.pantoli@univaq.it
[2] Antares Innovation, Via Crispi 35, 67100 L'Aquila, Italy

Abstract. This work deals on the design of a multisensorial anemometer able to provide an accurate measurement of both wind speed and direction. The system is based on thermal anemometry that is, probably, the preferable way to measure instantaneous wind velocity in any weather condition and surrounding. The application here proposed is based on a commercial flow probe, the IST FS5 that shows a robust design without moving parts, small dimensions and is suitable to operate up to 150 °C and a wind speed of 100 m/s. In addition, the sensor is organized as a pattern of probes. In this way, being the analysis based on differential measurements, analyzing the signal provided by each sensor is possible to perform an accurate evaluation of both the wind speed and direction. A microcontroller realizes the data management and wind flow identification process.

Keywords: Actuators · Automation system · Microcontroller · Power line · Sensors

1 Introduction

The environmental meteorological monitoring has always been a field of interest for the human being. The possibility to measure instantaneous phenomena and provide predictions about certain future events can definitely have a positive impact in our life and it is becoming a primary need in many activities. Wind monitoring, for instance, is essential in many areas of interest; see for example sports like sail or skiing, structures as bridges or skyscrapers, places as airports, beyond of urban environments. Continuous and accurate measurements are often required also in absence of local and fixed stations. This necessity brings to the development of portable applications and to the design of innovative systems, thanks to the availability of new technologies and sensors.

Currently, the most used sensor for anemometric systems and measurements is the electromechanical sensor, typically adopted in fixed stations. This solution has been developed over the years and allows reaching even very high performance, thanks also to the progress of technology and circuit architectures. On the other hand, the large area occupation and a continuous need of maintenance for the mechanical parts make this system inadequate for portable applications or critical environments. Alternatives are

B. Andò et al. (eds.), *Sensors*, Lecture Notes in Electrical Engineering 431,
DOI 10.1007/978-3-319-55077-0_42

based on the measurement of pressure difference or on heat exchange with the air flow and the emergence of new solid-state electronic sensors allowed novel approaches in the development of compact anemometric systems, without moving parts.

In this perspective, temperature-based anemometer technique is the best candidate for portable systems. This method could be implemented in different ways, classified as CCA (Constant Current Anemometer), CVA (Constant Voltage Anemometer) and CTA (Constant Temperature Anemometer). Thermal anemometry is probably the preferable way to measure instantaneous wind velocity in any conditions [1–8]. The working principle is based on the cooling effect of the airflow on a heated body. Convective heat transfer from a heated element (typically a resistor heated by an electrical current) to a fluid or gas flow is a function of the velocity of the flow itself, the element relative temperature and the physical properties of the medium. The application here proposed is based on a commercial flow sensor, the IST FS5 [9, 10] used at constant temperature and the power needed to keep it constant is an indirect measure of the heat exchanged with the air flow. Mapping the relationship between the output voltage and the wind speed, is possible to obtain the flow velocity. In addition, the designed thermal anemometer is organized as a pattern of sensors. In this way, being the analysis based on differential measurements, analyzing the signal provided by each sensor is possible to perform an accurate evaluation of both the wind speed and direction. The logical section for the data management and wind flow identification process is implemented by means of a microcontroller and in this first prototype, it has been realized with an Arduino board programmed accordingly.

2 Thermal Anemometry

Let us consider a heated resistor, immersed in a fluid or gas flow; assuming that the resistor is in thermal equilibrium with its environment, the electrical power input is equal to the power lost to convective heat transfer:

$$P = (T_e - T_0) \cdot A_e \cdot h = I^2 R_e \tag{1}$$

where I is the input current, R_e is the resistance of the element, A_e is the affected surface area of the element and h is the heat transfer coefficient of the resistor itself. The term $T_e - T_0$ expresses the difference between the resistor temperature and the fluid (or gas) temperature respectively. As well known, the resistance of the element R_e is also a function of temperature:

$$R_e = R(T_{ref})\left[1 + \alpha \cdot (T_e - T_{ref})\right] \tag{2}$$

where α is the thermal coefficient of the resistor and T_{ref} is the reference temperature.

The heat transfer coefficient h of the resistor is a function of the fluid velocity, as suggested by King's law:

$$h = a + b \cdot v^n; \quad n \sim 0.5 \tag{3}$$

where a and b are coefficient obtained by a previous calibration of the heated resistive element. Combining the Eqs. (1), (2) and (3), we have:

$$a + b \cdot \vec{v}^n = \frac{I^2 R(T_{ref})\left[1 + \alpha \cdot (T_e - T_{ref})\right]}{(T_e - T_0) \cdot A_e} \tag{4}$$

and by inverting this equation, it is possible to calculate the medium flow velocity.

3 System Architecture

The application here proposed is based on a commercial flow sensor, the IST FS5 (Fig. 1a), which shows a robust design without moving parts, small dimensions and is suitable to operate up to 150 °C and a wind speed of 100 m/s [9, 10].

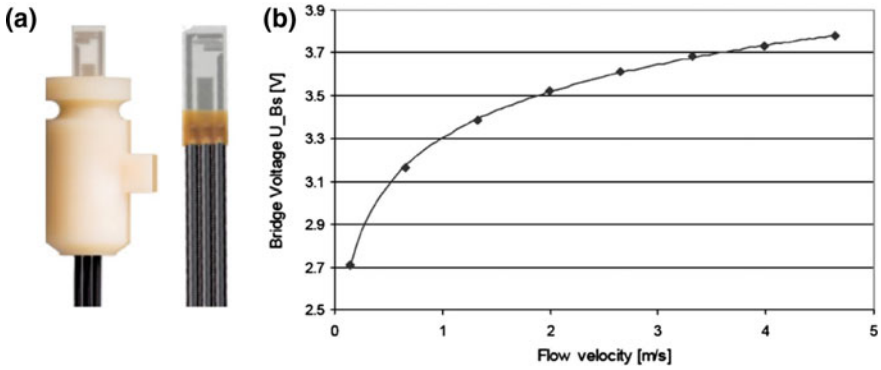

Fig. 1. **a** The IST FS5 mass flow sensor; **b** Typical flow measured *curve*

The device makes use of a special ceramic plane used as base plane, with low thermal conductivity, and thermal resistors. The resistive structure consists of two platinum resistors, used as heater and temperature sensor, respectively. The whole device has also a special passivation, making this sensor suitable even for fluid measurements.

In this application, we adopted a CTA method with the sensor, in order to measure the speed of the airflow, since a constant temperature anemometric strategy can provide a better resolution then CCA and CVA strategies [1, 2].

For the information measurement extraction, we implemented a feedback controlled Wheatston bridge, as in Fig. 2. In the scheme, the sensor represents the two low branches of the bridge, where R5 is the heater and R6 is the temperature sensor of the device. The latter is used to compensate for the medium temperature variation. Resistance value of R1, R2 and R3 is properly calculated, in order to keep the bridge

balanced in normal conditions. In particular, the resistor R3 allows to keep a medium temperature difference on the heater, that is essential for a correct measurement operation, since if the flow were suddenly slow down, the sensor might burn out in a constant-current anemometer. For gas applications (airflow, for instance), this temperature difference should be about 30 K and the proper R3 resistance value can be calculated by the following expression:

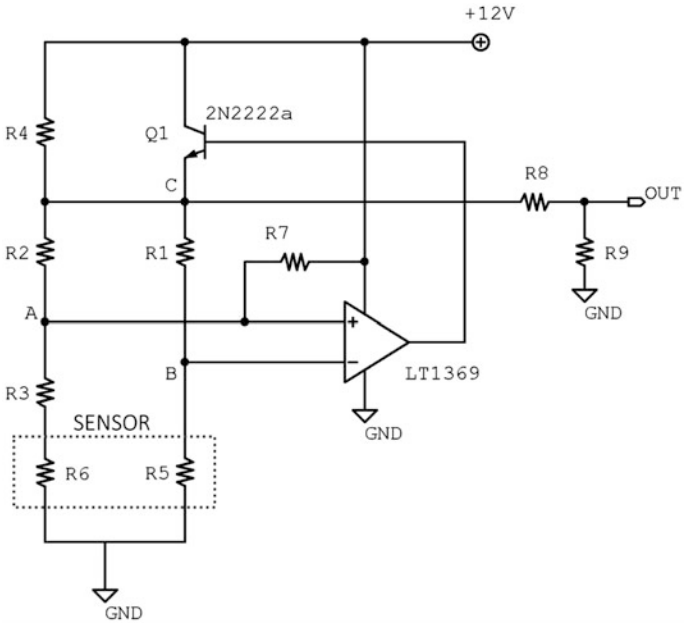

Fig. 2. The single flow sensor interface

$$R3 \approx \alpha \cdot R_0 \cdot \Delta T \approx 140\,\Omega \quad \text{where} \quad \alpha = 0.003902\,k^{-1},\ R_0 = 1200\,\Omega. \tag{5}$$

When an airflow over the sensor surface occurs, the bridge undergoes an unbalance, so the differential output of the bridge, $(V_A - V_B)$, is different from zero. When the difference is greater than zero (the resistance value of the heater decreases, due to the cooling effect of the airflow), the output of the comparator switches at high level, activating the transistor Q1. Therefore, an extra current is injected in the circuit, rebalancing the bridge and keeping constant the temperature of the sensor. A nominal bias current is guaranteed to the bridge by resistor R4, even when Q1 is off. Since the bridge is always balanced, the resistance and temperature of the heater are constant, thus the fluid velocity become a function of input current and flow temperature, simplifying the expression (4) as follows:

$$a + b \cdot \vec{v}^n = \frac{I^2 R_h}{A_h(T_h - T_0)} \tag{6}$$

where R_h and T_h are intended to be the resistance and temperature of the heater.

For a conventional thermal anemometer sensor—the so called "hot-wire sensor"—there is only a heater, that is a wire crossed by a current, which is inserted in a single branch of the bridge. In this case, an external temperature sensor is needed, in order to measure the flow temperature; for instance, the velocity is a function of the input current and the medium temperature as well, as shown in (6). The IST FS5 device provides a built-in temperature sensor, R6 in the scheme, that allows a compensation of the airflow temperature effect directly in the bridge, thus the airflow expression simply become a function of the input current only, or rather of the voltage of the C node in Fig. 2. Therefore, the above equation could be expressed and simplified as follows:

$$V_C = V_0 \cdot \sqrt{1 + k \cdot \vec{v}^n} \tag{7}$$

where V_C is the CTA voltage output, k is a fluid dependent constant and $\vec{v}$ is the air velocity. The term V_0 represents a free convection offset, due to the constant temperature difference between the heater and the air. A previous characterization of the circuit response with a known wind source allows calculating the airflow constant k, so to obtain the voltage-to-wind speed characteristic curve as in Fig. 1b, which is not linear for this sensor. Bu using at least three sensors, arranged for instance in a pattern as in Fig. 3, is it possible to calculate the effective cooling airflow speed, by analyzing the velocity components measured by the three sensors (Fig. 4).

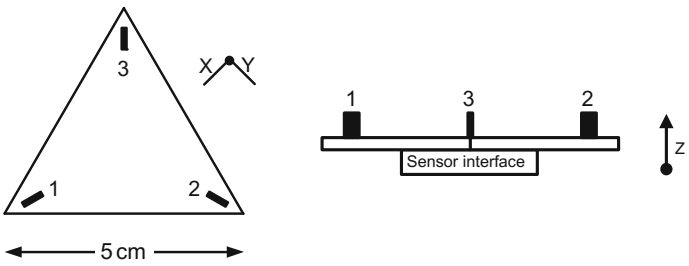

Fig. 3. The flow sensor pattern

Under those circumstances, a first prototype of the anemometric system has been implemented. The whole sensors conditioning circuit includes three Wheatstone bridges as shown in Fig. 3, since we used three sensors in this first test, for both velocity and direction detection of the wind, as mentioned before.

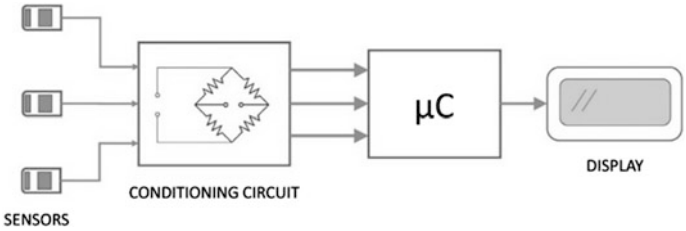

Fig. 4. The complete system architecture scheme

The proposed system, see Fig. 5, has been characterized with a known wind source and some results are shown in Fig. 6. The characteristic transfer function of each sensor has already been shown in Fig. 1b; so particular emphasis has been put in the capability to analyze also the wind direction, that is usually not possible with a single flow sensor. As illustrated in Fig. 6, the sensor has a fast response to any variation of the wind direction and also a good resolution versus the flow intensity. In fact, with a constant source the output voltage of the sensor interface shows a maximum variation of about 200 mV.

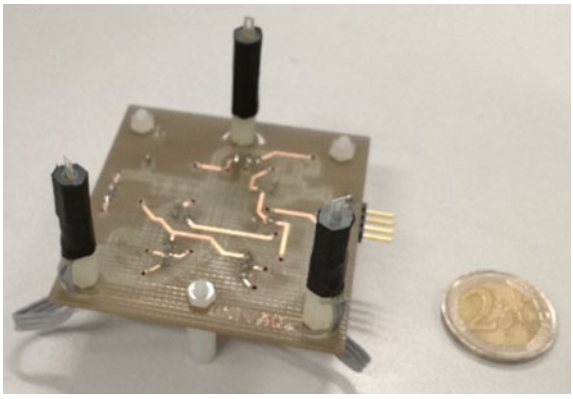

Fig. 5. The sensors board

The proposed solution appears to be suitable also for integration and further benefits both in term of performance, space occupation and power consumption can be achieved with the introduction of advanced circuitry solutions for data manipulation and transmission both in voltage and current mode [11–22] and an improved solution is currently under design.

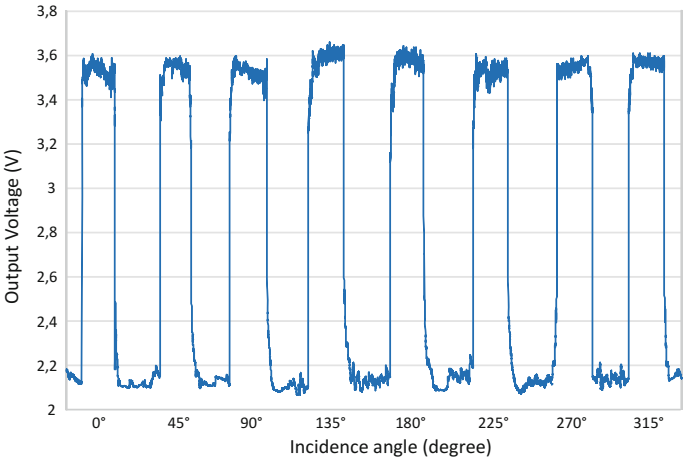

Fig. 6. Output voltage of the sensor interface as a function of the stepped-varied wind direction

4 Conclusions

The paper deals on the design of a low-cost thermal anemometer able to measure both wind speed and directions. It is a robust solution realized through a pattern of probes making use of CTA technique. The base element of the sensor is a commercial device, the FS5 from IST. The sensors interface embeds both analog and digital circuitry for data manipulation and conditioning. The digital data manipulation has been demanded to an Arduino board in the first prototype, useful for testing and characterization of both sensors and interface, but and advanced and fully integrated sensor solution is currently under design.

References

1. F. Feyzi, M. Kornberger, N. Rachor, B. Ilk, Development of two multisensor hot-film measuring techniques for free-flight experiments, in *ICIASF'89 Record. International Congress on Instrumentation in Aerospace Simulation Facilities, 1989* (Gottingen, 1989), pp. 443–449
2. T.S.J. Lammerink, N.R. Tas, G.J.M. Krijnen, M. Elwenspoek, A new class of thermal flow sensors using $\Delta T = 0$ as a control signal, in *MEMS 2000. The Thirteenth Annual International Conference on Micro Electro Mechanical Systems*, *2000* (Miyazaki, 2000), pp. 525–530
3. J.P. Rodriguez, C.R. Perez, Advanced sensor for optimal orientation and predictive maintenance of high power wind generators, in *IECON 02. IEEE 2002 28th Annual Conference of the Industrial Electronics Society*, vol. 3, 2002, pp. 2167–2172

4. B.A.J. Hernandez, E.M. Hernandez, J.Y.M. Perez, M.R.C. Lopez, Arrangement of temperature sensors as a wind sensor, in *2006 3rd International Conference on Electrical and Electronics Engineering* (Veracruz, 2006), pp. 1–4
5. H.I. Schlaberg, Y. Liu, Z. Li, S. Liu, Wind speed and direction measurement with narrowband ultrasonic sensors using dual frequencies, *Renewable Power Generation Conference (RPG 2013)*, 2nd edn. (IET, Beijing, 2013), pp. 1–4
6. M. Ghassemi, M. Farzaneh, Coupled computational fluid dynamics and heat transfer modeling of the effects of wind speed and direction on temperature increase of an ice-covered FRP live-line tool. IEEE Trans. Power Delivery **30**(5), 2268–2275 (2015)
7. B.A.J. Hernandez, E.M. Hernandez, J.Y.M. Perez, M.R.C. Lopez, Arrangement of temperature sensors as a wind sensor, in *2006 3rd International Conference on Electrical and Electronics Engineering*, 6–8 Sept 2006, pp. 1–4
8. K. Okamoto, T. Ohhashi, M. Asakura, K. Watanabe, A digital anemometer, in *Instrumentation and Measurement Technology Conference, 1993. IMTC/93. Conference Record*, IEEE, 18–20 May 1993, pp. 59–63
9. Flow Sens FS5/FS5A thermal mass flow sensor for all-purpose use in gases, IST AG technical paper
10. FS5 thermal mass flow sensor for various gas flow applications, IST AG datasheet
11. P. Branchi, L. Pantoli, V. Stornelli, G. Leuzzi, RF and microwave high-Q floating active inductor design and implementation. Int. J. Circuit Theory Appl. **43**(8), 1095–1104 (2015)
12. L. Pantoli, V. Stornelli, G. Leuzzi, Class AB tunable active inductor. Electron. Lett. **51**(1), 65–67 (2015)
13. L. Pantoli, V. Stornelli, G. Leuzzi, Tunable active filters for RF and microwave applications. J. Circuits Syst. Comput. **23**, 1450088 (2014)
14. L. Pantoli, V. Stornelli, G. Leuzzi, Low voltage high-order agile active filter for microwave applications, in *2013 European Microwave Conference* (*EuMC*) (Nuremberg, 2013), pp. 1203–1206
15. V. Stornelli, L. Pantoli, G. Leuzzi, G. Ferri, Fully differential DDA based fifth and seventh order Bessel low pass filters and buffers for DCR radio systems. Analog Integr. Circ. Sig. Process. **75**(2), 305–310 (2013)
16. L. Pantoli, V. Stornelli, G. Leuzzi, A single-transistor tunable filter for Bluetooth applications, in *2012 7th European Microwave Integrated Circuits Conference* (*EuMIC*) (Amsterdam, 2012), pp. 889–892
17. L. Pantoli, V. Stornelli, G. Leuzzi, Low-noise tunable filter design by means of active components. Electron. Lett. **52**(1), 86–88 (2016)
18. V. Stornelli, Low voltage low power fully differential buffer. J. Circuits Syst. Comput. **18**(3), 497–502 (2009)
19. G. Ferri, V. Stornelli, A. di Simone, A CCII-based high impedance input stage for biomedical applications. J. Circuits Syst. Comput. **20**(8), 1441–1447 (2011)
20. V. Stornelli, G. Ferri, A 0.18 μm CMOS DDCCII for portable LV-LP filters. Radioengineering **22**(2), 434–439 (2013)
21. G. Ferri, V. Stornelli, A. Celeste, Integrated rail-to-rail low-voltage low-power enhanced DC-gain fully differential operational transconductance amplifier. ETRI J. **29**(6), 785–792 (2007)
22. G. Leuzzi, V. Stornelli, L. Pantoli, S. Del Re, Single transistor high linearity and wide dynamic range active inductor. Int. J. Circuit Theory Appl. **43**(3), 277–285 (2015)

Remotely Controlled Terrestrial Vehicle Integrated Sensory System for Environmental Monitoring

Emiliano Zampetti(✉), Paolo Papa, Francesco Di Flaviano, Lucia Paciucci, Francesco Petracchini, Nicola Pirrone, Andrea Bearzotti, and Antonella Macagnano

CNR Istituto sull'Inquinamento Atmosferico (CNR-IIA), Via Salaria km 29,300, Monterotondo, RM, Italy
e.zampetti@iia.cnr.it

Abstract. In this paper we show the developing and the applications of a remotely controlled terrestrial vehicle (or Unmanned Ground Vehicles—UGV) provided with an integrated sensory system for environmental monitoring. The developed system is aimed to monitor some of the key air pollutants and harmful compounds, usable in contaminated sites at high risk to human health. The system is a 4WD radio-controlled vehicle, with small dimensions and low weight, complemented by a sensory system based on hybrid sensors technology (e.g. optic, electrochemical, gravimetric, etc…). These features allow this system to be easily used when inspection missions are required, before or after any environmental disaster. It is able to measure, in few minutes, the atmospheric particulate matter (PM1, PM2.5, PM10), CO_2 and CO, H_2S, SO_2, NO_2 in the range between 15 and 5000 ppb. Moreover, it is equipped with a telemetry system for the remote-controlled navigation, including a high-resolution camera, a GPS antenna, an anemometer and proximity sensors. The core of the device is a microprocessor board able to assist the navigation, acquiring values from sensors, transfer/record data and control tens input/outputs up to a distance of 1 km. In this work we report some information regarding the integration, the calibration and the data related to the monitoring of a waste landfill in the closing phase, during the construction of the extractor for generated biogas.

Keywords: UGV · Monitoring system · Gas sensors

1 Introduction

Unmanned Ground (UGV), Air (UAV), Surface (USV) and Underwater (UUV) vehicles are useful in a wide field of civil applications such as: environmental monitoring, agricultural surveys, emergency and disaster relief [1–5]. There are companies that sell UGVs that are able to detect leaks of oil and gas in the infrastructure, ensuring human safety. Other companies that offer UGVs able to enter into pipe systems to monitor toxic waste and chemical or radioactive material. In research field, there are USVs capable of sail the oceans and to report to scientific communities the measured data, anywhere in the world. Advances in the electronics integration and software are

B. Andò et al. (eds.), *Sensors*, Lecture Notes in Electrical Engineering 431,
DOI 10.1007/978-3-319-55077-0_43

steadily increasing bringing the autonomous UGV navigation system towards low costs with excellent level of reliability. At the same time, the growing demand of data related to environmental pollution by policy makers, citizens and the scientific community have stimulated the development of UGV with on-board environmental monitoring systems.

We therefore propose a UGV system aimed to monitor some of the key air pollutants and harmful compounds, usable in contaminated sites at high risk to human health. In this paper we show the details of development and an application of a remotely controlled terrestrial vehicle with sensory system integrated for environmental monitoring. In particular, we report the results obtained from a measurement campaign that consisted in the monitoring of the diffused emissions in a waste landfill area.

2 Experimental and Results

Proposed system consisted a 4WD (all-wheel drive) radio-controlled vehicle, with small dimensions and low weight, complemented by a sensory system based on hybrid sensors technology [6, 7]. Such a sensory system assembled within a terrestrial vehicle, is able to measure: atmospheric particulate matter, CO_2, CO, H_2S, SO_2 and NO_2. Starting from a commercial radio-controlled model (by Traxxas) we have designed and developed a complete system that includes: vehicle, air sampling system for gases and particles, a sealed measuring sensors chamber, a camera with wide angle lens and an electronic controlling board (electronic) as depicted in the sketch (Fig. 1). The air sampling system commutates between two distinct phase. During the measure, it delivers the air (to be analyzed) to the sensors chamber. In the cleaning phase, it creates the zero air, using a filter cartridge (Filter) and then delivers it to the sensor chamber.

An integrated optical particles counter (OPC-N2 by Alphasense Ltd) was used to measure the amount of PM in the sampled air. The data generated by the OPC are divided into three main classes, PM1, PM2.5 and PM10. The OPC sends the data to the electronics that gets the data every 2 s. The CO_2 concentration (0-5000 ppm) was measured by a NDIR sensor (IRC-A1 by Alphasense Ltd). Electrochemical sensors (by Alphasense Ltd) were used to measure the concentrations of CO, H_2S, SO_2 and NO_2 in the range between 15 and 5000 ppb. The electronic board was equipped with a telemetry system for the remote-controlled navigation, which includes: (i) a high-resolution camera; (ii) a GPS antenna; (iii) an anemometer and (iv) proximity sensors. The core of the electronics was a microprocessor board able to assist the navigation, acquire values from sensors, transfer/record data and to control tens of input/outputs up to a distance of 1 km.

After the integration phase the system was tested in various scenarios, with different soils structure and composition, to check the UGV navigation performances (see Fig. 2).

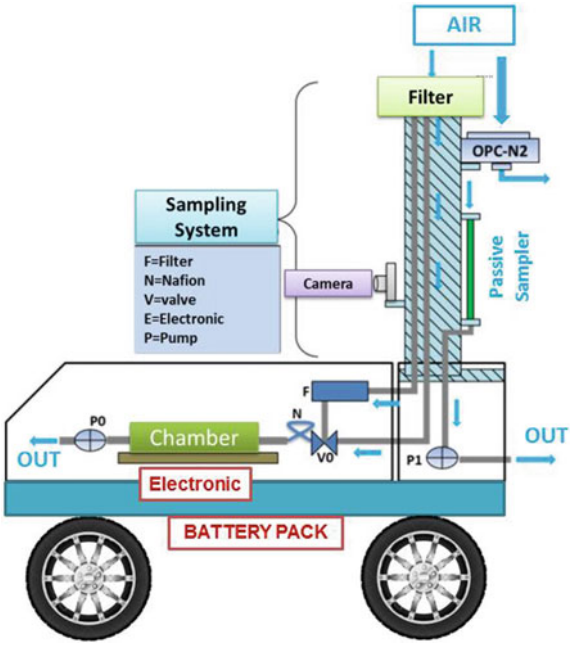

Fig. 1 Sketch of developed system

Fig. 2 Pictures of developed system during the campaign in landfill (*on the right*). The overall dimensions are 70 × 50 × 30 cm and 4 kg of weight + 2 kg of maximum payload

Before assembling, we checked and calibrated the sensors with accurate, precise and qualitatively controlled analytical instruments commonly used in our lab to measure and quantify the analyte concentrations in air. In Fig. 3 some example of dynamic sensor responses are shown, in particular in Fig. 3c the sensor responses obtained when the UGV navigated near to a traffic zone are reported.

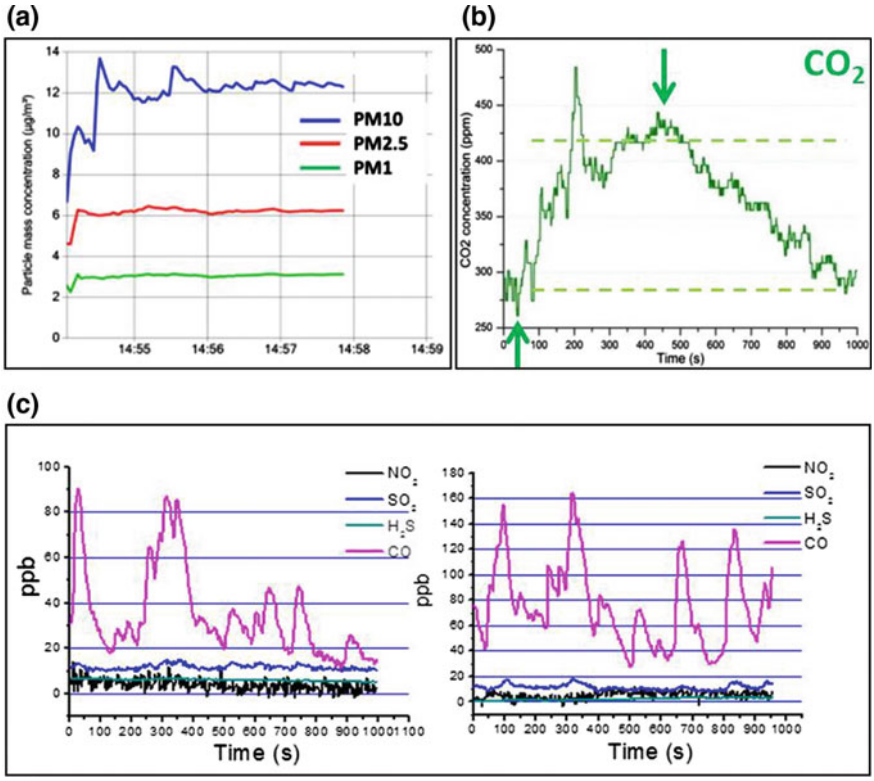

Fig. 3 Transient measurements of PM (**a**), CO_2 (**b**) and other gases during the test campaigns (**c**). In case (**c**) the system has monitored the air surrounding a traffic zone

In order to validate in a real scenario our monitoring system, we have performed several measurements in a waste landfill (about 60,000 m^2) where was in progress the developing of a biogas system. The developed UGV has monitored the gases and particles concentrations in six points of interest closed to the extraction pipes (P0,…, P5). In Fig. 4 we report the values of two gases amounts (CO_2, H_2S) recorded during the campaign. P0 an P5 were outside the landfill site about 200 m from the boundary. P1 and P3 were two points located in a part of landfill (Closed) where the extraction pipes were connected to the biogas system. P2 and P4 were located in a portion of landfill "Open" where the biogas system was to be completed. The results highlight that in the "Open" area the CO_2, H_2S concentrations were more higher than those in the "Closed" area. This result has confirmed the state of progress of the biogas system.

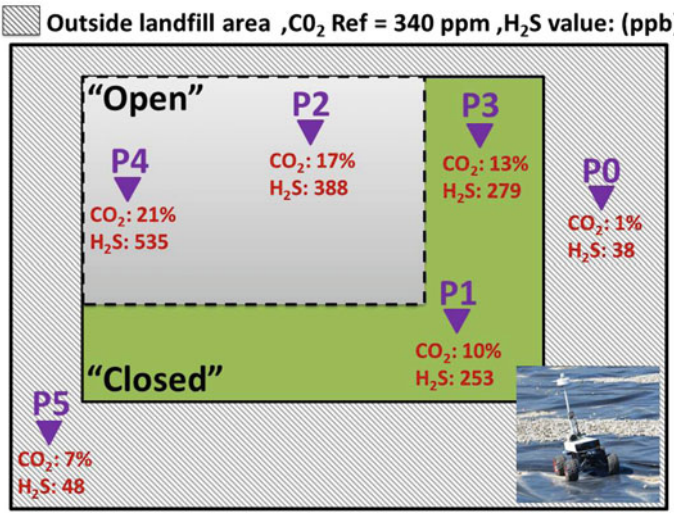

Fig. 4 Results of CO_2 and H_2S mean values for six points of interest (P0,…, P5), measured during the campaign in landfill are reported. The "Open" area means a part of landfill to be completed, vice versa the "Closed" means a completed part

3 Conclusions

We have developed and tested in a real scenario, a remotely controlled terrestrial vehicle (or Unmanned Ground Vehicles—UGV) integrated with a sensory system for environmental monitoring. The system was able to monitor atmospheric particulate matter (PM1, PM2.5, PM10), CO_2, H_2S, SO_2 and NO_2. We have validated the functioning of our system during a measurement campaign performed in a waste landfill where a biogas system was under construction. The results highlight that in the "Open" area (where the biogas system was to be completed) the CO_2, H_2S concentrations were more higher than that in the "closed" area (where the extraction pipes were connected to the biogas system). This result have confirmed the state of progress of the biogas system.

References

1. D. Floreano, R.J. Wood, Science, technology and the future of small autonomous drones. Nature **521**, 460–466 (2015)
2. J.J. Roldán, G. Joossen, D. Sanz, J. del Cerro, A. Barrientos, Mini-UAV based sensory system for measuring environmental variables in greenhouses. Sensors **15**, 3334–3350 (2015)
3. A. Ruiz-Larrea, J.J. Roldán, M. Garzón, J. del Cerro, A. Barrientos, A UGV approach to measure the ground properties of greenhouses. Adv. Intell. Syst. Comput. **418** (2016)
4. V. Meiser, R. Henke, D. Šeatović, T. Rotach, H. Hesselbarth, Autonomous unmanned ground vehicle as sensor carrier for agricultural survey tasks, in *Proceedings International Conference of Agricultural Engineering*. Zurich, 06–10 July 2014, Ref: C0266

5. G. Belloni, M. Feroli, A. Ficola, S. Pagnottelli, P. Valigi, A COTS-based mini unmanned aerial vehicle (SR-H3) for security, environmental monitoring and surveillance operations: design and test, in *European Robotics Symposium 2008*, *STAR 44*, pp. 73–82
6. F. De Cesare, E. Di Mattia, S. Pantalei, E. Zampetti, V. Vinciguerra, F. Canganella, A. Macagnano, Use of electronic nose technology to measure soil microbial activity through biogenic volatile organic compounds and gases release. Soil Biol. Biochem. **43**, 2094–2107 (2011)
7. M. Bernabei, K.C. Persaud, S. Pantalei, E. Zampetti, R. Beccherelli, Large-scale chemical sensor array testing biological olfaction concepts. IEEE Sens. J. **12**(11), 3174–3183 (2012)

Micro-nano Technologies, Electronic Systems for Sensors

A Compact Low-Offset Instrumentation Amplifier with Wide Input and Output Ranges

Massimo Piotto[1], Simone Del Cesta[2], Giovanni Argenio[2], Roberto Simmarano[3], and Paolo Bruschi[2(✉)]

[1] IEIIT-Pisa, CNR, via G. Caruso 16, 56122 Pisa, Italy
[2] Dipartimento di Ingegneria dell'Informazione, Università di Pisa, Via G. Caruso 16, Pisa, Italy
p.bruschi@iet.unipi.it
[3] Sensichips S.r.l., via delle Valli 46, Latina, Italy

Abstract. In this work, a new architecture for the design of very compact instrumentation amplifiers is proposed. The amplifier has been specifically developed for use as a versatile block for sensor interfacing. The most innovative feature of the proposed cell is the wide input common mode range, which has a margin to both power rails as small as 200 mV. The circuit, which has been implemented with the 3.3 V CMOS devices of the UMC 0.18 μm process, operates with supply voltage in the 1.4–3.6 V range. An input offset voltage standard deviation of 8 μV has been obtained using chopper modulation combined with gain enhancement of the output current mirrors. The amplifier performances are estimated by means of accurate electrical simulations.

Keywords: Instrumentation amplifier · Chopper modulation · Sensor interface

1 Introduction

The instrumentation amplifier (in-amp) is one of the most versatile block for sensor interfacing. The in-amp can be used to read the small-output signals of Wheatstone bridges, (strain gauges, magneto-resistors), thermoelectric sensors and Hall sensors. The development of complex Systems on a Chip, including several readout channels inside a single integrated circuit, is demanding the development of very compact instrumentation amplifiers. The current trend towards low supply voltages imposes smaller and smaller margins of the input and output ranges with respect to the power rails. The well-known three op-amp instrumentation amplifier is a sub-optimal solution in terms of area and suffers from input differential range clipping when the input common mode voltage approaches either rails. The achievement of an acceptable common-mode rejection ratio (CMRR) with a three op-amp architecture requires individual trimming of on-chip resistors, increasing production costs and complicating the circuit layout [1]. The popular indirect current feedback [2, 3] architecture (ICF) is more compact, has better CMRR performances, but is not suitable to achieve rail-to-rain input ranges, since it is not possible to precisely stabilize the input transconductance over wide common mode voltage intervals. Furthermore, ICF-based amplifiers yield excellent performances only when designed to provide high voltage

B. Andò et al. (eds.), *Sensors*, Lecture Notes in Electrical Engineering 431,
DOI 10.1007/978-3-319-55077-0_44

gains, while are practically unusable for unity gain settings, due to saturation of the input transconductors. Current-balancing in-amps [4] are extremely simple and compact, but, again, their structure does not allow for rail-to-rail input ranges.

Recently, we proposed a novel in-amp architecture [5, 6], which combines an almost rail-to-rail e input common mode range with extreme compactness, high speed, compatibility with low supply voltages and intrinsically high CMRR. The amplifier exploited chopper modulation to reduce offset and flicker noise. In this work, we describe a modified version of the earlier amplifier, consisting in application of gain-enhancement [7, 8] to the output stage. The benefit in terms of input referred offset is demonstrated by means of electrical simulations.

2 Description of the Amplifier Architecture

The principle of operation of the proposed amplifier is illustrated in Fig. 1. The two input transconductors, together with M_1 and M_2, form two embedded operational amplifiers, whose output nodes are V_{SP} and V_{SN}, respectively. The two op-amps are closed in unity-gain configuration, so that the input signals V_{IP} and V_{IN} are copied to V_{SP} and V_{SN}, respectively.

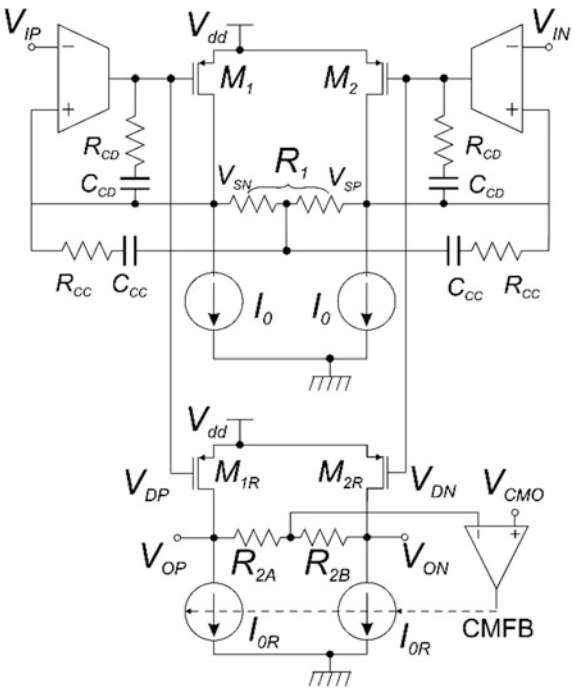

Fig. 1. Simplified schematic view, illustrating the principle of operation of the amplifier

In this way, the current in R_1 is proportional to the input differential voltage, V_{ID}, and the following equation can be written for M_1 and M_2 drain currents:

$$I_{D1} - I_{D2} = 2V_{ID}/R_1 \tag{1}$$

Currents I_{D1} and I_{D2} are copied into M_{1R} and M_{2R}, which, together with resistors R_{2A}, R_{2B} and current sources I_{OR}, form the output stage. As a result, the current flowing through the R_{2A}, R_{2B} series is a copy of the current in R_1. Defining $R_2 = R_{2A} + R_{2B}$, the output differential voltage is given by:

$$V_{OD} \equiv V_{OP} - V_{ON} = V_{ID}\frac{R_2}{R_1} \tag{2}$$

The amplifier gain is simply given by R_2/R_1 resistance ratio. The common mode feedback sub-circuit (CMFB in Fig. 1) sets the output common mode voltage to $V_{dd}/2$ in order to maximize the output swing. The principle underlying Eq. (1) was proposed several decades ago for precision voltage-to-current converters [9]. However, in previous implementations, feedback-enhanced source or emitter follower stages are used to replicate the input differential voltage across the reference resistor R_1. Consequently, rail-to-rail input ranges cannot be achieved with earlier architectures. In the circuit of Fig. 1, which we have proposed for the first time in Ref. [5], replication of the input voltage across R_1 relies on common source stages (i.e. M_1 and M_2), which have an output swing that approaches both power rails. In order to allow V_{SP} and V_{SN} to track the input signals over an as wide as possible range, complementary *p-n* input pairs have been adopted for the transconductors. Stability of the two embedded operational amplifiers has been obtained by means of Miller compensation, implemented by the C_{CD}-R_{CD} series. Additional compensation is applied to the common mode domain using the C_{CC}-R_{CC}, series, due to critical stability issues found in the design phase.

The actual circuit, which was described in Refs. [5, 6], used cascode structures for M_1, M_2, M_{1R}, M_{2R} and current sources I_0 and I_{0R}. This implied a slight degradation of the input and output ranges, but it was necessary to improve precision of current replication from R_1 to R_2. Reduction of the input offset voltage and flicker noise, which are severe drawbacks peculiar to compact CMOS amplifiers, has been obtained by means of chopper modulation.

Experimental tests performed on several samples after preliminary data publication of Ref. [6], showed that random input offset voltage was much larger than expected. Analysis of the circuit revealed that the offset derived from MOSFETs in the common gate stage of the cascode structures, which were not affected by the benefit of chopper modulation. This problem cannot be solved by moving the chopper demodulators from the input to the output of the common gate stages, since the intrinsic switched-capacitor parasitic resistance of the modulators would alter the amplifier gain.

In this work, we have applied a gate-enhancement strategy to enclose the common gate devices into feedback loops, reducing their impact on the amplifier offset. The proposed circuit is shown in Fig. 2. Input transconductors OTA-IN receive the input voltage from the chopper modulator shown on the left of the figure. Demodulation is operated by S_{B1}, at the input of M_3–M_4 common gate stage. Modulator S_{B2} is

necessary, as customary, to shift the offset and flicker contribution of M_7–M_8 current sources to high frequencies. In order to improve matching between the M_1, M_2 pair and its M_{1R}, M_{2R} replica, S_D dummy modulator, driven by a constant "0" logical value, has been placed in the input section.

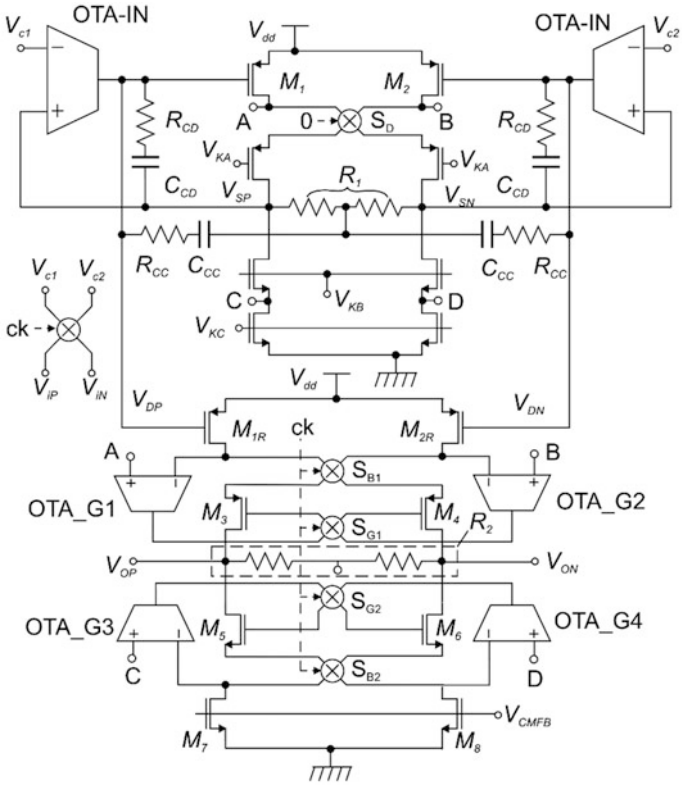

Fig. 2. Proposed instrumentation amplifier. The CMFB circuit has not been shown for the sake of simplicity. Modulator S_D is driven by a constant "0" logic value

Gain enhancement is applied to all common gate devices in the output stage. Considering M_3–M_4 differential common gate stage, we note that gate voltages are driven in a closed loop fashion by transconductors OTA-G1 and OTA-G2.

The effect of this solution is that M_{1R} and M_{2R} drain-source voltages closely track M_1, M_2 ones, respectively, with low sensitivity to M_3 and M_4 parameters. This improves further the circuit linearity and gain accuracy but, more importantly, suppresses the mentioned effect of M_3–M_4 on the amplifier offset. Clearly, M_{1R}–M_{2R} drain-source voltage mismatch is now dominated by mismatch of OTA-G1,2 offset voltages. For this reason, modulator S_{G1} swaps the two transconductors at any clock transition, shifting the transconductor offset to high frequencies. The same procedure is applied to M_5–M_6 common gate devices by means OTA-G3, OTA-G4 transconductors and S_{G2} modulator.

Output common mode stabilization has been obtained as in Fig. 1, by means of a differential amplifier that picks-up the middle-point voltage of resistor R_2, compares it to the target value and drives M_7–M_8 current sources (I_{0R} in Fig. 1) accordingly.

Input transconductors OTA-IN consist of simple folded cascode differential amplifiers, shown in the simplified schematic view of Fig. 3.

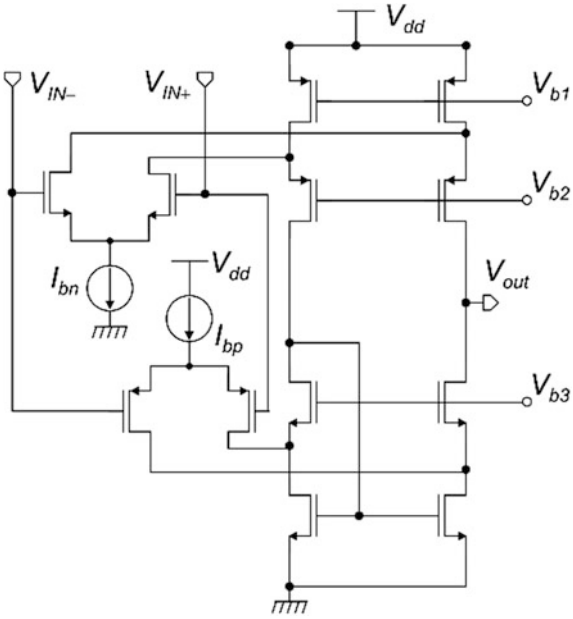

Fig. 3. Simplified schematic view of OTA-IN transconductors

The differential currents of the complementary input pairs are combined in the output cascode structure. Devices have been sized to obtain input common mode ranges that exceed the power rails. The typical transconductance variation of this stage, occurring when the input common mode voltage is swept from ground to V_{dd}, does not impact on the DC and low frequency characteristics of the feedback loops built around the OTA-IN stage, so that constant-Gm approaches have not adopted. Transconductors OTA-G1,2 are *p*-type, simple differential amplifiers while *n*-type versions have been used for OTA-G3,4 in order to match the required quiescent voltage levels.

3 Simulation Results

The amplifier has been designed using the 0.18 μm CMOS process of UMC. All MOSFETs used in the amplifier belong to the 3.3 V subset: this choice was made in order to allow operation up to 3.6 V supply voltages. Combination of regular and low threshold devices available in the 3.3 V subset of the process has been used to maximize the interval of applicable supply voltages and facilitate voltage level

matching inside the gain-enhancement stages. Polysilicon resistors have been used for R_1 and R_2. Resistance R_2 was set to 300 kΩ, while R_1 was implemented as a programmable resistor string. Possible values, selectable by means of digitally controlled switches, were 300, 25, 15, and 7.5 kΩ, corresponding to amplifier gains of 1, 12, 20 and 40. The total supply current is 90 μA, while the minimum supply voltage was 1.4 V. The total area of the cell, estimated from a preliminary layout, was $270 \times 270\ \mu m^2$.

Simulations shown in Figs. 4, 5 and 6 refer to a gain of 20. Figure 4 shows the output differential voltage as a function of the input differential voltage for two V_{dd} values, indicated in the figure. This result has been obtained with a DC sweep with the chopper clock fixed to a constant logic value.

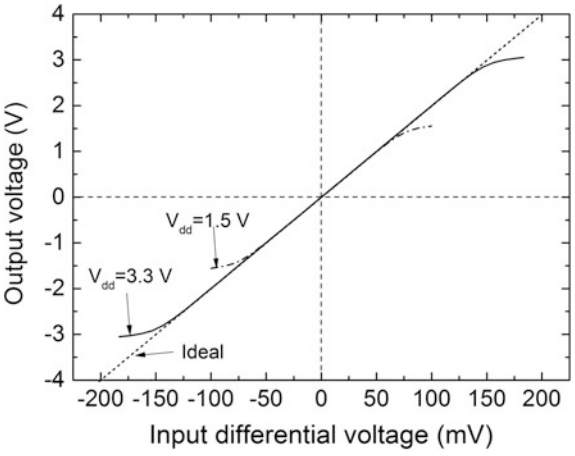

Fig. 4. Output voltage as a function of input differential voltage for two V_{dd} values, indicated in the figure. The amplifier gain was set to 20

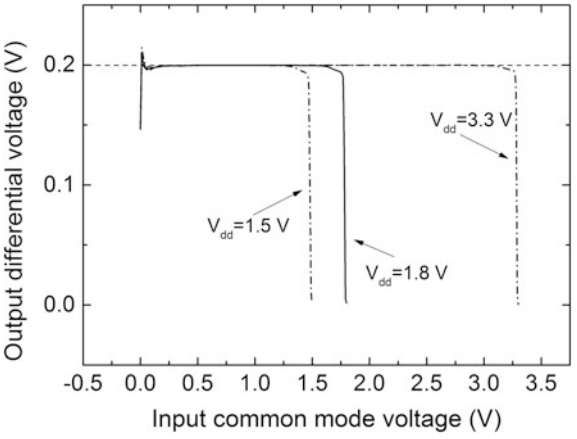

Fig. 5. Output voltage as a function of input common mode voltage, for a 10 mV differential mode voltage. The gain was set to 20

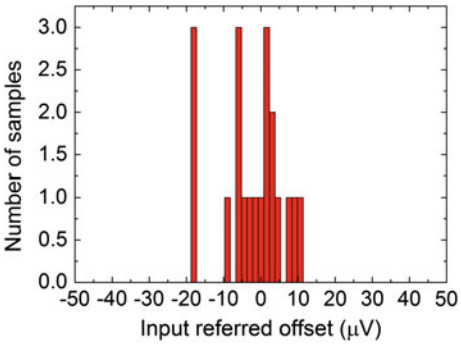

Fig. 6. Histogram of input referred offset voltage obtained by means of 20 Monte Carlo Transient simulations, post-processed to extract the average value of the output voltage out of the chopper ripple

The output swing is limited by two different mechanisms, depending on the supply voltage. In the case of V_{dd} = 1.5 V, deviation from the linearity is due to the minimum voltage drop of the cascode structures shown in Fig. 2, while for V_{dd} = 3.3 V it is the maximum current that can be delivered to R_2 by M_{1R} and M_{2R} to be exceeded. This limit is dictated by the amplifier bias current that was optimized for the low V_{dd} case.

Figure 5 shows the dependence of the output voltage on the input common mode voltage, for a fixed input differential signal (10 mV).

Note that the input common mode voltage starts to affect the output voltage only when the distance from one of the rails falls below 200 mV, confirming that an almost-rail-to-rail performance has been actually achieved.

The input referred offset voltage was estimated from the output offset obtained by means of transient simulations. The resulting output waveforms have been averaged over a clock cycle in order to extract the mean value, which would be otherwise concealed by the relatively large offset ripple. The histogram in Fig. 6 represents the result of 20 Monte Carlo runs.

The estimated standard deviation is 8 μV, which has to be compared with the 50 μV value obtained with the previous version of the circuit. This result confirms the effectiveness of the combination of chopper modulation and gain enhancement. It should be observed that, differently from previous works regarding much less compact in-amps [3, 10], no strategies have been implemented to reduce the output ripple. This is not a limitation for use in acquisition systems where ripple rejection can be performed in the digital domain, exploiting, for example, the decimation filter of a delta-sigma analog-to-digital converter.

References

1. J. Szynowsky, CMRR analysis of instrumentation amplifiers. Electron. Lett. **19**, 547–549 (1975)
2. B.J. Van den Dool, J.H. Huijsing, Indirect current feedback instrumentation amplifier with a common-mode input range that includes the negative rail. IEEE J. Solid-State Circ. **28**, 743–749 (1993)
3. R. Wu, J.H. Huijsing, K.A. Makinwa, A current-feedback instrumentation amplifier with a gain error reduction loop and 0.06% untrimmed gain error. IEEE J. Solid-State Circ. **46**(12), 2794–2806 (2011)
4. R.F. Yazicioglu, P. Merken, R. Puers, C. Van Hoof, A 60 μW 60 nV/$\sqrt{\text{Hz}}$ Readout front-end for portable biopotential acquisition systems. IEEE J. Solid State Circ. **14**, 1100–1110 (2007)
5. F. Del Cesta, A.N. Longhitano, P. Bruschi, R. Simmarano, A wide input range instrumentation amplifier for impedance spectroscopy applications. Ph.D. Research in Microelectronics and Electronics (PRIME), Villach (Austria), (2013) pp. 65–68
6. P. Bruschi, F. Del Cesta, A.N. Longhitano, M. Piotto, R. Simmarano, A very compact CMOS instrumentation amplifier with nearly rail-to-rail input common mode range. In: 40th European Solid State Circuits Conference (ESSCIRC),Venice Lido, Italy, 22–26 Sept. (2014), pp. 323–326
7. R.J. Baker, *CMOS Circuit Design Layout and Simulation*, 3rd edn. (Wiley Hoboken, New Jersey, 2010), pp. 808–809
8. F. Sebastiano, F. Butti, R. Van Veldhoven, P. Bruschi, A 0.07 mm^2 2-channel instrumentation amplifier with 0.1% gain matching in 0.16 μm CMOS. in *IEEE International Solid-State Circuits Conference Digest of Technical Papers (ISSCC)*, San Francisco, CA, 9–13 Feb. (2014) pp. 294–295
9. A.T. Van Zanten, J.H. Huijsing, An accurate integrated voltage-to-current converter. IEEE J. Solid State Circ. SC-10, 432–436 (1975)
10. F. Butti, P. Bruschi, M. Dei, M. Piotto, A compact instrumentation amplifier for MEMS thermal sensor interfacing. Analog Integr. Circ. Sig. Process **72**, 585–594 (2012)

Improving the Performance of an AMR-Based Current Transducer for Metering Applications

G. Betta[1], D. Capriglione[2(✉)], L. Ferrigno[1], and A. Rasile[1]

[1] Department of Electrical and Information Engineering, University of Cassino and Southern Lazio, via G. Di Biasio, 43, 03043 Cassino, Italy
[2] Department of Industrial Engineering, University of Salerno, Via Giovanni Paolo II, 132 - 84084 Fisciano, Italy
dcapriglione@unisa.it

Abstract. In Medium Voltage (MV) applications, innovative solutions for voltage and current measurements are investigated in this last years. In particular, technical solutions characterized by proper metrological performance and at the same time small size, low cost, and simple integrability with communication networks are followed with the aim of operating within the modern industrial context and in the smart grid. In these scenarios, the paper describes a current transducer thought for industrial applications and based on a cheap commercial AMR sensor. A deep experimental analysis is carried out to verify the metrological performance of the proposed system for both Direct and Alternate Current operating, and to verify the influence of the environmental temperature on the input-output characteristic. The obtained results have shown that the proposed system allows reaching metrological performance suitable for typical MV applications if the temperature compensation is carried out.

Keywords: AMR sensor · Contact-free current measurements · Magnetic field · Medium voltage applications

1 Introduction

The measurements of electrical quantities in the context of electricity distribution networks, has always been a very important task. In particular, in recent years, with the advent of smart grids, the functions of the measuring devices have become increasingly complex, and the requests are changed according to the needs of the network [1]. Currently we can assist to the migration from the use of conventional measurement transformers to the use of modern sensors capable of monitoring voltages and currents line, as well as the flow of power, for which the costs and overall dimensions significantly are less than the previous solutions [2]. In particular, the efforts of current research activity in the field are mainly addressed to provide measuring devices able to offer adequate performance (for the context) and at the same time showing a low installation complexity, small size, low processing complexity and contained costs [1–2]. Focusing the attention on current measurements, there are solutions which in part could warrant these requests, but although presenting a low installation complexity and proper measurement performance, require complex conditioning electronics and

B. Andò et al. (eds.), *Sensors*, Lecture Notes in Electrical Engineering 431,
DOI 10.1007/978-3-319-55077-0_45

relatively high costs [3]. As an example, among the main kind of sensors that respond to these demands we find:

- Inductive sensors: the highest performance are achieved with ones base on Rogowski coil [3]. Using techniques of precision winding, the coils are produced so that the output value ensures insensitivity to interference generated by the external magnetic field and is not affected by the position of the current conductor inside the bull. Basically, a current measurement system based on Rogowski coil sensor is constituted by the combination of a coil and an electronic circuitry. The main features of these types of systems are the wide dynamic range, high linearity in frequency, high isolation, immune to large loads, low installation complexity.
- Optical Sensors: based on the Faraday effect for current measurements [1–3]. The current sensor, is constituted by a suitably shaped glass block within which the polarized light sent from an optical fiber follows a closed path around a central hole in which the conductor is passed, of which one wants to measure the flow; at the end of the path the light is collected by another optical fiber that transports it to the reading unit that measures the rotation of the polarization plane by the Faraday effect. These type of sensors are generally capable of measuring currents up to 2 kA. Also the power necessary for the operation of the sensors is provided by an optical signal, thus obtaining a complete electrical insulation between the reading unit and the field sensors [4]. Optical techniques used also have several advantages, such as easier isolation, a wider bandwidth, higher dynamic range and immunity to electromagnetic interference.
- Magnetic field sensors: typically based on silicon, of small size, good spatial resolution, adequate sensitivity for many applications. In particular we find giant magnetoresistance sensors, GMR, characterized by a multilayer structure with alternating thin films, metal type, and ferromagnetic conductor (non-magnetic), that in the presence of an external magnetic field, provide changes in electrical resistance of the functional material that ranges from 10 to 20% up to 70% [5].
  In addition to the GMR, there is also another class of magnetic field sensors based on the magnetoresistive effect, the AMR (anisotropic magnetoresistive). The structure is composed of nickel-iron of a thin film (permalloy) deposited on a silicon wafer and structured so as to have a functional material filament (resistive), whose resistance changes up to 2–3% in the presence of a magnetic field [6]. In practice, 4 magnetoresistence are arranged in the typical configuration of a Wheatstone bridge, which allows to measure both the intensity and the direction of the magnetic field, supposed uniaxial [6].

Summarizing, the main disadvantages linked to the use of inductive sensors with high measuring accuracy is mainly the cost of implementation, while for the optical sensors, derive mainly from the sensitivity of the optical fiber to multiple parameters, and then to the difficulty of separating the contribution related to the electric quantity of interest from others; furthermore, as for the Rogowsky coils, the cost of the overall system is still significantly higher than solutions that include the use of magnetic field sensors [3].

The importance of the innovative sensors to giant magnetoresistance, is related to the improvement of various relevant factors for the industrial application of GMR sensors [5], such as greater strength measuring sensitivity to an external magnetic field,

associated to the more accentuated decrease of the electric resistance (10–20%), compared to AMR sensors (2–3%). The amplitude of the signal does not depend on the frequency of the magnetic field applied, tolerate very intense magnetic fields (100 T) without damage, linearity of the R/H curve (98% in the range of 10–70% of the applied magnetic field, temperature stability equal to about 0.15%/°C, heat tolerance up to 150 °C broad range of the external magnetic field variation, from 0 to 300 Gauss [5]. On the other hand, they require external control circuitry able to constantly ensure a proper axis of magnetization of the reference and an offset on the output signal compensation, due to the magnetization of the same sensor. Also a single GMR sensor only measures the intensity of the external magnetic field and not his hand [5–7].

As it regards the AMR sensors, instead, even though offer features less accurate, as the range of magnetic field intensity up to 100 Gauss, linearity in the band up to a few MHz and temperature dependence, their constructive structure provides for the internal use of self-magnetization systems (set/reset) and offset compensation, which allow a much simpler development complexity compared to GMR [8].

This paper proposes a measurement device for current, based on the effect of magnetic field. The principle of operation is based on detecting the magnetic field produced by the current that flows through a conductor, using the Biot-Savart law [8]. The sensor used belongs to the category AMR (anisotropic magneto resistive), it in fact is based on the effect magnetoresistive, that is, on the variation of the internal resistivity of the sensor, in the presence of a magnetic field [8].

2 Brief Recall of AMR Sensors

The magnetoresistive sensors, allow to make the magnetic field measurements, taking advantage of the physical properties of some materials called AMR (Anisotropic Magneto Resistive) or anisotropic materials whose resistance varies with the variation of the external magnetic field. In particular, for this type of sensor, the resistivity, ρ, of the material is related to the external magnetic field according to one of the relation $\cos^2\theta$ type, where θ is the angle between the magnetization M and the current vector I [8], where M is a vector quantity with which we quantify the magnetic effects related to mini dipoles that are created or are present at an internal of the material (Fig. 1).

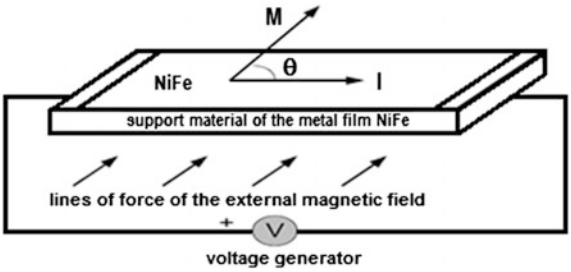

Fig. 1. Angle between the current direction (I) and the magnetization (M)

The deposition of the functional material occurs in the presence of an external magnetic field, so as to determine a preferred direction of magnetization. This makes anisotropic material, but it improves the response characteristic in terms of repeatability, low noise and low hysteresis of the output signals.

Due to the above-mentioned anisotropy, the greatest resistivity variation in the presence of a magnetic field will occur when the electric current flows in a direction parallel to the axis of the preferential magnetization. When a magnetic field is applied in a direction orthogonal to said axis, the magnetization vector rotates by an angle, and this causes a variation of the resistance to the passage of electric current that drives the device. In the measurement configuration, this will cause a relative change of resistance, and a proportional voltage signal, the output at the terminals of the Wheatstone bridge. The characterization of the behavior of this device, furthermore, indicates that the relative change of resistance is linear when the magnetic field and current are placed at an angle of 45°. For this reason, resistive film they are deposited on each of the places filaments at 45° to the preferential direction of magnetization, so that the output signal is generated in the linear response region of the bridge.

There are various techniques by means of which it is possible to obtain a linear relationship within wide values of magnetic field, ±6 Gauss [8]. The sensor consists of 4 resistors, Fig. 2, connected in a diamond constituting a Wheatstone bridge, this leads to a differential type output represented by OUT+ and OUT− pins, while the bridge of resistors is fed via pins V_{bridge} and GND. The sensor output reading may be performed, with an operational amplifier in subtractor configuration or by means of an instrumentation amplifier [8].

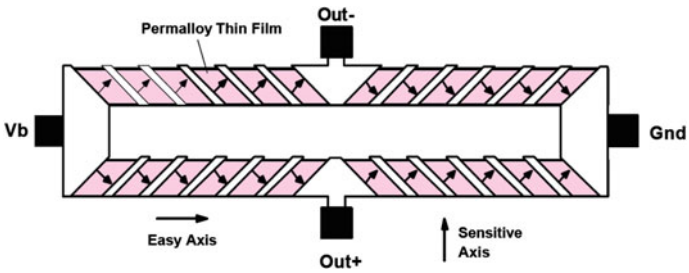

Fig. 2. The internal AMR sensor structure, magneto resistors in the Wheatstone bridge

This solution is not optimal in reality, since, the Wheatstone bridge has an offset voltage that will add up or escape to the output voltage. For this reason, it is possible to exploit an offset circuit, reached by pins “Offset+” and “Offset−“. These are connected to a small inner winding to the same sensor and disposed in such a manner that the magnetic field that is to be generated when current flows go to add up or subtract with the magnetic field component with respect to which the sensor is sensitive. This winding is generally used within a negative feedback loop in order to make the automatic zeroing. The current which is circular can make is generally a few tens of mA and the winding resistance is between 2.5 and 3.5 Ω, while the generated magnetic field is an average of 51 mA/Gauss.

One of the most complicated parts with which the designer must challenge themselves, but which are of magnetoresistive sensors among the most sensitive sensors to detect magnetic fields, are pins SET and RESET (S/R+ and S/R−), positive and negative, respectively [8]. As said, the resistivity is dependent on the angle θ between the vector of magnetized organization M and the current vector I. Due to strong external magnetic fields, such direction may be altered causing a deterioration of the sensitivity of the sensor itself. This is not damaged but due to a "memory" effect which keeps the magnetization vector M shifted with respect to that originally set, the sensor will not work in its maximum performance [8]. By means of the pin S/R+ and S/R−, which are connected to another internal winding of the switch it is possible to restore the initial conditions, "storing" the sensor. The magnetic field generated by this new winding must obtain the direction such as to modify the vector M, which is different from that which it should have in the case of the winding connected to pins Offset+ and Offset−. In particular, while in the case of the winding associated offset flowing a DC current of a few tens of mA, in the winding associated with the function of Set and Reset flow several amperes, up to 4 A, but in a pulsed way. The pulse should have a duration of 2 s, and the pulse width of the current ranges from 0.5 to 4 A, since in some cases it has no interest in obtaining the best sensitivity allowed by the sensor.

This winding allows to obtain maximum sensitivity of the sensor thanks to the fact that properly restores the magnetization vector. For this purpose, however, it is only necessary the impulse of Set or Reset. The distinction between the two pulses is only in the direction of the current, in particular the pulse Set is such that the current enters S/R + and comes out from S/R−, while for the Reset pulse is reversed reasoning, that is, the current flows out from S/R+ and entering S/R− [8].

As previously mentioned, the sensor provides a measurement of the output voltage of the differential type, which is performed by means of a Wheatstone bridge. Typically, the output voltage is few mV, therefore, it is needed to amplify such quantity for improving the measurement sensitivity. Figure 3 shows the schematic of the amplifier used. It is composed of an operational amplifier, in a differential configuration, with a gain equal to 100. Such a circuit has been realized for each sensor axis.

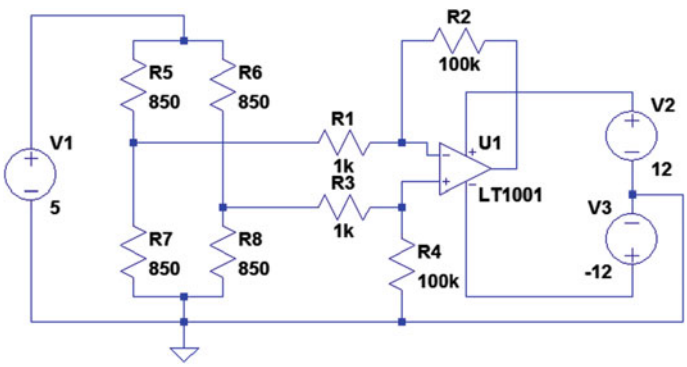

Fig. 3. Schematic of the amplification circuit

3 Experimental Characterization

An experimental analysis has been made for analyzing the metrological performance of the realized system [9, 10]. The measuring station (see Fig. 4) can be divided into two main parts: the stimulus generation and detection. The part of stimulus generation involves the use of a current source capable of generating different current values both DC and AC for different frequency values. The detection part comprises the system composed by the sensor for the detection of magnetic field and by measurement instrumentation (digital multi-meter and oscilloscope) for acquiring the sensor signal output. The device characterization has been made by considering tests with different DC and AC current values, and for different frequency values. During all tests, the environmental temperature was kept constant at a value of 25 °C.

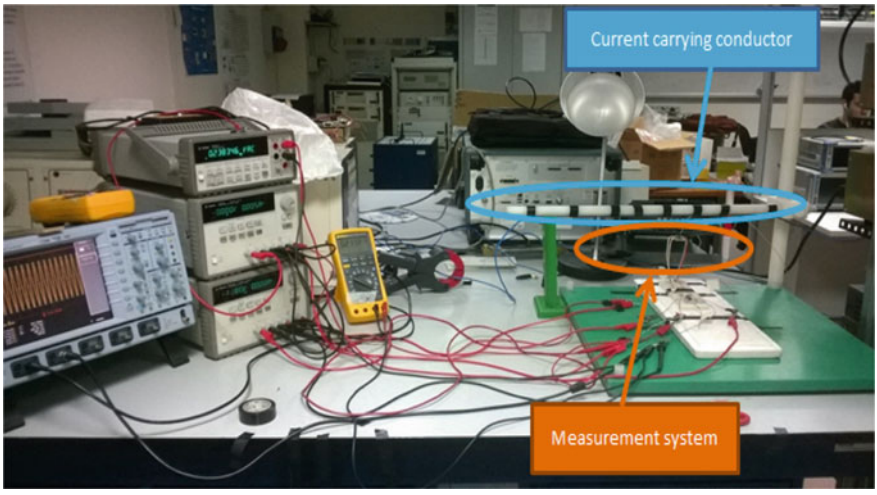

Fig. 4. The measuring station

The obtained results are reported in Figs. 5 and 6. They show that the sensor response well approximate a straight line, and therefore, the relation between the sensor output voltage and the current, can be expressed as:

$$I = \left(\frac{V_{rms} + 76.605}{77.605} - 1 \right) \times 10 \tag{1}$$

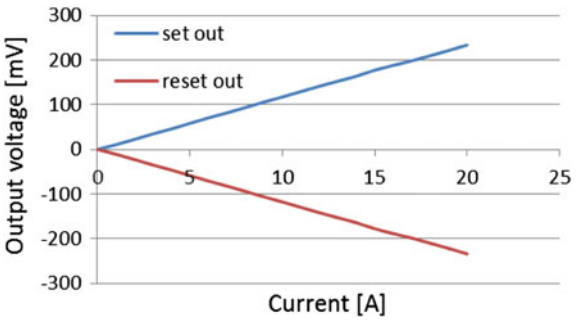

Fig. 5. The DC output characteristic of set and reset

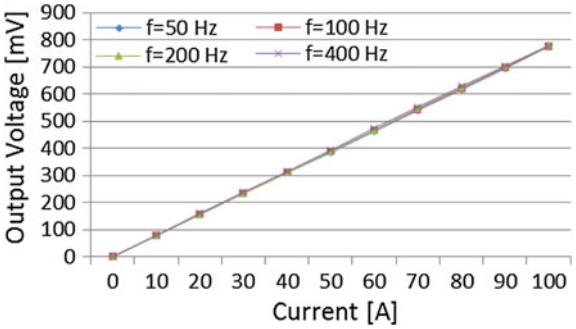

Fig. 6. The AC output characteristic for different values of frequency

Once defined the input-output relationship of the sensor, the percentage error for different current values and frequencies is reported in Fig. 7. It shows that the error is always below 0.2%.

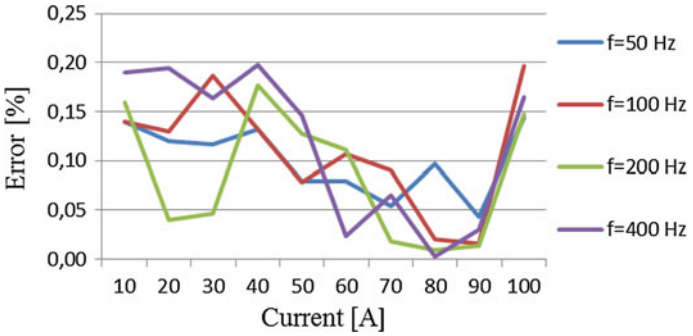

Fig. 7. The percentage error for different frequency values

From this first analysis, we can say that the AMR sensor presents an excellent performance for the current measurement, especially for the medium-voltage applications, where the current value lie in the range 50–100 A. However the linearity is assured if the magnetic field is inside ±6 Gauss.

4 Temperature Influence and Compensation

One of the factors that must always be taken into account when making the characterization of a device for measuring electrical quantities, is certainly the temperature. For this reason it was necessary to observe the HMC1022 sensor response to changes of this magnitude. The characterization was carried out by observing the variation of the response of the sensor, the frequency of 50 Hz, for different current values, with the range of temperature changing from 30 to 100 °C, in steps of 5 °C.

From an initial check of the results, it is evident that, as the temperature increases, the sensor output tends to decrease. This variation can therefore lead to a greater error than the one found in the preceding paragraph-tooth. It is therefore, very important to understand if, when the temperature varies, the sensor response still tends to be linear. This behavior is shown in Fig. 8.

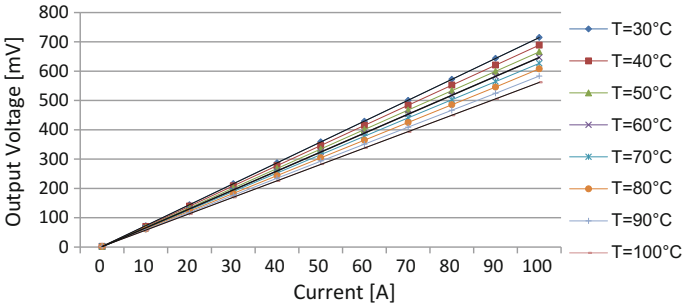

Fig. 8. The output characteristic for different values of temperature

Looking at the graph, it is evident that the sensor input-output curve is still linear even if with the curve slope depends on the temperature. As result, this behavior brings to a significance increasing of the percentage error which can assume also values close to 30%, if the Eq. (1), achieved for the environmental temperature of 25 °C, is used to estimate the current flowing in the wire. These results are shown in Fig. 9. Nevertheless, it is possible to perform a characterization of the sensor as a function of the operating temperature, and then obtain a new output equation of the system:

$$I = \left(\frac{V_{rms} + 76.605 - kT}{77.605 - kT} - 1 \right) \times 10 \tag{2}$$

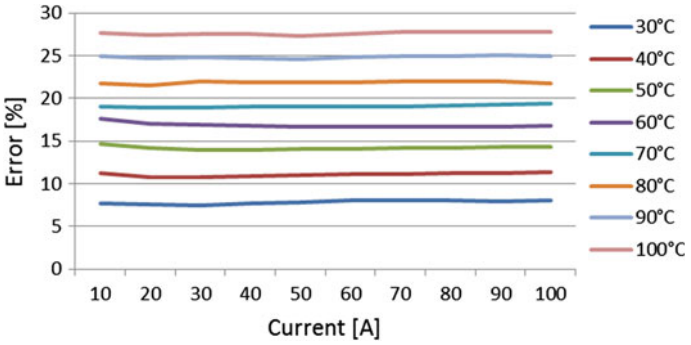

Fig. 9. Percentage error for different temperatures when the Eq. (1) is used whatever be the actual environmental temperature

where "*T*" is the actual operating temperature and "*k*" is a suitable correction factor. In this way, it is possible to apply the Eq. (2) in order to compensate the sensor output with respect to the temperature.

As result, repeating the tests for different temperatures, once again the percentage errors are all confined within the 0.2% limit, as shown in Fig. 10. Of course, this aspects would suggest to add a temperature sensor to the system thus allowing to adjust the input-output I/O curve in the basis of the temperature.

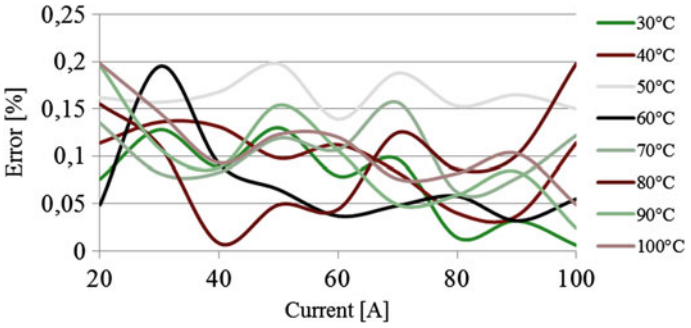

Fig. 10. Percentage error for different temperature values when the temperature compensation is performed

So, ultimately, for optimal performance, it is necessary to equip the measuring system of a simple temperature sensor, which interacts by means of a microprocessor, modifies the characteristic equation of the sensor as the temperature varies.

5 Conclusions

The realized device allows measuring the current flowing in a wire without contact by means of the measurement of the magnetic field due to the unknown current. If a temperature compensation is made, the achieved metrological performance are acceptable for the context of MV applications and are comparable with ones of competitor solutions. The proposed system offers considerable advantages in terms of cost, conditioning circuit complexity and overall size. Current efforts are focused on the development of methods for increasing the immunity of the system to external disturbances [11]. Future developments will concern with the design and PCB realization of the system which will include a temperature sensor, a microprocessor for data processing and communication management.

References

1. D.M. Parker, N.D. McCollough, Medium-voltage sensors for the smart grid: lessons learned. 2011 IEEE Power and Energy Society General Meeting, July 2011, pp. 1–7. doi:10.1109/PES.2011.6039775
2. V. Proca, N. Paduraru, Methods for non-conventional measuring sensor integration in the medium voltage electrical equipment. Power Tech, 2005 IEEE Russia, June 2005, pp. 1–6. doi:10.1109/PTC.2005.4524774
3. Die Messung der magnetische Spannung, Archiv für Elektrotechnik, 1, Pt.4, pp. 141–150 (1912)
4. Ll. Martínez-León, A. Díez, J. L. Cruz, M. V. Andrés, Frequency-output fiber-optic voltage sensor for high-voltage lines. IEEE Photonics Technol. Lett. **13**(9), 996–999 (2001)
5. Datasheet: AA and AB—series analog sensors. Available on-line at http://www.nve.com/
6. A. Bernieri, G. Betta, L. Ferrigno, M. Laracca, Multi-frequency Eddy current testing using a GMR based instrument. Int. J. Appl. Electromagn. Mech. **39**(1), 355–362 (2012). doi:10.3233/JAE-2012-1482
7. A. Bernieri, G. Betta, L. Ferrigno, M. Laracca, A biaxial probe for nondestructive testing on conductive materials. IEEE Trans. Instrum. Meas. **53**(3), 678–684 (2004)
8. Application note: AN 209 magnetic current sensing. Available on-line at https://aerospace.honeywell.com/
9. L. Angrisani, E. Atteo, D. Capriglione, L. Ferrigno, G. Miele, An efficient experimental approach for the uncertainty estimation of QoS parameters in communication networks. *2010 IEEE Instrumentation and Measurement Technology Conference (I2MTC)*, Austin (TX, USA), May 2010, pp. 1186–1191. doi:10.1109/IMTC.2010.5488077
10. L. Angrisani, D. Capriglione, L. Ferrigno, G. Miele, Packet jitter measurement in communication networks: a sensitivity analysis. IEEE International Workshop on Measurements and Networking, Anacapri (NA), Italy, 10–11 Oct 2011, pp. 146–151
11. G. Betta, D. Capriglione, L. Ferrigno, G. Miele, Experimental investigation of the electromagnetic interference of ZigBee transmitters on measurement instruments. IEEE Trans. Instrum. Meas. **57**, 2118–2127. doi:10.1109/TIM.2008.922105

Derived Non-contact Continuous Recording of Blood Pressure Pulse Waveform by Means of Vibrocardiography

Luigi Casacanditella(✉), Gloria Cosoli, Sara Casaccia, Lorenzo Scalise, and Enrico Primo Tomasini

Department of Industrial Engineering and Mathematical Sciences, Università Politecnica delle Marche, v. Brecce Bianche, 60131 Ancona, Italy
l.casacanditella@univpm.it

Abstract. Blood Pressure (BP) is considered a significant indicator of cardiac risk. By providing information about the hemodynamic load on the heart, BP detected in a central site may have added value with respect to the more familiar peripheral arterial pressure (i.e. measured on the brachial artery). Laser Doppler Vibrometry (LDV) has been demonstrated to be a reliable non-contact technique to measure the cardiovascular signals and parameters. LDV has a high sensitivity of acquisition and it is able to measure the skin vibrations related to cardiac activity when the laser beam is pointed in correspondence of the carotid artery. The obtainable vibrational signal (i.e. a velocity signal), VibroCardioGram (VCG), can provide relevant physiological parameters, including Heart Rate (HR) as well as more advanced features encoded in the contour of the pulse waveform. In this work, the authors aim to discuss the possibility of deriving the blood pressure signal from the vibrations of the carotid artery detected by LDV. 6 healthy participants were tested; the VCG was calibrated by means of diastolic and mean arterial pressure values measured by means of an oscillometric cuff. An exponential model was applied to the VCG signal of each participant in order to derive the pressure waveform from the displacement of the investigated vessel. Results show an average difference of around 20% between systolic pressure measured at brachial level (i.e. peripheral pressure value) and systolic pressure derived from VCG signal measured over the carotid artery (i.e. central pressure). This is consistent with the literature describing the physiological increase of Systolic Blood Pressure (SBP) and Pressure Pulse (PP) at increased distances from the heart (because of the presence of reflected waves). Moreover, the average measured displacements of the carotid artery are physiologically reliable (i.e. hundreds of micrometers). LDV seems to have the potential of correctly detecting the pressure waveform without contact. However, a comparison with a reference method is required to validate the proposed measurement technique.

Keywords: Blood pressure · Laser doppler vibrometry · Arterial wall displacement

B. Andò et al. (eds.), *Sensors*, Lecture Notes in Electrical Engineering 431,
DOI 10.1007/978-3-319-55077-0_46

1 Introduction

Vital signs, such as Heart Rate (HR) and Blood Pressure (BP), are fundamental to determine the wellbeing of people. Several cardiovascular pathologies can be predicted by means of central BP assessment, which is considered an important predictive factor, even more than peripheral BP [1, 2]. Its continuous recording permits the assessment of fundamental parameters related to cardiac activity (e.g. HR) and to pulse waveform (e.g. dicrotic notch). Intra-arterial pressure catheters, containing miniature pressure transducers, represent the gold standard for the measurement of time-continuous pressure signal [3], but is uncomfortable and unsuitable for routine monitoring. Applanation tonometry is a contact non-invasive technique for the assessment of the local pressure waveform, but shows some relevant drawbacks [2]. In fact, there is a lack of studies validating the method versus invasive techniques in a general population, and for that the application of such transfer function is still subject to debate. Moreover, the application of arterial tonometry is particularly challenging in obese subjects. Other studies show alternative techniques to evaluate central BP non-invasively; in [2], intravascular magnetic resonance (MR) is used to assess blood pressure waveform. A 1.5 T [T] MR scanner has been used, just above the sino-tubular junction, to evaluate the aortic area curves. This technique allows to directly measure the variation of the vessel section during the cardiac cycle, but needs a calibration model to derive the pressure waveform from the aortic traversal area. Pulse-Wave-based Ultrasound Manometry (PWUM) is another non-invasive method that combines Pulse Wave Imaging (PWI) and vessel diameter measurements for the assessment of central BP [4]. It is based on the ultrasound scanning of the cross-section of the vessel, in order to measure its diameter variation during cardiac cycle. The use of LDV for the measurement of cardiovascular signals is datable at more of 10 years ago [5]. The first reason of the introduction of this technique has been the non-contact capability of LDV to measure the skin vibrations, in particular where it is really difficult the application of the electrodes (i.e. in burnt subjects or preterm neonates [6]). The acquisition of the carotid signal on the carotid artery with LDV provides a vibrocardiographic signal (VCG), consequent to mechanical cardiovascular events. Many studies have focused their attention to the extent of cardiovascular parameters from carotid artery [7–13]. In a previous work [14], the authors have made the hypothesis of using LDV to non-invasively assess the blood pressure waveform. The aim of this work is to discuss the feasibility of the application of a mathematic model to derive the arterial pressure signal, at carotid level, from the vibrational signal measured by means of a Laser Doppler Vibrometer.

2 Materials and Methods

LDV method was tested in a preliminary study on 6 healthy subjects. Participants was informed about the test and they filled a consent form to permit the study of their data.

2.1 Measurement Setup

VCG and electrocardiographic (ECG) signals were acquired simultaneously thanks to a proper A/D board (PowerLab 4/25T, 12-bit resolution). The VCG signals were measured with a single point LDV system (Polytec PDV100; calibration accuracy ±0.05 mm/s, bandwidth 0.05 Hz–22 kHz, spot diameter <1 mm, sensitivity 0.2 V/(mm/s)). The Polytec PDV100 utilizes Class 2 (eye safe) beam at 633 nm wavelength. The native output of the LDV system is a velocity signal.

Three 2-mins trials were made for each participant. Furthermore, a conventional oscillometric method was used to simultaneously assess BP at brachial level (P monitor model UA-767BT-Ci from A&D Instruments, accuracy: ±3 mm Hg).

Three measures of blood pressure was acquired for each trials and a mean of the diastolic and systolic values was considered.

During the trials, the participants were asked to lie supine and stay relaxed.

The vibrometer was placed on a tripod at a distance of 50 cm from the subject and it was pointed perpendicularly to the skin of the participant, over the left common carotid artery. A hydrating lotion (45% zinc oxide) was spread on the neck over the carotid site to improve the reflectivity of the skin and, consequently, the quality of the measurement (i.e. signal-to-noise ratio). In the present work, the carotid artery was located by a palpation method on the neck, identifying the point of maximum pulsation of the carotid artery.

A sketch of the measurement setup is represented in Fig. 1.

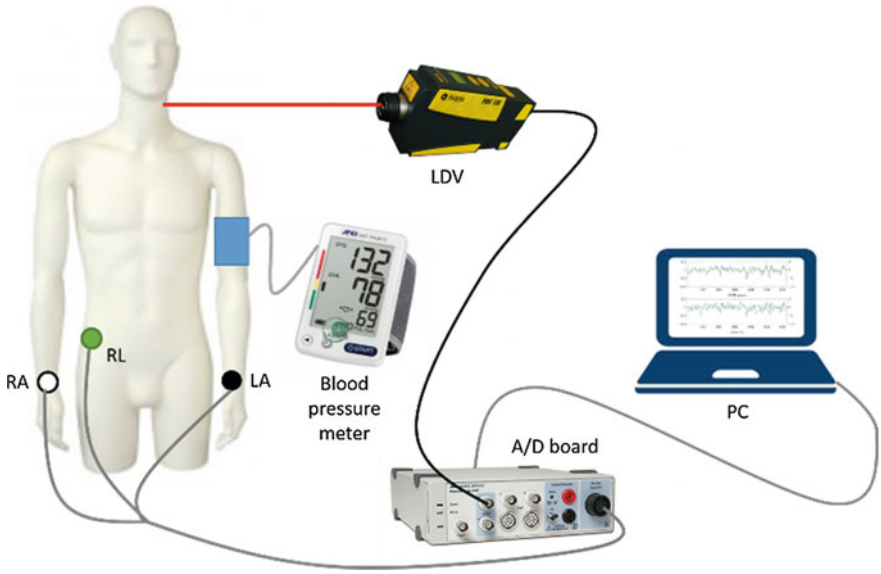

Fig. 1. Sketch of the measurement setup: LDV and ECG were connected to the same acquisition board; BP meter was applied on the *left* arm at brachial level

2.2 Signal Processing

The signal processing consists of the steps reported in Fig. 2 and after described in detail.

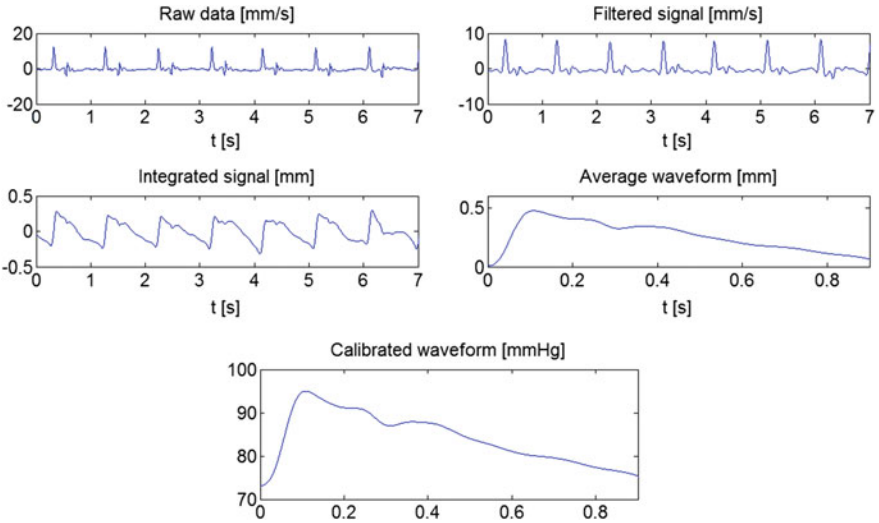

Fig. 2. Steps of the signal processing

- *Signal filtering*: a 3rd order Butterworth bandpass filter was applied to raw data. 0.1–30 Hz and 0.1–40 Hz were the two frequency bands considered for VCG and ECG signals, respectively.
- *Signal integration*: VCG (i.e. velocity signal) was integrated to obtain a displacement signal, which has to be calibrated to obtain absolute BP values. An operation of detrend was performed on the displacement signal to achieve a mean value equal to zero.
- *Computation of the average waveform*: ECG signal was used to correctly separate the single heartbeat in VCG signal. This allowed to detect the onset and the offset of the single heart beats in the displacement signal. Then, each heartbeat was re-sampled according to the mean heart period detected from ECG signal.
- *Application of the calibration model*: It was assumed that there is an exponential relationship between arterial pressure waveform and arterial cross-section [7]. Diastolic BP and Mean Arterial Pressure (MAP) values were supposed to remain fairly constant throughout the whole arterial tree. The systolic BP value extracted from the resulting pressure waveform was compared to the corresponding oscillometric BP value obtained from the brachial artery. The applied model relates the displacement d(t) achieved from LDV data to the arterial pressure waveform p(t), as described in (1) [15]:

$$p(t) = \mathrm{e}^{(\alpha(A(t))/A_d)} \tag{1}$$

where:

$\alpha = \frac{A_d}{A(t)-A_d} \ln\left(\frac{SBP}{DBP}\right)$ is a calibration parameter that quantifies the stiffness of the vessel;

$A(t) = \frac{\pi d(t)^2}{4}$ is the transversal cross circular section of the vessel;

A_d is the diastolic value of the transversal section of carotid when pressure assumes its diastolic value.

3 Results

Table 1 shows the comparison between the systolic pressure measured by means of the oscillometric cuff at brachial level and the one obtained from the calibration of the VCG signal (i.e. the maximum peak of the calibrated pressure waveform).

Table 1. Systolic pressure measured at brachial level, systolic pressure derived from VCG signal and percentage difference between systolic values measured in the two different site

	Brachial systolic pressure (mmHg)	Carotid systolic pressure (mmHg)	Percentage increase (%)
Subject 1	111	84	29
Subject 2	126	104	21
Subject 3	117	100	17
Subject 4	107	92	16
Subject 5	98	85	15
Subject 6	99	80	23

Moreover, the displacement waveforms were discussed, in order to evaluate if the measured artery wall movements are consistent with the ones in literature. In Fig. 3, an example of displacement waveform is reported.

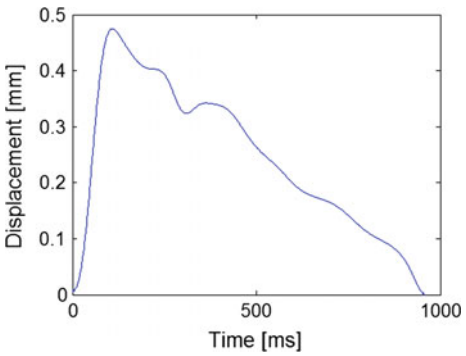

Fig. 3. Example of average displacement waveform (subject 4)

The mean values of the average displacement waveforms are the following ones (Table 2).

Table 2. Average displacement for the six participants

Subject	Average displacement (μm)
1	220
2	203
3	197
4	186
5	191
6	207

4 Discussion and Conclusions

In this preliminary study, the authors have been tested on six subjects the possibility of obtaining the pressure waveform from the integrated VCG signal, calibrated by means of brachial diastolic and mean blood pressure values measured via oscillometric method, using an exponential model [15].

The pressure values measured in the obtained waveforms have been compared with the ones measured at brachial level. The obtained systolic differences are comparable to the ones in literature (20%) [3] and express the physiological increase of systolic pressure (Fig. 4) from the central to peripheral sites.

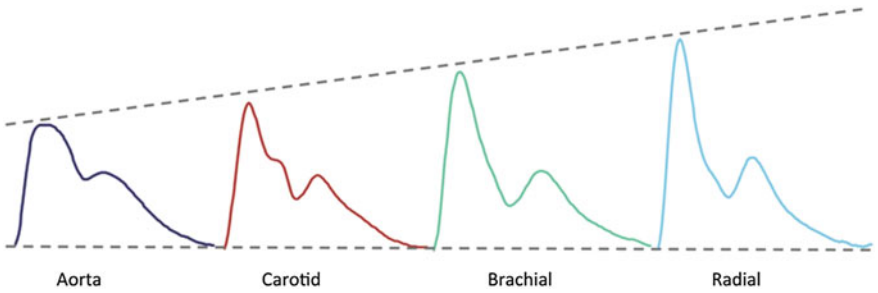

Fig. 4. Physiological variation in the pressure waveform throughout the arterial tree

Moreover, the average measured displacement shows values physiologically correct [3], that is of hundreds of micrometers [16].

The use of LDV to measure the displacement of carotid artery allows to observe the mechanical events related to hemodynamics with a very high sensitivity, but it involves the contribution of reflection phenomena, which may be not related to the investigated vessel.

A deeper investigation of the physiological dynamics is required in order to distinguish carotid features from the other mechanical events detected by LDV and to obtain a more accurate pressure waveform.

Moreover, the comparison with a reference method (i.e. arterial tonometry or intravascular catheter) is required to validate the described measurement method and processing algorithm.

References

1. J. Sharman, M. Stowasser, R. Fassett, T. Marwick, S. Franklin, Central blood pressure measurement may improve risk stratification. J. Hum. Hypertens. **22**(12), 838–844 (2008)
2. M.A. Quail, J.A. Steeden, D. Knight, P. Segers, A.M. Taylor, V. Muthurangu, Development and validation of a novel method to derive central aortic systolic pressure from the MR aortic distension curve. J. Magn. Reson. Imaging JMRI **40**(5), 1064–1070 (2014)
3. McDonald's blood flow in arteries, in *Theoretical, Experimental and Clinical Principles*, 6th edn. (CRC Press, 29-July-2011) [Online]. Available: https://www.crcpress.com/McDonalds-Blood-Flow-in-Arteries-Sixth-Edition-Theoretical-Experimental/Nichols-ORourke-Vlachopoulos/9780340985014. Accessed 16 Apr 2016
4. J. Vappou, J. Luo, K. Okajima, M. Di Tullio, E.E. Konofagou, Non-invasive measurement of local pulse pressure by pulse wave-based ultrasound manometry (PWUM). Physiol. Meas. **32**(10), 1653–1662 (2011)
5. M. Pinotti, N. Paone, F.A. Santos, E.P. Tomasini, *Carotid Artery Pulse Wave Measured by a Laser Vibrometer*, vol 3411 (1998), pp. 611–616
6. L. Scalise, N. Bernacchia, I. Ercoli, P. Marchionni, Heart rate measurement in neonatal patients using a webcamera, in *2012 IEEE International Symposium on Medical Measurements and Applications Proceedings (MeMeA)*, 2012, pp. 1–4
7. L. Scalise, U. Morbiducci, Non-contact cardiac monitoring from carotid artery using optical vibrocardiography. Med. Eng. Phys. **30**(4), 490–497 (2008)
8. S. Casaccia, E.J. Sirevaag, E. Richter, J.A. O'Sullivan, L. Scalise, J.W. Rohrbaugh, Decoding carotid pressure waveforms recorded by laser Doppler vibrometry: effects of rebreathing, in *AIP Conference Proceedings*, vol 1600, 2014, pp. 298–312
9. P.H. Lai, J.A. O'Sullivan, M. Chen, E.J. Sirevaag, A.D. Kaplan, J.W. Rohrbaugh, A robust feature selection method for noncontact biometrics based on Laser Doppler Vibrometry, in *Biometrics Symposium, 2008. BSYM '08*, 2008, pp. 65–70
10. M. Chen, J.A. O'Sullivan, N. Singla, E.J. Sirevaag, S.D. Kristjansson, P.H. Lai, A.D. Kaplan, J.W. Rohrbaugh, Laser Doppler vibrometry measures of physiological function: evaluation of biometric capabilities. IEEE Trans. Inf. Forensics Secur. **5**(3), 449–460 (2010)
11. A. Campo, P. Segers, H. Heuten, I. Goovaerts, G. Ennekens, C. Vrints, R. Baets, J. Dirckx, Non-invasive technique for assessment of vascular wall stiffness using laser Doppler vibrometry. Meas. Sci. Technol. **25**(6), 65701 (2014)
12. G. Cosoli, L. Casacanditella, E.P. Tomasini, L. Scalise, The non-contact measure of the heart rate variability by laser doppler vibrometry: comparison with electrocardiography. Meas. Sci. Tecnol. (in press)
13. E.J. Sirevaag, S. Casaccia, E.A. Richter, J.A. O'Sullivan, L. Scalise, J.W. Rohrbaugh, Cardiorespiratory interactions: noncontact assessment using laser Doppler vibrometry. Psychophysiology, p. n/a-n/a, Mar 2016
14. Non-contact assessment of blood pressure wave by means of vibrocardiography [Online]. Available: https://www.researchgate.net/publication/282867958_Non-contact_assessment_of_blood_pressure_wave_by_means_of_vibrocardiography. Accessed 15 June 2016

15. S.J. Vermeersch, E.R. Rietzschel, M.L. De Buyzere, D. De Bacquer, G. De Backer, L.M. Van Bortel, T.C. Gillebert, P.R. Verdonck, P. Segers, Determining carotid artery pressure from scaled diameter waveforms: comparison and validation of calibration techniques in 2026 subjects. Physiol. Meas. **29**(11), 1267–1280 (2008)
16. C.L. Desjardins, L.T. Antonelli, E. Soares, *A Remote and Non-contact Method for Obtaining the Blood-Pulse Waveform with a Laser Doppler Vibrometer*, vol 6430 (2007), pp. 64301C–64301C–9

A Fall Detector Based on Ultra-Wideband Radar Sensing

Giovanni Diraco(✉), Alessandro Leone, and Pietro Siciliano

National Research Council of Italy—Institute for Microelectronics and Microsystems, Lecce, Italy
giovanni.diraco@le.imm.cnr.it

Abstract. Falls in the elderly have been recognized worldwide as a major public health problem. Nevertheless, falls cannot be detected efficiently yet, due to open issues on both sensing and processing sides. The most promising sensing approaches raise concerns for privacy issues (e.g., video-based approaches) or low acceptability rate (e.g., wearable approaches); whereas on the processing side, the commonly used methodologies are based on supervised techniques trained with both positive (falls) and negative (ADL-Activity of Daily Living) samples, both simulated by healthy young subjects. As a result of such a training protocol, fall detectors inevitably exhibit lower performance when used in real-world situations, in which monitored subjects are older adults. The aim of this study is to investigate a fully privacy-preserving and high-acceptance sensing technology, i.e. ultra-wideband radar sensor, together with a novelty detection methodology based exclusively on real ADL data from monitored elderly subject. The use of the UWB novelty detection methodology allowed to significantly improve detection performance in comparison to traditional supervised approaches.

Keywords: Fall detection · Range sensing · Ultra-wideband radar sensor · Machine learning · Novelty detection

1 Introduction

Nowadays, the most industrialized countries around the world are facing an unprecedented aging of their population. The fastest growing age group is 65 years and older which is expected to cover over a quarter of the population within the next four decades [1].

This demographic phenomenon, also known as "aging society", has a direct impact on healthcare and elderly care sectors, as well as substantial financial and social implications. In particular, the depletion of healthcare resources is largely attributable to age-related injuries, of which the large majority are associated with falls [2, 3]. In fact, each year about one in three older adults aged 65 or more experiences at least a fall, with serious injuries (e.g., from skeletal fracture to death) in 25% of cases [4, 5].

Among fall-related consequences the so-called "long lie" after a fall (for an hour or more) is particularly critical because it has been associated with pneumonia, dehydration, hypothermia, and high mortality rate (i.e., one in two seniors who reported a

B. Andò et al. (eds.), *Sensors*, Lecture Notes in Electrical Engineering 431,
DOI 10.1007/978-3-319-55077-0_47

long lie died within six months) [6]. In addition, long lies even after a non-injury fall may contribute to the onset of "fear of falling" and social isolation.

In the scenario depicted above, automatic fall detection has become a very active research area, aiming to substantially reduce the worst consequences of falls among the elderly by automatically detecting and signalling the occurrence of a fall event in order to ensure a prompt assistance to the fallen person.

The remainder of the paper is organized as follows: Sect. 2 analyses the state-of-the-art of fall detection solutions, highlighting related works based on radar systems; Sect. 3 starts by giving some background information on the UWB radar technology adopted in this study and, afterwards, describes the experimental setup and collected data, then continues detailing the processing framework, and finally presents the metrics used for performance evaluation; the achieved experimental results and discussion are in Sect. 4; some conclusive remarks are, finally, provided in Sect. 5.

2 State-of-the-Art Analysis

The nowadays available fall detection solutions can be roughly subdivided into two main categories, wearable-based and ambient-based solutions [7]. The most elementary wearable device consists of a push-button worn and actuated by a senior in case of fall. Obviously, such manually-actuated solutions cannot help in case of falls resulting in a lack of conscience or upper extremity paralysis.

Wearable-based automatic fall detectors are based on small-sized devices worn by the senior (usually embedded in garments, belts, etc.), equipped with sensor measuring translational and rotational rates of body's parts like torso and/or limbs, and able to automatically send help requests in case of detected fall [8]. Normally, such devices use MEMS (microelectromechanical systems) accelerometer and compass sensors in conjunction with some dedicated hardware for online processing and wireless radio communication. Arguably the most stringent requirements they need to be able to satisfy are minimum size and maximum battery life, which are conflicting requirements that are very difficult to meet in real-life applications. In addition, wearable approaches have to deal with issues related to their usage (usability) and acceptance (acceptability) by the user. In this regard, well-known issues are related with forgetting to wear (e.g., after having a bath) or to recharge, accidental damaging, wrong wearing position, and refusing to wear (e.g., due to fear of stigma) [7].

Regarding the ambient-based category, these solutions are based on different kinds of ambient-installed sensors which can be further classified as contact and contactless solutions. In the first case, pressure or contact vibration sensors are integrated on surfaces hit by the person's body during a fall, such as floor, carpet, bed, chair, and so on [9]. Although the affordability of these sensors, ambient contact solutions require an accurate design or redesign of the home environment making them quite expensive and cumbersome.

In the second case, on the other hand, involved sensing approaches do not require any kind of contact with the environment; the most investigated solutions are based on audio, video and range sensing. Audio- and video-based systems use, respectively, microphones and cameras in order to perform acoustic and visual scene analysis. Fall

detectors based on these approaches, especially video-based, are considered reasonably reliable and affordable, although they raise many privacy concerns (e.g., recordings may be accessed by unauthorized users) [7].

Range-based systems use sound or electromagnetic waves outside the human perceptible spectrum. As sensing elements they can use SONAR (Sound Navigation and Ranging), LIDAR/LADAR (Light Detection and Ranging), Range camera and RADAR (Radio Detection and Ranging) sensors [10]. Their main strength lies in the fact that, being active range systems, they are almost totally independent from environmental conditions (e.g., surrounding sounds, lighting, electromagnetic fields). Another important strength is that they work outside the human perceptible spectrum, and thus their range data are not directly usable for obtaining privacy-sensitive information.

Among all range systems mentioned above, the most promising and thoroughly investigated are those based on range cameras and radars. Range camera systems are able to provide, at high frame rates (e.g., up to 50 fps) and within a wide field-of-view (e.g., up to 70°), dense depth images of a scene suitable for real-time 3d visual analysis. Several authors demonstrated the feasibility of using TOF (Time-Of-Flight) or SL (Structured-Light) range cameras for accurately detecting falls [7]. Although the richness of range data provided by TOF/SL cameras, nevertheless they are based on (near-)infrared light waves and so are subject to occlusion problems which are particularly frequent in home environments. In addition, even if only depth data are used (i.e., range cameras usually provide both range and intensity images), privacy concerns are not fully resolved since the person's silhouette is visible as well.

2.1 Related Works Using Radars

Radar-based systems present many interesting aspects for fall detection, and more general for in-home health monitoring. In fact, they are able to penetrate obstacles so that do not suffer from occlusion problems, and are conceived to deal with highly cluttered and noisy environments. Furthermore, radar systems are much more privacy-preserving than range cameras, since radar data are not directly usable for obtaining any kind of privacy-sensitive information.

By using radar-based systems, various human activities, including falls, can be effectively detected (e.g., high detection rates) via Doppler analysis of their motion signatures. The radar systems adopted for this kind of analysis typically uses narrowband waveforms, in order to achieve high Doppler resolution, especially in presence of fast-moving targets [10].

However, ultra-wideband (UWB) systems, and particularly Impulse-Radio (IR) UWB ones, offer several advantages over narrowband systems, such as low power spectral density (i.e., very difficult to be intercepted, low interferences), short pulse duration (i.e., high penetrating power, multipath immunity, high-speed short-range data transmission), low cost and low power architecture (i.e., almost "all-digital") [11]. For that reasons, IR-UWB radar has emerged as a multi-purpose technology whose application range spans from detection and measurement of vital signs to human localization/tracking (also through walls), activity detection/classification, and even

secure high-throughput wireless communication, just to name a few of its possible uses. Although fall detection has also been demonstrated using UWB radar, nonetheless, to the best of authors' knowledge, these studies were based almost exclusively on Stepped-Frequency Continuous-Wave (SFCW) systems, which do not offer the same advantages as IR-UWB ones.

On the processing side, the methodologies commonly used for fall detection are based either on threshold approaches or supervised machine learning techniques tuned/trained with both positive (falls) and negative (ADL-Activity of Daily Living) samples, both simulated by healthy young subjects. As a result, due to such a tuning/training protocol, fall detectors inevitably exhibit lower performance when used in real-world situations, in which monitored subjects are older adults [7]. The lack of real-world fall data is an issue common to all fall detection studies, nevertheless only few studies considered datasets collected from real falls of older adults. The number of fall events included in such (not public yet) datasets, however, is low and the fall mechanisms are not adequately documented.

In spite of this unresolved issue, very few attempts have been made to address the fall-detection problem from the complementary point of view, that is, to train the algorithms with only ADLs and then detect falls as novelties or anomalies. To the best of the author's knowledge, the studies that attempted to do so all used data provided by accelerometer sensors embedded in smartphones [12, 13] or other wearable devices [14], whereas there are no studies in the literature that used radar-based systems to detect falls as novelties/anomalies.

3 Materials and Methods

The purpose of the study presented in this paper is to investigate the ability of micro-Doppler features, obtained with a monostatic IR-UWB radar sensor, to represent micro-movements involved during both ADLs and falls, in a way which is useful for addressing the problem of detecting real-world falls by means of a novelty detection methodology. All details about sensing, experimental setting, processing and performance evaluation are provided in this section.

3.1 Ultra-Wideband Radar Sensing

The radar sensor adopted in this study is based on the monostatic sensor module P410 manufactured by Time Domain [15], which is connected via USB to an Embedded PC (EPC). Both devices, P410 and EPC, are presented in Fig. 1. The P410 is a state-of-the-art IR-UWB radar, working from 3.1 to 5.3 GHz centred at 4.3 GHz, covering a distance range of about 30 m, having good object penetrating capabilities and compact (7.6 × 8.0 × 1.6 cm) board dimensions. The P410 is equipped with an omnidirectional antenna, which in this study has been modified by adding a planar back reflector in order to reduce the azimuth pattern to around 100°. Range data from the P410 are processed by the Embedded PC (EPC), which has low computational profile (i.e., Intel Atom processor based), low power consumption (25 W) and reduced (13.2 × 9.5 × 3.7 cm) dimensions.

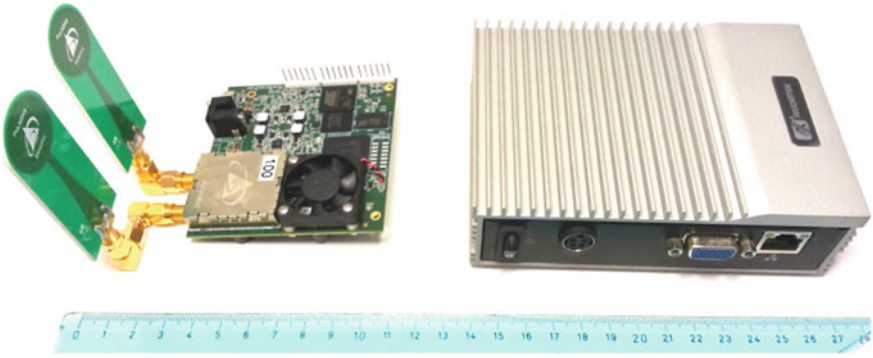

Fig. 1. UWB radar sensor P410 (*left*) and embedded PC (*right*)

The EPC runs the processing algorithms, including (as better explained in the following) pre-processing steps and machine learning, for detection of fall events in real-time following a novelty discovering methodology.

3.2 Experimental Setup and Data Acquisition

The experiments were conducted in home-like setting, as pictorially represented in Fig. 2. The P410 was accommodated at about one meter from the floor. For comparison reasons, also a TOF range camera MESA SR4000 [16] was wall-mounted at the height of about 2.40 m with respect the floor.

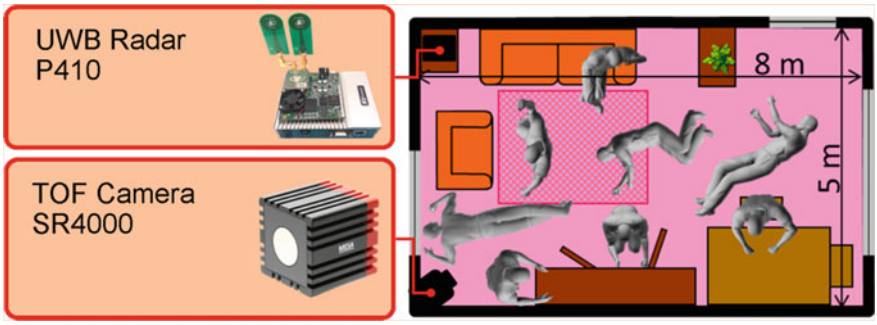

Fig. 2. Home-like setting used for data collection

Both ADLs and falls were performed in a home-like setting by involving ten healthy subjects divided into two age groups of avg. 24 and 48 years old, respectively. Falls were simulated by following the protocol suggested by Noury et al. [17]. For each participant, a total amount of 436 actions were collected, of which 30 were simulated falls and the remaining were daily activities such as walking, sitting down, standing up, and so on.

3.3 Processing Framework

On the algorithmic side, there are three main stages: pre-processing, feature extraction, and event detection. Regarding the pre-processing stage, the scattered radar signal is first filtered by a 16th-order Butterworth (bandpass 3.1–5.3 GHz) and then by a 3-tap FIR motion filter in order to improve the signal-to-clutter ratio. The resulting range profiles are normalized in amplitude and time within a sliding window of time length 1.5 s and distance range up to 8 m. The time duration of 1.5 s was experimentally determined, as that able to discriminate both fast actions (e.g., falls) and slow ones (e.g., voluntary lying down). Amplitudes and times-of-arrival (TOAs) are estimated by peak analysis and tracked with Kalman filter in order to isolate the only target of interest (i.e., the monitored subject). The pre-processed radar signal is shown in Fig. 3.

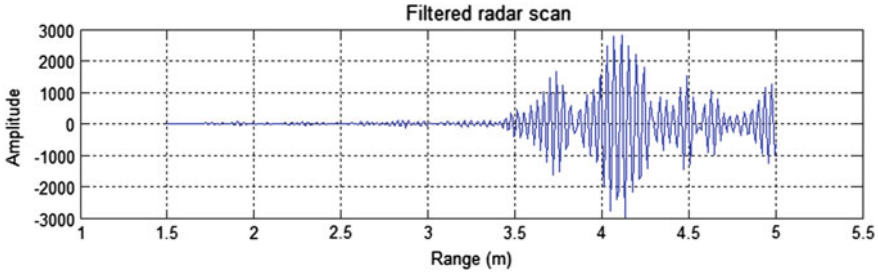

Fig. 3. Pre-processed radar signal referred to a person moving inside a room at a distance of about 4 m from the radar sensor

The extracted features are based on the micro-Doppler effect which is briefly introduced as follows. As well known, the relative motion between radar and target introduces a Doppler frequency shift which relates directly to the radial velocity: movements towards (away from) the radar introduce a positive (negative) frequency shift. Furthermore, a human target consists of different parts (e.g., head, torso, legs, etc.) which move at different velocities during the same action (e.g., walking, sitting, etc.). The multiple Doppler shifts produced by these smaller motions are referred to as micro-Doppler features. The feature extraction process starts by computing the Doppler spectrogram which represents the signal power distribution over velocity (x-axis) and distance (y-axis). In Fig. 4, the Doppler spectrograms of radar scans taken during a simulated fall (Fig. 4a) and walking activity (Fig. 4b) are presented. As evident from Fig. 4a, the spectrogram exhibits horizontally aligned peaks (micro-Doppler) related to movements of body's parts during the fall event. The Doppler spectrogram is computed by applying the short-time Fourier transform to the analytic form of the radar signal. Hence, the micro-Doppler features are extracted by convolving the spectrogram with a Gaussian filter and summing the power spectrum at all distances for each frequency, in order to obtain one-dimensional micro-Doppler signatures as those reported in Fig. 4c, d associated with the simulated fall (Fig. 4a) and the walking activity (Fig. 4b), respectively.

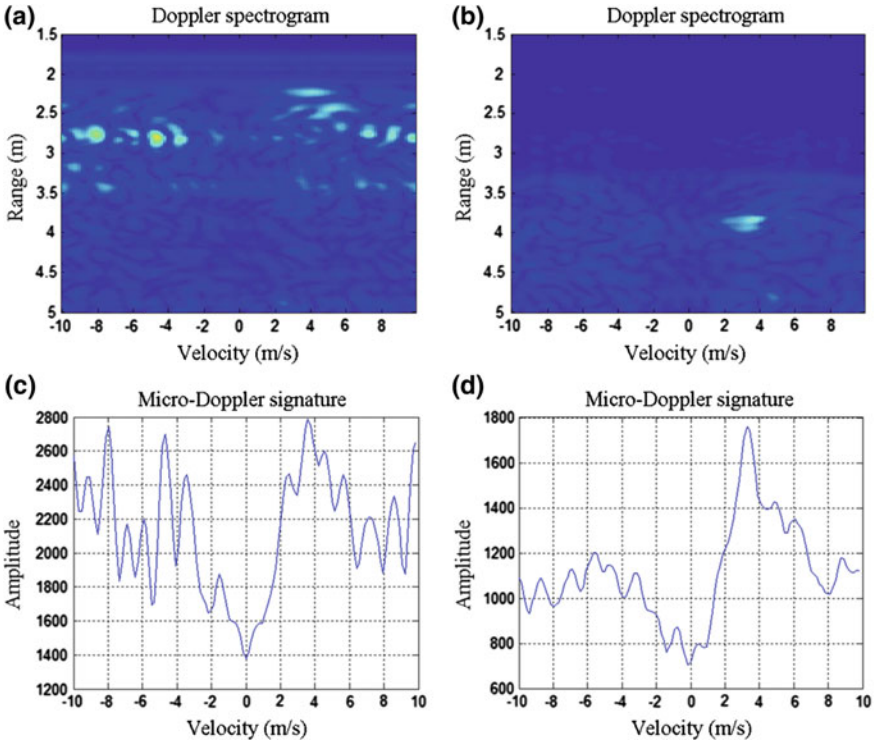

Fig. 4. Doppler spectrum (**a**) and micro-Doppler signature (**c**) of a radar scan referred to a person falling down at a distance of about 3 m from the sensor. Doppler spectrum (**b**) and micro-Doppler signature (**d**) of a radar scan referred to a person walking at a distance of about 4 m from the sensor

The event detection stage deals with the recognition of a fall occurrence from the extracted features. The commonly used methodologies are based on supervised machine learning techniques trained with both positive (falls) and negative (ADLs) samples, both simulated by healthy young subjects. As a result, due to such a training protocol, fall detectors inevitably exhibit lower performance when used in real-world situations, in which monitored subjects are older adults [7]. In order to address this problem and to improve fall detection performance under real-life conditions, an unsupervised approach has been used in which the fall occurrence is detected as a "novelty" with respect the usual daily activities performed by the monitored subject. In the suggested unsupervised approach, novelties are detected using votes casted by multiple one-class K-means classifiers [18]. For evaluation purpose, a classical supervised detector based on Support Vector Machine (SVM) [19] has been also experimented and its performance compared with the unsupervised one.

Furthermore, to have an additional term of comparison, TOF range data captured with the SR4000 were processed using the fall detection approaches described in [20] and the extracted features (i.e., the person's centroid temporal trend) were classified using SVM.

3.4 Performance Evaluation

The SVM-based supervised approach was evaluated with both P410 and SR4000 data. More specifically, ADLs and falls performed by the young group were used for training, whereas falls performed by the older group were used for testing. During the training phase, 738 daily actions and 90 falls were used. During the testing phase, instead, the remaining 492 daily actions and 60 falls were used.

Regarding the K-means-based unsupervised approach, since it is oriented to detect falls as novelties among daily "normal" activities (e.g., walking, sitting down, standing up, etc.), it has been validated involving the same subject in both observation and testing phases. The observation phase lasted for about 95 min for each subject (i.e., 190 actions), after which the testing phase started and 30 falls/person were performed.

Fall detection performance was evaluated, according to Noury et al. [17], in terms of sensitivity and specificity which are defined as follows:

$$\text{Sensitivity} = \text{TP}/(\text{TP} + \text{FN}),$$
$$\text{Specificity} = \text{TN}/(\text{TN} + \text{FP}),$$

where TP, TN, FP, and FN are respectively the True Positives, True Negatives, False Positives, and False Negatives.

4 Experimental Results and Discussion

As summarized in Table 1, the novelty-based unsupervised approach outperformed the (UWB) supervised one without requiring any fall-based training, and thus more reproducible in real-life scenarios. Furthermore, the novelty-based UWB performance was comparable with that obtained using the more specialized TOF vision-based sensing approach. However, it is worth noting that the unsupervised approach requires a preliminary calibration phase during which almost all daily "normal" activities should be observed and labelled as not-fall. In this study, such a calibration phase lasted 95 min per subject, but in real-world it may take much longer depending on habits of monitored subject.

Table 1. Experimental results

Approach	Sensitivity (%)	Specificity (%)
Novelty UWB[a]	91	89
Supervised UWB[b]	86	75
Supervised TOF[b]	95	97

[a]Trained with ADLs and tested with falls, both simulated by the same subject
[b]Trained with falls simulated by the young group and tested with falls simulated by the older group

The use of the UWB novelty detection methodology allowed to significantly improve detection performance in comparison to the supervised one, exhibiting performance comparable with that obtained using the more specialized TOF vision-based sensing approach. The presented system may find application for continuous indoor monitoring of older adults living alone. In fact, after a period of observation (i.e., unsupervised training), the system can reliably detect fall events against daily activities. The presence of moving objects (e.g., chairs, sofas, etc.) in the room does not interfere with the event detection, since the Kalman filter allows tracking of peaks associated with a human target in the radar signal.

Furthermore, it is worth to note that because of the high penetrating ability of the UWB radar, the presence of medium-sized objects (e.g., tables, chairs, etc.) between radar sensor and human target does not raise any occlusion problem. Instead, the most serious noise source in indoor environments is the clutter signal containing reflections from stationary structures (e.g., walls, furniture, etc.). In this study the clutter signal has been strongly attenuated by motion filtering the radar signal. However, this technique is not quite effective for through-wall sensing, in which case more sophisticated clutter removal techniques should be adopted.

As already mentioned, the system reliably detects falls when only one person is present in the room (i.e., a living-alone elderly). When two or more people are present, on the other hand, the system takes into account only the movement patterns of the person nearest to the radar sensor, and thus it is able to detect only falls of the nearest subject. Additionally, when two or more people stay at the same radial distance with respect to the radar sensor, their motion patterns may interfere, affecting the detection performance.

5 Conclusion

The main contribution of this work concerns the investigation and validation, in a home-like setting, of a fall detector based on IR-UWB radar sensor able to detect falls as novelties. Moreover, the problem of performance under real-life conditions has been addressed by suggesting an unsupervised approach not requiring fall-based training but only a subject-specific calibration phase based on observation of daily activities. Preliminary results are very encouraging, showing the effectiveness to achieve good detection performance under real-life conditions through IR-UWB-based Doppler analysis and novelty detection, which were not investigated together up to now.

The ongoing work is focused, on one hand, on extending the proposed system to detect falls in multi-user scenarios (e.g., in community dwellings) by facing the multi-target/multi-detection association problem. On the other hand, the future work is to investigate the use the UWB radar sensor also for continuous and unobtrusive in-home monitoring of vital parameters.

References

1. *World Population Prospects: The 2010 Revision* (United Nations, New York)
2. J.C. Davis et al., International comparison of cost of falls in older adults living in the community: a systematic review. Osteoporos. Int. **21**(8), 1295–1306 (2010)

3. S. Heinrich, K. Rapp, U. Rissmann, C. Becker, H.H. König, Cost of falls in old age: a systematic review. Osteoporos. Int. **21**(6), 891–902 (2010)
4. K.E. Ensrud et al., Study of osteoporotic fractures research group. Frailty and risk of falls, fracture, and mortality in older women: the study of osteoporotic fractures. J. Gerontol. A Biol. Sci. Med. Sci. **62**(7), 744–751 (2007)
5. K.E. Ensrud et al., A comparison of frailty indexes for the prediction of falls, disability, fractures, and mortality in older men. J. Am. Geriatr. Soc. **57**(3), 492–498 (2009)
6. J. Fleming, C. Brayne, Inability to get up after falling, subsequent time on floor, and summoning help: prospective cohort study in people over 90. BMJ **337**, a2227 (2008)
7. R. Igual, C. Medrano, I. Plaza, Challenges, issues and trends in fall detection systems. Biomed. Eng. **12**(66), 1–66 (2013)
8. F. Bagalà et al., Evaluation of accelerometer-based fall detection algorithms on real-world falls. PLoS ONE **7**(5), e37062 (2012)
9. M. Mubashir, L. Shao, L. Seed, A survey on fall detection: principles and approaches. Neurocomputing **100**, 144–152 (2013)
10. M.G. Amin, Y.D. Zhang, F. Ahmad, K.D. Ho, Radar signal processing for elderly fall detection: the future for in-home monitoring. IEEE Sig. Proc. Mag. **33**(2), 71–80 (2016)
11. C. Nguyen, J. Han, *Time-Domain Ultra-Wideband Radar, Sensor and Components: Theory, Analysis and Design* (Springer Science & Business Media, Berlin, 2014)
12. C. Medrano, R. Igual, I. Plaza, M. Castro, Detecting falls as novelties in acceleration patterns acquired with smartphones. PLoS ONE **9**(4), e94811 (2014)
13. D. Micucci, M. Mobilio, P. Napoletano, F. Tisato, Falls as anomalies? An experimental evaluation using smartphone accelerometer data. J Ambient Intell Humanized Comput. 1–13 (2015)
14. A. Lisowska, G. Wheeler, V. Inza, I. Poole, An evaluation of supervised, novelty-based and hybrid approaches to fall detection using silmee accelerometer data, in *Proceedings of IEEE CCVW*, 2015, pp. 10–16
15. Time Domain (2015, May 27). PulsON® P410 radar kit [Online]. Available: http://www.timedomain.com/
16. MESA Imaging (2016, Jun 16). SR4000/SR4500 User Manual V 3.0 [Online]. Available: http://www.realtechsupport.org/UB/SR/range_finding/SR4000_SR4500_Manual.pdf
17. N. Noury et al., Fall detection-principles and methods, in *Proceedings of 29th IEEE EMBS*, Aug 2007, pp. 1663–1666
18. T. Kanungo et al., An efficient k-means clustering algorithm: analysis and implementation. Pattern Anal. Mach. Intell. IEEE Trans. **24**(7), 881–892 (2002)
19. C. Cortes, V. Vapnik, Support-vector networks. Mach. Learn. **20**(3), 273–297 (1995)
20. A. Leone, G. Diraco, P. Siciliano, Detecting falls with 3D range camera in ambient assisted living applications: a preliminary study. Med. Eng. Phys. **33**(6), 770–781 (2011)

Capacitance Humidity Micro-sensor with Temperature Controller and Heater Integrated in CMOS Technology

M. Elkhayat[1(✉)], S. Mangiarotti[1], M. Grassi[1], P. Malcovati[1], and A. Fornasari[2]

[1] Department of Electrical, Computer, and Biomedical Engineering, University of Pavia, Pavia, Italy
moataz.elkhayat@universitadipavia.it
[2] Texas Instruments, Milano, Italy

Abstract. This paper wants to study the possibility of generating predictable relative humidity variations with temperature on a capacitive humidity sensor. Software and a circuit temperature control will be analyzed. The precision of both systems is remarkable. A possible application is in the field of self-diagnostics for humidity sensors.

Keywords: Relative humidity · Absolute humidity · Humidity sensor · Temperature control · Polyamide · CMOS

1 The Capacitive Humidity Sensor

A capacitive humidity sensor exploits a polymer as sensitive element (typically Polyimide) whose dielectric constant varies with changes in humidity (RH), approximately linearly. This leads to a corresponding change in the capacitance (as a simple rule, assuming a parallel-plate structure, the relation between the capacitance geometry and the dielectric properties between is $C = \varepsilon_0 \varepsilon_r A/d$). The sensor and temperature control circuit are today frequently made through a single integrated chip [1–4].

2 What Is the Relation Between Relative Humidity and Temperature?

Local variations of relative humidity can be obtained on the sensor through variations of the temperature. The mathematical model is expressed in the following equation:

$$RH = \frac{P_T \mu_{H_2O}}{6.11} \exp\left(\frac{-17.625T}{243.04 + T}\right)(\%) \quad (1)$$

where RH is the relative humidity, P_T the atmospheric pressure, μ_{H_2O} the molar fraction of water present in air, and T the temperature expressed °C. By controlling the

B. Andò et al. (eds.), *Sensors*, Lecture Notes in Electrical Engineering 431,
DOI 10.1007/978-3-319-55077-0_48

temperature of the sensor, it is possible to compare the measurements of the capacitance (RH) of the sensor to the mathematical model given in Eq. (1). If the amount of water in the air does not change (μ_{H_2O} constant), the temperature variation produces a variation in relative humidity.

Changing at local level (sensor) the temperature is relatively simple the Joule effect. The humidity sensor, indeed, includes a of 250 Ω resistance that is used as a heater to modify the temperature internally when current passing through it. Another resistance with higher value (2.5 kΩ) allows us to read the corresponding temperature value (using a suitable resistance-temperature conversion circuit). Regarding from Eq. (1), it is clear that, if μ_{H_2O} remains constant (the measurement takes place in a short time) the temperature variation will dominate the relative humidity change.

3 Software Implementation for Temperature Control

The adjustment of the temperature values was produced by a PI controller, calibrated according to an appropriate algorithm (Ziegler-Nichols rules). A voltage source is connected to the integrated heater (resistance) to provide a certain current, while a digital multi-meter is used to read the instantaneous values of the resistor (and hence the temperature) of the sensor. The temperature of the sensor changes with the applied voltage according to the values reported in Table 1. The step response of the system is shown in Fig. 1. The capacitance of the sensor has been read out through a "capacitance-to-digital converter". The detected capacitance values are converted into the corresponding relative humidity values according to the graph of initial calibration of the sensor. The control loop is implemented in LabVIEW environment.

Table 1. Response of the open loop system when the voltage supplied changes

V(V)	T (°C)	T_o (°C)	V^2	R*heater* (Ω)	Delta (T)	P (Watt)
1	23.765	23.306	1	250.4131	0.459	0.003993
2	25.107	23.196	4	251.7199	1.911	0.015891
3	27.336	23.145	9	253.7719	4.191	0.035465
4	30.44	23.193	16	256.5223	7.247	0.062373
5	34.76	23.312	25	260.3032	11.448	0.096042
6	40.041	23.492	36	264.8941	16.549	0.135903
7	45.696	23.679	42	269.8153	22.017	0.155662

The comparison between the measurements of the capacitance values and the mathematical model given by equation verifies the hypothesis, as shown in Fig. 2. The difference between the measurement values and the mathematical model ranges between ±1% RH due to the uncertainty of the capacitance measurements or the limited variations in ambient conditions

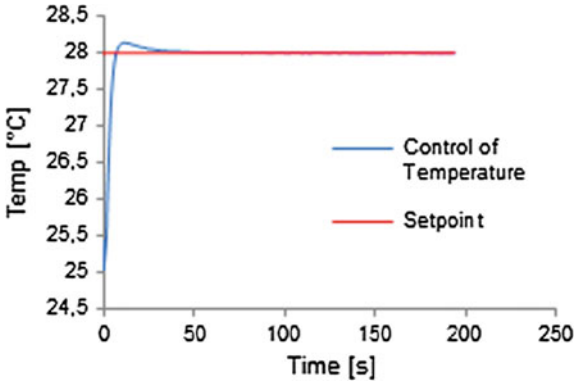

Fig. 1. PI controller: step response with ΔT = 3 °C

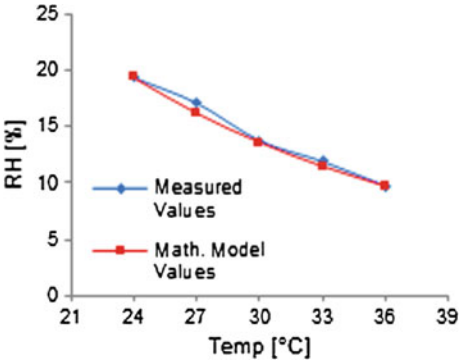

Fig. 2. Comparison between RH measurements and -mathematical model

4 Circuit Implementation for Temperature Control

The temperature control loop shown in Fig. 3 is driven by a PI (proportional-Integral) controller with parameters $K_p = 10$, $T_I = 1.04$ s. Gain and integrator op-amp are realized using switched-capacitor (SC) techniques, driven by two non-overlapped clock phases: ϕ1 and ϕ2 with a frequency of 100 Hz. The integrator op-amp is followed by a comparator whose output is connected to a power n-MOS featuring W = 1000 µm and L = 0.4 µm which delivers the required current to R*heater*.

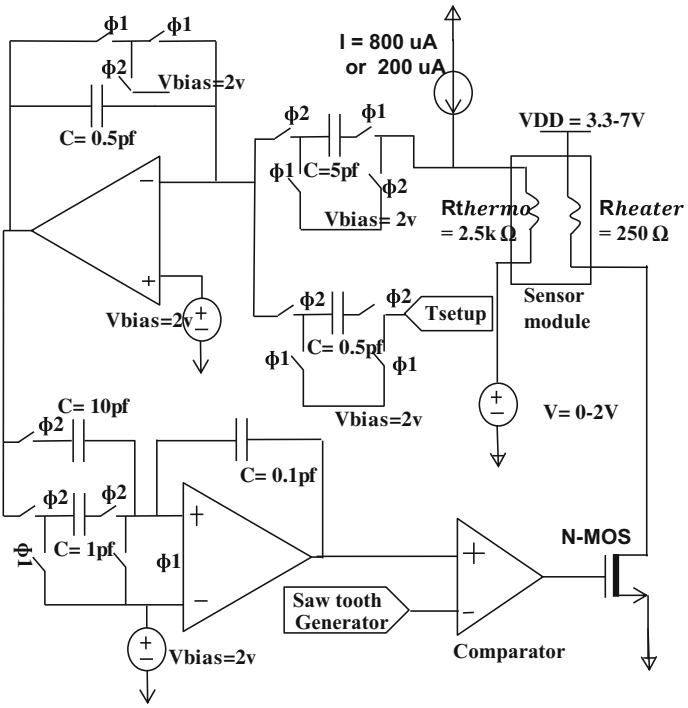

Fig. 3. Temperature control system schematic architecture

The thermal coupling inside the sensor between R*heater* and Rt*hermo* resistors has been modeled in VerilogA for transistor level system simulations. The first resistor has a terminal connected to the power n-MOS to regulate the temperature, while the other terminal is connected to an external voltage supply which can vary 3.3 and 7 V depending on the range of temperature). The temperature signal from the second resistor (2.5 kΩ) biased by a programmable current generator is converted into a voltage and amplified by a factor of 10 by a first SC stage. In particular, the bias current of 800 μA is used with the bias voltage of 0 V in the range 24–27 °C, while the bias current of 200 μA is used with 2 V bias voltage in the range 27–34 °C. For higher temperatures, the current will go further down (e.g. 100 μA). The frequency of the saw-tooth waveform applied to the inverting input of the comparator is 1 MHz and the loop gain is 1000. The system was simulated in Cadence environment at transistor level. The achieved accuracy is in order of 0.005 °C in a temperature range of 50 °C.

Figure 4 shows the layout of the chip realized in 0.35 μm CMOS technology. The chip area is 0.25 mm^2 and 21 pins are used. It is expected in the future to have one complete integrated chip for industrial applications.

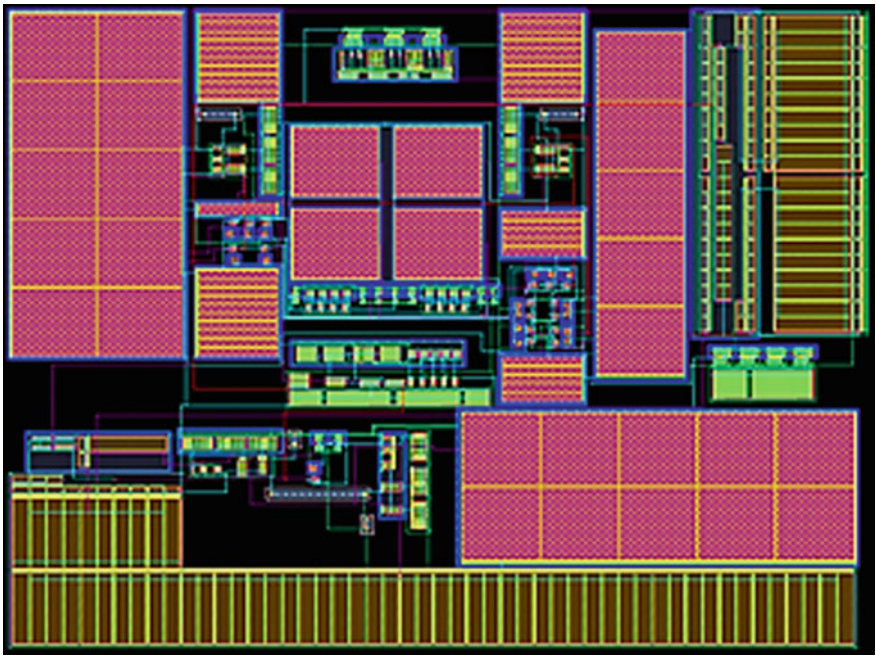

Fig. 4. Temperature control system layout

4.1 From the Laboratory to Industrial Application

The results reported in this paper demonstrate that a change in relative humidity can be actually achieved locally on the sensor by means of a temperature variation, using a temperature control circuit implemented in CMOS technology.

There are many applications for temperature control in humidity sensors, ranging from the simple heating of the sensor in order to eliminate condensation or accumulation of water on the sensor, to the sensor self-diagnostic in order to identify damages. Moreover, the temperature accuracy obtained with the integrated control circuit enables the possibility of sensor self-calibration, strongly improving its performance and reliability over time.

References

1. D. Cartasegna et al., Smart RFID label for monitoring the preservation conditions of food, in *Proceedings of the IEEE ISCAS* (2009), pp. 1161–1164
2. C.L. Zhao et al., A fully packaged CMOS interdigital capacitive humidity sensor with polysilicon heaters. IEEE Sens. J. **11**(11), 2986–2992 (2011)
3. N. Lazarus et al., CMOS-MEMS capacitive humidity sensor. J. Microelectromech. Syst. **19** (1), 183–191 (2010)
4. J.H. Kim et al., High sensitivity capacitive humidity sensor with a novel polyimide design fabricated by MEMS technology, in *IEEE International Conference on Nano/Micro Engineered and Molecular Systems* (2009)

Voltage-Mode Analog Interfaces for Differential Capacitance Position Transducers

G. Ferri[1(✉)], F.R. Parente[1], V. Stornelli[1], G. Barile[1], G. Pennazza[2], and M. Santonico[2]

[1] Department of Industrial and Information Engineering and Economics, University of L'Aquila, L'Aquila, Italy
giuseppe.ferri@univaq.it
[2] University Campus Bio-Medico di Roma, Rome, Italy

Abstract. A fully-analog integrated electronic interface for the detection and measurement of differential capacitive position sensors is shown. The read-out circuit, performing a differential capacitive to voltage conversion, has been developed in a standard 0.35 μm CMOS technology with low-voltage/low-power characteristics. The interface has shown a good accuracy, in particular the relative percentage error is lower than 0.8% for the simulations of the integrated solution. When compared to other solutions in the literature, sensitivity (*S*) and resolution (*res*) data on a practical case-study of position sensor are satisfactory so validating the architecture to be a good candidate as first stage in analog front-ends for differential capacitive sensor data measurements.

Keywords: Differential capacitive sensor · Ratiometric sensors · Position sensors · Capacitance measurement · Sensor interface · Analog front-end

1 Introduction

The detection of very small quantities of physical, chemical and biological measurands is typically employed through suitable sensors and related interfaces, developed either with discrete elements or through integrated circuits in CMOS technology. Electronic front-ends are particularly important for a suitable reading of the measurand [1–5]. When the measurand variation is converted into a capacitance, the sensor is named capacitive sensor and this capacitive change can be converted into a more easily electrical quantity. Capacitive sensors are employed in different modern applications, such as in detecting position, displacement, acceleration, fluid level [6–12].

Differential (or ratiometric) capacitive sensors constitute a particular case of these kinds of transducers. They have suitable applications in hair flow motion, accelerometers, position or rotation detection, force, etc. [13–18].

Figure 1 shows a typical differential capacitive structure: two capacitors in series are formed by two fixed electrodes (conductive plates) and one, movable in the middle, which changes its position from nominal one owing to sensing effect. The variations in the two series capacitances are of complementary kind.

B. Andò et al. (eds.), *Sensors*, Lecture Notes in Electrical Engineering 431,
DOI 10.1007/978-3-319-55077-0_49

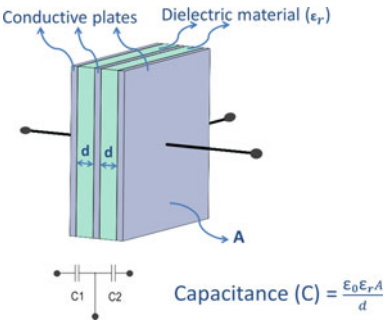

Fig. 1. Differential capacitance transducer

The electronic front-end has the task to measure and amplify the (differential) capacitive change detected by the sensor. The employment of a differential capacitive structure helps to reduce resolution problems related to low capacitive variations and common mode disturbs. In the literature, a differential capacitive sensing is performed in different ways: capacitance-to-frequency conversion, capacitance-to-phase conversion, switched-capacitor analog-to-digital technique, current-integrating threshold detection based technique [19–21]. Other interfaces utilize transimpedance or charge amplifiers, performing a capacitance-to-voltage conversion in continuous time [22].

In this paper we give evidence to the interface design of differential capacitive sensors. Recently, in [23], the authors have proposed for the first time a fully-analog front-end performing differential capacitance measurements through the reading of a voltage. In this paper, a development in the output reading of this interface as well as novel simulations on a different application are presented also for the integrated design of the active blocks.

2 Differential Capacitance Sensors and Proposed Interface

This work is addressed to consider a differential position capacitive sensor, to which a variation in the relative distance between the plates may occur.

In this case C_1 and C_2 capacitances can be expressed according to (1):

$$C_{1,2} = \frac{C_0}{2}\frac{1}{(1 \mp x)} \tag{1}$$

being C_0 the total capacitance of the transducer. We can notice that the measurand x can be expressed as independent from C_0 value, being:

$$x = \frac{C_1 - C_2}{C_1 + C_2} \tag{2}$$

The development of the read-out circuitry for differential capacitive sensors is an important challenge, except if the classical capacitive AC bridge is considered. This analogue interface gives a differential output voltage proportional to x variable only for low values of x, according to the factor $V_{IN}/2$. In order to increase this factor, we have recently proposed an analog interface [23], based on the cascade of an integrator and a differentiator containing the capacitive differential sensor. We here propose a development in the output reading of this interface as well as novel simulations on a different application. The read-out circuit is shown in Fig. 2 as block scheme and in Fig. 3 at component level.

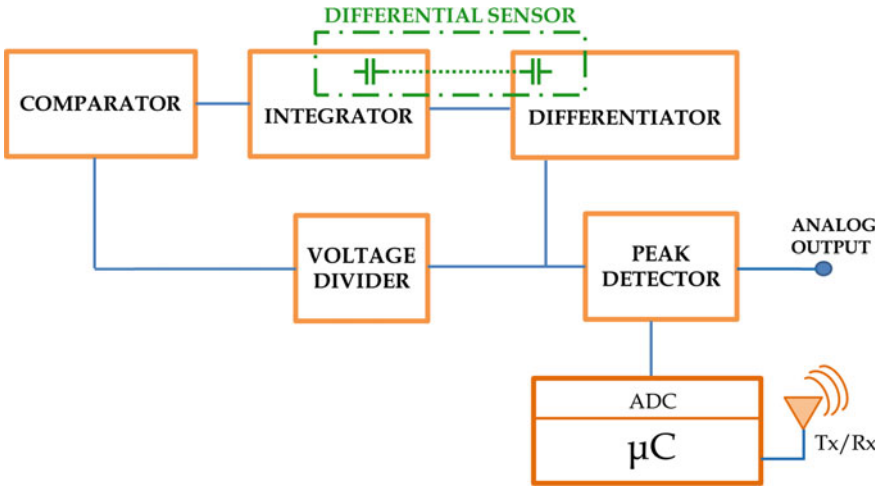

Fig. 2. The proposed interface block scheme

Beside the integrator/differentiator configurations, an additional circuitry (comparator, voltage divider) automatically generates a square-wave signal. The peak detector has been employed to give the DC level of the maximum output voltage. A digital data acquisition system (formed by an ADC [24] and a microcontroller) has been implemented establishing a communication by using a Tx/Rx structure. The utilized microcontroller is an ATMEGA328P from Atmel that integrates a 8 bit ADC whereas the radio link is established by a low power commercial transceiver (NFC21) with on board integrated antenna. Two dedicated boards have been externally connected and tested. The interconnection with the designed interface has been performed by on board mounted wires.

Concerning the amplifier block, the circuit in Fig. 3 has been designed in an integrated version in a standard CMOS technology, suitable for portable applications. A straightforward analysis gives the following equation for the output voltage value:

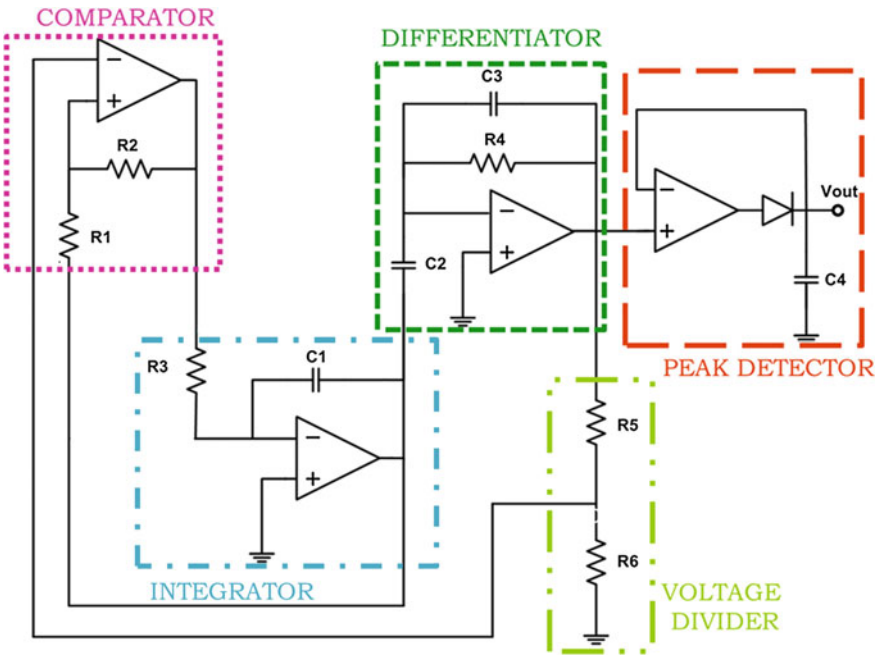

Fig. 3. The analog part of the proposed interface architecture: C_1 and C_2 are the differential capacitor

$$V_{out}(x) = V_k \cdot \frac{1-x}{1+x} \tag{3}$$

being V_k a constant value (in Volt), given by $(R_4{*}V_{DD,SAT})/R_3$, where $V_{DD,SAT}$ is the amplifier saturation supply voltage (amplifier non idealities can be considered negligible), given by the peak detector.

Starting from parallel plate capacitor model, we can consider the distance variation case, respectively, as

$$C = \frac{\varepsilon A}{d_0 \mp \Delta d} \tag{4}$$

In particular, in (4), we consider a possible capacitive variation Δd, related to a change of the initial distance d_0, between the capacitor plates. Considering both the capacitance variations where x is expressed by (2) and (4), the ratiometric equation becomes:

$$x = \frac{C_1 - C_2}{C_1 + C_2} = \frac{\Delta d}{d_0} \tag{5}$$

from which, (3) becomes:

$$V_{out}(x) = V_k \cdot \frac{d_0 - \Delta d}{d_0 + \Delta d} \tag{6}$$

3 OTA Design for CMOS Integrated Solution

We have suitably designed an integrated version of the proposed interface, at transistor level, in a standard CMOS technology (AMS 0.35 μm), through the development of Operational Transconductance Amplifiers (OTAs) as active blocks, having the same internal topology and transistors (reported in Fig. 4). The application of analog microelectronic design techniques has allowed to obtain good low-voltage (±1.65 V) low-power (<5 mW) OTA performances, whereas a meticulous attention has been paid to obtain good Slew-rate (SR) and input voltage offset characteristics. Passive components are employed on-chip, so the circuit is suitable for very compact applications.

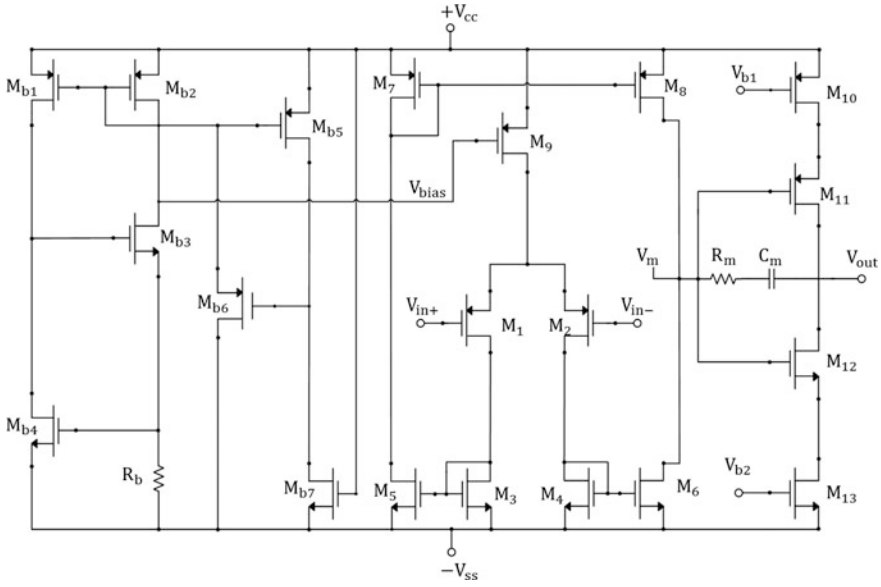

Fig. 4. The proposed OTA topology and its biasing circuit

The OTA shown in Fig. 4 has two stages: a symmetrical OTA as input stage (M_1–M_9), chosen for its low systematic offset and a cascoded class-AB output stage (M_{10}–M_{13}) ensuring full dynamic output range.

In the input stage, the choice of *p-MOS* input transistors, for the first stage (i.e., M_1–M_2), guarantees a reduced low-frequency noise level ensured also by a proper layout design. Considering ideal matched conditions between the transistor couples M_1–M_2,

M_3–M_4, M_5–M_6 and M_7–M_8, its output impedance, evaluated at the internal node V_M, and its voltage gain can be expressed as follows, respectively:

$$R_{OUT\_V_M} \cong rds_{M6} // rds_{M8} \tag{7}$$

$$A_{V_M} \cong B \cdot gm_{M1} \cdot R_{OUT\_V_M} \tag{8}$$

being B the ratio between $(W/L)_5$ and $(W/L)_3$, equal to that between $(W/L)_6$ and $(W/L)_4$.

The OTA output stage is a class-AB inverter amplifier, in a push–pull configuration with source degenerations, which guarantees a further voltage gain, a better output dynamic range, a better control of the output current and a high output impedance.

This stage has been properly frequency-compensated through the use of Rm and Cm passive elements and transistor M_{14} implementing the pole splitting and the zero cancellation. The OTA output impedance, evaluated at V_{OUT} node, and the voltage gain of the output stage can be expressed as follows, respectively:

$$\begin{aligned} R_{OUT} \cong & [rds_{M10} + rds_{M11} + rds_{M10} rds_{M11} (gm_{M11} + gmb_{M11})] \\ & // [rds_{M12} + rds_{M13} + rds_{M12} rds_{M13} (gm_{M12} + gmb_{M12})] \end{aligned} \tag{9}$$

$$A_{V_{OUT}} \cong \left[\left(\frac{gm_{M11}}{1 + rds_{M10}(gm_{M11} + gmb_{M11} + \frac{1}{rds_{M11}})} \right) + \left(\frac{gm_{M12}}{1 + rds_{M13}(gm_{M12} + gmb_{M12} + \frac{1}{rds_{M12}})} \right) \right] R_{OUT} \tag{10}$$

The total open loop DC voltage gain of the designed *OTA* is simply obtained by the multiplication of (8) and (10) gains. A supply-independent current source allows to obtain a high *SR* value, through the injection of a biasing current independent both from supply voltage variation (e.g. battery discharge) up to relatively high variations respect to the nominal value (higher than ±10%), and from temperature drifts of the whole OTA. This current reference is completed by a "start-up" circuit [25], which allows to operate in the correct non-zero working point. The complete current generator for OTA biasing is formed by transistors M_{b1}–M_{b4} and resistance R_b, and the start-up circuit (M_{b5}–M_{b7}). Table 1 reports the OTA main parameter values obtained with simulations.

The following values have been considered for the passive components employed in the integrated version of the interface: C_0 = 10 pF (variation = ±50%), R_1 = R_2 = R_5 = R_6 = 100 kΩ, R_4 = 680 kΩ, R_3 = 150 kΩ, C_3 = 1 pF.

4 Results

Theoretical and simulated output voltage results are shown in Fig. 5. The output range has been optimized, for the x variation, in the most part of the supply range.

Table 1. OTA main characteristics: simulated results

OTA main parameters	Simulated values
Voltage supply	±1.65 V
External voltage V_{b1}	−0.3 V
External voltage V_{b2}	1 V
Power dissipation	0.8 mW
GBW	38 MHz
Output resistance	1.5 MΩ
Output dynamic range	97%
Open loop DC voltage gain	62 dB
Slew-rate	28 V/μs
Input voltage offset	86 μV
Input equivalent noise	180 nV/sqrt(Hz) @1 kHz
CMRR	53 dB
$V_{DD,SAT}$	1.6006 V

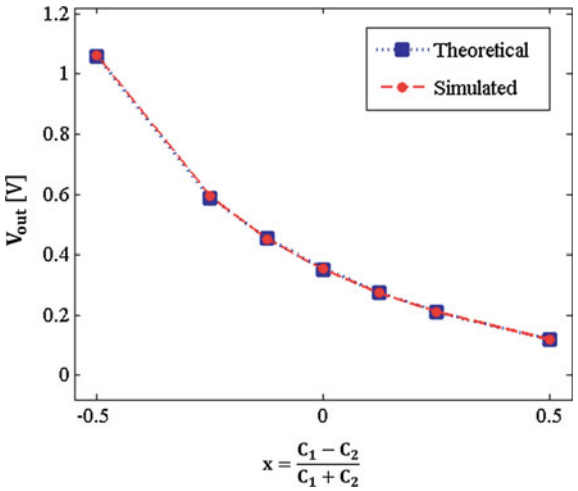

Fig. 5. Output voltage versus x (theoretical and simulated results)

As shown in Fig. 6, the relative error, defined as in [25], is always lower, in absolute value, than 0.8%, so the proposed interface shows a good accuracy.

We have considered two basic parameters in sensors and interfaces that are sensitivity and resolution [25]. Sensitivity (S) is defined as the ratio between output parameter (in this case, output voltage) and the measurand. Then, from (6) sensitivity is given by:

$$S = \frac{\partial V_{out}}{\partial(\Delta d)} = [2d_0 V_k] \frac{1}{(d_0 + \Delta d)^2} \tag{11}$$

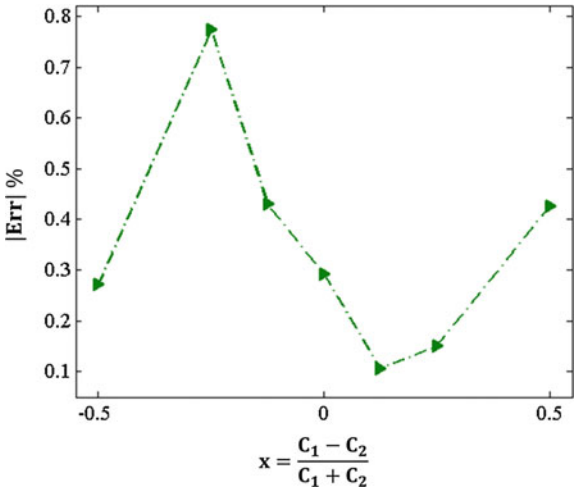

Fig. 6. Relative percentage error versus x for the integrated solution

Having considered a commercial position sensor of 10 pF capacitance [26] and its possible initial distance of d_0 = 100 μm we obtained the theoretical sensitivity trend shown in Fig. 7 (variation = ±50%).

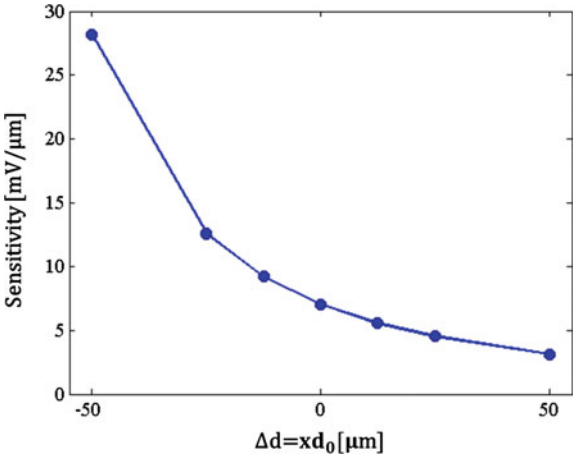

Fig. 7. Theoretical sensitivity trend versus Δd for the integrated solution

Starting from sensitivity definition and having evaluated a 500 μV output voltage noise we obtained the resolution trend shown in Fig. 8.

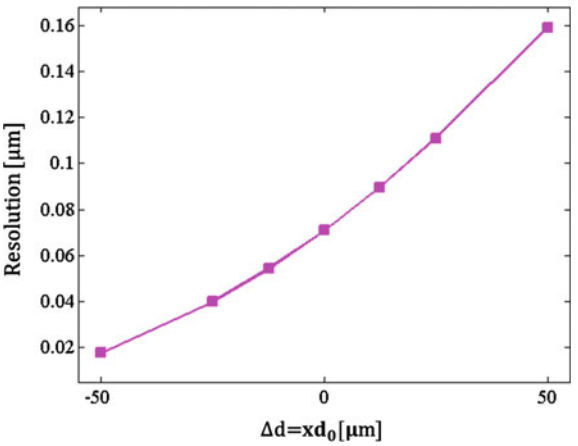

Fig. 8. Resolution trend versus Δd for the integrated solution

5 Conclusions

We have presented an analog interface for the detection and quantification of differential capacitive sensors. Waiting for the integrated interface fabrication, simulations on the designed CMOS integrated OTA-based interface have been performed. They have a good agreement with the theoretical expectations. Sensitivity and resolution have been determined in a practical case, showing satisfactory values. This sensor interface could be applied to a wide range of application such as measurement of displacement, distance and position. In particular, the proposed circuit is suitable for those applications requiring precision positioning, such as in lithography.

References

1. N. Ida, *Sensors, Actuators, and Their Interfaces—A Multidisciplinary Introduction* (Sc. Tech Publishing, 2013)
2. C. Falconi, E. Martinelli, C. Di Natale, A. D'Amico, P. Malcovati, A. Baschirotto, V. Stornelli, G. Ferri, Electronic interfaces. Sens. Actuators B **121**, 295–329 (2007)
3. A. Baschirotto, S. Capone, A. D'Amico, C. Di Natale, V. Ferragina, G. Ferri, L. Francioso, M. Grassi, N. Guerrini, P. Malcovati, E. Martinelli, P. Siciliano, A portable integrated wide-range gas sensing system with smart A/D front-end. Sens. Actuators B **130**(1), 164–174 (2008)
4. A. De Marcellis, A. Depari, G. Ferri, A. Flammini, D. Marioli, V. Stornelli, A. Taroni, Uncalibrated integrable wide-range single-supply portable interface for resistance and parasitic capacitance determination. Sens. Actuators B **132**(2), 477–484 (2008)
5. G. Ferri, V. Stornelli, A. De Marcellis, A. Flammini, A. Depari, Novel CMOS fully integrated interface for wide-range resistive sensor arrays with parasitic capacitance estimation. Sens. Actuators B **130**(1), 207–215 (2008)

6. R. Puers, Capacitive sensors: when and how to use them. Sens. Actuators **A37–A38**, 93–105 (1993)
7. L.K. Baxter, *Capacitive sensors* (IEEE Press Series on Electronics Technology Series, New York, 1996)
8. E.B. Mohammed, M. Rehman, Digital capacitive angular-position sensor, in *Proceedings of the IEE Science, Measurement and Technology*, vol 150, Issue 1 (2003), pp. 15–18
9. F.N. Toth, G.C.M. Meijer, A low-cost, smart capacitive position sensor. IEEE Trans. Instrum. Measur. **41**(6) (1992)
10. H. Gu, C. Sterzik, Capacitive touch hardware design guide, in *Texas Instruments Design Guide* (2013)
11. E.C. Tan, A. Wahab, K.M. Low, Application of capacitive coupling to the design of an absolute-coordinate pointing device. IEEE Trans. Instrum. Measur. **54**(5), 2099–2104 (2005)
12. T. Singh, T. Sæther, T. Ytterdal, Current-mode capacitive sensor interface circuit with single-ended to differential output capability. IEEE Trans. Instrum. Measur. **58**, 3914–3920 (2009)
13. G. Scotti, S. Pennisi, P. Monsurrò, A. Trifiletti, 88-A 1-MHz stray-insensitive CMOS current-mode interface IC for differential capacitive sensors. IEEE Trans. Circuits Syst. I Regul. Pap. **61**(7), 1905–1916 (2014)
14. M.N. Horenstein, J.A. Perreault, T.G. Bifano, Differential capacitive position sensor for planar MEMS structures with vertical motion. Sens. Actuators **80**, 53–61 (2000)
15. F. Reverter, O. Casas, Interfacing differential capacitive sensors to microcontrollers: a direct approach. IEEE Trans. Instrum. Measur. **59**(10), 2763–2769 (2010)
16. J.C. Lötters, A sensitive differential capacitance to voltage converter for sensor applications. IEEE Trans. Instrum. Measur. **48**(1), 89–96 (1999)
17. A.M.K. Dagamesh, Interfacing of differential-capacitive biomimetic hair flow-sensors for optimal sensitivity, J. Micromech. Microeng. **23**(3) (2013)
18. R.A. Brookhuis, T.S.J. Lammerink, R.J. Wiegerink, Differential capacitive sensing circuit for a multi-electrode capacitive force sensor. Sens. Actuators A **23**(4), 168–179 (2015)
19. T.G. Constandinou, J. Georgiou, C. Toumazou, A micropower front-end interface for differential-capacitive sensor systems, in *IEEE International Symposium on Circuits and Systems* (2008) pp. 2474–2477
20. B. George, V.J. Kumar, Switched capacitor signal conditioning for differential capacitive sensors. IEEE Trans. Instrum. Measur. **56**(3), 913–917 (2007)
21. N.M. Mohan, A.R. Shet, S. Kedarnath, V.J. Kumar, Digital converter for differential capacitive sensors. IEEE Trans. Instrum. Measur. **57**, 2576–2581 (2008)
22. K. Mochizuki, K. Watanabe, T. Masuda, A high-accuracy high-speed signal processing circuit of differential-capacitance transducers. IEEE Trans. Instrum. Measur. **47**, 1244–1247 (1998)
23. G. Ferri, F.R. Parente, V. Stornelli, G. Pennazza, M. Santonico, A. D'Amico, A standard CMOS technology fully-analog differential capacitance sensor front-end, in *Proceedings of International Workshop on Advances in Sensors and Interfaces* (Gallipoli, June 2015), pp. 152–157
24. G. Bonfini, A.S. Brogna, C. Garbossa, L. Colombini, M. Bacci, S. Chicca, F. Bigongiari, N. C. Guerrini, G. Ferri, An ultra low power switched opamp-based 10-bit integrated ADC for implantable biomedical applications. IEEE Trans. Circuits Syst. I **51**(1), 174–177 (2004)
25. A. De Marcellis, G. Ferri, in *Analog Circuits and Systems for Voltage-Mode and Current-Mode Sensor Interfacing Applications* (Springer, New York, 2011)
26. http://www.nanopositioning.com/products/nanosensors/nanosensors-nxc-series. Accessed 9 June 2016

CCII-Based Linear Ratiometric Capacitive Sensing by Analog Read-Out Circuits

G. Ferri[1(✉)], F.R. Parente[1], V. Stornelli[1], G. Barile[1], G. Pennazza[2], and M. Santonico[2]

[1] Department of Industrial and Information Engineering and Economics, University of L'Aquila, L'Aquila, Italy
giuseppe.ferri@univaq.it
[2] University Campus Bio-Medico di Roma, Rome, Italy

Abstract. Two electronic interfaces performing a differential (or ratiometric) sensor capacitance to voltage conversion are here presented. The output signal is proportional to the measurand variation *x*. The two read-out circuits differ themselves in their input stage: the first has an input current-to-voltage conversion, while the second one employs an input voltage source. Both of the solutions utilize commercial second generation current conveyors (CCIIs) as active blocks, in particular AD844. Theoretical analysis, simulated and experimental results have shown a good accuracy. Considering a capacitance variation due to the relative distance change, interface sensitivity (*S*) and resolution (*res*) values are constant and satisfactory: for the first solution, $S = 8.54$ V/μm and $res = 674$ pm (capacitance resolution value is 89.85 fF, that is −79 dB), while, for the second one, $S = 8.13$ V/μm and $res = 814$ pm (capacitance resolution value is 108.5 fF, that is −77 dB).

Keywords: Differential capacitive sensor · CCII · Current mode · Analog front-end

1 Introduction

Capacitive sensors are solid-state devices that reveal and quantify variations of physical, chemical or biological parameters the change of a capacitor. They are typically formed by two metal parallel plates separated by an insulator layer [1] and can be employed in applications as accelerometers [2], position sensors [3], pressure sensors [4] etc., where capacitance values can range from less than 1 pF up to hundreds of pF or even to nF. Their interfaces are based on the conversion of the capacitive value and variation into a voltage, a frequency (or period), a phase, etc. [5–7].

Differential (or ratiometric) sensors are a sub-set of these capacitive sensors employed to reduce resolution problems related to low capacitive variations and common mode disturbs. They have suitable applications in hair flow motion, accelerometers, position or rotation detection, force, etc. Figure 1 shows a simple schematization of a ratiometric capacitive sensor consisting in a three plates capacitive system with two fixed plates. The simplest differential sensing element is the capacitive

B. Andò et al. (eds.), *Sensors*, Lecture Notes in Electrical Engineering 431,
DOI 10.1007/978-3-319-55077-0_50

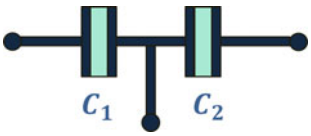

Fig. 1 Differential capacitance sensor structure

AC half-bridge where two capacitors change their value in a complementary way under a stimulus; unfortunately, this topology shows a reduced and not constant sensitivity.

In the literature, some analog interfaces for the ratiometric capacitive sensing have been proposed, based mainly on operational amplifiers [7–11], while current-mode interfaces are typically related to other sensor interfaces [12–17]. In this paper we propose two current conveyor-based interfaces performing a capacitive-to-voltage conversion, showing good and constant values of sensitivity and resolution.

2 The Current-Mode Interfaces

Considering Fig. 1, if the distance between the electrodes is changing, C_1 and C_2 have the following variations:

$$C_{1,2} = \frac{C_0}{2}\frac{1}{(1 \mp x)} \tag{1}$$

being C_0 the total capacitance of the transducer [9], from which measurand x can be expressed as independent from C_0 value as follows:

$$x = \frac{C_1 - C_2}{C_1 + C_2} \tag{2}$$

Figure 2 shows the first proposed interface (employing a current source as input signal), based on second generation current-conveyors (CCIIs).

From the properties of the ideal CCII ($V_X = V_Y$, $I_X = I_Z$ for the CCII+ and $I_X = -I_Z$ for the CCII−) [12], a straightforward analysis gives:

$$V_{out,pp}(x) = R_L' I_{IN,pp} \cdot \left[\frac{C_o}{C_o + C_3}x + \frac{C_3}{C_o + C_3}\right] \tag{3}$$

being R_L' the parallel impedance between the load resistance R_L (see Fig. 2) and the impedance parasitic component at CCII Z node at working frequency (R_Z) and $I_{IN,pp}$ the peak-to-peak value of the input current.

The second interface here proposed (Fig. 3) shows an input stage employing a CCII-based voltage-to-current converter [12]; in this manner, the voltage input signal can be more easily injected through a standard laboratory waveform generator.

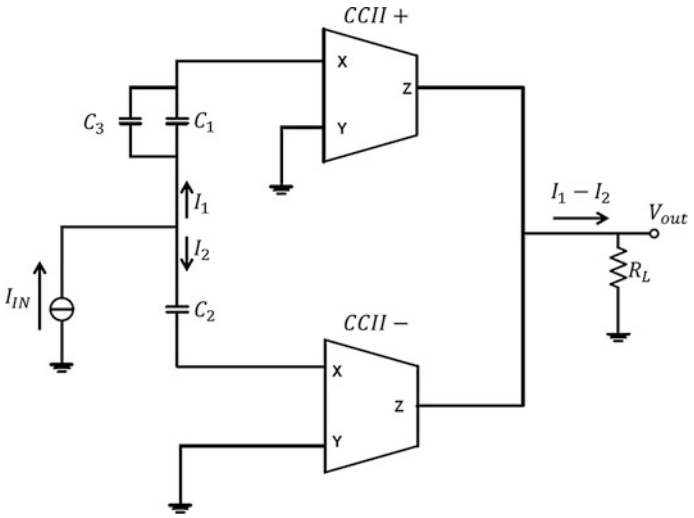

Fig. 2 The first proposed interface (C_1 and C_2 form the differential capacitive sensors)

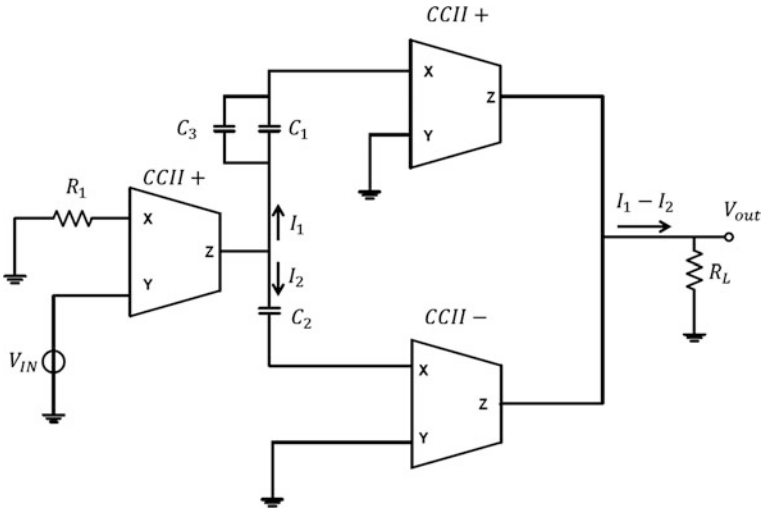

Fig. 3 The second proposed interface (C_1 and C_2 form the differential capacitive sensors) including the voltage to current converter as input stage

In this case, Eq. (3) becomes:

$$V_{out,pp}(x) = R'_L \frac{V_{IN,pp}}{R'_1} \cdot \left[\frac{C_o}{C_o + C_3} x + \frac{C_3}{C_o + C_3} \right] \tag{4}$$

being R_L' the parallel impedance between the load resistance R_L and the impedance parasitic component at CCII Z node at working frequency (R_Z), R_1' the series

impedance between the resistance R_1 and the impedance parasitic component at CCII X node at working frequency (R_X) and $V_{IN,PP}$ the peak-to-peak value of the input voltage.

3 Results

For experimental measurements we have employed AD844 component as CCII+, while CCII− is implemented through a cascade of two AD844 devices [12]. The following nominal values have been considered: working frequency = 10 kHz and R_L = 60 kΩ; concerning the input signal amplitude, we chose $I_{IN,pp}$ = 1 mA for the first interface and $V_{IN,pp}$ = 1 V, R_1 = 1 kΩ for the second one. Furthermore, having considered AD844 parasitic components at the working frequency (R_X = 50 Ω, R_Z = 3 MΩ), we have obtained R_1' = 1.05 kΩ and R_L' = 57.629 kΩ. We have considered a ratiometric capacitance sensing application, having a base-line value C_O of 800 pF and a 10% maximum relative variation (x). The transducer behavior has been emulated, in the experimental phase, by two capacitors. The value of C_3 has been set to 100 pF.

Starting from parallel plate capacitor model, we considered a possible capacitive variation related to a change in the initial distance between the capacitor plates, d_o:

$$C_{1,2} = \frac{\varepsilon A}{(d_0 \mp \Delta d)} \tag{5}$$

The ratiometric equation becomes:

$$x = \frac{C_1 - C_2}{C_1 + C_2} = \frac{\Delta d}{d_0} \tag{6}$$

Concerning the first solution (shown in Fig. 2), we have performed only simulations that have been compared with the theory. Figure 4 shows the theoretical and

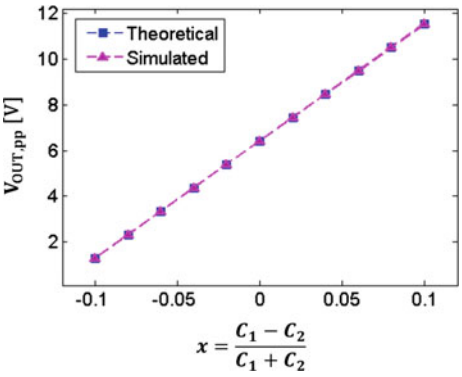

Fig. 4 First interface: output voltage (theoretical, simulated) versus x

simulated output voltages versus x parameter. The output range has been optimized, for the considered x variation, in the most part of the supply range. The relative percentage error is always lower, in absolute value, than 0.1%, so the proposed interface shows a good accuracy.

Having considered a MEMS application (d_0 = 3 μm), the sensitivity is constant and valued about S = 8.54 V/μm. Sensitivity definition has been expressed according to [17]. Having evaluated a 576 nV output voltage noise, we have a resolution in terms of distance variation of about 674 pm, i.e., as capacitive value, of 89.85 fF (that is about −79 dB).

Concerning the second solution (Fig. 3), Fig. 5 shows the output voltage versus the measurand x. Theoretical, simulated (through Orcad-Spice software) and experimental results (averaged on 10 different measurements) are in a good agreement. Uncertainty on the experimental data has been expressed through the standard deviation: it is lower than 0.025 for the whole measurements. The relative percentage error has been calculated for the averaged experimental data is lower than 0.2% between simulations and theory and than 3% between theory and measurements.

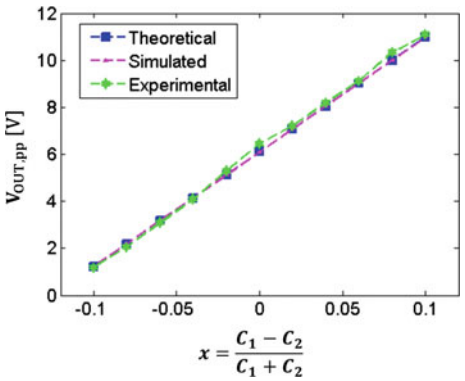

Fig. 5 Second interface: output voltage (theoretical, simulated, measured) versus x

Then, having considered d_0 = 3 μm, sensitivity value for the second interface is constant and valued about 8.13 V/μm. Having evaluated a 662 nV output voltage noise, we have a resolution of about 814 pm for the above mentioned case. This spatial resolution value corresponds to a capacitance resolution of 108.5 fF (that is about −77 dB). A suitable ADC [18] has been utilized for better reading of the output voltage.

A comparison of the main characteristics of the presented interfaces, with respect to those reported in the literature, is here presented in Table 1. We underline the fact that the works reported in [6, 10] are related to a single ended capacitive sensor (despite the second one is showing a differential output and its approach is also applicable to ratiometric sensors). The here proposed circuits show better values of sensitivity and resolution (in dB), also being constant for each operating point.

Table 1

Ref. number	Application	Approach	Type of conversion	Technology	Measurable capacitance features	Accuracy (error)	Sensitivity	Resolution
[2]	Micro-accelerometers	VM	switched-capacitor (A/D conversion)	Integrated	Csens > 80 pF	n.a.	0.26–1.6 V/g	1.6 μg/√Hz
[5]	MEMS	VM	switched-capacitor (A/D conversion)	Discrete	C_0 = 500 pF (C_1 = C_2 = 250 pF) Range ±50%	± 0.03%	n.a	at least 10 pF (−34 dB)
[6]	Grounded capacitive sensors	VM	C to Period (A/D conversion)	Integrated 0.7 μm CMOS	C_0 = 100 pF/−2 μF	Non-linearity error = 0.2%	n.a	n.a.
[7]	MEMS	VM	C to Phase	Integrated 0.35 μm CMOS	C_0 = 10 pF Range ±50%	± 0.02%	n.a	n.a.
[8]	Differential capacitive sensors	VM	C to Period (A/D conversion)	Discrete	C_0 = 400 pF (C_1 = C_2 = 200 pF) Range ±50%	± 0.2%	n.a	10 pF (−32 dB)
[9]	Accelerometers	VM	C to V	Discrete	C_0 = 20 pF Range ±120%	ΔV = 1.5 mV	0.1 mV/fF	20 fF (−60 dB)
[10]	Capacitive/resistive sensors	VM	C to V	Integrated 0.8 μm CMOS	C_0 = 1 pF Range ±75%	Non-linearity error =1%	n.a	1.13 fF (−59 dB)
[11]	Biomimetic hair flow sensors	VM	C to V	Integrated 0.35 μm CMOS	C_0 = 25 pF Range ±30%	0.5–3.4%	6–21 mV/μm	23–83 nm (from −77 to −65 dB)
This work 1st sol.	Differential capacitive sensors	CM	C to V	Discrete	C_0 = 800 pF (C_1 = C_2 = 400 pF) Range ±10%	0.01–0.09%	constant 8.54 V/μm	674 pm 89.85 fF (−79 dB)
This work 2nd sol.	Differential capacitive sensors	CM	C to V	Discrete	C_0 = 800 pF (C_1 = C_2 = 400 pF) Range ±10%	< 0.2% (simul.) < 3.2% (meas.)	constant 8.13 V/μm	814 pm 108.5 fF (−77 dB)

Note: VM = Voltage mode; CM = Current mode

4 Conclusions

We have shown two novel current-mode analog interfaces for revealing and measuring ratiometric capacitive sensors. Experimental measurements have been performed on a discrete element board, employed through a commercial CCII (AD844). Both of our proposed architectures have shown a good agreement with the theoretical expectations. Sensitivity and resolution (showing constant values for each considered working point) have been determined in a practical case, showing satisfactory values.

References

1. L.K. Baxter, *Capacitive sensors: design and applications*, vol. 1 (John Wiley & Sons, New York, 1996)
2. N. Yazdi, H. Kulah, K. Najafi, Precision readout circuits for capacitive microaccelerometers. Proc. IEEE Sens. 24–27 (2004)
3. M.N. Horenstein, J.A. Perreault, T.G. Bifano, Differential capacitive position sensor for planar MEMS structures with vertical motion. Sens. Actuators **80**, 53–61 (2000)
4. R.E. Oosterbroek, T.S.J. Limmerink, J.W. Berenshot, G.J.M. Krijnen, M.C. Elwenspoek, A. van den Berg, A micromachined pressure/flow-sensor. Sens. Actuators **77**, 167–177 (1999)
5. B. George, V.J. Kumar, Switched capacitor signal conditioning for differential capacitive sensors. IEEE Trans. Instrum. Measur. **56**, 913–917 (2007)
6. Q. Jia, G. Meijer, X. Li, C. Guan, An integrated interface for grounded capacitive sensors, in *Proceedings of the 4th IEEE Sensors Conference*. Irvine. Oct 2005, pp. 4–5
7. T.G. Constandinou, J. Georgiou, C. Toumazou, A micropower front-end interface for differential-capacitive sensor systems, in *Proceedings of the IEEE International Symposium on Circuits and Systems.* Seattle. May 2008, pp. 2474–2477
8. N.M. Mohan, A.R. Shet, S. Kedarnath, V.J. Kumar, Digital converter for differential capacitive sensors. IEEE Trans. Instrum. Meas. **57**, 2576–2581 (2008)
9. K. Mochizuki, K. Watanabe, T. Masuda, A high-accuracy high-speed signal processing circuit of differential-capacitance transducers. IEEE Trans. Instrum. Meas. **47**, 1244–1247 (1998)
10. T. Singh, T. Sæther, T. Ytterdal, Current-mode capacitive sensor interface circuit with single-ended to differential output capability. IEEE Trans. Instrum. Meas. **58**, 3914–3920 (2009)
11. G. Ferri, F.R. Parente, V. Stornelli, G. Pennazza, M. Santonico, A. D'Amico, A standard CMOS technology fully-analog differential capacitance sensor front-end, in *Proceedings of the International Workshop on Advanced Sensor Interface*. Gallipoli. June 2015, pp. 152–157
12. G. Ferri, N.C. Guerrini, *Low-voltage low-power CMOS current-conveyors* (Kluwer Academic Publisher, Boston, 2003)
13. G. Ferri, A. De Marcellis, C. Di Carlo, V. Stornelli, A. Flammini, A. Depari, D. Marioli, E. Sisinni, A CCII-based low-voltage low-power read-out circuit for DC-excited resistive gas sensors. IEEE Sens. J. **9**, 2035–2041 (2009)
14. G. Ferri, V. Stornelli, A. di Simone, A CCII-based high impedance input stage for biomedical applications. J. Circuits Syst. Comput. **20**(8), 1441–1447 (2011)
15. V. Stornelli, G. Ferri, A 0.18 μm CMOS DDCCII for portable LV-LP filters. Radioengineering **22**(2), 434–439 (2013)

16. C. Falconi, G. Ferri, V. Stornelli, A. De Marcellis, D. Mazzieri, A. D'Amico, Current-mode high-accuracy high-precision CMOS amplifiers. IEEE Trans. Circuits Syst. II **55**(5), 394–398 (2008)
17. A. De Marcellis, G. Ferri, *Analog Circuits and Systems for Voltage-Mode and Current-Mode Sensor Interfacing Applications* (Springer, 2011)
18. G. Bonfini, A.S. Brogna, C. Garbossa, L. Colombini, M. Bacci, S. Chicca, F. Bigongiari, N. C. Guerrini, G. Ferri, An ultra low power switched opamp-based 10-bit integrated ADC for implantable biomedical applications. IEEE Trans. Circuits Syst. **51**, 174–177 (2004)

Integrable Autonomous Devices for WSNs

L. Pantoli, A. Leoni, F.R. Parente, V. Stornelli(✉), and G. Ferri

Department of Industrial and Information Engineering and Economics,
University of L'Aquila, L'Aquila, Italy
vincenzo.stornelli@univaq.it

Abstract. We here present an energy harvesting system for low power sensor applications. The system is a dual band architecture able to capture the largest amount of EM radiation available in the urban environment and to provide an autonomous device potentially with infinitive cycle of use. The device is tuned to receive both GSM and Wi-Fi frequencies and a power battery loading circuitry is available on board to guarantee the required energy for the autonomous sensor to work. The whole system, designed using a discrete board, has been also conceived in order to be completely integrated in a standard CMOS technology.

Keywords: Energy harvesting · Autonomous sensors · Low-voltage low-power integrated circuits

1 Introduction

Gathering energy from ambient environment and converting it into an usable electrical energy is an innovative and appealing way to feed small, wireless and autonomous devices commonly used in wearable electronics or in Wireless Sensor Network (WSN) systems [1–7]. Good performances with longevity constrain for the recovering of environmental energy system is mandatory, even if the latter are intrinsically not constant either in time or concerning their input power [8–13]. An appropriate harvesting design can lead to this goal and can actually represent a new frontier in the development of energy optimization techniques, which started from low power design and evolved into power-aware design methods for circuit and systems for any kind of application [14–32]. In this perspective, although the interest in WSN research is increasing, several fundamental issues remain unsolved and, among them, some are very important in sight of the long-term operation of the systems. In any case, whatever would be the constraints under investigation, the desire for a long system lifetime is always a common goal. We here describe a system for energy harvesting with the aim to capture the largest amount of EM radiation in the urban environment. It is based on a dual band architecture and handles both GSM and Wi-Fi signals with a high energy conversion efficiency in the full band and specifically onto the two working frequencies, pointed to 936 MHz and 2.4 GHz, so to catch the largest amount of EM radiation available in the surroundings. Defining the harvester efficiency as the ratio between the rectified power and the input one, the proposed circuit shows an efficiency greater than 50% for an incoming power between −5 and 15 dBm thanks to a suitable design both

B. Andò et al. (eds.), *Sensors*, Lecture Notes in Electrical Engineering 431,
DOI 10.1007/978-3-319-55077-0_51

of the networks and the control system. A prototype board has been fabricated and tested and experimental results are also herewith shown.

2 Architecture Overview

The harvester block scheme is described in Fig. 1. It is composed by two energy conversion channels (named "Low Power" and "Medium Power") designed to manage different power levels at both the reference frequencies and to collect the recovered energy into a common regulation and storage section. The "Low Power" channel is set as the default path. According to the incoming power level and comparing the rectified voltage with a reference voltage threshold, the ultralow power voltage comparator selects afterwards the suitable channel of the receiver to proper handle the EM radiation. The "Low Power" channel deals with power ranging from −20 to 5 dBm while the "Medium Power" one relates to power levels ranging from 5 to 20 dBm. The subsequent regulation and storage section consists of an ultralow voltage Step-Up Converter, that boosts the input voltage and decouples the harvester from the storage and load section. Finally, a common load is used for further utilizations.

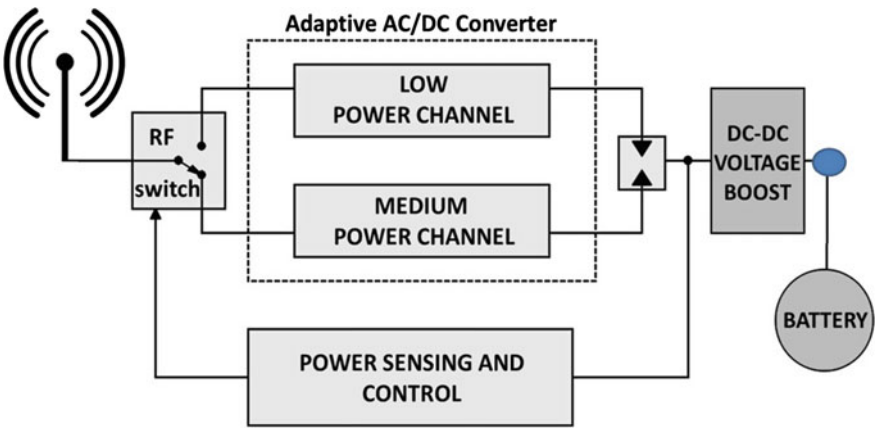

Fig. 1. Proposed dual band harvester block diagram for autonomous sensors

The harvester has been designed and optimized for its simultaneous operation at mobile GSM transmissions (936 MHz) and Wi-Fi broadcasting connections (2.4 GHz).

The harvester indeed is able to support the whole system in a "long-life" use of the system where it is used and directly answers the growing demand for sensors which need to be integrated into either batteries (that become, in our case, rechargeable) or totally self-powered wireless systems.

3 Prototype Device Details and Measurements

We here define the system efficiency as the ratio between the total amount of power delivered to the load and the amount of power that the receiving antenna could inject in a perfectly matched circuit. The schematic of the standalone rectifiers is shown in Fig. 2a, as they have been implemented into the prototype board used for test measurements (Fig. 2b).

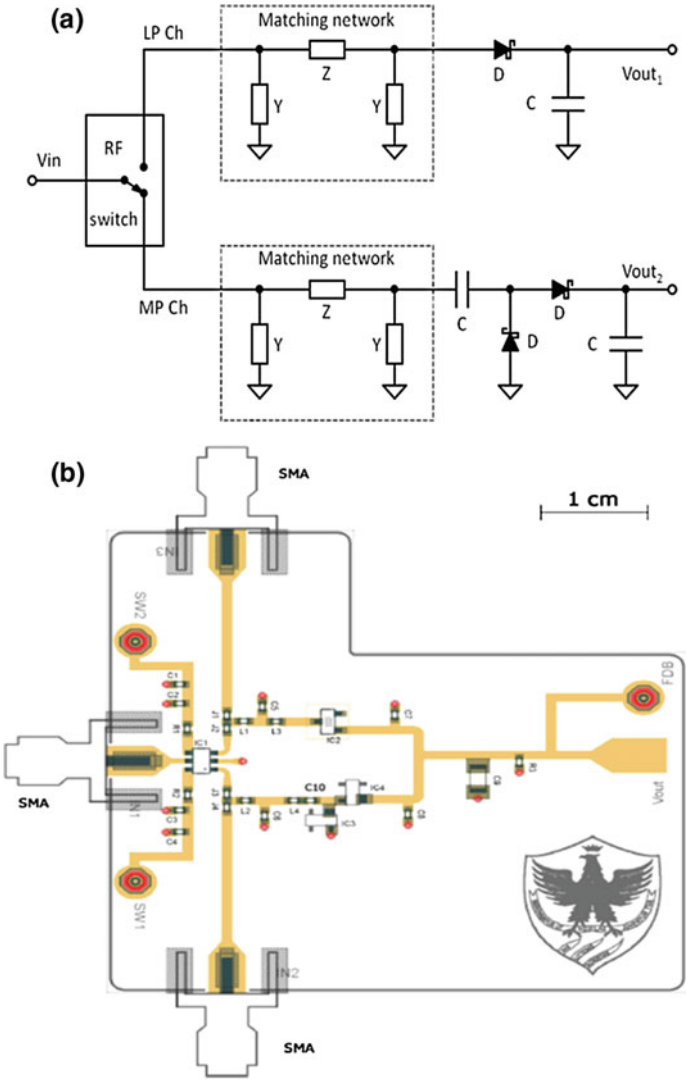

Fig. 2. **a** Multi-power harvester scheme. **b** Test board

The low power signal handling is achieved with a Schottky diode, characterized by a very low threshold voltage. The chosen device is *HSMS2850* provided by Avago Technologies: it is a zero bias detector, series-mounted and able to provide high sensitivity to the circuit response. Our tests have demonstrated that the designed "*Low Power*" circuit is very performing for low power levels, between −20 dBm and about 5 dBm, while working at higher power levels the performance drops because the rectified power transfer loses its incremental growth and changes slope tending to a constant limited value. This is because of the diode characteristics, not performing well for relatively high voltages. This consideration justifies the use "*Medium Power*" channel, suggesting the need to use a more complex configuration. The "*Medium Power*" channel implements, in fact, a voltage multiplier designed with two detector diodes *HSMS2865*, always provided by Avago. Test measurements (Fig. 3) confirmed all the theoretical results, showing that the output power got its maximum values for input levels, located at the two main frequencies of 936 MHz (GSM band) and 2.4 GHz (WiFi).

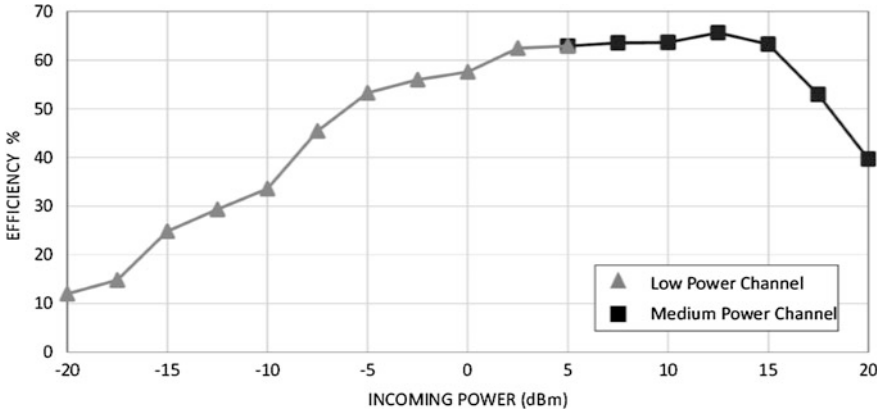

Fig. 3. Conversion efficiency

Generally we have got an efficiency greater than 50% for an incoming power between −5 and 15 dBm that decreases outside this range even though it remains high due to the a suitable design of the matching networks and of the control system. Figure 1 block parts have been fabricated in preliminary printed circuit boards in order to allow standalone functionality tests (Fig. 4) and assembled in our laboratory with a commercial multiband antenna, furnished by TAOGLAS, named TG.31.8112W.

Experimental measurements on the full system have been performed considering free sources provided by commercial devices as a mobile GMS phone and a Wi-Fi router. The sources have been considered both separately (one feeder per time) and simultaneously by feeding the harvester at different distances, so confirming the theoretical expectations.

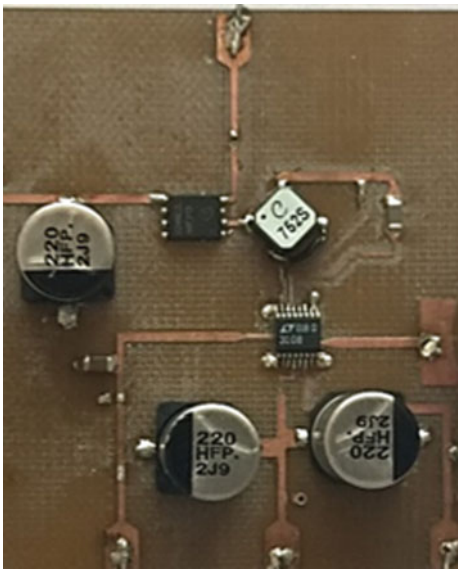

Fig. 4. DC/DC regulator and storage section

4 Conclusions

A dual band architecture for high conversion efficiency energy harvesting system has been here proposed. The harvester can simultaneously operate at two main frequencies, 936 MHz and 2.4 GHz and the experimental results have confirmed that the energy harvester final architecture can be easily interconnected with low power sensors for either recharging or powering purposes, to get a real "life-long autonomous" cycle of employment of the system.

References

1. K. Al Agha, M.-H. Bertin, T. Dang, A. Guitton, P. Minet, T. Val, J.-B. Viollet, Which wireless technology for industrial wireless sensor networks? The development of OCARI technology. IEEE Trans. Ind. Electron. **56**(10), 4266–4278 (2009)
2. A. Liberale, E. Dallago, A.L. Barnabei, G. Torelli, G. Venchi, Ultra low-voltage supervisor for energy scavenging system, in *Proceedings of the 11th Conference on Ph.D. Research Microelectron. Electron* (*PRIME*). Glasgow, Scotland, UK, June 29–July 02, 2015
3. Y. Tan, S. Panda, Optimized wind energy harvesting system using resistance emulator and active rectifier for wireless sensor nodes. IEEE Trans. Power Electron. **26**(99), 1 (2011)
4. S.E. Lyshevski, High-power density miniscale power generation and energy harvesting systems. Energy Convers. Manag. **52**(1), 46–52 (2011)
5. A. Karalis, J. Joannopoulos, M. Soljacic, Efficient wireless non-radiative mid-range energy transfer. Ann. Phys. **323**(1), 34–48 (2008)

6. V.C. Gungor, G.P. Hancke, Industrial wireless sensor networks: challenges, design principles, and technical approaches. IEEE Trans. Ind. Electron. **56**(10), 4258–4265 (2009)
7. M. Ferri, D. Pinna, E. Dallago, P. Malcovati, 0.35 μm CMOS solar scavenger with power storaging mangement system, in *Proceedings of IEEE Ph.D. Research in Microelectronics and Electronics* (*PRIME*) (Cork, Ireland, 2009). 12–17 July 2009
8. A.L. Barnabei, E. Dallago, P. Malcovati, A. Liberale, An improved ultra-low-power wireless sensor-station supplied by a photovoltaic harvester, in *9th Conference on Ph.D. Research in Microelectronics and Electronics* (*PRIME*), 2013, pp. 205–208
9. A. Dolgov, R. Zane, Z. Popovic, Power management system for online low power RF energy harvesting optimization. IEEE Trans. Circuits Syst. I Regul. Pap. **57**(7), 1802–1811 (2010)
10. S.L. Brunton, C.W. Rowley, S.R. Kulkarni, C. Clarkson, Maximum power point tracking for photovoltaic optimization using ripple-based extremum seeking control. IEEE Trans. Power Electron. **25**(10), 2531–2540 (2010)
11. M.A. Hannan, F.A. Azidin, A. Mohamed, Multi-sources model and control algorithm of an energy management system for light electric vehicles. Energy Convers. Manag. **62**, 123–130 (2012)
12. Y. Levron, D. Shmilovitz, A power management strategy for minimization of energy storage reservoirs in wireless systems with energy harvesting. IEEE Trans. Circuits Syst. I Regul. Pap. 1–11 (2010)
13. R.-Y. Kim, J.-S. Lai, B. York, A. Koran, Analysis and design of maximum power point tracking scheme for thermoelectric battery energy storage system. IEEE Trans. Industr. Electron. **56**(9), 3709–3716 (2009)
14. G. Leuzzi, V. Stornelli, S. Del Re, A tuneable active inductor with high dynamic range for band-pass filter applications. IEEE Trans. Circuits Syst. II Express Briefs **58**(10), 647–651 (2011)
15. V. Janicek, M. Husak, J. Jakovenko, J. Formanek, Design and fabrication of 3D electrostatic energy harvester. Radioeng. J. **21**(1) (2012)
16. L. Pantoli, V. Stornelli, G. Leuzzi, Low voltage high-order agile active filter for microwave applications, in *2013 European Microwave Conference* (*EuMC*) (Nuremberg, 2013), pp. 1203–1206
17. V. Stornelli, Low voltage low power fully differential buffer. J. Circuits Syst. Comput. **18**(3), 497–502 (2009)
18. L. Pantoli, V. Stornelli, G. Leuzzi, Class AB tunable active inductor. Electron. Lett. **51**(1), 65–67 (2015). doi:10.1049/el.2014.3877
19. H. Xiao, H. Shao, K. Yang, F. Yang, W. Wang, Multiple timescale energy scheduling for wireless communication with energy harvesting devices. Radioengineering **21**(3) (2012)
20. V. Stornelli, L. Pantoli, G. Leuzzi, G. Ferri, Fully differential DDA-based fifth and seventh order Bessel low pass filters and buffers for DCR radio systems. Analog Integr. Circ. Sig. Process. **75**(2), 305–310 (2013)
21. B. Merabet, L. Cirio, H. Takhedmit, F. Costa, C. Vollaire, B. Allard, O. Picon, Low-cost converter for harvesting of microwave electromagnetic energy. IEEE Energy Convers. Congr. Exp. 2592–2599 (2009)
22. G. Ferri, V. Stornelli, A. Celeste, Integrated rail-to-rail low-voltage low-power enhanced DC-gain fully differential operational transconductance amplifier. ETRI J. **29**(6), 785–793 (2007)
23. G. Ferri, V. Stornelli, A. Di Simone, A CCII-based high impedance input stage for biomedical applications. J. Circuits Syst. Comput. **20**(8), 1441–1447 (2011)

24. V. Stornelli, G. Ferri, A single current conveyor-based low voltage low power bootstrap circuit for ElectroCardioGraphy and ElectroEncephaloGraphy acquisition systems. Analog Integr. Circ. Sig. Process. **79**(1), 171–175 (2014)
25. V. Stornelli, G. Ferri, A 0.18 μm CMOS DDCCII for portable LV-LP filters. Radioengineering **22**(2), 434–439 (2013)
26. V. Stornelli, L. Pantoli, G. Leuzzi, High quality factor L-band active inductor-based band-pass filters. J. Circuits Syst. Comput. **22**(03) (2013)
27. G. Leuzzi, V. Stornelli, L. Pantoli, S. Del Re, Single transistor high linearity and wide dynamic range active inductor. Int. J. Circuit Theory Appl. **43**(3), 277–285 (2015)
28. P. Branchi, L. Pantoli, V. Stornelli, G. Leuzzi, RF and microwave high-Q floating active inductor design and implementation. Int. J. Circuit Theory Appl. **43**(8), 1095–1104 (2015)
29. A. De Marcellis, G. Ferri, N.C. Guerrini, G. Scotti, V. Stornelli, A. Trifiletti, A novel low-voltage low-power fully differential voltage and current gained CCII for floating impedance simulations. Microelectron. J. **40**(1), 20–25 (2009)
30. A. De Marcellis, C. Di Carlo, G. Ferri, V. Stornelli, A CCII-based wide frequency range square waveform generator. Int. J. Circuit Theory Appl. **41**(1), 1–13 (2013)
31. L. Pantoli, V. Stornelli, G. Leuzzi, Tunable active filters for RF and microwave applications, J. Circuits Syst. Comput. **23** (2014)
32. L. Pantoli, V. Stornelli, G. Leuzzi, A single-transistor tunable filter for Bluetooth applications, in *2012 7th European Microwave Integrated Circuits Conference* (*EuMIC*) (Amsterdam, 2012), pp. 889–892

A Low Cost Flexible Power Line Communication System

L. Pantoli[1(✉)], M. Muttillo[1], V. Stornelli[1], G. Ferri[1], and T. Gabriele[2]

[1] Department of Industrial and Information Engineering and Economics, University of L'Aquila, 67100 L'Aquila, Italy
leonardo.pantoli@univaq.it
[2] 2Bite s.r.l., via Saragat snc, 67100 L'Aquila, Italy

Abstract. The present work focuses its attention on the definition of a home automation system based on power line communication. A low cost and non invasive system has been developed and tested with successful results. It is based on the Cypress CY8CPLC10, an integrated power line communication chip which embeds both a PHY modem and a network protocol stack. The information management and data generation processes are demanded to a microcontroller, in this first prototype, being implemented with a standard Arduino board. Combining the use of a microcontroller with a power line modem makes possible to manage sensors and actuators in the neighbors through the power grid and without modifying the electrical and network systems.

Keywords: Actuators · Automation system · Microcontroller · Power line · Sensors

1 Introduction

Nowadays, electricity is the main resource for both human wellness and productivity. In this sense, home and urban automation are benefiting of great efforts from the designers with the dual aims of improving the quality of live and preserving the natural resources. Also communication systems are widely increasing themselves thanks to a variety of interests, from safety to information purposes. In this scenario, the mix of different skills and knowledge is straightforward and leads to the definition of innovative applications [1–10] and systems for human wellness [11–22]. Home automation systems are enhancing the convenience, safety, comfort, and energy efficiency of a growing number of homes around the world. Smart homes are realized by means of sensors, advanced appliances, actuators and user interfaces that communicate by means of interconnections. Usually, they are realized with dedicated, physical networks or by means of RF and wireless links. Anyway, both the solutions experiment some drawbacks that rely on the necessity to modify or expand the electrical system for wiring solutions or to occupy useful bandwidth in the local wireless network. In this scenario, the solution here presented and based on power line communications represents an adequate and feasible alternative to realize efficient and non-invasive automation systems. In particular, the proposed solution embeds different key points valuable for

B. Andò et al. (eds.), *Sensors*, Lecture Notes in Electrical Engineering 431,
DOI 10.1007/978-3-319-55077-0_52

home applications and environmental monitoring, allowing to achieve the following characteristics:

- Simplicity
- Ease of installation
- Reliability
- Robustness.

The system has been developed and tested with successful results. It is based on a microcontroller and the Cypress CY8CPLC10, an integrated power line communication chip which embeds both a PHY modem and a network protocol stack, allowing a robust communication between different nodes. Combining the use of a microcontroller with a power line modem makes possible to manage sensors and actuators in any place in the neighbors through the power grid and without modifying the electrical and network systems. In addition, the choice of the Cypress chip gives further advantages in terms of available features, since it allows a bidirectional half duplex communication, FSK modulation and errors correction codes. All these characteristics improve the overall quality of the system permitting robust communications also on old electrical systems.

2 Hardware Architecture

The architecture of the proposed power line module is showed in Fig. 1. The electrical grid is used for by-directional communications between different nodes, which in home environment can represent control units, user devices or appliances. The overall functionality is guaranteed by the use of a microcontroller combined with the communication chip. The microcontroller interprets the user requests and generates the corresponding message to transmit. The information reaches the powerline device through an I2C serial bus and the Cypress CY8CPLC10 [23] is responsible of the data

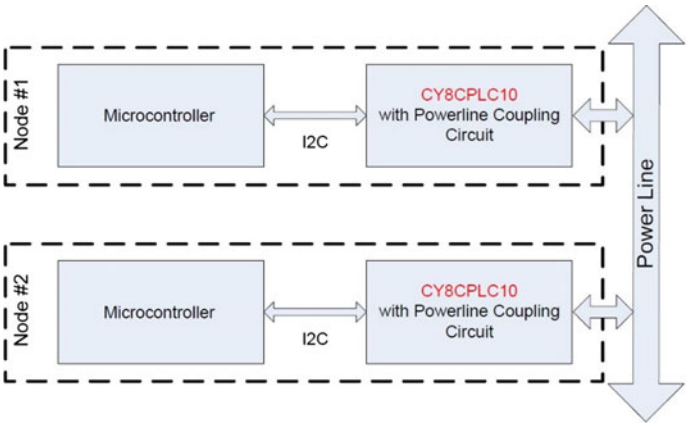

Fig. 1. Proposed communication scheme

transmission, since it embeds both a network protocol and an FSK modem. The main characteristics of the chosen device are listed below:

- PHY Modem
- 2400 bps Frequency Shift Keying modulation
- Optimized powerline network protocol
- Half-Duplex bi-directional communication
- 8-bit CRC Error Detection code
- I2C communication protocol at 50, 100 and 400 kHz
- Full compatibility with 110–240 V AC and 12–24 V AC/DC network voltages
- Fulfillment of CENELEC EN50065-1:2001 and FCC Part 15 rules.

The receiver node demodulates the network signal in the reverse way and transfers the information to the control unit in order to perform the requested action.

In this first prototype, a standard Arduino board with ATMEGA microcontroller has been used and programmed accordingly; the choice has been useful also for testing purposes, since keeping advantage of the features provided by Arduino, the system has been tested in different working modes, both as data link and as communication channel.

A typical scheme of a home automation utility is illustrated in Fig. 2. The proposed communication system shown in Fig. 1 has been completed and enhanced with a designed Bluetooth module and an actuator combined with a generic load. Thanks to the Bluetooth module, the full system can be controlled and monitored with any Bluetooth application, as for instance, the "*Arduino Bluetooth Control Developer*" freely available for Android devices. In this way, a smartphone or tablet can be enough to check and change the status of any appliance connected to a power line node.

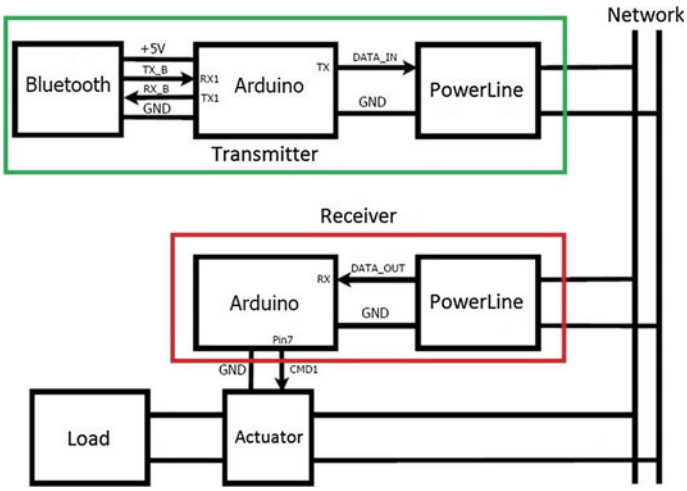

Fig. 2. Basic scheme of the communication system for home appliances

In addition, a front-end to be used between the power line chip and the electrical network is also necessary and has been designed for filtering and amplifying the generated signal, in compliance with the CENELEC and FCC standards. The transmitter filter is a pass-band network realized in the Chebyshev topology with operational amplifiers and it shows a centre frequency of 133 kHz. It has a gain of 16.5 dB with an in-band delta gain of 1.5 dB and an out-of-band attenuation that allows to obtain −20 dBc at 150 kHz and −50 dBc at second harmonic. The transmission chain ends with a further op-amp-based amplification stage that provides an additional gain of 12 dB and is designed with a push-pull output stage, useful to drive the low-impedance loads of the power line. The receiver chain instead, has an input, pass-band filter realized in the Butterworth topology, with an insertion loss of 1 dB and a 3 dB bandwidth of 60 kHz.

3 Prototype and Test

The hardware architecture described above has been implemented and tested in home environment. The TX/RX module, which embeds the selected Cypress device, the Bluetooth module and the signal conditioning circuitry, has been realized as a standalone board and a photo of the top side of the prototype is shown in Fig. 3.

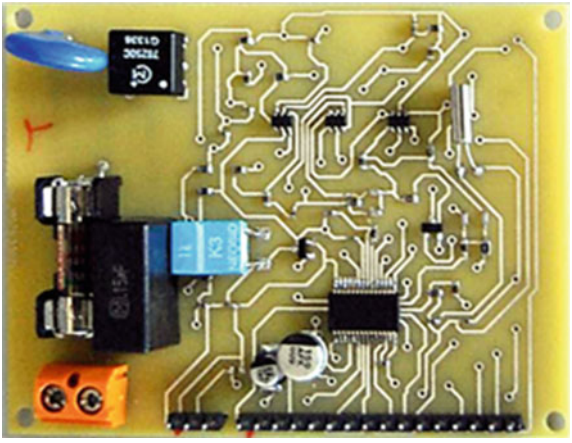

Fig. 3. Prototype of the TX/RX transmission module

The socket strip in the lower side of the pcb allows to connect the board to both the Arduino board and the electrical grid. The full connection scheme of the test system is illustrated in the next Fig. 4. Clearly, the Atmega microcontroller on the Arduino board has been programmed accordingly in order to provide the full functionality of the system. In this application, the breadboard prototyping board has been used for testing purposes to check the node features and the transmission modes. Also the actuator and a typical appliance or user device have been simulated on the breadboard with a generic load and a led diode.

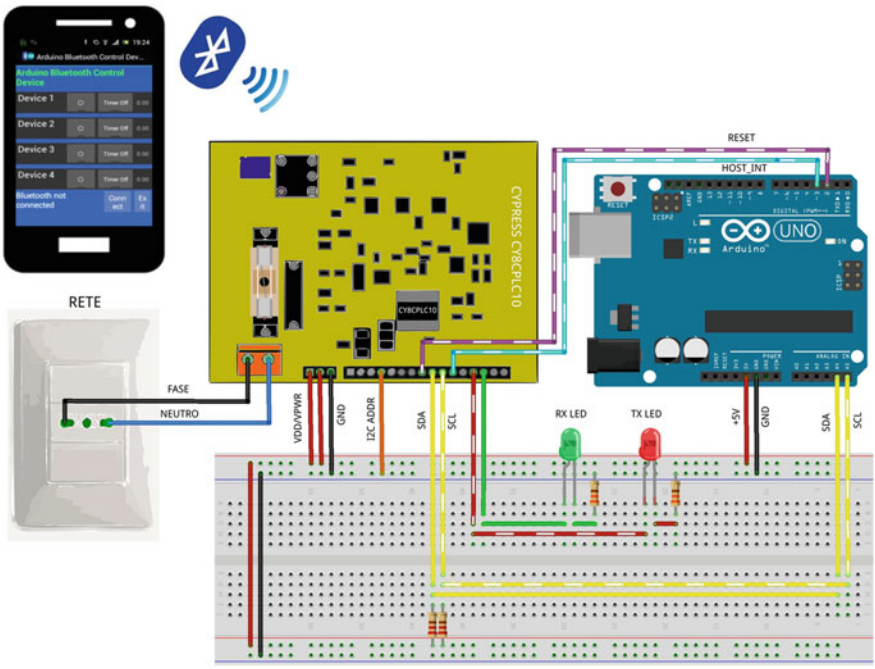

Fig. 4. Full scheme of the test system

As an example of application, in Fig. 5 is plotted a transmission signal measured with an oscilloscope. The electrical grid signal is simulated with a sinusoidal signal at the frequency of 50 Hz and a 12 V peak-to-peak amplitude. This carrier is used to

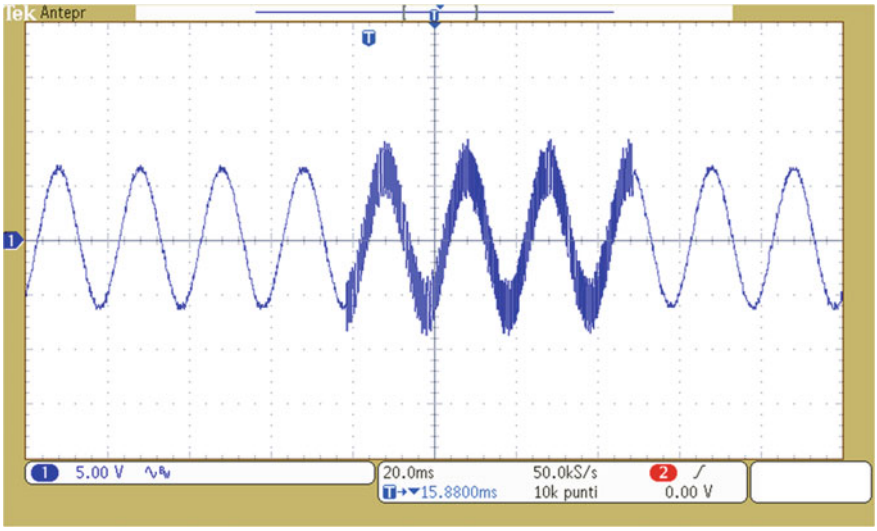

Fig. 5. Example of measured 50 Hz signal with a FSK modulated transmitted information

transport the information through an FSK modulation and the modulated signal is superimposed to it.

It is important to note that both the generation of information and data conversion of the communication signals have been demanded to the microcontroller and have required the development of dedicated algorithms and code in order to correctly interpret the used needs and aims.

A comparison of the main characteristics of the proposed solutions with respect to other literary solutions is reported in Table 1. Further benefits both in term of performance and integrability can be achieved with the introduction of advanced circuitry solutions for data manipulation and transmission both in voltage and current mode [24–38] and an improved solution is currently under design.

Table 1. Table of comparison between different literary solutions

	[1]	[2]	[3]	[4]	This work
Transmission mode	Bluetooth	ZigBee	X10	ASK modulation	FSK modulation
Communication mode	RF	RF	Powerline	Powerline	Powerline
Encryption	Yes	Yes	No	No	No
Data rate	3 Mbps	>20 kbps	20–200 bps	1200 bps	2400 bps
Ability to work as repeaters	Yes	Yes	No	No	Yes
Transmission range	~350 m	~60 m	~30 m	>10 m	~100 m (1000 m with repeaters)

4 Conclusions

The paper deals on the design of a new home automation system based on power line communication systems. The Cypress CY8CPLC10 and a microcontroller have been used to realized a low cost and non invasive solution for home environment and it has been tested with successfully results. Beyond the cost, the potentialities of the proposed solution rely on the capability to cover high transmission range and good data rate, offering a robust transmission system through the power grid also on old electrical systems and without modifying them.

References

1. R. Piyare, M. Tazil, Bluetooth based home automation system using cell phone, in *IEEE 15th International Symposium on Consumer Electronics* (Singapore, 2011), pp. 192–195
2. K. Gill, S. Yang, F. Yao, Lu Xin, A zigbee-based home automation system. IEEE Trans. Consum. Electron. **55**, 422–430 (2009)
3. K. Baraka, M. Ghobril, S. Malek, R. Kanj, A. Kayssi, Low cost Arduino/Android based energy-efficient home automation system with smart task scheduling, in *2013 Fifth*

International Conference on Computational Intelligence, Communication Systems and Networks, 2013
4. A. Al-Dweik, M. Al-Qutayri, R. Hamila, Sensor network architecture for deployment over low-voltage powerlines, in *2010 10th International Conference on Information Sciences Signal Processing and their Applications* (*ISSPA*), 2010, pp. 385–388
5. C. Withanage, R. Ashok, C. Yuen, K. Otto, A comparison of the popular home automation technologies, in *Innovative Smart Grid Technologies—Asia* (*ISGT Asia*), *2014*. IEEE, 20–23 May 2014 pp. 600,605
6. V. Harshad, K. Vamsi, Power line communication based home automation and electricity distribution system, in *IEEE International Symposium on Power Line Communications and Its Applications.* Italy, 2011, pp. 1–6
7. G. Bal, N. Daldal, Design and implamentation of microcontroller based temperature measurement and control system using power line communication, in *4rd IEEE International Conference on Power Engineering, Energy and Electrical Drivers*, 2013, pp. 740–741
8. S.H. Ju, Y.H. Lim, M.S. Choi, J.-M. Baek, S.-Y. Lee, An efficient home energy management system based on automatic meter reading, in *IEEE International Symposium on Power Line Communication and Its Applications.* April 2011, pp. 479–484
9. U. Braun, Bridging the gap with Broadband Powerline (BPL) technology, in *2011 2nd IEEE PES International Conference and Exhibition on Innovative Smart Grid Technologies* (*ISGT Europe*). 5–7 Dec 2011, pp. 1–7
10. A. Sanz, P.J. Piñero, S. Miguel, J.I. Garcia, Real problems solving in PRIME networks by means of simulation, in *2013 IEEE 17th International Symposium on Power Line Communications and Its Applications Real*, 2013, pp. 285–290
11. P. An, X. Chen, J. Wang, S. Zhou, X. Shan, Analysis on application of repeater technology in powerline communications networks, in Proceedings of the IEEE International Symposium on Power Line Communications and its Applications. Pisa, Italy. Mar 2007, pp. 273–277
12. C. Jin, T. Kunz, Smart home networking: combining wireless and powerline networking, in *2011 7th International Wireless Communications and Mobile Computing Conference* (*IWCMC*). 4–8 July 2011, pp. 1276–1281
13. W. Gouret, F. Nouvel, G. El-Zein, Powerline communication on automotive network, in *Proceedings of the IEEE 65th VTC-Spring.* Apr 2007, pp. 2545–2549
14. A. Depari, P. Ferrari, A. Flammini, S. Rinaldi, E. Sisinni, A. Vezzoli, On the use of prime powerline communication in industrial applications: modbus a first testcase, in *2013 IEEE International Instrumentation and Measurement Technology Conference* (*I2MTC*). May 2013, pp. 587–592
15. S.C. Pereira, A.S. Caporali, I.R.S. Casella, Power line communication technology in industrial networks, in *2015 International Symposium on Power Line Communications and Its Applications* (*ISPLC*). 29 Mar 2015–1 Apr 2015, pp. 216–221
16. G. Dozio, A. Rivero, A. Bernaschina, D. Rivola, V. Medici, G. Montù, HAC: hardware design for a smart-home and smart-grid decentralised load management system, in *2015 IEEE 24th International Symposium on Industrial Electronics* (*ISIE*), 3–5 June 2015, pp. 699-704
17. Y.-J. Lin, H. Latchman, L. Minkyu, S. Katar, A power line communication network infrastructure for the smart home, in *IEEE Wireless Communications*, vol. 9. IEEE, Dec 2002, pp. 104–111
18. G. Mathisen, A.M. Tonello, WIRENET: an experimental system for in-house powerline communication, in Proceedings of the IEEE International Symposium on Power Line Communications and its Applications (ISPLC). Mar 2006, pp. 137–142

19. I. Berganza, A. Sendin, J. Arriola, Prime: powerline intelligent metering evolution, in *SmartGrids for Distribution*, *2008*. *IET-CIRED*, 2008, pp. 1–3
20. M.C. Bali, C. Rebai, S-FSK modem design and experimental validation for robust narrowband powerline communication, in *2014 IEEE International Instrumentation and Measurement Technology Conference* (*I2MTC*) *Proceedings*, 12–15 May 2014, pp. 1251–1255
21. M.K. Varma, Z.A. Jaffery, Ibraheem, Advances of broadband power line communication and its application, in *2015 Annual IEEE India Conference* (*INDICON*). 17–20 Dec 2015, pp. 1–6
22. A. Ricci, E. Smargiassi, D. Mancini, I. De Munari, V. Aisa, P. Ciampolini, Wr@p: a "last-meter" technology for energy-aware networked appliances, in *2011 IEEE International Symposium on Power Line Communications and Its Applications* (*ISPLC*), 3–6 Apr 2011, pp. 193–198
23. CY8CPLC10 Datasheet, Cypress Semiconductor Corporation, Aug 2015
24. P. Branchi, L. Pantoli, V. Stornelli, G. Leuzzi, RF and microwave high-Q floating active inductor design and implementation. Int. J. Circuit Theory Appl. **43**(8), 1095–1104 (2015)
25. L. Pantoli, V. Stornelli, G. Leuzzi, Class AB tunable active inductor. Electron. Lett. **51**(1), 65–67 (2015)
26. L. Pantoli, V. Stornelli, G. Leuzzi, Tunable active filters for RF and microwave applications. J. Circuits Syst. Comput. **23**, 1450088 (2014)
27. L. Pantoli, V. Stornelli, G. Leuzzi, Low voltage high-order agile active filter for microwave applications, in *2013 European Microwave Conference* (*EuMC*) (Nuremberg, 2013), pp. 1203–1206
28. V. Stornelli, L. Pantoli, G. Leuzzi, G. Ferri, Fully differential DDA based fifth and seventh order Bessel low pass filters and buffers for DCR radio systems. Analog Integr. Circ. Sig. Process. **75**(2), 305–310 (2013)
29. L. Pantoli, V. Stornelli, G. Leuzzi, A single-transistor tunable filter for Bluetooth applications, in *2012 7th European Microwave Integrated Circuits Conference* (*EuMIC*). Amsterdam, 2012, pp. 889–892
30. L. Pantoli, V. Stornelli, G. Leuzzi, Low-noise tunable filter design by means of active components. Electron. Lett. **52**(1), 86–88 (2016)
31. G. Leuzzi, V. Stornelli, L. Pantoli, S. Del Re, Single transistor high linearity and wide dynamic range active inductor. Int. J. Circuit Theory Appl. **43**(3), 277–285 (2015)
32. V. Stornelli, L. Pantoli, G. Leuzzi, High quality factor L-band active inductor-based band-pass filters. J. Circuits Syst. Comput. **22**(03), 1350014 (2013)
33. G. Ferri, V. Stornelli, A. Celeste, Integrated rail-to-rail low-voltage low-power enhanced DC-gain fully differential operational transconductance amplifier. ETRI J. **29**(6), 785–792 (2007)
34. V. Stornelli, Low voltage low power fully differential buffer. J. Circuits Syst. Comput. **18**(3), 497–502 (2009)
35. G. Ferri, V. Stornelli, A. di Simone, A CCII-based high impedance input stage for biomedical applications. J. Circuits Syst. Comput. **20**(8), 1441–1447 (2011)
36. V. Stornelli, G. Ferri, A 0.18 μm CMOS DDCCII for portable LV-LP filters. Radioengineering **22**(2), 434–439 (2013)
37. A. De Marcellis, G. Ferri, N.C. Guerrini, G. Scotti, V. Stornelli, A. Trifiletti, A novel low-voltage low-power fully differential voltage and current gained CCII for floating impedance simulations. Microelectron. J. **40**(1), 20–25 (2009)
38. A. De Marcellis, C. Di Carlo, G. Ferri, V. Stornelli, A CCII-based wide frequency range square waveform generator. Int. J. Circuit Theory Appl. **41**(1), 1–13 (2013)

MEMS-Based Transducers (CMUT) and Integrated Electronics for Medical Ultrasound Imaging

Alessandro S. Savoia(✉) and Giosuè Caliano

Dipartimento di Ingegneria, Università degli Studi Roma Tre, via della Vasca Navale 84, 00146 Rome, Italy
alessandro.savoia@uniroma3.it

Abstract. Capacitive Micromachined Ultrasonic Transducers (CMUTs) are MEMS transducers fabricated on silicon that have reached technological maturity, representing today a valid alternative to piezoelectric transducers in medical ultrasound imaging applications, offering larger bandwidth and better thermal efficiency. The growing interest for this new technology is based in the increased compatibility with 3D electronics integration methods that allow integrating, on the same chip, the transducers and the electronics, thereby enabling the realization of high-performance and low-cost devices. This paper summarizes the research activity carried out at the Acoustoelectronics Laboratory (ACULAB) of Roma Tre University on the integration of CMUTs and analog front-end electronics in ultrasound medical imaging probes for volumetric imaging applications.

Keywords: MEMS · Micromachined ultrasonic transducer · CMUT · 3D-integration · Analog front-end · ASIC · Ultrasound imaging · Sparse array

1 Introduction

Micromachined ultrasonic transducers (MUTs) [1] are emerging as a valid alternative for next generation ultrasound imaging systems. MEMS technology employed for MUT microfabrication provides higher flexibility in the design and improved reproducibility as compared to conventional piezoelectric ultrasonic transducer technology. These characteristics, together with an easier integration with front-end electronic circuits, make MUTs attractive for the realization of advanced imaging systems such as volumetric real-time ultrasound scanners.

The Acoustoelectronics Laboratory (ACULAB, Roma Tre University, Italy) research is focused on capacitive micromachined ultrasonic transducers (CMUTs) and includes design, modeling, microfabrication, interconnection and packaging materials, characterization, electronics and system integration [2–4]. Significant results have been obtained in the development of CMUT probes for medical ultrasound imaging and biometric applications [5–9]. In the last years, ACULAB's research was devoted to advanced ultrasound imaging applications [10], and particular effort has been dedicated to the integration of CMUTs and front-end electronics. A fully-integrated, low-power analog front-end circuit, consisting in a high-voltage unipolar pulser and a low-power

B. Andò et al. (eds.), *Sensors*, Lecture Notes in Electrical Engineering 431,
DOI 10.1007/978-3-319-55077-0_53

transimpedance low-noise amplifier, was specifically designed for 1D CMUT arrays operating in the 1–15 MHz range [11, 12] covering a wide range of imaging applications. Further, a novel method for the compensation of CMUT harmonic distortion was proposed and implemented in a 200 V unipolar pulser integrated circuit [13] demonstrating a reduction of the second-harmonic distortion of more than 30 dB, meeting typical requirements of nonlinear medical imaging applications. Current research at ACULAB is devoted to the development of a 256-element 2D CMUT probe based on a Fermat's spiral sparse array configuration [14]. The new CMUT probe head is achieved by hybrid 3D-integration of a CMUT spiral array and a 256-channel analog front-end ASIC, based on the previously developed pulser and receive topologies. This paper summarizes the activities carried out on these research topics, the ongoing developments, and the expected results.

2 Analog Front-End Integrated Electronics

In [11, 12], we reported on the development of a fully-integrated, low-power analog front-end circuit, which consisted in a high-voltage unipolar pulser and a low-noise charge amplifier, specifically designed for 1D CMUT arrays operating in the 1–15 MHz range. The proposed circuit comprised a high-voltage unipolar driver, a transmit/receive (T/R) switch, and an ultra-low-noise charge amplifier (LNA), which were conveniently co-designed in order to minimize the power consumption and the parasitic capacitance. The high-voltage drivers allowed us to generate unipolar pulses up to 100 V amplitude. The T/R switch was carefully designed to achieve protection of the LNA input during transmission while keeping the parasitic resistance low during reception. The LNA is based on a transimpedance topology using a capacitive feedback, providing large bandwidth and improved noise-power performance as compared to resistive feedback topologies. ASIC prototypes, based on the circuit schematic shown in Fig. 1, were designed in collaboration with the Analog Integrated Circuits Laboratory (Department of Electrical, Computer and Biomedical Engineering, University of Pavia, Italy), and fabricated using a BCD-SOI technology available at STMicroelectronics (Cornaredo, Italy). Experimental characterization was carried out in conjunction with a 10 MHz CMUT linear array, previously developed for medical imaging applications [8].

In order to reduce the effects of the electrostatic nonlinearity on the CMUT transmission operation, we proposed [13] a linearization method aimed at pre-compensating the second harmonic distortion using unipolar excitation pulses. The method consists in applying signal predistortion by acting on the amplitude, duty cycle, and slope of the rising and falling edges, of the trapezoidal excitation pulses. We determined the pulse-shaping parameters using an open-loop charge control algorithm that uses electrical impedance data, estimated at several bias voltages, to identify the CMUT non-linear behavior. A 0–200 V unipolar pulser circuit, based on the topology shown in Fig. 2, consisting in a digitally-controlled current generator yielding trapezoidal pulse-shaping capability when connected to a capacitive load, was designed in collaboration with the Analog Integrated Circuits Laboratory (Department of Electrical, Computer and Biomedical Engineering, University of Pavia, Italy), and fabricated

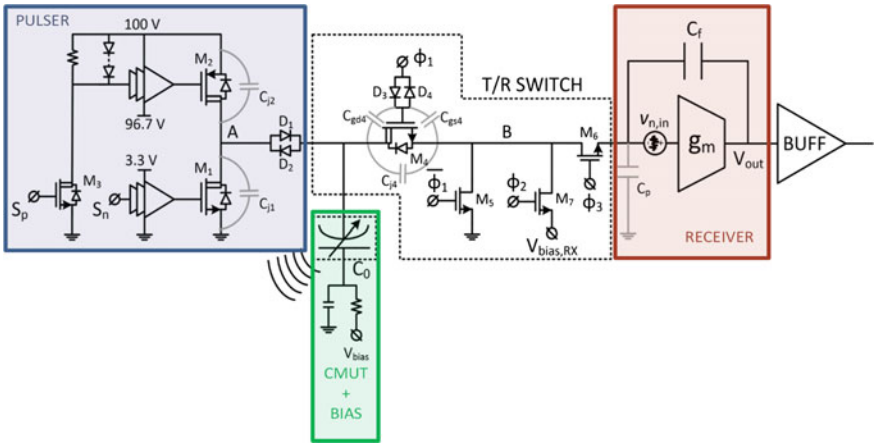

Fig. 1. Simplified schematic of the CMUT transciever

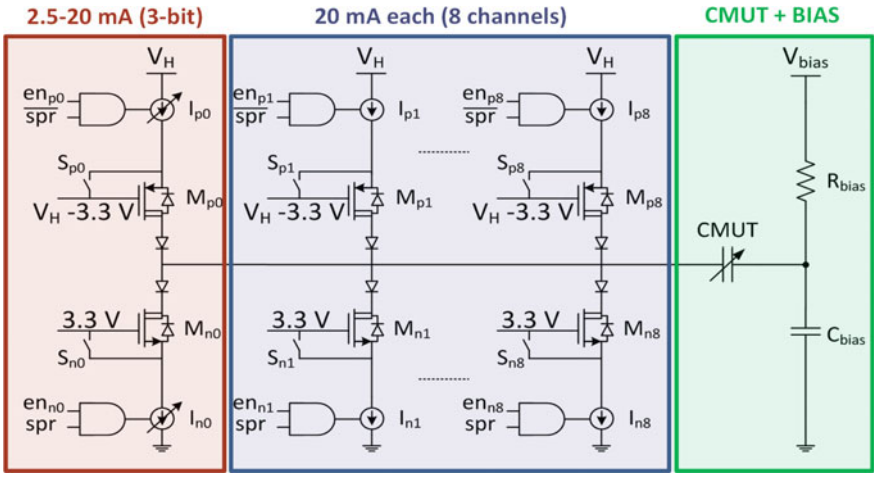

Fig. 2. Simplified schematic of the high-voltage unipolar pulser. The output of the pulser is connected to the CMUT array element electrode while the DC bias is fed through an external high-voltage generator using an off-chip R-C network

using a BCD-SOI technology available at STMicroelectronics. The pulser was tested with a 10 MHz CMUT linear array developed for medical imaging applications [8].

First transmit pressure measurements were performed proving a second-harmonic reduction of more than 20 dB, resulting in a harmonic-to-fundamental ratio (HFR) below −30 dB, which makes the use of such configuration suitable for typical nonlinear imaging operation. We here report additional experimental results achieved by optimizing the CMUT nonlinear parameter extraction. We measured the acoustic pressure signal at 4.6 mm from the transducer surface, by exciting the CMUT with a 10 MHz, 20-cycle, 100 V trapezoidal pulse train. The excitation signal was generated by programming the pulser using the parameters achieved with the predistortion

algorithm, fed with a set of electrical impedance measurements performed on the CMUT at different bias voltages in the 140–240 V range. Figure 3 shows the measured hydrophone signal. The negative peak pressure amplitude is 400 kPa, while the HFR is approximately −45 dB. The measured performance is fully compatible with nonlinear ultrasound imaging applications.

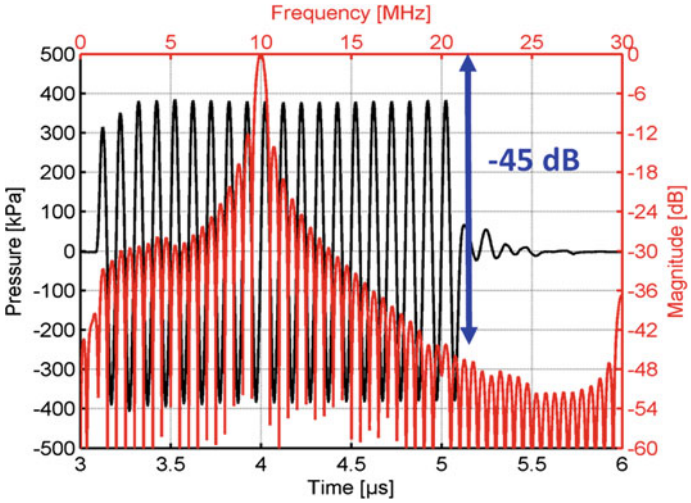

Fig. 3. Hydrophone pressure signal measured at 4.6 mm from the transducer surface, obtained by exciting the CMUT with a 10 MHz, 20-cycle, 100 V trapezoidal pulse train

An updated version of the CMUT transceiver, characterized by the same topology presented in [11, 12], but provided with the transmission driver proposed in [13], is currently under implementation on a 256-element ASIC with transmit beamforming capability. This ASIC is part of the 3D-integrated hybrid multi-chip-module (MCM), described in the following section, based on a sparse 2D CMUT array configuration.

3 CMUT Array Design, Microfabrication and Packaging of the 3D-Integrated Module

In order to reduce the complexity related to the high element and channel count typically required by volumetric imaging applications, we investigated [14], in collaboration with the Microelectronic System Design Laboratory (MSDLab, Information Engineering Department, University of Florence, Italy), the possibility of designing the layout of large circular arrays with limited number of elements according to particular sparse spatial distributions. We proposed to use the Fermat's spiral pattern with spatial density modulation. This deterministic, aperiodic, and balanced positioning procedure aims at guaranteeing uniform performance over a wide range of steering angles. We showed that this approach allows increasing the probe sensitivity while simplifying the design of the transmit section, which does not involve element dependent amplitude

control. We compared the performance of several 256-element sparse array configurations, testing different spatial density modulation functions, and found that a good trade-off is achieved by a 60λ spiral array with 1.0λ elements and Blackman density tapering window. With this configuration, the grating lobe level is −16 dB, the lateral resolution is lower than 6.0λ, the depth of field is 120λ and, the average contrast is 10.3 dB, while the sensitivity remains in a 5 dB range for a wide selection of steering angles. Compared with a dense array configuration yielding the equivalent performance in terms of acoustic beam characteristics, the number of elements is reduced by a 8.3 factor (i.e. 256 vs. 2136).

A physical implementation of this spiral array configuration is currently under development using the CMUT Reverse Fabrication Process (RFP) [3]. The array was dimensioned considering an operation frequency of 7.5 MHz. The single element size is 200 μm (1.0λ), whilst the array size is 10 mm (50λ). A Blackman window was used as a density tapering function. Figure 4 shows the physical layout of the spiral array under development, consisting of 256 elements each composed of 12 CMUT circular cells arranged in a hexagonal tiling and electrically connected in parallel.

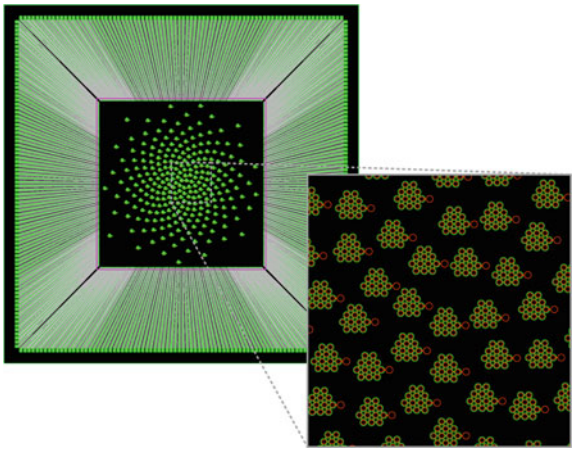

Fig. 4. Physical layout of the spiral array CMUT implementation

We have established a 3D-integration process whose goal is to bond two dice, containing respectively a MEMS (CMUT) array and an ASIC (multichannel AFE). The shape of the two dice is square being their size different. In particular, the smaller ASIC die, containing the 256-channel AFE circuits and the transmit beamforming digital logic, is connected to the MEMS die using flip-chip bonding, while the larger MEMS die, containing the 256-element CMUT spiral array, is used also to connect the final hybrid MCM to the external circuits using wire bonding. We follow a die-to-die (ASIC die on MEMS) bonding approach using Cu-pillar + SnAg solder bumping on the ASIC, and pre-applied epoxy-based underfill on the MEMS, being this procedure compatible with wafer-level packaging, which is our future objective. With reference to

Fig. 5, the MEMS die (a) contains the 2D CMUT array in the central part. Each CMUT array element, depicted as a red circle, is accessible through a circular pad, shown as a blue circle. A further set of circular pads, of the same shape and size of the element pads, are linearly disposed along a square perimeter surrounding the CMUT array area. The pads laying on the square perimeter are individually routed to larger pads, shown as green rectangles, laying close to the edges of the MEMS die. Figure 5b shows the ASIC die in which a number of circular pads, shown in blue, is arranged in order to symmetrically match the positions of all of the circular pads on the MEMS die (a). The two dice are aligned and electrically bonded, through solder-reflow-based interconnection, and mechanically attached, through epoxy adhesion. The described 3D-integration process in currently under development.

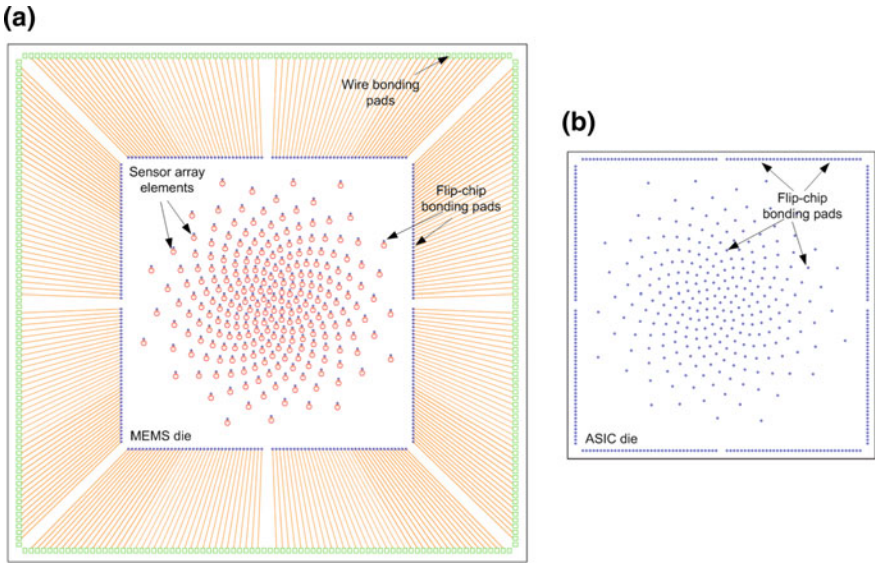

Fig. 5. Shape and layout of the features of the **a** MEMS die and of the **b** ASIC die

The obtained hybrid module is then processed following the CMUT RFP [3]. With reference to Fig. 6, the MCM is aligned and wire bonded to a rigid-flex PCB using a 50 µm-diameter Al wire (Fig. 6a). A thermally conductive heat sink is then coupled to the exposed side of the ASIC die, and an epoxy resin is applied in order to encapsulate the wire bonds and to mechanically support both the thin portion of the hybrid module, i.e. the routing part of the MEMS die, and the PCB (Fig. 6b). The assembly is then housed in a container with an opening used to access the exposed side of the MEMS die. Then, the entire silicon substrate is wet-etched in order to release the sensor array (Fig. 6c). Finally, the entire device is encapsulated with a special polymeric elastomer acting both as a protection, and as an insulating and an acoustical matching layer. As a result, we obtain a compact-size probe head, connectable to in-probe PCBs by means of commercial board-to-board connectors.

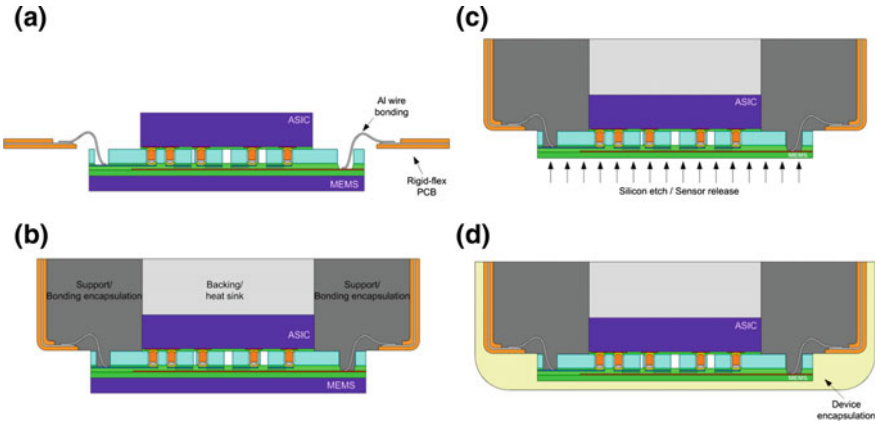

Fig. 6. Description of the assembly process-flow performed on the hybrid module

Figure 7a shows a 3D mechanical representation of the spiral probe head resulting from the described packaging process. We tested this process on a squared-shape dice, with similar dimensions, containing a recently fabricated dual-linear (crisscross) array [15]. Figure 7b shows a picture of a completed probe head.

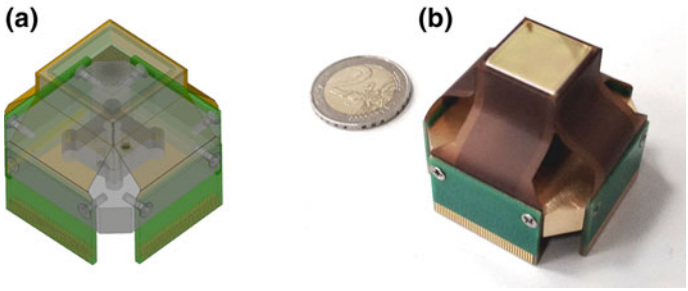

Fig. 7. **a** 3D mechanical model of the spiral probe head. **b** Photo of a dual-linear (crisscross) array microfabricated and packed using CMUT RFP

Finally, we show in Fig. 8 a 3D mechanical model of the interior of the probe under development, where the probe head is connected to four PCBs containing auxiliary electronics and the connectors used to interface the module to the ultrasound scanner by means of a multi-coaxial cable.

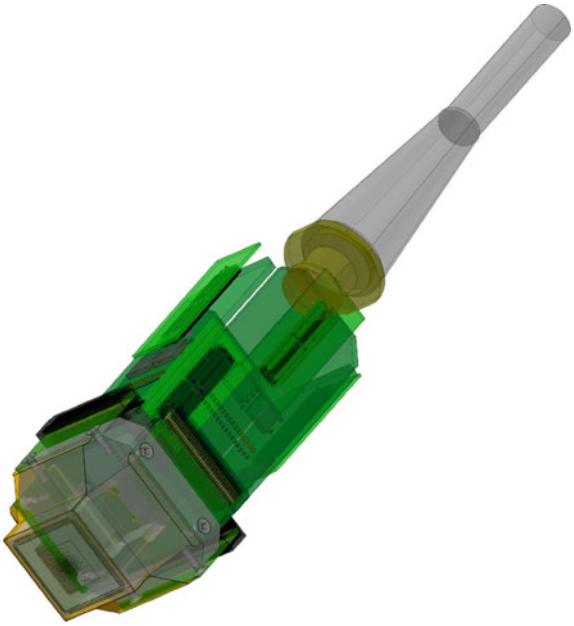

Fig. 8. 3D mechanical model of the interior of the 256-element CMUT spiral probe

4 Conclusions

This paper presented the research activity recently carried out by ACULAB on the integration of CMUTs with analog front-end electronics. A new CMUT probe is under development. The probe head contains a multi-chip-module achieved by hybrid 3D-integration of a CMUT spiral array and a 256-channel analog front-end ASIC.

This work is funded by the national government and the European Union through the ENIAC JU project DeNeCoR under grant agreement number 324257, and by the Italian Ministry of Education, University and Research (PRIN 2010–2011).

References

1. M. Pappalardo, G. Caliano, A.S. Savoia, A. Caronti, Micromachined ultrasonic transducers, in *Piezoelectric and Acoustic Materials for Transducer Applications*, 2008, pp. 453–478
2. A. Caronti, G. Caliano, R. Carotenuto, A. Savoia, M. Pappalardo, E. Cianci, V. Foglietti, Capacitive micromachined ultrasonic transducer (CMUT) arrays for medical imaging. Microelectron. J. **37**, 770–777 (2006)
3. A. Bagolini, A.S. Savoia, A. Picciotto, M. Boscardin, P. Bellutti, N. Lamberti, G. Caliano, PECVD low stress silicon nitride analysis and optimization for the fabrication of CMUT devices. J. Micromech. Microeng. **25** (2015)
4. A. Caronti, A. Coppa, A. Savoia, C. Longo, P. Gatta, B. Mauti, A. Corbo, B. Calabrese, G. Bollino, A. Paz, G. Caliano, M. Pappalardo, Curvilinear capacitive micromachined

ultrasonic transducer (CMUT) array fabricated using a reverse process, in *Proceedings of the IEEE Ultrason. Symposium,* 2008, pp. 2092–2095
5. A. Iula, A. Savoia, G. Caliano, Capacitive micro-fabricated ultrasonic transducers for biometric applications. Microelectron. Eng. **88**, 2278–2280 (2011)
6. A. Savoia, G. Caliano, A. Iula, C. Longo, A. Caronti, R. Carotenuto, M. Pappalardo, Design and fabrication of a cMUT probe for ultrasound imaging of fingerprints, in *Proceedings of the IEEE Ultrason. Symposium*, 2010, pp. 1877–1880
7. A. Savoia, G. Caliano, R. Carotenuto, C. Longo, P. Gatta, A. Caronti, E. Cianci, V. Foglietti, M. Pappalardo, Enhanced echographic images obtained improving the membrane structural layer of the cMUT probe, in *Proceedings of the IEEE Ultrason. Symposium*, 2005, pp. 1960–1963
8. A. Savoia, G. Caliano, B. Mauti, M. Pappalardo, Performance optimization of a high frequency CMUT probe for medical imaging, in *Proceedings of the IEEE Ultrason. Symposium*, 2011, pp. 600–603
9. A.S. Savoia, G. Caliano, M. Pappalardo, A CMUT probe for medical ultrasonography: from microfabrication to system integration. IEEE Trans. Ultrason. Ferroelectr. Freq. Control **59**, 1127–1138 (2012)
10. G. Matrone, A. Savoia, M. Terenzi, G. Caliano, F. Quaglia, G. Magenes, A volumetric CMUT-based ultrasound imaging system simulator with integrated reception and μ-beamforming electronics models. IEEE Trans. Ultrason. Ferroelectr. Freq. Control **61**, 792–804 (2014)
11. M. Sautto, D. Leone, A. Savoia, D. Ghisu, F. Quaglia, G. Caliano, A. Mazzanti, A CMUT transceiver front-end with 100-V TX driver and 1-mW low-noise capacitive feedback RX amplifier in BCD-SOI technology, in *European Solid-State Circuits Conference*, 2014, pp. 407–410
12. A.S. Savoia, G. Caliano, A. Mazzanti, M. Sautto, A.D. Leone, D.U. Ghisu, F. Quaglia, An ultra-low-power fully integrated ultrasound imaging CMUT transceiver featuring a high-voltage unipolar pulser and a low-noise charge amplifier, in *Proceedings of the IEEE Ultrason. Symposium*, 2014, pp. 2568–2571
13. A.S. Savoia, G. Scaglione, G. Caliano, A. Mazzanti, M. Sautto, F. Quaglia, Second-harmonic reduction in CMUTs using unipolar pulsers, in *Proceedings of the IEEE Ultrason. Symposium, IUS 2015*, 2015
14. A. Ramalli, E. Boni, A.S. Savoia, P. Tortoli, Density-tapered spiral arrays for ultrasound 3-D imaging. IEEE Trans. Ultrason. Ferroelectr. Freq. Control **62**, 1580–1588 (2015)
15. A. Savoia, V. Bavaro, G. Caliano, A. Caronti, R. Carotenuto, P. Gatta, C. Longo, M. Pappalardo, Crisscross 2D cMUT array: beamforming strategy and synthetic 3D imaging results, in *Proceedings of the IEEE Ultrason. Symposium*, 2007, pp. 1514–1517